Donor-acceptor functionalized coordination cages for photoinduced charge separation

This dissertation is submitted for the degree of

“Doctor rerum naturalium”

TU Dortmund

Department of Chemistry and Chemical Biology

Laura Neukirch

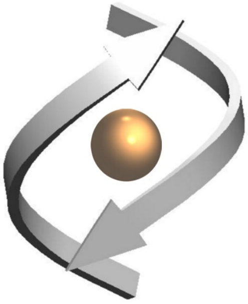

technische universität
dortmund

RESOLV
RUHR EXPLORES SOLVATION
CLUSTER OF EXCELLENCE - EXC 2033

The work presented in this dissertation has been carried out between June 2021 and May 2025 in the Department of Chemistry and Chemical Biology at TU Dortmund.

Principal advisor:	Prof. Dr. Guido H. Clever Department of Chemistry and Chemical Biology TU Dortmund
Coexaminer:	Prof. Dr. Andreas Steffen Department of Chemistry and Chemical Biology TU Dortmund
Submission:	May 2025

Abstract

Natural systems master intricate tasks with high efficiency and selectivity. Key to this are large biomolecules whose three-dimensional architectures are assembled via dynamic interactions. The latter enable efficient formation of the structure as well as structural reorganization, for example under altered conditions. Enticed by this, supramolecular chemists design large molecules of increasing complexity and functionality by exploiting dynamic bonds which spare the need for multi-step organic synthesis. A subfield utilizes the kinetically labile coordination bond between Pd(II) metal nodes and bis-pyridyl organic ligands L. The resulting assemblies Pd_nL_{2n} are called cages when they possess a cavity and can serve as hosts for binding, stabilizing, or converting guest molecules. Moreover, they are utilized as scaffolds for arranging different functionalities, implemented in the organic ligands, in space. For all potential applications it is of pivotal importance to control the self-assembly outcome since structure and function are closely connected.

The first part of the thesis focuses on gaining control over the nuclearity of coordination rings Pd_nL_{2n}. In order to establish relationships between the ligand geometry and the self-assembly outcome, stiff organic ligands were employed. A ligand with a binding angle of 84° proved to be suitable for the self-assembly into a homoleptic five-membered ring Pd_5L_{10} across various conditions. Noteworthy, it is the first of its kind that does not require a template for its formation. The crystal structures of two five-membered rings, based on ligands with ideal and non-ideal geometries, were obtained and their comparison underscores the crucial role of the ligand bent angle. These results are furthermore supported by DFT computations. Based on geometrical considerations, theoretical models were derived that correlate the ligand bent angle with the ring nuclearity.

Moreover, cages were used as a modular platform for studying the dependency of the rate constant of electron transfer between organic donor and acceptor ligands on the thermodynamic driving force of the process. For this, a library of nine donor-acceptor cages, based on three different donor (D) and three different acceptor (A) ligands, was synthesized. Importantly, the so-called shape complementarity strategy was applied which allowed for the selective self-assembly into *cis*-$Pd_2D_2A_2$ cages. Hence, donor and acceptor moieties are positioned in defined distances and orientations. After thorough structural characterization of the cages, their ground state photophysical and electrochemical properties were investigated. Owing to the different half-wave potentials and excited state energies of the ligands, the thermodynamic driving forces for the electron transfer processes vary by up to 1.2 eV. The excited state dynamics were studied with pump-probe transient absorption spectroscopy. Across the cages, the largest part of the ligand-to-ligand charge separated state decays with a time constant of around 100 ps. Excitingly, correlation of the thermodynamic and kinetic data for this dominating charge recombination process showed that an increase in exergonicity is accompanied by a decrease of the electron transfer rate constant, indicating that the process lies in the Marcus inverted region. These results will allow for the targeted design of donor-acceptor cages with long-lived charge separated states in the future, for example for applications in photoredox catalysis.

Lastly, studies towards photoredox active soft materials based on coordination cages were undertaken. Functionalization of the donor ligand of one of the *cis*-$Pd_2D_2A_2$ cages with nonpolar alkyl chains endowed the cage with amphiphilicity. Preliminary results indicate that the cage assembles into agglomerates with a diameter of around 100 nm in the tested polar organic solvents. Furthermore, first steps towards the incorporation of the amphiphilic donor-acceptor cages into aqueous micellar solutions based on amphiphilic block copolymers were carried out.

Such systems offer two differentiable environments, that are the nonpolar micellar core and the bulk water phase. Selective enrichment of these two environments with suitable redox active compounds might allow for vectorial electron transfer across the micellar interface in the future.

Overall, the work presented in this thesis expands the toolbox of design approaches for Pd_nL_{2n} assemblies with a particular structure and function.

Zusammenfassung

Komplexe Prozesse laufen in natürlichen Systemen mit hoher Effizienz und Selektivität ab. Grundlage hierfür sind große Biomoleküle, dessen dreidimensionale Architektur auf Basis von dynamischen Interaktionen assembliert. Neben einer effizienten Strukturbildung ermöglichen diese Interaktionen strukturelle Reorganisationen, zum Beispiel unter veränderten Umgebungsbedingungen. Dies inspiriert supramolekulare Chemiker, große Moleküle mit zunehmender Komplexität und Funktionalität darzustellen. Hierbei werden ebenfalls dynamische Bindungen genutzt, wodurch die mehrschrittige organische Synthese vermieden werden kann. Ein Teilgebiet der supramolekularen Chemie nutzt die kinetisch labile koordinative Bindung zwischen Pd(II) Metallzentren und Bis-Pyridin-Liganden L. Die gebildeten Assemblierungen Pd_nL_{2n} werden als Käfige bezeichnet, wenn sie eine Kavität besitzen und werden als Wirte für die Bindung, Stabilisierung und Umwandlung von Gästen untersucht. Außerdem werden sie als Gerüste zur räumlichen Anordnung von Funktionalitäten, welche durch die organischen Liganden eingebracht werden, genutzt. Weil Struktur und Funktion eng miteinander verbunden sind, ist es für alle potenziellen Anwendungen von zentraler Bedeutung, das Ergebnis der Selbstassemblierung kontrollieren zu können.

Der erste Teil dieser Arbeit konzentriert sich darauf, Kontrolle über die Nuklearität von Koordinationsringen Pd_nL_{2n} zu gewinnen. Mit dem Ziel, eine Beziehung zwischen der Ligandengeometrie und dem Ergebnis der Selbstassemblierung aufzustellen, wurden rigide organische Liganden eingesetzt. Ein Ligand mit einem Bindungswinkel von 84° hat sich als geeignet für die Selbstassemblierung zu einem homoleptischen fünf-gliedrigen Ring Pd_5L_{10} erwiesen. Erwähnenswert ist, dass dies der erste seiner Art ist, welcher kein Templat für seine selektive Bildung benötigt. Es wurden die Kristallstrukturen von zwei fünf-gliedrigen Ringen erhalten, welche auf Liganden mit idealen und nicht-idealen Geometrien basieren. Ihr Vergleich unterstreicht die entscheidende Rolle des Bindungswinkels des Liganden. Dieses Ergebnis wird durch DFT Berechnungen gestützt. Basierend auf geometrischen Überlegungen wurden theoretische Modelle hergeleitet, welche den Bindungswinkel des Liganden mit der Nuklearität des Rings korrelieren.

Des Weiteren wurden Käfige als modulare Plattform genutzt, um die Geschwindigkeitskonstante des Elektronentransfers zwischen organischen Donor- und Akzeptorliganden in Abhängigkeit der thermodynamischen Triebkraft dieses Prozesses zu untersuchen. Hierfür wurden neun Donor-Akzeptorkäfige basierend auf drei Donor- (D) und drei Akzeptorliganden (A) synthetisiert. Die selektive Selbstassemblierung zu *cis*-$Pd_2D_2A_2$ Käfigen wurde durch die Anwendung des sogenannten Formkomplementaritätsprinzips gewährleistet. Donor- und Akzeptoreinheiten befinden sich im Käfig folglich in einem definierten Abstand und einer definierten Orientierung zueinander. Nach einer gründlichen Charakterisierung der Struktur der Käfige wurden ihre photophysikalischen Eigenschaften im elektronischen Grundzustand sowie ihre elektrochemischen Eigenschaften untersucht. Aufgrund der unterschiedlichen Halbstufenpotentiale und Energien der elektronisch angeregten Zustände der Liganden variieren die thermodynamischen Triebkräfte für die Elektronentransferprozesse um bis zu 1.2 eV. Die lichtinduzierten Prozesse wurden mit Pump-Probe transienter Absorptionsspektroskopie untersucht. Allgemein wurde beobachtet, dass der Großteil der Ligand-zu-Ligand ladungsseparierten Zustände mit einer Zeitkonstante von ungefähr 100 ps rekombiniert. Spannenderweise korrelieren die thermodynamischen und kinetischen Daten dieses Rekombinationsprozesses in der Hinsicht, dass mit zunehmender Exergonizität die Geschwindigkeitskonstante sinkt. Dies deutet darauf hin, dass der Prozess in der Marcus-invertierten Region liegt. Basierend auf diesen Ergebnissen können in der Zukunft gezielt Donor-

Akzeptor Käfige mit langlebigen ladungsseparierten Zuständen designet werden, zum Beispiel für Anwendungen in der Photoredox-Katalyse.

Im letzten Projekt dieser Arbeit wurden erste Schritte zur Realisierung von photoredox aktiven weichen Materialien basierend auf Koordinationskäfigen unternommen. Der Donorligand von einem der *cis*-$Pd_2D_2A_2$ Käfige wurde mit unpolaren Alkylketten funktionalisiert, wodurch der Käfig einen amphiphilen Charakter aufweist. Vorläufige Ergebnisse deuten darauf hin, dass der Käfig in Agglomerate mit einem Durchmesser von ungefähr 100 nm in den untersuchten polaren organischen Lösungsmitteln assembliert. Zusätzlich wurden erste Untersuchungen hinsichtlich der Einbettung der amphiphilen Donor-Akzeptor-Käfige in wässrige mizellare Lösungen basierend auf amphiphilen Blockcopolymeren durchgeführt. Solche Systeme weisen zwei unterscheidbare Umgebungen auf, das sind der unpolare mizellare Kern und die wässrige Phase. In der Zukunft könnte eine selektive Anreicherung von geeigneten redox-aktiven Verbindungen in die beiden Phasen den vektoriellen Elektronentransfer über die mizellare Grenzfläche ermöglichen.

Insgesamt erweitern die in dieser Dissertation präsentierten Arbeiten das Repertoire an Ansätzen für das Design von Pd_nL_{2n} Assemblierungen mit spezifischer Struktur und Funktion.

Contents

1. Introduction

Contents of this chapter are written up for publication:

L. Neukirch, G. H. Clever* *Chem. Sci., submitted*.

Topological Variety and Self-Sorting in Homo- and Heteroleptic Pd_nL_{2n} Metallo-Supramolecular Assemblies (Review article)

E. Benchimol, L. Neukirch, A. Walther, G. H. Clever*

Chromophore-Based Coordination Cages (Review article)

1.1. Motivation

According to the annual statistics of the energy institute, over 80% of the energy consumed globally in 2023 stemmed from fossil fuels.[1] Fossil fuels are depleting and their combustion leads to the emission of greenhouse gases.[2] While operating nuclear power plants stands out in terms of low carbon emissions, it comes with the disadvantage of the need for long-term storage of nuclear waste.[3,4] Owing to these drawbacks of fossil fuel combustion and nuclear power paired with the growing energy demand, a full transition towards renewable energy sources is desirable.

Nature has optimized the capture and conversion of energy over billions of years, allowing for the creation of all biomass surrounding us, majorly through photosynthesis, i.e. the conversion of light energy into chemical energy. In principle, the daily irradiance could supply the world with sufficient energy for multiple years.[5] Therefore, natural photosynthesis is often regarded as a blueprint for light conversion. While the overall efficiency of photosynthesis is low (< 10%[6]), light harvesting occurs with exceptionally high yields, i.e. nearly each absorbed photon contributes to charge separation.[7] This high efficiency can be traced back to the choice of chromophores as well as their spatial arrangement in the light-harvesting apparatuses. The latter finetunes the photophysical properties of the chromophores and endows the energy transfer processes with directionality.[8,9] This inspires chemists to design systems in which multiple chromophores are meticulously arranged in space with the aim to control the fate of their excited states.[10,11]

1.2. Inspiration from nature: photosynthetic apparatus of *Rhodobacter sphaeroides*

Rhodobacter sphaeroides is a purple non-sulfur bacterium with a very diverse metabolism.[12,13] Important for the following is that the bacterium can capture light for producing high energy compounds, i.e. it is facultative phototrophic. Its light harvesting apparatus is well studied. Therefore, it was chosen here to discuss nature's strategies for mastering efficient photon capture. The light harvesting apparatus of the bacterium consists of light harvesting complex 2 (LHC2) and LHC1, the latter surrounds the reaction center (RC). LHC1 is dimeric[14,15] and a simplified overall chromophore organization is shown in Fig 1b.[16]

LHC2s majorly serve as antennae, absorbing light and funneling the energy with minimal losses to LHC1. The structure of LHC2 was resolved by cryo electron microscopy and consists of nine cyclically arranged protein subunits that each bind three bacteriochlorophyll *a* (BChl *a*) molecules and one carotenoid (see Fig. 1c for the chromophore arrangement).[17] In the upper circle, nine BChl *a* molecules are arranged with a Mg-Mg distance of ca. 21 Å. Owing to their absorption maximum at 800 nm, they are referred to as B800. In contrast to this, the 18 BChl *a* molecules B850 in the lower circle are more densely packed (Mg-Mg distance: 9 Å), allowing for excitonic coupling which is mainly responsible for their red-shifted and broadened absorbance. The carotenoids possess a structural and photoprotective function but also broaden the absorption of the LHC2 within the visible region.[8]

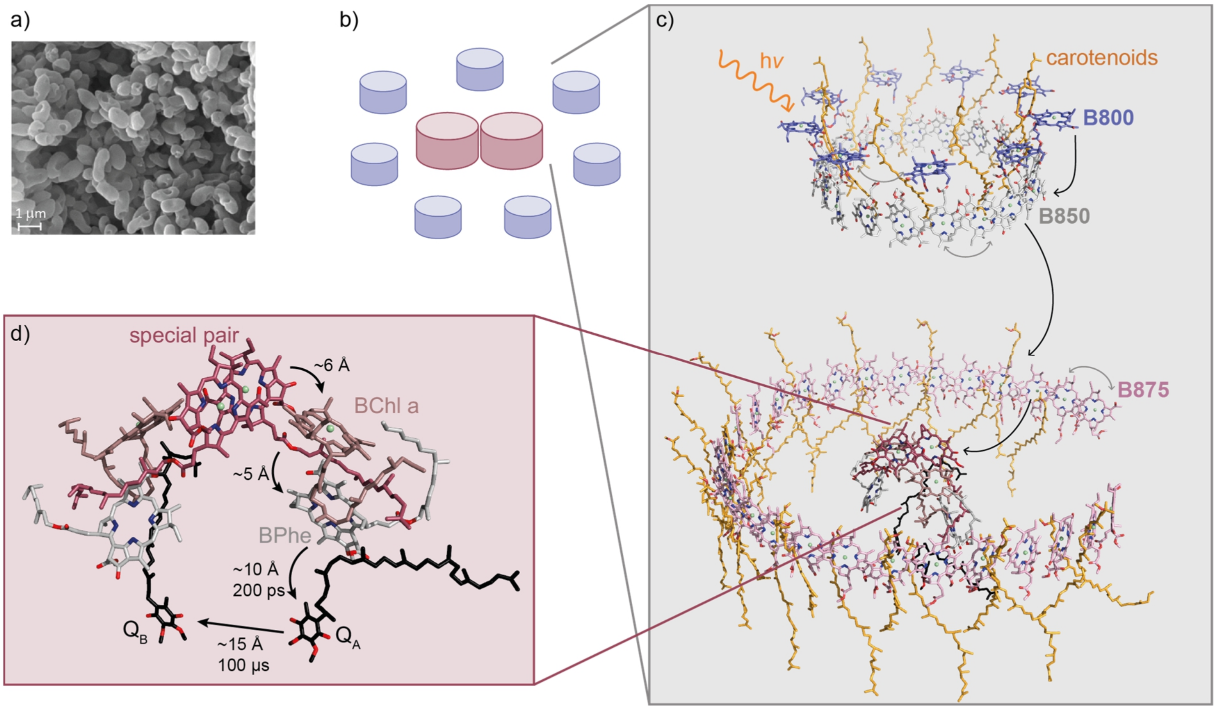

Fig. 1 Overview of the light-harvesting processes in *Rhodobacter sphaeroides*; a) scanning electron micrograph of the bacterium (reproduced with permission from ref[18]); b) simplified overview of the arrangement of LHC1 (purple) and LHC2 (blue); c) chromophore arrangement in LHC1 (bottom)[14] and LHC2 (top)[17] along with the homo- (gray arrows) and hetero- (black arrows) energy transfer processes; d) redox active molecules in the RC along with electron transfer processes (black arrows).[14,19]

The LHC1s accept excitation energy from the LHC2s or absorb light by themselves and transfer it to the reaction center. The organization of the proteins and chromophores in LHC1 is reminiscent to the one of LHC2: BChl *a* molecules are non-covalently attached to protein subunits. The latter oligomerize to give a cyclic arrangement of protein-chromophore complexes.[14] The absorption of the BChl *a* molecules in LHC1 is finetuned in a way that their absorption is further redshifted to 875 nm. Hence, energy can migrate without losses within the three cycles (B800→B800, B850→B850, B875→B875) but directionality is endowed through the different absorption energies of the BChl *a* molecules and hetero energy transfer occurs towards the reaction center. The overall energy transfer cascade is hence B800 (LHC2) → B850 (LHC2) →B875 (LHC1) → RC. In the last energy transfer step, the excitation energy is transferred to a BChl dimer within the reaction center, the so-called special pair $BChl_2$. Here, a noteworthy distance of 40 Å has to be bridged; accordingly, this step is comparably slow (20-50 ps). However, this distance prohibits electron transfer between RC($BChl_2^+$) and LHC1 which would quench the B875 excited state, exploiting that electron transfer has a much steeper distance-dependence as compared to energy transfer.[8,20] The excited special pair transfers an electron over an accessory BChl *a* to a bacteriopheophytin (BPhe) (Fig. 1d). The edge-to-edge distances are in both cases ca. 5 Å and they occur in sum within a couple of ps. Next, the electron is transferred to a quinone Q_A (~10 Å, 200 ps) and then to quinone Q_B (~15 Å, 100 µs). Through this stepwise electron transfer, the distance between electron and hole is increased, avoiding unproductive charge recombination. However, it comes with an overall loss of free energy in order to make each step thermodynamically feasible. Regarding the choice of chromophore, BChl *a* has a sufficiently long excited state lifetime for enabling the energy and electron transfer processes with near-unity efficiencies and it comes with a broad and strong absorption (only the Q_y transition was discussed here).[17,19] Reduction of the quinones leads to proton uptake and the protonmotive force drives ATP synthesis.[21]

While we can learn from the mutual arrangement of the chromophores in the light-harvesting systems, mimicking the framework that holds them in space – i.e. the proteins – is not desirable, not the least owing to their fragility. Instead, antenna chromophores as well as donor and acceptor moieties have been connected in a covalent fashion, often via conjugated or non-conjugated bridges (Fig. 2a).[22–33] For example, Schuster, Guldi, and coworkers reported a zinc-porphyrin (ZnP)-fullerene (C_{60}) dyad in 2004 (Fig. 2b).[34] The authors found that the interactions between the ZnP donor and the C_{60} acceptor are weak in the ground state. However, photoexcitation of the dyad was followed by electron transfer affording the ZnP radical cation and, presumably, the C_{60} radical anion. The charge recombination rate constant was shown to be strongly solvent-dependent (99 ps in tetrahydrofuran, 1 ns in toluene).

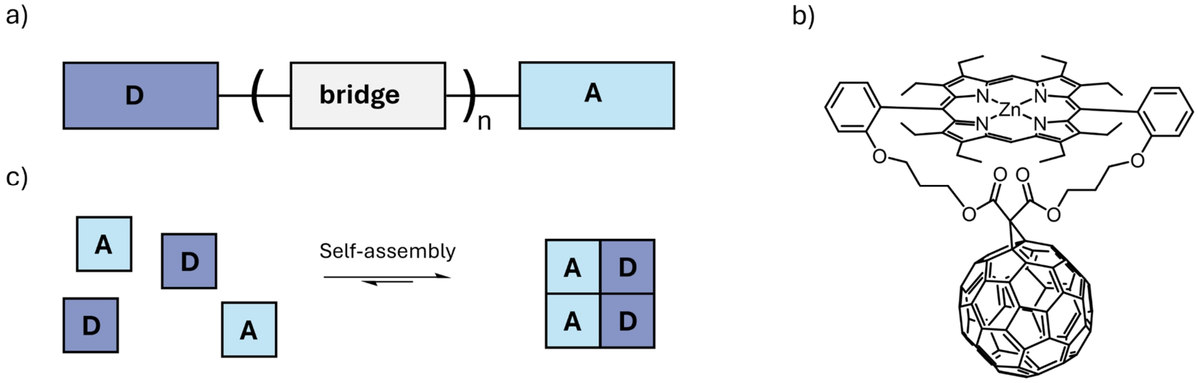

Fig. 2a) Schematic illustration of a donor-bridge-acceptor system; b) structure of the zinc-porphyrin-fullerene dyad studied by Schuster, Guldi, and coworkers;[34] c) schematic illustration of the self-assembly into a supramolecular donor-acceptor system.

The investigation of organic donor-acceptor compounds provided insights into important structure-property relationships, such as the dependence of the electron transfer rate constant on the donor-acceptor distance[24,25,29,31] and orientation,[22,23,31] driving force,[27,30] and electronic coupling.[28] However, the synthesis of such purely covalent systems is usually time- and resource consuming. Supramolecular chemistry is an attractive alternative as it allows connecting multiple building blocks in a single step.[35] This is schematically shown for donor and acceptor building blocks in Fig. 2c. The assembly to supramolecular structures can result from dynamic covalent,[36–38] hydrogen-bonding interactions[39–42] or metal coordination.[43–51]

1.3. Coordination cages

The coordination-driven self-assembly of bridging organic ligands and metal ions can afford coordination polymers, metal-organic frameworks (MOFs), or discrete nanoscale architectures such as cages and rings.[52–54] Coordination cages based on a variety of metal-ligand combinations have been reported. The first coordination cage, based on Mg(II) cations, was described in 1988 by Saalfrank.[55] The field was further pioneered by Raymond who introduced tetrahedral cages based on Ga(III) metal nodes and catecholate-terminated ligands.[56,57] The group of Nitschke employs octahedral metal ions such as Zn(II) or Fe(II) and pyridylimine-terminated ligands that are formed during the self-assembly via imine condensation („subcomponent self-assembly") to form tetrahedral or cubic cages, amongst other topologies.[58] Major contributions in the field were furthermore achieved by Stang and coworkers who focus on metallacages and metallacycles with Pt(II) nodes.[51,59]

A subfield of metal-coordination driven assemblies utilizes Pd(II) as metal nodes and nitrogen-based ligands, such as pyridines or isoquinolines (Fig. 3).[50] The benefits of this metal-ligand combination include the diamagnetism of Pd(II) (allowing for analysis via NMR spectroscopy) and the reliability of the square planar coordination geometry (facilitating the rational design). Moreover, the Pd(II)-nitrogen bond has a relatively high thermodynamic stability while the ligand exchange kinetics are rather fast. The latter enables error-correction during the self-assembly process, usually allowing for obtaining the thermodynamically most stable product in quantitative yields which hence spares the need for post-synthesis purification. The preparation of molecular hosts based on this metal-ligand combination traces back decades. For example, Fujita reported in 1990 a molecular square $Pd_4L_4(en)_4$, which was obtained through the combination of ethylene diamine (en) *cis*-protected Pd(II) and 4,4'-bipyridine L and was shown to encapsulate a small organic molecule in water.[60] With "naked" Pd(II), i.e. in the absence of protecting ligands, self-assembly with bent bis-mono dentate ligands leads to architectures with the stoichiometry Pd_nL_{2n} (Fig. 3). In this regard, McMorran and Steel were the first to report a Pd_2L_4 helicate in 1998.[61] Since these initial reports, the field of Pd(II)-based coordination assemblies flourished.[48,50,62] In the early stages, researchers primarily focused on accessing novel structural motifs, often driven by their aesthetics. In recent years, however, the research transitioned towards imbuing cages with functionality.[63] Pd(II)-based cages have been investigated as high affinity binders[64–66] and reaction vessels.[67–69] Furthermore, chromophores,[70] luminophores,[71–73] (photo)redox active moieties,[74–77] and solubility controlling groups for steering higher-order assembly[78–80] have been implemented into the assemblies.

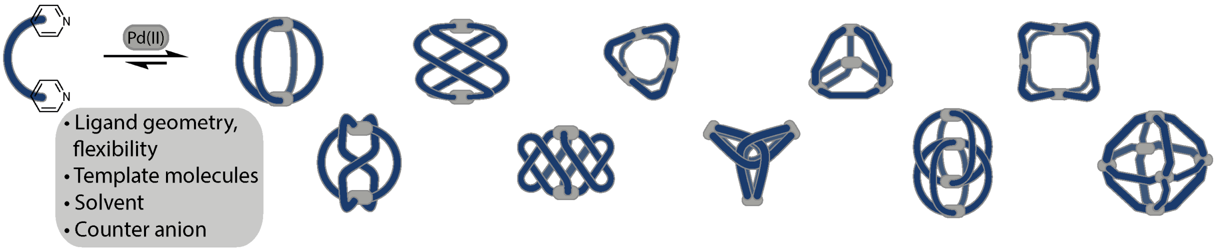

Fig. 3 Structural diversity of homoleptic Pd_nL_{2n} assemblies (n = 2,3,4,6). Factors governing the formation of a particular assembly are listed in the box.

Across the range of potential applications, predictability of the self-assembly outcome is of pivotal importance as structure and function are closely related. For example, for designing a high-affinity binder, both the chemical nature of the ligand (e.g. large π-surface for π-π interactions) and the size of the assembly must match the properties of the guest. And, similar to the chromophore arrangement in the photosynthesis apparatus, distance and orientation of chromophoric ligands can affect their photophysical properties.[81,82] Therefore, the structural diversity of Pd_nL_{2n} assemblies along with guidelines governing the formation of a particular nuclearity and topology will be discussed first. Next, strategies for achieving integrative self-sorting to defined heteroleptic assemblies, that are assemblies based on different kinds of ligands, will be presented. These discussions will be limited to Pd_nL_{2n} assemblies where n = 2-8, meaning assemblies formed from unprotected Pd(II) and bis-monodentate ligands, owing to their relevance for this work. The second part of the introduction focuses on coordination cages with chromophore-based ligands and emergent phenomena in these cages such as energy and electron transfer.

1.3.1. Homoleptic assemblies with n = 2

Pd_2L_4 assemblies represent the most extensively researched Pd_nL_{2n} family member and various of them have been equipped with functionalities. Dinuclear cages are obtained with rigid ligands possessing collinear binding vectors, i.e. binding angles α close to 0°. The latter corresponds to the angle between the two donor vectors. A prominent example for a so-called lantern-shaped cage is $[Pd_2\mathbf{1a}_4]^{4+}$ (Fig. 4a), which was reported by Hooley and coworkers in 2010.[83] In this type of cage, the aromatic system of the ligand is perpendicular to the Pd-Pd axis, allowing for inward-directed functionalities. Lusby and coworkers exploited the endohedral protons of the pyridines in $[Pd_2\mathbf{1a}_4]^{4+}$ for binding quinones via hydrogen bonding interactions[84] and a homologous cage $[Pd_2\mathbf{1b}_4]^{4+}$ was utilized for catalyzing cycloadditions.[85–87] Moreover, the inward-directed nitrogen atoms of the pyridine backbones in $[Pd_2\mathbf{1b}_4]^{4+}$ enabled encapsulation of cisplatin via hydrogen bonding, as shown by Lewis and Crowley.[88] Clever and coworkers equipped a lantern-shaped cage with endohedral substituents; more precisely, electron-withdrawing groups were attached to an electron-rich backbone via C-C double bonds.[89] The electronic push-pull character led to rotation around the double bond whose dynamics were modulated upon self-assembly and upon guest encapsulation.

By contrast, the π-surface of the ligands in capsules shields the cavity, enabling encapsulation of neutral aromatic guests of suitable size. For example, Clever and coworkers reported on capsule $[Pd_2\mathbf{2}_4]^{4+}$ with triptycene-based ligand **2**[65,90] (Fig. 4b) as well as on a similar capsule $[Pd_2\mathbf{17a}_4]^{4+}$ with a slightly altered ligand (Fig. 5c).[91] Driven by π-π interactions, the cages act as fullerene receptors, allowing for solubilization of the latter in polar organic solvents. Moreover, a photochemically generated fullerene radical anion was shown to possess a significantly increased lifetime within this shielded environment. Yoshizawa and coworkers constructed a capsule with ligands **3** based on anthracene (Fig. 4c); here, eight anthracenes surround the cavity, thus creating a hydrophobic confined space.[66] In combination with the solubility of the capsule in aqueous solution, which can be attributed to their methoxy ethoxy substituents, this capsule binds a wide range of neutral guests. A closer look at the structure of the capsule reveals helical twisting of the ligands. Decoration of the capsules with chiral saccharide-based moieties leads to enrichment of one of the two helical enantiomers, meaning that the chirality is transferred to the assembly framework.[92] This helical chirality, on the other hand, results in chiral induction on fullerene and other neutral guests. Clever and coworkers also achieved chirality transfer to fullerenes by employing a Pd_2L_4 capsule with an intrinsically chiral ligand, derived from Tröger's base.[93]

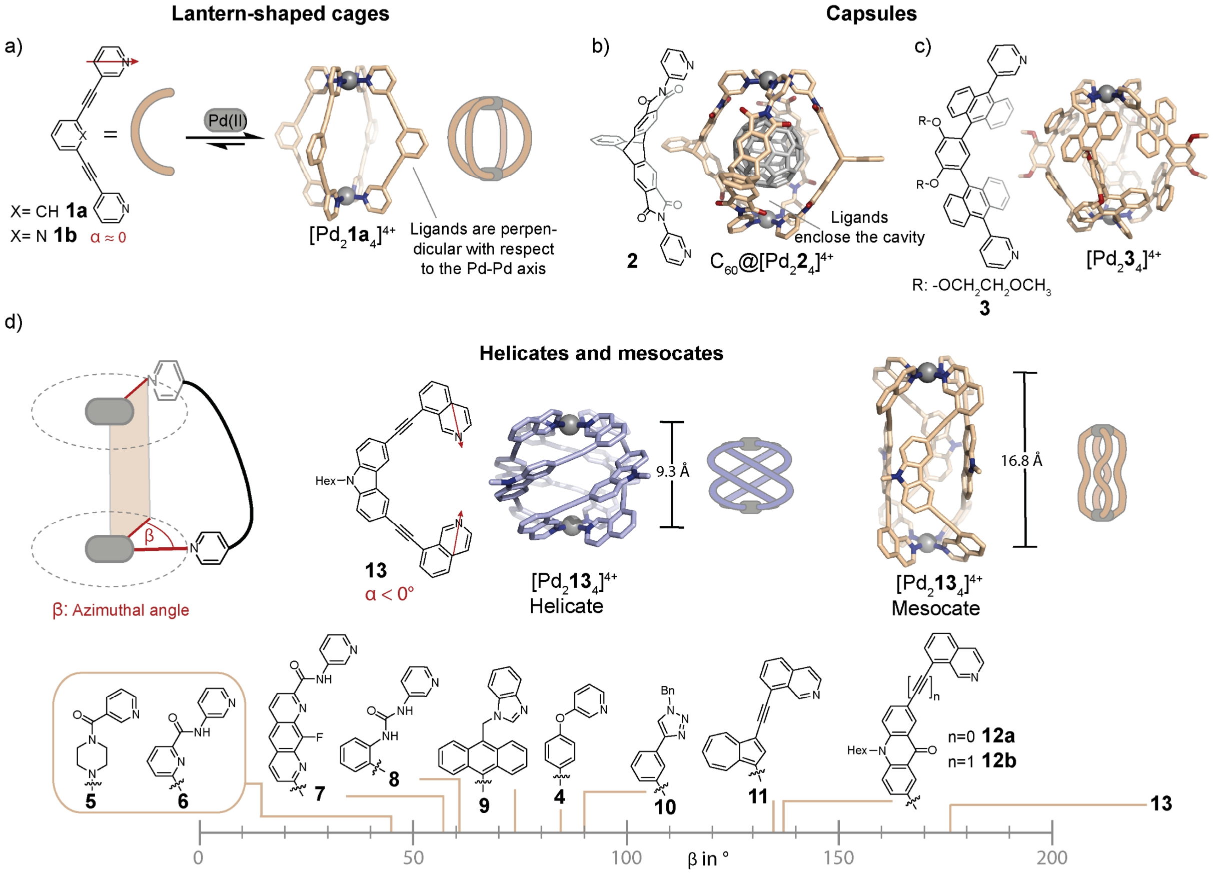

Fig. 4a) Illustration of the ligand binding angle α, self-assembly into lantern-shaped cage $[Pd_2\mathbf{1}_4]^{4+}$ and X-ray structure of $[Pd_2\mathbf{1a}_4]^{4+}$;[83] b) X-ray structure of host-guest complex $C_{60}@[Pd_2\mathbf{2}_4]^{4+}$;[90] c) X-ray structure of capsule $[Pd_2\mathbf{3}_4]^{4+}$; d) illustration of the azimuthal angle β and X-ray structures of helicate and mesocate $[Pd_2\mathbf{13}_4]^{4+}$ [94] as well as overview of the azimuthal angles β of published Pd_2L_4 helicates.[61,95–104] For the determination of the azimuthal angles, see appendix, section 1.6.

Helical twisting of the ligands, as was just described for capsule $[Pd_2\mathbf{2}_4]^{4+}$, can be a result of a) the ligand geometry,[70,101,103] b) steric demand at the backbone[100] or donor site,[105] and c) favorable ligand-to-ligand interactions.[106,107] The helicity can furthermore be influenced by solvents and counter anions.[94,98] As a measure for the degree of helicity, the azimuthal angle β can be utilized which corresponds to the angle between the two coordination bonds (Fig. 4d). Earlier mentioned helicate $[Pd_2\mathbf{4}_4]^{4+}$, synthesized by McMorran and Steel, was found to have a counter anion dependent helicity: anions with smaller diameters trigger a shrinkage along the Pd-Pd axis, whereby the helicity is increased.[95] Among the tested anions, the greatest helicity of β = 85° was attained with iodine. Chand and coworkers constructed helicates with β = 85° with ligand **5**, based on piperazine,[96] and ligand **6** with flexible amide linkers[97] in 2010 and 2012, respectively. Moreover, ligand **7** reported by Gan, also possessing amide linkers, forms a helicate-mesocate equilibrium that can be shifted towards the helicate upon addition of $B_{12}F_{12}{}^{2-}$ and towards the mesocate in the presence of tetrafluoroborate.[98] Urea-spaced ligand **8** forms a helicate with ClO_4^- while a non-helical cage is assembled in the presence of NO_3^-.[99] For anthracene-based ligand **9** with benzimidazole donors, the helicate is favored owing to repulsive steric interactions between the bulky cores.[100] Crowley and coworkers reported on helicates with ligands **10** with imidazole donors that are spaced by 1,3-benzene.[104] Presumably, the helicate is formed due to the convergence of the donor vectors and is stabilized by π-π-interactions. Several helicates based on ligands with 8-isoquinoline donor groups were described by the Clever group. Owing to their highly convergent donor vectors (i.e. α < 0), the ligands must twist in order to bridge the Pd(II) centers while maintaining a square planar coordination geometry. The helicates are further stabilized by inter-ligand π-π interactions. 8-Isoquinoline terminated ligands based on azulene

(**11**)[101] and acridone (**12a**,**b**)[102,103] resulted in helicates with azimuthal angles between 130 and 140°. Aiming at even greater azimuthal angles, Clever and coworkers synthesized strongly convergent carbazole-based ligand **13**.[94] Depending on the counter anion employed for the self-assembly, helicates with β = 171-176° were observed. Moreover, the helicate was found to be in a solvent- and counter anion-dependent equilibrium with its corresponding mesocate. In the latter, the ligands are V-shaped and the azimuthal angle equals zero; consequently, the assembly is expanded along its Pd-Pd axis (Fig. 4d).

Attractive inter-ligand interactions can furthermore favor the self-assembly into interlocked and interwoven architectures. In 2020, the Clever group examined the self-assembly of ligand **14**, based on a peptidic macrocycle.[108] Owing to its high flexibility, formation of the entropically favored mononuclear complex $[Pd_1\mathbf{14}_2]^{2+}$ was observed at first. However, self-assembly in acetonitrile, followed by the addition of chloride or triflimide resulted in the obtention of a dinuclear assembly $[Pd_2\mathbf{14}_4]^{4+}$. The X-ray structure revealed that two mononuclear complexes, in which the Pd(II) centers are *cis*-chelated, are mechanically interlocked. Overall, the structure is stabilized through π-π interactions between the ligands, the embedding of the pyridine within the peptidic macrocycle of the neighboring ligand, as well as electrostatic interactions in the central cation-anion-cation arrangement (Fig. 5a).

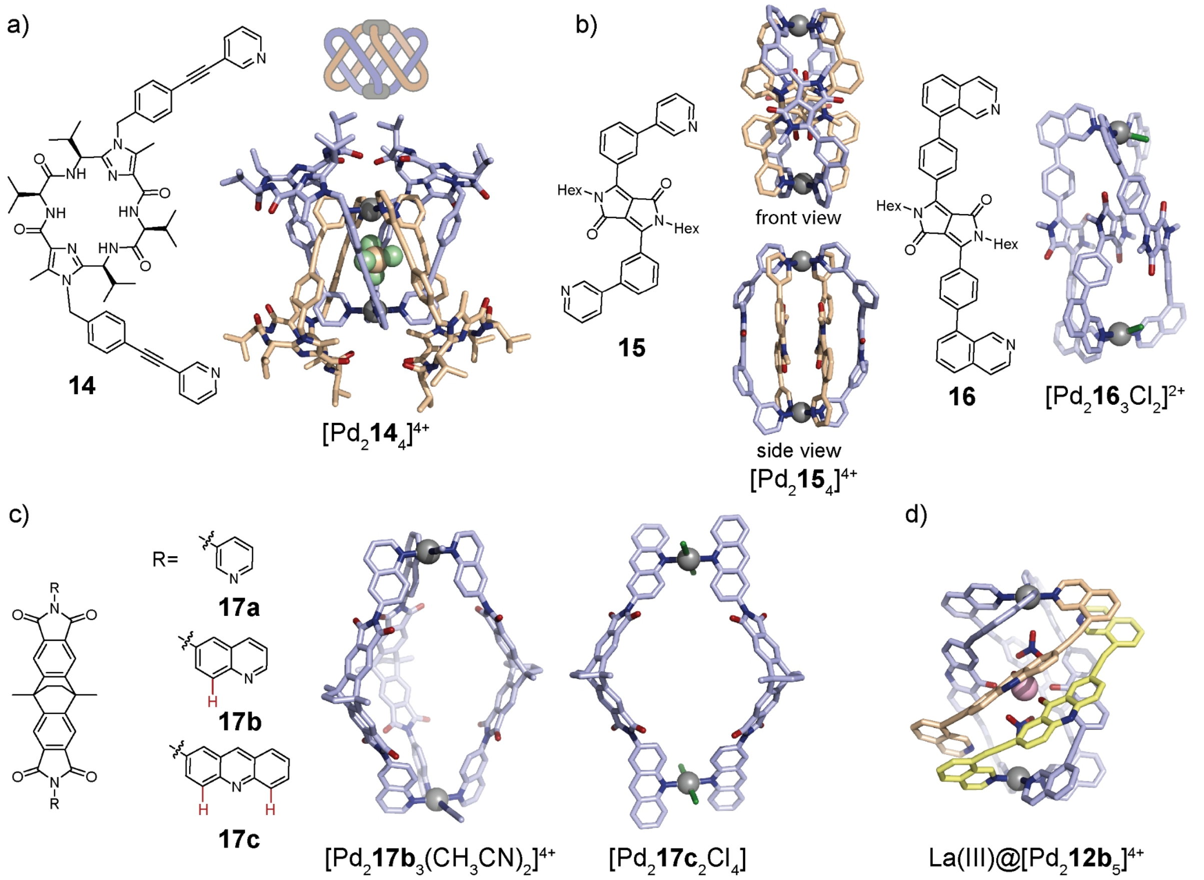

Fig. 5a) Interlocked lemniscates $[Pd_2\mathbf{14}_4]^{4+}$;[108] b) double bridged ravel $[Pd_2\mathbf{15}_4]^{4+}$ (left) and single bridged ravel $[Pd_2\mathbf{16}_4]^{4+}$ (right);[81] c) bowl $[Pd_2\mathbf{17b}_3(CH_3CN)_2]^{4+}$ (left) and ring $[Pd_2\mathbf{17c}_2Cl_4]$ (right) (positions on the Pd(II) nodes that are not bound to organic ligands are occupied by solvent molecules or halides) ;[91,105] d) penta-stranded helicate La(III)@$[Pd_2\mathbf{12b}_5]^{4+}$.[107]

Our group also found a self-penetrated homoleptic motif.[81] Double-bridged ravel $[Pd_2\mathbf{15}_4]^{4+}$ is based on ligand **15**, possessing two key attributes: strongly inward-directed bonding vectors and diketopyrrolopyrrole backbones, well-known for engaging in π-π-stacking interactions. For the formation of the peculiar structure, two ligands adopt an S-shaped conformation and cross in the center of the cavity. The two outer ligands adopt a helical twist (Fig. 5b). Diketopyrrolopyrrole derivative **16** which is terminated with isoquinoline donors was investigated in addition. Again, the binding vectors are convergent; however, in this case more sterically demanding. As a result, single-bridged ravel [Pd$_2$**16**$_3$(CH$_3$CN)$_2$]$^{4+}$ is observed which possesses "free" coordination sites (meaning that they are occupied by solvent molecules or halides). Similarly to [Pd$_2$**15**$_4$]$^{4+}$, two ligands cross in the centrum of the cavity but only one ligand occupies the outer position. This leads to three instead of four stacked diketopyrrolopyrrole moieties (Fig. 5b), altering the assemblies photophysical properties, as will be discussed later. The principle of maximum site occupancy is also challenged in the case of ligand **17**, whose pyridine-version **17a** forms a classical capsule [Pd$_2$**17a**$_4$]$^{4+}$.[91,105] Ligand **17b**, equipped with 6-quinoline, assembles to bowl [Pd$_2$**17d**$_3$(CH$_3$CN)$_2$]$^{4+}$ when ligand and Pd(II) salt are combined in a 3:2 ratio. In this manner, steric repulsion between the inward-pointing quinoline protons (Fig. 5c, red) is reduced. The steric congestion at the donor site was further increased by equipping the ligand with acridine donors, possessing two protons that are collinear to the coordination bonds. Consequently, self-assembly into ring [Pd$_2$**17c**$_2$(CH$_3$CN)$_4$]$^{4+}$ was favored. This structural variance, controlled by the steric bulk at the donor site, resulted in differences in the assemblies' host-guest chemistry: while capsule [Pd$_2$**17a**$_4$]$^{4+}$ was shown to bind fullerene C$_{60}$, bowl [Pd$_2$**17b**$_3$(CH$_3$CN)$_2$]$^{4+}$ could additionally encapsulate larger C$_{70}$, and ring [Pd$_2$**17c**$_2$(CH$_3$CN)$_4$]$^{4+}$ did not show fullerene binding at all. Contrasting with the just described examples, Severin and coworkers discovered a penta-stranded helicate La(III)@[Pd$_2$**12b**$_5$]$^{4+}$ (Fig. 5d).[107] This work was enticed by the observation that a fifth ligand **12b** interacts with initially reported helicate [Pd$_2$**12b**$_4$]$^{4+}$.[103] The penta-stranded arrangement was stabilized through incorporation of oxophilic La(III), exploiting the high density of carbonyl groups within the helicate.

1.3.2. Homoleptic assemblies with n = 3-8

In 2006, Fujita and coworkers reported that ligand **18** assembles with a Pd(II) triflate salt into three-membered ring [Pd$_3$**18**$_6$]$^{6+}$.[81] With nitrate or tetrafluoroborate salts, however, pseudo-tetrahedral [Pd$_4$**18**$_8$]$^{8+}$ was obtained (Fig. 6). In this structure, two edges are double-bridged and the remaining edges are single-bridged while in a „real" tetrahedron, all edges are equivalent. For simplicity, this structure is referred to as tetrahedron in the following. The Fujita group also investigated the effect of prolongation of the ligand: when **18** was prolonged by one phenyl moiety, an equilibrium between ring and tetrahedron was observed with nitrate and triflate salts, albeit again with a strong preference for the three-membered ring when the triflate salt was employed. In 2022, Mukherjee investigated the ring-tetrahedron equilibrium with ligand **19**, which is similar in shape compared to **18** but possesses a wider backbone.[109] With the tetrafluoroborate salt in DMSO, a mixture of tetrahedron [Pd$_4$**19**$_8$]$^{8+}$ and three-membered ring [Pd$_3$**19**$_6$]$^{6+}$ was yielded, whereas only [Pd$_4$**19**$_8$]$^{8+}$ was observed under two other tested conditions (Fig. 6). Van't Hoff analysis of the equilibrium disclosed that the ring is enthalpically and the tetrahedron entropically favored. Similar thermodynamic trends were observed for a second ligand with the same geometry.

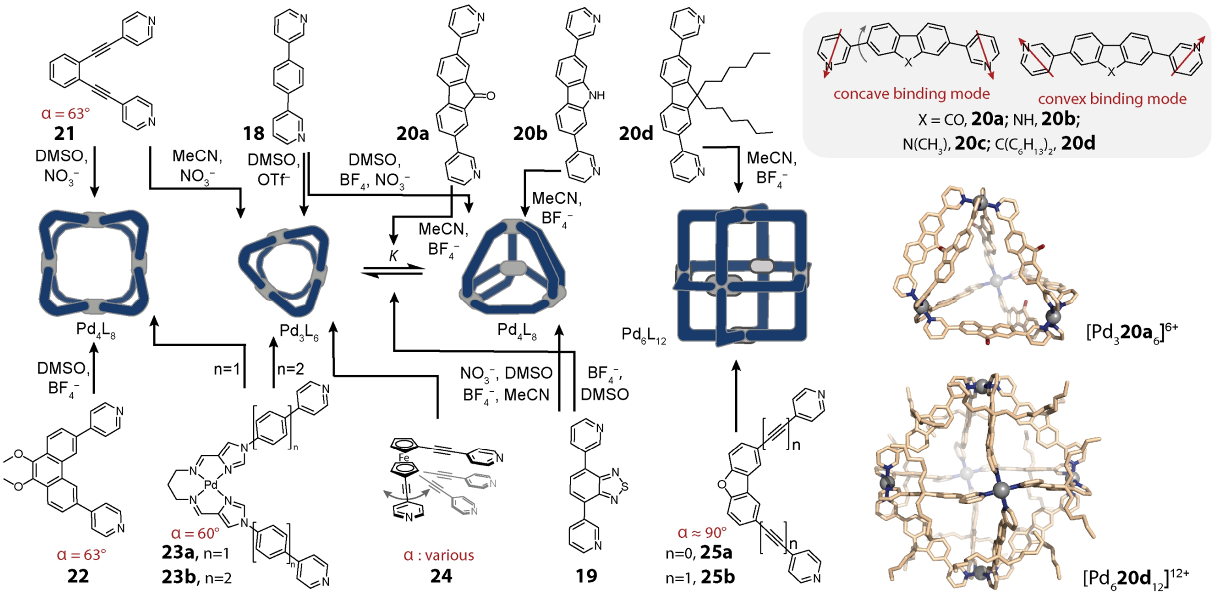

Fig. 6 Overview of homoleptic rings, tetrahedra, and octahedra Pd_nL_{2n} (n = 3,4,6). For ligands with *para*-pyridines, binding angles α are specified in red.[103,109–117]

Furthermore, the Clever group examined the self-assembly outcome of various fluorene-derived ligands differing in their electronic situation and in the backbone-centered steric demand.[112,113] When the flat ligands are considered, two binding scenarios, the convex and the concave binding mode, can be distinguished (Fig. 6, gray box). The actual binding situation can lie between these two boundary cases. A situation in which the two pyridines point in opposite directions would not lead to a defined assembly. For the sake of comparability, the assemblies in acetonitrile with tetrafluoroborate anions will be described only. Ligands **20a** and **20c** based on fluorenone and methyl-carbazole, respectively, assemble into a mixture of three-membered rings and tetrahedra. Ligand **20b** based on *N*-unsubstituted carbazole forms tetrahedron [Pd$_4$**20b**$_8$]$^{8+}$. Conversely, ligand **20d**, equipped with hexyl chains, assembles into octahedron [Pd$_6$**20d**$_{12}$]$^{12+}$ without formation of the lower-nuclearity assemblies (Fig. 6). The X-ray crystal structure reveals that the ligands adopt a convex binding mode, wherefore the backbone-centered steric bulk is located on the cage's exterior. Occupation of double-bridged edges in a potential ring or tetrahedron would lead to steric clash, explaining the observed outcome. Topology control through backbone-centered steric bulk was also achieved by Severin and coworkers. For this, the authors designed clathrochelate-based ligands that are similar in geometry to ligand **18** and possess a varying backbone thickness.[118,119] Next, they showed that the ligand with the smallest bulk was still able to assemble to a Pd$_4$L$_8$ tetrahedron while self-assembly of ligands bearing a thicker backbone resulted in the formation of octahedra Pd$_6$L$_{12}$. In contrast to the aforementioned work, not only the chains at the exterior but the overall bulk of the ligands is increased leading to a reduction of the cavity volume.

In contrast to bis-monodentate ligands with *meta*-pyridines, which tend to form equilibria between three-membered rings and tetrahedra, analogous ligands terminated with *para*-pyridines are often found to form three- and four-membered rings (Fig. 6). The bent angle calculated based on the flat ligand describes the binding situation of these ligands more accurately as compared to the *meta*-pyridine siblings since rotation around the backbone/linker-pyridine bond is not associated with a change in the angle. In 2007, Fujita and coworkers described the self-assembly of ligand **21**, possessing a bent angle of 63°, into four-membered ring [Pd$_4$**21**$_8$]$^{8+}$ with a Pd(II) nitrate salt in DMSO.[110] By contrast, three-membered ring [Pd$_3$**21**$_6$]$^{6+}$ was yielded when acetonitrile was used as the solvent. In the solid state, the cavity of [Pd$_4$**21**$_8$]$^{8+}$ is occupied by an aggregate of DMSO and nitrate molecules, suggesting that the four-membered ring $[Pd_4\mathbf{21}_8]^{8+}$ might be favored due to a templation effect. In accordance with this, addition of various other solvents to $[Pd_4\mathbf{21}_8]^{8+}$ in DMSO resulted in a shift in the equilibrium towards $[Pd_3\mathbf{21}_6]^{6+}$. Phenanthrene-based ligand **22**, reported by the Clever group, has a similar bent angle and was found to assemble into four-membered ring $[Pd_4\mathbf{22}_8]^{8+}$ in DMSO with a tetrafluoroborate salt.[103] A complicated mixture of three- and four-membered rings as well as a tetrahedron was obtained when the same reaction was carried out in acetonitrile.[120] Moreover, assembly in acetonitrile with a nitrate salt led to two mechanically interlocked four-membered rings. In 2023, Li and coworkers compared the self-assembly of two ligands **23a** and **23b** with a bent angle of 60°, solely differing in their length, under the same conditions.[114] Intriguingly, shorter ligand **23a** formed four-membered ring $[Pd_4\mathbf{23a}_8]^{8+}$ while longer ligand **23b** yielded three-membered ring $[Pd_3\mathbf{23b}_6]^{6+}$. Hence, presumably, the higher flexibility of the longer derivative **23b** allowed for bending of the ligand and hence for the formation of the entropically favored smaller assembly. Crowley and coworkers studied the self-assembly of ferrocene-based ligand **24** which can, owing to its rotational flexibility, adopt a variety of different bent angles (Fig. 6).[115] The authors observed formation of a three-membered ring $[Pd_3\mathbf{24}_6]^{6+}$ with a tetrafluoroborate as well as with a hexafluoroantimonate salt in acetonitrile. Presumably, this can again be reasoned with the entropic advantage of the three-membered ring. Ligands with a rectangular geometry, in other words with bent angles of 90°, assemble into cubes with an octahedral arrangement of the Pd(II) nodes (Fig. 6). The first cube $[Pd_6\mathbf{25b}_{12}]^{12+}$ was published in 2009 by Fujita and coworkers.[116] In a similar fashion, shorter ligand **25a** and an analogous ligand based on carbazole, assemble into cubes, as was shown by the group of Reek.[117] The authors exploited the large cavity for the encapsulation of fullerenes and demonstrated that the affinity for fullerenes can be tuned based on the electronic properties of the ligand.

The just described examples show that an increase in the binding angle is associated with the formation of assemblies of higher nuclearity – from dinuclear over tri- and tetranuclear to hexanuclear species. Most interestingly, pentanuclear homoleptic species remain unreported for bis-pyridyl ligands. A sole example for a Pd_5L_{10} species, where L is equipped with benzimidazole donors, was reported by Sun and coworkers in 2017 and its formation can be traced back to a template effect.[121] More precisely, the authors found that ligand **26** can yield three- to seven-membered rings, strictly depending on the anion present in solution. Three-, six-, and seven-membered rings were obtained via direct assembly with the NO_3^-, BF_4^-, and PF_6^-/OTf^- salts, respectively (red arrows in Fig. 7). Contrarily, four- and five-membered rings were only accessible via ring-to-ring transformations: $[Pd_4\mathbf{26}_8]^{8+}$ is yielded through addition of HSO_4^- to preformed $[Pd_6\mathbf{26}_{12}]^{12+}$ or $[Pd_7\mathbf{26}_{14}]^{14+}$ (dark blue arrows) and $[Pd_5\mathbf{26}_{10}]^{10+}$ via addition of $Mo_7O_{24}^{6-}$ to any of the assemblies (beige arrows). The high adaptability of ligand **26** was attributed to a) its acidic C-H protons, possibly engaging in specific interactions with the anionic templates and b) the pronounced flexibility of ligand **26** owing to its methylene group.

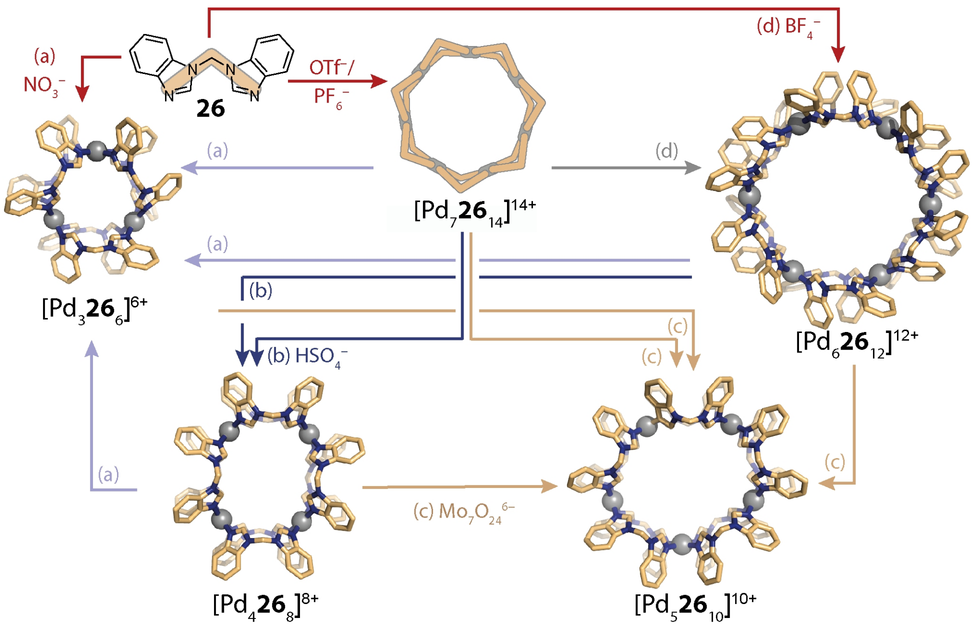

Fig. 7 Anion-templated self-assembly of ligand **26** into rings $[Pd_n\mathbf{26}_{2n}]^{2n+}$ (n = 3-7); red arrows: synthesis starting from the ligand; light blue, dark blue, and beige arrows: synthesis through ring-to-ring transformation; (a) to (d) indicate the anion of the salt added for triggering the ring-to-ring transformation ((a): NO_3^-, (b): HSO_4^-, (c) $Mo_7O_{24}^{6-}$, (d) BF_4^-).[121]

Further reported topologies include a double trefoil knot reported by Clever and coworkers.[122] In this Pd_3L_6 architecture, neighboring Pd(II) centers are double bridged, similarly to the three-membered rings, but the ligands are intertwined. Kuroda reported in 2008 on the first quadruply interlocked double cage Pd_4L_8;[123] the Clever group deciphered guidelines for their formation[124,125] and thoroughly investigated their anion binding capabilities.[126–128] Only recently, a triply interlocked double cage Pd_4L_8 was described for the first time by employing a long furane-based ligand.[129] The backbone and the pyridine donors possess complementary electronic properties and engage in π-π interactions. Theoretical calculations support that these interactions are crucial for the formation of the intercalated architecture. Furthermore, the Severin group showed that acridone-based helicate $[Pd_2\mathbf{12b}_4]^{4+}$ reorganizes into a low-symmetry, tetranuclear structure $[Pd_4\mathbf{12b}_8]^{8+}$ upon addition of a Li(I) salt.[130] This architecture holds two pockets that encapsulate Li(I) in a tetrahedral environment. Lützen and coworkers accessed a pseudo rotaxane-like cage-in-ring structure $Pd_2L_4@Pd_4L_8$ by employing a long BODIPY-based ligand.[131] Formation of the tetranuclear species with this banana-shaped ligand relied on flipping of the pyridines for achieving a greater bent angle. The BODIPY moieties of the central lantern-shaped cage are slipped into the clefts of the four-membered ring, allowing for stabilization of the structure by π-π interactions.

1.3.3. Heteroleptic assemblies

The vast progress on Pd(II) based homoleptic coordination assemblies has provided researchers in the field with some guidelines for the design of assemblies with a particular geometry and nuclearity. However, homoleptic assemblies show limited potential for applications since they carry only one kind of ligand – the component which usually dictates the overall functionality of the cage. For example, emerging phenomena like energy and electron transfer, as discussed in section 1.4., rely on the combination of different functional moieties. This enticed researchers to explore the self-assembly of different kinds of ligands to heteroleptic coordination cages.[63,132] In the absence of factors favoring a particular self-assembly outcome, the combination of differentiable ligands results in the formation of cages with various stoichiometries and stereo configurations.[133] Working with such statistical mixtures impedes the assignment of observed properties to a specific structure and hence its optimization.[75] Additionally, only a fraction of the assemblies possesses the desired properties. The number of possible isomers can be reduced by employing *cis*-protected Pd(II) cations. This allowed for integrative self-sorting to defined heteroleptic assemblies when combined with strategies exploiting steric bulk, as shown by Fujita,[134] or differently charged donor groups, as reported by Mukherjee.[135,136] Strategies for mastering integrative self-sorting with free Pd(II) have been developed by Clever,[103,113,137] Crowley,[138] Hooley,[139] and Severin.[140]

Clever and coworkers endowed banana-shaped ligands with sterically demanding groups at the coordination site for steering integrative self-sorting in 2018.[137] This strategy was coined coordination sphere engineering (CSE). Acridone-based ligands **27** were equipped with picoline moieties possessing either inward (***i*-27**) or outward (***o*-27**) oriented methyl groups (Fig. 8a). A homoleptic coordination environment is disfavored owing to steric congestion. Therefore, bowls $[Pd_2\mathbf{27}_3(CH_3CN)_2]^{4+}$ and rings $[Pd_2\mathbf{27}_2(CH_3CN)_4]^{4+}$ are obtained when one of the ligands is reacted with Pd(II). Excitingly, upon combination of both ligands ***i*-27** and ***o*-27** with Pd(II), heteroleptic cage $[Pd_2\boldsymbol{i}\text{-}\mathbf{27}_2\boldsymbol{o}\text{-}\mathbf{27}_2]^{4+}$ is obtained selectively. This can be traced back to lower steric hindrance in this architecture combined with satisfaction of the principle of maximum site occupancy. The X-ray crystal structure of a mononuclear complex $[Pd_1 2\text{-picolin}_4]^{2+}$ in combination with DFT computations support that the *cis*-isomer is energetically more favorable than a potential *trans*-isomer.

Integrative self-sorting can also be fostered through attractive interactions within the coordination sphere, as was shown by Crowley and coworkers in 2016.[138] Ligands **28a** and **28b** vary solely in the presence or absence of the *ortho* amino groups attached to the pyridines of **28a**. The authors observed that addition of **28a** to preformed homoleptic cage $[Pd_2\mathbf{28b}_4]^{4+}$ results in ligand exchange to yield heteroleptic cage $[Pd_2\mathbf{28a}_2\mathbf{28b}_2]^{4+}$. Again, DFT computations point towards a preference for the *cis*-configurated cage which can be explained by the possibility for H-bonding interactions (Fig. 8b). Importantly, *cis*-$[Pd_2\mathbf{28a}_2\mathbf{28b}_2]^{4+}$ could not be assembled in a direct fashion through combination of the two ligands and Pd(II) cations or via cage-to-cage transformation starting with the two homoleptic cages, suggesting that it is metastable. In agreement with this, DFT computations predict the homoleptic cage $[Pd_2\mathbf{28a}_4]^{4+}$ to be thermodynamically favored.

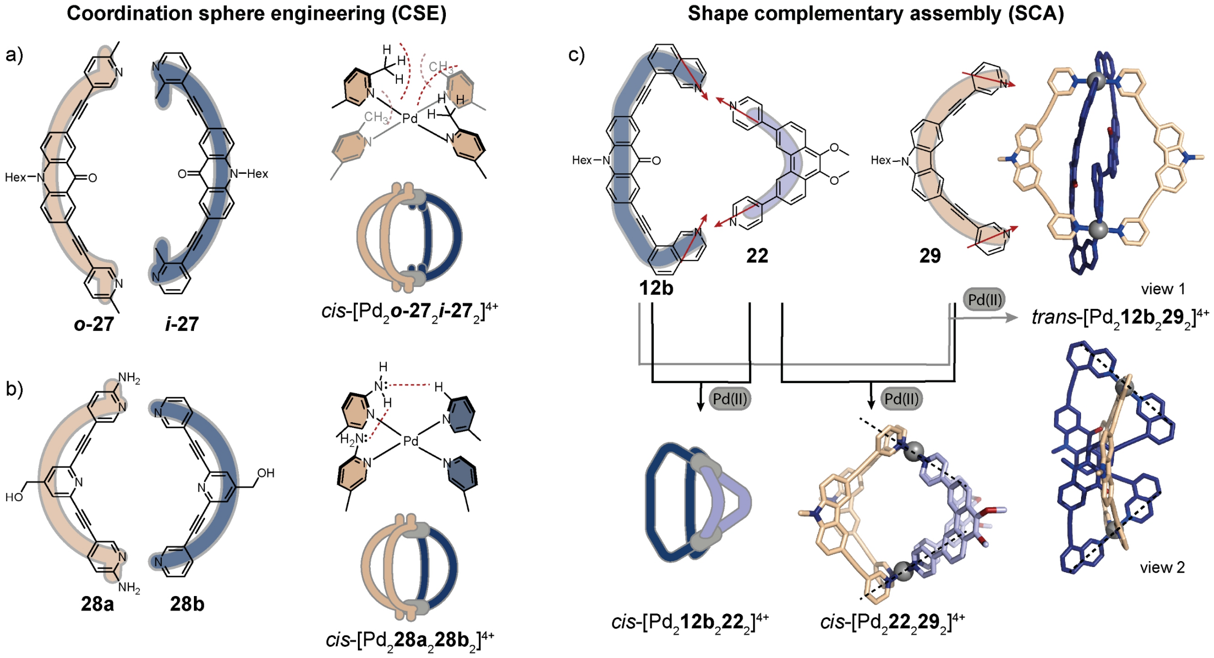

Fig. 8 Strategies for the integrative self-sorting to $Pd_2A_2B_2$-type cages; a) steric bulk close to the coordination site allows for the integrative self-sorting to *cis*-$[Pd_2\mathbf{\textit{i}\text{-}27}_2\mathbf{\textit{o}\text{-}27}_2]^{4+}$ with picolyl-ligands **27**;[137] b) H-bonding interactions close to the coordination site allow for the formation of metastable *cis*-$[Pd_2\mathbf{28a}_2\mathbf{28b}_2]^{4+}$;[138] c) shape complementary assembly approach for accessing *cis*-$[Pd_2\mathbf{22}_2\mathbf{12b/29}_2]^{4+}$ and *trans*-$[Pd_2\mathbf{12b}_2\mathbf{29}_2]^{4+}$.[103,141]

Defined heteroleptic assemblies based on other metal-ligand combinations have been realized through the design of geometrically complementary ligands. For example, heteroleptic Cu(II)-based coordination cages have been reported by Zhou[142] and Stang described heteroleptic metal-organic rings based on Pt(II) and Pd(II).[143] Moreover, concerning Pd_nL_{2n} assemblies, Fujita showed in 2014 that heteroleptic spheres $Pd_{12}A_{12}B_{12}$ can be obtained by combining ligands that solely differ in their length.[144] Clever and coworkers developed the so-called shape complementary assembly (SCA) strategy for the integrative self-sorting into *cis*- and *trans*-$Pd_2A_2B_2$ cages in 2016 and 2017.[103,141] A convergent ligand, such as **12b** or **29**, is combined with a divergent ligand, such as **22**. The geometric complementarity of the ligands allows for the formation of heteroleptic *cis*-$[Pd_2\mathbf{12b/29}_2\mathbf{22}_2]^{4+}$, in which the Pd(II) centers are coordinated in a square planar fashion while the ligands are not significantly conformationally strained. This results in tilted $Pd(donor)_4$ planes (Fig. 8c). In addition, the corresponding homoleptic assemblies are disfavored from an enthalpic viewpoint, owing to the twisting of the ligands in helicate $[Pd_2\mathbf{12b}_4]^{4+}$, as well as from an entropic viewpoint, due to the higher nuclearity of ring $[Pd_4\mathbf{22}_8]^{8+}$. It was shown that the heteroleptic cage can be accessed via different pathways, underscoring its thermodynamic stability. Addition of ligand **12b** to heteroleptic *cis*-$[Pd_2\mathbf{29}_2\mathbf{22}_2]^{4+}$ results in the transformation into *cis*-$[Pd_2\mathbf{12b}_2\mathbf{22}_2]^{4+}$, ascribable to the better geometric complementarity of **12b** and **22** as opposed to **29** and **22**. Interestingly, combination of ligands **12b** and **29** with Pd(II) affords *trans*-$[Pd_2\mathbf{12b}_2\mathbf{29}_2]^{4+}$. Here, ligands **12b** cross the centrum of the cavity which enables *trans* coordination despite the highly convergent nature of the ligand.

The SCA strategy was applied for combining different functionalities, carried by the organic ligands, within the cages. For example, Clever and coworkers combined an intrinsically chiral ligand with an emissive ligand. The overall assembly showed circularly polarized luminescence (CPL) stemming from the initially achiral ligand (described more in depth in section 1.4.2).[145,146] Moreover, appending one kind of ligand in *cis*-$[Pd_2A_2B_2]^{4+}$ cages with hydrophobic chains allowed for the formation of amphiphilic cages, as was shown by our group (section 4.1).[78,79]

In a joint experimental and theoretical approach, Jelfs and Lewis attempted to develop a protocol for predicting the integrative self-sorting of shape complementary ligands based on cheap computational methods.[147] The predictions lacked, however, in accuracy which can presumably be traced back to the simplicity of the applied model in which solvent and counter anion effects as well as ligand flexibility are not captured. These effects can severely influence the integrative self-sorting, as was recently shown by us in cooperation with the Kast group.[148] The reported system exclusively self-sorted into heteroleptic *cis*-$Pd_2\mathbf{12b}_2L_2$ in DMSO while the equilibrium shifted towards the homoleptic assemblies when the solvent was changed to acetonitrile. Experimental van't Hoff analysis in combination with theoretical investigations suggested that the solvation entropy plays a key role in the solvent-dependent equilibrium shift.

The number of possible isomers and hence the complexity of the system rises when more than two differentiable ligands are combined. Zhang and coworkers described the stepwise formation of $Pd_2A_3B_1$ and $Pd_2A_2B_1C_1$-type cages by merging the CSE approach and endohedral steric bulk.[149,150] The latter strategy based on a similar ligand combination was applied earlier by Hooley and coworkers;[139] however, without additional bulk at the coordination site the heteroleptic cage was not obtained in a selective fashion. Clever and coworkers also utilized the CSE approach for the self-assembly of a series of $Pd_2A_3B_1$ cages.[151] Our group furthermore reported on *cis*- or *trans*-$Pd_2A_2B_1C_1$-type cages by combining the SCA approach with inter-ligand interactions or stoichiometry control, respectively.[113,152] Ligand **17a** features geometric complementarity with short ligands **20** enabling the selective formation of *cis*-$[Pd_2\mathbf{17a}_2\mathbf{20}_2]^{4+}$ cages. While being similar in shape, ligands **20a** and **20d** possess different electronic properties allowing for $CH_3\cdots\pi$ interactions if they sit adjacent to each other within the assembly ("adjacent backbone interaction", ABI). For this reason, a 1:1:1:2 mixture of Pd(II), **20a**, **20d**, and **17a** selectively affords *cis*-$[Pd_2\mathbf{17a}_2\mathbf{20a}_1\mathbf{20d}_1]^{4+}$ (Fig. 9a). Owing to its spring-like nature, ligand **17a** can also adopt nearly collinear binding vectors, as can be seen in the corresponding homoleptic cage $[Pd_2\mathbf{17a}_4]^{4+}$. Consequently, when two equivalents of **17a** were combined with convergent ligand **16** and divergent ligand **20d**, one equivalent of each, self-assembly into *trans*-$[Pd_2\mathbf{17a}_2\mathbf{16}_1\mathbf{20d}_1]^{4+}$ was observed.

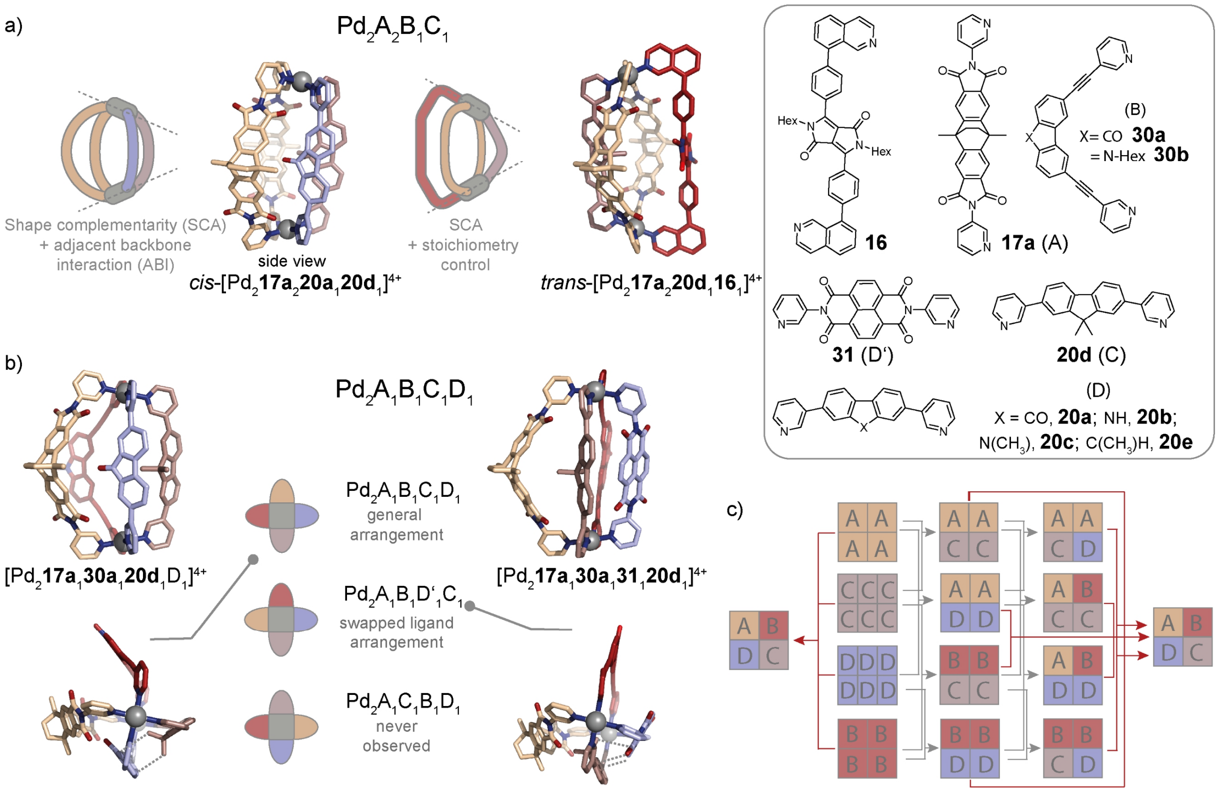

Fig. 9a) Structures of *cis*- and *trans*-$Pd_2A_2B_1C_1$ cages;[113,152] b) possible ligand arrangements in $Pd_2A_1B_1C_1D_1$ cages; c) schematic illustration of various cage-to-cage transformation pathways to afford $Pd_2A_1B_1C_1D_1$.[113]

In 2024, the Clever group described the selective self-assembly into $Pd_2A_1B_1C_1D_1$-type cages under thermodynamic control – a milestone achievement within the field.[113] This was again achieved through the combination of the SCA and ABI approaches. More precisely, convergent ligands **17a** (A) and **30a** (B) were combined with divergent ligands **20d** (C) and **20a** (D) and Pd(II) in a 1:1:1:1:1 ratio. Intriguingly, out of 55 possible homo- and heteroleptic assemblies, a single cage carrying all four ligands was afforded. By taking the two above-mentioned strategies into account, two isomers are possible, $[Pd_2\mathbf{17a}_1\mathbf{30a}_1\mathbf{20a}_1\mathbf{20d}_1]^{4+}$ ($Pd_2A_1B_1D_1C_1$) and $[Pd_2\mathbf{17a}_1\mathbf{30a}_1\mathbf{20d}_1\mathbf{20a}_1]^{4+}$ ($Pd_2A_1B_1C_1D_1$), of which only the latter is obtained (Fig. 9b). Presumably, incorporation of one count of ligand **17a** is favored since it allows for sufficient flexibility to adapt to a suitable N···N distance. Importantly, the cage could be afforded via multiple different pathways, corroborating its thermodynamic stability. An analogous $Pd_2A_1B_1C_1D_1$-type was formed when ligand **30b**, which is similar in shape to **30a**, was employed as ligand B. Furthermore, ligand **20a** (D) could be replaced by ligands **20b**, **20c**, and **20e**, that feature a π-surface suitable for CH_3···π interactions with **20d** as well. When ligand **31** based on naphthalenediimide (NDI) is employed as ligand D', the ligand arrangement is swapped (Fig. 9b). Here, ligand C offers its π-surface for CH_3···π interactions with ligand D'. This change in the ligand orientations presumably affects the geometric complementarity to ligands **17a** and **30a**, resulting in the swapped arrangement. The various types of heteroleptic dinuclear cages, $Pd_2A_2B_2$, $Pd_2A_3B_1$, $Pd_2A_2B_1C_1$, $Pd_2A_1B_1C_1D_1$ (*cis*- and *trans*-configurated where applicable), have also been synthesized by the Hiraoka group.[153] In these cases, a pathway-dependent approach was used, meaning that the self-assembly occurs in multiple steps and the outcome is not necessarily the thermodynamic product.

The SCA approach has been extended for the realization of heteroleptic three- and four-membered rings $Pd_3A_3B_3$ and $Pd_4A_4B_4$ by the Clever group.[72] Moreover, a heteroleptic tetrahedron was assembled from fluorene-based ligands with varying backbone-centered steric bulk, exploiting that the Pd_4L_8 tetrahedron features two differentiable edges (Fig. 6). This can be regarded as a steric variant of the aforementioned ABI approach.[112] Pill-shaped tetranuclear cages with the stoichiometry $Pd_4A_6B_2$ (or $Pd_4A_4B_2C_2$) were formed by bridging two Pd_2A_3 (or Pd_2A_2B)-type bowls with terephthalate[91] or strongly divergent bis-pyridyl ligands.[153] Chand and Yoshizawa described a $Pd_5A_5B_5$ ring,[154] also termed "truncated molecular star" and the group of Mukherjee constructed a trigonal prismatic cage $Pd_6A_6B_6$.[155] The group of Severin assembled tetrahedra $Pd_4A_4B_4$, trigonal prismatic and antiprismatic cages $Pd_6A_6B_6$ as well as tetragonal prismatic ones $Pd_8A_8B_8$.[140,156] Some of the just listed architectures, namely the pill-shaped and prismatic cages, are not possible to realize in a homoleptic fashion as they rely on two different ligand geometries. This shows that the heteroleptic self-assembly can not only be used as a tool for increasing the functional but also the structural diversity.

1.4. Chromophore-based coordination cages

Having covered the design principles for Pd(II)-based cages, this section aims at presenting coordination cages which have been equipped with chromophores with a particular focus on phenomena that emerge from the spatial proximity of multiple dyes. While cages based on various metal-ligand combinations will be explored, special emphasis will be put on Pd(II)-based cages for understanding how the Pd(II) nodes interfere with the ligand excited state properties.

The section follows the structure of a Jablonski diagram (Fig. 10):[157] Absorption of a photon with an energy of 1.8 to 3.3 eV leads to a colored compound (by our human eyes). The excited state can be deactivated through collisions or internal conversion (IC) or via emission of fluorescence. Furthermore, the system can undergo intersystem crossing (ISC) to a triplet state which can be deactivated via emission of phosphorescence. In the case of an adjacent energy or electron acceptor, the excitation energy can be transferred, leading to an electronically excited acceptor, or an electron can be transferred, leading to an electron-hole pair.

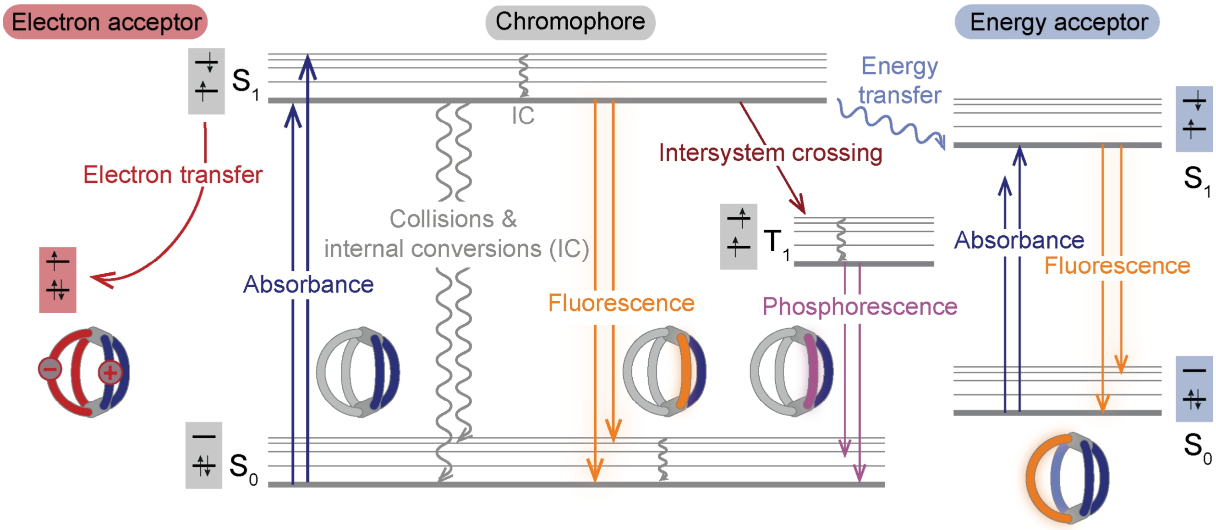

Fig. 10 Jablonski diagram showing the possible excited state process for a chromophore (gray) as well as for the chromophore in the presence of a suitable electron (red) or energy acceptor (blue).

1.4.1. Absorption

In 2021, the Clever Lab started to implement well-known „blockbuster” dyes in coordination cages and helicates.[70] Importantly, the employed coal-tar class of chromophores contain dialkyl amine functionalities (Fig. 11a) which are auxochromic groups, meaning that removing them, e.g. through the attachment of the typical alkyne or phenyl linkers, would drastically change the dyes' absorption properties. This was circumvented by the usage of piperazine linkers. Ligands **DYE-P**, equipped with pyridine donors, assemble into lantern-shaped cages $[Pd_2\textbf{DYE-P}_4]^{4+}$ while ligands **DYE-Q**, equipped with strongly convergent isoquinoline donor groups, assemble into helicates $[Pd_2\textbf{DYE-Q}_4]^{4+}$, consistent with the trends described in section 1.3.1. The strong absorption in the visible region was exploited for the recognition of chiral guests of suitable size by circular dichroism (CD) spectroscopy: addition of an anionic chiral guest to lantern-shaped cages or a mixture of *M*- and *P*-helicates, that are rapidly interconverting, led to the rise of a CD band in the visible range. This can be attributed to chiral induction as only the ligands but not the chiral guest absorb in this region. Hence, this work focused on the strategy for the integration of chromophores into cages to render rather flat dyes into three-dimensional assemblies for chiral recognition.

In a later study by the Clever group, Pd_2L_4 cages and helicates with ligands based on the blue chromophore azulene were investigated.[101] Interestingly, addition of a sulfonate guest to one of the cages resulted in a transformation into a distorted tetrahedron Pd_4L_8, which provided a suitable pocket for the sulfonate in terms of size and charge. Owing to the absorption in the visible region, this could be followed by the naked eye.

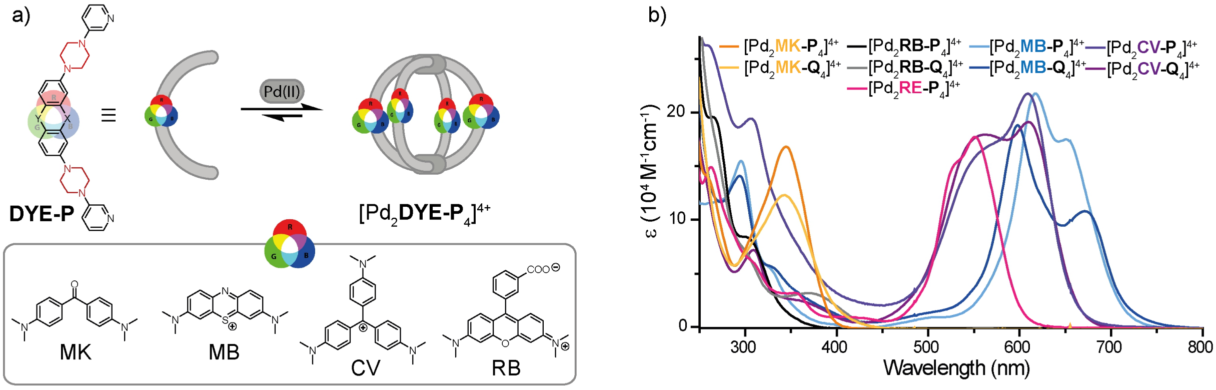

Fig. 11 Assembly of $[Pd_2\textbf{DYE-P}_4]^{4+}$ cages with bis-monodentate organic ligands **DYE-P** based on well-known chromophores MK, MB, CV, RB (structures in box); b) UV-Vis absorption spectra of the corresponding cages and helicates; reproduced and modified from ref[70] (*open access*).

In 2013, the Nitschke group reported on a M_4L_6-type tetrahedron with M = Zn(II) or Fe(II), respectively, and ligands based on boron dipyrromethene (BODIPY).[158] Binding of different anionic guests was accompanied by a color change. This allowed for the qualitative analysis of the anions with test strips coated with the cage. A later study by the same group found that BODIPY ligands sitting on the edges of M_4L_6 tetrahedra engage in dipole-dipole coupling.[159]

Besides embedding a chromophoric moiety into the organic ligands, the color can also stem from transitions in which the metal vertex is involved, such as metal-to-ligand charge transfer (MLCT) states. Examples for this are the tetrahedral cages Fe_4L_6 of the group of Nitschke. The color of the cages was exploited for following the phase transfer of the cage between different solvent layers.[160,161]

Absorption in the visible region was furthermore exploited for studying intrinsic chirality of coordination cages by CD spectroscopy. Landmark studies were published by

Lützen,[162,163] Natarajan,[164] and Clever[165] reporting on the self-assembly of chiral organic ligands based on BINOL, bimesityl, and helicene, respectively. Across these works it was found that the CD signal of the assemblies is increased compared to the ones of the free ligands. Furthermore, besides the earlier mentioned guest-to-host chirality transfer, also guest-induced modulation of the helical pitch[165] and host-to-guest chirality transfer[93] was probed via CD spectroscopy.

1.4.2. Luminescence

In 2023, the Clever group reported on another family of dye-based assemblies, this time with a focus on interactions between a varying number of stacked chromophores.[81] Formation of the diketopyrrolopyrrole (DPP)-based architectures was accomplished by altering the linker and donor group of the bis-monodentate ligands and consequently their binding vectors (Fig. 12a). Ligand **DPP1** with a comparably large bent angle forms three-membered ring $[Pd_3\textbf{DPP1}_6]^{6+}$. Here, the DPP moieties of ligands bridging the same edge possess a distance of ~ 9 Å, i.e. do not engage in π-π-stacking interactions. Isoquinoline-equipped ligand **DPP2** forms heteroleptic *trans*-$[Pd_2\textbf{DPP2}_2\textbf{CBZ}_2]^{4+}$ when combined with ligand **CBZ**, similarly to what has been reported by the group beforehand (section 1.3.3.).[141] In this architecture, the two **DPP** ligands crossing through the center of the cavity engage in π-π-stacking (distance ~ 4 Å). Ligand **DPP2** forms homoleptic single-bridged ravel $[Pd_2\textbf{DPP2}_3(CH_3CN)_2]^{4+}$ with an array of three stacked DPP moieties due to steric reasons (the two remaining coordination sites are occupied by solvent molecules). The highest count of four stacked chromophores was observed for the double-bridged ravel $[Pd_2\textbf{DPP3}_4]^{4+}$ of ligand **DPP3** (more details on the topologies in section 1.3.1.). Possible communication between the chromophores was investigated by steady state absorption and emission spectroscopy (Fig. 12b, c). First, with an increasing number of stacked chromophores in $[Pd_3\textbf{DPP1}_6]^{6+}$, $[Pd_2\textbf{DPP2}_3(CH_3CN)_2]^{4+}$, and $[Pd_2\textbf{DPP3}_4]^{4+}$, the absorption band in the visible region broadens and shifts bathochromically. Second, the redshift of the emission band between free ligand and assembly increases, and the emission quantum yield (QY) decreases (21%, 3%, 0.7%). While the observed photophysical properties for the homoleptic assemblies can hence be traced back to the number of closely interacting chromophoric moieties, heteroleptic cage $[Pd_2\textbf{DPP2}_2\textbf{CBZ}_2]^{4+}$ stands out with an exceptionally high QY for Pd(II)-based cages (over 50%) and its spectra do not follow the same trends. Presumably, intra-assembly excitation energy transfer between **CBZ** and **DPP2** accounts for this phenomenon.

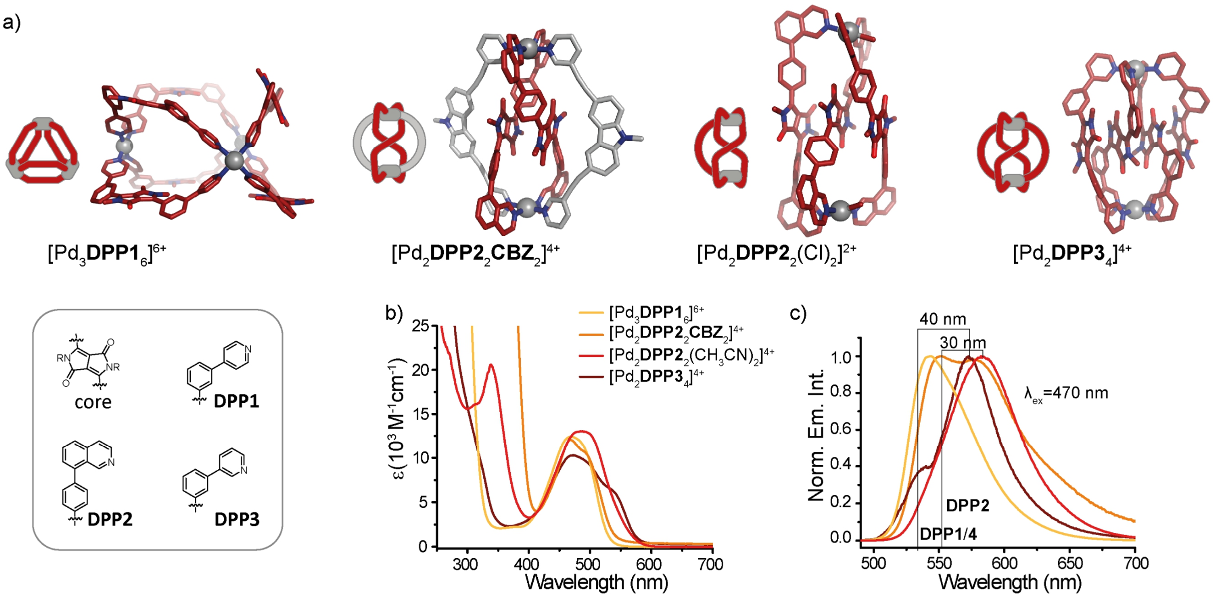

Fig. 12a) Structures of Pd(II)-based coordination assemblies $[Pd_3\mathbf{DPP1}_6]^{6+}$, $[Pd_2\mathbf{DPP2}_2\mathbf{CBZ}_2]^{4+}$, $[Pd_2\mathbf{DPP2}_3Cl_2]^{2+}$ (DFT calculated structure), and $[Pd_2\mathbf{DPP3}_4]^{4+}$, featuring a varying number of stacked DPP moieties; b) UV-Vis absorption and c) emission spectra of the assemblies; b) and c) reproduced from ref.[81] (*open access*).

Aside from the just described **DPP**-based systems, emissive coordination assemblies based on Pd(II) remain rare. Other examples include three- and four-membered rings as well as a heteroleptic tetrahedron, all with fluorenone based ligands, reported by the Clever group.[72,112] Furthermore, the group of Zysman-Colman reported four-membered rings Pd_4L_8 with ligands L based on phosphorescent Ru(II) or Ir(III) complexes.[166,167] The scarcity of luminescent Pd(II) assemblies can be explained by the open-shell nature of Pd(II) i.e. photoinduced charge transfer to Pd(II) represents for most assemblies a fast, dark excited state deactivation pathway.

Yoshizawa and coworkers nicely showcased this phenomenon by studying the photophysical properties of a range of capsules $[M_2\mathbf{ANT}_4]^{4+}$ assembled from anthracene-based ligands **ANT** with varying metal ions (M = Pd(II), Pt(II), Co(II), Cu(II), Ni(II), Mn(II), Zn(II), Hg(II)) (Fig. 13a).[168–170] Depending on the metal, the width of the band as well as the vibronic progression stemming from the absorption of the anthracene ligand changes slightly. However, overall, the different assemblies are pale yellow except for $[Cu_2\mathbf{ANT}_4]^{4+}$. The latter also shows solvatochromism: intensity and position of a low-energy band that can be assigned to a Cu(II)-centered d-d transition change upon switching the solvent. Moreover, the anthracene-centered emission of the assemblies showed to be highly dependent on the nature of the metal ion: the blue emission of the ligand with a QY of ~ 80% was completely retained in $[Zn_2\mathbf{ANT}_4]^{4+}$, weak emission was observed for the cages with Mn(II), Ni(II), and Hg(II) (the latter is not shown here) while complete emission quenching occurred for Pd(II), Pt(II), Co(II), and Cu(II) (Fig. 13b).

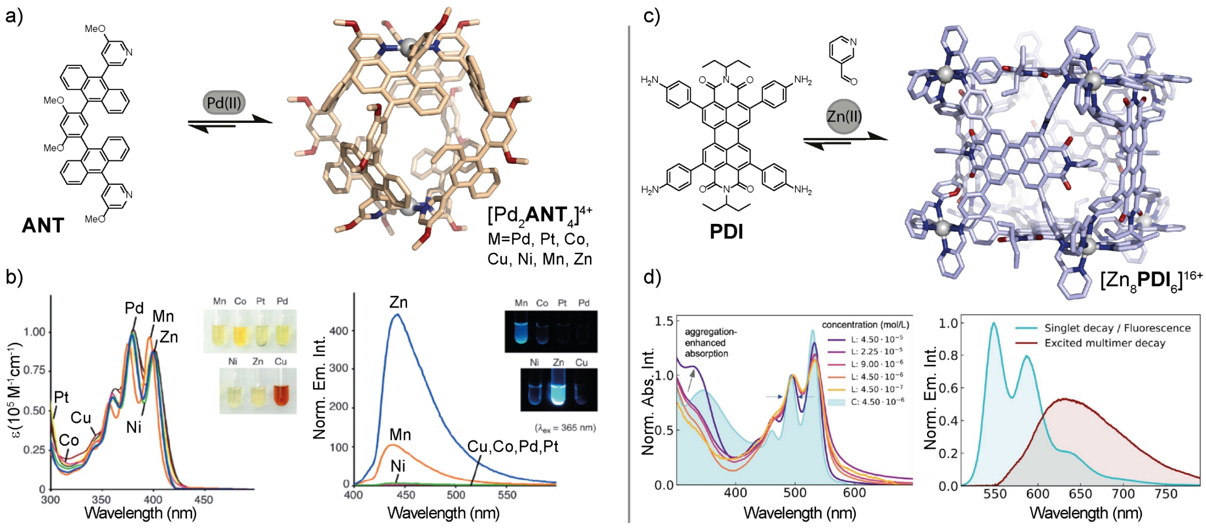

Fig. 13a) Self-assembly of capsules [M$_2$**ANT**$_4$]$^{4+}$ (M = Pd, Pt, Co, Cu, Ni, Mn, Zn) and X-ray structure of [Pd$_2$**ANT**$_4$]$^{4+}$; b) UV-Vis absorption (left) and emission spectra (right) of the capsules, reproduced with permission from ref[169] ; c) Self-assembly and X-ray structure of cube [Zn$_8$**PDI**$_6$]$^{16+}$; d) UV-Vis absorption spectra of [Zn$_8$**PDI**$_6$]$^{16+}$ and **PDI** at different concentrations (left) and emission spectra of [Zn$_8$**PDI**$_6$]$^{16+}$(right, prompt singlet state emission in cyan, delayed emission in red), reproduced and modified from ref[82] (*open access*).

For simultaneously exploiting ligand-based emission and the perks of working with Pd(II), Crowley[73] as well as Kühn[171] attached organic fluorophores and phosphorescent Ru(II) complexes, respectively as exohedral pending groups on the ligands. This strategy allowed at least for partial retention of the luminescent properties. However, the fluorophores have a comparably large distance from the cavity, making it less suitable for applications which rely on interactions between adjacent ligands or between ligands and guest (such as induced chirality and luminescence quenching upon guest binding).

The benign nature of Zn(II) vertexes in the context of the assemblies' photophysical properties was exploited by the groups of Feldmann and Nitschke for constructing an emissive cube [Zn$_8$**PDI**$_6$]$^{16+}$ through sub-component self-assembly of ligand **PDI** (based on perylene diimide, PDI), picolinal, and Zn(II) (Fig. 13c).[82] Free ligand **PDI** suffers from excited state quenching through intramolecular rotations and vibrations as well as from uncontrolled aggregation. Hence, the linewidth of the $S_0 \rightarrow S_1$ absorption of **PDI** is rather broad and at a certain threshold concentration, an additional feature arises owing to aggregation-induced absorption (Fig. 13d). Furthermore, dilute solutions of the ligands are non-emissive. Upon aggregation, only little emission is recovered (QY ~ 0.1%) and the vibrational progression indicates H-type aggregation. By contrast, the vibronic progression of the $S_0 \rightarrow S_1$ absorption of **PDI** is defined in cube [Zn$_8$**PDI**$_6$]$^{16+}$ and mirror-image emission with a 100-fold increase in emission intensity is observed. The combination of the restriction of intramolecular motion and the absence of strong inter-chromophore coupling in the ground state hence ensures high electronic purity of the **PDI** moieties. Furthermore, upon photoexcitation a new emission band was observed, which is absent in the steady state emission spectra (Fig. 13d). This was assigned to an excited multimer, meaning that an unknown number of chromophoric moieties couple within the cube in the excited state. In-depth investigation with transient absorption spectroscopy furthermore revealed that this state and a triplet state serve as excitation reservoirs for repopulating the singlet state, leading to delayed fluorescence. Similarly, the group of Sun reported on ligand-centered excited multimer emission in lanthanide-based cubes.[172]

Würthner and coworkers observed that encapsulation of polyaromatic hydrocarbons (PAHs) into a tetrahedral cage Zn$_4$L$_6$ with PDI-based ligands results in quenching of the emission of the latter, which is of interest for PAH detection.[173] The group of Nitschke reported on a water soluble, fluorescent tetrahedron Zn_4L_6 with ligands based on triazatriangulenium, i.e. the ligands increased the overall positive charge of the cage.[174] This cage was exploited for sensing nucleotides through emission quenching upon encapsulation.

In addition, the self-assembly into cages represents an attractive tool for enhancing the emission of so-called aggregation-induced emission luminophores.[175,176] Commonly, the emission of the latter is quenched in the non-aggregated form since molecular rotations and/or vibrations lead to efficient excited state deactivation. These dynamics significantly slow down upon aggregation and emission becomes a competitive pathway. In a similar fashion, molecular motion can be suppressed upon self-assembly; for this, the term coordination-enhanced emission was coined. Examples for this include works by groups of Stang[177] and Zhang[178] on luminescent Pt(II)-based cages with tetraphenylethylene (TPE) chromophores.

Chromophores that are positioned in a chiral environment can furthermore emit CPL, which is of interest for the development of advanced optical materials and sensors. For quantification of the CPL signal, the luminescence dissymmetry factor g_{lum} value is used, which corresponds to the normalized difference between left- and right-handed emitted light.[179] Self-assembly was exploited for connecting emissive and chiral moieties. The Clever group synthesized a $Pd_2A_2B_2$-type heteroleptic cage by combining a fluorenone-based ligand A, which keeps its emission within the assembly, with a chiral helicene-based ligand B.[145] The helicene-based ligand leads to an overall chiral conformation of the cage, allowing for CPL from the initially achiral fluorenone-based ligand. In a follow-up study, the helicene-based ligand was replaced by a non-aromatic chiral ligand derived from cyclohexane.[146] This allowed for enhancing the g_{lum}-value and an unambiguous assignment of the emission band to the fluorenone-based ligand. Importantly, the g_{lum} value is influenced by magnitude and relative orientation of electric and magnetic transition dipole moments of the CPL emitter.[180,181] In the described example, the dissymmetry factor of the system is low (~ 10^{-3}) owing to the small magnetic and large electric transition dipole moment of organic fluorophores. By contrast, lanthanides stand out with their magnetic-dipole allowed transitions, resulting in large dissymmetry factors.[180] For achieving efficient CPL, they must be situated in a chiral environment in close proximity to antenna-chromophores. The latter sensitize the lanthanide emission, allowing these systems to overcome the low extinction coefficients which is an intrinsic drawback of lanthanide emitters. In multiple works, the self-assembly to helicates and cages has been exploited for combining chiral moieties, antenna chromophores, and lanthanides. Major contributions in this field were published by the group of Sun[182–184] among others.[185,186]

1.4.3. Photoinduced energy transfer

Multiple groups observed energy transfer between similar (energy migration) or different chromophores which have been brought into spatial proximity in coordination cages or in their host-guest complexes. The first study on energy transfer in coordination cages was reported by the group of Tahara, who investigated a Pd(II)-based octahedral cage with triazine panels ("Fujita's cage") with an acridine guest.[187] Through a combination of steady state and time-resolved emission spectroscopy, the authors found that photoexcitation of the host is followed by energy transfer to the acridine guest which subsequently deactivates through the emission of fluorescence. In a later study, a bis-anthracene guest, more electron rich in nature, was encapsulated into the same host.[188] The host-guest complex possessed an emissive charge transfer state. More precisely, it was found that the photoexcited guest undergoes three different radiative decay processes: fluorescence from a locally excited state, fluorescence from a twisted, guest-centered charge transfer state and emission from a host-guest charge transfer state.

Ward and coworkers encapsulated pyrene-derivative **PYR** into emissive cube $[Cd_8\mathbf{NAP}_{12}]^{16+}$ (Fig. 16a).[189] Stepwise addition of **PYR** to a solution of the host was accompanied by a progressive reduction of the emission of the host while the emission of **PYR** increased, albeit its small extinction coefficient at the excitation wavelength. Displacement of **PYR** through the addition of a competitive guest led to recovery of the emission of $[Cd_8\mathbf{NAP}_{12}]^{16+}$ and diminishment of the one of **PYR**, evidencing that host-guest-complexation was a prerequisite for the energy transfer process. In a similar fashion, He and coworkers investigated energy transfer between a Zn_8L_6 box, where L is a TPE-based ligand, and two anionic energy acceptor guests.[190] For one host-guest complex, the output energy was used for promoting a dehalogenation reaction. In the second system, fine-tuning of the host-to-guest ratio allowed for the generation of white light.

The group of Zysman-Colman reported on a cube Pd_6L_{12} with a carbazole-based ligand (90° bent angle, as described in section 1.3.2.), functionalized with benzophenone, in order to endow the ligand with thermally-activated delayed fluorescence properties.[191] While the latter was not retained in the cage, the short-lived fluorescence was not fully quenched. Addition of guest Rose Bengal to the cage resulted in gradual quenching of the emission of the cage accompanied by a rise in the emission of the guest. Owing to a suitable overlap of the emission spectrum of the host and the absorption spectrum of the guest, the authors proposed Förster resonance energy transfer (FRET) as likely mechanism. In another work, the group investigated energy transfer in rings Pd_4L_8 based on chiral Ir(III) metalloligands.[167] An Ir(III) complex possessing blue phosphorescence was chosen as an energy transfer partner for the red-phosphorescent host. The authors followed addition of the host to the guest by emission spectroscopy, unveiling guest-to-host energy transfer. Owing to the little spectral overlap, the authors suggested that energy transfer occurs via the Dexter exchange mechanism.

Zhang and coworkers reported on ligand-to-ligand energy transfer in prismatic Pt(II)-based coordination cages.[178] In $[Pt_8\mathbf{TPE}_2\mathbf{MeBn}_4]^{8+}$, energy is transferred from the photoexcited dimethoxy benzene-based pillar **MeBn** to the **TPE**-based faces (Fig. 14a). The authors observed that upon titration of **TPE** to a mixture of **MeBn** and the metal precursor, the emission of **MeBn** gradually decreases and the emission at > 500 nm, stemming from the **TPE** faces, rises. When pillar **RhB**, appended with Rhodamine B, is used for the formation a prismatic cage, which is otherwise analogous to the just described one, the direction of energy transfer is reversed, i.e. excitation of the **TPE** faces is followed by energy transfer to the **RhB** pillars whose emission is then observed (Fig. 14b). Yang and coworkers observed a similar face-to-pillar energy transfer process in $[Pt_8\mathbf{TPE}_2\mathbf{BDY2}_4]^{8+}$ when BODIPY-based pillars **BDY2** were used (Fig. 14c).[192] The cage and Nile Red as second energy acceptor were incorporated into vesicular structures based on amphiphilic polymers. This brought the cage and Nile Red in sufficient spatial proximity for triggering a two-step energy transfer process, i.e. excitation of the **TPE** faces results overall in emission from Nile Red. The authors were further able to show that the system photocatalyzes a dehalogenation reaction.

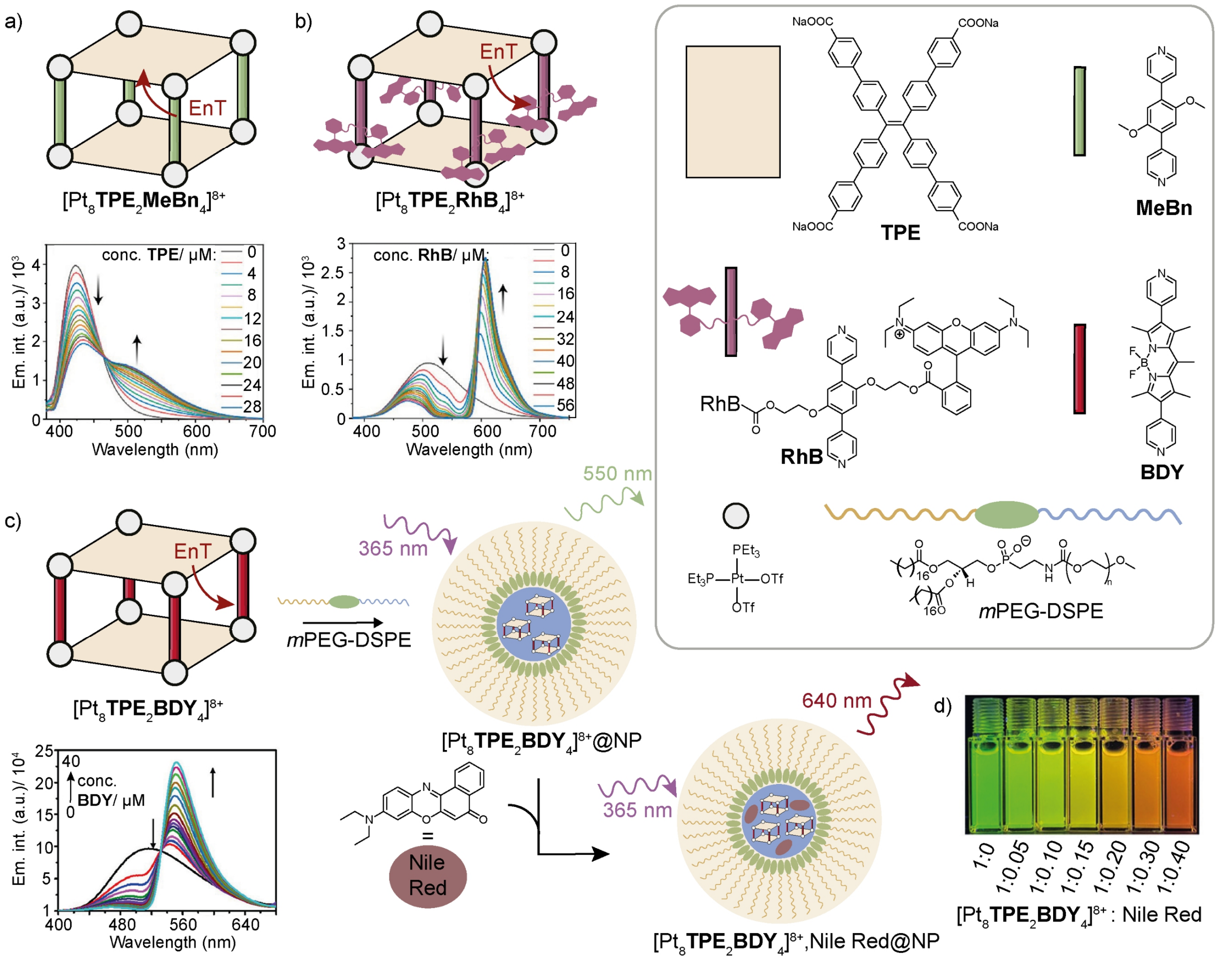

Fig. 14 Ligand-to-ligand photoinduced energy transfer in prismatic Pt(II)-based coordination cages; a) pillar-to-face energy transfer, emission spectra for the titration of **TPE** to a mixture of **MeBn** and Pt(PEt$_3$)$_2$(OTf)$_2$; b) face-to-pillar energy transfer, emission spectra for the titration of **RhB** to a mixture of **TPE** and Pt(PEt$_3$)$_2$(OTf)$_2$; c) face-to-pillar energy transfer, emission spectra for the titration of **BDY** to a mixture of **TPE** and Pt(PEt$_3$)$_2$(OTf)$_2$, illustration of two-step energy transfer in nanoparticles (NP) loaded with [Pt$_8$**TPE**$_2$**BDY**$_4$]$^{8+}$ and Nile Red, and photographs of [Pt$_8$**TPE**$_2$**BDY**$_4$]$^{8+}$@NP with varying concentrations of Nile Red under illumination, emission spectra and photograph reproduced and modified with permission from refs[178,192] .

Mukherjee and coworkers brought prismatic cages Pt$_8$TPE$_2$L$_4$, whereby TPE serves as energy donor, in close proximity to small molecule energy acceptors via formation of vesicular structures[193] or via aggregation[194] to achieve energy transfer. Stang also reported on bimolecular energy transfer between a Pt$_6$A$_2$B$_3$ prismatic cage and a small molecule energy acceptor following a static mechanism.[195] Zhang and coworkers investigated energy transfer from a prismatic cage Pt$_{12}$A$_2$B$_3$ to a naphthalimide derivative, known for its aggregation caused quenching properties.[196] In the presence of the cage, the emission of the naphthalimide derivative, sensitized by energy transfer from the TPE faces of the cage, can be observed in both, solution and solid state. The energy transfer efficiency is lower in solution, which the authors assigned to weak host-guest properties. In a follow-up study, a host with a larger π-surface was designed, which led to an enhancement of the host-guest affinity in solution.[197] Photophysical characterization of a host-guest complex with a PDI derivate as guest revealed host-to-guest energy transfer. Furthermore, adjustment of the host-to-guest ratio allowed for white light generation.

Multiple works on photoinduced energy transfer in metal-organic rings have been reported by Würthner[198–200] and Yang[201–203] which are not discussed here further. However, an in-depth study of energy transfer in Pt(II)-based rings, reported by Pistolis, will be highlighted owing to the investigation of energy migration. The authors combined a BODIPY Pt(II) tecton **BDY2** with either linear (**PDI2**) or convergent (**PDI3**) PDI-based ligands that assembled to heteroleptic rings [Pt_8**BDY2**$_4$**PDI2**$_4$]$^{8+}$ and [Pt_4**BDY2**$_2$**PDI3**$_2$]$^{4+}$, respectively.[204] With a *cis*-protected Pt(II) source, ligand **PDI2** furthermore assembles to homoleptic ring [Pt_4**PDI2**$_4$]$^{4+}$ (Fig. 15a). Steady state spectroscopy revealed that excitation of the BODIPY chromophores in the heteroleptic rings contributes to the PDI emission while the BODIPY emission is quenched. Furthermore, pump-probe emission spectroscopy unveiled that the time constant for the fast decay of the emission of the BODIPY moieties matches the time constant for a second rise component of the emission of PDI, evidencing energy transfer from **BDY2** to PDI with time constants of ($\tau = 55$ ps [Pt_8**BDY2**$_4$**PDI2**$_4$]$^{8+}$) and ($\tau = 26$ ps [Pt_4**BDY2**$_2$**PDI3**$_2$]$^{4+}$), respectively. The difference in energy transfer rates between the two rings can be explained based on the varying donor-acceptor distances within the framework of Förster's theory. For getting insight into energy migration between the **PDI** ligands, the authors compared the fluorescence anisotropy decay of the three rings with the one of free ligand **PDI2**, in which energy migration can be excluded as anisotropy decay channel (no adjacent PDI). Owing to the symmetrical nature of the rings, it was assumed that energy migration occurs with a single rate constant k_{hopp} (Fig. 15b). The closer the adjacent PDI moieties are in the metal-organic ring, the faster is the anisotropy decay, hence the faster is the energy migration ([Pt_4**PDI2**$_4$]$^{4+}$: $\tau = 1.25$ ps, [Pt_4**BDY2**$_2$**PDI3**$_2$]$^{4+}$: $\tau = 33.5$ ps, [Pt_8**BDY2**$_4$**PDI2**$_4$]$^{8+}$: $\tau = 216$ ps, and **PDI2**: $\tau = 330$ ps). Theoretical calculations underpin that energy migration also occurs via the Förster mechanism. Energy migration was also found in porphyrin zinc(II) boxes, as described by Osuka and coworkers.[205] The authors thoroughly studied the fluorescence decay, transient absorption, as well as transient absorption and emission anisotropy decay of the boxes. Furthermore, they varied the distance between the chromophores through incorporation of a different number of phenyl linkers and found that energy hopping can be described based on the Förster theory. Indications for energy hopping between adjacent chromophoric ligands was also reported for Raymond's Ga(III) cage Ga_4L_6.[206]

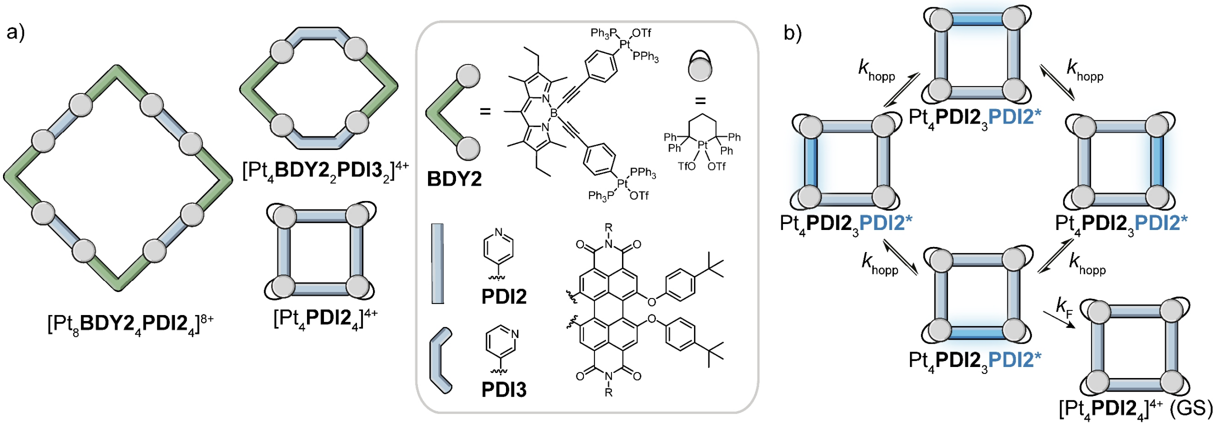

Fig. 15 Structures of metal-organic rings [Pt_8**BDY2**$_4$**PDI2**$_4$]$^{8+}$, [Pt_4**BDY2**$_2$**PDI3**$_2$]$^{4+}$, and [Pt_4**PDI2**$_4$]$^{4+}$ and of the respective ligands; b) illustration of the kinetic scheme for energy migration in [Pt_4**PDI2**$_4$]$^{4+}$.[204]

Application of photoinduced energy transfer in coordination cages include lanthanide-emission sensitization as already touched upon in the last section. Here, the organic ligands act as antenna for sensitizing emission of the lanthanide nodes. Initial works on helicates have been carried out by Bünzli, Hopfgartner, and Piguet.[207–209] Landmark studies on this with cages have been carried out by the group of Sun.[182,210] Recently, they reported on upconversion in lanthanide-based cages.[172] Furthermore, cages have been exploited for singlet oxygen sensitization, i.e. energy transfer occurs from a photosensitzer, that is either part of the cage framework or encapsulated within the cage, to oxygen.[117,211–214] In contrast to the earlier mentioned undesirable consequences of heavy metals on the excited state photophysics of the cages, their presence can lead to promotion of ISC (heavy atom effect) and hence to an increase of the sensitization efficiency. For example, Preston and Crowley reported on a three-membered ring Pd_3L_6 with ligands L based on Pt(II) complexes.[215] With a singlet-oxygen sensitive colorimetric probe, the authors evidenced the singlet oxygen sensitization capability of the ring. Anthracene, which can be incorporated into the clefts of the ring, is converted into 9,10-dihydro-9,10-epidioxyanthracene in the presence of light, oxygen, and the metal-organic ring. This showcases how multiple properties of the assembly, here the host-guest and photosensitizing properties, act in synergy for one emerging function.

1.4.4. Photoinduced electron transfer

The group of Ward reported on photoinduced electron transfer from a cubic coordination cage to encapsulated guests. The cage consists of naphthalene-based ligands **NAP** and Cd(II) nodes ($[Cd_8\mathbf{NAP}_{12}]^{16+}$)[189] or alternating Zn(II) and Os(II) nodes ($[Os_4Zn_4\mathbf{NAP}_{12}]^{16+}$),[216] respectively (Fig. 16a). Use of closed-shell metal Cd(II) as vertices allows for a retention of the emission of ligand **NAP** in the free host $[Cd_8\mathbf{NAP}_{12}]^{16+}$. However, encapsulation of guest **TCB** leads to a gradual quenching of the ligand-centered emission. In order to get insight into the nature of the quenching, the authors investigated the host and the host-guest complex with transient absorption spectroscopy. For the free host, excitation of the naphthalene array (290 nm) results in broadened positive signals at around 380 and 550 nm owing to the singlet-singlet excited state absorption. In contrast, in the presence of the guest, the absorbance between 380-460 nm is increased and a new feature at 450 nm arises (Fig. 16b). These spectral changes can be explained by the formation of the naphthyl radical cation and the guest radical anion. The host-to-guest charge separated state decays within 160 ps. Fluorescence quenching upon guest encapsulation was shown for two other electron-acceptor guests; however, the excited state dynamics of these systems were not investigated. Aiming at long-lived excited states, the authors incorporated Os(II) nodes into the cage. For this, the kinetically inert mononuclear Os(II) complexes were synthesized, followed by coordination to Zn(II), leading to cage $[Os_4Zn_4\mathbf{NAP}_{12}]^{16+}$. Encapsulation of guest **TCB** and two other small, neutral electron deficient molecules is accompanied by a quenching of the phosphorescence of the Os(II) complex, indicative for host-to-guest electron transfer. Transient absorption spectroscopy revealed that photoexcitation into the ^{1}MLCT manifold of the Os(II) coordination complexes leads to rise and decay of an ^{3}MLCT state for both, a mononuclear reference complex and cage $[Os_4Zn_4\mathbf{NAP}_{12}]^{16+}$. In the presence of electron acceptor guests, the rise and decay of the features of the host-to-guest charge separated state were observed. For the host-guest complex with **TCB**, the grow-in of the feature at 460 nm assignable to $\mathbf{TCB}^{\cdot-}$ is particularly visible (Fig. 16b). For the three complexes with different electron acceptor guests, rise and decay of the features occur on similar time scales, more precisely within 20 ps and 200 ps, respectively. Two elegant control experiments were performed to assure that electron transfer relies on the spatial proximity within the host guest complex and does not occur on the intermolecular level: first, a photophysically innocent but higher affinity guest was added to the $\mathbf{TCB}@[Os_4Zn_4\mathbf{NAP}_{12}]^{16+}$ complex. Second, they combined guest **TCB** with a mononuclear Os(II) reference complex. In both experiments, the features of the host-to-guest charge separated state were absent.

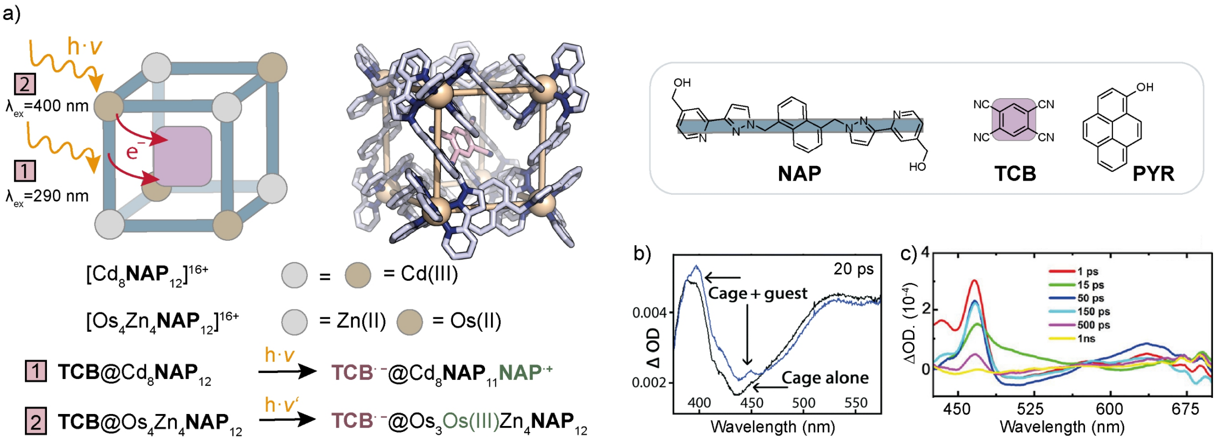

Fig. 16a) Schematic representation of light-induced electron transfer pathways in host-guest complexes **TCB**@[Cd$_8$**NAP**$_{12}$]$^{16+}$ and **TCP**@[Os$_4$Zn$_4$**NAP**$_{12}$]$^{16+}$ and X-ray structure of **TCB**@[Cd$_8$**NAP**$_{12}$]$^{16+}$; b) normalized transient difference spectra of [Cd$_8$**NAP**$_{12}$]$^{16+}$ (black) and **TCB**@[Cd$_8$**NAP**$_{12}$]$^{16+}$ (blue) at a time delay of 20 ps (λ_{ex} = 290 nm); c) transient difference spectra of **TCP**@[Os$_4$Zn$_4$**NAP**$_{12}$]$^{16+}$ at different time delays (λ_{ex} = 400 nm); transient difference spectra reproduced and modified from refs[189,216] (*open access*).

In 2022, the Clever group reported on host-to-guest electron transfer within a lantern-shaped cage.[217] The donor cage [Pd$_2$**PTZ-Ph**$_4$]$^{4+}$ is based on phenyl-spaced phenothiazine ligand **PTZ-Ph** and an anthraquinone disulfonate **ANQ-DS** was used as electron accepting guest (Fig. 17a). The combination of these two redox active moieties was used in purely organic donor-acceptor systems beforehand[218] and by the same group also for ligand-to-ligand electron transfer in Pd(II)-based double cages,[75] as will be discussed later. The steady state absorption spectrum of **ANQ-DS**@[Pd$_2$**PTZ-Ph**$_4$]$^{4+}$ is mainly a superposition of the spectra of its components, indicating that electronic communication between the donor cage and the acceptor guest in the electronic ground state is negligible. The excited state dynamics of the free host and the host-guest complex were studied separately. Photoexcitation of the phenothiazine-based ligands in the free host leads to population of the excited singlet state with maxima at 450 and 613 nm (Fig. 17c). In accordance with the completely quenched fluorescence in the cage, these features disappear within 0.7 ps and new features at 500 and 700 nm arise. The latter are assigned to the phenothiazine radical cation, formed through charge transfer to the Pd(II) nodes. This ligand-to-metal charge transfer (LMCT) state decays quickly ($\tau \sim 0.9$ ps). In the presence of the guest **ANQ-DS**, the phenothiazine excited singlet state decays quicker, indicating the existence of an additional decay channel, and a slight hypsochromic shift of the 613 nm band is observed. The latter coincides with the band of the guest radical anion, showing that host-to-guest electron transfer occurred. This host-to-guest charge separated state (HGCS) decays within 2.5 ps (Fig. 17b). Hence, assuming that the LMCT dynamics are similar in the free host and in the host-guest complex, a yield of $\Phi_{HG} = k_{HG}/(k_{LM}+k_{HG})$ = 44% can be determined.

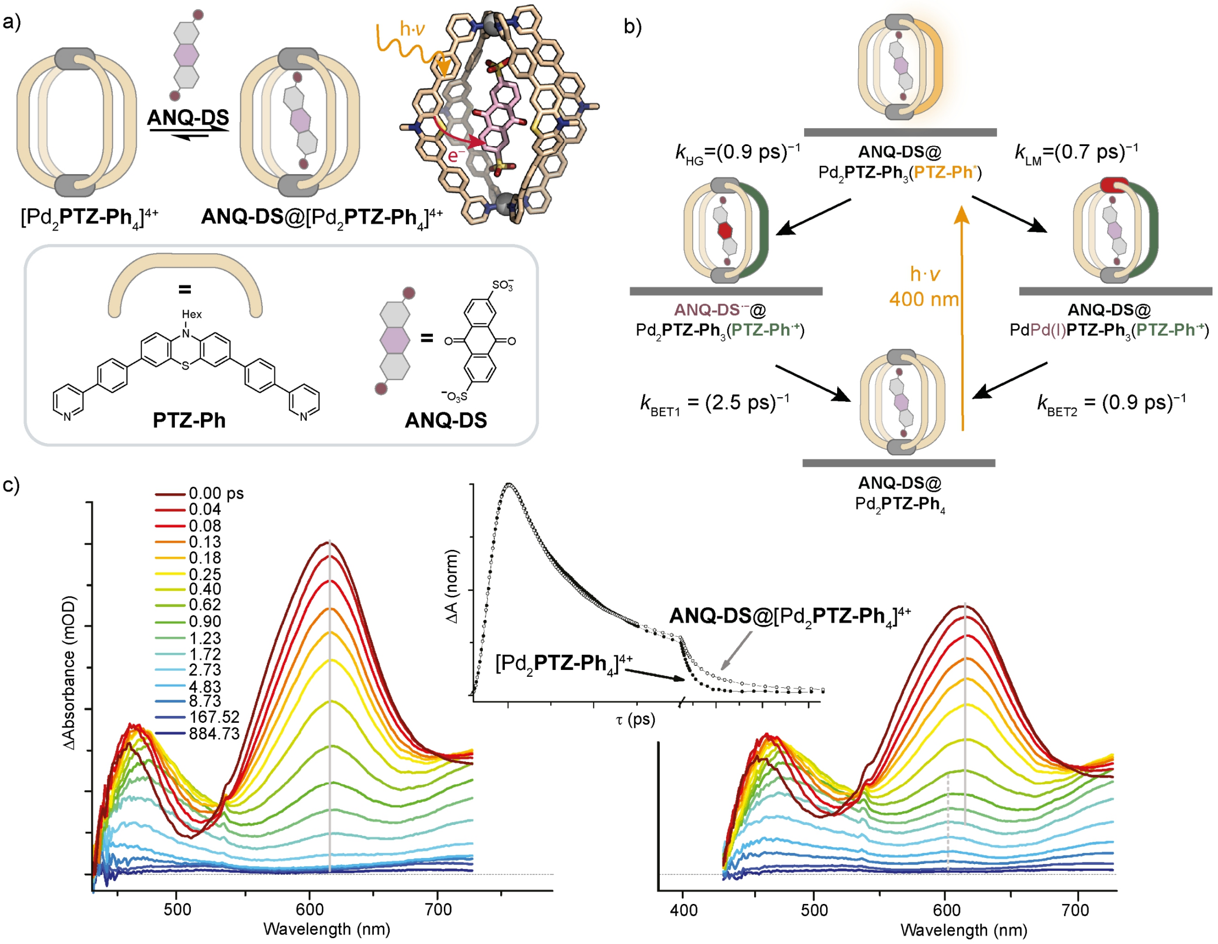

Fig. 17a) Structure of host-guest system **ANQ-DS**@[Pd$_2$**PTZ-Ph**$_4$]$^{4+}$; b) overview of excited state processes in **ANQ-DS**@[Pd$_2$**PTZ-Ph**$_4$]$^{4+}$; c) transient difference spectra at various time delays for free host [Pd$_2$**PTZ-Ph**$_4$]$^{4+}$ (left) and host-guest complex **ANQ-DS**@[Pd$_2$**PTZ-Ph**$_4$]$^{4+}$ (right), and their kinetic traces at 613 nm (middle), transient difference spectra and decay traces reproduced and modified from ref[217] (*open access*).

Many other works report on indications for photoinduced electron transfer between host and guest, often proposed as an explanation for the quenched emission of the host-guest complex. For example, the group of Zysman-Colman reported on gradual quenching of a Pd$_6$L$_{12}$ cube upon addition of fluorescein as guest.[191] Supported by a negative free energy for photoinduced electron transfer, estimated based on the ground state electrochemical and photophysical properties, the authors concluded that light-induced electron transfer from fluorescein to the carbazole ligands of the host occurs. In another fashion, Shionoya and coworkers studied a Zn-porphyrin derivate functionalized with pyridine donors which form a dimer upon addition of Ag(I).[219] The distance between the two porphyrins allows for intercalation of flat aromatics, such as 1,4-naphthoquinone. Upon addition of the latter, the emission of the porphyrin dimer is quenched, suggesting the presence of host-to-guest electron transfer. In 2011 and 2014, Mukherjee, Chi, and Stang reported on metal-organic rings and cages for the sensing of nitroaromatics.[220,221] More precisely, the fluorescence intensity of the assemblies decreased in the presence of nitroaromatic compounds which was used as a readout and traced back to photoinduced electron transfer.

Contrasting with the numerous examples for light-induced charge separation between host and guest, ligand-to-ligand electron transfer in coordination cages is significantly less explored. In 2016 and 2017, the Clever group reported on heteroleptic interlocked double cages [Pd$_4$**PTZ**$_n$**ANQ**$_{(8-n)}$]$^{8+}$ (n = 0-8) with a statistical distribution of phenothiazine-based ligand **PTZ** and anthraquinone-based ligand **ANQ** within the cage framework.[75,222] Noteworthy, a mixture of the preformed homoleptic double cages [Pd_4**PTZ**$_8$]$^{8+}$ and [Pd_4**ANQ**$_8$]$^{8+}$ is kinetically stable (Fig. 18a). This is attributable to the mechanical interlocking and advantageous for control experiments with a mixture of the purely homoleptic cages. Electrochemical investigations showed that formation of the double cage is accompanied by an anodic shift for the donor ligand and by a cathodic shift for the acceptor ligand. No further shift is observed in the heteroleptic double cages which would point towards strong electronic interactions in the ground state. However, the steady state absorption spectrum of the heteroleptic cage [Pd_4**PTZ**$_n$**ANQ**$_{(8-n)}$]$^{8+}$ (n = 0-8) cannot be reproduced by the sum of the spectra of the homoleptic cages [Pd_4**PTZ**$_8$]$^{8+}$ and [Pd_4**ANQ**$_8$]$^{8+}$, for instance in the low-energy region where charge transfer bands are expected, indicating that there is some kind of electronic communication (Fig. 18b). Deep insight into the excited state dynamics was gained by investigating the ligands, homoleptic double cages, and heteroleptic [Pd_4**PTZ**$_n$**ANQ**$_{(8-n)}$]$^{8+}$ (n = 0-8) with transient absorption spectroscopy in the visible and the mid infrared probe (IR) region. In short, photoexcitation of ligand **ANQ** and its homoleptic cage [Pd_4**ANQ**$_8$]$^{8+}$ leads to population of the excited singlet state, followed by intersystem crossing. Free ligand **PTZ** forms a long-lived emissive state. In contrast, the emission of the homoleptic cage [Pd_4**PTZ**$_8$]$^{8+}$ is quenched and instead, ultrafast rise of the features of the phenothiazine radical cation are observed. This was attributed to an LMCT state, decaying within 1.3 ps. Upon photoexcitation of the donor-acceptor cage mixture, a spectrum resembling the superposition of donor radical cation and acceptor radical anion was observed, indicating that ligand-to-ligand electron transfer occurred (Fig. 18c). Importantly, such a spectrum was not observed for the kinetically stable mixture of the two homoleptic cages [Pd_4**PTZ**$_8$]$^{8+}$ and [Pd_4**ANQ**$_8$]$^{8+}$, showing that electron transfer relies on the spatial proximity of **PTZ** and **ANQ** within the donor-acceptor cage and does not occur intermolecularly. However, a definite conclusion about the formation of the acceptor radical anion was difficult solely based on the transient difference spectra in the visible region owing to the broad and featureless absorption of the anthraquinone radical anion which overlaps with the one of the phenothiazine radical cation. The transient difference spectra in the IR probe region, on the other hand, provided unambiguous proof for the formation of both radical ions upon photoexcitation of [Pd_4**PTZ**$_n$**ANQ**$_{(8-n)}$]$^{8+}$ (n = 0-8).[222] Triexponential fit of the decay trace(s) led to τ_1 = 3.6 ps (82%), τ_2 = 44 ps (12%), and τ_3 > 1.5 ns (6%) for the lifetimes of the ligand-to-ligand charge separated state. It is worth noting that more than three different charge separated states might be formed, which is realistic regarding the number of different donor-acceptor distances in the statistical mixture of double cages. Owing to the statistical distribution of donor and acceptor moieties, the lifetimes cannot be assigned to a specific charge-separated state, impeding optimization of the arrangement of the photoredox active moieties. This shortcoming will become a major motivation for the design of defined donor-acceptor cages in this thesis.

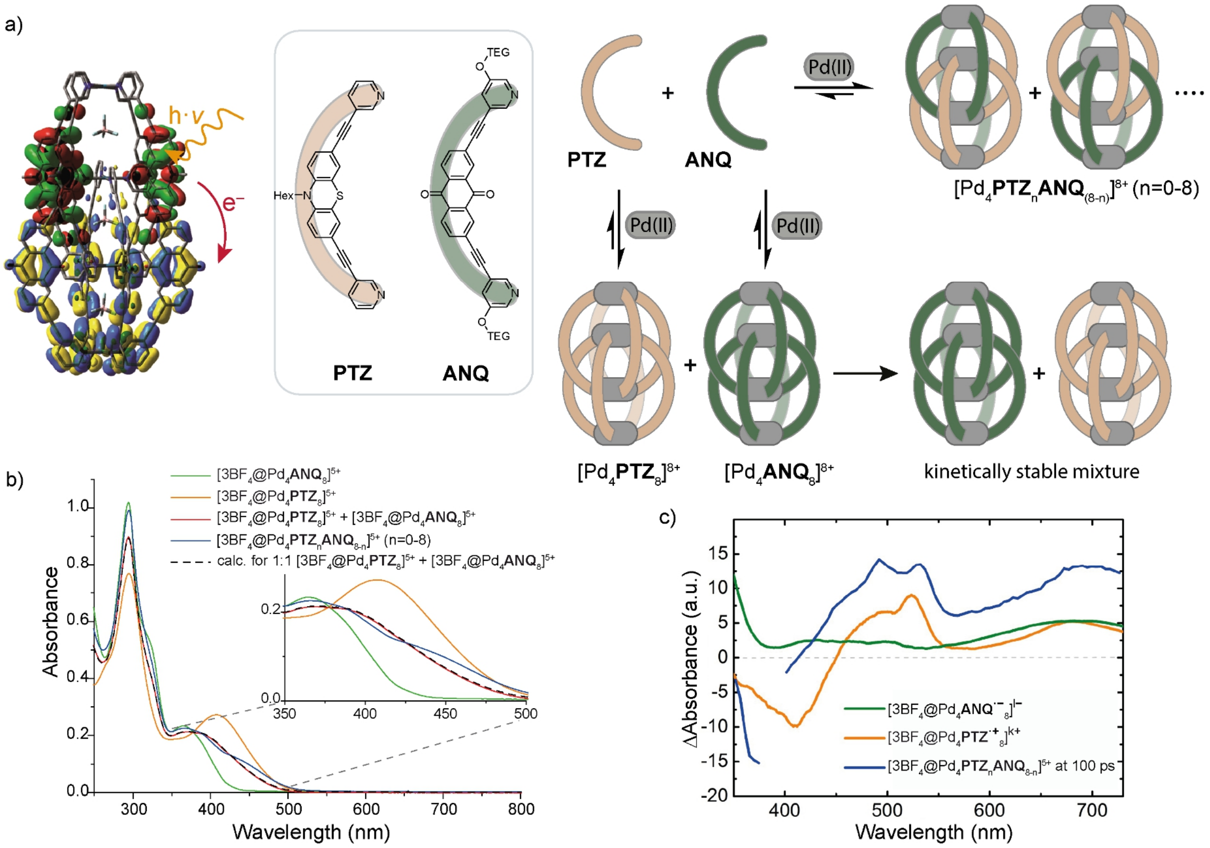

Fig. 18a) Overview of structures of ligands **PTZ** and **ANQ** as well as their homoleptic and heteroleptic cages; b) steady state absorption spectra of homoleptic double cages, their sum and the kinetically stable mixture, as well as of the heteroleptic double cage; c) transient difference spectra of [Pd_4**PTZ**$_n$**ANQ**$_{(8-n)}$]$^{8+}$ (n = 0-8) at a time delay of 100 ps compared to the difference spectra of the electrochemically generated radical ions of the homoleptic cages; b) and c) reproduced and modified with permission from ref[75].

Coordination cages or host-guest complexes that show photoredox activity have been applied for solar fuel production which includes proton reduction,[223,224] H_2S splitting,[225,226] and CO_2 reduction.[227,228] For this, three processes must occur in succession: photon capture, electron transfer, and promotion of the reaction in which the solar fuel is formed. The functional components required for proton reduction are a photosensitizer and a metal with a suitable reduction potential in vicinity as well as a sacrificial electron donor for regeneration of the photosensitizer. Su and coworkers achieved combining the first two components within octahedral cage Pd_6L_8 with Ru(II) metalloligand L.[229] Indeed, photoinduced electron transfer from the metallo-ligand to the Pd(II) nodes was followed by hydrogen evolution. Interestingly, the hydrogen evolution efficiency was affected by the presence of a redox active tetrathiafulvalene guest. Further studies revealed that the guest acted as an electron relay between the cage and the sacrificial electron donor. In other reports on coordination cages for hydrogen evolution, such as those reported by Duan,[224,230] He,[231,232] or Reek,[233,234] only one of the components (i.e. the photosensitizer or the redox active metal) was incorporated into the cage framework while the other one was encapsulated as guest.

Cages in general are promising nanosized reaction vessels since the confined space can increase the local catalyst as well as substrate concentration, enable preorganization, and can endow the reaction with regio- and stereoselectivity. In chromophore-based cages, these properties are paired with photo(redox) activity, making them highly attractive for the promotion of photoinduced reactions.[228,235,236] Fundamental work in this regard has been carried out by the group of Fujita, mostly with his “classical” octahedral cage Pd_6L_4 with L being based on triazine. These reactions include the demethylenation of cyclopropanes,[237] the photooxidation of alkanes[238] and of triquinancene,[239] as well as the alkyne hydration.[240] In the mentioned reactions, photoexcitation of the host leads to substrate activation through substrate-to-host electron transfer. Catalytic turnover, however, was impeded by product inhibition. Su and coworkers used homochiral octahedral cage Pd_6L_8 (with L based on a Ru(II) metallo-ligand) for promoting a photosensitized oxidative biaryl coupling[241] and a [2+2] photodimerization,[242] both in a regio- and enantioselective fashion. The authors also used Pd_6L_8 for promoting a [2+2] cycloaddition of α,β-unsaturated carbonyls.[243] Importantly, across these works, only catalytic amounts of the cage were required. The group of Dasgupta exploited the electron-deficient nature of earlier mentioned triazine-based cage Pd_6L_4, initially reported by Fujita, for the formation of charge transfer complexes with encapsulated aromatic substrates.[244] Photoexcitation into the charge transfer band activates the substrate by guest-to-host electron transfer leading to carbon-centered radicals. This allowed for driving reactions that need harsh conditions and/or metal catalysts otherwise, e.g. the activation of sp-hybridized C-H bonds for coupling of acetylenes,[244] the activation of sp^3-hybridized C-H bonds,[245] and the activation of styrene.[246] Very recently, the group also reported on the [4+2] cycloaddition of arylethynes in a cage with similar electronic properties but a more open shape.[247] Across these works, the electronic properties of the cage allowed for the attained reactivity but the confinement contributed to the selectivity of the reactions.

Overall, coordination cages based on various metal-ligand combinations have been equipped with chromophores and fluorophores. The spatial proximity of different photoactive components resulted in emergent phenomena that were not observed in the isolated chromophores, such as electron transfer.[75] In some cases, the modularity of the self-assembly was utilized for deducing the effect of structural changes on the excited state properties.[81,204] The modularity has, however, not yet been exploited for establishing relationships between the design of the donor-acceptor cage and the observed electron transfer rate constant. Given the importance of the precisely orchestrated electron transfer rate constants in the photosynthetic system for achieving high efficiency, understanding of the factors governing the kinetics is pivotal for designing artificial light-harvesting systems.

1.5. Marcus theory of electron transfer

Rudolph A. Marcus published in a series of papers around 1960 a theory which describes the dependency of the electron transfer rate constant k_{ET} on the free energy change ΔG^0, the reorganization energy λ, and the electronic matrix element H_{DA}.[248–250] The original theory was developed for outer sphere electron transfer reactions, meaning that the coordination spheres remain unchanged (no bonds are formed or broken).[249,251] For deriving the relationship, Marcus approximated the potential energy surfaces of reactants and products (both with surrounding solvent molecules) as parabolas in analogy to the harmonic oscillator. Product and reactant parabola possess the same force constant and are offset in energy by ΔG^0 (Fig. 19a). This is a fair approximation as no large displacement from the equilibrium geometry is expected for electron transfer. The theory was initially developed for non-adiabatic or weakly adiabatic electron transfer, i.e. the coupling between the potential energy surfaces of reactants and products is weak. For this reason, the Franck-Condon principle can be applied: electron transfer occurs suddenly, i.e. the nuclear position does not change, and hence the transfer occurs at the intersection of the two parabolas. Determining the intersection allows for deriving equation 1 for the activation barrier $\Delta G^{\neq}$.

$$\Delta G^{\neq} = \frac{(\Delta G^0 + \lambda)^2}{4\lambda} \tag{1}$$

The reorganization energy λ corresponds to the energy difference between reactant and product parabolas in the equilibrium geometry of the reactants. Equation 1 shows that $\Delta G^{\neq}$ has a parabolic dependency on ΔG^0, giving rise to three regimes (Fig. 19b). When the driving force is small, electron transfer accelerates with increasing driving force (Marcus normal region). This is intuitive and can be understood from the parabolas shown in a): when the light red product parabola is displaced to smaller energies, the height of the intersection decreases at first. Upon further increasing the driving force, the product parabola crosses the ones of the reactants in the equilibrium configuration, leading to barrierless electron transfer i.e. the rate constant is maximal. According to equation 1, this occurs for $-\Delta G^0 = \lambda$. Further increasing the exergonicity leads to an increase in the activation barrier and hence to deceleration of electron transfer (Marcus inverted region).

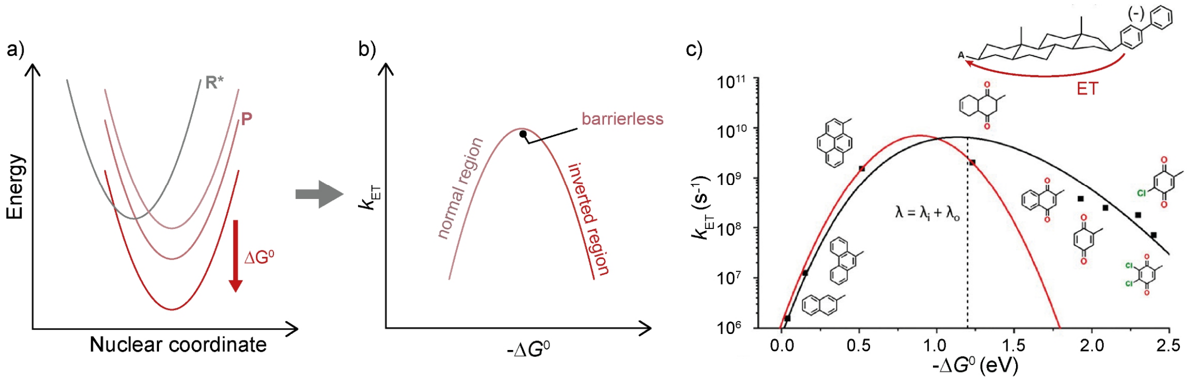

Fig. 19a) Schematic representation of reactant (R*) and product (P) parabolas for the normal region (light red), barrierless region (middle red), and inverted region (dark red); b) parabolic dependence of the electron transfer rate constant k_{ET} on the driving force $-\Delta G^0$ according to classical Marcus theory; c) plot of k_{ET} versus $-\Delta G^0$ for intramolecular electron transfer in solution observed by Closs and Miller in 1984; reproduced and modified with permission from ref[249].

Within the framework of Marcus theory, the overall rate constant k_{ET} can be obtained with equation 2. The electronic matrix element H_{DA} corresponds to the electronic coupling between the reactant and product states.

$$k_{\mathrm{ET}} = \frac{(2\pi)^2}{h} \cdot \frac{H_{\mathrm{DA}}^2}{\sqrt{4\pi\lambda k_{\mathrm{b}} T}} \exp(-\frac{\Delta G^{\neq}}{k_{\mathrm{b}} T}) \tag{2}$$

Only around 25 years after Marcus' theoretical prediction, the inverted region was experimentally observed for electron transfer reactions in solution. Miller and Closs studied the electron transfer kinetics between a 4-biphenylyl anion, generated through a pulse of solvated electrons, and different acceptors. Variation of the latter allowed for covering driving forces between 0 and 2.4 eV (Fig. 19c).[32] Importantly, donor and acceptor were connected through a rigid steroid bridge. This allowed for gaining control over the donor-acceptor distance and for studying electron transfer on an intramolecular level. Hence, in contrast to studies performed beforehand,[252–255] electron transfer was not diffusion-limited at high driving forces. Up to a driving force of 0.6 eV, the electron transfer rate increases with increasing driving force by around three orders of magnitudes, corresponding to the normal region, and then falls off at driving forces of 1.2 eV and higher, marking the inverted region. Noteworthy, the rate constants in the inverted region are larger than predicted by equation 2 (red curve in Fig. 19c). Fitting to the so-called semiclassical Marcus or Marcus-Levich-Jortner equation yields a better fit (back curve). This refined equation incorporates vibronic coupling which is more pronounced in the inverted region, resulting in an asymmetric shape of the curve.[256,257] Marcus was awarded the Chemistry Nobel prize in 1992 for his work on electron transfer[248] and his theory is applied in various fields, including the understanding of enzymatic redox reactions[258–260] and photosynthesis[261,262] as well as research on organic photovoltaic systems[263,264] and organic semiconductors,[265] among others.

1.6. Appendix

The azimuthal angles β were either directly taken from the original publication, when available, or were calculated based on the X-ray crystal structures. For the latter, the nitrogen-Pd(II) bonds were described as vectors pointing from nitrogen to Pd(II). These were then used for determining the angle between the two nitrogen-Pd(II) bonds of the same ligand. In the last step, the average of the four azimuthal angles was calculated.[94]

1.7. References

[1] Statistical Review of World Energy, 73rd edition, can be found under: www.energyinst.org/statistical-review, last visit: April 2025.

[2] L. Bruhwiler, S. Basu, J. H. Butler, A. Chatterjee, E. Dlugokencky, M. A. Kenney, A. McComiskey, S. A. Montzka, D. Stanitski, *Clim. Chang.* **2021**, *165*, 12.

[3] T. Jin, J. Kim, *Renew. Sustain. Energy Rev.* **2018**, *91*, 464.

[4] T. A. Kurniawan, M. H. D. Othman, D. Singh, R. Avtar, G. H. Hwang, T. Setiadi, W. Lo, *Ann. Nucl. Energy* **2022**, *166*, 108736.

[5] N. S. Lewis, D. G. Nocera, *Proc. Natl. Acad. Sci.* **2006**, *103*, 15729.

[6] R. E. Blankenship, D. M. Tiede, J. Barber, G. W. Brudvig, G. Fleming, M. Ghirardi, M. R. Gunner, W. Junge, D. M. Kramer, A. Melis, T. A. Moore, C. C. Moser, D. G. Nocera, A. J. Nozik, D. R. Ort, W. W. Parson, R. C. Prince, R. T. Sayre, *Science* **2011**, *332*, 805.

[7] A. Verméglio, P. Joliot, *Trends Microbiol.* **1999**, *7*, 435.

[8] R. J. Cogdell, A. Gall, J. Köhler, *Q. Rev. Biophys.* **2006**, *39*, 227.

[9] R. Y. Pishchalnikov, D. D. Chesalin, A. P. Razjivin, *Int. J. Mol. Sci.* **2021**, *22*, 10031.

[10] P. D. Frischmann, K. Mahata, F. Würthner, *Chem. Soc. Rev.* **2012**, *42*, 1847.

[11] M. R. Wasielewski, *Acc. Chem. Res.* **2009**, *42*, 1910.

[12] E. Orsi, J. Beekwilder, G. Eggink, S. W. M. Kengen, R. A. Weusthuis, *Biotechnol. Bioeng.* **2021**, *118*, 531.

[13] M. Grattieri, *Photochem. Photobiol. Sci.* **2020**, *19*, 424.

[14] P. Cao, L. Bracun, A. Yamagata, B. M. Christianson, T. Negami, B. Zou, T. Terada, D. P. Canniffe, M. Shirouzu, M. Li, L.-N. Liu, *Nat. Commun.* **2022**, *13*, 1977.

[15] C. Jungas, J. Ranck, J. Rigaud, P. Joliot, A. Verméglio, *EMBO J.* **1999**, *18*, 534.

[16] S. Baghbanzadeh, I. Kassal, *Phys. Chem. Chem. Phys.* **2016**, *18*, 7459.

[17] P. Qian, D. J. K. Swainsbury, T. I. Croll, P. Castro-Hartmann, G. Divitini, K. Sader, C. N. Hunter, *Biochemistry* **2021**, *60*, 3302.

[18] S. Subudhi, S. K. Mogal, N. R. Kumar, T. Nayak, B. Lal, H. Velankar, T. A. R. Kumar, P. V. C. Rao, N. V. Choudary, G. Shah, S. Gandham, *Int. J. Hydrog. Energy* **2016**, *41*, 13979.

[19] J. H. Golbeck *Photosynthetic Reaction Centers: So little time, so much to do.* Biophysics textbooks online (http://www. biophysics. org/btol), **2003**.

[20] C. C. Moser, C. C. Page, R. J. Cogdell, J. Barber, C. A. Wraight, P. L. Dutton, *Adv. Protein Chem.* **2003**, *63*, 71.

[21] E. Altamura, P. Albanese, R. Marotta, F. Milano, M. Fiore, M. Trotta, P. Stano, F. Mavelli, *Proc. Natl. Acad. Sci.* **2021**, *118*, e2012170118.

[22] R. J. Cave, P. Siders, R. A. Marcus, *J. Phys. Chem.* **1986**, *90*, 1436.

[23] A. Helms, D. Heiler, G. McLendon, *J. Am. Chem. Soc.* **1991**, *113*, 4325.

[24] M. R. Wasielewski, M. P. Niemczyk, *J. Am. Chem. Soc.* **1984**, *106*, 5043.

[25] O. S. Wenger, *Acc. Chem. Res.* **2011**, *44*, 25.

[26] M. Holzapfel, C. Lambert, *J. Phys. Chem. C* **2008**, *112*, 1227.

[27] A. J. Ward, A. Ruseckas, M. M. Kareem, B. Ebenhoch, L. A. Serrano, M. Al-Eid, B. Fitzpatrick, V. M. Rotello, G. Cooke, I. D. W. Samuel, *Adv. Mater.* **2015**, *27*, 2496.

[28] T. Higashino, T. Yamada, M. Yamamoto, A. Furube, N. V. Tkachenko, T. Miura, Y. Kobori, R. Jono, K. Yamashita, H. Imahori, *Angew. Chem.* **2016**, *128*, 639.

[29] M. Kuss-Petermann, O. S. Wenger, *J. Am. Chem. Soc.* **2016**, *138*, 1349.

[30] A. L. Jones, K. S. Schanze, *J. Phys. Chem. A* **2020**, *124*, 21.

[31] R. M. Williams, *Photochem. Photobiol. Sci.* **2010**, *9*, 1018.

[32] J. R. Miller, L. T. Calcaterra, G. L. Closs, *J. Am. Chem. Soc.* **1984**, *106*, 3047.

[33] P. P. Levin, P. F. Pluzhnikov, V. A. Kuzmin, *Chem. Phys. Lett.* **1988**, *147*, 283.

[34] D. I. Schuster, P. Cheng, P. D. Jarowski, D. M. Guldi, C. Luo, L. Echegoyen, S. Pyo, A. R. Holzwarth, S. E. Braslavsky, R. M. Williams, G. Klihm, *J. Am. Chem. Soc.* **2004**, *126*, 7257.

[35] G. M. Whitesides, B. Grzybowski, *Science* **2002**, *295*, 2418.

[36] M. E. Briggs, A. I. Cooper, *Chem. Mater.* **2017**, *29*, 149.

[37] F. Beuerle, B. Gole, *Angew. Chem. Int. Ed.* **2018**, *57*, 4850.

[38] M. Mastalerz, *Angew. Chem. Int. Ed.* **2010**, *49*, 5042.

[39] L. R. MacGillivray, J. L. Atwood, *Nature* **1997**, *389*, 469–472.

[40] J. Rebek, *Acc. Chem. Res.* **2009**, *42*, 1660–1668.

[41] S. K. Yang, S. C. Zimmerman, *Isr. J. Chem.* **2013**, *53*, 511.

[42] L. J. Prins, D. N. Reinhoudt, P. Timmerman, *Angew. Chem. Int. Ed.* **2001**, *40*, 2382.

[43] M. M. J. Smulders, I. A. Riddell, C. Browne, J. R. Nitschke, *Chem. Soc. Rev.* **2012**, *42*, 1728.

[44] M. Pan, K. Wu, J.-H. Zhang, C.-Y. Su, *Coord. Chem. Rev.* **2019**, *378*, 333.

[45] F. Würthner, C.-C. You, C. R. Saha-Möller, *Chem. Soc. Rev.* **2004**, *33*, 133.

[46] C. M. Hong, R. G. Bergman, K. N. Raymond, F. D. Toste, *Acc. Chem. Res.* **2018**, *51*, 2447.

[47] M. Fujita, M. Tominaga, A. Hori, B. Therrien, *Acc. Chem. Res.* **2005**, *38*, 369.

[48] D. Bardhan, D. K. Chand, *Chem. Eur. J.* **2019**, *25*, 12241.

[49] S. De, K. Mahata, M. Schmittel, *Chem. Soc. Rev.* **2010**, *39*, 1555.

[50] M. Han, D. M. Engelhard, G. H. Clever, *Chem. Soc. Rev.* **2014**, *43*, 1848.

[51] T. R. Cook, P. J. Stang, *Chem. Rev.* **2015**, *115*, 7001.

[52] S. Pullen, G. H. Clever, *Acc. Chem. Res.* **2018**, *51*, 3052.

[53] S. Kitagawa, R. Kitaura, S. Noro, *Angew. Chem. Int. Ed.* **2004**, *43*, 2334.

[54] A. Y. Robin, K. M. Fromm, *Coord. Chem. Rev.* **2006**, *250*, 2127.

[55] R. W. Saalfrank, A. Stark, K. Peters, H. G. von Schnering, *Angew. Chem. Int. Ed.* **1988**, *27*, 851.

[56] M. Scherer, D. L. Caulder, D. W. Johnson, K. N. Raymond, *Angew. Chem. Int. Ed.* **1999**, *38*, 1587.

[57] D. L. Caulder, C. Brückner, R. E. Powers, S. König, T. N. Parac, J. A. Leary, K. N. Raymond, *J. Am. Chem. Soc.* **2001**, *123*, 8923.

[58] D. Zhang, T. K. Ronson, J. R. Nitschke, *Acc. Chem. Res.* **2018**, *51*, 2423.

[59] B. Olenyuk, J. A. Whiteford, A. Fechtenkötter, P. J. Stang, *Nature* **1999**, *398*, 796.

[60] M. Fujita, J. Yazaki, K. Ogura, *J. Am. Chem. Soc.* **1990**, *112*, 5645.

[61] D. A. McMorran, P. J. Steel, *Angew. Chem. Int. Ed.* **1998**, *37*, 3295.

[62] Z. T. Avery, J. L. Algar, D. Preston, *Trends Chem.* **2024**, *6*, 352.

[63] S. Pullen, J. Tessarolo, G. H. Clever, *Chem. Sci.* **2021**, *12*, 7269.

[64] W.-L. Jiang, B. Huang, X.-L. Zhao, X. Shi, H.-B. Yang, *Chem* **2023**, *9*, 2655.

[65] S. Hasegawa, A. Baksi, B. Chen, G. H. Clever, *Org. Mater.* **2022**, *4*, 222.

[66] M. Yoshizawa, L. Catti, *Acc. Chem. Res.* **2019**, *52*, 2392.

[67] Y. Xue, X. Hang, J. Ding, B. Li, R. Zhu, H. Pang, Q. Xu, *Coord. Chem. Rev.* **2020**, *430*, 213656.

[68] H. Takezawa, M. Fujita, *Bull. Chem. Soc. Jpn.* **2021**, *94*, 2351.

[69] T. K. Piskorz, V. Martí-Centelles, R. L. Spicer, F. Duarte, P. J. Lusby, *Chem. Sci.* **2023**, *14*, 11300.

[70] I. Regeni, B. Chen, M. Frank, A. Baksi, J. J. Holstein, G. H. Clever, *Angew. Chem. Int. Ed.* **2021**, *60*, 5673.

[71] B. Aikman, R. Bonsignore, B. Woods, D. Doellerer, R. Scotti, C. Schmidt, A. A. Heidecker, A. Pöthig, E. J. Sayers, A. T. Jones, A. Casini, *Dalton Trans.* **2022**, *51*, 7476.

[72] K. E. Ebbert, E. Benchimol, A. Platzek, C. Drechsler, J. Openy, S. Hasegawa, J. J. Holstein, G. H. Clever, *Angew. Chem. Int. Ed.* **2024**, *63*, e202413323.

[73] A. B. S. Elliott, J. E. M. Lewis, H. van der Salm, C. J. McAdam, J. D. Crowley, K. C. Gordon, *Inorg Chem* **2016**, *55*, 3440.

[74] M. Frank, J. Hey, I. Balcioglu, Y. Chen, D. Stalke, T. Suenobu, S. Fukuzumi, H. Frauendorf, G. H. Clever, *Angew. Chem. Int. Ed.* **2013**, *52*, 10102.

[75] M. Frank, J. Ahrens, I. Bejenke, M. Krick, D. Schwarzer, G. H. Clever, *J. Am. Chem. Soc.* **2016**, *138*, 8279.

[76] V. Croué, S. Krykun, M. Allain, Y. Morille, F. Aubriet, V. Carré, Z. Voitenko, S. Goeb, M. Sallé, *New J. Chem.* **2017**, *41*, 3238.

[77] R. A. S. Vasdev, J. A. Findlay, A. L. Garden, J. D. Crowley, *Chem Commun* **2019**, *55*, 7506.

[78] S. Saha, Y.-T. Chen, S. Ganta, M. Gilles, B. Holzapfel, P. Lill, H. Rehage, C. Gatsogiannis, G. H. Clever, *Chem. Eur. J.* **2022**, *28*, e202103406.

[79] S. Saha, B. Holzapfel, Y.-T. Chen, K. Terlinden, P. Lill, C. Gatsogiannis, H. Rehage, G. H. Clever, *J. Am. Chem. Soc.* **2018**, *140*, 17384.

[80] S. Ganta, C. Drechsler, Y. Chen, G. H. Clever, *Chem. Eur. J.* **2022**, *28*, e202104228.

[81] I. Regeni, R. Chowdhury, K. Terlinden, S. Horiuchi, J. J. Holstein, S. Feldmann, G. H. Clever, *Angew. Chem. Int. Ed.* **2023**, *62*, e202308288.

[82] I. Heckelmann, Z. Lu, J. C. A. Prentice, F. Auras, T. K. Ronson, R. H. Friend, J. R. Nitschke, S. Feldmann, *Angew. Chem. Int. Ed.* **2023**, *62*, e202216729.

[83] P. Liao, B. W. Langloss, A. M. Johnson, E. R. Knudsen, F. S.

Tham, R. R. Julian, R. J. Hooley, *Chem. Commun.* **2010**, *46*, 4932.

[84] D. P. August, G. S. Nichol, P. J. Lusby, *Angew. Chem. Int. Ed.* **2016**, *55*, 15022.

[85] V. Martí-Centelles, A. L. Lawrence, P. J. Lusby, *J Am Chem Soc* **2018**, *140*, 2862.

[86] R. L. Spicer, A. D. Stergiou, T. A. Young, F. Duarte, M. D. Symes, P. J. Lusby, *J. Am. Chem. Soc.* **2020**, *142*, 2134.

[87] T. A. Young, V. Martí-Centelles, J. Wang, P. J. Lusby, F. Duarte, *J. Am. Chem. Soc.* **2020**, *142*, 1300.

[88] J. E. M. Lewis, E. L. Gavey, S. A. Cameron, J. D. Crowley, *Chem Sci* **2011**, *3*, 778.

[89] M. Krick, J. Holstein, C. Würtele, G. H. Clever, *Chem. Commun.* **2016**, *52*, 10411.

[90] S. Hasegawa, S. L. Meichsner, J. J. Holstein, A. Baksi, M. Kasanmascheff, G. H. Clever, *J. Am. Chem. Soc.* **2021**, *143*, 9718.

[91] B. Chen, J. J. Holstein, S. Horiuchi, W. G. Hiller, G. H. Clever, *J. Am. Chem. Soc.* **2019**, *41*, 8907.

[92] H. Sasafuchi, M. Ueda, N. Kishida, T. Sawada, S. Suzuki, Y. Imai, M. Yoshizawa, *Chem* **2024**, 102332.

[93] E. Benchimol, H. M. O'Connor, B. Schmidt, N. Bogo, J. J. Holstein, J. I. Lovitt, S. Shanmugaraju, C. J. Stein, T. Gunnlaugsson, G. H. Clever, *Angew. Chem. Int. Ed.* **2025**, *64*, e202421137.

[94] W. M. Bloch, S. Horiuchi, J. J. Holstein, C. Drechsler, A. Wuttke, W. Hiller, R. A. Mata, G. H. Clever, *Chem. Sci.* **2023**, *14*, 1524.

[95] P. J. Steel, D. A. McMorran, *Chem. Asian J.* **2019**, *14*, 1098.

[96] H. S. Sahoo, D. K. Chand, *Dalton Trans.* **2010**, *39*, 7223.

[97] D. Tripathy, A. K. Pal, G. S. Hanan, D. K. Chand, *Dalton Trans.* **2012**, *41*, 11273.

[98] Q. Lin, L. Gao, B. Kauffmann, J. Zhang, C. Ma, D. Luo, Q. Gan, *Chem. Commun.* **2018**, *54*, 13447.

[99] M. Sarkar, H. Dasary, D. K. Chand, *J. Organomet. Chem.* **2021**, *950*, 121984.

[100] L.-P. Zhou, Q.-F. Sun, *Chem. Commun.* **2015**, *51*, 16767.

[101] A. Walther, I. Regeni, J. J. Holstein, G. H. Clever, *J. Am. Chem. Soc.* **2023**, *145*, 25365.

[102] E. Benchimol, K. E. Ebbert, A. Walther, J. J. Holstein, G. H. Clever, *Chem. Eur. J.* **2024**, e202401850.

[103] W. M. Bloch, Y. Abe, J. J. Holstein, C. M. Wandtke, B. Dittrich, G. H. Clever, *J. Am. Chem. Soc.* **2016**, *138*, 13750.
[104] J. D. Crowley, E. L. Gavey, *Dalton T* **2010**, *39*, 4035.

[105] B. Chen, S. Horiuchi, J. J. Holstein, J. Tessarolo, G. H. Clever, *Chem. Eur. J.* **2019**, *25*, 14921.

[106] R. A. S. Vasdev, L. F. Gaudin, D. Preston, J. P. Jogy, G. I. Giles, J. D. Crowley, *Front. Chem.* **2018**, *6*, 563.

[107] S. Sudan, F. Fadaei-Tirani, K. Severin, *Chem. Commun.* **2023**, *59*, 8258.

[108] T. R. Schulte, J. J. Holstein, L. Schneider, A. Adam, G. Haberhauer, G. H. Clever, *Angew. Chem. Int. Ed.* **2020**, *59*, 22489.

[109] A. Kumar, R. Banerjee, E. Zangrando, P. S. Mukherjee, *Inorg. Chem.* **2022**, *61*, 2368.

[110] K. Suzuki, M. Kawano, M. Fujita, *Angew. Chem. Int. Ed.* **2007**, *46*, 2819.

[111] D. K. Chand, K. Biradha, M. Kawano, S. Sakamoto, K. Yamaguchi, M. Fujita, *Chem. Asian J.* **2006**, *1*, 82.

[112] J. Tessarolo, H. Lee, E. Sakuda, K. Umakoshi, G. H. Clever, *J. Am. Chem. Soc.* **2021**, *143*, 6339.

[113] K. Wu, E. Benchimol, A. Baksi, G. H. Clever, *Nat. Chem.* **2024**, *16*, 584.

[114] Y.-Y. Ge, X.-C. Zhou, J. Zheng, J. Luo, Y.-L. Lai, J. Su, H.-J. Zhang, X.-P. Zhou, D. Li, *Inorg. Chem.* **2023**, *62*, 4048.

[115] R. A. S. Vasdev, J. A. Findlay, D. R. Turner, J. D. Crowley, *Chem. Asian J.* **2021**, *16*, 39.

[116] K. Suzuki, M. Tominaga, M. Kawano, M. Fujita, *Chem. Commun.* **2009**, 1638.

[117] E. O. Bobylev, D. A. Poole, B. de Bruin, J. N. H. Reek, *J. Am. Chem. Soc.* **2022**, *144*, 15633.

[118] M. D. Wise, J. J. Holstein, P. Pattison, C. Besnard, E. Solari, R. Scopelliti, G. Bricogne, K. Severin, *Chem. Sci.* **2015**, *6*, 1004.

[119] S. M. Jansze, G. Cecot, M. D. Wise, K. O. Zhurov, T. K. Ronson, A. M. Castilla, A. Finelli, P. Pattison, E. Solari, R. Scopelliti, G. E. Zelinskii, A. V. Vologzhanina, Y. Z. Voloshin, J. R. Nitschke, K. Severin, *J. Am. Chem. Soc.* **2016**, *138*, 2046.

[120] W. M. Bloch, J. J. Holstein, B. Dittrich, W. Hiller, G. H. Clever, *Angew. Chem. Int. Ed.* **2018**, *57*, 5534.

[121] T. Zhang, L.-P. Zhou, X.-Q. Guo, L.-X. Cai, Q.-F. Sun, *Nat. Commun.* **2017**, *8*, ncomms15898.

[122] D. M. Engelhard, S. Freye, K. Grohe, M. John, G. H. Clever, *Angew. Chem. Int. Ed.* **2012**, *51*, 4747.

[123] M. Fukuda, R. Sekiya, R. Kuroda, *Angew. Chem. Int. Ed.* **2008**, *47*, 706.

[124] T. R. Schulte, M. Krick, C. I. Asche, S. Freye, G. H. Clever, *RSC Adv.* **2014**, *4*, 29724.

[125] S. Freye, R. Michel, D. Stalke, M. Pawliczek, H. Frauendorf, G. H. Clever, *J. Am. Chem. Soc.* **2013**, *135*, 8476.

[126] S. Freye, J. Hey, A. Torras-Galán, D. Stalke, R. Herbst-Irmer, M. John, G. H. Clever, *Angew. Chem. Int. Ed.* **2012**, *51*, 2191.

[127] M. Frank, M. D. Johnstone, G. H. Clever, *Chem. Eur. J.* **2016**, *22*, 14104.

[128] R. Zhu, J. Lübben, B. Dittrich, G. H. Clever, *Angew. Chem. Int. Ed.* **2015**, *54*, 2796.

[129] P. Montes-Tolentino, A. S. Mikherdov, C. Drechsler, J. J. Holstein, G. H. Clever, *Angew. Chem. Int. Ed.* **2025**, e202423810.

[130] S. Sudan, F. Fadaei-Tirani, R. Scopelliti, K. E. Ebbert, G. H. Clever, K. Severin, *Angew. Chem. Int. Ed.* **2022**, *61*, e202201823.

[131] M. Käseborn, J. J. Holstein, G. H. Clever, A. Lützen, *Angew. Chem. Int. Ed.* **2018**, *57*, 12171.

[132] W. M. Bloch, G. H. Clever, *Chem. Commun.* **2017**, *53*, 8506.

[133] M. Frank, L. Krause, R. Herbst-Irmer, D. Stalke, G. H. Clever, *Dalton Trans.* **2014**, *43*, 4587.

[134] M. Yoshizawa, M. Nagao, K. Kumazawa, M. Fujita, *J Organomet Chem* **2005**, *690*, 5383.

[135] A. K. Bar, S. Raghothama, D. Moon, P. S. Mukherjee, *Chem. Eur. J.* **2012**, *18*, 3199.

[136] A. K. Bar, G. Mostafa, P. S. Mukherjee, *Inorg. Chem.* **2010**, *49*, 7647.

[137] R. Zhu, W. M. Bloch, J. J. Holstein, S. Mandal, L. V. Schäfer, G. H. Clever, *Chem Eur. J.* **2018**, *24*, 1297.

[138] D. Preston, J. E. Barnsley, K. C. Gordon, J. D. Crowley, *J. Am. Chem. Soc.* **2016**, *138*, 10578.

[139] A. M. Johnson, R. J. Hooley, *Inorg. Chem.* **2011**, *50*, 4671.

[140] R. Li, F. Fadaei-Tirani, R. Scopelliti, K. Severin, *Chem. Eur. J.* **2021**, *27*, 9439.

[141] W. M. Bloch, J. J. Holstein, W. Hiller, G. H. Clever, *Angew. Chem. Int. Ed.* **2017**, *56*, 8285.

[142] J.-R. Li, H.-C. Zhou, *Nat. Chem.* **2010**, *2*, 893.

[143] P. J. Stang, B. Olenyuk, *Acc. Chem. Res.* **1997**, *30*, 502.

[144] Q. Sun, S. Sato, M. Fujita, *Angew. Chem. Int. Ed.* **2014**, *53*, 13510.

[145] K. Wu, J. Tessarolo, A. Baksi, G. H. Clever, *Angew. Chem. Int. Ed.* **2022**, *61*, e202205725.

[146] J. Tessarolo, E. Benchimol, A. Jouaiti, M. W. Hosseini, G. H. Clever, *Chem. Commun.* **2023**, *59*, 3467.

[147] A. Tarzia, W. Shan, V. Posligua, C. J. T. Cox, L. Male, B. D. Egleston, R. L. Greenaway, K. E. Jelfs, J. E. M. Lewis, *Chem. Eur. J.* **2025**, *31*, e202403336.

[148] K. E. Ebbert, F. Sendzik, L. Neukirch, L. Eberlein, A. Platzek, P. Kibies, S. M. Kast, G. H. Clever, *Angew. Chem. Int. Ed.* **2024**, e202416076.

[149] Y. Liu, S. Liao, W. Dai, Q. Bai, S. Lu, H. Wang, X. Li, Z. Zhang, P. Wang, W. Lu, Q. Zhang, *Angew. Chem. Int. Ed.* **2023**, *62*, e202217215.

[150] W.-T. Dai, T.-T. Liu, Q. Bai, Z. Zhang, P. Wang, W. Lu, Q. Zhang, *Sci. China Chem.* **2024**, 1.

[151] R.-J. Li, J. Tessarolo, H. Lee, G. H. Clever, *J. Am. Chem. Soc.* **2021**, *143*, 3865.

[152] E. Benchimol, I. Regeni, B. Zhang, M. Kabiri, J. J. Holstein, G. H. Clever, *J. Am. Chem. Soc.* **2024**, *146*, 6905.

[153] T. Abe, N. Sanada, K. Takeuchi, A. Okazawa, S. Hiraoka, *J. Am. Chem. Soc.* **2023**, *145*, 28061.

[154] S. Prusty, K. Yazaki, M. Yoshizawa, D. K. Chand, *Chem. Eur. J.* **2017**, *23*, 12456.

[155] P. Howlader, P. Das, E. Zangrando, P. S. Mukherjee, *J. Am. Chem. Soc.* **2016**, *138*, 1668.

[156] S. Sudan, R.-J. Li, S. M. Jansze, A. Platzek, R. Rudolf, G. H. Clever, F. Fadaei-Tirani, R. Scopelliti, K. Severin, *J. Am. Chem. Soc.* **2021**, *143*, 1773.

[157] R. Winter, F. Noll, C. Czeslik, **2011**, DOI 10.1007/978-3-8348-8143-4.

[158] P. P. Neelakandan, A. Jiménez, J. R. Nitschke, *Chem. Sci.* **2014**, *5*, 908.

[159] A. J. Musser, P. P. Neelakandan, J. M. Richter, H. Mori, R. H. Friend, J. R. Nitschke, *J. Am. Chem. Soc.* **2017**, *139*, 12050.

[160] N. Mihara, T. K. Ronson, J. R. Nitschke, *Angew. Chem. Int. Ed.* **2019**, *58*, 12497.

[161] B. T. Nguyen, A. B. Grommet, A. Tron, M. C. A. Georges, J. R. Nitschke, *Adv. Mater.* **2020**, *32*, 1907241.

[162] C. Gütz, R. Hovorka, C. Klein, Q. Jiang, C. Bannwarth, M. Engeser, C. Schmuck, W. Assenmacher, W. Mader, F. Topić, K. Rissanen, S. Grimme, A. Lützen, *Angew. Chem. Int. Ed.* **2014**, *53*, 1693.

[163] C. Gütz, R. Hovorka, G. Schnakenburg, A. Lützen, *Chem. Eur. J.* **2013**, *19*, 10890.

[164] S. Ghorai, S. Maji, B. Paul, K. Samanta, S. K. Sen, R. Natarajan, *Chem. Asian J.* **2023**, e202201312.

[165] T. R. Schulte, J. J. Holstein, G. H. Clever, *Angew. Chem. Int. Ed.* **2019**, *58*, 5562.

[166] D. R. Martir, D. B. Cordes, A. M. Z. Slawin, D. Escudero, D. Jacquemin, S. L. Warriner, E. Zysman-Colman, *Chem. Commun.* **2018**, *54*, 6016.

[167] D. R. Martir, D. R. Martir, D. Escudero, D. Jacquemin, D. B. Cordes, A. M. Z. Slawin, H. A. Fruchtl, S. L. Warriner, E. Z. Colman, *Chem. Eur. J.* **2017**, *23*, 14358-.

[168] Z. Li, N. Kishi, K. Hasegawa, M. Akita, M. Yoshizawa, *Chem. Commun.* **2011**, *47*, 8605.

[169] Z. Li, N. Kishi, K. Yoza, M. Akita, M. Yoshizawa, *Chem. Eur. J.* **2012**, *18*, 8358.

[170] N. Kishi, M. Akita, M. Yoshizawa, *Angew. Chem. Int. Ed.* **2014**, *53*, 3604.

[171] A. Schmidt, M. Hollering, J. Han, A. Casini, F. E. Kühn, *Dalton Trans.* **2016**, *45*, 12297.

[172] X.-F. Duan, L.-P. Zhou, H.-R. Li, S.-J. Hu, W. Zheng, X. Xu, R. Zhang, X. Chen, X.-Q. Guo, Q.-F. Sun, *J. Am. Chem. Soc.* **2023**, *145*, 23121.

[173] P. D. Frischmann, V. Kunz, F. Würthner, *Angew. Chem.* **2015**, *127*, 7393.

[174] A. J. Plajer, E. G. Percástegui, M. Santella, F. J. Rizzuto, Q. Gan, B. W. Laursen, J. R. Nitschke, *Angew. Chem. Int. Ed.* **2019**, *58*, 4200.

[175] J. Yu, L. Sun, C. Wang, Y. Li, Y. Han, *Chem. Eur. J.* **2021**, *27*, 1556.

[176] Y. Li, J. Zhang, H. Li, Y. Fan, T. He, H. Qiu, S. Yin, *Adv. Opt. Mater.* **2020**, *8*, 1902190.

[177] C. Lu, M. Zhang, D. Tang, X. Yan, Z. Zhang, Z. Zhou, B. Song, H. Wang, X. Li, S. Yin, H. Sepehrpour, P. J. Stang, *J. Am. Chem. Soc.* **2018**, *140*, 7674.

[178] Z. Zhang, Z. Zhao, L. Wu, S. Lu, S. Ling, G. Li, L. Xu, L. Ma, Y. Hou, X. Wang, X. Li, G. He, K. Wang, B. Zou, M. Zhang, *J. Am. Chem. Soc.* **2020**, *142*, 2592.

[179] W. R. Kitzmann, J. Freudenthal, A. M. Reponen, Z. A. VanOrman, S. Feldmann, *Adv. Mater.* **2023**, *35*, e2302279.

[180] F. Zinna, L. D. Bari, *Chirality* **2014**, *27*, 1.

[181] G. Longhi, E. Castiglioni, J. Koshoubu, G. Mazzeo, S. Abbate, *Chirality* **2016**, *28*, 696.

[182] X.-Z. Li, C.-B. Tian, Q.-F. Sun, *Chem Rev* **2022**, *122*, 6374.

[183] Z. Wang, L.-P. Zhou, T.-H. Zhao, L.-X. Cai, X.-Q. Guo, P.-F. Duan, Q.-F. Sun, *Inorg. Chem.* **2018**, *57*, 7982.

[184] S.-J. Hu, X.-Q. Guo, L.-P. Zhou, D.-N. Yan, P.-M. Cheng, L.-X. Cai, X.-Z. Li, Q.-F. Sun, *J Am Chem Soc* **2022**, *144*, 4244.

[185] Y. Zhou, H. Li, T. Zhu, T. Gao, P. Yan, *J. Am. Chem. Soc.* **2019**, *141*, 19634.

[186] Y. B. Tan, Y. Okayasu, S. Katao, Y. Nishikawa, F. Asanoma, M. Yamada, J. Yuasa, T. Kawai, *J. Am. Chem. Soc.* **2020**, *142*, 17653.

[187] H. Hosoi, S. Yamaguchi, T. Tahara, *Chem. Lett.* **2005**, *34*, 618.

[188] J. K. Klosterman, M. Iwamura, T. Tahara, M. Fujita, *J. Am. Chem. Soc.* **2009**, *131*, 9478.

[189] J. R. Piper, L. Cletheroe, C. G. P. Taylor, A. J. Metherell, J. A. Weinstein, I. V. Sazanovich, M. D. Ward, *Chem. Commun,* **2017**, *53*, 408.

[190] D. Li, X. Liu, L. Yang, H. Li, G. Guo, X. Li, C. He, *Chem. Sci.* **2023**, *14*, 2237.

[191] D. R. Martir, A. Pizzolante, D. Escudero, D. Jacquemin, S. L. Warriner, E. Zysman-Colman, *ACS Appl. Energy Mater.* **2018**, *1*, 2971.

[192] P.-P. Jia, Y.-X. Hu, Z.-Y. Peng, B. Song, Z.-Y. Zeng, Q.-H. Ling, X. Zhao, L. Xu, H.-B. Yang, *Inorg. Chem.* **2022**, *62*, 1950.

[193] Z. Zhang, Z. Zhao, Y. Hou, H. Wang, X. Li, G. He, M. Zhang, *Angew. Chem. Int. Ed.* **2019**, *58*, 8862.

[194] A. Kumar, R. Saha, P. S. Mukherjee, *Chem. Sci.* **2021**, *12*, 5319.

[195] Y. Li, S. S. Rajasree, G. Y. Lee, J. Yu, J.-H. Tang, R. Ni, G. Li, Kendall. N. Houk, P. Deria, P. J. Stang, *J. Am. Chem. Soc.* **2021**, *143*, 2908.

[196] H. Liu, Z. Zhang, C. Mu, L. Ma, H. Yuan, S. Ling, H. Wang, X. Li, M. Zhang, *Angew. Chem. Int. Ed.* **2022**, *61*, e202207289.

[197] H. Liu, C. Guo, Z. Zhang, C. Mu, Q. Feng, M. Zhang, *Chem. Eur. J.* **2023**, *29*, e202203926.

[198] F. Würthner, A. Sautter, *Org. Biomol. Chem.* **2002**, *1*, 240.

[199] C. You, C. Hippius, M. Grüne, F. Würthner, *Chem. Eur. J.* **2006**, *12*, 7510.

[200] A. Sautter, B. K. Kaletaş, D. G. Schmid, R. Dobrawa, M. Zimine, G. Jung, I. H. M. van Stokkum, L. D. Cola, R. M. Williams, F. Würthner, *J. Am. Chem. Soc.* **2005**, *127*, 6719.

[201] Y. Qin, L.-J. Chen, Y. Zhang, Y.-X. Hu, W.-L. Jiang, G.-Q. Yin, H. Tan, X. Li, L. Xu, H.-B. Yang, *Chem. Commun.* **2019**, *55*, 11119.

[202] Y. Qin, L.-J. Chen, F. Dong, S.-T. Jiang, G.-Q. Yin, X. Li, Y. Tian, H.-B. Yang, *J. Am. Chem. Soc.* **2019**, *141*, 8943.

[203] P.-P. Jia, L. Xu, Y.-X. Hu, W.-J. Li, X.-Q. Wang, Q.-H. Ling, X. Shi, G.-Q. Yin, X. Li, H. Sun, Y. Jiang, H.-B. Yang, *J. Am. Chem. Soc.* **2021**, *143*, 399.

[204] N. Karakostas, A. Kaloudi-Chantzea, E. Martinou, K. Seintis, F. Pitterl, H. Oberacher, M. Fakis, J. K. Kallitsis, G. Pistolis, *Faraday Discuss.* **2015**, *185*, 433.

[205] I.-W. Hwang, T. Kamada, T. K. Ahn, D. M. Ko, T. Nakamura, A. Tsuda, A. Osuka, D. Kim, *J. Am. Chem. Soc.* **2004**, *126*, 16187.

[206] D. M. Dalton, S. R. Ellis, E. M. Nichols, R. A. Mathies, F. D. Toste, R. G. Bergman, K. N. Raymond, *J. Am. Chem. Soc.* **2015**, *137*, 10128.

[207] J.-C. G. Bünzli, C. Piguet, *Chem. Rev.* **2002**, *102*, 1897.

[208] C. Piguet, J.-C. G. Bünzli, G. Bernardinelli, G. Hopfgartner, S. Petoud, O. Schaad, *J. Am. Chem. Soc.* **1996**, *118*, 6681.

[209] C. Piguet, G. Bernardinelli, G. Hopfgartner, *Chem. Rev.* **1997**, *97*, 2005.

[210] C.-L. Liu, R.-L. Zhang, C.-S. Lin, L.-P. Zhou, L.-X. Cai, J.-T. Kong, S.-Q. Yang, K.-L. Han, Q.-F. Sun, *J. Am. Chem. Soc.* **2017**, *139*, 12474.

[211] Y.-Y. Liu, H.-J. Yu, Y.-P. Wang, C.-J. Li, X.-F. Wang, C.-G. Ye, H.-L. Yao, M. Pan, C.-Y. Su, *Mater. Chem. Front.* **2022**, *6*, 948.

[212] S. Pullen, S. Löffler, A. Platzek, J. J. Holstein, G. H. Clever, *Dalton Trans.* **2020**, *49*, 9404.

[213] P. P. Neelakandan, A. Jiménez, J. D. Thoburn, J. R. Nitschke, *Angew. Chem. Int. Ed.* **2015**, *127*, 14586.

[214] S. Bhattacharyya, M. Venkateswarulu, J. Sahoo, E. Zangrando, M. De, P. S. Mukherjee, *Inorg. Chem.* **2020**, *59*, 12690.

[215] D. Preston, J. J. Sutton, K. C. Gordon, J. D. Crowley, *Angew. Chem. Int. Ed.* **2018**, *57*, 8659.

[216] J. S. Train, A. B. Wragg, A. J. Auty, A. J. Metherell, D. Chekulaev, C. G. P. Taylor, S. P. Argent, J. A. Weinstein, M. D. Ward, *Inorg Chem* **2019**, *58*, 2386.

[217] S. Ganta, J.-H. Borter, C. Drechsler, J. J. Holstein, D. Schwarzer, G. H. Clever, *Org. Chem. Front.* **2022**, *9*, 5485.

[218] S. Bay, T. Villnow, G. Ryseck, V. Rai-Constapel, P. Gilch, T. J. J. Müller, *ChemPlusChem* **2013**, *78*, 137.

[219] T. Nakamura, H. Ube, M. Shionoya, *Angew. Chem. Int. Ed.* **2013**, *52*, 12096.

[220] A. Dubey, A. Mishra, J. W. Min, M. H. Lee, H. Kim, P. J. Stang, K.-W. Chi, *Inorg. Chim. Acta* **2014**, *423*, 326.

[221] M. Wang, V. Vajpayee, S. Shanmugaraju, Y.-R. Zheng, Z. Zhao, H. Kim, P. S. Mukherjee, K.-W. Chi, P. J. Stang, *Inorg. Chem.* **2011**, *50*, 1506.

[222] J. Ahrens, M. Frank, G. H. Clever, D. Schwarzer, *Phys. Chem. Chem. Phys.* **2017**, *19*, 13596.

[223] S. Chen, K. Li, F. Zhao, L. Zhang, M. Pan, Y.-Z. Fan, J. Guo, J. Shi, C.-Y. Su, *Nat. Commun.* **2016**, *7*, 13169.

[224] X. Jing, C. He, Y. Yang, C. Duan, *J. Am. Chem. Soc.* **2015**, *137*, 3967.

[225] X. Jing, Y. Yang, C. He, Z. Chang, J. N. H. Reek, C. Duan, *Angew. Chem. Int. Ed.* **2017**, *129*, 11921.

[226] Y. Yang, H. Li, X. Jing, Y. Wu, Y. Shi, C. Duan, *Chem. Commun.* **2021**, *58*, 807.

[227] D. Liu, H. Ma, C. Zhu, F. Qiu, W. Yu, L.-L. Ma, X.-W. Wei, Y.-F. Han, G. Yuan, *J. Am. Chem. Soc.* **2024**, *146*, 2275.

[228] R. Ham, C. J. Nielsen, S. Pullen, J. N. H. Reek, *Chem. Rev.* **2023**, *123*, 5225.

[229] K. Wu, K. Li, S. Chen, Y.-J. Hou, Y.-L. Lu, J.-S. Wang, M.-J. Wei, M. Pan, C.-Y. Su, *Angew. Chem. Int. Ed.* **2019**, *59*, 2639.

[230] C. He, J. Wang, L. Zhao, T. Liu, J. Zhang, C. Duan, *Chem. Commun.* **2012**, *49*, 627.

[231] L. Yang, C. He, X. Liu, J. Zhang, H. Sun, H. Guo, *Chem. Eur. J.* **2016**, *22*, 5253.

[232] H. Wang, L. Li, X. Li, C. He, *Isr. J. Chem.* **2018**, *59*, 273.

[233] H. Yu, C. He, J. Xu, C. Duan, J. N. H. Reek, *Inorg. Chem. Front.* **2016**, *3*, 1256.

[234] S. S. Nurttila, R. Becker, J. Hessels, S. Woutersen, J. N. H. Reek, *Chem. Eur. J.* **2018**, *24*, 16395.

[235] D. Hong, L. Shi, X. Liu, H. Ya, X. Han, *Molecules* **2023**, *28*, 4068.

[236] Y. Peng, Z. Su, M. Jin, L. Zhu, Z.-J. Guan, Y. Fang, *Dalton Trans.* **2023**, *52*, 15216.

[237] W. Cullen, H. Takezawa, M. Fujita, *Angew. Chem. Int. Ed.* **2019**, *58*, 9171.

[238] M. Yoshizawa, S. Miyagi, M. Kawano, K. Ishiguro, M. Fujita, *J. Am. Chem. Soc.* **2004**, *126*, 9172.

[239] T. Murase, Y. Nishijima, M. Fujita, *Chem. Asian J.* **2012**, *7*, 826.

[240] T. Murase, H. Takezawa, M. Fujita, *Chem. Commun.* **2011**, *47*, 10960.

[241] J. Guo, Y. Xu, K. Li, L. Xiao, S. Chen, K. Wu, X. Chen, Y. Fan, J. Liu, C. Su, *Angew. Chem. Int. Ed.* **2017**, *129*, 3910.

[242] J. Guo, Y. Fan, Y. Lu, S. Zheng, C. Su, *Angew. Chem. Int. Ed.* **2020**, *59*, 8661.

[243] J.-S. Wang, K. Wu, C. Yin, K. Li, Y. Huang, J. Ruan, X. Feng, P. Hu, C.-Y. Su, *Nat. Commun.* **2020**, *11*, 4675.

[244] D. Roy, S. Paul, J. Dasgupta, *Angew. Chem. Int. Ed.* **2023**, *62*, e202312500.

[245] A. Das, I. Mandal, R. Venkatramani, J. Dasgupta, *Sci. Adv.* **2019**, *5*, eaav4806.

[246] S. Ghosal, A. Das, D. Roy, J. Dasgupta, *Nat. Commun.* **2024**, *15*, 1810.

[247] K. K. Yadav, R. Tyagi, V. K. Voora, J. Dasgupta, **2025**, DOI 10.26434/chemrxiv-2025-sffb5.

[248] R. A. Marcus, *Angew. Chem. Int. Ed.* **1993**, *32*, 1111.

[249] E. J. Piechota, G. J. Meyer, *J. Chem. Educ.* **2019**, *96*, 2450.

[250] R. A. Marcus, N. Sutin, *Biochim. Biophys. Acta (BBA) - Rev. Bioenerg.* **1985**, *811*, 265.

[251] T. P. Silverstein, *J. Chem. Educ.* **2012**, *89*, 1159.

[252] J. Eriksen, C. S. Foote, *J. Phys. Chem.* **1978**, *82*, 2659.

[253] R. Scheerer, M. Graetzel, *J. Am. Chem. Soc.* **1977**, *99*, 865.

[254] C. R. Bock, T. J. Meyer, D. G. Whitten, *J. Am. Chem. Soc.* **1975**, *97*, 2909.

[255] D. Rehm, A. Weller, *Isr. J. Chem.* **1970**, *8*, 259.

[256] J. Ulstrup, J. Jortner, *J. Chem. Phys.* **1975**, *63*, 4358.

[257] V.G. Levich *Adv. Electrochem. Electrochem. Eng.* **1966**, *4*, 249.

[258] R. A. Marcus, *J. Chem. Phys.* **2006**, *125*, 194504.

[259] F. Yu, V. M. Cangelosi, M. L. Zastrow, M. Tegoni, J. S. Plegaria, A. G. Tebo, C. S. Mocny, L. Ruckthong, H. Qayyum, V. L. Pecoraro, *Chem. Rev.* **2014**, *114*, 3495

[260] J. R. Winkler, H. B. Gray, *Chem. Rev.* **2014**, *114*, 3369.

[261] C. C. Moser, P. L. Dutton, *Adv. Photosynth. Respir.* **2006**, 583.

[262] D. N. LeBard, V. Kapko, D. V. Matyushov, *J. Phys. Chem. B* **2008**, *112*, 10322.

[263] J. Bisquert, R. A. Marcus, *Top. Curr. Chem.* **2013**, *352*, 325.

[264] Y. Zhao, W. Liang, *Chem. Soc. Rev.* **2011**, *41*, 1075.

[265] Z. Shuai, W. Li, J. Ren, Y. Jiang, H. Geng, *J. Chem. Phys.* **2020**, *153*, 080902.

Scope of the thesis

The work presented in this thesis aims at contributing to the rational design approaches for coordination assemblies of a particular size and function.

On one hand, the self-assembly into coordination rings Pd_nL_{2n} ($n = 3$-5) is studied. Stiff bis-monodentate ligands are chosen for sketching a relationship between the ligand bent angle and the ring size. The ligand geometry is adjusted to allow for the beforehand unreported self-assembly into a homoleptic five-membered ring Pd_5L_{10} in the absence of a template (chapter 2).

On the other hand, the photoinduced processes in donor-acceptor cages are studied. A strategy for the non-statistical self-assembly is applied for realizing a library of donor-acceptor cages with the same stoichiometry and stereoconfiguration but varying redox active moieties. The ground state photophysical and electrochemical properties are thoroughly investigated for estimating the thermodynamic driving forces for charge separation and recombination. Next, the ultrafast photoinduced dynamics are studied and correlated to the thermodynamic driving forces in the framework of Marcus theory (chapter 3).

Lastly, the first steps towards incorporation of photoredox active cages into soft materials are undertaken. One of the donor-acceptor cages is anisotropically modified with nonpolar chains for endowing it with amphiphilicity. The higher order self-assembly and their incorporation into aqueous solutions of polymeric micelles is studied (chapter 4).

2. Self-assembly of five-membered rings Pd_5L_{10} by ligand angle adjustment

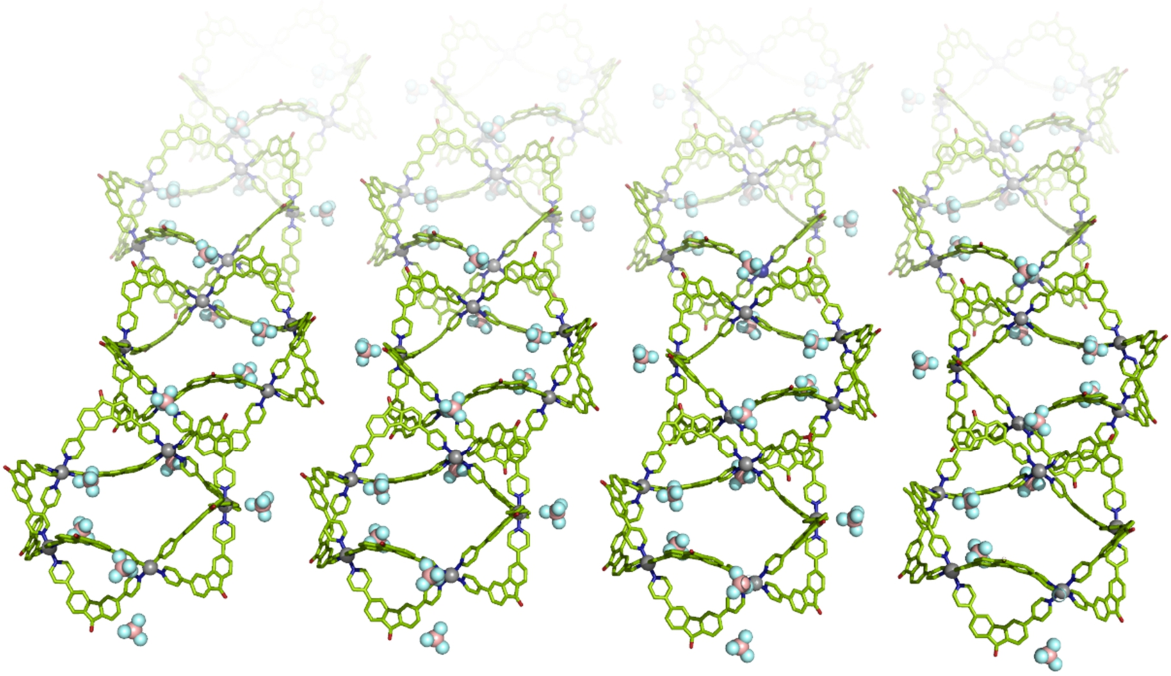

Contents of this chapter are published in:

L. Neukirch, M. D. Kulas, J. J. Holstein and G. H. Clever*

Non-Templated Assembly of D5h-Symmetric Pd5L10 Rings by Precise Ligand Angle Adjustment

Chem. Eur. J., **2024**, *30*, e202400132.

2.1. Motivation

Controlling the size and shape of supramolecular assemblies is of high importance for the design of suitable host architectures. While counter anion templation allows the exclusive formation of coordination assemblies of a particular size,[1] it comes with the disadvantage of an occupied cavity. Removal of the counter anion can result in structural reorganization when the assembly is based on dynamic metal-ligand bonds such as Pd(II) pyridine bonds. Therefore, an attractive approach for gaining control over the assembly size is the design of organic ligands featuring a suitable geometry. The group of Fujita studied the dependency of the ligand bent angle on the size of Pd_nL_{2n} spheres ($n \geq 6$)[2–4] but such a systematic study has not yet been performed for smaller assemblies. Moreover, while several three-[5–7] and four-membered[5,6,8,9] rings were reported for assemblies based on Pd(II) and bis-pyridyl ligands, five-membered rings remain rare. The sole example of a homoleptic ring Pd_5L_{10} was achieved with a benzimidazole ligand and a templating anion by Sun and coworkers (section 1.3.2).[1] Yoshizawa and Chand reported on a heteroleptic ring $Pd_5A_5B_5$.[10]

In general, compounds with five-fold symmetry have garnered particular interest[11] and five-membered supramolecular architectures were reported based on other metal-ligand combinations. Examples for this include the circular helicates reported by Lehn[12,13] and the pentafoil knots reported by Leigh (Fig. 1a)[14] that are based on Fe(II) metal nodes and bipyridine ligands. Selection of the particular ring size can be traced back to a template effect of the central chloride anion, engaging in $CH\cdots Cl^-$ as well as long-range electrostatic $Fe(II)\cdots Cl^-$ interactions.[15] Moreover, Nitschke and coworkers used a penta-amino functionalized corannulene, i.e. an organic component featuring five-fold symmetry, as subcomponent for the assembly with formyl phenanthroline and Co(II) or Zn(II) metal ions to yield D_5-symmetric cages (Fig. 1b).[16] The group of Dunbar showed that bis-pyridyl tetrazine assembles with Ni(II) into Pd_4L_4-type squares when tetrafluoroborate or perchlorate anions are used while a pentagonal Pd_5L_5 is formed upon self-assembly with hexafluoroantimonate (Fig. 1c).[17,18] Additionally, Newkome assembled a five-membered ring M_5L_5 with bis-terpyridine functionalized carbazole and different metal ions (Fig. 1d).[19]

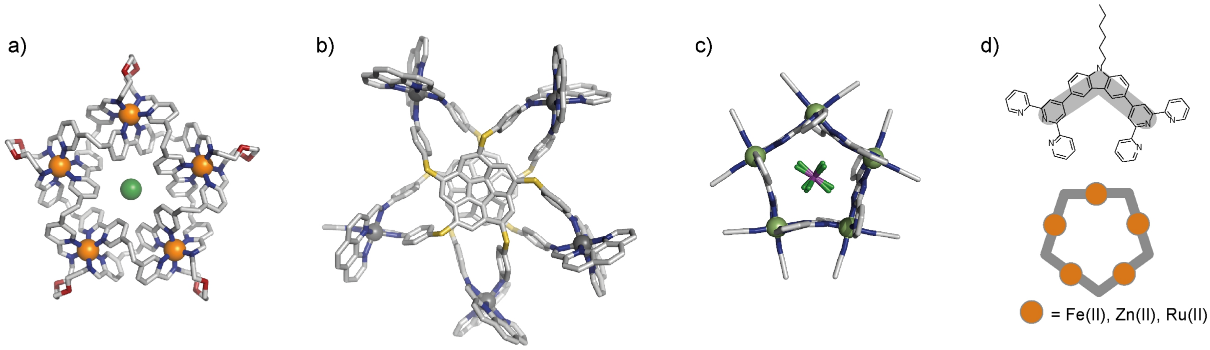

Fig. 1 Five-membered supramolecular architectures based on different metal-ligand combinations; a) Leigh's pentafoil knot with a central chloride anion;[14] b) Nitschke's D_5-symmetric cage (shown with Zn(II) metal centers);[16] c) Dunbar's Ni_5L_5 ring with a central hexafluoroantimonate anion;[18] d) Newkome's M_5L_5 ring.[19]

Owing to the missing guidelines for the design of coordination rings Pd_nL_{2n} (n = 3-5) and the rarity of five-membered rings Pd_5L_{10}, this work aims at:

1) studying the self-assembly of bis-pyridyl ligands and Pd(II) into five-membered rings Pd_5L_{10} in the absence of a template and

2) drawing a relationship between the ligand binding angle and the nuclearity for three- to five-membered rings.

2.2. Self-assembly into coordination rings

For the design of ligands with a suitable geometry for the formation of three- and five-membered rings, it was considered that lantern-shaped cages Pd_2L_4 are obtained with ligands with collinear binding vectors $\alpha \approx 0°$,[20] four-membered rings Pd_4L_8 with ligands possessing an angle α of 63°,[8] and cubes Pd_6L_{12} with ligands with rectangular geometry ($\alpha \approx 90°$) (section 1.3.2.).[21] Short ligands were designed (i.e. without linker) owing to their lower flexibility. The latter promises a more predictable self-assembly outcome.

For the self-assembly into a three-membered ring, dithienothiophene-based ligand **L1** was synthesized in one step via a Suzuki cross-coupling (appendix, section 2.7.2). In a concave binding situation of the flat ligand, the binding angle amounts to 28°, i.e. lies half-way in between the ones forming lantern-shaped cages and four-membered rings, respectively. For the self-assembly, a 1.4 mM solution of the ligand was combined with $[Pd(CH_3CN)_4](BF_4)_2$ in DMSO-d_6 and heated for 3 h at 70 °C. These self-assembly conditions ($[Pd(CH_3CN)_4](BF_4)_2$, DMSO-d_6) were chosen for the sake of comparability with other works on coordination rings.[8] In the ^1H NMR spectrum, the signals of all protons but most prominently for protons a and b, that are adjacent to the nitrogen donor, are downfield shifted (Fig. 2b). This is characteristic for the coordination to Pd(II) which is accompanied by a reduction in the electron density close to the donor site. With a ^1H DOSY NMR experiment, a diffusion coefficient of $D_H = 5.93 \cdot 10^{-11}\ m^2 \cdot s^{-1}$ was obtained. This corresponds to a hydrodynamic radius of 12.5 Å according to the Stokes-Einstein equation, assuming that the species is spherical.[22] In the electrospray ionization (ESI) mass spectrum, prominent peaks for $[Pd_3\mathbf{L1}_6+nBF_4]^{6-n+}$ (n = 0-3) were observed (Fig. 2c). Aside from a three-membered ring, a double trefoil knot structure was reported for this sum formula.[23] However, the small length of ligand **L1** and, more tangibly, the single set of signals observed in the ^1H NMR spectrum, which attests a high symmetry of the assembly, strongly points towards the formation of a three-membered ring $[Pd_3\mathbf{L1}_6]^{6+}$.

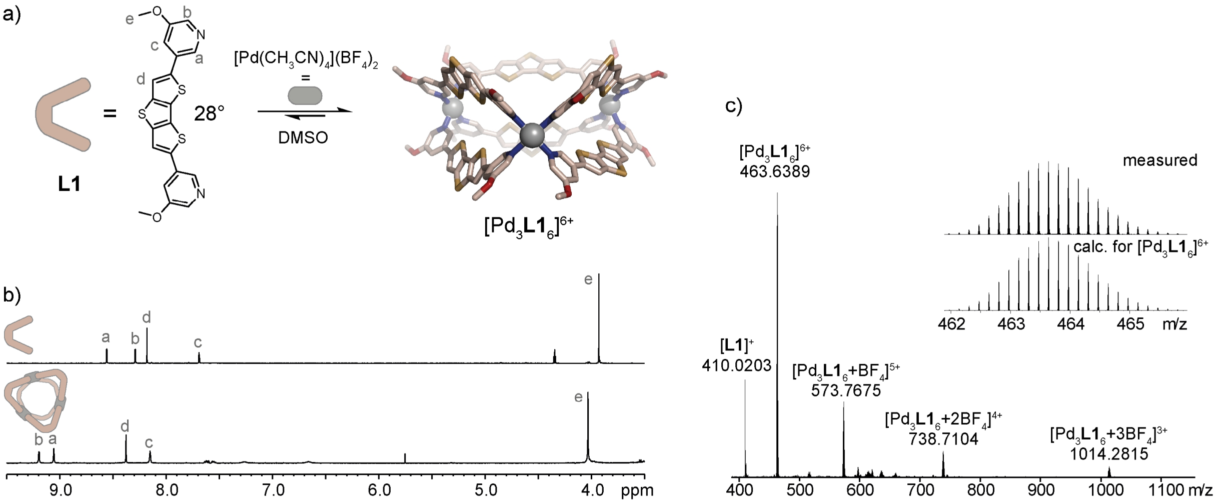

Fig. 2 Self-assembly of three-membered ring $[Pd_3\mathbf{L1}_6]^{6+}$; a) self-assembly scheme and DFT-optimized structure of $[Pd_3\mathbf{L1}_6]^{6+}$; b) ^1H NMR spectra of ligand **L1** (top) and $[Pd_3\mathbf{L1}_6]^{6+}$ (bottom) (600 MHz, 500 MHz, 298 K, DMSO-d_6); c) ESI mass spectrum of $[Pd_3\mathbf{L1}_6]^{6+}$.

Aiming at accessing five-membered rings with bis-pyridyl ligands, the self-assembly of fluorenone-based ligand **L2** with a bent angle of 84°, lying in between the angles of ligands forming four-membered rings and octahedra, respectively, was examined under the same conditions (Fig. 3). The ligand was reported beforehand in the context of heteroleptic cages.[24] Again, a downfield shift of the ^1H NMR signals assignable to the pyridine protons a and b was observed, indicating coordination to Pd(II). A single set of signals reveals that an assembly of high symmetry formed. In comparison to the ^{1}H NMR spectrum of $[\mathrm{Pd}_3\mathbf{L1}_6]^{6+}$, the signals are broadened, suggesting formation of a larger species. In agreement with this, ^{1}H DOSY NMR yielded a hydrodynamic radius of 16.8 Å. Finally, investigation with ESI mass spectrometry disclosed that a pentanuclear species $[\mathrm{Pd}_5\mathbf{L2}_{10}]^{10+}$ was afforded. Yellow, block-shaped single crystals suitable for synchrotron X-ray diffraction were grown by slow vapor diffusion of toluene into an acetonitrile solution of the assemblies of **L2**. In agreement with the experiments carried out in solution, the diffraction experiment unraveled a cyclic arrangement of the ligands in the pentanuclear species. The ring crystallized in space group *P*nma with one half of the ring per asymmetric unit and a mirror-plane passing through the cyclically arranged Pd(II) nodes (Fig. 3, 6a).

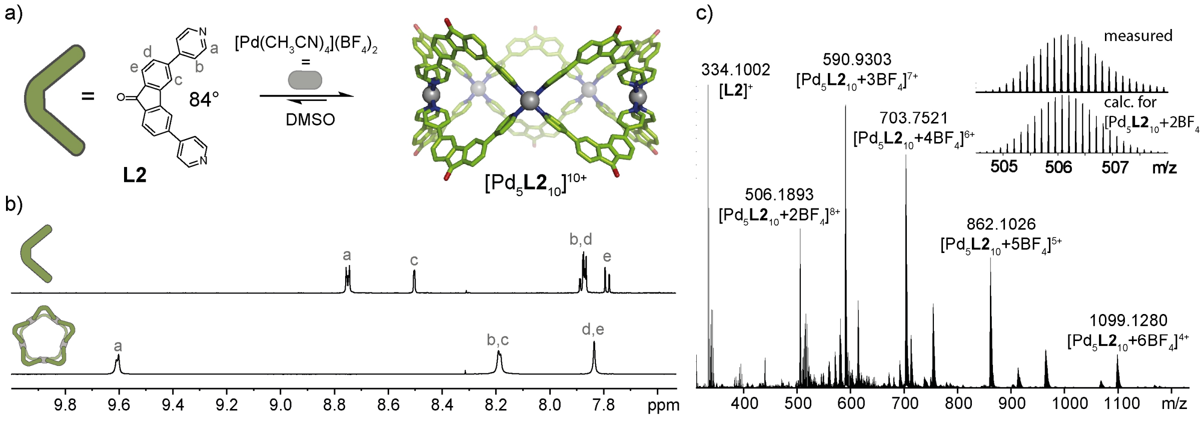

Fig. 3 Self-assembly of five-membered ring $[\mathrm{Pd}_5\mathbf{L2}_{10}]^{10+}$; a) self-assembly scheme and X-ray crystal structure of $[\mathrm{Pd}_5\mathbf{L2}_{10}]^{10+}$; b) ^{1}H NMR spectra of ligand **L2** (top) and $[\mathrm{Pd}_5\mathbf{L2}_{10}]^{10+}$ (bottom) (500 MHz, 700 MHz, 298 K, DMSO-d_6); c) ESI mass spectrum of $[\mathrm{Pd}_5\mathbf{L2}_{10}]^{10+}$.

For ensuring that the formation of $[\mathrm{Pd}_5\mathbf{L2}_{10}]^{10+}$ can be traced back to a suitable ligand geometry rather than to favorable reaction conditions, the self-assembly of **L2** was tested with different counter anions, across various concentrations, and in different solvents (appendix, section 2.7.4). The self-assembly of **L2** with triflate and hexafluorophosphate salts, respectively, led to one set of slightly broadened signals in the ^{1}H NMR, reminiscent of the five-membered ring formed with the tetrafluoroborate salt (Fig. 4). Moreover, the ESI mass spectrum evidenced formation of $[\mathrm{Pd}_5\mathbf{L2}_{10}]^{10+}$ with both counter anions, excluding strong counter anion templation. Next, the self-assembly was studied at ligand concentrations ranging from 0.6 to 11.1 mM. Across five tested concentrations, the five-membered ring $[\mathrm{Pd}_5\mathbf{L2}_{10}]^{10+}$ was obtained as sole assembly; however, at concentrations ≤ 1.1 mM, the free ligand was observed along with the assembly. The self-assembly of **L2** with $[\mathrm{Pd}(\mathrm{CH}_3\mathrm{CN})_4](\mathrm{BF}_4)_2$ in acetonitrile and dimethylformamide (DMF) resulted in a mixture of different species. In both solvents, tetra-, penta-, and hexanuclear species were observed in the ESI mass spectrum. Penta- and hexanuclear species are most probably assignable to a five-membered ring and a cube, respectively. The ^{1}H NMR spectrum in DMF features well-separated signals, that allowed for assignment of the signals to three distinct species. Two of them possess high symmetry (one set of signals) and are probably assignable to the penta- and hexanuclear structures. The third species gives rise to a 1:1 split of the signals and can therefore presumably be assigned to a pseudo-tetrahedron. Overall, across the conditions investigated, the five-membered ring is the main species or one of the main species.

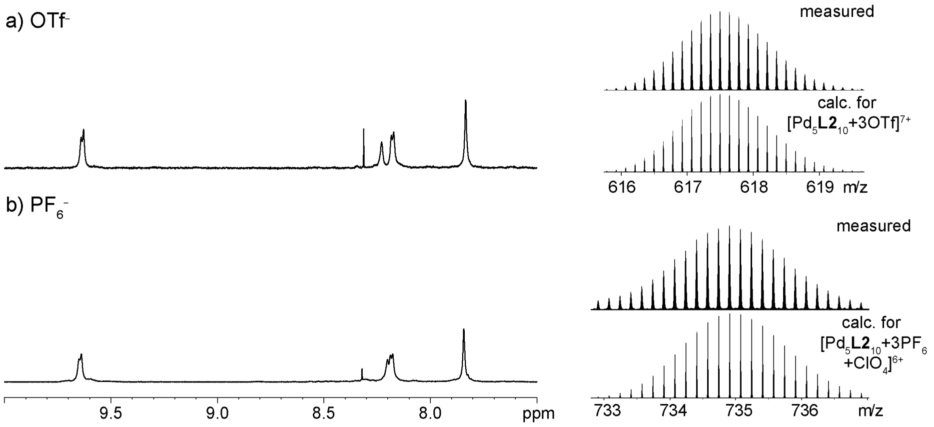

Fig. 4 Self-assembly of ligand **L2** with a) [Pd(CH$_3$CN)$_4$](CF$_3$SO$_3$)$_2$ (left: ^{1}H NMR spectrum (500 MHz, 298 K, DMSO-*d*$_6$), right: isotopic pattern of the ESI mass spectrum, OTf$^-$ = CF$_3$SO$_3^-$), b) [Pd(CH$_3$CN)$_4$](PF$_6$)$_2$ (left: ^{1}H NMR spectrum (500 MHz, 298 K, DMSO-*d*$_6$), right: isotopic pattern of the ESI mass spectrum).

In order to explore how small deviations in the ligand bent angle affect the self-assembly outcome, small rigid ligand **L3** was designed. **L3** possesses a high structural similarity with fluorenone-based ligand **L2** but differs in the substitution of the central five-membered ring which translates into a narrower binding angle of 78°. The ligand was synthesized via Suzuki cross coupling (appendix, section 2.7.2). Next, a 1.4 mM solution of ligand **L3** was combined with [Pd(CH$_3$CN)$_4$](BF$_4$)$_2$ in DMSO-*d*$_6$ and heated for 3 h at 70 °C. The ^{1}H NMR spectrum revealed formation of two distinct species of high symmetry with an integral ratio of 1:0.2 (Fig. 5b). For the main species, ^{1}H DOSY NMR yielded a hydrodynamic radius of 14.8 Å which lies in between the ones of three- and five-membered rings [Pd$_3$**L1**$_6$]$^{6+}$ and [Pd$_5$**L2**$_{10}$]$^{10+}$, pointing towards the formation of a tetranuclear species. In agreement with this, the ESI mass spectrum showed predominant peaks for [Pd$_4$**L3**$_8$+nBF$_4$]$^{6-n+}$ (n = 1-5). Pentanuclear [Pd$_5$**L3**$_{10}$]$^{10+}$ was identified as minor species in the mass spectrum (Fig. 5c). Aside from four-membered rings, interlocked lantern-shaped cages, tetrahedra, and twisted bridged bowls (see chapter 1.3.2.) obey the sum formula Pd$_4$L$_8$. However, the reduced symmetry of these species would result in signal splitting which is not observed in the ^{1}H NMR spectrum of [Pd$_4$**L3**$_8$]$^{8+}$. The tetranuclear assembly of ligand **L3** is therefore assigned to a four-membered ring. Self-assembly of ligand **L3** with [Pd(CH$_3$CN)$_4$](BF$_4$)$_2$ in acetonitrile and DMF resulted in the formation of a mixture of tetra-, penta-, and hexanuclear species (appendix, section 2.7.4). In contrast to the mixtures obtained with ligand **L2** with a slightly larger bent angle, only traces of the hexanuclear species were observed in the ESI mass spectrum, attesting the preference of ligand **L3** for species of lower nuclearity.

2. Self-assembly of five-membered rings Pd5L10 by ligand angle adjustment

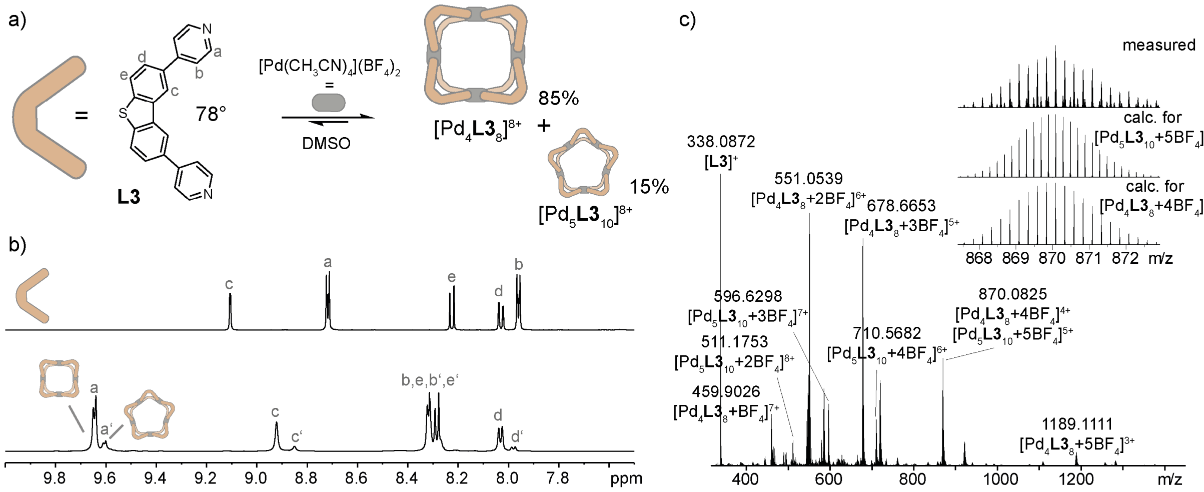

Fig. 5 Self-assembly of ligand **L3** into an equilibrated mixture of $[\mathrm{Pd}_4\mathbf{L3}_8]^{8+}$ and $[\mathrm{Pd}_5\mathbf{L3}_{10}]^{10+}$; a) self-assembly scheme; b) ^{1}H NMR spectra of ligand **L3** (top) and a mixture of $[\mathrm{Pd}_4\mathbf{L3}_8]^{8+}$ and $[\mathrm{Pd}_5\mathbf{L3}_{10}]^{10+}$ (bottom) (600 MHz, 298 K, DMSO-d_6); c) ESI mass spectrum of $[\mathrm{Pd}_4\mathbf{L3}_8]^{8+}$ and $[\mathrm{Pd}_5\mathbf{L3}_{10}]^{10+}$.

Slow diffusion of toluene into a solution of the assemblies of **L3** in DMF-d_7 yielded colorless block-shaped single crystals. Investigation with synchrotron X-ray diffraction unveiled that five-membered ring $[\mathrm{Pd}_5\mathbf{L3}_{10}]^{10+}$ had crystallized. When comparing the crystal structures of $[\mathrm{Pd}_5\mathbf{L2}_{10}]^{10+}$ and $[\mathrm{Pd}_5\mathbf{L3}_{10}]^{10+}$, the non-ideal, too narrow binding angle of ligand **L3** for the self-assembly into a five-membered ring becomes visible (Fig. 6). Firstly, for $[\mathrm{Pd}_5\mathbf{L3}_{10}]^{10+}$, the arrangement of the Pd(II) nodes deviates more strongly from an ideal pentagon, which possesses an interior angle of 108°. More precisely, the Pd-Pd-Pd angles range between 106 and 109° in $[\mathrm{Pd}_5\mathbf{L2}_{10}]^{10+}$ and between 102 and 119° in $[\mathrm{Pd}_5\mathbf{L3}_{10}]^{10+}$ (appendix, section 2.7.5). Secondly, the distribution of the distances between two backbones bridging the same edge varies less in $[\mathrm{Pd}_5\mathbf{L2}_{10}]^{10+}$ (d = 12.5-13.8 Å) as compared to in $[\mathrm{Pd}_5\mathbf{L3}_{10}]^{10+}$ (d = 12.4-14.8 Å) (distances were measured between the edges of the backbones, i.e. for ligand **L2** between the two carbonyl oxygen atoms and for ligand **L3** between the sulfur atoms). Thirdly, the coordination environment is more strained in $[\mathrm{Pd}_5\mathbf{L3}_{10}]^{10+}$: the Pd-N-C(ipso) angle, which amounts ideally to 180°, is only slightly smaller in $[\mathrm{Pd}_5\mathbf{L2}_{10}]^{10+}$ (171-179°) but adopts values of 166-180° in $[\mathrm{Pd}_5\mathbf{L3}_{10}]^{10+}$. While these observations could simply stem from crystal packing effects, they indicate higher conformational strain of $[\mathrm{Pd}_5\mathbf{L3}_{10}]^{10+}$ as compared to $[\mathrm{Pd}_5\mathbf{L2}_{10}]^{10+}$ which is in agreement with the observation that ligand **L3** preferentially forms a four-membered ring in solution.

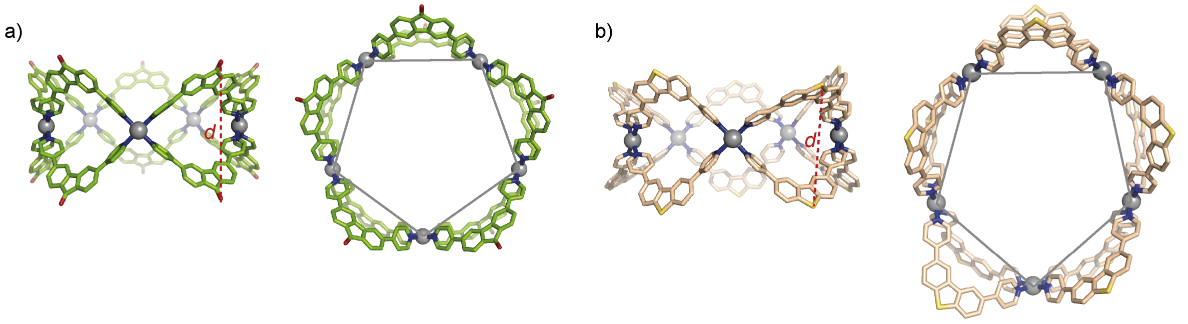

Fig. 6a) X-ray crystal structure of $[\mathrm{Pd}_5\mathbf{L2}_{10}]^{10+}$ (left: front view, right: top view); b) X-ray crystal structure of $[\mathrm{Pd}_5\mathbf{L3}_{10}]^{10+}$ (left: front view, right: top view); indicated with red dotted line: distances between two backbones bridging the same edge; gray lines connect two adjacent Pd(II) nodes.

2.3. DFT computations: conformational strain

For supporting that the conformational strain is decisive for the preference for either the four-or the five-membered ring, the difference in strain associated with a ring-to-ring transformation was investigated with DFT computations. The coordination rings were first subjected to a geometry optimization (B3LYP/Def-SVP). Next, a single point energy calculation was performed (wb97xd/Def-SVP). The energy for the transformation of four-membered into five-membered rings can be obtained with equation 1. In order to mainly account for the difference in conformational strain, the energy values of the rings were corrected by the electrostatic repulsion ΔE_{Coul} between the Pd(II) complexes. The latter corresponds to the difference in energy between the cyclically arranged $[\mathrm{Pdpy}_4]^{2+}$ complexes and the respective number of complexes that are in infinite distance to each other (eq. 2, Fig. 8). For this, the $[\mathrm{Pdpy}_4]^{2+}$ complexes were carved out of the rings.

$$\Delta E(\mathrm{Pd}_4 \rightarrow \mathrm{Pd}_5, \mathbf{L2}) = 4 \cdot E(\mathrm{Pd}_5\mathbf{L2}_{10}) - 5 \cdot E(\mathrm{Pd}_4\mathbf{L2}_{10}) \tag{1}$$

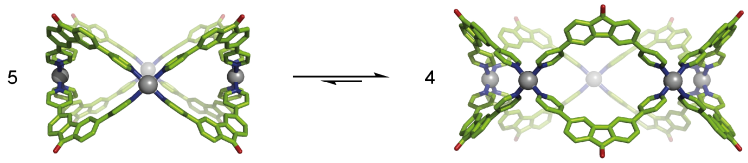

Fig. 7 Transformation of four-membered rings $[\mathrm{Pd}_4\mathbf{L2}_8]^{8+}$ into five-membered rings $[\mathrm{Pd}_5\mathbf{L2}_{10}]^{10+}$; shown are the DFT-optimized ring structures.

$$\Delta E_{\mathrm{Coul}}, \mathrm{Pd}_5\mathbf{L2}_{10} = E(\mathrm{Pd}_5\mathrm{py}_{20}) - 5 \cdot E(\mathrm{Pdpy}_4) \tag{2}$$

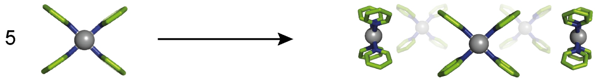

Fig. 8 Representation of the calculation of the Coulomb repulsion ΔE_{Coul} which corresponds to the destabilization of the cyclic arrangement of the $[\mathrm{Pdpy}_4]^{2+}$ complexes (right) relative to the complexes in infinite distance to each other (left).

Intuitively, the Coulomb repulsion in the five-membered rings exceeds the one in the four-membered rings (Tab. 1). Moreover, the Coulomb repulsion is slightly larger for rings with ligand **L3** as compared to the ones with ligand **L2**. This can be traced back to the smaller Pd-Pd distance in rings based on **L3** (distances in the DFT-optimized structures: $[\mathrm{Pd}_4\mathrm{L}_8]^{8+}$ (**L2**: 14.0 Å, **L3**: 13.6 Å), $[\mathrm{Pd}_5\mathrm{L}_{10}]^{10+}$ (**L2**: 14.5 Å, **L3**: 14.1 Å)), most probably due to its smaller bent angle.

Overall, the difference in conformational strain associated with the ring-to-ring transformation is then obtained with equation 3. For ligand **L2**, the transformation into the five-membered ring is strongly favored ($E_{\mathrm{S}}(\mathrm{Pd}_4 \rightarrow \mathrm{Pd}_5$, **L2**$) = -39.7$ kJ/mol), in line with the experimentally observed exclusive formation of this ring, while for ligand **L3**, the transformation is slightly disfavored ($E_{\mathrm{S}}(\mathrm{Pd}_4 \rightarrow \mathrm{Pd}_5$, **L3**$) = +4.6$ kJ/mol). Again, this is in accordance with the experimentally observed formation of a mixture of rings of both sizes with the four-membered rings as the main species. Attempting to refine the computations, DMSO was added as an implicit solvent for the single point energy calculation by using the SCRF method. This resulted in a reduction of the energies $E_{\mathrm{S}}(\mathrm{Pd}_4 \rightarrow \mathrm{Pd}_5)$ of the ring-to-ring transformations for both ligands. While the trends still match the experimental observations in the sense that the five-membered ring is more strongly favored for ligand **L2** than for ligand **L3**, the absolute energies cannot explain the experimental results ($E_{\mathrm{S}}(\mathrm{Pd}_4 \rightarrow \mathrm{Pd}_5$, **L2**$) = -91.5$ kJ/mol, $E_{\mathrm{S}}(\mathrm{Pd}_4 \rightarrow \mathrm{Pd}_5$, **L3**$) = -26.7$ kJ/mol) (see appendix, section 2.7.6). These calculations only consider enthalpic contributions. The entropic advantage of the formation of the smaller four-membered ring is not captured which might explain the overestimated preference for the five-membered ring.

$$E_S(\mathrm{Pd}_4 \rightarrow \mathrm{Pd}_5, \mathbf{L2}) = \\ 4 \cdot \left(E(\mathrm{Pd}_5\mathbf{L2}_{10}) - \Delta E_{\mathrm{Coul}}, \mathrm{Pd}_5\mathbf{L2}_{10}\right) - 5 \cdot \left(E(\mathrm{Pd}_4\mathbf{L2}_8) - \Delta E_{\mathrm{Coul}}, \mathrm{Pd}_4\mathbf{L2}_8\right) \tag{3}$$

Tab. 1 Single point energies E obtained by DFT computations (wb97xd/Def-SVP) and Coulomb repulsions ΔE_{Coul} obtained with equation 2.

	$[\mathrm{Pd}_4\mathbf{L2}_8]^{8+}$	$[\mathrm{Pd}_5\mathbf{L2}_{10}]^{10+}$	$[\mathrm{Pd}_4\mathbf{L3}_8]^{8+}$	$[\mathrm{Pd}_5\mathbf{L3}_{10}]^{10+}$
E in kJ/mol	−23780005.73	−29724602.31	−29763591.91	−37204065.48
ΔE_{Coul} in kJ/mol	2142.67	3093.11	2183.51	3152.63

2.4. Geometrical relationship between the ligand bent angle and the ring nuclearity

Aiming at quantifying the observed dependence of the ring nuclearity on the ligand binding angle, a geometrical relationship was derived. For this, the ligands were approximated as stiff, triangular flaps sitting on the edges of a regular n-gon (flaps in green, plane of the n-gon in blue for n = 5, Fig. 9b). The internal angle β of a regular n-gon depends on the number of vertexes n according to equation 4.

$$\beta = \frac{(\mathrm{n}-2)}{\mathrm{n}} \cdot 180° \tag{4}$$

Trigonometric relationships were used for connecting the number of vertexes n with the angle β_1 of the triangular flap, which will be referred to as theoretical ligand binding angle. The height h of the triangle in the pentagon plane can be expressed as a function of β and the base b (eq. 5). For obtaining an expression for the height h_1 of the triangular flap, the angle of the flap relative to the pentagon plane must be fixed. By assuming that they adopt an angle of 45°, the height h_1 can be expressed as a function of β (eq. 6). With the height h_1 and the base b, which both triangles share, an expression for β_1 can be obtained (eq. 7). Considering the earlier mentioned relationship between β and the number of vertexes (eq. 4), equation 8 is obtained which allows for the calculation of the theoretical ligand binding angle β_1 based on the nuclearity n or vice versa.

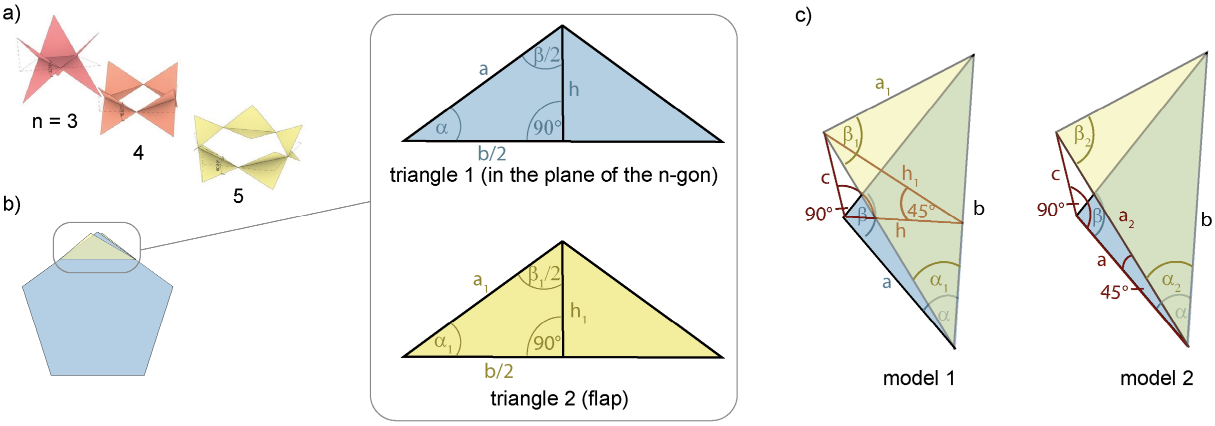

Fig. 9 Geometrical model for n-membered rings; a) representation of model 1 for n = 3-5; b) representation of angles and lengths in the triangle that lies in the pentagon plane (blue) and the triangle representing the stiff ligand ("flap", yellow); c) assumptions drawn in model 1 (left) and 2 (right).

$$\tan\left(\frac{\beta}{2}\right) = \frac{\mathrm{b}}{2 \cdot \mathrm{h}} \quad \leftrightarrow \quad \mathrm{h} = \frac{\mathrm{b}}{2 \cdot \tan\left(\frac{\beta}{2}\right)} \tag{5}$$

$$\cos(45°) = \frac{h}{h_1} = \frac{b}{h_1 \cdot 2 \cdot \tan\left(\frac{\beta}{2}\right)} \leftrightarrow h_1 = \frac{b}{\cos(45°) \cdot 2 \cdot \tan(\frac{\beta}{2})} \tag{6}$$

$$\tan\left(\frac{\beta_1}{2}\right) = \frac{b}{2 \cdot h_1} = \tan(\frac{\beta}{2}) \cdot \cos(45°) \tag{7}$$

$$\beta_1 = 2 \cdot \arctan(\frac{1}{\sqrt{2}} \cdot \tan\left(90° \cdot \frac{(n-2)}{n}\right)) \tag{8}$$

In order to evaluate the applicability of the model, the theoretical binding angles β_1 were calculated for the ring sizes n = 3, 4, and 5 and compared with the binding angles of the ligands introduced in this work and ligands reported beforehand (Tab. 2, Fig. 10). The theoretical angles β_1 trend as an upper bound for a given ring nuclearity meaning that they are somewhat overestimated. There are two factors that contribute to a deviation of the theoretical angle β_1 from the binding angle of the ligand: first, the ligand flexibility is not considered in the model. A ligand that features a suitable geometry for a particular ring size in its stiff, flat form will still assemble to a ring of lower nuclearity as long as the entropic advantage of the formation of the smaller ring outcompetes the enthalpic disadvantage of the bending of the aromatic plane. This leads to an underestimation of the theoretical bent angle. Second, fixing the flap at a 45° angle with respect to the plane of the n-gon leads to angles between the edges of the triangular flaps that are smaller than 90°, i.e. there is a deviation from the square planar coordination geometry in the model (see appendix, section 2.7.7) which is not observed in the X-ray structures and DFT models. This deviation to smaller values leads to an overestimation of the bent angle. These two factors are counteractive; the systematic overestimation indicates that the second effect predominates.

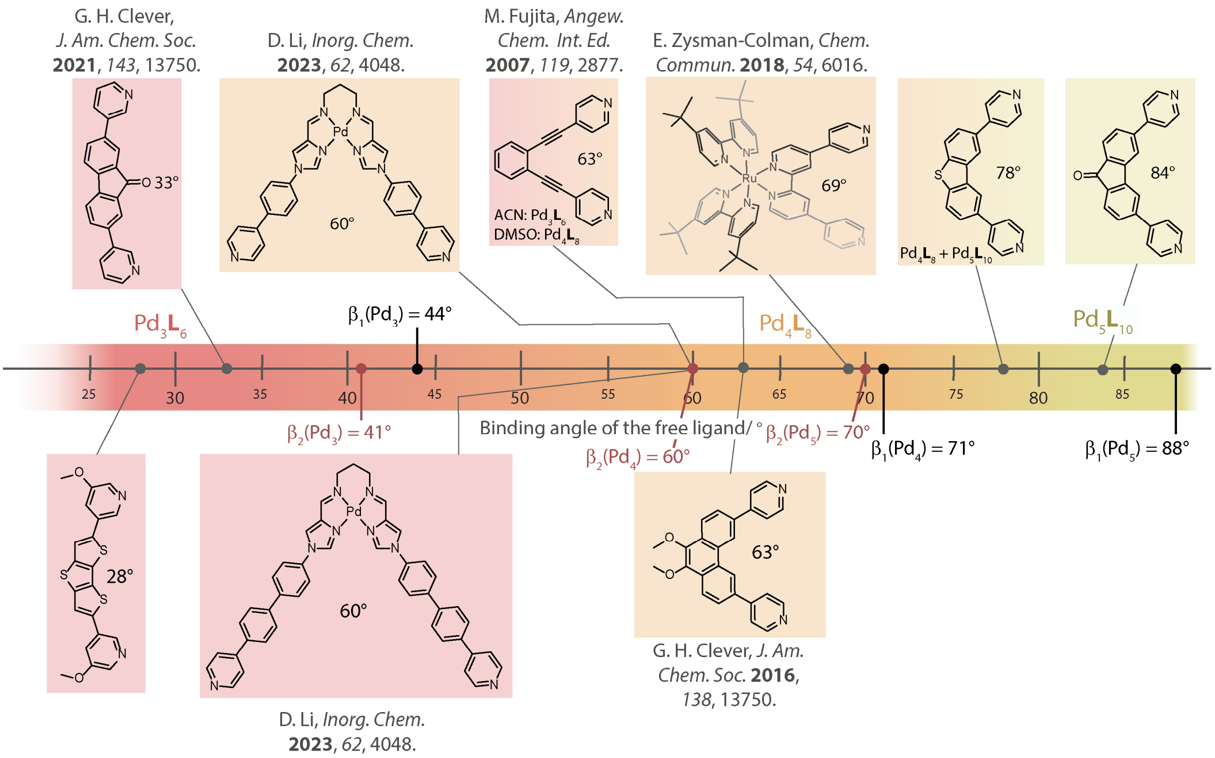

Fig. 10 Structures and bent angles of ligands that were experimentally shown to form Pd_nL_{2n} (n = 3-5) coordination rings in comparison with the theoretical angles β_1 (black) and β_2 (red) derived according eq. 8 and 9 (note that the nuclearity of the ring is indicated by the color of the rectangle (red = Pd_3L_6, orange = Pd_4L_8, green = Pd_5L_{10}). If not mentioned otherwise, the self-assembly was carried out with $[Pd(CH_3CN)_4](BF_4)_2$ in DMSO.[5–9]

Attempting at improving the geometrical model, the angle between the edges of the triangles (in plane and flap) was fixed to 45° (Fig. 9c), i.e. this second model assumes a square planar coordination geometry as observed in the X-ray structures and DFT models. Again, trigonometric relationships allowed for the derivation of an equation connecting a theoretical binding angle β_2 with the ring nuclearity n (eq. 9, for derivation see appendix, section 2.7.7).

$$\beta_2 = 2 \cdot \arcsin\left(\frac{\sqrt{2}}{2} \cdot \sin\left(90° \cdot \frac{(n-2)}{n}\right)\right) \tag{9}$$

For n = 4 and n = 5, the theoretical angle β_2 of the second model is slightly and significantly underestimated, respectively. This can probably be explained by the omission of the ligand flexibility. Three-membered rings are reported with ligands with binding angles between 28° to 63° which possess, however, an overall higher flexibility owing to the *meta*-pyridine donors, alkyne-, or phenyl linkers.[5–7] The value of β_2 = 41.4° is therefore realistic based on the ligands which have been investigated until now (Fig. 10).

Overall, the derived geometrical models allow for an estimation of the formed nuclearity and for an explanation of the observed trends, they lack, however, in accuracy. The reason for this is that the ligand flexibility as well as solvent and counter anion effects are not captured. Model 1 is better suited than model 2 for rough approximations since the systematic underestimation of the bent angle due to the neglect of the ligand flexibility is counterbalanced by an overestimation due to the deviation from the square planar geometry in the model.

Tab. 2 Overview of theoretical binding angles β_1 and β_2 for the ring sizes n = 3-5 obtained with model 1 and model 2, respectively, in comparison to the binding angles of the free ligands **L1**, **L2** (this work) and **22**,[8] all selectively assembling to a ring of the respective size with $[Pd(CH_3CN)_4](BF_4)_2$ in DMSO.

n	theoretical angle β_1	theoretical angle β_2	ligand angle
3	44.4°	41.4°	28° (**L1**)
4	70.5°	60.0°	63° (**22**)
5	88.5°	69.8°	84° (**L2**)

2.5. X-ray crystal structure packing

Contrarily to triangles, squares, and hexagons, the two dimensional Euclidean space cannot be tiled with regular pentagons (Fig. 11a). The reason for this is their interior angle of 108° which is not a divisor of 360°. Consequently, when trying to arrange pentagons around one vertex, one creates either an overlap or a gap. Pentagon tessellation is possible when the requirement for the regular pentagon is relaxed or when additional shapes are included. This has enticed artists and mathematicians for centuries; famous pentagon tilings were for example constructed by Albrecht Dürer.[25]

Due to this peculiarity of the periodic arrangement of pentagons, the crystal lattice arrangement of $[Pd_5\mathbf{L2}_{10}]^{10+}$ was examined more closely. In a single layer, the five-membered rings are arranged in zigzag chains (horizontal direction in Fig. 11b,c), multiple of these chains are arranged in a parallel fashion (vertical direction in Fig. 11b,c) and separated by rhombic gaps (gray in Fig. 11b). Even though the crystal lattice arrangement cannot directly be compared with the period arrangement of n-gons owing to the three-dimensionality of the molecules themselves, the solvent molecules, and the counter anions, one can say in a rough approximation that the rhombic gaps allow for the periodic arrangement of the pentagon-shaped rings. In the second layer, the zigzag chains are arranged with a slight offset wherefore they cover the gaps of the first layer (Fig. 11d). The third layer is then similar to the first layer (Fig. 11e).

2. Self-assembly of five-membered rings Pd5L10 by ligand angle adjustment

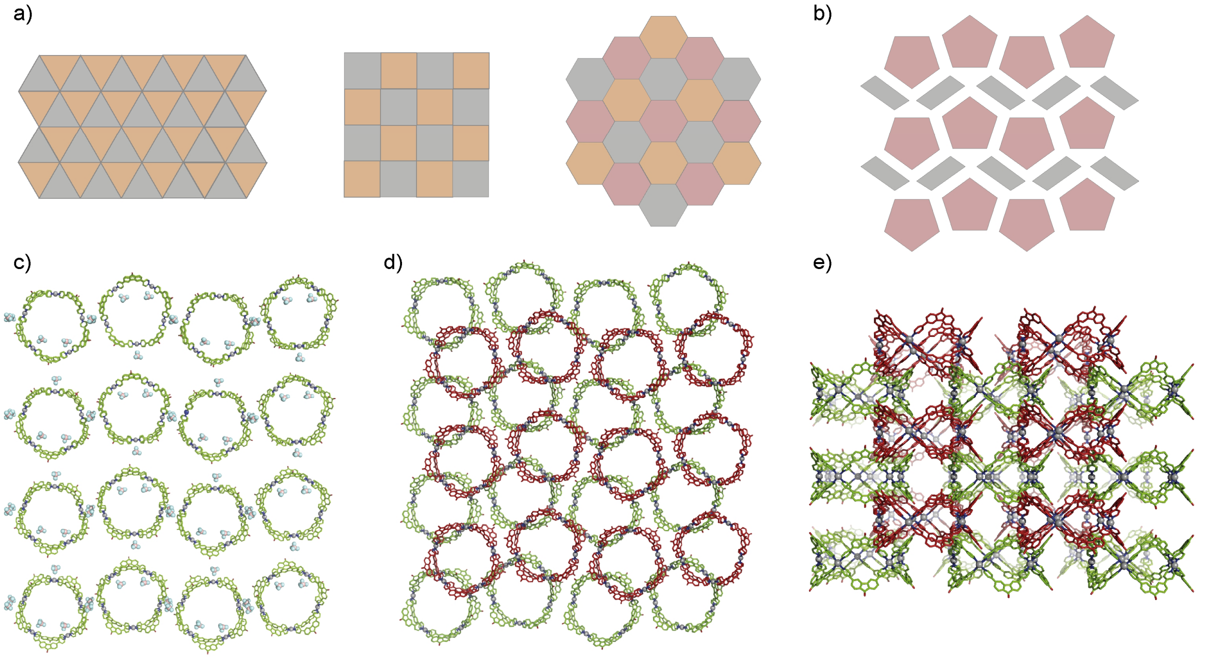

Fig. 11a) Tessellation with triangles, squares, and hexagons; b) schematic representation of the arrangement of $[\mathrm{Pd}_5\mathbf{L2}_{10}]^{10+}$ rings observed in one layer of the X-ray crystal lattice; c) the arrangement of $[\mathrm{Pd}_5\mathbf{L2}_{10}]^{10+}$ rings observed in one layer of the X-ray crystal lattice; d) the arrangement of two adjacent layers of $[\mathrm{Pd}_5\mathbf{L2}_{10}]^{10+}$ rings in the X-ray crystal lattice (top view); e) the arrangement of four adjacent layers of $[\mathrm{Pd}_5\mathbf{L2}_{10}]^{10+}$ rings in the X-ray crystal lattice (side view); note that the counter anions were omitted in d) and e) for clarity.

2.6. Conclusion

Based on the rough trends between the ligand binding angle and the nuclearity of Pd_nL_{2n} rings reported in the literature,[8,21] short ligands **L1** (28°) and **L2** (84°) were designed for the formation of three- and five-membered rings, respectively. This rational strategy allowed for the hitherto unprecedented formation of a five-membered homoleptic ring $[Pd_5\mathbf{L2}_{10}]^{10+}$ that does not require a template for its formation. Indeed, ring $[Pd_5\mathbf{L2}_{10}]^{10+}$ was shown to assemble as sole product at various concentrations as well as with different counter anions. It is, however, in a solvent-dependent equilibrium with tetra- and hexanuclear species. For gaining more insight into the relationship between the ligand bent angle and the ring nuclearity, ligand **L3** was synthesized which is structurally similar to ligand **L2** but features a narrower binding angle that lies in between the angles of ligands forming four- and five-membered rings. Intriguingly, ligand **L3** assembled with Pd(II) into a mixture of four- and five-membered rings with the former as the main species. Comparison of the X-ray crystal structures of $[Pd_5\mathbf{L2}_{10}]^{10+}$ and $[Pd_5\mathbf{L3}_{10}]^{10+}$ indicates that the ring based on narrower ligand **L3** exhibits higher conformational strain, which is in accordance with the equilibrium between two ring sizes observed in solution. The difference in strain associated with the transformation of a four- into a five-membered ring was studied by DFT computations for ligands **L2** and **L3**. The transformation is accompanied by a strong release in strain for **L2** and a slight increase in strain for **L3**, supporting that the conformational strain plays a decisive role for the self-assembly outcome. In order to correlate the ligand binding angle and the ring nuclearity, two models were constructed based on geometrical principles. While one of the models can reproduce the observed trends, an accurate prediction of the self-assembly outcome solely based on geometrical considerations is hampered since the ligand flexibility as well as counter anion and solvent effects are not captured.

For enhancing the understanding and predictability of the self-assembly into Pd_nL_{2n} coordination rings, more thorough DFT computational studies could be carried out in the future. For example, solvent and counter anions could be included in an explicit fashion.

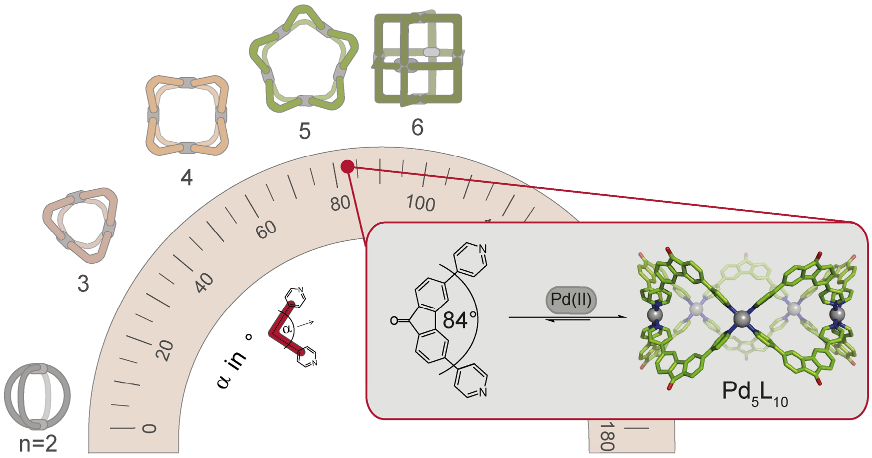

Fig. 12 Illustration of the control of the nuclearity of Pd_nL_{2n} assemblies through the ligand binding angle α. Adjustment of the angle to 84° allowed for the exclusive formation of a beforehand unreported D_{5h}-symmetric ring Pd_5L_{10}.

2.7. Appendix

2.7.1. General methods

NMR spectroscopy

NMR spectra were measured on the spectrometers Bruker AV 500 Avance NEO, AV 500 Avance III HD, AV 600 Avance III HD, and AV 700 Avance III HD. The chemical shifts were calibrated to the solvent lock signal (DMSO: 2.50 ppm for ^{1}H, 39.52 for ^{13}C; ACN: 1.94 ppm for ^{1}H, 118.26 for ^{13}C; DMF: 8.03 ppm for ^{1}H). The chemical shifts δ are given in ppm and the coupling constants J in Hz. The spectra were recorded in standard 5 mm NMR tubes at 298 K. All ^{1}H DOSY NMR spectra were measured on the spectrometers Bruker AV 500 Avance NEO at 500 MHz. Moreover, they were measured with a *dstebpgp3s* pulse sequence with diffusion delays D20 of 0.08 to 0.10 s and gradient powers P30 of 2500 to 2800 µs.[26,27] To obtain the diffusion coefficient D, T1 analyses of the corresponding signals in the 1D spectra using the STEJSKAL-TANNER equation were performed.[28,29] For the calculation of the hydrodynamic radii r_H the STOKES-EINSTEIN equation was used.[22]

Mass spectrometry

Mass spectrometry data were measured on Bruker ESI-timsTOF (electrospray ionization-trapped ion mobility-time of flight) and Bruker compact high-resolution LC mass spectrometers (positive/negative mode). For calibration of the TOF devices, Agilent ESI-Low Concentration Tuning Mix was used. All measured and calculated values are given in *m/z*.

2.7.2. Ligand synthesis

Ligand **L2** was synthesized as reported before.[24]

Ligand **L1**

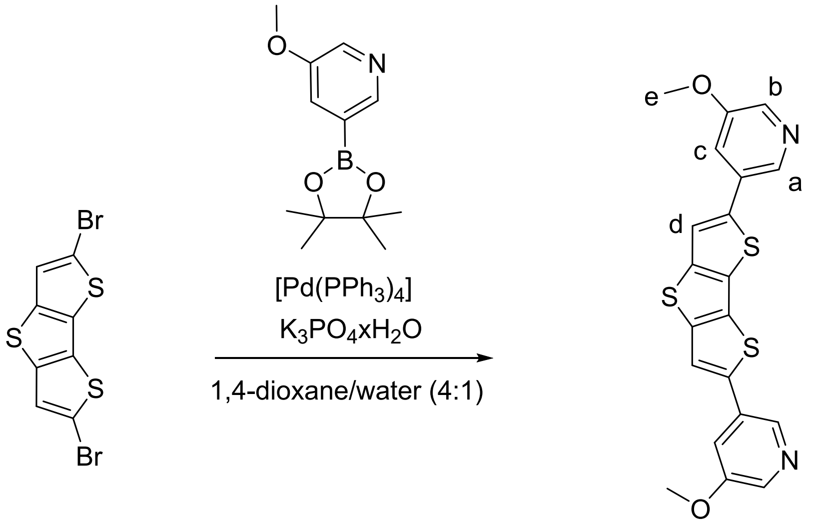

Scheme 1 Synthesis of **L1**.

2,6-dibromodithieno[3,2-b:2',3'-d]thiophene (0.206 g, 0.58 mmol, 1.0 eq), 3-methoxy-5-pyridine boronic acid pinacol ester (0.649 g, 2.76 mmol, 4.8 eq.), potassium phosphate monohydrate (1.340 g, 5.81 mmol, 10.0 eq.), and [Pd(PPh$_3$)$_4$] (0.067 g, 0.06 mmol, 0.1 eq.) were suspended in a mixture of 1,4-dioxane and water (4:1). The reaction mixture was degassed via freeze-pump-thaw cycles and then heated at 90 °C for 22 h. After cooling to room temperature, the reaction mixture was extracted with chloroform. The combined organic layers were washed with water and brine and dried over magnesium sulfate. The solvent was removed *in vacuo*. The crude was further purified by column chromatography (EtOAc with TEA (1%):EtOH 100:0 to 0:100) to yield **L1** as a yellow-brown solid (0.068 g, 29%).

^{1}H NMR (600 MHz, DMSO-d_6): δ = 8.56 (d, J = 1.85, 1H; a), 8.29 (d, J = 2.71, 1H; b), 8.18 (s, 1H; d), 7.69 (dd, J = 2.74, J = 1.95, 1H; c), 3.93 (s, 3H; e).

^{13}C NMR (151 MHz, DMSO-d_6): δ = 155.69, 142.29, 140.68, 138.23, 137.11, 130.45, 129.94, 119.62, 116.65, 56.02.

ESI MS: *m/z* calc. for [**L1**]$^+$: 410.0212; found: 410.0202

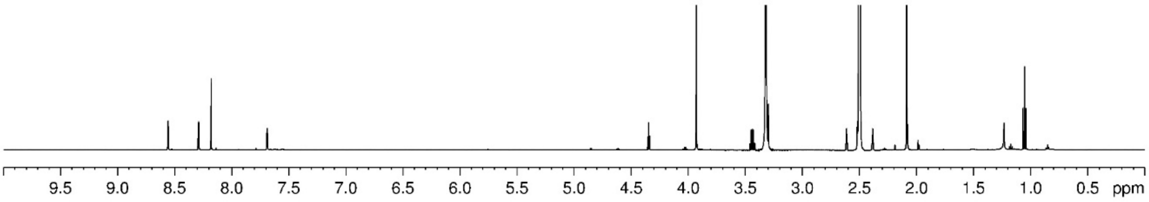

Fig. 13 ^{1}H NMR (600 MHz, 298 K, DMSO-d_6) of **L1**.

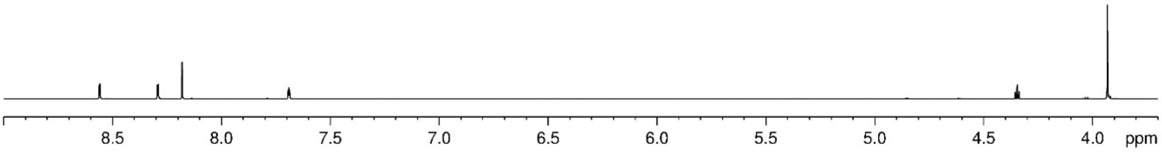

Fig. 14 Partial ^{1}H NMR (600 MHz, 298 K, DMSO-d_6) of **L1**.

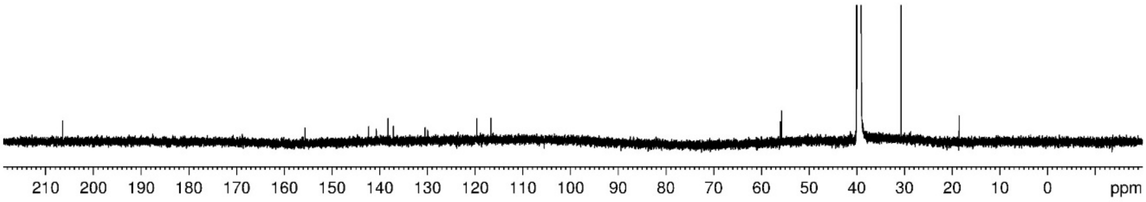

Fig. 15 ^{13}C NMR (151 MHz, 298 K, DMSO-d_6) of **L1**.

Ligand **L3**

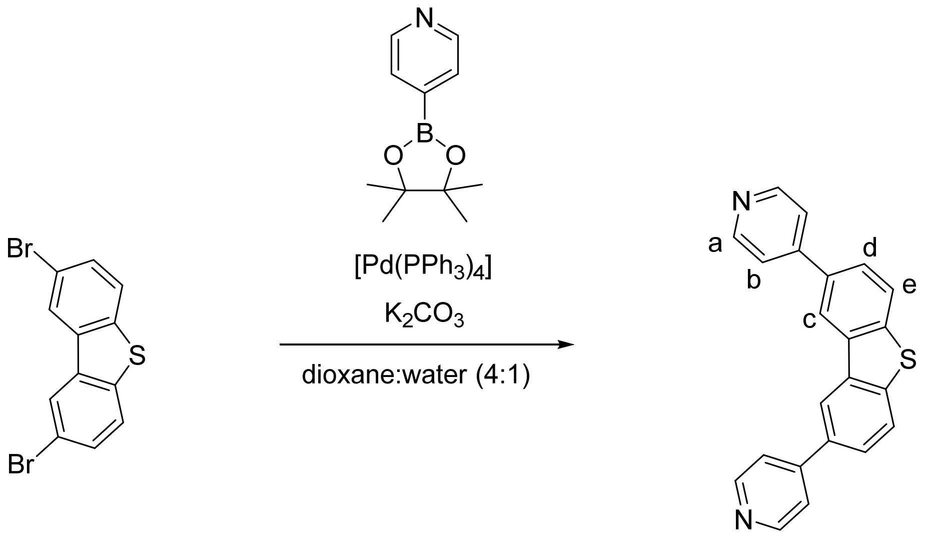

Scheme 2 Synthesis of **L3**.

A mixture of 2,8-dibromodibenzo[b,d]thiophene (0.700 g, 2.05 mmol, 1.0 eq.), 4-pyridine boronic acid pinacol ester (1.680 g, 8.19 mmol, 4.0 eq.), potassium carbonate (0.707 g, 5.12 mmol, 2.5 eq.), and [Pd(PPh$_3$)$_4$] (0.236 g, 0.20 mmol, 0.1 eq.) was suspended in a mixture of dioxane and water (4:1). The reaction mixture was degassed by argon purging for 30 min and then heated at 90 °C for 22 h. After cooling to room temperature, the reaction mixture was extracted with chloroform. The combined organic layers were washed with water and brine and dried over magnesium sulfate. After removal of the solvent *in vacuo* the crude product was further washed with ice-cold acetonitrile and cold diethylether to yield **L3** as a white powder (0.388 g, 56%).

^{1}H NMR (600 MHz, DMSO-d_6): δ = 9.11 (d, J = 1.70, 1H; c), 8.72 (dd, J = 4.26, 1.70, 2H; a), 8.22 (d, J = 8.36, 1H; e), 8.03 (dd, J = 8.40, 1.86, 1H; d), 7.96 (dd, J = 4.25, 1.70, 2H; b).

^{13}C NMR (151 MHz, DMSO-d_6): δ = 150.29, 146.67, 140.14, 135.85, 133.98, 125.83, 123.92, 121.36, 120.84.

ESI MS: *m/z* calc. for [**L3**]$^+$: 338.0872; found: 338.0872

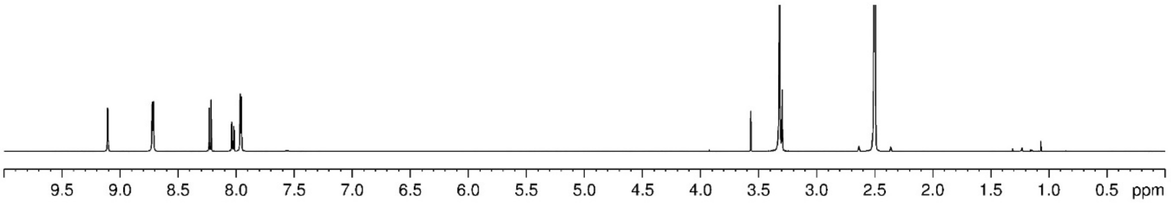

Fig. 16 ^{1}H NMR (600 MHz, 298 K, DMSO-d_6) of **L3**.

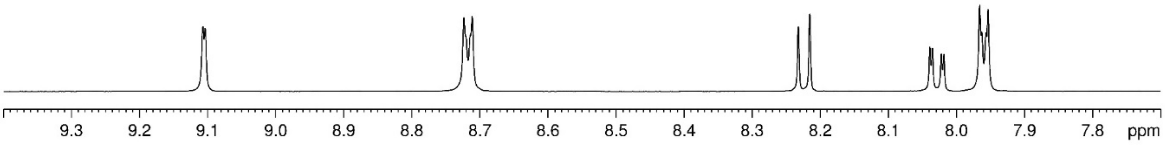

Fig. 17 Partial ^{1}H NMR (600 MHz, 298 K, DMSO-d_6) of **L3**.

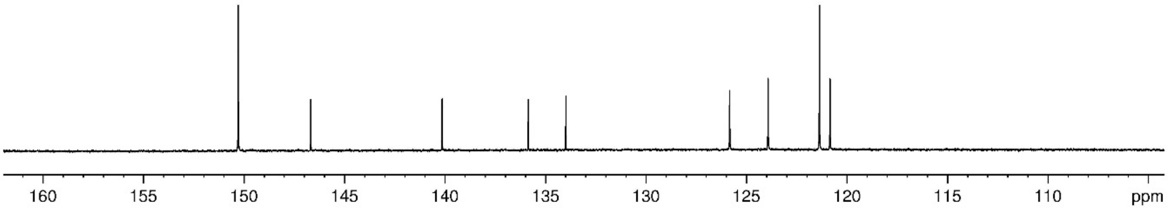

Fig. 18 ^{13}C NMR (151 MHz, 298 K, DMSO-d_6) of **L3**.

2.7.3. Self-assembly into coordination rings

Three-membered ring [Pd$_3$L1$_6$]$^{6+}$

Solutions of ligand **L1** (500 µL, 1.4 mM, 0.70 µmol) and [Pd(CH$_3$CN)$_4$](BF$_4$)$_2$ (35 µL, 15 mM, 0.53 µmol) in DMSO-d_6 were combined. The reaction mixture was heated at 70 °C for 3 h.

^{1}H NMR (500 MHz, DMSO-d_6): δ = 9.20 (d, J = 2.36, 1H; b), 9.06 (d, J = 1.17, 1H; a), 8.38 (s, 1H; d), 8.15 (br, 1H; c), 4.03 (s, 3H; e).

^{13}C NMR (151 MHz, DMSO-d_6): δ = 157.26, 143.70, 137.50, 133.59, 131.56, 130.43, 128.80, 128.72, 121.38, 56.70.

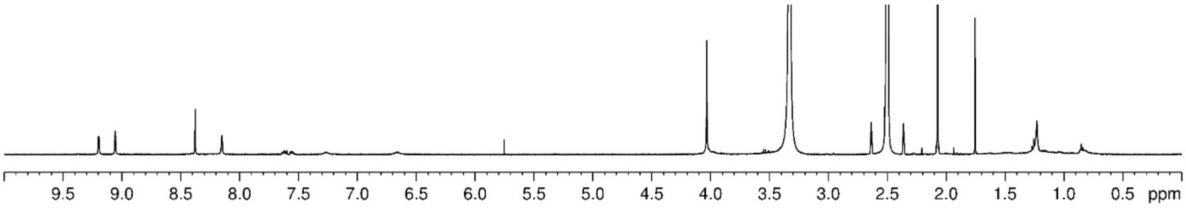

Fig. 19 ^{1}H NMR (500 MHz, 298 K, DMSO-d_6) of [Pd$_3$**L1**$_6$]$^{6+}$.

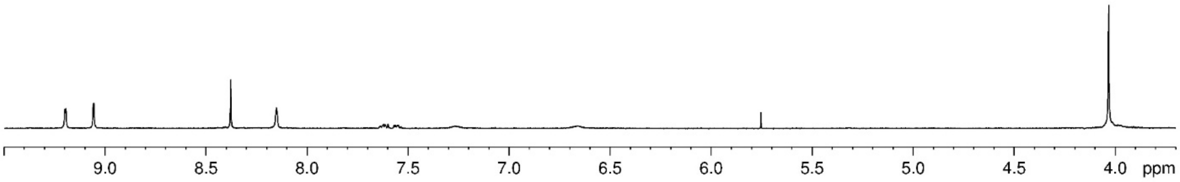

Fig. 20 Partial ^{1}H NMR (500 MHz, 298 K, DMSO-d_6) of [Pd$_3$**L1**$_6$]$^{6+}$.

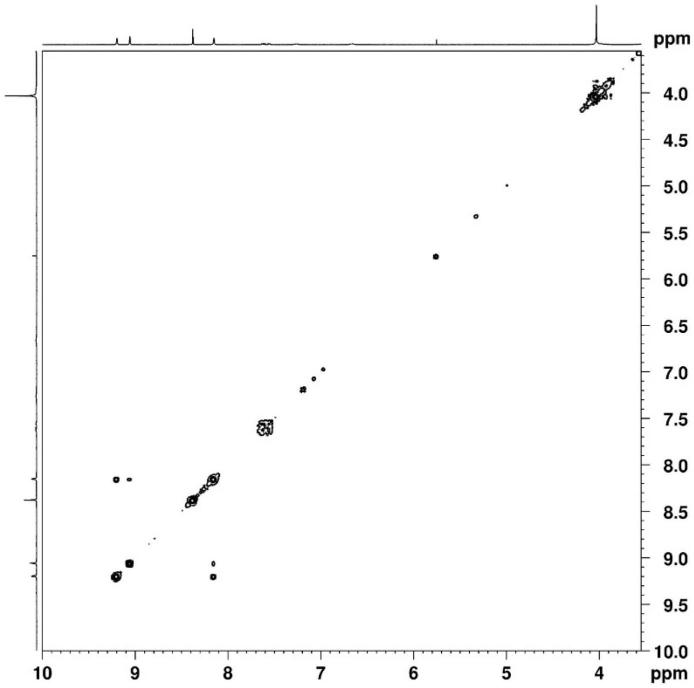

Fig. 21 Partial ^1H-^1H COSY NMR (500 MHz, 298 K, DMSO-*d*$_6$) of [Pd$_3$**L1**$_6$]$^{6+}$.

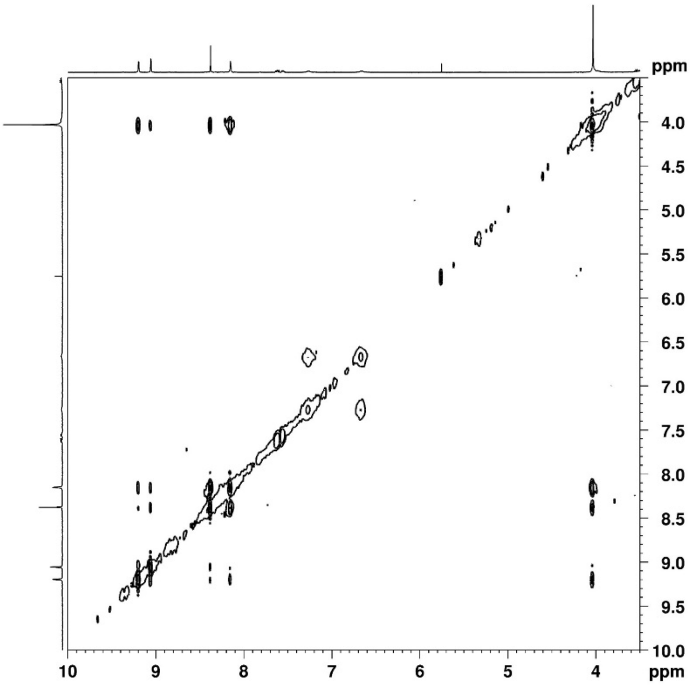

Fig. 22 Partial ^1H-^1H NOESY NMR (500 MHz, 298 K, DMSO-*d*$_6$) of [Pd$_3$**L1**$_6$]$^{6+}$.

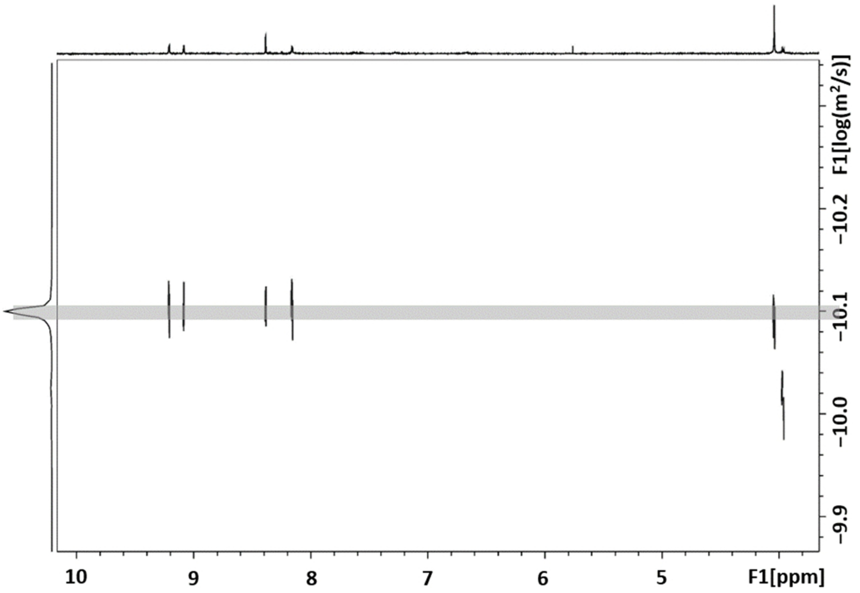

Fig. 23 Partial ^{1}H DOSY NMR (500 MHz, 298 K, DMSO-d_6) of [Pd$_3$**L1**$_6$]$^{6+}$ (D_H = 7.97 · 10^{-11} m^2 · s^{-1}, R_H = 12.5 Å).

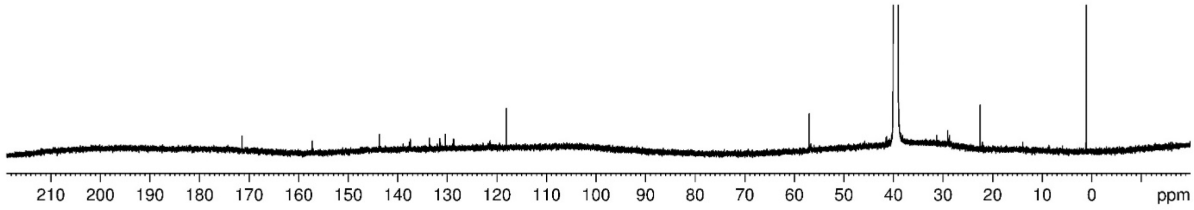

Fig. 24 ^{13}C NMR (151 MHz, 298 K, DMSO-d_6) of [Pd$_3$**L1**$_6$]$^{6+}$.

Five-membered ring [Pd$_5$L2$_{10}$]$^{10+}$

Solutions of ligand **L2** (500 µL, 1.4 mM, 0.70 µmol) and [Pd(CH$_3$CN)$_4$](BF$_4$)$_2$ (30 µL, 15 mM, 0.45 µmol) in DMSO-d_6 were combined. The reaction mixture was heated at 70 °C for 5 h.

^{1}H NMR (700 MHz, DMSO-d_6): δ = 9.60 (d, J = 5.84, 2H; a), 8.20-8.16 (m, 3H; b,c), 7.83 (br, 2H; d,e).

^{13}C NMR (176 MHz, DMSO-d_6): δ = 191.51, 151.21, 150.40, 143.92, 141.85, 134.70, 129.00, 125.29, 125.07, 121.30.

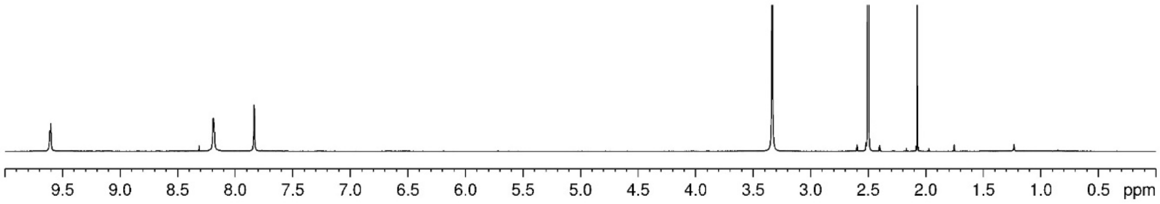

Fig. 25 ^{1}H NMR (700 MHz, 298 K, DMSO-d_6) of [Pd$_5$**L2**$_{10}$]$^{10+}$.

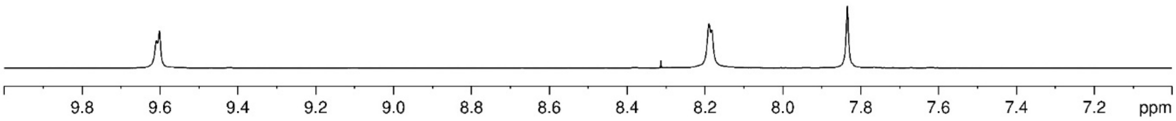

Fig. 26 Partial ^{1}H NMR (700 MHz, 298 K, DMSO-d_6) of [Pd$_5$**L2**$_{10}$]$^{10+}$.

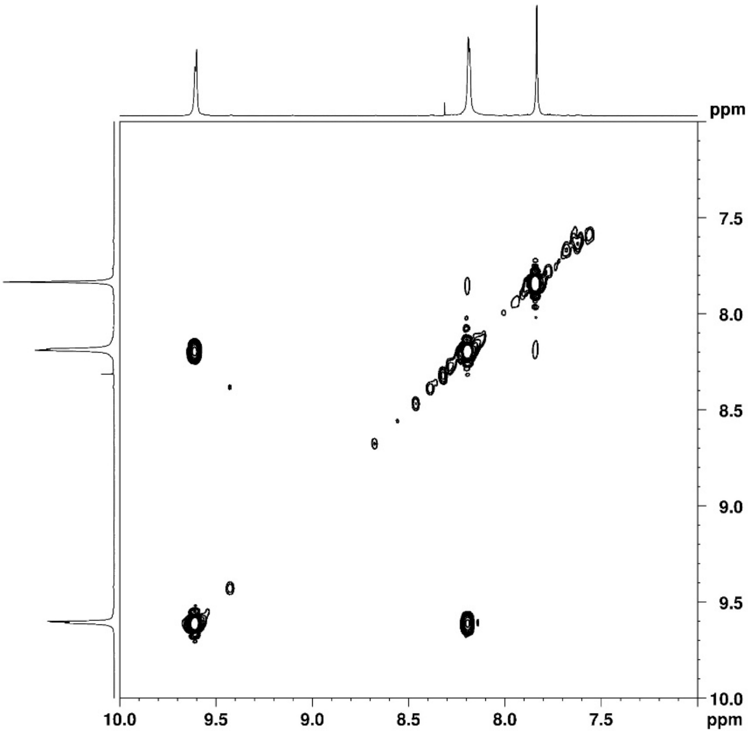

Fig. 27 Partial ^{1}H-^{1}H COSY NMR (700 MHz, 298 K, DMSO-d_6 of [Pd$_5$**L2**$_{10}$]$^{10+}$.

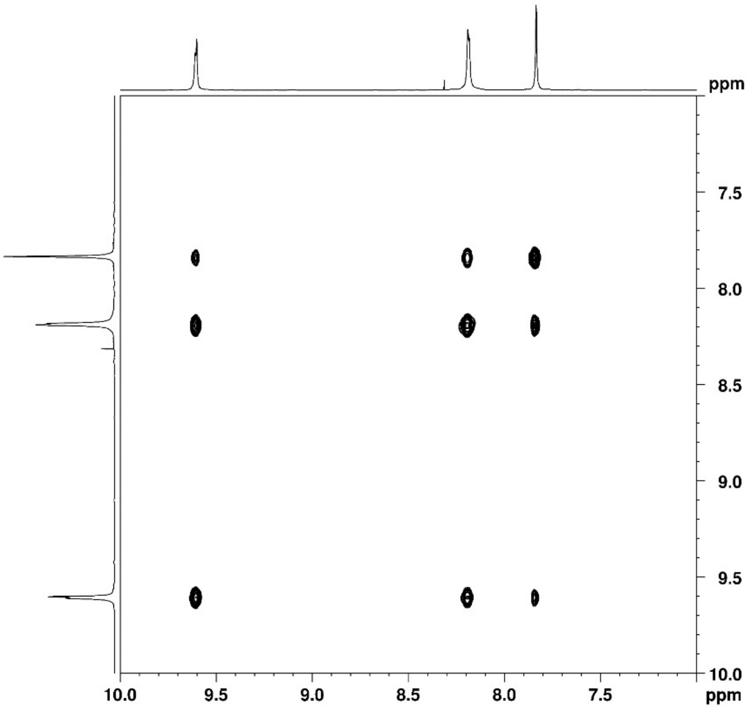

Fig. 28 Partial ^{1}H-^{1}H NOESY NMR (700 MHz, 298 K, DMSO-d_6) of [Pd$_5$**L2**$_{10}$]$^{10+}$.

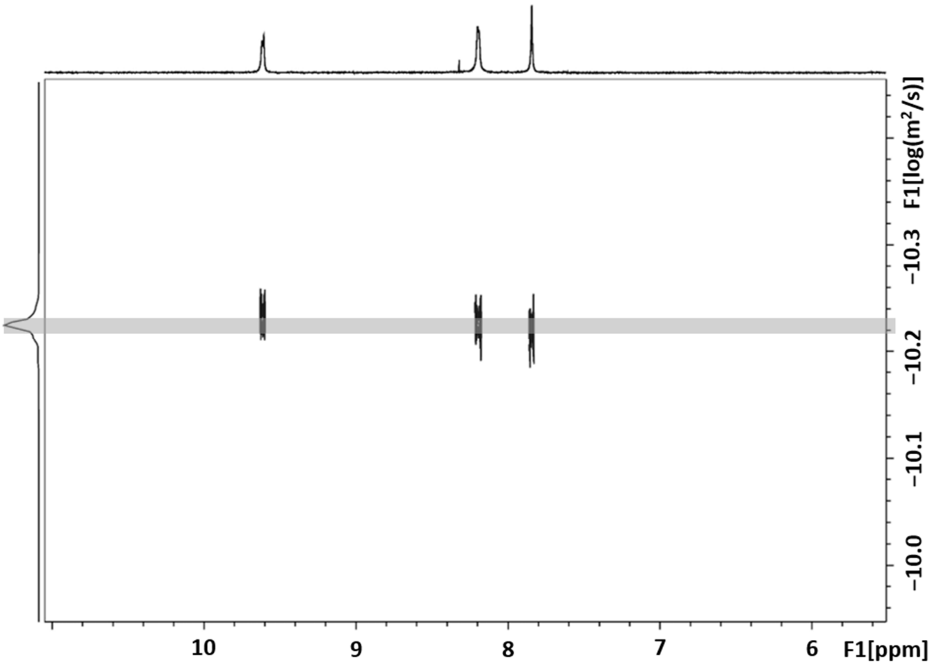

Fig. 29 Partial ^{1}H DOSY NMR (500 MHz, 298 K, DMSO-d_6) of [Pd$_5$**L2**$_{10}$]$^{10+}$ (D_H = 5.93 · 10^{-11} m^2 · s^{-1}, R_H = 16.8 Å).

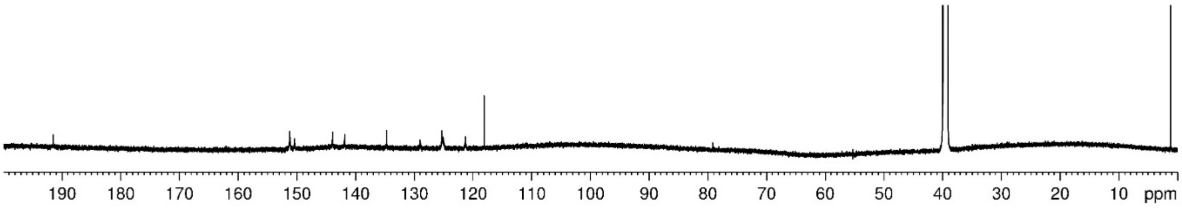

Fig. 30 ^{13}C NMR (176 MHz, 298 K, DMSO-d_6) of [Pd$_5$**L2**$_{10}$]$^{10+}$.

Equilibrated mixture of [Pd$_4$L3$_8$]$^{8+}$ and [Pd$_5$L3$_{10}$]$^{10+}$

Solutions of ligand **L3** (500 µL, 1.4 mM, 0.70 µmol) and [Pd(CH$_3$CN)$_4$](BF$_4$)$_2$ (30 µL, 15 mM, 0.45 µmol) in DMSO-d_6 were combined. The reaction mixture was heated at 70 °C for 3 h. Four-membered ring [Pd$_4$**L3**$_8$]$^{8+}$ was formed as major product (85%; signal assignment a, b...) and five-membered ring [Pd$_5$**L3**$_{10}$]$^{10+}$ as minor product (15%; signal assignment a', b'...).

^{1}H NMR (600 MHz, DMSO-d_6): δ = 9.65 (d, J = 5.96, 2H; a), 9.61 (d, J = 5.96, 0.4H; a'), 8.92 (s, 1H; c), 8.85 (s, 0.2 H; c'), 8.32-8.26 (m, 3.6H; b,e,b',e'), 8.03 (d, J = 8.37, 1H; d), 7.98 (d, J = 8.47, 0.2H; d').

^{13}C NMR (151 MHz, DMSO-d_6): δ = 151.59, 151.45, 151.22, 150.94, 142.09, 141.97, 135.70, 135.63, 132.42, 132.01, 126.47, 126.01, 125.36, 124.93, 124.68, 122.17.

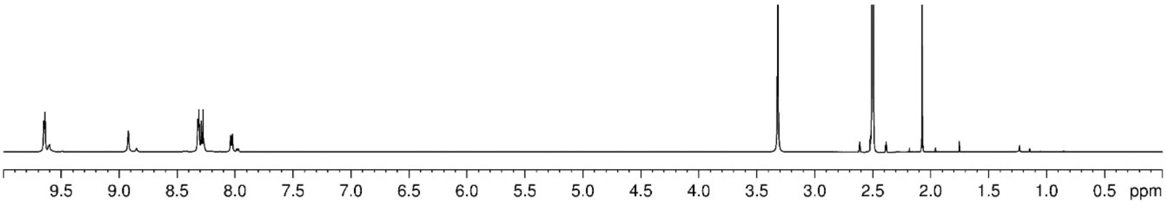

Fig. 31 ^{1}H NMR (600 MHz, 298 K, DMSO-d_6) of a mixture of [Pd$_4$**L3**$_8$]$^{8+}$ and [Pd$_5$**L3**$_{10}$]$^{10+}$.

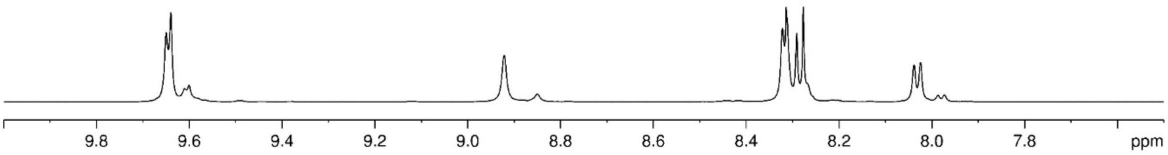

Fig. 32 Partial ^{1}H NMR (600 MHz, 298 K, DMSO-d_6) of a mixture of [Pd$_4$**L3**$_8$]$^{8+}$ and [Pd$_5$**L3**$_{10}$]$^{10+}$.

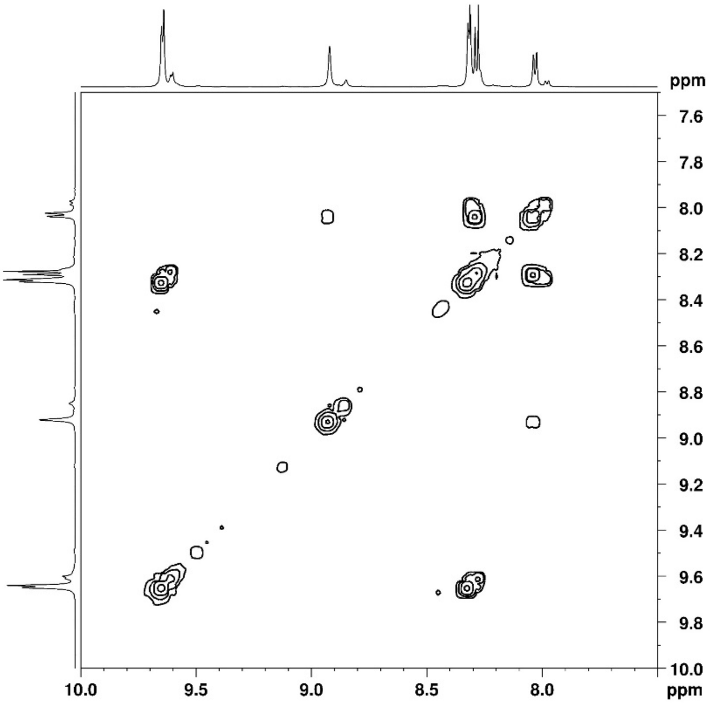

Fig. 33 Partial ^{1}H-^{1}H COSY NMR (600 MHz, 298 K, DMSO-d_6) of a mixture of [Pd$_4$**L3**$_8$]$^{8+}$ and [Pd$_5$**L3**$_{10}$]$^{10+}$.

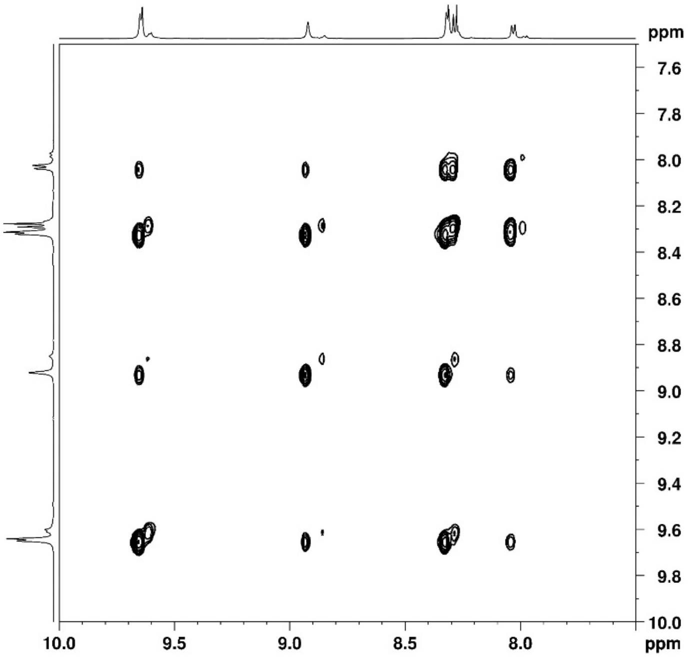

Fig. 34 Partial ^{1}H-^{1}H NOESY NMR (600 MHz, 298 K, DMSO-d_6) of a mixture of [Pd$_4$**L3**$_8$]$^{8+}$ and [Pd$_5$**L3**$_{10}$]$^{10+}$.

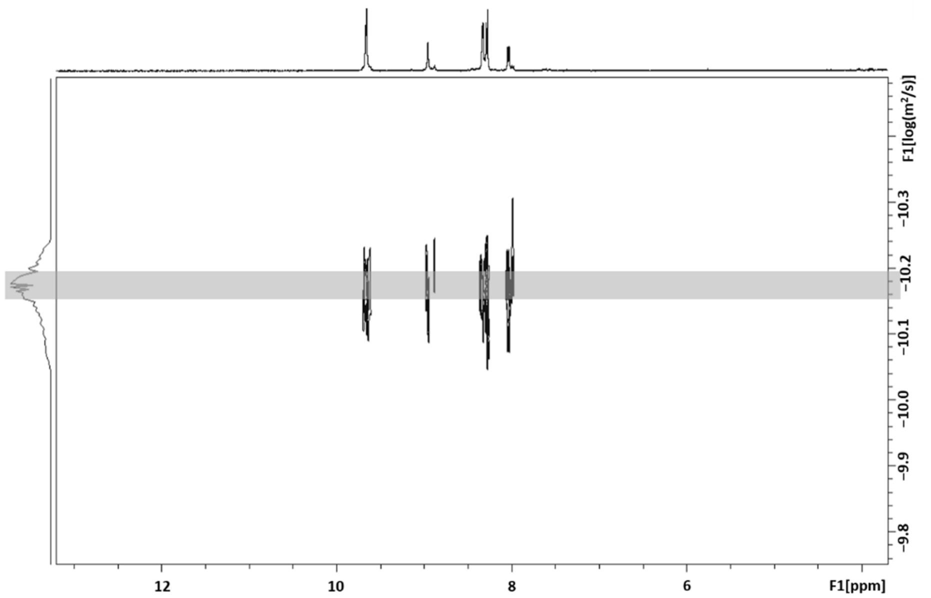

Fig. 35 Partial ^{1}H DOSY NMR (500 MHz, 298 K, DMSO-d_6) of a mixture of $[Pd_4\mathbf{L3}_8]^{8+}$ ($D_H = 6.74 \cdot 10^{-11}\ m^2 \cdot s^{-1}$, $R_H = 14.8$ Å) and $[Pd_5\mathbf{L3}_{10}]^{10+}$ (diffusion data for minor species not resolved).

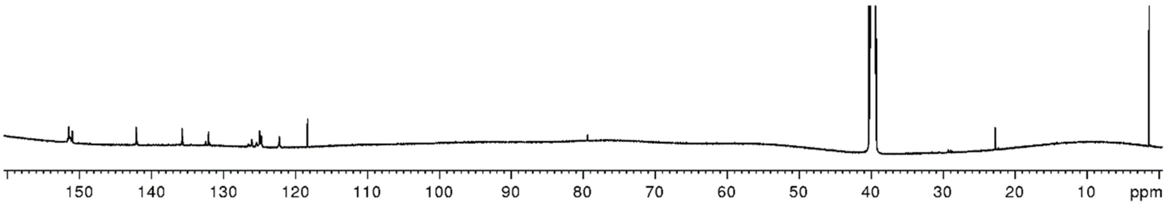

Fig. 36 ^{13}C NMR (151 MHz, 298 K, DMSO-d_6) of a mixture of $[Pd_4\mathbf{L3}_8]^{8+}$ and $[Pd_5\mathbf{L3}_{10}]^{10+}$.

2.7.4. Self-assembly of **L2** and **L3** under varying conditions

2.7.4.1. Concentration dependency

A suspension of ligand **L^1** in DMSO-d_6 (260 µL (a), 130 µL (b), 26 µL (c), 13 µL (d), 21 mM, 5.46 µmol (a), 2.73 µmol (b), 0.55 µmol (c), 0.27 µmol (d)), DMSO-d_6 (0 µL (a), 247 µL (b), 444 µL (c), 467 µL (d)), and a solution of $[Pd(CH_3CN)_4](BF_4)_2$ in DMSO-d_6 (233.3 µL (a), 116.6 µL (b), 23.3 µL (c), 11.7 µL (d), 15 mM, 3.50 µmol (a), 1.75 µmol (b), 0.35 µmol (c), 0.18 µmol (d)) were combined. The reaction mixture was heated at 70 °C for 26 h. The chemical shifts of the assembly are identical to the ones of the five-membered ring $[Pd_5\mathbf{L2}_{10}]^{10+}$. At low concentrations (c,d) partial disassembly of the ring into the free ligand is observed (signals of the free ligand are marked with yellow circles). No other assembly is observed, showing that the five-membered ring $[Pd_5\mathbf{L2}_{10}]^{10+}$ is the favored species at all of the tested concentrations.

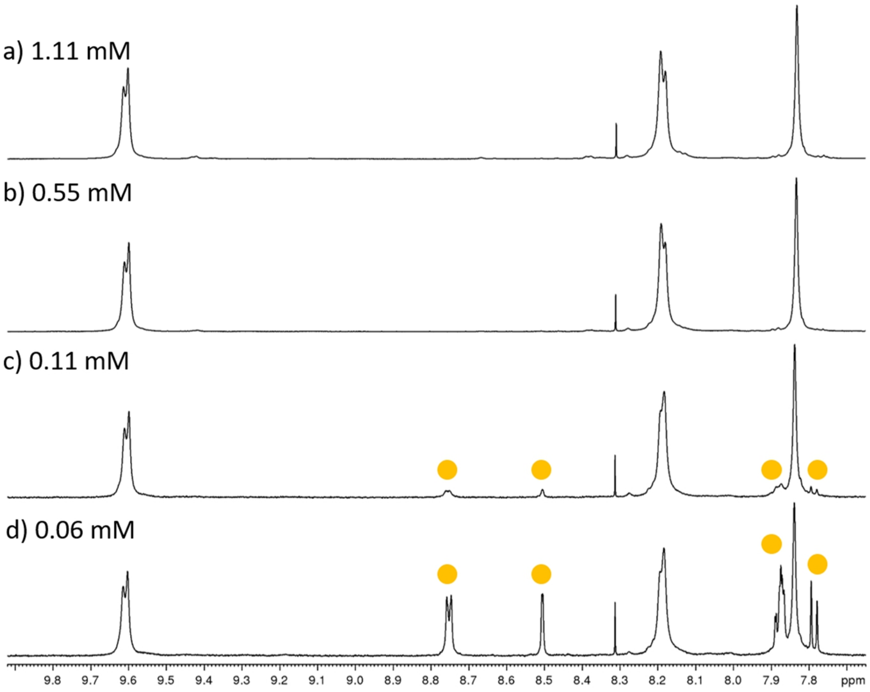

Fig. 37 Partial ^{1}H NMR (500 MHz, 298 K, DMSO-d_6) of the self-assembly of **L2** to $[Pd_5\mathbf{L2}_{10}]^{10+}$ at different ring concentrations in DMSO-d_6. Signals marked with a yellow circle belong to the free ligand **L2**.

2.7.4.2. Counter anion dependency

Assembly with hexafluorophosphate counter anions: Solutions of ligand **L2** (500 µL, 2.8 mM, 1.40 µmol) and $[Pd(CH_3CN)_4](PF_6)_2$ (60 µL, 15 mM, 0.90 µmol) in DMSO-d_6 were combined. The reaction mixture was heated at 70 °C for 5 h.

^{1}H NMR (500 MHz, DMSO-d_6): δ = 9.64 (d, J = 5.63, 2H), 8.22-8.14 (m, 3H), 7.83 (s, 2H).

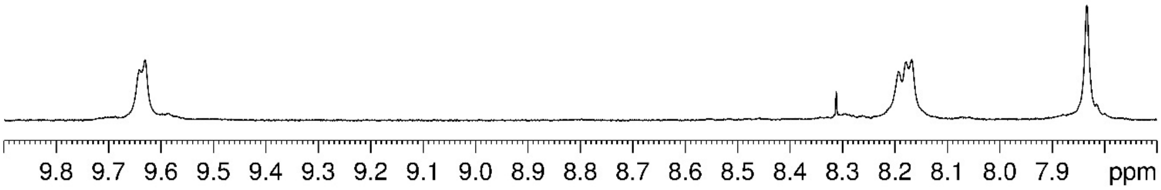

Fig. 38 Partial ^{1}H NMR (500 MHz, 298 K, DMSO-d_6) of $[Pd_5\mathbf{L2}_{10}](PF_6)_{10}$.

2. Self-assembly of five-membered rings Pd5L10 by ligand angle adjustment

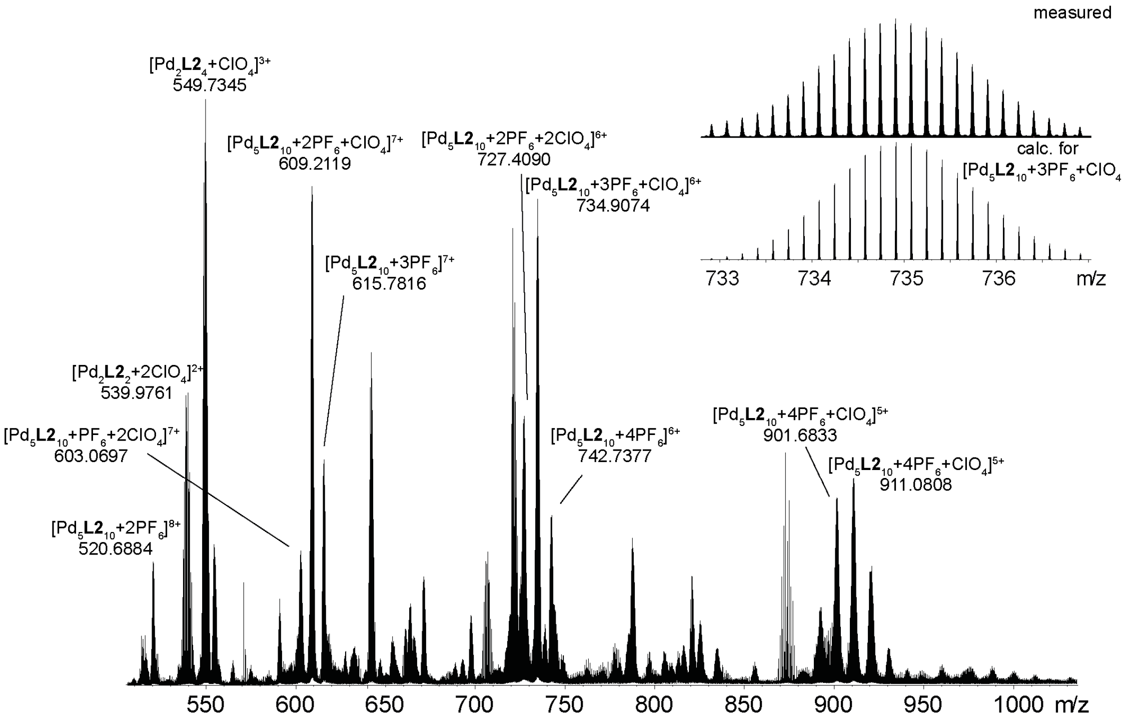

Fig. 39 ESI mass spectrum $[\mathrm{Pd_5}\mathbf{L2}_{10}+n\mathrm{PF_6}]^{(10-n)+}$. The inset shows a comparison of the measured and calculated isotopic pattern. Despite a contamination of the sample (or mass spectrometer) with perchlorate anions, all assemblies were identified as five-membered rings.

Assembly with triflate counter anions: Solutions of ligand **L2** (500 µL, 1.4 mM, 0.70 µmol) and $[\mathrm{Pd(CH_3CN)_4}](\mathrm{CF_3SO_3})_2$ (35 µL, 15 mM, 0.53 µmol) in DMSO-d_6 were combined. The reaction mixture was heated at 70 °C for 15 h.

^{1}H NMR (500 MHz, DMSO-d_6): δ = 9.64 (d, J = 6.08, 2H), 8.23 (s, 1H), 8.18 (d, J = 5.66, 2H), 7.83 (s, 2H).

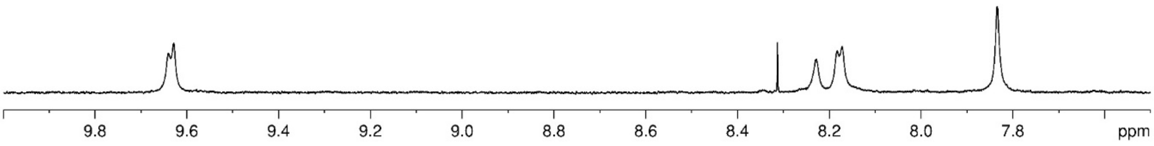

Fig. 40 Partial ^{1}H NMR (500 MHz, 298 K, DMSO-d_6) of $[\mathrm{Pd_5}\mathbf{L2}_{10}](\mathrm{CF_3SO_3})_{10}$.

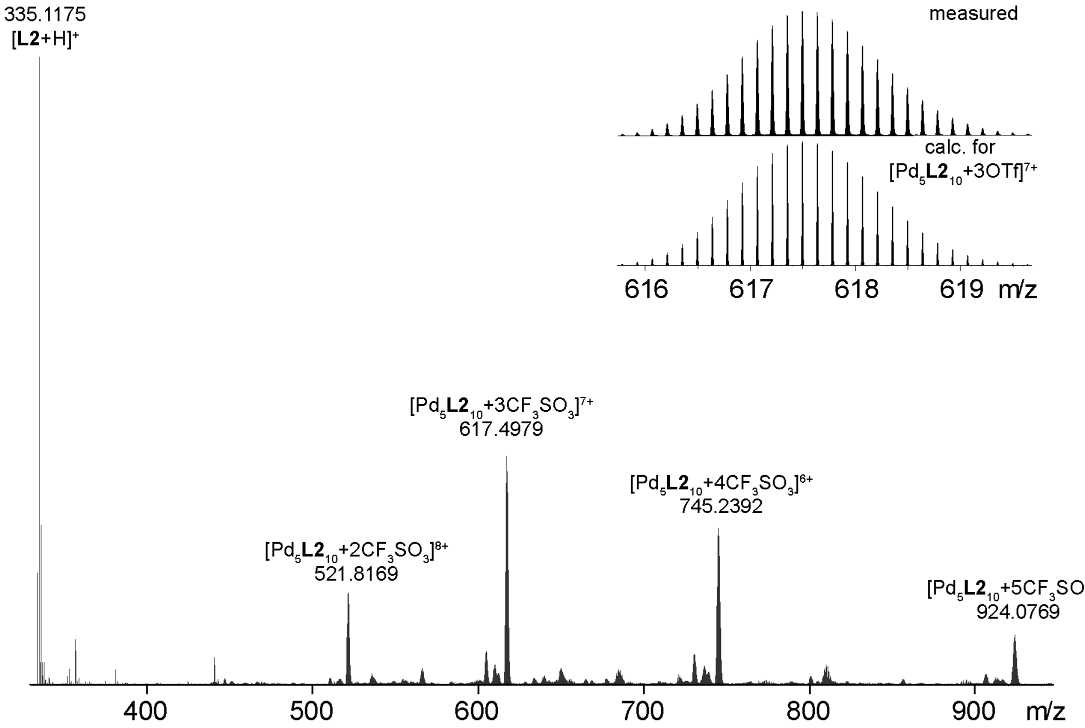

Fig. 41 ESI mass spectrum $[Pd_5\mathbf{L2}_{10}+nCF_3SO_3]^{(10-n)+}$. The inset shows a comparison of the measured and calculated isotopic pattern.

2.7.4.3. Solvent dependency

Solutions of ligand **L2** or **L3** (500 µL, 1.4 mM, 0.70 µmol) and $[Pd(CH_3CN)_4](BF_4)_2$ (30 µL, 15 mM, 0.53 µmol) in either CD_3CN or DMF-*d*$_7$ were combined. The reaction mixture was heated at 70 °C for overnight. The formation of mixtures of tetranuclear $[Pd_4\mathbf{L}_8]^{8+}$ (for $[Pd_4\mathbf{L2}_8]^{8+}$ most probably a pseudo-tetrahedron, see below), pentanuclear $[Pd_5\mathbf{L}_{10}]^{10+}$, and hexanuclear (most probably octahedral) $[Pd_6\mathbf{L}_{12}]^{12+}$ was observed by means of high-resolution mass spectrometry and NMR analysis.

Self-assembly of L2 in CD_3CN

^{1}H NMR (500 MHz, CD_3CN): δ = 9.41-9.39 (m, 0.3H), 9.36 (d, *J*= 6.79, 2H), 9.29 (d, *J* = 6.70, 0.8H), 9.10 (d, *J*= 6.87, 0.8H), 8.94 (d, *J* = 6.87, 0.8H), 8.83 (d, *J* = 6.96, 0.6H), 8.36-8.35 (m, 0.4H), 8.34-8.33 (m, 0.4H), 8.09 (d, *J* = 6.96, 1H), 8.04 (d, *J* = 6.96, 0.8H), 8.01-8.00 (m, 1H), 7.98 (dd, *J* = 5.06, *J* = 1.65, 2.4H), 7.94 (d, *J* = 6.80, 0.8H), 7.93-7.62 (m, 9H).

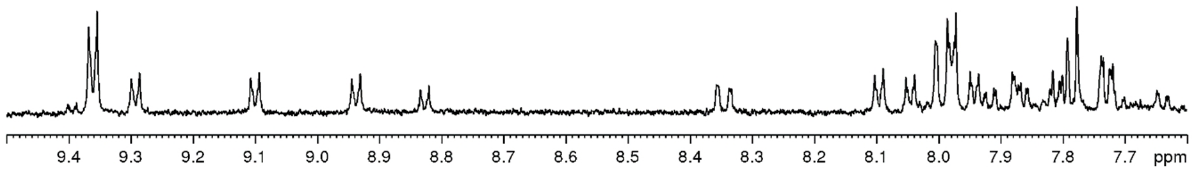

Fig. 42 Partial ^{1}H NMR (500 MHz, 298 K, CD_3CN) of the self-assembly of **L2** in CD_3CN.

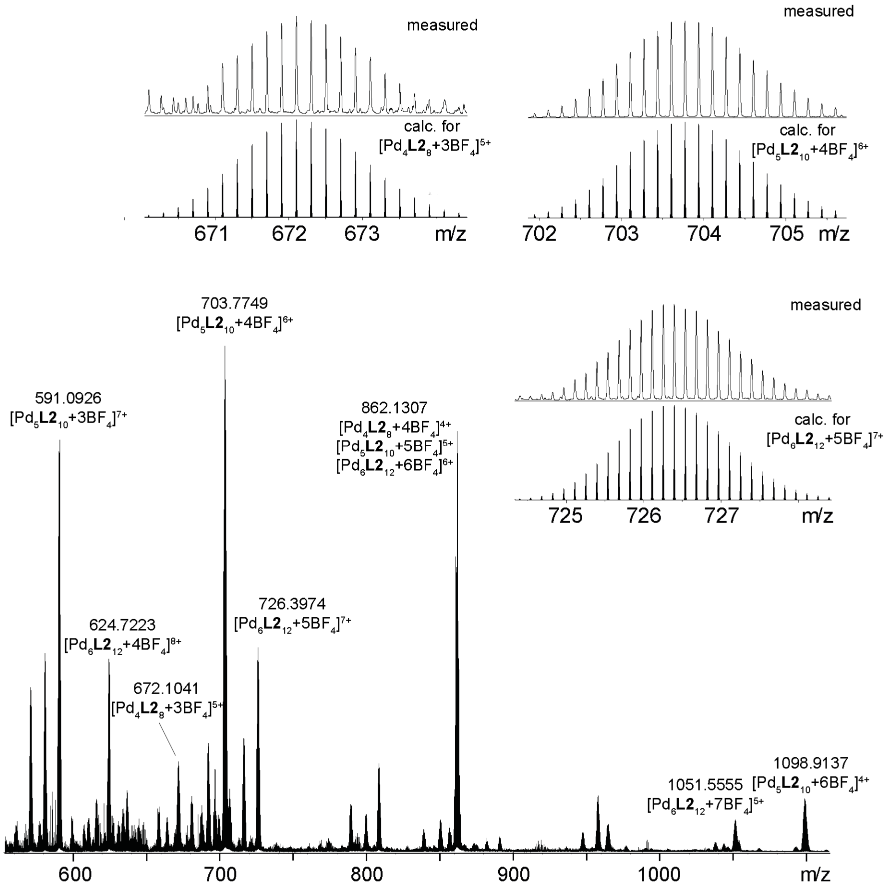

Fig. 43 ESI mass spectrum of the self-assembly of **L2** in CD_3CN. The inset shows a comparison of the measured and calculated isotopic patterns for $[Pd_4\mathbf{L2}_8+3BF_4]^{5+}$, $[Pd_5\mathbf{L2}_{10}+4BF_4]^{6+}$, and $[Pd_6\mathbf{L2}_2+5BF_4]^{7+}$.

Self-assembly of L2 in DMF-d_7

Self-assembly of **L2** in DMF-d_7 leads to three species. Thereof, one shows signal splitting (1:1). For signal assignment: species 1: a-e; species 2: a'-e' and a''-e''; species 3: a'''-e'''. Due to the 1:1 signal splitting, species 2 is assigned to a pseudo-tetrahedral assembly in which two edges are doubly-bridged and four edges are singly-bridged.[7]

^{1}H NMR (600 MHz, DMF-d_7): δ = 9.85 (d, *J* = 6.56, 1.3H; a), 9.81 (d, *J* = 6.37, 1H; a'), 9.65 (d, *J* = 6.56, 1H; a''), 9.59 (d, *J* = 6.56, 2H; a'''), 8.73 (s, 1.5H; c''+c'''), 8.49 (d, *J* = 5.05, 1.2H; b''), 8.45 (d, *J* = 5.05, 2.3H; b'''), 8.29 (d, *J* = 4.54, 1.4H; b), 8.26-8.19 (m, 2.9H; b'+c+d''), 8.13 (dd, *J* = 7.75, 1.10, 1.2H; d'''), 7.94 (d, *J* = 7.52, 0.9H; d), 7.87-7.77 (m, 3.8H; e+c'+d'+e'+e''+e''').

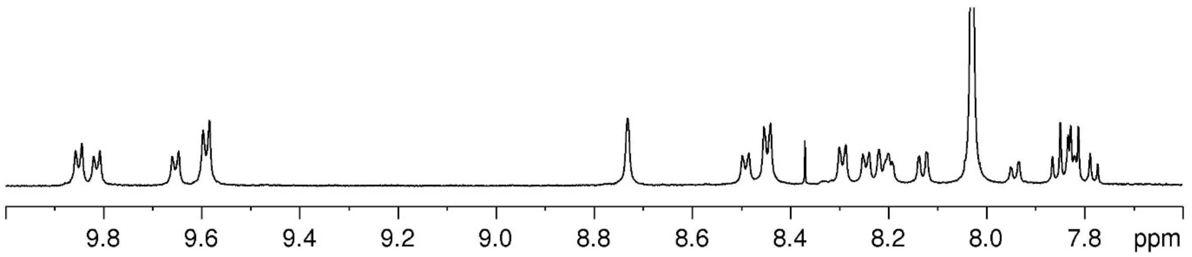

Fig. 44 Partial ^{1}H NMR (600 MHz, 298 K, DMF-d_7) of the self-assembly of **L2** in DMF-d_7.

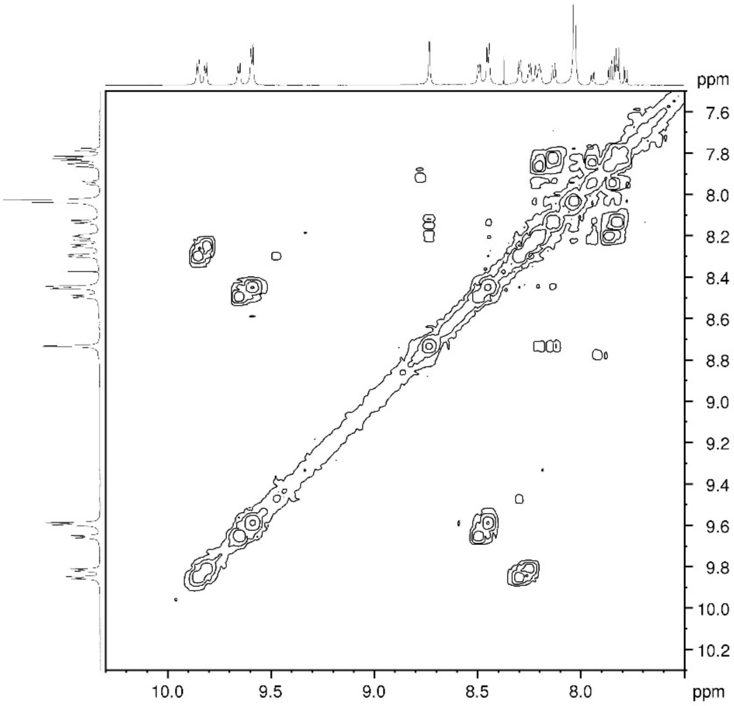

Fig. 45 Partial ^{1}H-^{1}H COSY NMR (600 MHz, 298 K, DMF-d_7) of the self-assembly of **L2** in DMF-d_7.

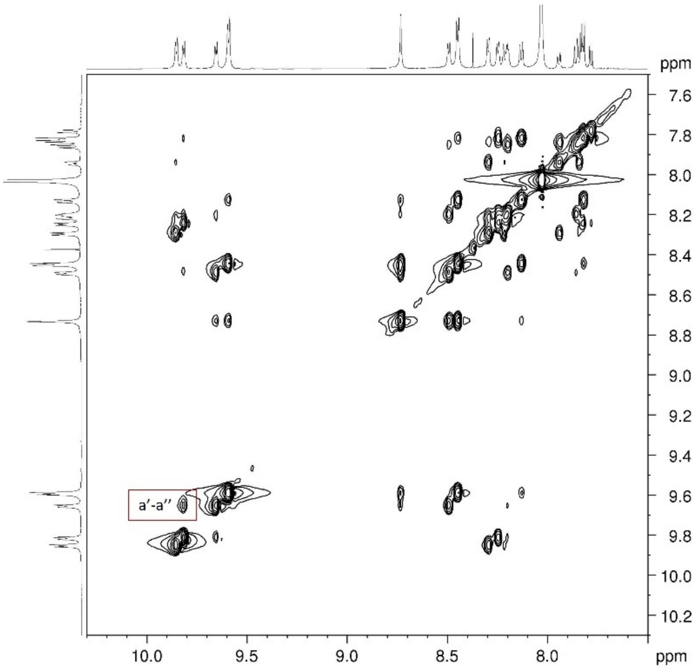

Fig. 46 Partial ^{1}H-^{1}H NOESY NMR (600 MHz, 298 K, DMF-d_7) of the self-assembly of **L2** in DMF-d_7. The highlighted NOE contact shows that signal sets a'-e' and a''-e'' belong to the same species.

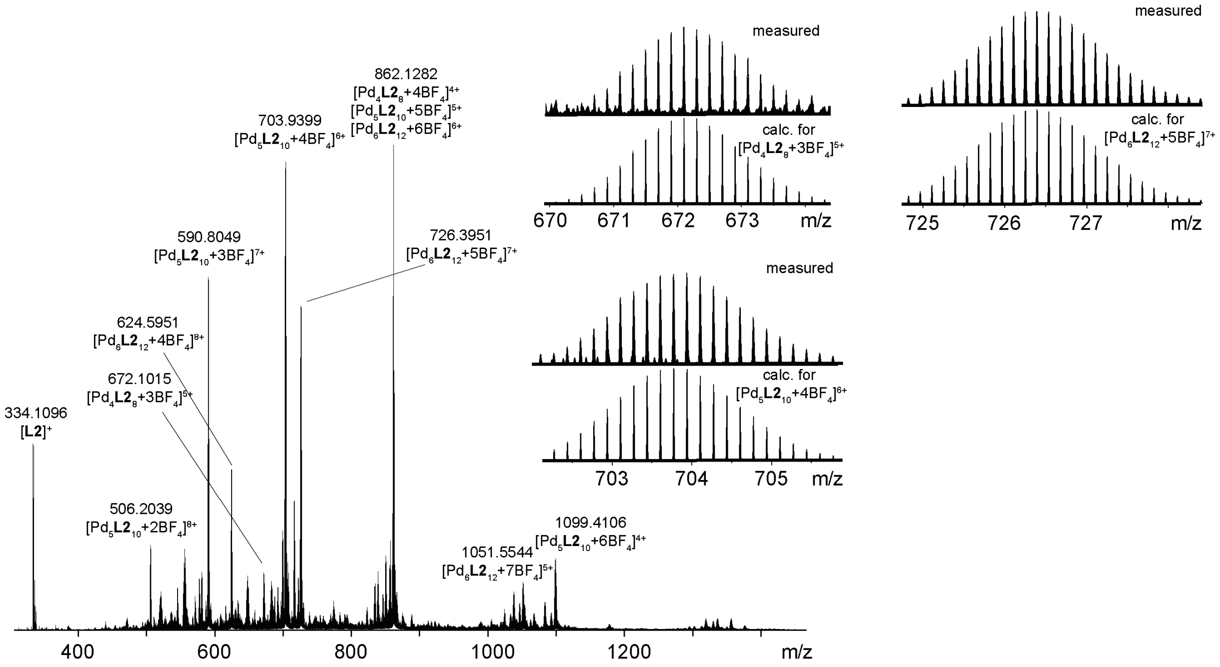

Fig. 47 ESI mass spectrum of the self-assembly of **L2** in DMF-d_7. The inset shows a comparison of the measured and calculated isotopic patterns for $[Pd_4\mathbf{L2}_8+3BF_4]^{5+}$, $[Pd_5\mathbf{L2}_{10}+4BF_4]^{6+}$, and $[Pd_6\mathbf{L2}_{12}+5BF_4]^{7+}$.

Self-assembly of L3 in CD_3CN

^{1}H NMR (500 MHz, CD_3CN): δ = 9.42 (d, J = 6.76, 0.8H), 9.38 (d, J = 6.77, 2H), 8.87 (d, J = 6.76, 1.4H), 8.73 (d, J = 1.56, 0.5H), 8.65 (d, J = 1.67, 1H), 8.57 (d, J = 1.62, 0.7H), 8.16-8.12 (m, 3.7H), 8.08 (d, J = 6.86, 2.3H), 8.00 (d, J = 6.75, 1.6H), 7.90-7.86 (m, 1.8H).

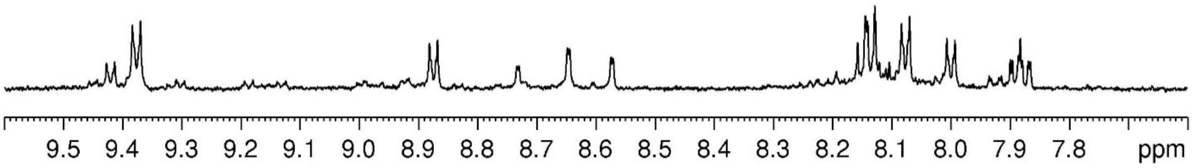

Fig. 48 Partial ^{1}H NMR (500 MHz, 298 K, CD_3CN) of the self-assembly of **L3** in CD_3CN.

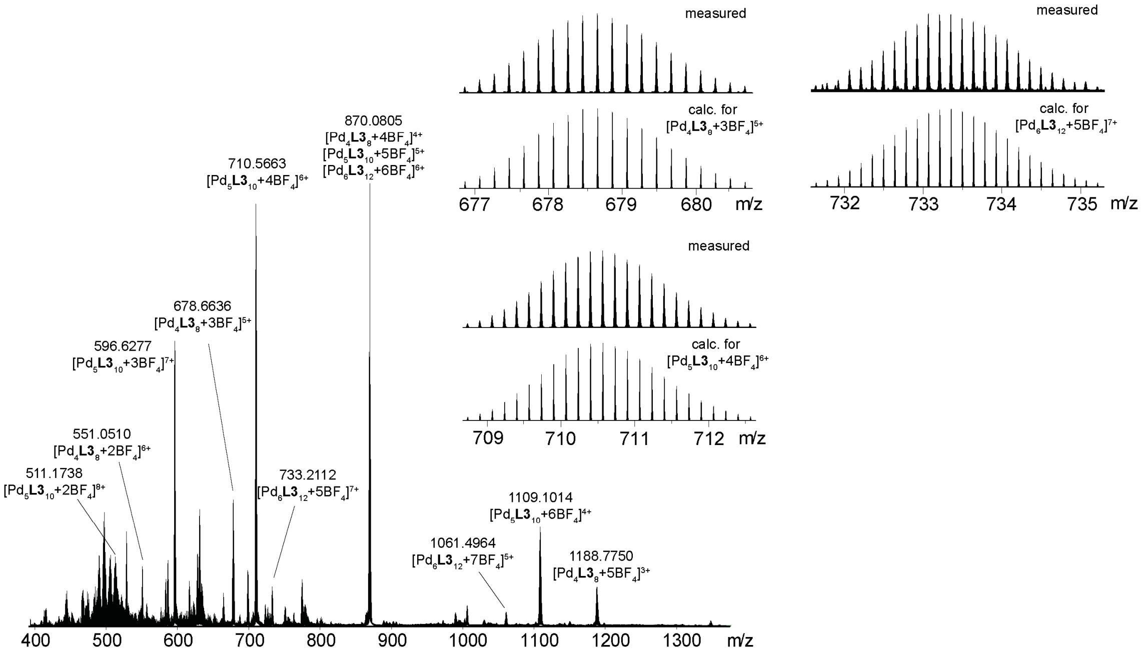

Fig. 49 ESI mass spectrum of the self-assembly of **L3** in CD_3CN. The inset shows a comparison of the measured and calculated isotopic patterns for $[Pd_4$**L3**$_8+3BF_4]^{5+}$, $[Pd_5$**L3**$_{10}+4BF_4]^{6+}$, and $[Pd_6$**L3**$_{12}+5BF_4]^{7+}$.

Self-assembly of L3 in DMF-*d*$_7$

^{1}H NMR (500 MHz, DMF-*d*$_7$): δ = 9.86-9.82 (m, 2.8H), 8.97 (s, 1H), 8.87 (s, 0.4H), 8.41 (d, *J* = 6.87, 2H), 8.38-8.30 (m, 3.2H), 8.21 (s, 0.7H), 8.14 (dd, *J* = 6.26, 1.37, 1.5H).

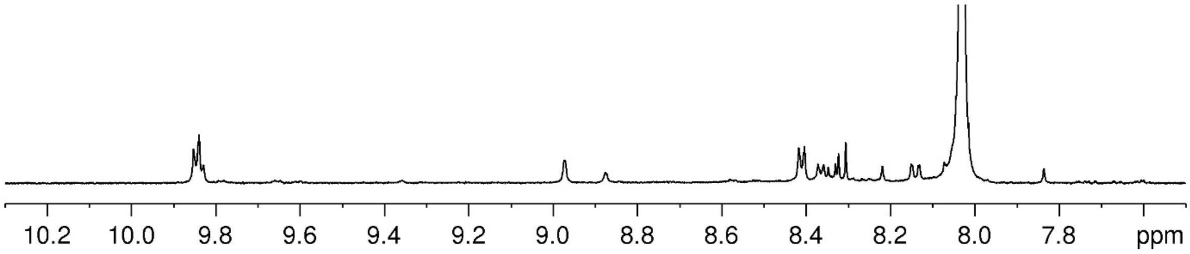

Fig. 50 Partial ^{1}H NMR (500 MHz, 298 K, DMF-*d*$_7$) of the self-assembly of **L3** in DMF-*d*$_7$.

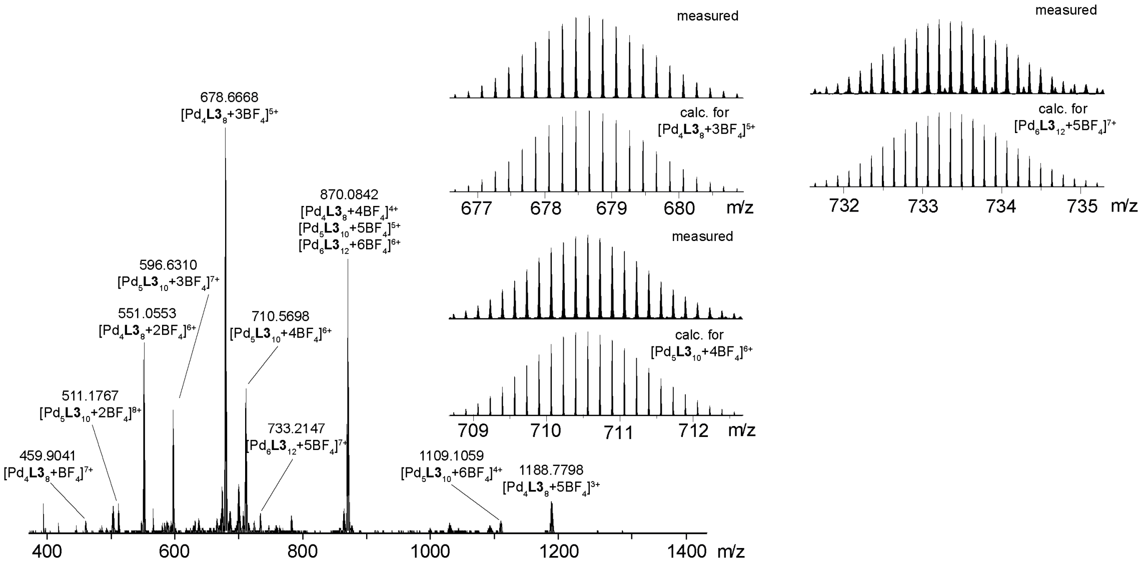

Fig. 51 ESI mass spectrum of the self-assembly of **L3** in DMF-d_7. The inset shows a comparison of the measured and calculated isotopic patterns for $[Pd_4\mathbf{L3}_8+3BF_4]^{5+}$, $[Pd_5\mathbf{L3}_{10}+4BF_4]^{6+}$, and $[Pd_6\mathbf{L3}_{12}+5BF_4]^{7+}$.

2.7.5. X-ray crystallography

Two supramolecular assemblies $[Pd_5\mathbf{L2}_{10}]^{10+}$ and $[Pd_5\mathbf{L3}_{10}]^{10+}$ were analyzed using single-crystal X-ray crystallography. The crystals of the supramolecular assemblies were extremely sensitive to loss of organic solvent. Due to very tiny crystal volumes, the analysis was further hampered by the limited scattering power. Gaining detailed structural insight required cryogenic crystal handling and highly brilliant synchrotron radiation. Diffraction data was collected during two beamtime shifts at macromolecular synchrotron beamline P11, PETRA III, at DESY, Hamburg.[30] Carefully adapted macromolecular refinement protocols employing geometrical restraint dictionaries, similarity restraints and restraints for anisotropic displacement parameters (ADPs) were applied. Details can be found in the discussions below. The refinement was carried out by Milan Kulas and Dr. Julian J. Holstein who also provided the texts and tables shown here.

Tab. 3 Crystallographic data of $[Pd_5\mathbf{L2}_{10}]^{10+}$ and $[Pd_5\mathbf{L3}_{10}]^{10+}$.

Compound	$[Pd_5\mathbf{L2}_{10}]^{10+}$	$[Pd_5\mathbf{L3}_{10}]^{10+}$
CIF ID	**Ln4t_syn**	**Ln10c**
CCDC no	**2297390**	**2297391**
Empirical formula	$C_{230}H_{140}B_5F_{20}N_{20}O_{10}Pd_5$	$C_{224}H_{146}B_5F_{20}N_{22}Pd_5S_{10}$
Formula weight	4309.66	4432.27
Temperature [K]	100(2)	100(2)
Crystal system	orthorhombic	monoclinic
Space group (number)	$Pnma$ (62)	$P2_1/c$ (14)
a [Å]	62.293(19)	16.980(17)
b [Å]	22.731(11)	49.902(17)
c [Å]	37.013(17)	53.89(2)
α [Å]	90	90
β [Å]	90	96.15(2)
γ [Å]	90	90
Volume [Å^3]	52410(38)	45403(52)
Z	4	4
ρ_{calc} [g/cm^3]	0.546	0.648
μ [mm^{-1}]	0.539	0.751
F(000)	8700	8956

Crystal size [mm^3]	0.040×0.030×0.010	0.010×0.005×0.005
Crystal color	yellow	yellow
Crystal shape	block	needle
Radiation	synchrotron (λ=1.03323 Å)	synchrotron (λ=1.03321 Å)
2Θ range [°]	2.48 to 43.31 (1.40 Å)	1.62 to 43.31 (1.40 Å)
Index ranges	$-44 \le h \le 44$ $-16 \le k \le 16$ $-26 \le l \le 26$	$-11 \le h \le 11$ $-35 \le k \le 33$ $-38 \le l \le 38$
Reflections collected	64820	58656
Independent reflections	10424 R_{int} = 0.0661 R_{sigma} = 0.0431	16003 R_{int} = 0.1089 R_{sigma} = 0.0929
Completeness to θ = 25.242°	99.7%	92.4%
Data / Restraints / Parameters	10424/2882/1327	16003/5340/2575
Goodness-of-fit on F^2	2.082	1.368
Final R indexes [$I \geq 2\sigma(I)$]	R_1 = 0.1902 wR_2 = 0.4814	R_1 = 0.1145 wR_2 = 0.3219
Final R indexes [all data]	R_1 = 0.2091 wR_2 = 0.5025	R_1 = 0.1427 wR_2 = 0.3511
Largest peak/hole [eÅ^3]	1.52/−0.71	0.60/−0.43

Crystal structure of [Pd$_5$L2$_{10}$]$^{10+}$ (Ln4t_syn)

Yellow block-shaped crystals of [Pd$_5$**L2**$_{10}$]$^{10+}$ were grown by slow vapor diffusion of toluene into the solution of [Pd$_5$**L2**$_{10}$]$^{10+}$ in acetonitrile at room temperature. Single crystals in mother liquor were pipetted onto a glass slide containing NVH oil. To avoid collapse of the crystal lattice, the crystal was quickly mounted onto a 0.2 mm nylon loop and immediately flash-cooled in liquid nitrogen. Crystals were stored at cryogenic temperature in dry shippers, in which they were safely transported to macromolecular beamline P11 at Petra III,[30] DESY, Hamburg, Germany. A wavelength of λ = 1.0332 Å was chosen using a liquid N$_2$ cooled double crystal monochromator. Single crystal X-ray diffraction data was collected at 100(2) K on a single axis goniometer, equipped with an Oxford Cryostream 800 instrument and an Eiger 2x 16M detector. 3600 diffraction images were collected in a 180° ϕ sweep at a detector distance of 154 mm, 100% filter transmission, 0.1° step width and 0.1 seconds exposure time per image. Data integration and reduction were undertaken using XDS.[31] The structure was solved by intrinsic phasing/direct methods using SHELXT[32] and refined with SHELXL[33] using 22 CPU cores for full-matrix least-squares routines on F^2 and ShelXle[34] as a graphical user interface and the DSR program plugin was employed for modeling.[35,36]

Specific refinement details for [Pd$_5$**L2**$_{10}$] **(Ln4t_syn)**

The structure was solved and refined in orthorhombic space group $Pnma$ (62) and only contains half of the [Pd$_5$**L2**$_{10}$]$^{10+}$ ring in the asymmetric unit. Four out of five tetrafluoroborate counterions were successfully modelled.

Stereochemical restraints for the **L^1** (residue FOP) ligands were generated by the GRADE program using the GRADE Web Server (http://grade.globalphasing.org) and applied in the refinement. A GRADE dictionary for SHELXL contains target values and standard deviations for 1,2-distances (DFIX) and 1,3-distances (DANG), as well as restraints for planar groups (FLAT). All displacements for non-hydrogen atoms were refined anisotropically. The refinement of ADP's for carbon, nitrogen and oxygen atoms was enabled by a combination of similarity restraints (SIMU) and rigid bond restraints (RIGU).[37] The contribution of the electron density from disordered counterions and solvent molecules, which could not be modeled with discrete atomic positions were handled using the SQUEEZE[38] routine in PLATON.[39] The solvent mask file (.fab) computed by PLATON was included in the SHELXL refinement via the ABIN instruction leaving the measured intensities untouched.

Tab. 4 C^{ipso}-N-Pd and Pd-Pd-Pd angles in the crystal structure of [Pd$_5$**L2**$_{10}$]$^{10+}$.

atom-atom-atom	angle (°)
C20_6-N23_6-Pd1_1	177.69(112)
C20_3-N23_3-Pd1_1	178.62(100)
C1_3-N4_3-Pd2_1	170.92(82)
C20_2-N23_2-Pd2_1	177.16(104)
C1_2-N4_2-Pd3_1	177.30(115)
C1_4-N4_4-Pd3_1	173.45(95)
C20_4-N23_4-Pd4_1	175.90(122)
C1_5-N4_5-Pd4_1	171.94(122)
C20_5-N23_5-Pd5_1	172.18(114)
C1_6-N4_6-Pd5_1	171.92(146)
Pd2_1-Pd1_1-Pd5_1	106.14(5)
Pd1_1-Pd5_1-Pd4_1	110.87(5)
Pd5_1-Pd4_1-Pd3_1	105.10(4)
Pd4_1-Pd3_1-Pd2_1	108.49(3)
Pd3_1-Pd2_1-Pd1_1	109.39(4)

Tab. 5 Carbonyl-C to carbonyl-C distances between the fluorenone backbones of ligands bridging the same edge in the crystal structure of [Pd$_5$**L2**$_{10}$]$^{10+}$.

C - C	distance (Å)
C13_2 - C13_2_$1	13.8203 (0.0273)
C13_3 - C13_3_$1	13.1939 (0.0292)
C13_4 - C13_4_$1	12.6784 (0.0284)
C13_5 - C13_5_$1	12.5377 (0.0314)
C13_6 - C13_6_$1	13.3755 (0.0344)

Crystal structure of [Pd$_5$L3$_{10}$]$^{10+}$ (Ln10c)

Yellow needle-shaped crystals of [Pd$_5$**L3**$_{10}$]$^{10+}$ were grown by slow vapor diffusion of toluene into the solution of [Pd$_5$**L3**$_{10}$]$^{10+}$ in acetonitrile at room temperature. Single crystals in mother liquor were pipetted onto a glass slide containing NVH oil. To avoid collapse of the crystal lattice, the crystal was quickly mounted onto a 0.2 mm nylon loop and immediately flash-cooled in liquid nitrogen. Crystals were stored at cryogenic temperature in dry shippers, in which they were safely transported to macromolecular beamline P11 at Petra III,[30] DESY, Hamburg, Germany. A wavelength of λ = 1.0332 Å was chosen using a liquid N$_2$ cooled double crystal monochromator. Single crystal X-ray diffraction data was collected at 100(2) K on a single axis goniometer, equipped with an Oxford Cryostream 800 instrument and an Eiger 2x 16M detector. 3600 diffraction images were collected in a 180° ϕ sweep at a detector distance of 154 mm, 75% filter transmission, 0.1° step width and 0.2 seconds exposure time per image. Data integration and reduction were undertaken using XDS.[31] The structure was solved by intrinsic phasing/direct methods using SHELXT[32] and refined with SHELXL[33] using 22 CPU cores for full-matrix least-squares routines on F^2 and ShelXle[34] as a graphical user interface and the DSR program plugin was employed for modeling.[35,36]

Specific refinement details for $[Pd_5L3_{10}]^{10+}$ (Ln10c)

The structure was solved and refined in monoclinic space group $P21/\mathrm{n}$ (14) and contains a full $[Pd_5\mathbf{L}^2{}_{10}]^{10+}$ ring in the asymmetric unit. Five out of ten tetrafluoroborate counterions and two acetonitrile solvent molecules were successfully modelled.

Stereochemical restraints for the **L3** (residue DBT) ligands and acetonitrile solvent molecules (residue ACN) were generated by the GRADE program using the GRADE Web Server (http://grade.globalphasing.org) and applied in the refinement. A GRADE dictionary for SHELXL contains target values and standard deviations for 1,2-distances (DFIX) and 1,3-distances (DANG), as well as restraints for planar groups (FLAT). All displacements for non-hydrogen atoms were refined anisotropically. The refinement of ADPs for carbon, nitrogen and oxygen atoms was enabled by a combination of similarity restraints (SIMU) and rigid bond restraints (RIGU).[37] The contribution of the electron density from disordered counterions and solvent molecules, which could not be modeled with discrete atomic positions were handled using the SQUEEZE[38] routine in PLATON.[39] The solvent mask file (.fab) computed by PLATON was included in the SHELXL refinement via the ABIN instruction leaving the measured intensities untouched.

Tab. 6 C^{ipso}-N-Pd and Pd-Pd-Pd angles in the crystal structure of $[Pd_5\mathbf{L3}_{10}]^{10+}$.

atom-atom-atom	angle (°)
C1_8-N4_8-Pd2_1	177.23(109)
C20_7-N23_7-Pd2_1	175.13(116)
C20_9-N23_9-Pd2_1	174.37(106)
C1_10-N4_10-Pd2_1	171.09(96)
C1_5-N4_5-Pd4_1	174.18(96)
C20_6-N23_6-Pd4_1	165.77(102)
C20_8-N23_8-Pd4_1	177.95(123)
C1_7-N4_7-Pd4_1	176.02(99)
C1_6-N4_6-Pd5_1	173.00(103)
C20_4-N23_4-Pd5_1	176.48(129)
C20_5-N23_5-Pd5_1	170.97(115)
C20_11-N23_11-Pd5_1	174.30(114)
C1_2-N4_2-Pd3_1	176.85(120)
C1_4-N4_4-Pd3_1	174.25(99)
C1_11-N4_11-Pd3_1	176.93(112)
C20_3-N23_3-Pd3_1	179.70(139)
Pd2_1-Pd1_1-Pd3_1	102.20(3)
Pd1_1-Pd2_1-Pd4_1	106.45(3)
Pd2_1-Pd4_1-Pd5_1	115.72(2)
Pd3_1-Pd5_1-Pd4_1	96.75(3)
Pd5_1-Pd3_1-Pd1_1	118.81(3)

Tab. 7 Sulfur to sulfur distances between the dibenzothiophene backbones of ligands bridging the same edge in the crystal structure of $[Pd_5\mathbf{L3}_{10}]^{10+}$.

C - C	distance (Å)
S13_10 - S13_9	12.5722 (0.0175)
S13_8 - S13_7	14.7528 (0.0198)
S13_6 - S13_5	12.4462 (0.0168)
S13_4 - S13_11	14.5749 (0.0185)
S13_2 - S13_3	14.5544 (0.0178)

2.7.6. Computational studies

Calculation of binding angles

Models of the free ligands were built with the software Spartan[40] and were then geometry-optimized using the semiempirical PM6 method without constraints and afterwards by DFT calculations (B3LYP/Def2SVP) using Gaussian.[41] The binding angle refers here to the angle between the two donor vectors of the respective ligands (vectors defined within the pyridines as pointing from C4 to N1). For ligands with meta-pyridine donor groups, the binding angles were determined from the flat ligand as various binding angles can be adopted by rotation of the pyridine moiety against the ligand backbone. Here, a concave binding mode was chosen over a convex binding mode as the former more closely resembles the binding angle adopted in entropically favored assemblies of low nuclearity.[7]

DFT optimization of coordination rings and single point energy calculations

Models of the rings were built with the software Spartan[40] and were then optimized using the semiempirical PM6 method without constraints. The pre-optimized structures were then subjected to a further geometry optimization by DFT calculations (B3LYP/Def2-SVP) using Gaussian 16.[41] Single-point energy calculations of the rings, single or cyclically arranged [Pd(II)pyridine$_4$]$^{2+}$ complexes (as described in the main text) were performed using Gaussian 16 (wb97cd/Def2SVP).[41]

Tab. 8 Single point energies E obtained by DFT computations (wb97xd/Def-SVP) with implicit solvent (SCRF model, DMSO) and Coulomb repulsions ΔE_{Coul} obtained with equation 2.

	$[\mathrm{Pd_4}\mathbf{L2}_8]^{8+}$	$[\mathrm{Pd_5}\mathbf{L2}_{10}]^{10+}$	$[\mathrm{Pd_4}\mathbf{L3}_8]^{8+}$	$[\mathrm{Pd_5}\mathbf{L3}_{10}]^{10+}$
E in kJ/mol	−23784279.43	−29730368.97	−29767647.93	−37209560.84
ΔE_{Coul} in kJ/mol	41.74	55.36	42.01	58.26

Tab. 9 Energies ΔE for the ring-to-ring transformations and for the Coulomb repulsion-corrected ring-to-ring transformations E_{S} for the models computed with implicit solvent (SCRF model, DMSO), determined with equations 1 and 3.

	L2	**L3**
$\Delta E(\mathrm{Pd_4} \rightarrow \mathrm{Pd_5})$ in kJ/mol	−78.77	−3.70
$E_{\mathrm{S}}(\mathrm{Pd_4} \rightarrow \mathrm{Pd_5})$ in kJ/mol	−91.48	−26.70

2.7.7. Geometrical model

Representation of geometric model 1 for n-gons with n = 3-5

The models were constructed with Andreas Walther (http://www.v-cube.de/).

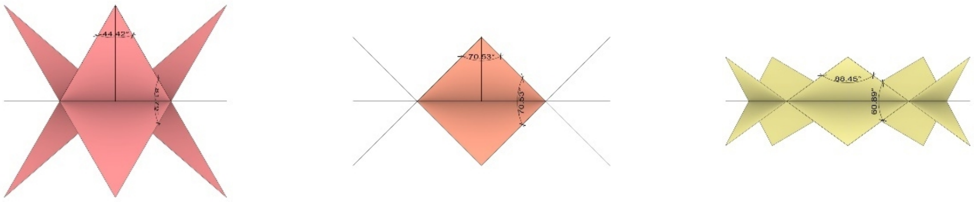

Fig. 52 Geometric models (side view) of 3- (left), 4- (middle), and 5-membered (right) ring. Specified are the interior angles of the protruding triangles (44.42°, 70.53°, 88.45°) and the angles between the two edges of the two triangles sharing the middle point on the edge of the pentagon (81.79°, 70.53°, 60.89°). In this model, the latter angles deviate from the ideally 90° angles dictated by the square-planar coordination of the Pd(II) cations, sitting on these positions, leading to an additional bending of the ligand planes, as also experimentally observed.

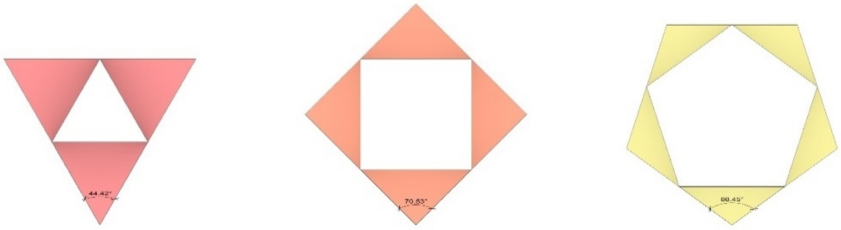

Fig. 53 Geometric models (top view) of 3- (left), 4- (middle), and 5-membered (right) ring. Specified are the interior angles of the protruding triangles (44.42°, 70.53°, 88.45°).

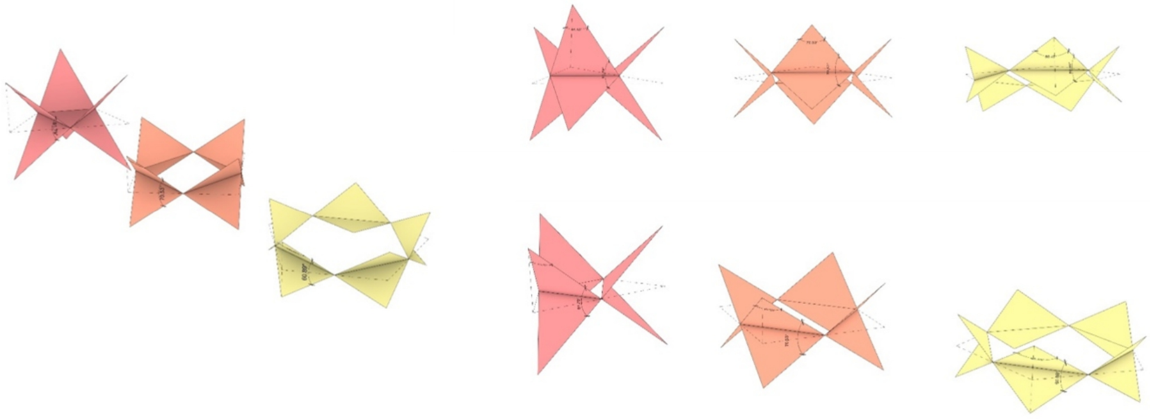

Fig. 54 Further models of the 3- (left), 4- (middle), and 5-membered (right) rings. Specified are the interior angles of the protruding triangles (44.42°, 70.53°, 88.45°) and the angles between the two edges of the two triangles sharing the edge of the pentagon (81.79°, 70.53°, 60.89°).

Derivation of geometric model 2

For deriving the second model, the angle between the flap (ligand, yellow) and the pentagon plane (blue) is set to 45°, according to a square planar coordination geometry. From this, equation 10 follows:

$$\cos(45°) = \frac{a}{a_2} \tag{10}$$

For both triangles, the angle β can be expressed as a function of the edges:

$$\sin\left(\frac{\beta}{2}\right) = \frac{b}{2 \cdot a} \tag{11}$$

$$\sin\left(\frac{\beta_2}{2}\right) = \frac{b}{2 \cdot a_2} \tag{12}$$

Solving for b and equating leads to:

$$a \cdot \sin\left(\frac{\beta}{2}\right) = a_2 \cdot \sin\left(\frac{\beta_2}{2}\right) \tag{13}$$

From equations 10 and 13 as well as the relationship between β and the ring nuclearity n, it follows:

$$\beta_2 = 2 \cdot \arcsin\left(\cos(45°) \cdot \sin\left(\frac{\beta}{2}\right)\right) = 2 \cdot \arcsin\left(\cos(45°) \cdot \sin\left(\frac{(n-2)}{2 \cdot n} \cdot 180°\right)\right) \tag{14}$$

2.8. References

[1] T. Zhang, L.-P. Zhou, X.-Q. Guo, L.-X. Cai, Q.-F. Sun, *Nat. Commun.* **2017**, *8*, ncomms15898.

[2] K. Harris, D. Fujita, M. Fujita, *Chem. Commun.* **2013**, *49*, 6703.

[3] Y. Zhang, H. Gan, C. Qin, X. Wang, Z. Su, M. J. Zaworotko, *J. Am. Chem. Soc.* **2018**, *140*, 17365.

[4] D. Fujita, Y. Ueda, S. Sato, N. Mizuno, T. Kumasaka, M. Fujita, *Nature* **2016**, *540*, 563.

[5] Y.-Y. Ge, X.-C. Zhou, J. Zheng, J. Luo, Y.-L. Lai, J. Su, H.-J. Zhang, X.-P. Zhou, D. Li, *Inorg. Chem.* **2023**, *62*, 4048.

[6] K. Suzuki, M. Kawano, M. Fujita, *Angew. Chem. Int. Ed.* **2007**, *119*, 2877.

[7] J. Tessarolo, H. Lee, E. Sakuda, K. Umakoshi, G. H. Clever, *J. Am. Chem. Soc.* **2021**, *143*, 6339.

[8] W. M. Bloch, Y. Abe, J. J. Holstein, C. M. Wandtke, B. Dittrich, G. H. Clever, *J. Am. Chem. Soc.,* **2016**, *138*, 13750.

[9] D. R. Martir, D. B. Cordes, A. M. Z. Slawin, D. Escudero, D. Jacquemin, S. L. Warriner, E. Zysman-Colman, *Chem. Commun.* **2018**, *54*, 6016.

[10] S. Prusty, K. Yazaki, M. Yoshizawa, D. K. Chand, *Chem. Eur. J.* **2017**, *23*, 12456.

[11] F. Spaepen, *Nature* **2000**, *408*, 781.

[12] B. Hasenknopf, J. Lehn, B. O. Kneisel, G. Baum, D. Fenske, *Angew. Chem. Int. Ed.* **1996**, *35*, 1838.

[13] B. Hasenknopf, J. Lehn, N. Boumediene, E. Leize, A. V. Dorsselaer, *Angew. Chem. Int. Ed.* **1998**, *37*, 3265.

[14] J.-F. Ayme, J. E. Beves, D. A. Leigh, R. T. McBurney, K. Rissanen, D. Schultz, *Nat. Chem.* **2012**, *4*, 15.

[15] J.-F. Ayme, J. E. Beves, C. J. Campbell, G. Gil-Ramírez, D. A. Leigh, A. J. Stephens, *J. Am. Chem. Soc.* **2015**, *137*, 9812.

[16] T. K. Ronson, Y. Wang, K. Baldridge, J. S. Siegel, J. R. Nitschke, *J. Am. Chem. Soc.* **2020**, *142*, 10267.

[17] C. S. Campos-Fernández, R. Clérac, J. M. Koomen, D. H. Russell, K. R. Dunbar, *J. Am. Chem. Soc.* **2001**, *123*, 773.

[18] C. S. Campos-Fernández, B. L. Schottel, H. T. Chifotides, J. K. Bera, J. Bacsa, J. M. Koomen, D. H. Russell, K. R. Dunbar, *J. Am. Chem. Soc.* **2005**, *127*, 12909.

[19] S.-H. Hwang, P. Wang, C. N. Moorefield, L. A. Godínez, J. Manríquez, E. Bustos, G. R. Newkome, *Chem. Commun.* **2005**, 4672.

[20] P. Liao, B. W. Langloss, A. M. Johnson, E. R. Knudsen, F. S. Tham, R. R. Julian, R. J. Hooley, *Chem. Commun.* **2010**, *46*, 4932.

[21] K. Suzuki, M. Tominaga, M. Kawano, M. Fujita, *Chem. Commun.* **2009**, 1638.

[22] A. Einstein, *Ann. Phys.* **1905**, *322*, 549.

[23] D. M. Engelhard, S. Freye, K. Grohe, M. John, G. H. Clever, *Angew. Chem. Int. Ed.* **2012**, *51*, 4747.

[24] A. Platzek, S. Juber, C. Yurtseven, S. Hasegawa, L. Schneider, C. Drechsler, K. E. Ebbert, R. Rudolf, Q. Yan, J. J. Holstein, L. V. Schäfer, G. H. Clever, *Angew. Chem. Int. Ed.* **2022**, *61*, e202209305.

[25] R. Lück, *Mater. Sci. Eng.: A* **2000**, *294*, 263.

[26] A. Jerschow, N. Müller, *J. Magnetic. Reson.* **1996**, *123*, 222.

[27] A. Jerschow, N. Müller, *J. Magn. Reson.* **1997**, *125*, 372.

[28] M. A. Einstein, *J. Food Sci.* **1976**, *41*, 383.

[29] J. E. Tanner, E. O. Stejskal, *J. Chem. Phys.* **1968**, *49*, 1768.

[30] A. Burkhardt, T. Pakendorf, B. Reime, J. Meyer, P. Fischer, N. Stübe, S. Panneerselvam, O. Lorbeer, K. Stachnik, M. Warmer, P. Rödig, D. Göries, A. Meents, *Europ. Phys. J. Plus* **2016**, *131*, 56.

[31] W. Kabsch, *Acta Crystallogr. Sect. D* **2010**, *66*, 125.

[32] G. M. Sheldrick, *Acta Crystallogr. Sect. A* **2015**, *71*, 3.

[33] G. M. Sheldrick, *Acta Crystallogr. C* **2015**, *71*, 3.

[34] C. B. Hübschle, G. M. Sheldrick, B. Dittrich, *J. Appl. Crystallogr.* **2011**, *44*, 1281.

[35] D. Kratzert, J. J. Holstein, I. Krossing, *J. Appl. Crystallogr.* **2015**, *48*, 933.

[36] D. Kratzert, I. Krossing, *J. Appl. Crystallogr.* **2018**, *51*, 928.

[37] A. Thorn, B. Dittrich, G. M. Sheldrick, *Acta Crystallogr. Sect. A* **2012**, *68*, 448.

[38] A. L. Spek, *Acta Crystallogr. Sect. C* **2015**, *71*, 9.

[39] A. L. Spek, *Acta Crystallogr. Sect. D* **2009**, *65*, 148.

[40] SPARTAN Wavefunction, Inc., Spartan` 18 Parallel Suite, Irvine (USA), **2018**.

[41]. J. Frisch, G. W. Trucks, H. B. Schlegel et al., Gaussian, Inc., Gaussian 16, Revision C.01, Wallingford CT (USA) **2016**.

3. Systematic study of donor-acceptor cages

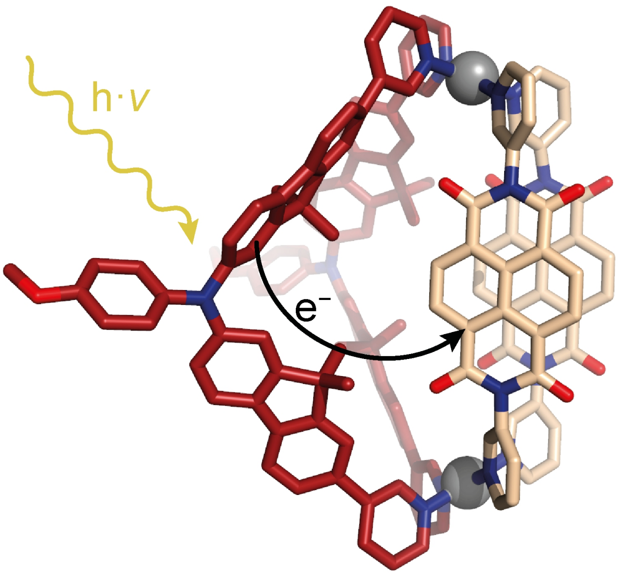

Results of this chapter are currently compiled for publication:

L. Neukirch, P. T. Cesana, R. Naumann, B. Schmidt, S. Afshar, E. Benchimol, K. Heinze*, G. S. Schlau-Cohen*, G. H. Clever*

Photoinduced Charge Separation in Donor-Acceptor Functionalized Coordination Cages - A Systematic Study

3.1. Motivation

While the coordination-driven self-assembly into cages has been exploited for bringing electron donor and acceptor moieties in spatial proximity,[1] the modularity of the underlying approach was so far not used for drawing systematic structure-function relationships. For the donor-acceptor cages herein investigated, „function" refers to the excited state properties, which decide on whether the system is suitable for a certain application. Donor-acceptor cages hold promise for application in photoredox catalysis owing to their cavity which is surrounded by the photoredox active moieties and can be exploited for substrate binding.[2,3] Encapsulation results in an increased local concentration and the spatial constraints of the cage can endow a reaction with selectivity. Moreover, coordination cages could be used as a platform for studying electron transfer rates between redox active moieties positioned in defined distances and orientations. These insights could then steer the development of novel materials for applications in photovoltaics and artificial photosynthesis. With regards to the excited state properties, a long-lived charge separated state is desirable for most applications as it increases the probability of the occurrence of a second electron transfer step, e.g. to a substrate or to an electrode, as opposed to unproductive back electron transfer.[4,5] Predicting the electron transfer rate constant is, however, challenging.[6] By contrast, the thermodynamic driving force for the process can be predicted relatively reliable based on the halfwave potentials of the donor and acceptor moieties.[7] Therefore, this work is focused on studying the free-energy dependency of the rate constant for the back electron transfer in donor-acceptor cages with the aim to contribute to the rational design of functional coordination cages.

For accomplishing this goal, a library of donor-acceptor cages covering a range of electron transfer driving forces is designed. In contrast to the beforehand reported statistical mixture of donor-acceptor cages,[1,8] discrete cages (with regards to their stoichiometry and stereoconfiguration) are envisioned. This should reduce the number of concomitantly occurring excited state processes and hence improve the chances of being able to assign the observed rates to a particular process. In order to achieve this, the SCA approach is applied: convergent donor ligands are combined with divergent acceptor ligands to yield *cis*-$[Pd_2D_2A_2]^{4+}$ cages. Inspired by literature reports,[9–11] donor ligands based on phenyl-carbazole (**CBZ**), triaryl amine (**TAA**), and phenothiazine (**PTZ**) and acceptor ligands based on naphthalene diimide (**NDI**), pyromellitic diimide (**PMDI**), and fluorenone (**FRO**) were employed (Fig. 1a).

In the first step, the constituent organic ligands are designed and synthesized. This is followed by the self-assembly into the heteroleptic cages under suitable conditions and thorough characterization of their structures. Next, the ground state photophysical and electrochemical properties of ligands, homoleptic, and heteroleptic cages are investigated. These studies are required for a) determining a suitable wavelength for electronic excitation, b) acquiring the absorption spectra of oxidized and reduced cages, serving as references for the interpretation of the transient difference spectra, and c) calculation of the driving force for the electron transfer processes. Insight into the excited state dynamics of the cages is then gained by applying transient absorption spectroscopy. The combination of the kinetic and thermodynamic data represents the culmination of the project. In addition, DFT calculations were performed to support the experimental data.

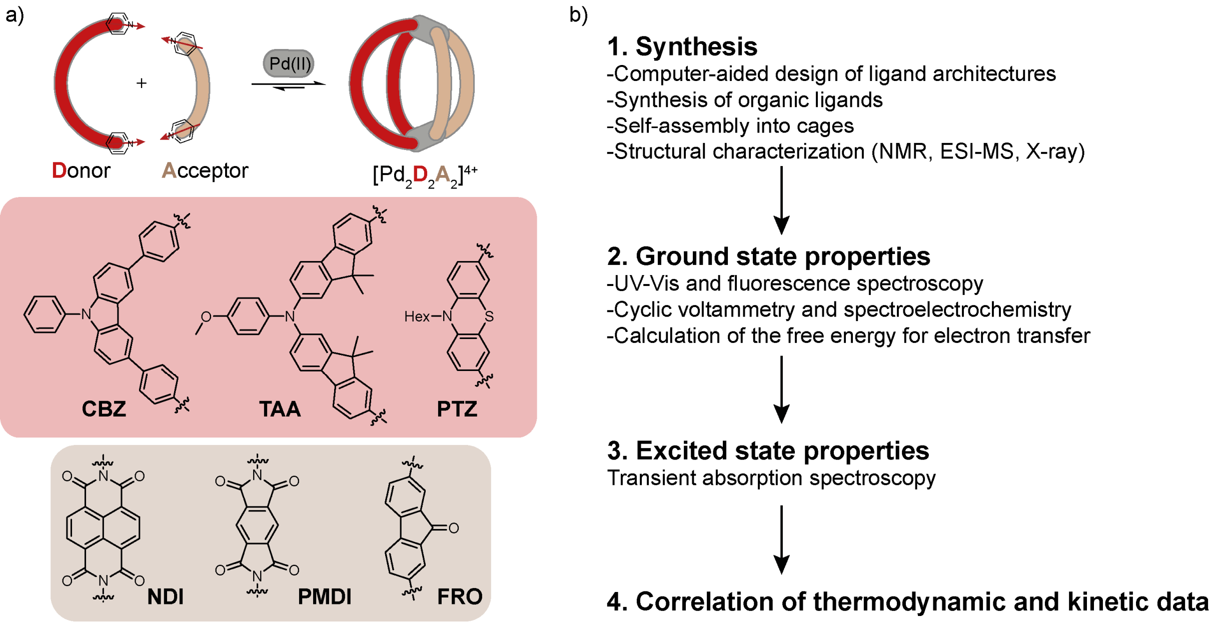

Fig. 1 Procedure for the systematic investigation of electron transfer in $[Pd_2D_2A_2]^{4+}$ donor-acceptor cages.

3.2. State of the art

Two of the cages in the library investigated in this work have been previously synthesized and studied. Dr. Jacopo Tessarolo designed cage $[Pd_2\mathbf{TAA}_2\mathbf{FRO}_2]^{4+}$ with triarylamine-based ligand **TAA** and fluorenone-based ligand **FRO** (Fig. 2) and Dr. Kai Wu synthesized a similar cage with a phenothiazine-based donor $[Pd_2\mathbf{PTZ}_2\mathbf{FRO}_2]^{4+}$. The interpretation of the data obtained in this PhD project is based on the results obtained with these two cages. Since they are unpublished, selected transient difference spectra will be shown and described here.

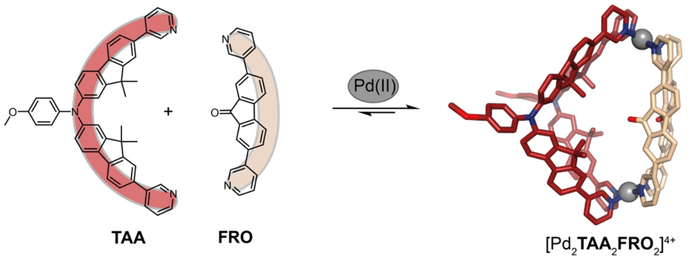

Fig. 2 Self-assembly of discrete donor-acceptor functionalized coordination cage $[Pd_2\mathbf{TAA}_2\mathbf{FRO}_2]^{4+}$.

In the case of $[Pd_2\mathbf{TAA}_2\mathbf{FRO}_2]^{4+}$, the photoinduced processes were examined for ligands, homoleptic assemblies, and donor-acceptor cages using a transient absorption setup with 375, 385, or 400 nm pump pulses and probe pulses in the visible (time resolution about 100 fs) and IR (time resolution about 500 fs). The time constants were obtained by single wavelength fitting. Measurement and analysis were carried out by the group of Prof. Dirk Schwarzer, Max-Planck-Institute for Multidisciplinary Science, Göttingen.

Photoexcitation of the **FRO** ligand in DMSO leads to population of its singlet excited state with an absorption maximum at around 580 nm and a lifetime > 1 ns (Fig. 3a). This is in great accordance with its intense steady state fluorescence. Next, the photoinduced dynamics of the homoleptic assemblies of **FRO** were probed in the IR region in acetonitrile. Again, bands attributable to a long-lived S_1 state were observed. Even though a direct comparison between the two data sets cannot be drawn due to the different probed regions and solvents used, it can be concluded that coordination to Pd(II) only has a small effect on the excited state pathways of this acceptor ligand, similar to what has been observed for the anthraquinone acceptor ligand used in the preceding work.[1,8] Photoexcitation of the **TAA** ligand in DMSO is accompanied by ground state bleaching (400 nm), stimulated emission (440 nm) and excited state absorption (550 and 630 nm), probably from a locally excited state. These features disappear within a few ps while features at 470 and 610 nm arise. Presumably, this is attributable to an excited state species with charge transfer character ($S_{1,CT}$). Under the same conditions, the homoleptic donor cage [Pd$_2$**TAA**$_4$]$^{4+}$ shows immediately after photoexcitation a spectrum resembling the one of the $S_{1,CT}$ state of the **TAA** ligand (Fig. 3b). However, consistently with the quenched emission, these features decay within ~180 fs, giving rise to a spectrum that resembles the one of the **TAA** radical cation. Similar to what has been observed for the **PTZ** double cage (section 1.4.4.),[1,8] this is assigned to the formation of an LMCT state. Interestingly, the LMCT state in [Pd$_2$**TAA**$_4$]$^{4+}$ decays with the time constants τ_1 = 1.3 ps (75%) and τ_2 = 200 ps (25%) while such a long time constant was absent in [Pd$_4$**PTZ**$_8$]$^{8+}$. In heteroleptic [Pd$_2$**TAA**$_2$**FRO**$_2$]$^{4+}$, the decay of the **TAA** excited singlet state is again accompanied by the rise of features at 470 and > 750 nm. However, the features remain of high intensity once the short dynamic is over (Fig. 3c). This indicates the presence of an additional decay channel involving the **FRO** acceptor. Single wavelength fitting yielded the lifetimes τ_1 = 0.9 ps (56%), τ_2 = 200 ps (25%) and τ_3 = 500 ps (30%) for the **TAA** radical cation. The short dynamic was again assigned to the decay of an LMCT state while the two longer dynamics were assigned to back electron transfer between acceptor and donor ligands sitting in *cis* (τ_2) or in *trans* (τ_3) position to each other. The two LLCS states give rise to the same spectral features; for assignment, it was assumed that the electron transfer rate constant decreases with increasing distance between donor and acceptor moieties.[12]

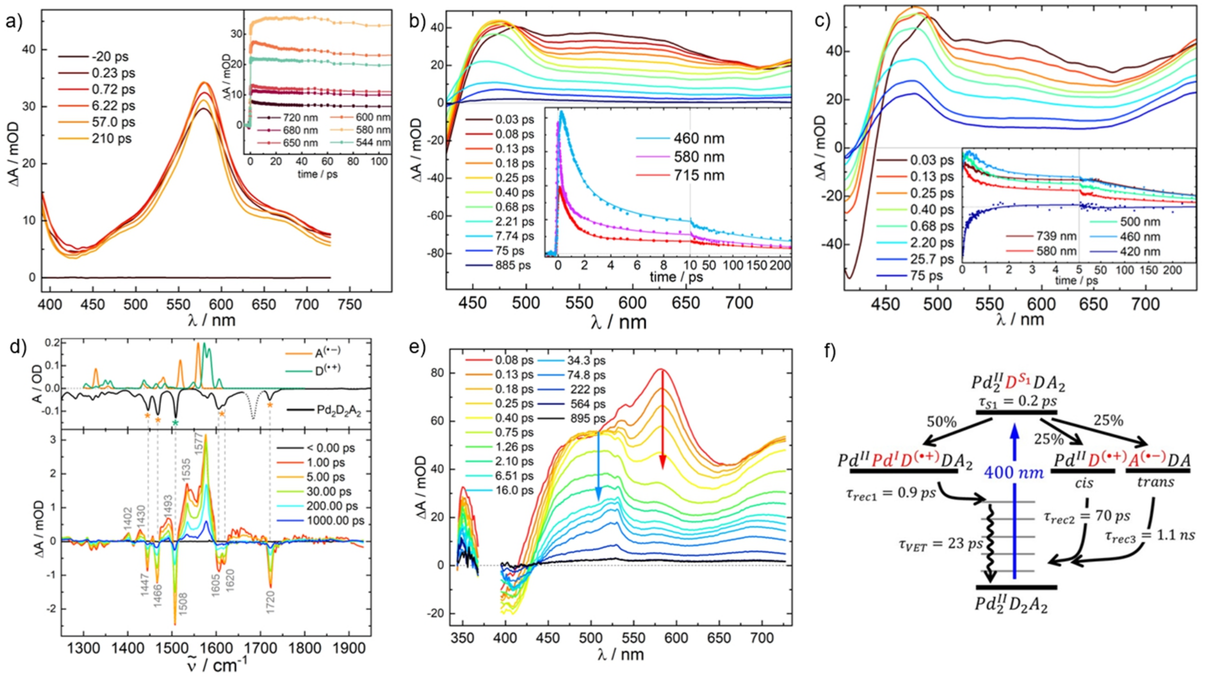

Fig. 3a-e) Transient difference spectra for selected time delays and decay traces for selected wavelengths (a) **FRO** (DMSO, λ_{ex} = 375 nm); b) [Pd$_2$**TAA**$_4$]$^{4+}$ (DMSO, λ_{ex} = 375 nm); c) [Pd$_2$**TAA**$_2$**FRO**$_2$]$^{4+}$ (DMSO, λ_{ex} = 375 nm); d) [Pd$_2$**TAA**$_2$**FRO**$_2$]$^{4+}$ (CH$_3$CN, λ_{ex} = 400 nm); e) [Pd$_2$**PTZ**$_2$**FRO**$_2$]$^{4+}$ (CH$_3$CN, λ_{ex} = 385 nm); f) schematic overview of excited state dynamics in [Pd$_2$**TAA**$_2$**FRO**$_2$]$^{4+}$.

Definite conclusions on ligand-to-ligand electron transfer solely based on the TA spectra in the visible are difficult to draw, owing to the broad absorption of the **FRO** acceptor radical anion between 500 and 650 nm. In contrast, the TA spectra in the IR probe region show bands that coincide well with the calculated IR absorption bands of the **FRO** radical anion. The features decay with lifetimes similar to τ_2 and τ_3 obtained for the same cage in the UV-Vis region (Fig. 3d). After the fast decay of the LMCT state, the ground state is recovered within around 23 ps, which is assigned to vibrational cooling.

The excited state dynamics of cage [Pd$_2$**PTZ**$_2$**FRO**$_2$]$^{4+}$ in acetonitrile upon excitation with a 385 nm pulse were investigated by probing in the visible region. Photoexcitation leads to population of the **PTZ** excited singlet state, absorbing at 585 nm. This state decays within around 200 fs, giving rise to features at 520 and 700 nm, assignable to the **PTZ** radical cation as well as at 580 nm, owing to the absorption of the **FRO** radical anion (Fig. 3e). The **PTZ** radical cation decays with the lifetimes τ_1 = 1.1 ps (55%), τ_2 = 110 ps (41%) and τ_3 > 2ns (4%).

The overall excited state processes in this type of donor-acceptor cage are summarized in figure 3f: the population of the excited singlet state of the donor ligand is followed by charge transfer to one of the metal nodes (here shown as charge separation to yield Pd(I) since the spectral features of the **TAA** radical cation are observed). Alternatively, electron transfer to one of the acceptor ligands, sitting either in *cis*- or in *-trans* position to the initially excited donor, occurs. While the LMCT state decays quickly (τ_1), the LLCS states decay slower (τ_2, τ_3).

3.3. Synthesis of ligands and cages

3.3.1. Synthesis of the ligands

The synthesis of the organic ligands is described in the appendix (section 3.11.2).

3.3.2. Synthesis of $[Pd_2\mathbf{CBZ}_2A_2]^{4+}$ cages

For the synthesis of $[Pd_2\mathbf{CBZ}_2\mathbf{NDI}_2]^{4+}$, $[Pd_2\mathbf{CBZ}_2\mathbf{PMDI}_2]^{4+}$, and $[Pd_2\mathbf{CBZ}_2\mathbf{FRO}_2]^{4+}$ an equal ratio of the two ligands **CBZ** and **NDI**, **PMDI**, or **FRO** was combined with a small excess of $[Pd(CH_3CN)_4](BF_4)_2$ and heated at 70 °C. The synthesis was either carried out with a ligand concentration of 1.4 mM in CD_3CN and heating for three days or with a ligand concentration of 2.8 mM in DMSO-d_6 and heating for 1.5 h followed by lyophilization and redissolution in CD_3CN.

The aromatic region of the ^1H NMR spectra of ligands **CBZ** and **NDI**, homoleptic assemblies $[Pd_2\mathbf{CBZ}_4]^{4+}$ and $[Pd_3\mathbf{NDI}_6]^{6+}$, $[Pd_4\mathbf{NDI}_8]^{8+}$ and donor-acceptor cage $[Pd_2\mathbf{CBZ}_2\mathbf{NDI}_2]^{4+}$ are shown in figure 4. Coordination of ligand **CBZ** to Pd(II) leads to the formation of a lantern-shaped cage (synthesis in DMSO, followed by lyophilization and redissolution in CD_3CN (appendix, section 3.11.3)), wherefore the signals of the protons close to the pyridine nitrogen experience a downfield shift and a single set of signals is observed. The spectrum of the homoleptic assemblies of the **NDI** ligand is more complex: a mixture of a three-membered ring (set a''-e'') and a tetrahedron is obtained.[13] The latter gives rise to two sets of signals (a-e, a'-e') due to singly and doubly-bridged edges. In the heteroleptic cage, one set of signals is observed for all protons of the **CBZ** ligand as well as for the pyridine protons of the **NDI** ligand – characteristic for the anticipated *cis*-$Pd_2A_2B_2$ structure.[14] By contrast, proton e which is located on the **NDI** backbone gives rise to two signals of equal intensity. The ESI mass spectrum shows dominant peaks for $[Pd_2\mathbf{CBZ}_2\mathbf{NDI}_2]^{4+}$ with one and two counter anions. Furthermore, ^1H DOSY NMR gives a similar log(D) value for all signals in the aromatic region, supporting that they are assignable to a single species. A hydrodynamic radius of $R_H = 11.3$ Å was obtained, which is in great accordance with the values reported for dinuclear Pd(II) cages.[13] Slow vapor diffusion of THF into a solution of $[Pd_2\mathbf{CBZ}_2\mathbf{NDI}_2]^{4+}$ in CD_3CN yielded single, transparent needle-shaped crystals suitable for synchrotron single crystal X-ray diffraction. The crystal structure confirms the formation of *cis*-$[Pd_2\mathbf{CBZ}_2\mathbf{NDI}_2]^{4+}$. The π-surfaces of the two **NDI** backbones enclose the cavity. One ligand half points towards the **CBZ** ligand and the other half points towards the neighboring **NDI** ligand. This conformation can explain the observed signal splitting. However, the conformation of the **NDI**s in the X-ray structure could also be a result of packing effects. While the conformation in solution remains unknown, the NMR splitting reveals that the free rotation of the **NDI** backbones is hindered. This might be due to CH⋯ π- or π-π interactions between the **NDI** moieties and/or due to steric constraints.

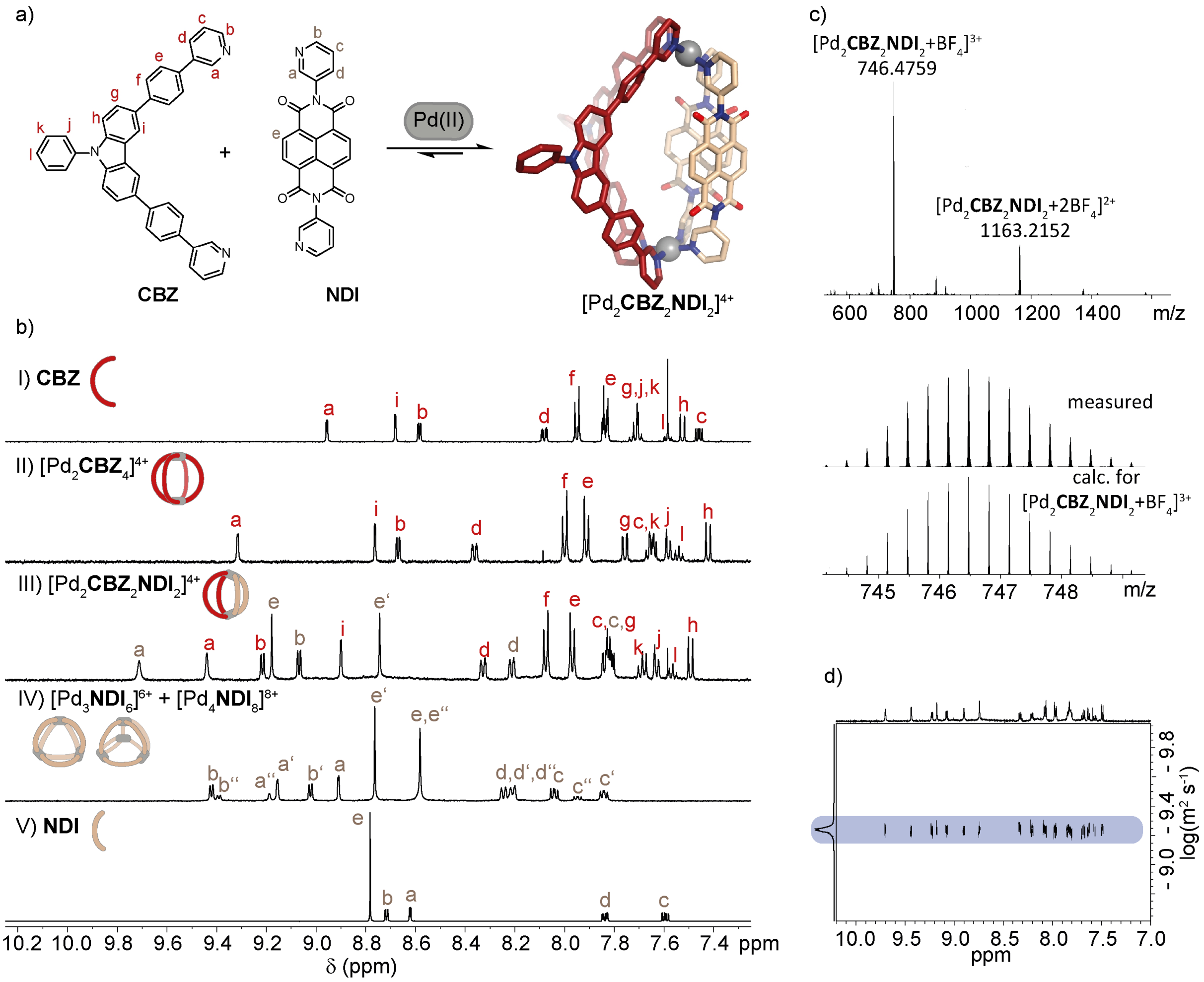

Fig. 4 Synthesis of $[Pd_2\mathbf{CBZ}_2\mathbf{NDI}_2]^{4+}$: a) synthesis scheme and X-ray structure; b) stack of aromatic regions of ^{1}H NMR spectra of ligands (I,V), homoleptic assemblies (II,IV) and $[Pd_2\mathbf{CBZ}_2\mathbf{NDI}_2]^{4+}$ (III); c) ESI mass spectrum, d) ^{1}H DOSY NMR.

A comparison of the ^{1}H NMR spectra of $[Pd_2\mathbf{CBZ}_2\mathbf{PMDI}_2]^{4+}$, ligand **CBZ**, $[Pd_2\mathbf{CBZ}_4]^{4+}$ and the homoleptic assembly of **PMDI** – three membered ring $[Pd_3\mathbf{PMDI}_6]^{6+}$ – is shown in figure 5. Owing to its low solubility in CD_3CN, a meaningful NMR spectrum of ligand **PMDI** could not be obtained. Again, the ^{1}H NMR spectrum of $[Pd_2\mathbf{CBZ}_2\mathbf{PMDI}_2]^{4+}$ shows one set of signals for the protons of **CBZ** and for the pyridine protons of **PMDI** as expected for a *cis*-$Pd_2A_2B_2$-type cage. The ESI mass spectrum shows prominent peaks for $[Pd_2\mathbf{CBZ}_2\mathbf{PMDI}_2\text{+n}BF_4]^{(4-n)+}$ (n = 0-2). In addition, ^{1}H DOSY NMR yielded a hydrodynamic radius of R_H = 11.0 Å, again in accordance with the formation of $[Pd_2\mathbf{CBZ}_2\mathbf{PMDI}_2]^{4+}$. In the ^{1}H NMR spectrum, the signal of proton e of the **PMDI** backbone is broadened to the point of disappearance in the baseline. This can be traced back to coalescence at room temperature. Hence, rotation of the **PMDI** backbone is faster as compared to the **NDI** backbone in the respective heteroleptic cages with **CBZ** counter ligand. There are two possible explanations for this discrepancy: first, the **PMDI** backbone has a smaller diameter as compared to **NDI**; therefore, rotation of the backbone might be sterically less restricted. Second, possible CH··· π- or π-π interactions should be weaker between two **PMDI** ligands as compared to between two **NDI** ligands owing to the smaller π-surface and number of CH protons of the former. In the geometry-optimized structure (B3LYP/def2-SVP), neighboring **PMDI** ligands are rotated by approximately 90° allowing for C-H··π interactions.

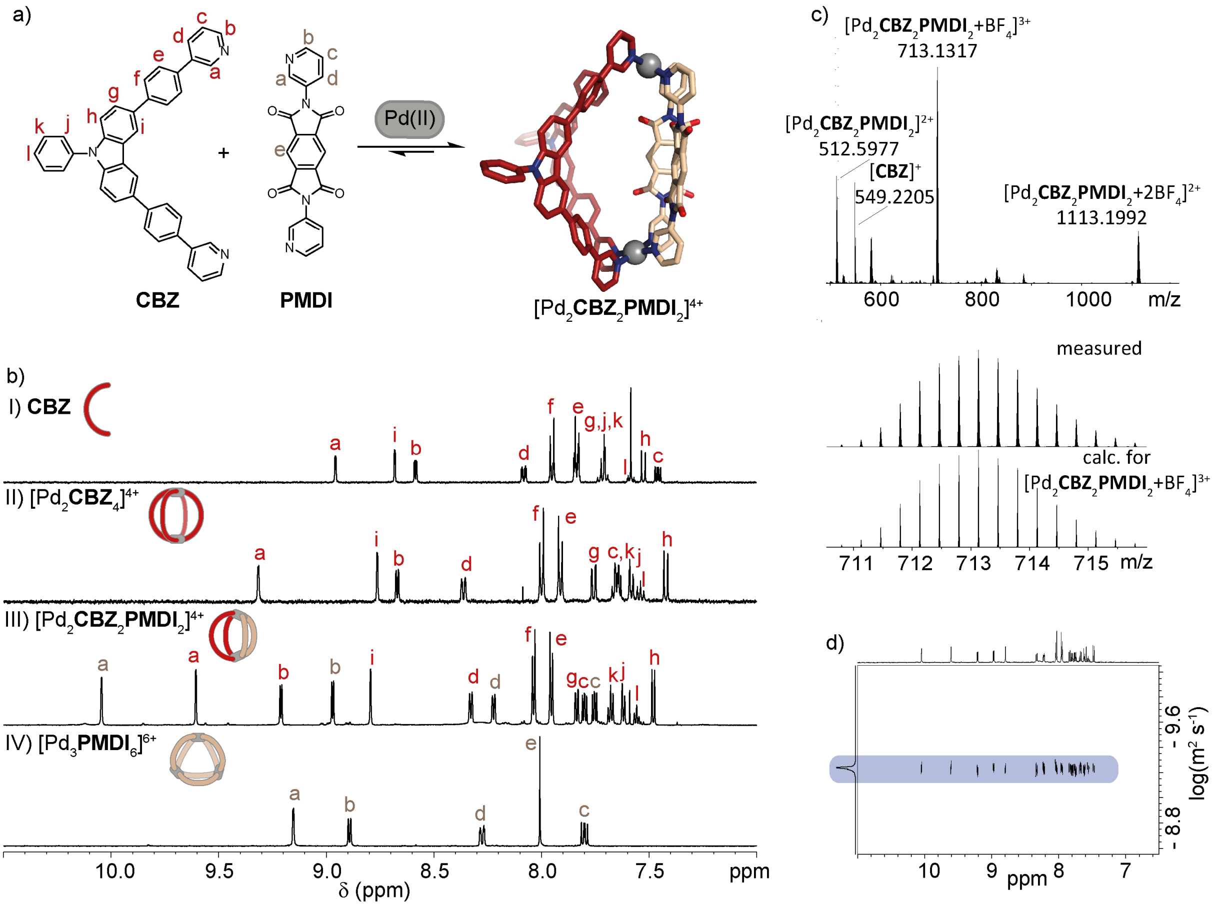

Fig. 5 Synthesis of $[Pd_2\textbf{CBZ}_2\textbf{PMDI}_2]^{4+}$: a) synthesis scheme and geometry-optimized structure (B3LYP/def2-SVP); b) stack of aromatic regions of ^{1}H NMR spectra of ligand **CBZ** (I), homoleptic assemblies (II,IV) and $[Pd_2\textbf{CBZ}_2\textbf{PMDI}_2]^{4+}$ (III); c) ESI mass spectrum; d) ^{1}H DOSY NMR.

The ^{1}H NMR spectrum of the analogous cage with acceptor ligand **FRO** and of the corresponding homoleptic assemblies is shown in figure 6. Similar to **NDI**, ligand **FRO** forms a mixture of homoleptic three-membered rings $[Pd_3\textbf{FRO}_6]^{6+}$ (set a''-g'') and tetrahedra $[Pd_4\textbf{FRO}_8]^{8+}$ (sets a-e, a'-e') when combined with Pd(II) in acetonitrile.[15] For the heteroleptic cage, one set of signals is observed and proton g of the **FRO** backbone is broadened, indicating that its rotation is somewhat restricted. Investigation with ESI-MS unequivocally showed that the formula of the assembly is $[Pd_2\textbf{CBZ}_2\textbf{FRO}_2]^{4+}$ and DOSY yielded a hydrodynamic radius of R_H = 11.4 Å. In the DFT-optimized model, the two **FRO** moieties are rotated by 90° allowing for CO··π interactions, similarly to what was observed for the **PMDI** analogue.

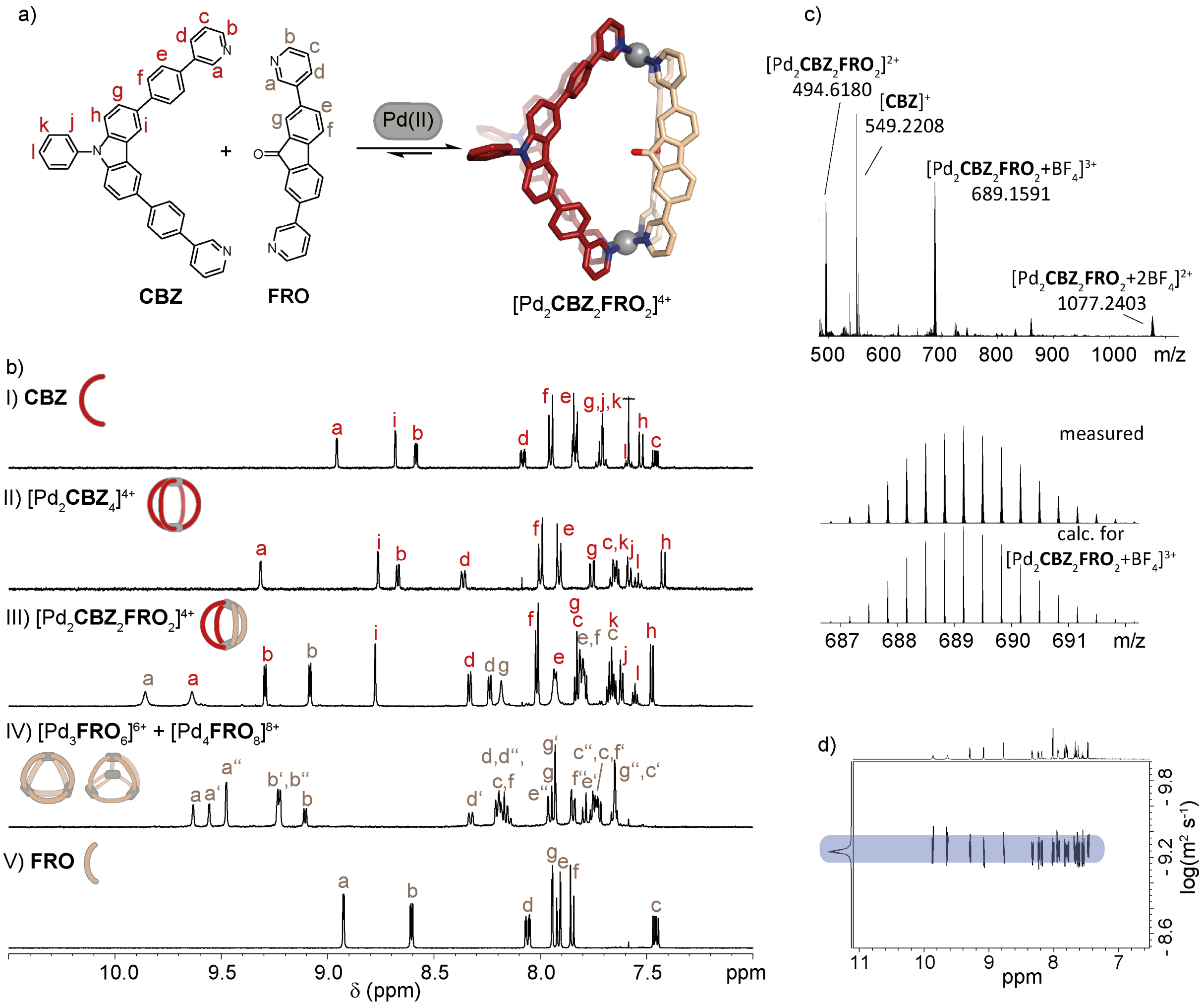

Fig. 6 Synthesis of [Pd$_2$**CBZ**$_2$**FRO**$_2$]$^{4+}$: a) synthesis scheme and geometry-optimized structure (B3LYP/def2-SVP); b) stack of aromatic regions of ^{1}H NMR spectra of ligands (I,V), homoleptic assemblies (II,IV) and [Pd$_2$**CBZ**$_2$**FRO**$_2$]$^{4+}$ (III); c) ESI mass spectrum; d) ^{1}H DOSY NMR.

3.3.3. Synthesis of [Pd$_2$**TAA**$_2$A$_2$]$^{4+}$ cages

Donor-acceptor cages with **TAA** ligands were yielded by combining an equal ratio of the two ligands **TAA** and **NDI**, **PMDI**, or **FRO** with a small excess of [Pd(CH$_3$CN)$_4$](BF$_4$)$_2$ followed by heating at 70 °C. Similar to cages with **CBZ** donor ligands, the synthesis was either carried out with 1.4 mM ligand solutions in CD$_3$CN for three days or with 2.8 mM ligand solutions in DMSO-*d*$_6$ for 1.5 h. Here, the structures of the new cages [Pd$_2$**TAA**$_2$**NDI**$_2$]$^{4+}$ and [Pd$_2$**TAA**$_2$**PMDI**$_2$]$^{4+}$ will be described.

The partial ^{1}H NMR spectra of ligands **TAA** and **NDI**, homoleptic assemblies [Pd$_2$**TAA**$_4$]$^{4+}$ and [Pd$_3$**NDI**$_6$]$^{6+}$, [Pd$_4$**NDI**$_8$]$^{8+}$, and donor-acceptor cage [Pd$_2$**TAA**$_2$**NDI**$_2$]$^{4+}$ are shown in figure 7. Similarly to [Pd$_2$**CBZ**$_2$**NDI**$_2$]$^{4+}$, one set of signals is observed for all protons except for protons e of the **NDI** backbone whose signal splits in two. The ESI mass spectrum shows prominent peaks for [Pd$_2$**TAA**$_2$**NDI**$_2$+BF$_4$]$^{3+}$ and [Pd$_2$**TAA**$_2$**NDI**$_2$+2BF$_4$]$^{2+}$. In addition, a hydrodynamic radius of R_H = 11.7 Å was obtained with ^{1}H DOSY, which is in great accordance with the radii of the cages with **CBZ** donor. Yellow, plate-shaped crystals suitable for X-ray diffraction were obtained by slow vapor diffusion of methyl *tert*-butyl ether into a solution of the heteroleptic cage in CD$_3$CN. The obtained structure is in accordance with the expected *cis*-[Pd$_2$**TAA**$_2$**NDI**$_2$]$^{4+}$ framework. In the solid-state structure, the two **NDI** ligands are cofacially arranged. The distance between the two π-surfaces of the **NDI** ligands in the crystal structure is 6.5 Å (measured between the central carbons similar to the measurements described in section 3.11.8).

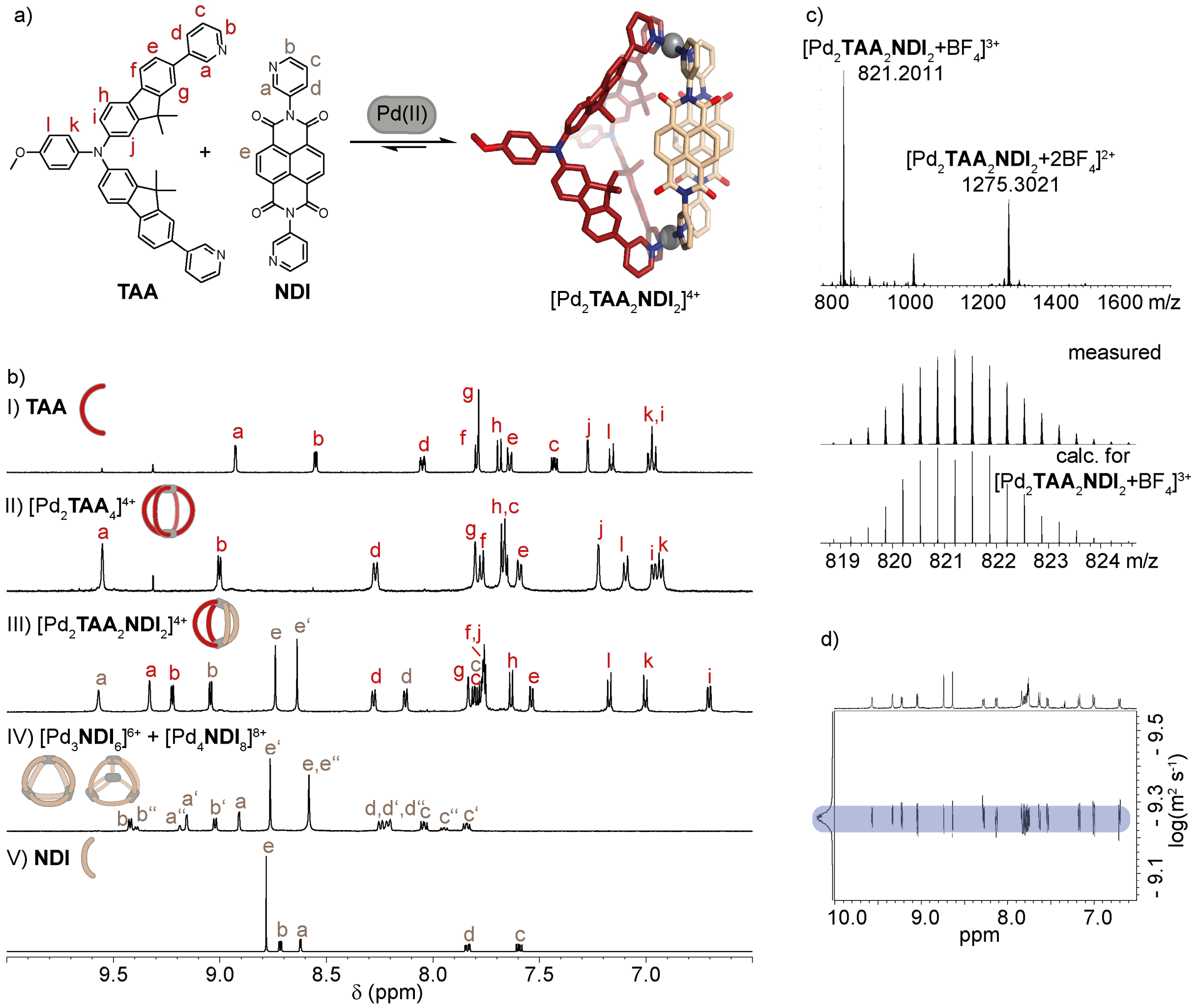

Fig. 7 Synthesis of [Pd$_2$**TAA**$_2$**NDI**$_2$]$^{4+}$: a) synthesis scheme and X-ray structure; b) stack of aromatic regions of ^{1}H NMR spectra of ligands (I,V), homoleptic assemblies (II,IV) and [Pd$_2$**TAA**$_2$**NDI**$_2$]$^{4+}$ (III); c) ESI mass spectrum; d) ^{1}H DOSY NMR.

Figure 8 shows the partial ^{1}H NMR spectra of the **TAA** ligand, the two homoleptic assemblies [Pd$_2$**TAA**$_4$]$^{4+}$ and [Pd$_3$**PMDI**$_6$]$^{6+}$, and heteroleptic cage [Pd$_2$**TAA**$_2$**PMDI**$_2$]$^{4+}$. The NMR spectrum of the heteroleptic cage shows one set of signals, the ESI mass spectrum shows prominent peaks for [Pd$_2$**TAA**$_2$**PMDI**$_2$+nBF$_4$]$^{(4-n)+}$ (n = 1,2), and ^{1}H DOSY NMR yielded a hydrodynamic radius of R_H = 11.0 Å, all in agreement with the formation of *cis*-[Pd$_2$**TAA**$_2$**PMDI**$_2$]$^{4+}$. A sharp signal is observed for proton e of the **PMDI** backbone meaning that the backbone rotates fast relative to the NMR timescale. This contrasts with the analogous cage with a **CBZ** donor in which the signals of proton e coalesced at room temperature in CD$_3$CN. The faster rotational dynamics of the **PMDI** ligand in the cage with the **TAA** counter ligand can be explained by the higher flexibility of the latter, which also affects the photophysical properties as will be shown later. In DMSO, no signal of proton e can be observed at room temperature due to broadening (appendix, section 3.11.3). Most probably, the rotation of the **PMDI** backbone is slower in the higher viscous DMSO and coalescence occurs at room temperature. Again, the geometry-optimized model suggests that two neighboring **PMDI** backbones are arranged in a perpendicular fashion allowing for C-H··π interactions.

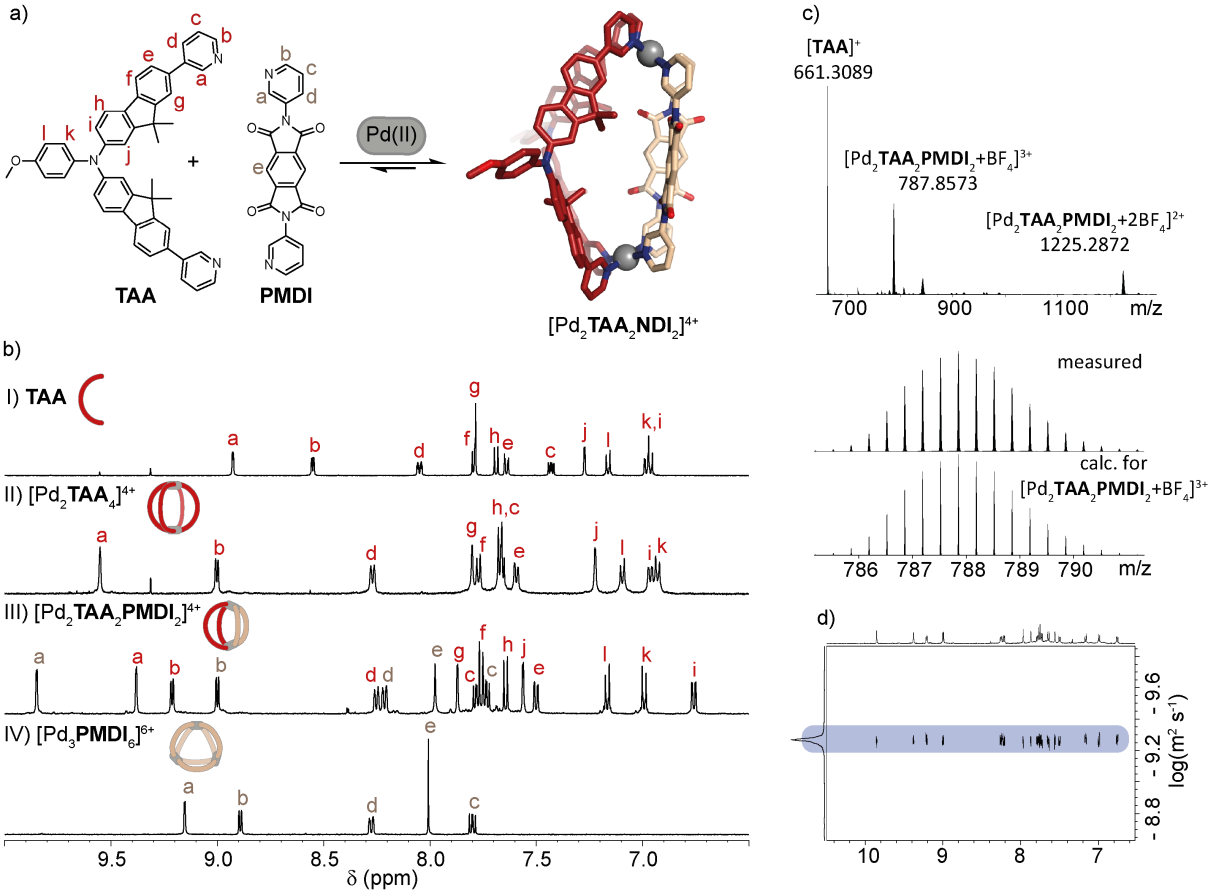

Fig. 8 Synthesis of [Pd$_2$**TAA**$_2$**PMDI**$_2$]$^{4+}$: a) synthesis scheme and geometry-optimized structure (B3LYP/def2-SVP); b) stack of aromatic regions of ^{1}H NMR spectra of ligand **TAA** (I), homoleptic assemblies (II,IV) and [Pd$_2$**TAA**$_2$**PMDI**$_2$]$^{4+}$ (III); c) ESI mass spectrum; d) ^{1}H DOSY NMR.

3.3.4. Synthesis of [Pd$_2$**PTZ**$_2$A$_2$]$^{4+}$ cages

The synthesis of [Pd$_2$**PTZ**$_2$**NDI**$_2$]$^{4+}$, [Pd$_2$**PTZ**$_2$**PMDI**$_2$]$^{4+}$, and [Pd$_2$**PTZ**$_2$**FRO**$_2$]$^{4+}$ were performed by combining **PTZ** and **NDI**, **PMDI**, or **FRO**, both at a concentration of 2.8 mM in DMSO-d_6, with a slight excess of Pd(II), followed by heating at 70 °C for 1.5 h. The solvent was removed by lyophilization and the solid stored at −20 °C under argon atmosphere due to the sensitivity of the **PTZ** ligand towards oxidation. For the investigations, the cages were dissolved in CD$_3$CN and used within one day. Here, the structures of the new cages [Pd$_2$**PTZ**$_2$**NDI**$_2$]$^{4+}$ and [Pd$_2$**PTZ**$_2$**PMDI**$_2$]$^{4+}$ will be described.

A comparison of the partial ^{1}H NMR spectra of ligands **PTZ** and **NDI**, homoleptic assemblies [Pd$_2$**PTZ**$_4$]$^{4+}$ and [Pd$_3$**NDI**$_6$]$^{6+}$, [Pd$_4$**NDI**$_8$]$^{8+}$, and donor-acceptor cage [Pd$_2$**PTZ**$_2$**NDI**$_2$]$^{4+}$ in CD$_3$CN is shown in figure 9. The **PTZ**-based ligand assembles in CD$_3$CN into interlocked double cage [Pd$_4$**PTZ**$_8$]$^{8+}$.[16] However, when DMSO-d_6 is used as the solvent, monomeric cage [Pd$_2$**PTZ**$_4$]$^{4+}$ is formed. This cage is kinetically stable at room temperature for hours after removal of the solvent and redissolving in CD$_3$CN. Here, the ^{1}H NMR spectrum of the monomeric cage is shown since the heteroleptic cages were synthesized in DMSO-d_6 as well and since the chemical environment of the **PTZ**-based ligand in the homoleptic dinuclear cage more closely resembles the one in the heteroleptic cage. The ^{1}H NMR spectrum of the heteroleptic cage shows one set of signals for the pyridine protons of the ligand **NDI** as well as the protons of ligand **PTZ**, again in accordance with the formation of a *cis*-configurated heteroleptic cage. Similar to what has been observed for [Pd$_2$**CBZ**$_2$**NDI**$_2$]$^{4+}$ and [Pd$_2$**TAA**$_2$**NDI**$_2$]$^{4+}$, the backbone protons e of the **NDI** ligand split in two signals of equal intensity owing to slow rotation of the **NDI** backbones relative to the NMR time scale. In contrast to the cages with **CBZ** or **TAA** donor, the ^{1}H-^{1}H COSY and ^{1}H-^{1}H NOESY spectra of [Pd$_2$**PTZ**$_2$**NDI**$_2$]$^{4+}$ and [Pd$_2$**PTZ**$_2$**PMDI**$_2$]$^{4+}$ do not display coupling between the protons of the pyridines and the protons of the **PTZ** backbone. For assignment, the ^{1}H-^{13}C HMBC spectrum was used which shows cross peaks between the alkyne carbon atoms and protons d of the pyridine and e,g of the backbone of **PTZ** (appendix, section 3.11.3). The cage was modelled by means of DFT computations. The model predicts that the two **NDI** backbones are oriented in a perpendicular fashion, presumably enabling C-H··π interactions.

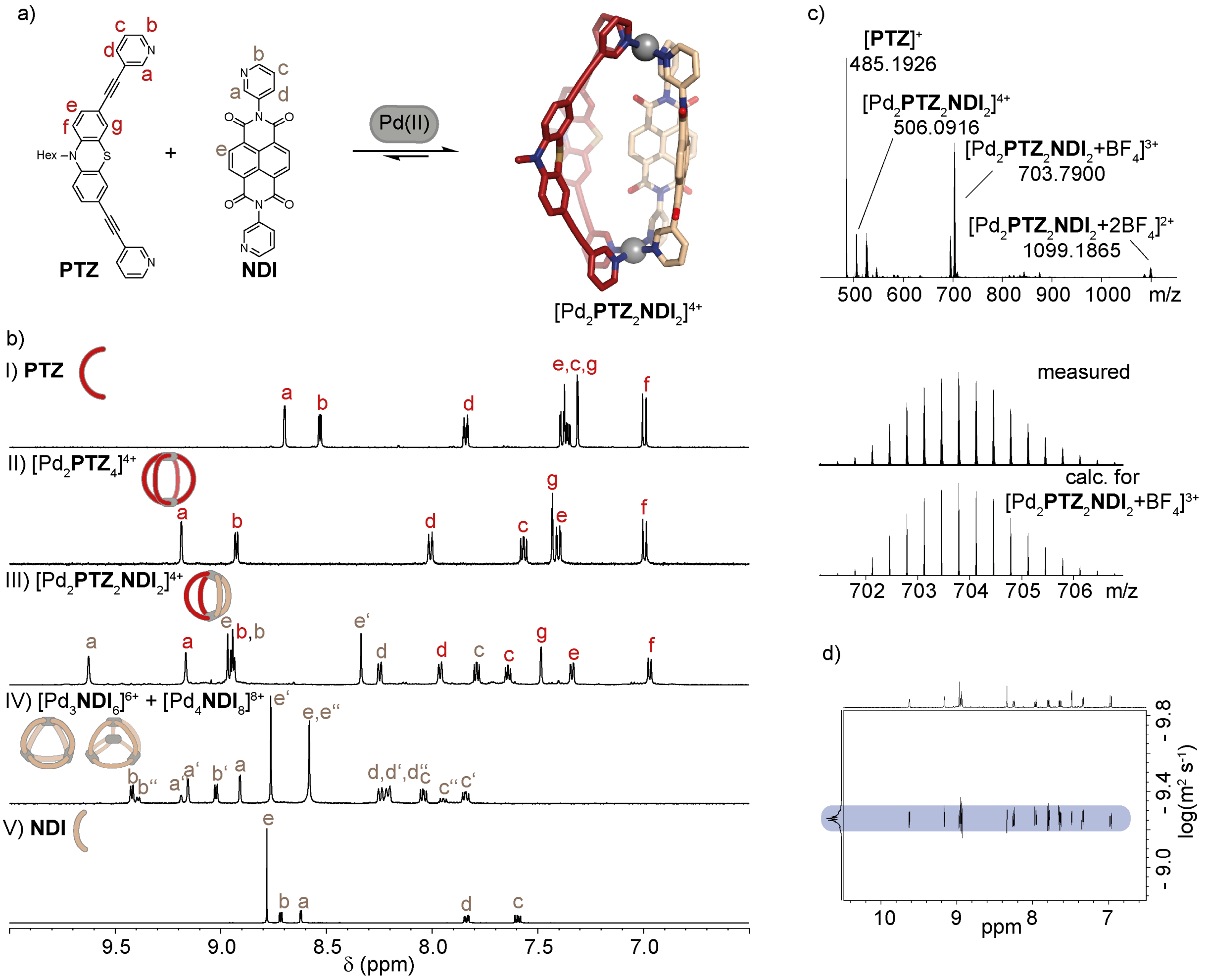

Fig. 9 Synthesis of [Pd$_2$**PTZ**$_2$**NDI**$_2$]$^{4+}$: a) synthesis scheme and geometry-optimized structure (B3LYP/def2-SVP); b) stack of aromatic regions of ^{1}H NMR spectra of ligands (I,V), homoleptic assemblies (II,IV) and [Pd$_2$**PTZ**$_2$**NDI**$_2$]$^{4+}$ (III); c) ESI mass spectrum; d) ^{1}H DOSY NMR.

The ^{1}H NMR spectrum of [Pd$_2$**PTZ**$_2$**PMDI**$_2$]$^{4+}$ shows one set of signals that differs from the ones of the homoleptic assemblies (Fig. 10). Similar to [Pd$_2$**CBZ**$_2$**PMDI**$_2$]$^{4+}$, no signal is observed for proton e of the backbone of **PMDI** at room temperature in CD$_3$CN due to coalescence. Again, slower rotation of the **PMDI** backbone in [Pd$_2$**PTZ**$_2$**PMDI**$_2$]$^{4+}$ as compared to in [Pd$_2$**TAA**$_2$**PMDI**$_2$]$^{4+}$ can be explained by the higher rigidity of the **PTZ** counter ligand as compared to the **TAA** ligand. ^{1}H DOSY NMR of the cage in CD$_3$CN gave a hydrodynamic radius of R_H = 9.78 Å and the ESI mass spectrum shows prominent peaks for [Pd$_2$**PTZ**$_2$**PMDI**$_2$+nBF$_4$]$^{(4-n)+}$ (n = 1,2). In the DFT-optimized structure, the two acceptor backbones are rotated by 90° relative to each other, similar to the DFT structures of the other donor-acceptor cages.

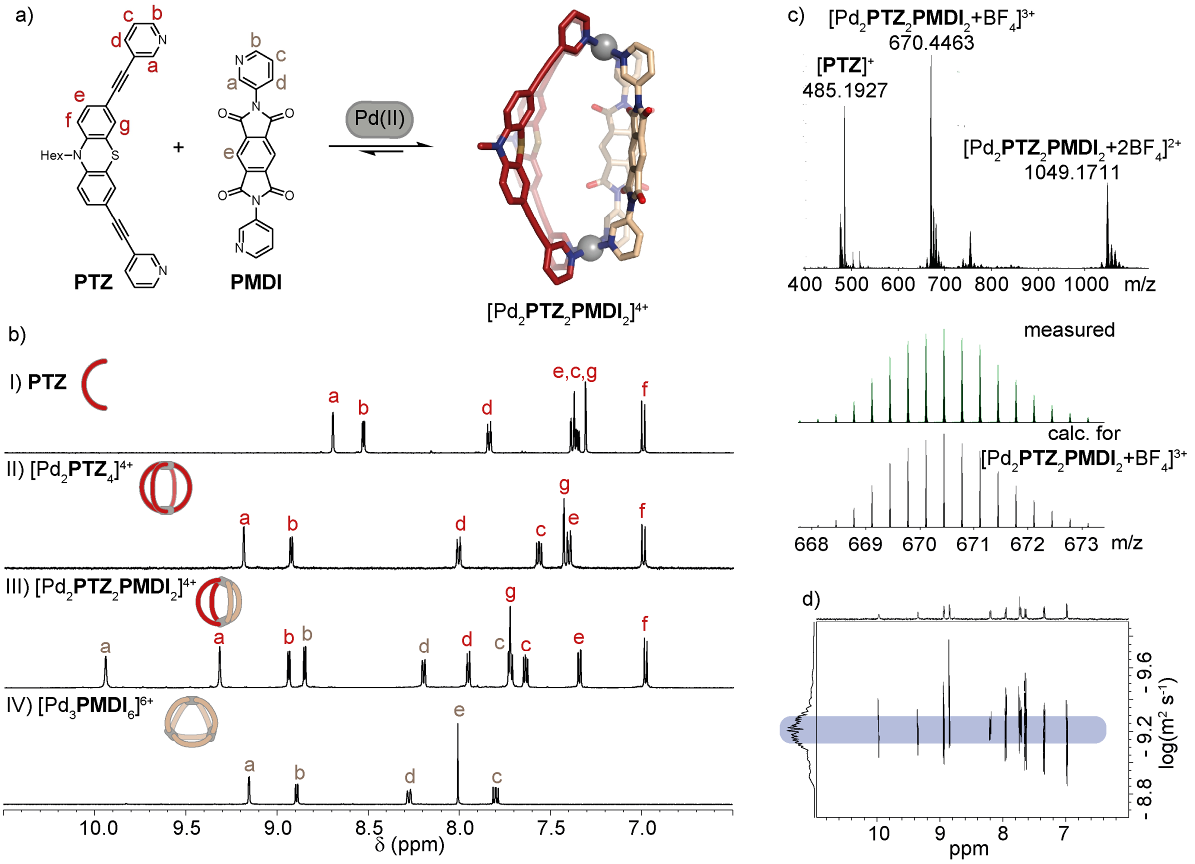

Fig. 10 Synthesis of $[Pd_2\mathbf{PTZ}_2\mathbf{PMDI}_2]^{4+}$: a) synthesis scheme and geometry-optimized structure (B3LYP/Def2SVP); b) stack of aromatic regions of ^1H NMR spectra of ligand **PTZ** (I), homoleptic assemblies (II,IV) and $[Pd_2\mathbf{PTZ}_2\mathbf{PMDI}_2]^{4+}$ (III); c) ESI mass spectrum; d) ^1H DOSY NMR.

Overall, all members of the library of donor-acceptor cages were successfully synthesized and were shown to feature a *cis*-$Pd_2A_2B_2$ structure. NMR spectroscopic analyses unveiled that the rotation of the acceptor backbones is somewhat hindered, and that this dynamic varies across the cages. The timescale of the rotation does not only depend on the acceptor ligand (faster for smaller **PMDI** than for **NDI**) but also on the respective counter ligand. While different conditions were required for the synthesis (**PTZ** cages only assembled cleanly in DMSO-d_6), all nine cages possess sufficient stability under the same conditions (acetonitrile as solvent, tetrafluoroborate as counter anion), allowing for a direct comparison of their electrochemical and photophysical properties.

3.4. Steady state absorption spectroscopy

3.4.1. Ligands and homoleptic assemblies

In the first step, the steady state absorption spectra of the free ligands were qualitatively compared with the ones of the corresponding homoleptic assemblies (Fig. 11,12). The **CBZ** ligand shows an absorption feature at 264 nm, an absorption maximum at 307 nm with a shoulder at 330 nm, and the absorption tails off at 370 nm. The homoleptic cage $[Pd_2\mathbf{CBZ}_4]^{4+}$ shows increased absorbance at $\lambda < 300$ nm as compared to the free ligand. Furthermore, the absorption is bathochromically shifted and extends up to 400 nm. The **TAA** donor ligand possesses an absorption band at 282 nm as well as a band at 388 nm with a shoulder at 350 nm. In the homoleptic cage $[Pd_2\mathbf{TAA}_4]^{4+}$, the former band is bathochromically shifted to 289 nm. The band at 388 nm does not show a shoulder and extends more into the visible region as compared to the free ligand. The **PTZ** donor ligand shows absorption maxima at 288 nm and 380 nm. In the kinetically stable monomeric cage [Pd$_2$**PTZ**$_4$]$^{4+}$, both maxima are slightly red shifted to 292 nm and 398 nm, respectively. Interestingly, a further redshift of the absorption bands to 295 nm and 408 nm is observed in the double cage [Pd$_4$**PTZ**$_8$]$^{8+}$. This might be a result of the close proximity of the ligands or a different accessible conformational landscape in the intercalated structure. A possible origin for the systematic bathochromically shifted absorption of the cage as compared to their constituent ligands is an increasing intra-ligand charge transfer character upon coordination to Pd(II). It is feasible that charge transfer occurs from the electron-rich backbones to the pyridines. As a result of the coordination, the electron density at the pyridines is reduced in the cages which would explain the modulation of the transition.

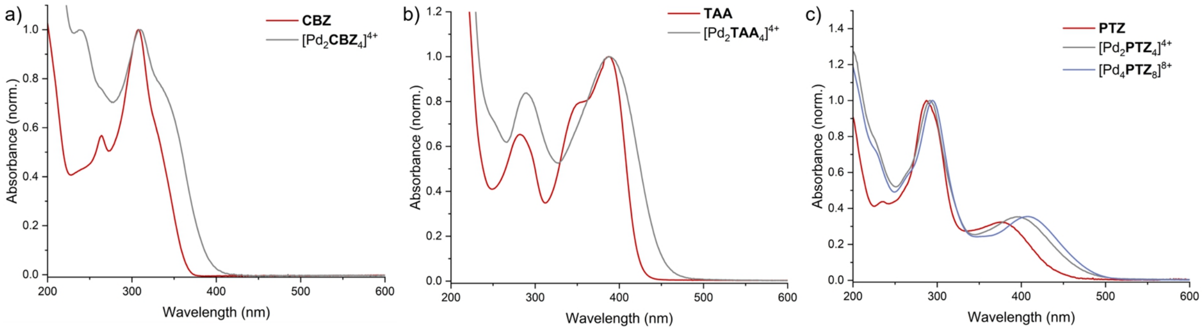

Fig. 11 Normalized absorption spectra of ligands: a) **CBZ**; b) **TAA**; c) **PTZ** (the spectrum of [Pd$_4$**PTZ**$_8$]$^{4+}$ was measured and published by Dr. Marina Frank[1]) (CH$_3$CN, 1 mm cuvette pathlength).

For the **NDI** acceptor ligand and the mixture of homoleptic ring [Pd$_3$**NDI**$_6$]$^{6+}$ and tetrahedron [Pd$_4$**NDI**$_8$]$^{8+}$, the vibronic bands of the S$_0$-S$_1$ transition are observed between 300 and 400 nm (Fig. 12a). The first vibronic band (v_0-v_0) at 376 nm has the highest oscillator strength in the free ligand. No shift of the absorption band is observed for the mixture of homoleptic assemblies; however, the vibronic progression changes. More precisely, the ratio of the intensities of the first and second vibronic bands ($I_{0\text{-}0}/I_{0\text{-}1}$) and of the first and third vibronic bands ($I_{0\text{-}0}/I_{0\text{-}2}$) changes from 1.2 to 0.95 and from 2.1 to 1.4, respectively. A possible origin of the vibronic redistribution is H-type excitonic coupling between the **NDI** moieties[17] or changes in the conformational landscape. The absorption spectra of the **PMDI** ligand and ring [Pd$_3$**PMDI**$_6$]$^{6+}$ were compared at equal concentrations due to the lack of a defined absorption band in the near UV and visible region. The absorption of both, ligand and ring tail into the near UV region and flattens off at around 350 nm for the ligand and at around 400 nm for the ring. Fluorenone-based ligand **FRO** shows an absorption maximum at 285 nm with two defined shoulders at 321 and 335 nm as well as a broad absorption band at 430 nm. In kinetically stable [Pd$_3$**FRO**$_6$]$^{6+}$, the high energy absorption band and the band in the visible region are hypsochromically shifted by 10 nm and 20 nm, respectively. Furthermore, the shoulders of the former feature appear less defined.

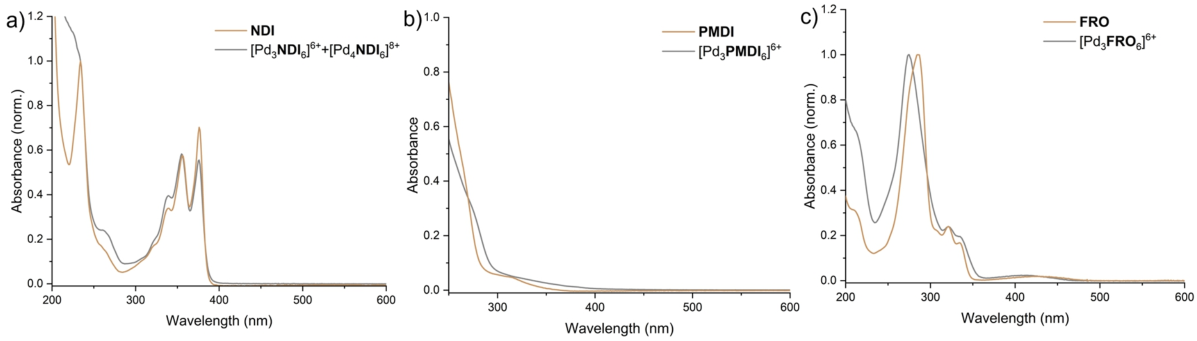

Fig. 12 Normalized absorption spectra of acceptor ligands and their homoleptic assemblies for a) **NDI**; b) **PMDI** (100 µM ligand concentration,); c) **FRO** (a), c) CH$_3$CN, b) DMSO, 1 mm cuvette pathlength).

3.4.2. Heteroleptic cages

In order to test for possible ground state interactions between donor and acceptor in the heteroleptic cages and to choose a suitable excitation wavelength for transient absorption spectroscopy, the photophysical properties of the donor-acceptor cages were investigated. The spectrum of each donor-acceptor cage is shown in comparison to the spectra of the corresponding homoleptic assemblies and the superposition thereof. If donor and acceptor ligands are fully independent in the heteroleptic cage, the calculated sum of the spectra of the homoleptic assemblies should coincide with the spectrum of the heteroleptic cage.

The absorption spectrum of $[Pd_2\mathbf{CBZ}_2\mathbf{NDI}_2]^{4+}$ shows a maximum at 312 nm, mostly stemming from the absorption of the **CBZ** ligand as well as at 337, 354, and 375 nm corresponding to the vibronic progression of the S_0-S_1 transition of the **NDI** ligand. The spectrum of $[Pd_2\mathbf{CBZ}_2\mathbf{NDI}_2]^{4+}$ can be reconstructed nearly perfectly based on the spectra of the homoleptic assemblies (Fig. 13a). The absorption spectrum of $[Pd_2\mathbf{CBZ}_2\mathbf{PMDI}_2]^{4+}$ shows features at 245 nm, mostly stemming from the **PMDI** acceptor and at 311 nm with a shoulder at 350 nm, attributable to the absorption of the **CBZ** donor. The latter features are slightly red shifted as compared to the features of the homoleptic cage $[Pd_2\mathbf{CBZ}_4]^{4+}$ (Fig. 13b). $[Pd_2\mathbf{CBZ}_2\mathbf{FRO}_2]^{4+}$ possesses a feature at 246 nm, mostly originating from the absorbance of the **CBZ** ligand, as well as a comparably sharp feature at 281 nm stemming from the **FRO** ligand. The broad absorption stemming from both ligands tails off at 400 nm. The characteristic absorption maximum of **FRO** in the heteroleptic cage is shifted by around 5 nm when compared to the spectrum of the homoleptic assembly. Aside from the small bathochromic shifts, the spectra of the heteroleptic cages with **CBZ** donor are in great accordance with the superposition of the spectra of the homoleptic assemblies. This indicates the absence of strong electronic communication between donor and acceptor in the ground state.

For triggering photoinduced electron transfer, it is advisable to excite into a low-energy absorption maximum of the donor ligand which does not show significant overlap with the absorption of the acceptor ligand. This reduces the number of concomitantly occurring excited state processes. For the series of cages $[Pd_2\mathbf{CBZ}_2A_2]^{4+}$, 350 nm is chosen as excitation wavelength. While for $[Pd_2\mathbf{CBZ}_2\mathbf{PMDI}_2]^{4+}$ and $[Pd_2\mathbf{CBZ}_2\mathbf{FRO}_2]^{4+}$ the **CBZ** donor is excited nearly completely selectively, photoexcitation of $[Pd_2\mathbf{CBZ}_2\mathbf{NDI}_2]^{4+}$ with $\lambda = 350$ nm leads to excitation of **CBZ** and **NDI** with nearly equal probabilities. The extinction coefficients at this wavelength range between $\varepsilon \approx 8\ mM^{-1} \cdot mm^{-1}$ and $\varepsilon \approx 12.6\ mM^{-1} \cdot mm^{-1}$ (Tab. 1).

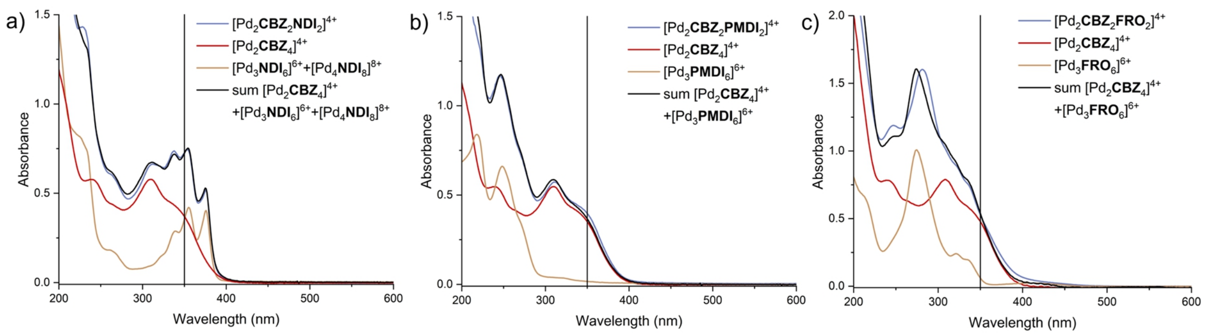

Fig. 13 Absorption spectra of donor-acceptor cages in comparison to the spectra of the corresponding homoleptic assemblies and the calculated sum of their spectra for a) $[Pd_2\mathbf{CBZ}_2\mathbf{NDI}_2]^{4+}$; b) $[Pd_2\mathbf{CBZ}_2\mathbf{PMDI}_2]^{4+}$; c) $[Pd_2\mathbf{CBZ}_2\mathbf{FRO}_2]^{4+}$ (*c*(ligand) = 200 µM, CH_3CN, 1 mm cuvette pathlength). The vertical line shows the excitation wavelength chosen for transient absorption spectroscopy.

Tab. 1 Extinction coefficients of $[Pd_2\mathbf{CBZ}_2A_2]^{4+}$ cages at 350 nm.

	$[Pd_2\mathbf{CBZ}_2\mathbf{NDI}_2]^{4+}$	$[Pd_2\mathbf{CBZ}_2\mathbf{PMDI}_2]^{4+}$	$[Pd_2\mathbf{CBZ}_2\mathbf{FRO}_2]^{4+}$
ε(350 nm)/ $mM^{-1}\cdot mm^{-1}$	12.58	7.92	10.57

The absorption spectrum of $[Pd_2\mathbf{TAA}_2\mathbf{NDI}_2]^{4+}$ exhibits absorption maxima at 295 nm, stemming from the **TAA** ligand, at 339, 356, and 376 nm corresponding to the S_0-S_1 transitions of the **NDI** ligand and at 408 nm. The latter might correspond to the red-shifted absorption of the **TAA** ligand. Furthermore, the vibronic progression of the **NDI** S_0-S_1 transition in the heteroleptic cage cannot be reproduced with the absorption spectra of the two homoleptic assemblies (Fig. 14a). $[Pd_2\mathbf{TAA}_2\mathbf{PMDI}_2]^{4+}$ exhibits an absorption feature at 250 nm which is slightly bathochromically shifted in comparison with $[Pd_3\mathbf{PMDI}_6]^{6+}$. Moreover, two absorption features at 358 and 403 nm are observed, rather reminiscent to the **TAA** ligand than to homoleptic $[Pd_2\mathbf{TAA}_4]^{4+}$. Again, the lowest energy absorption feature is red-shifted compared to the spectra of the homoleptic assemblies. For $[Pd_2\mathbf{TAA}_2\mathbf{FRO}_2]^{4+}$, a bathochromic shift of the characteristic **FRO** absorption feature is observed, similar to its sibling with **CBZ** donor. In addition, the low-energy absorption feature of the **TAA** ligand is shifted to 403 nm. The disparity between the spectra of the heteroleptic **TAA** cages and the corresponding sum of the spectra of the homoleptic cages might originate on one hand from electronic communication between the chromophores in the ground state. On the other hand, they might originate from a different conformational landscape accessible in the heteroleptic cages. This was observed to a smaller extent for the **CBZ** cages which were shown to be more rigid by NMR spectroscopy, supporting the second hypothesis.

For triggering photoinduced electron transfer, an excitation wavelength of 400 nm is suitable, as it allows for selective excitation of the **TAA** donor ligand in $[Pd_2\mathbf{TAA}_2\mathbf{NDI}_2]^{4+}$ and $[Pd_2\mathbf{TAA}_2\mathbf{PMDI}_2]^{4+}$. For $[Pd_2\mathbf{TAA}_2\mathbf{FRO}_2]^{4+}$, simultaneous excitation of the **FRO** acceptor might occur, however, with a significantly lower probability. The extinction coefficients of the donor-acceptor cages at $\lambda = 400$ nm are around $\varepsilon \approx 8\ mM^{-1}\cdot mm^{-1}$, the small differences are probably due to the experimental error (Tab. 2).

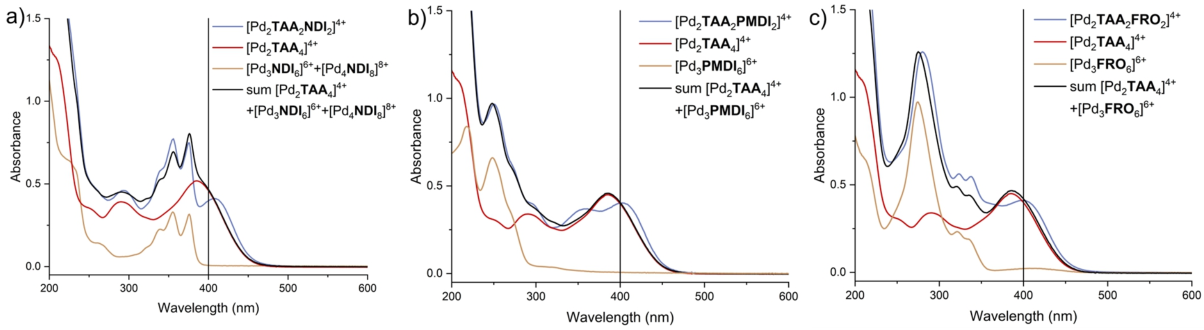

Fig. 14 Absorption spectra of donor-acceptor cages in comparison to the spectra of the corresponding homoleptic assemblies and the calculated sum of their spectra for a) $[Pd_2\mathbf{TAA}_2\mathbf{NDI}_2]^{4+}$; b) $[Pd_2\mathbf{TAA}_2\mathbf{PMDI}_2]^{4+}$; c) $[Pd_2\mathbf{TAA}_2\mathbf{FRO}_2]^{4+}$ (c(ligand) = 200 μM, CH_3CN, 1 mm cuvette pathlength). The vertical line shows the excitation wavelength chosen for transient absorption spectroscopy.

Tab. 2 Extinction coefficients of $[Pd_2\mathbf{TAA}_2A_2]^{4+}$ cages at 400 nm.

	$[Pd_2\mathbf{TAA}_2\mathbf{NDI}_2]^{4+}$	$[Pd_2\mathbf{TAA}_2\mathbf{PMDI}_2]^{4+}$	$[Pd_2\mathbf{TAA}_2\mathbf{FRO}_2]^{4+}$
ε(400 nm)/ $mM^{-1}\cdot mm^{-1}$	7.96	8.14	8.14

The spectrum of $[Pd_2\mathbf{PTZ}_2\mathbf{NDI}_2]^{4+}$ shows features at 296 nm, attributable to the **PTZ** absorption, the vibronic progression of the **NDI** S_0-S_1 transition at 338, 356, and 376 nm, as well as a feature at 400 nm assignable to the **PTZ** lowest-energy absorption (Fig. 15a). For [Pd$_2$**PTZ**$_2$**PMDI**$_2$]$^{4+}$, a feature of the **PMDI** ligand at 248 nm and features of the **PTZ** ligand at 296 and 402 nm are observed. Aside from a small bathochromic shift of the 400 nm-feature, the spectrum is in great accordance with the sum of the spectra of the homoleptic assemblies. The spectrum of [Pd$_2$**PTZ**$_2$**FRO**$_2$]$^{4+}$ displays features at 282 nm and at 400 nm, stemming from **FRO** and **PTZ** ligand, respectively. Similar to what has been observed for [Pd$_2$**CBZ**$_2$**FRO**$_2$]$^{4+}$ and [Pd$_2$**TAA**$_2$**FRO**$_2$]$^{4+}$, the feature of **FRO** is slightly red shifted. Overall, the absorption spectra of the heteroleptic cages with **PTZ** donor closely match the superposition of the spectra of the respective homoleptic assemblies, similar to what has been observed for the cages with **CBZ** donor.

As for the cages with **TAA** donor, an excitation wavelength of 400 nm allows for selectively exciting the donor ligand. The extinction coefficients of the **PTZ** cages at the excitation wavelength are around $\varepsilon \approx 5\ \mathrm{mM^{-1}\cdot mm^{-1}}$, hence somewhat lower than the ones of the corresponding **TAA** cages (Tab. 3).

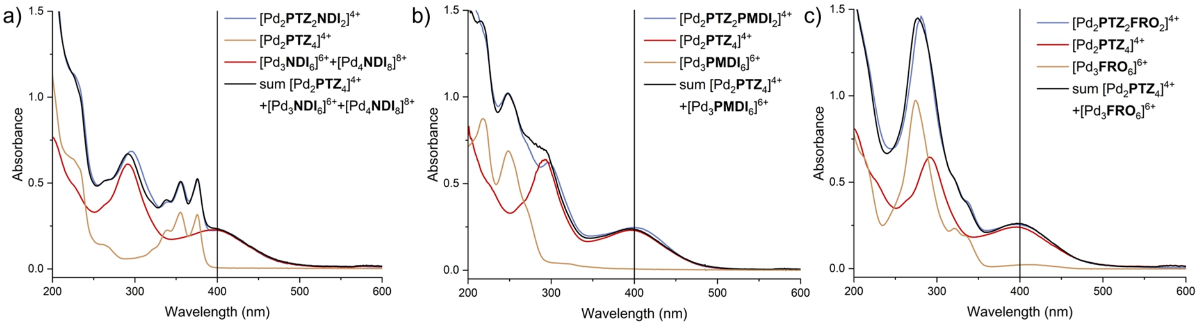

Fig. 15 Absorption spectra of donor-acceptor cages in comparison to the spectra of the corresponding homoleptic assemblies and the calculated sum of their spectra for a) [Pd$_2$**PTZ**$_2$**NDI**$_2$]$^{4+}$; b) [Pd$_2$**PTZ**$_2$**PMDI**$_2$]$^{4+}$; c) [Pd$_2$**PTZ**$_2$**FRO**$_2$]$^{4+}$ (*c*(ligand) = 200 µM, CH_3CN, 1 mm cuvette pathlength). The vertical line shows the excitation wavelength chosen for transient absorption spectroscopy.

Tab. 3 Extinction coefficients of [Pd$_2$**PTZ**$_2$A$_2$]$^{4+}$ cages at 400 nm.

	[Pd$_2$**PTZ**$_2$**NDI**$_2$]$^{4+}$	[Pd$_2$**PTZ**$_2$**PMDI**$_2$]$^{4+}$	[Pd$_2$**PTZ**$_2$**FRO**$_2$]$^{4+}$
ε(400 nm)/ mM^{-1}·mm^{-1}	4.73	5.03	5.13

3.5. Emission spectroscopy

For the determination of the free energy of photoinduced electron transfer, the energy of the excited singlet state of the donor is required. The latter is commonly estimated as the energy at which absorption and emission spectra intersect.[18] Due to the quenching of the emission of the donor ligand in homo- and heteroleptic Pd(II) assemblies owing to the formation of LMCT and LLCS states,[1,19] only the emission of the free donor ligands was studied.

Ligand **CBZ** shows an emission band at 410 nm featuring a Stokes shift of 102 nm (Fig. 16a). Absorption and emission spectra cross at 362 nm which corresponds to a singlet state energy of 3.42 eV. Ligand **TAA** shows a broad emission at 495 nm that is shifted by 108 nm as compared to the absorption maximum (Fig. 16b). The spectra intersect at 425 nm, corresponding to an energy of 2.92 eV. The emission properties of the **PTZ** ligand were reported beforehand; the ligand emits at around 500 nm and possesses a singlet state energy of 2.70 eV.[1,16]

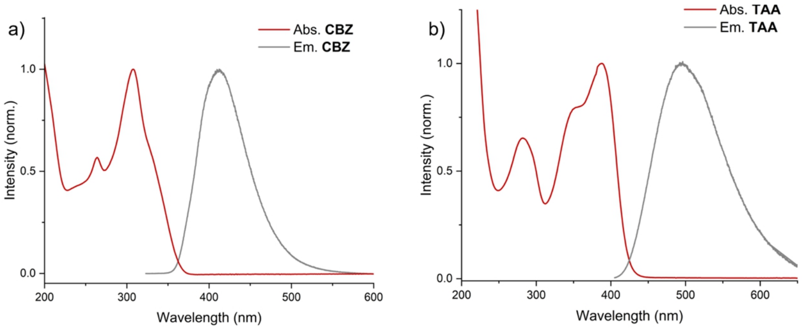

Fig. 16 Normalized absorption and emission spectra a) ligand **CBZ** (λ_{ex} = 308 nm); b) ligand **TAA** (λ_{ex} = 390 nm) (CH_3CN). Absorption and emission spectra of ligand **PTZ** are reported.[16]

3.6. Electrochemistry

The ligands, homoleptic assemblies and donor-acceptor cages were investigated by cyclic voltammetry. This allows for further insight into possible interactions between the redox active moieties in the ground state, for estimation of the frontier orbital energy levels and hence of the driving force for electron transfer, and for determination of the potential required for electrochemically reducing or oxidizing the ligands. The latter was exploited for acquisition of the absorption spectra of electrochemically generated donor radical cation and acceptor radical anion via spectroelectrochemistry. These spectra are required for interpreting the transient absorption spectra. First, the electrochemical characterization of **NDI** and **PMDI** ligands is described in depth. In the next step, the electrochemical properties of the homoleptic assemblies and of the donor-acceptor cages are described. In the last step, the electrochemical data are combined with the spectroscopic data for calculating the free energy of the electron transfer processes.

3.6.1. Ligands **NDI** and **PMDI**

The cyclic voltammogram of the **NDI** ligand was acquired at different scan rates in acetonitrile with $TBAPF_6$ as electrolyte (Fig. 17a, working electrode (WE): glassy carbon, counter electrode (CE): platinum wire, reference electrode (RE): $Ag/AgNO_3$). A first redox event with peak potentials of $E_{p2} = -0.92$ V and $E_{p1} = -0.85$ V, i.e. a half-wave potential of $E_{1/2} = -0.89$ V was observed. The peak-to-peak separation of $\Delta E_p = 0.07$ V is close to the ideal value of 0.057 V for electrochemically reversible redox processes.[20] A second reversible redox event occurs at $E_{1/2} = -1.31$ V with peak potentials of $E_{p2} = -1.33$ V and $E_{p1} = -1.27$ V. The observed potentials are in great accordance with those reported for the *para*-pyridine **NDI** analogue.[21] In accordance with the Randles-Sevcik equation, a linear relationship between the peak current and the square root of the scan rate is observed for all four processes (Fig. 17b).[20] This confirms a) that the redox events are electrochemically reversible and b) that the redox process involves freely diffusing species as opposed to electrode-adsorbed species.

Next, a solution of the free ligand in acetonitrile with $TBAPF_6$ as electrolyte was exposed to an electric potential slightly more negative as compared to the half-wave potential of the first reduction (Fig. 17c top, cuvette pathlength: 0.5 mm, WE: gold gauze, CE: platinum wire, RE: $Ag/AgNO_3$). Simultaneously, the changes in absorption were followed using a deuterium-halogen light source and optical fibers that conduct the light from the source to the spectroelectrochemical cell as well as from the cell to the spectrometer. The characteristic S_0-S_1 transition between 300 and 400 nm is bleached while a new intense absorption feature at 470 nm along with less intense features at 603, 705, and 785 nm arise, that can be assigned to the **NDI** radical anion.[22] When a more negative potential is applied, the just described features rise first but are bleached quickly concomitant with the appearance of two new absorption features at 415 nm and 620 nm, possessing shoulders at 395 nm and 575 nm, respectively (Fig. 17c, bottom). This absorption pattern was assigned to the **NDI** dianion.

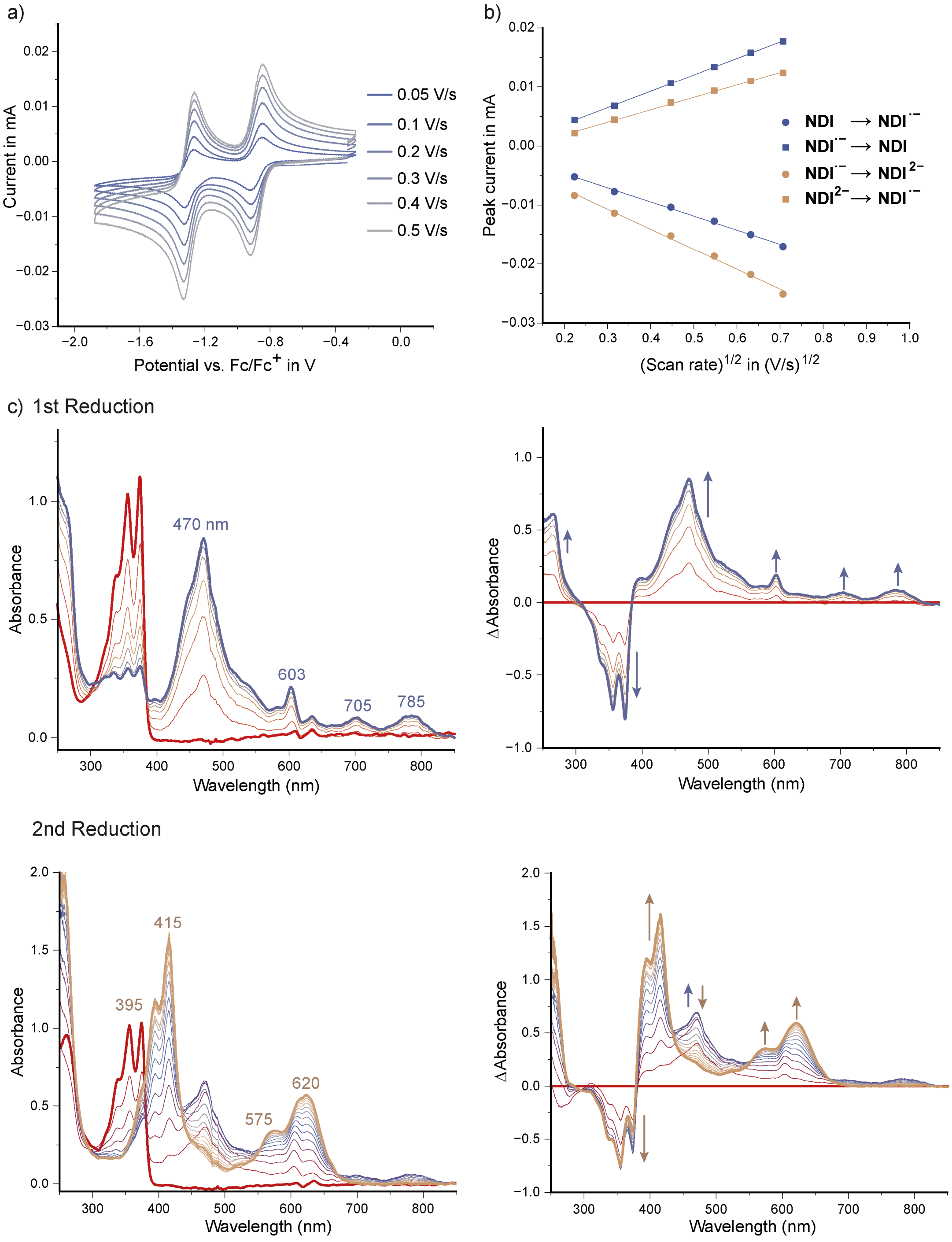

Fig. 17 Cyclic voltammograms of **NDI** ligand at different scan rates (*c* = 400 µM, CH_3CN, 0.1 M $TBAPF_6$, WE: glassy carbon, CE: platinum wire, RE: $Ag/AgNO_3$); b) plot of the peak currents of first and second reduction as well as of the re-oxidation events versus the square root of the scan rate; c) UV-Vis absorption spectra (left) and difference spectra (right) of the **NDI** ligand upon application of −1.1 V (top) and −1.3 V (bottom) (*c* = 750 µM, CH_3CN, 0.1 M $TBAPF_6$, WE: gold gauze, CE: platinum wire, RE: $Ag/AgNO_3$, cuvette pathlength: 0.5 mm).

Due to the low solubility of the **PMDI** ligand in acetonitrile, its electrochemical characterization was performed in DMSO. Furthermore, a platinum disc electrode was used as working electrode. A first reversible redox event with peak potentials of E_{p2} = −1.10 V and E_{p1} = −1.04 V, hence a half-wave potential of $E_{1/2}$ = −1.07 V, can be observed (Fig. 18a). At more negative potentials, a second redox event with $E_{1/2}$ = −1.61 V and peak potentials of E_{p2} = −1.65 V and E_{p1} = −1.57 V occurs. These values are in accordance with the half-wave potentials of **PMDI** derivatives reported in the literature.[23] The peak-to-peak separation of approximately 60 mV as well as the linear relationship between peak current and the square root of the scan rate show that the electron transfer occurs with freely diffusing species and is electrochemically reversible (Fig. 18b).

A direct comparison of the herein described cyclic voltammograms of **NDI** and **PMDI** is hampered by the different working electrodes and solvents used. However, a change of the working electrode did not affect the half-wave potentials of ligand **PMDI** (appendix, section 3.11.6). The electrochemical properties of ligands **PTZ**[1] and **TAA** (Tab. 4) are similar in different solvents, indicating that the solvent-dependency of the half-wave potentials is only small. Hence, these factors were neglected, and it can be concluded that ligand **PMDI** is a weaker electron acceptor as compared to ligand **NDI**.

The **PMDI** radical anion and the dianion were generated electrochemically and their formation was followed by UV-Vis absorption spectroscopy (Fig. 18c). The **PMDI** radical anion absorbs between 300 and 350 nm and possesses defined absorption maxima in the visible region at 420 nm and 655 nm as well as an intense absorption feature at 718 nm. Upon application of a more negative potential, formation of the radical anion is observed which then decays again due to the formation of the **PMDI** dianion. The UV absorption of the dianion is slightly red shifted as compared to the one of the radical anion. Furthermore, it possesses a small absorption feature at 420 nm and an intense feature at 556 nm.

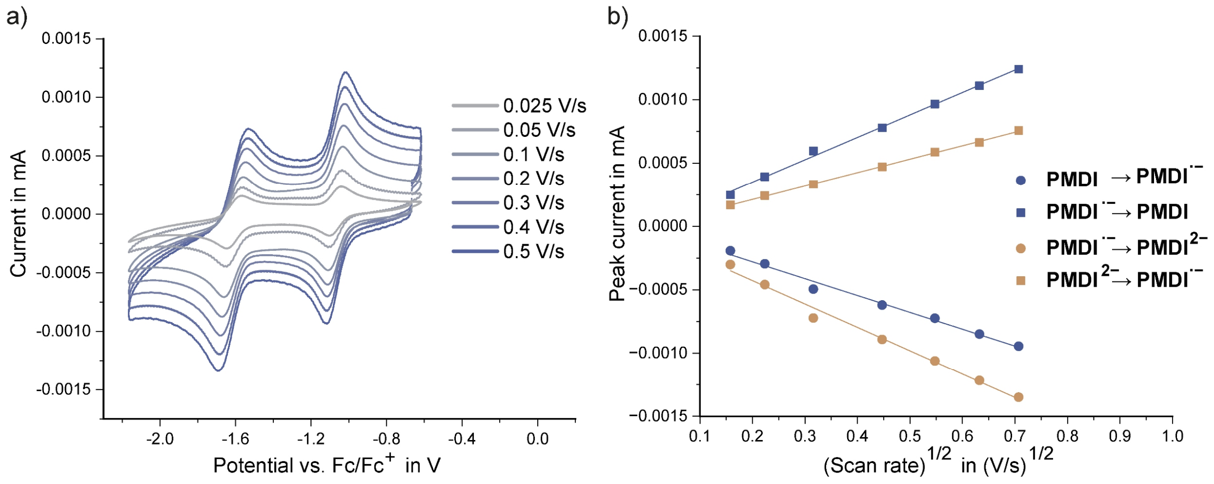

c) 1st Reduction

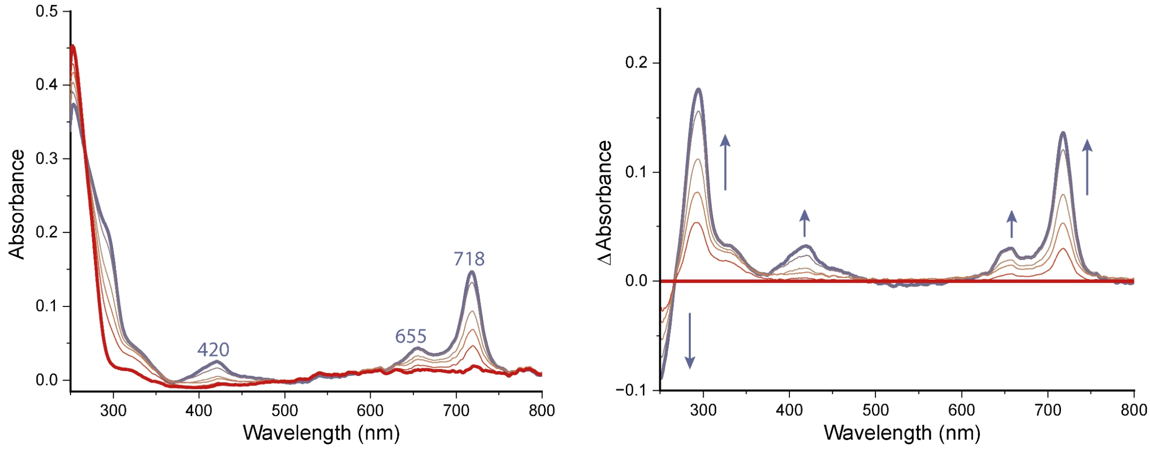

2nd Reduction

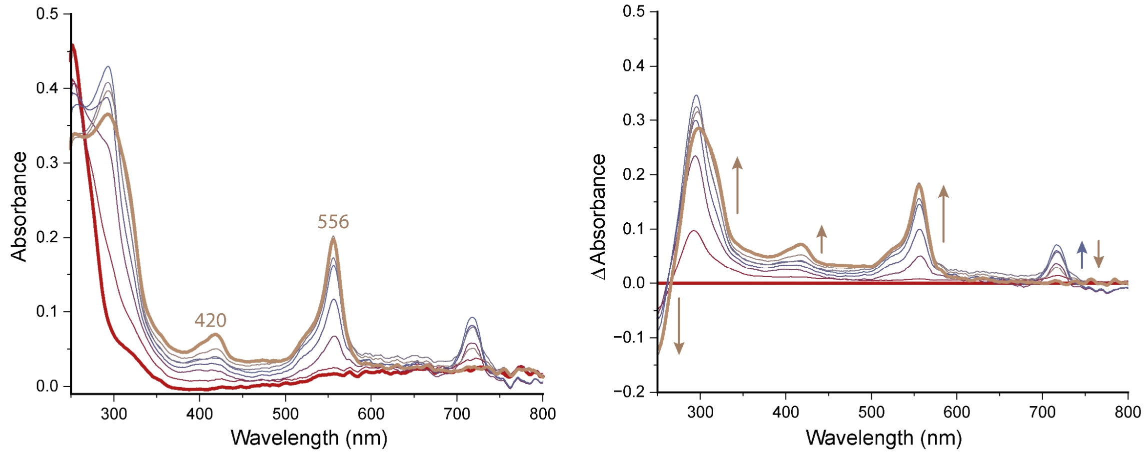

Fig. 18 Cyclic voltammograms of the **PMDI** ligand at different scan rates (*c* = 50 µM, DMSO, 0.1 M TBAPF$_6$, WE: platinum disc, CE: platinum wire, RE: Ag/AgNO$_3$); b) plot of the peak currents of first and second reduction as well as of the re-oxidation events versus the square root of the scan rate; c) UV-Vis absorption spectra (left) and difference spectra (right) of the **PMDI** ligand upon application of −1.3 V (top) and −1.9 V (bottom) (*c* = 100 µM, DMSO, 0.1 M TBAPF$_6$, WE: gold gauze, CE: platinum wire, RE: Ag/AgNO$_3$, cuvette pathlength: 0.5 mm).

3.6.2. Homo- and heteroleptic assemblies

The homoleptic assemblies and the donor-acceptor cages were investigated with cyclic voltammetry. The integrity of the assemblies at the large electrolyte concentration was confirmed by ^{1}H NMR.

The redox properties of the constituent ligands are overall well conserved in the assemblies. For example, the cyclic voltammogram of the cage $[\mathrm{Pd_2}\mathbf{TAA}_2\mathbf{NDI}_2]^{4+}$ shows a redox event at $E_{1/2}$ = +0.34 V assignable to the oxidation of the **TAA** donor ligand and two consecutive reductions of the **NDI** acceptor ligand at $E_{1/2}$ = −0.91 V and $E_{1/2}$ = −1.31 V (Fig. 19a, compare to Fig. 17 and appendix, section 3.11.6). Table 4 lists the half-wave potentials for ligands, homoleptic, and heteroleptic cages. Across the different donor ligands, the half-wave potential shifts anodically by around 0.05 V upon formation of a dinuclear cage. Possible reasons are the reduced electron density of the ligand upon coordination, the positive charge of the assembly, and a conformational change of the ligand upon oxidation which might lead to strain in the assembly. The anodic shift is somewhat larger (+0.12 V) upon formation of the $[\mathrm{Pd_4}\mathbf{PTZ}_8]^{8+}$ double cage, possibly due to the higher positive charge of the overall assembly and/or the close proximity of the redox centers. The half-wave potentials of the acceptor ligands are relatively similar in the free ligand as compared to in the homoleptic assemblies ($\Delta E_{1/2}$ = 0.01-0.02 V). Furthermore, for the **NDI** ligand, the half-wave potential of the donor-acceptor cage equals the one obtained for the homoleptic assemblies. For **PMDI** and **FRO**, a direct comparison of homoleptic assemblies and donor-acceptor cages is hampered by different experimental conditions. However, overall, the number of redox events as well as the half-wave potentials of the redox active moieties are similar in homoleptic and in the different donor-acceptor cages. This points towards the absence of strong electronic communication between donor and the acceptor ligands in the ground state. For strongly electronically couped redox active moieties, a shift and/or splitting of the redox waves would be expected.[24]

The half-wave potentials of the redox active moieties furthermore allow for comparing the electron donating strength of the donor ligands as well as the electron affinity of the acceptor ligands in the electronic ground state. The donor strength decreases in the order **TAA** > **PTZ** > **CBZ** and the acceptor strength decreases in the order **NDI** > **PMDI** > **FRO**.

Tab. 4 Half-wave potentials $E_{1/2}$ of the ligands, their homoleptic assemblies, and the donor-acceptor cages. The potentials are given in V and are referenced to Fc/Fc$^+$. If not mentioned otherwise, the conditions for the measurement were: solvent: CH_3CN, 0.1 M $TBAPF_6$, WE: glassy carbon, CE: platinum wire, RE: Ag/$AgNO_3$. [1]solvent: DMSO, [2]WE: Pt, [3]not measured due to low solubility, [4]a reliable value could not be obtained (appendix, section 3.11.6).

Donor	Ligand D	$[\mathrm{Pd}_n\mathrm{D}_{2n}]^{2n+}$	$[\mathrm{Pd_2D_2}\mathbf{NDI}_2]^{4+}$	$[\mathrm{Pd_2D_2}\mathbf{PMDI}_2]^{4+}$	$[\mathrm{Pd_2D_2}\mathbf{FRO}_2]^{4+}$
CBZ	0.80	-[3]	0.86	0.86	0.84
TAA	0.26, 0.29[1]	0.33 (n = 2)[1]	0.34	0.32	0.34[1]
PTZ	0.40	0.52 (n = 4)[1]	0.45	0.46	0.47
Acceptor	Ligand A	$[\mathrm{Pd}_n\mathrm{A}_{2n}]^{2n+}$	$[\mathrm{Pd_2}\mathbf{CBZ}_2\mathrm{A_2}]^{4+}$	$[\mathrm{Pd_2}\mathbf{TAA}_2\mathrm{A_2}]^{4+}$	$[\mathrm{Pd_2}\mathbf{PTZ}_2\mathrm{A_2}]^{4+}$
NDI	−0.89	−0.91 (n = 3,4)	-[4]	−0.91	−0.91
PMDI	−1.07[1,2]	−1.08 (n = 3)[1,2]	−1.13	−1.12	−1.11
FRO	−1.54[1]	−1.52 (n = 3,4)[1]	−1.57	−1.49[1]	−1.60

In the next step, the redox events in the cages were followed spectroscopically in order to obtain the spectra of the electrochemically generated radical ions. This is described here for three cages $[\mathrm{Pd_2}\mathbf{TAA}_2\mathbf{NDI}_2]^{4+}$, $[\mathrm{Pd_2}\mathbf{CBZ}_2\mathbf{PMDI}_2]^{4+}$, and $[\mathrm{Pd_2}\mathbf{PTZ}_2\mathbf{FRO}_2]^{4+}$ that cover the features of all three donor and all three acceptor ligands. The spectra of the remaining cages can be found in the appendix, section 3.11.6.

For the electrochemical oxidation of the **TAA** ligand in [Pd$_2$**TAA**$_2$**NDI**$_2$]$^{4+}$, a potential of +0.5 V was applied. This leads to the rise of absorption features at 315 nm, 450-500 nm, and a broad feature between 650-1000 nm. Concomitantly, the absorption between 350-450 nm decreases due to bleaching of the ground state (Fig. 19b). This spectrum is assigned to the **TAA** radical cation. A similar spectrum is obtained upon oxidation of cage [Pd$_2$**TAA**$_2$**NDI**$_2$]$^{4+}$, supporting the assignment (appendix, section 3.11.6). Electrochemical reduction of [Pd$_2$**TAA**$_2$**NDI**$_2$]$^{4+}$ with a potential of −1.2 V causes ground state bleaching between 300 and 400 nm, and at 420 nm. In addition, new features at 270 nm, 390 nm, 470 nm, 603 nm, 705 nm, and 785 nm arise. These new features coincide with the absorption features of the radical anion of the free **NDI** ligand (Fig. 17) while the feature at 390 nm is only observed in the donor-acceptor cage.

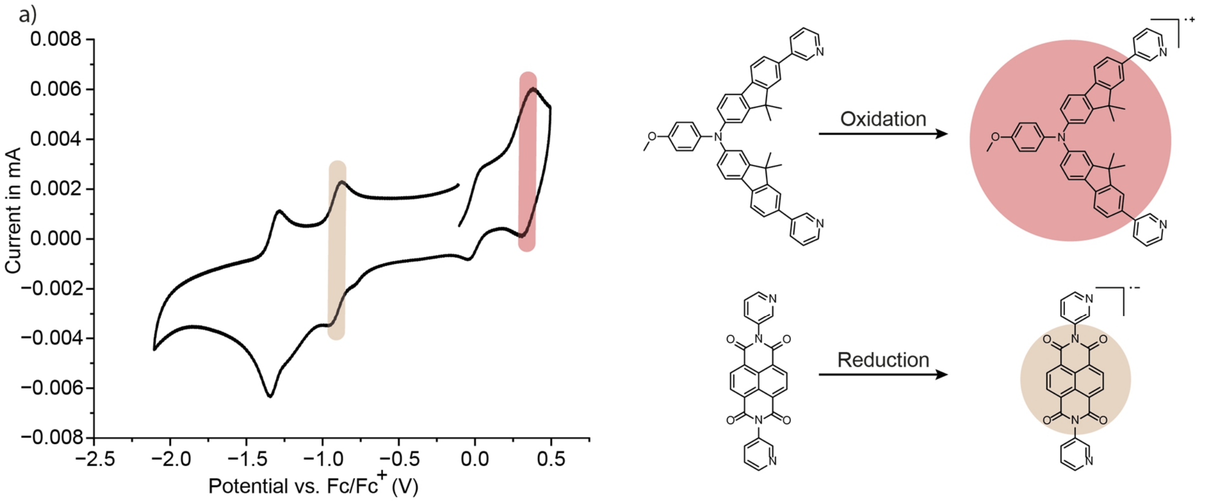

b) Oxidation

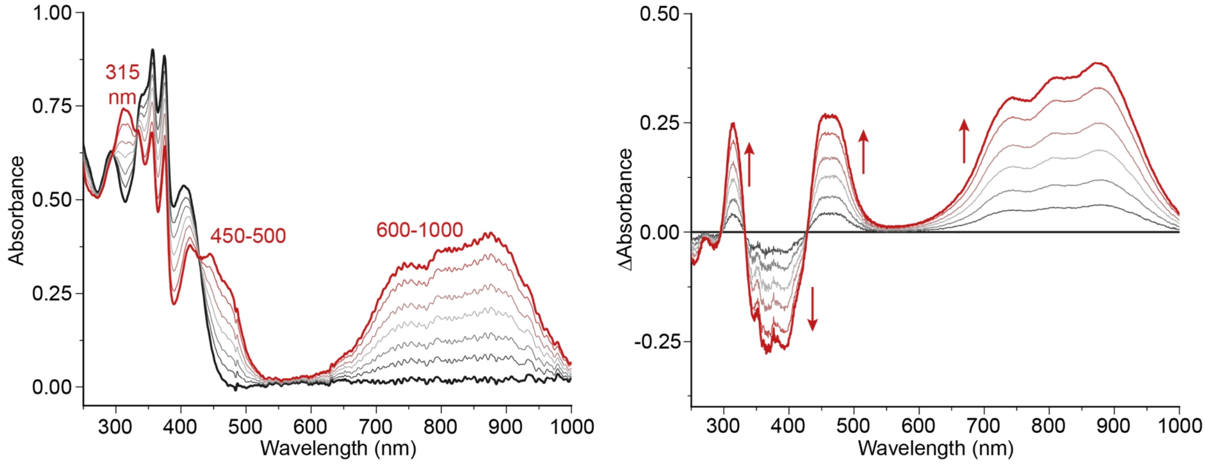

c) Reduction

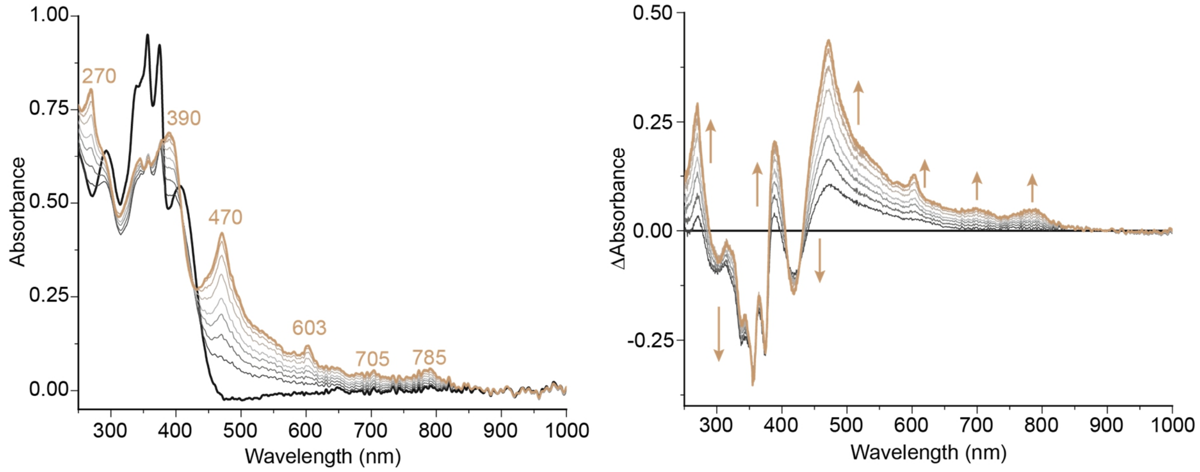

Fig. 19 Electrochemical characterization of $[Pd_2\textbf{TAA}_2\textbf{NDI}_2]^{4+}$: a) cyclic voltammogram of $[Pd_2\textbf{TAA}_2\textbf{NDI}_2]^{4+}$, the oxidation event is highlighted in red and the first reduction in beige (*c*(cage) = 80 μM, CH_3CN, 0.1 M $TBAPF_6$, WE: glassy carbon, CE: platinum wire, RE: $Ag/AgNO_3$, scan rate: 0.1 $V \cdot s^{-1}$); b) UV-Vis absorption spectra of the oxidation process (left: absorption spectra, right: difference spectra); c) UV-Vis absorption spectra of the 1st reduction process (left: absorption spectra, right: difference spectra) (*c*(cage) = 140 μM, CH_3CN, 0.1 M $TBAPF_6$, WE: gold gauze, CE: platinum wire, RE: $Ag/AgNO_3$, cuvette pathlength: 0.5 mm).

For investigating the cage integrity during the redox processes, the absorption was followed upon re-reduction of the oxidized cage and upon re-oxidation of the reduced cage. The processes were followed until no changes were observed in the UV-Vis spectrum. The initial and final states are shown in Fig. 20. Re-reduction of the oxidized cage leads to disappearance of the characteristic features of the triaryl amine radical cation $\mathbf{TAA}^{\cdot+}$ in the visible region. The final spectrum nearly perfectly overlaps with the ground state absorption spectrum of $[\mathrm{Pd}_2\mathbf{TAA}_2\mathbf{NDI}_2]^{4+}$. This supports that oxidation does not disturb the cage integrity, in accordance with studies on the chemical oxidation of heteroleptic **PTZ**-based double cages.[1] A strikingly different observation was made upon re-oxidation of the reduced cage: the characteristic absorption features of the **NDI** radical anion disappear concomitantly with a rise of the S_0-S_1 absorption of the **NDI**, in accordance with the reversible nature of its redox event. However, the final spectrum is hypsochromically shifted and the vibronic progression of the S_0-S_1 absorption of the **NDI** is altered (increased $I_{0\text{-}0}/I_{0\text{-}1}$). Hence, the final absorption spectrum resembles the absorption of the free ligands, indicating that the cage does not survive electrochemical reduction. It has to be mentioned that the experiments included bulk electrolysis, i.e. a constant potential was applied. These conditions are - with the scan rates chosen in this work - harsher as compared to the ones during cyclic voltammetry, where the potentials are only applied for a short period of time. Nevertheless, the half-wave potentials of the acceptor ligands in the cages should be taken with caution.

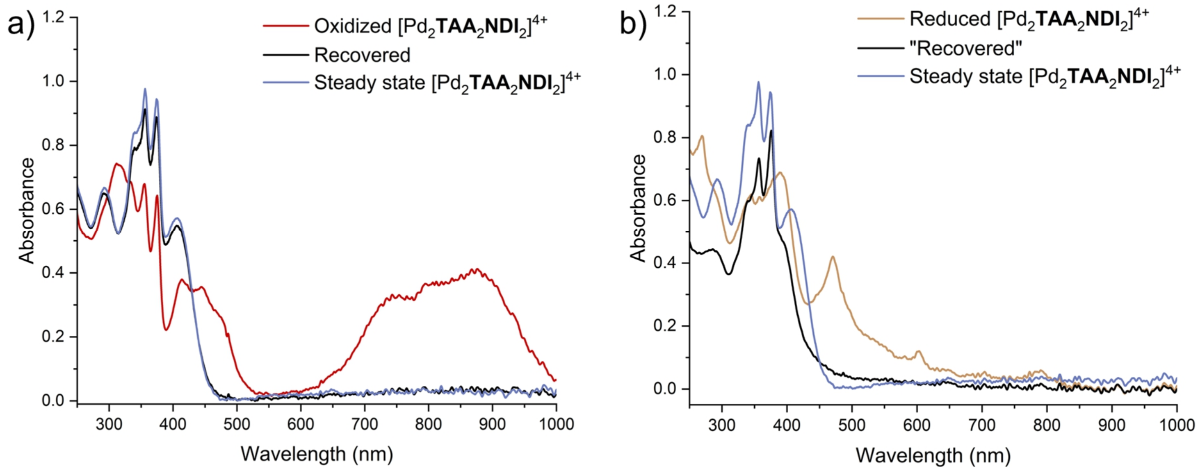

Fig. 20a) UV-Vis absorption spectra of $[\mathrm{Pd}_2\mathbf{TAA}_2\mathbf{NDI}_2]^{4+}$ after oxidation (red), after recovery (black) in comparison to the steady state spectrum (blue); b) UV-Vis absorption spectra of $[\mathrm{Pd}_2\mathbf{TAA}_2\mathbf{NDI}_2]^{4+}$ after reduction (beige), after recovery (black) in comparison to the steady state spectrum (blue) (*c*(cage) = 140 µM, CH_3CN, 0.1 M $TBAPF_6$, WE: gold gauze, CE: platinum wire, RE: $Ag/AgNO_3$, cuvette pathlength: 0.5 mm).

For oxidation of the **CBZ** ligand in $[\mathrm{Pd}_2\mathbf{CBZ}_2\mathbf{PMDI}_2]^{4+}$, a potential of +1.1 V was applied (Fig. 21). This resulted in bleaching of the ground state absorption in the UV region and the emergence of a feature at 425 nm as well as increased absorbance between 600 and 1100 nm with characteristic features at 720 and 940 nm. Most probably, these features can be assigned to the **CBZ** radical cation. Oxidation of $[\mathrm{Pd}_2\mathbf{CBZ}_2\mathbf{NDI}_2]^{4+}$ and $[\mathrm{Pd}_2\mathbf{CBZ}_2\mathbf{FRO}_2]^{4+}$ gave rise to a similar absorption pattern, supporting this conclusion (appendix, section 3.11.6). Application of a potential of −1.3 V led to increased absorbance in the UV region along with the rise of a small feature at 650 nm and an intense feature at 715 nm. Again, the spectrum closely resembles the one of the reduced free **PMDI** ligand except for the absence of a distinct feature at 420 nm (Fig. 18c). Instead, the absorbance of the reduced cage is somewhat broad between 400 and 600 nm.

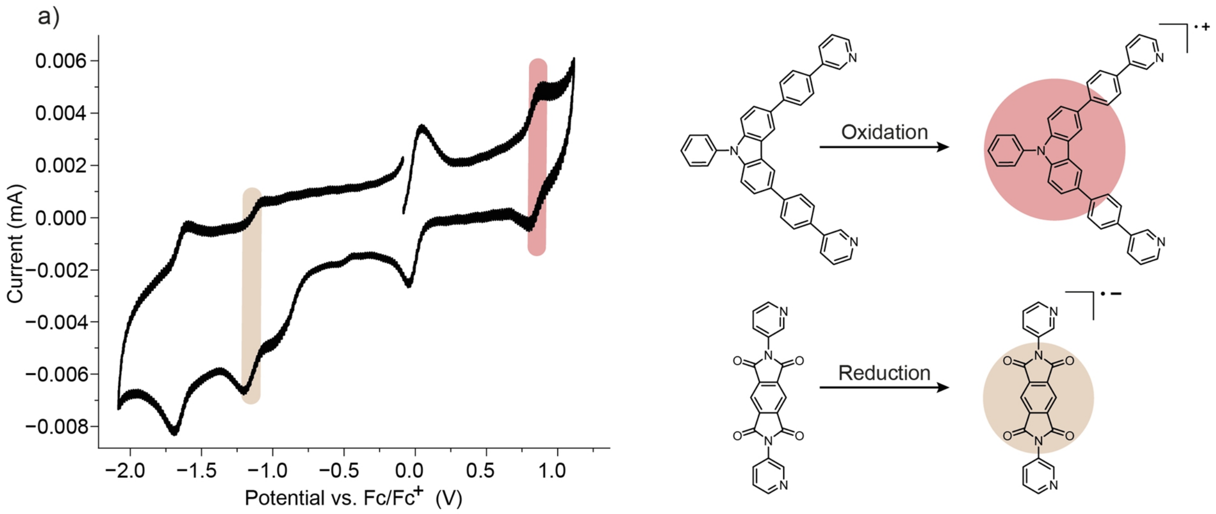

b) Oxidation

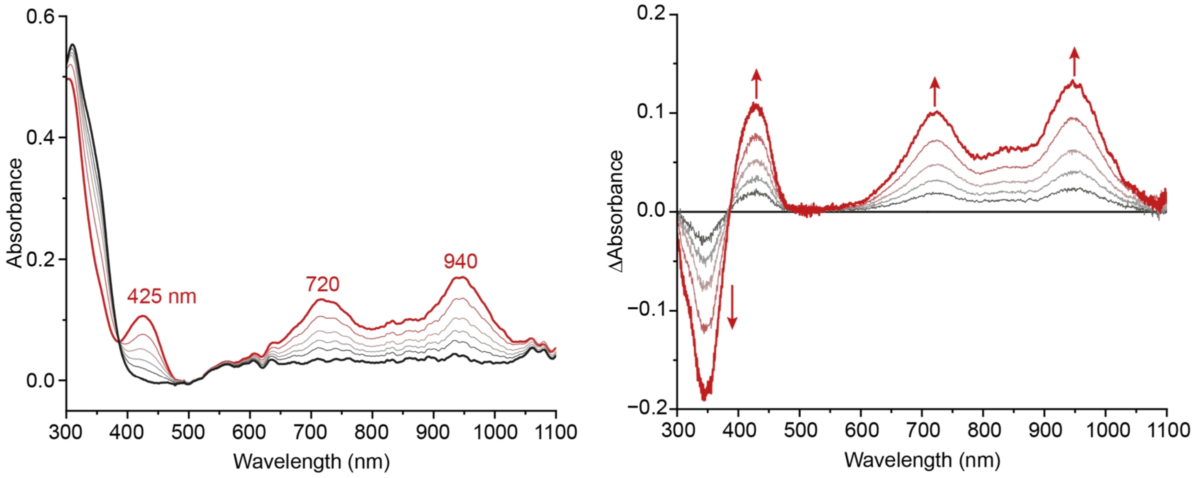

c) Reduction

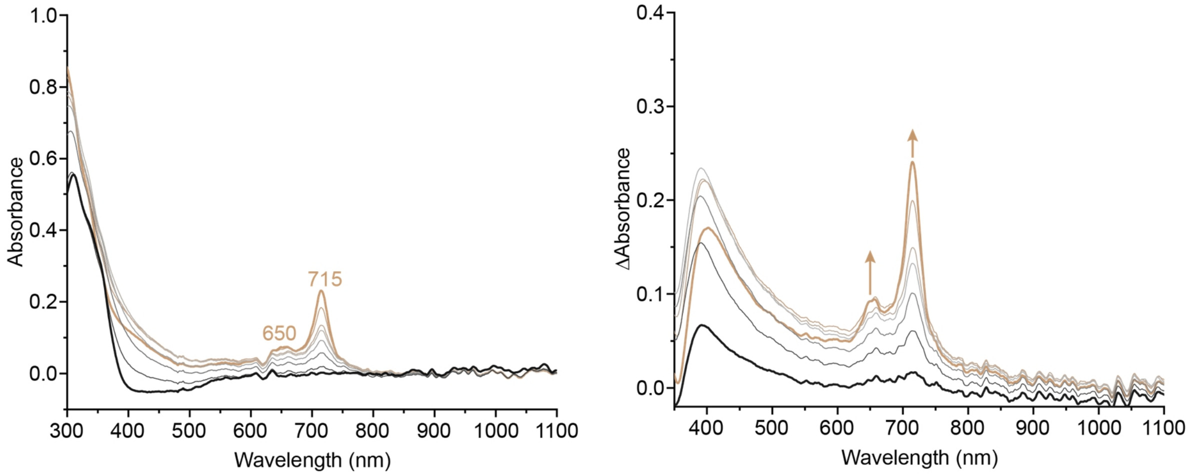

Fig. 21 Electrochemical characterization of $[\mathrm{Pd_2}\mathbf{CBZ_2PMDI_2}]^{4+}$: a) cyclic voltammogram of $[\mathrm{Pd_2}\mathbf{CBZ_2PMDI_2}]^{4+}$, the oxidation event is highlighted in red and the first reduction in beige (*c*(cage) = 25 µM, CH_3CN, 0.1 M $TBAPF_6$, WE: glassy carbon, CE: platinum wire, RE: $Ag/AgNO_3$, scan rate: 0.1 $V\cdot s^{-1}$); b) UV-Vis spectra of the oxidation process (left: absorption spectra, right: difference spectra); c) UV-Vis spectra of the reduction process (left: absorption spectra, right: difference spectra) (*c*(cage) = 60 µM, CH_3CN, 0.1 M $TBAPF_6$, WE: gold gauze, CE: platinum wire, RE: $Ag/AgNO_3$, cuvette pathlength: 0.5 mm).

In a similar fashion, the changes in absorption were monitored for the redox processes of $[Pd_2\mathbf{PTZ}_2\mathbf{FRO}_2]^{4+}$ (Fig. 22). Application of a potential of +0.6 V led to the rise of absorbance at 320 nm, 520 nm, and a broad band between 600 and 800 nm while the absorption between 350 and 450 nm is bleached. The feature at 520 nm possesses a shoulder at higher energy. This absorption pattern is in agreement with the radical cation of the **PTZ** ligand and the corresponding double cage.[1] Upon application of a potential of −1.8 V, the absorption between 300 and 400 nm rose along with a broad band between 400 and 700 nm, assignable to the **FRO** radical anion.

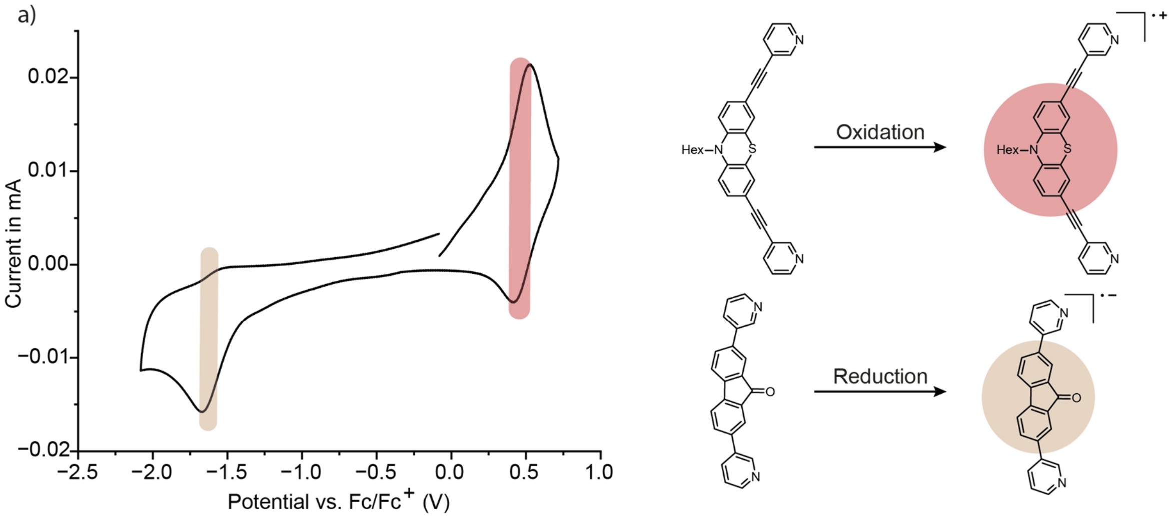

b) Oxidation

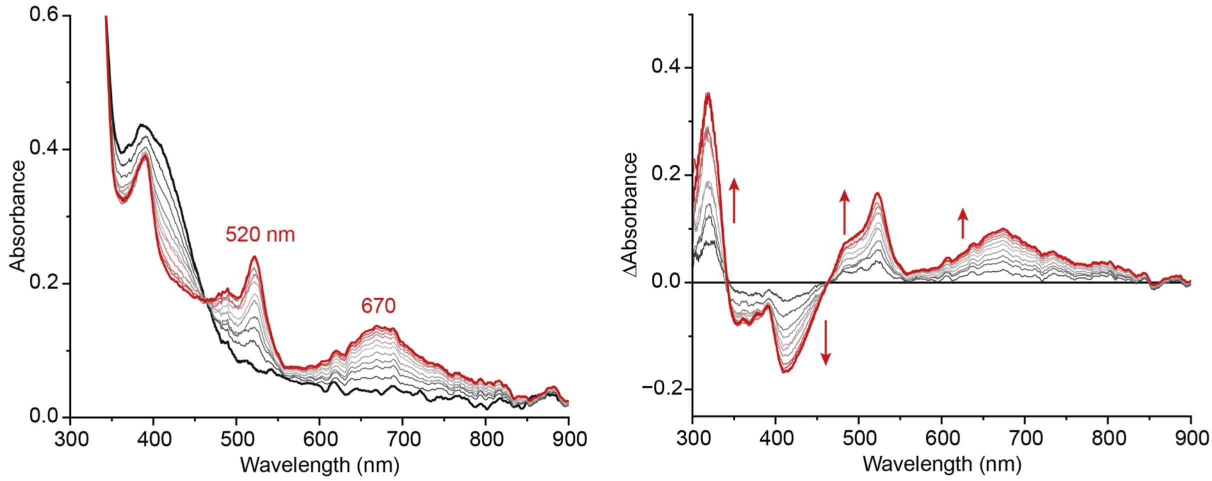

c) Reduction

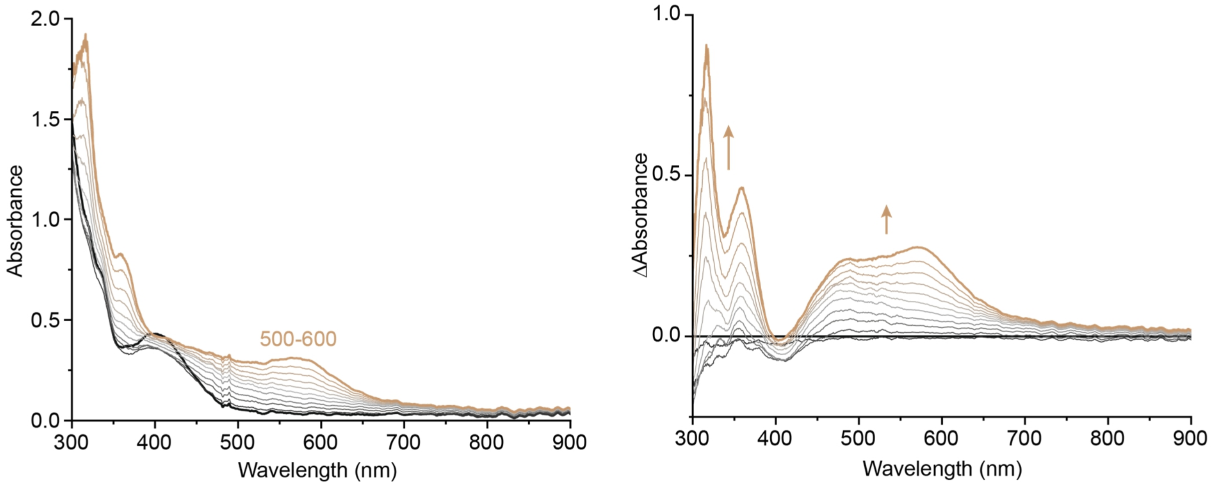

Fig. 22 Electrochemical characterization of [Pd$_2$**PTZ**$_2$**FRO**$_2$]$^{4+}$: a) cyclic voltammogram of [Pd$_2$**PTZ**$_2$**FRO**$_2$]$^{4+}$, the oxidation event is highlighted in red and the first reduction in beige (*c*(cage) = 160 µM, CH_3CN, 0.1 M $TBAPF_6$, WE: glassy carbon, CE: platinum wire, RE: Ag/$AgNO_3$, scan rate: 0.1 V·s^{-1}); b) UV-Vis spectra of the oxidation process (left: absorption spectra, right: difference spectra); c) UV-Vis spectra of the reduction process (left: absorption spectra, right: difference spectra) (*c*(cage) = 160 µM, CH_3CN, 0.1 M $TBAPF_6$, WE: gold gauze, CE: platinum wire, RE: Ag/$AgNO_3$, cuvette pathlength: 0.5 mm).

3.6.3. Calculation of the electron transfer driving forces

The driving forces for the photoinduced electron transfer and the thermal back electron transfer can be calculated based on the half-wave potentials of donor and acceptor moieties. For the following calculations, an average of the half-wave potentials obtained for a particular ligand in the different donor-acceptor cages was used in order to minimize the propagation of experimental errors ($E_{1/2}$(**CBZ**) = 0.85 V, $E_{1/2}$(**TAA**) = 0.33 V, $E_{1/2}$(**PTZ**) = 0.46 V, $E_{1/2}$(**NDI**) = −0.91 V, $E_{1/2}$(**PMDI**) = −1.13 V, $E_{1/2}$(**FRO**) = −1.58 V).

Since the redox events of all donor ligands (E_{ox}) are anodically shifted as compared to the redox events of the acceptor ligands (E_{red}), electron transfer in the electronic ground state would be endergonic:

$$\Delta G_{\mathrm{CS}} = -\mathrm{e} \cdot (E_{\mathrm{red}} - E_{\mathrm{ox}}) > 0 \tag{1}$$

However, photoexcitation of the donor ligand increases its reducing strength by its singlet state energy E_{00}. Furthermore, in order to account for the electrostatic attraction of the formed ions, a Coulomb term is included. The Coulomb term is distance-dependent; here, the distance between donor and acceptor ligands sitting in *cis* position was considered (appendix, section 3.11.8). However, in polar media such as acetonitrile, the term is relatively small (contributes here with up to 7% to ΔG). Overall, these considerations result in equation 2 for estimating the free energy for photoinduced electron transfer (PET).[7] The process is exergonic for all nine combinations, varying between −0.71 eV for $[\mathrm{Pd_2}\mathbf{PTZ}_2\mathbf{FRO}_2]^{4+}$ and −1.72 eV for $[\mathrm{Pd_2}\mathbf{TAA}_2\mathbf{NDI}_2]^{4+}$ (Tab. 5).

$$\Delta G_{\mathrm{PET}} = -\mathrm{e} \cdot (E_{\mathrm{red}} - E_{\mathrm{ox}}) - E_{00} - \frac{e^2}{4\pi\varepsilon_0\varepsilon_r d_{\mathrm{DA}}} < 0 \tag{2}$$

Back electron transfer (BET) is driven by the difference in the ground state redox potentials of the donor and the acceptor ligand (eq. 3).

$$\Delta G_{\mathrm{BET}} = \mathrm{e} \cdot (E_{\mathrm{red}} - E_{\mathrm{ox}}) + \frac{e^2}{4\pi\varepsilon_0\varepsilon_r d_{\mathrm{DA}}} < 0 \tag{3}$$

The free energy for back electron transfer varies between −1.20 eV for $[\mathrm{Pd_2}\mathbf{TAA}_2\mathbf{NDI}_2]^{4+}$ and −2.40 eV for $[\mathrm{Pd_2}\mathbf{CBZ}_2\mathbf{FRO}_2]^{4+}$. This is a reasonable range for studying the free energy-dependency of the electron transfer rate constant in the context of Marcus theory when compared to reported donor-acceptor systems.[25–27] Hence, overall, the variation of the redox active ligands allowed for tuning the thermodynamic driving forces for the electron transfer processes, as is schematically depicted in figure 23.

Tab. 5 Overview of the driving forces for the photoinduced forward electron transfer and for the back electron transfer determined with equations 2 and 3, respectively.

	$-\Delta G_{\mathrm{PET}}$ (eV)			$-\Delta G_{\mathrm{BET}}$ (eV)		
D↓ A→	**NDI**	**PMDI**	**FRO**	**NDI**	**PMDI**	**FRO**
CBZ	1.70	1.48	1.02	1.73	1.95	2.40
TAA	1.72	1.50	1.05	1.20	1.42	1.87
PTZ	1.38	1.16	0.71	1.32	1.54	1.99

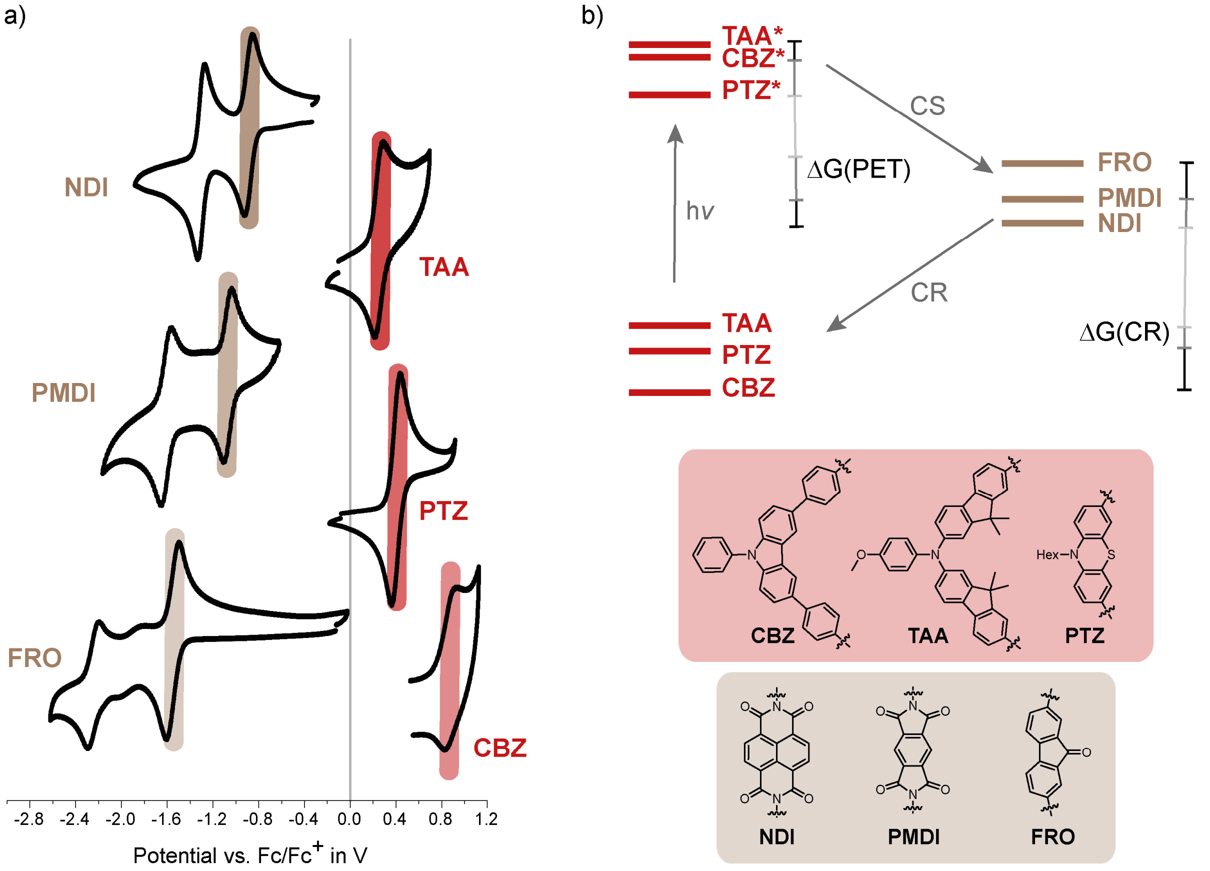

Fig. 23 Cyclic voltammograms of ligands **NDI**, **PMDI**, **FRO** (beige) and **TAA**, **PTZ,** and ligand **CBZ** (in [Pd$_2$**CBZ**$_2$**NDI**$_2$]$^{4+}$, for the cyclic voltammogram of the free ligand see appendix, section 3.11.6) (red); b) schematic overview of the relative energy levels in the donor-acceptor cages (up) and structure of the functional backbones (down).

3.7. Computational studies

The structures of all nine donor-acceptor cages were geometry-optimized by DFT computations (B3LPY/def2-SVP), followed by single point energy calculations (B3LPY/def2-TZVP). In order to approach the experimental conditions while keeping the model simple enough, an implicit solvent model was used (CPCM, acetonitrile) and the counter anions were neglected. The computations were carried out for 1) visualization of the frontier orbitals, 2) estimation of the energy of the unoccupied orbital localized at the Pd(II) nodes, 3) comparison of the frontier orbital energy levels obtained by DFT and experimentally.

For all cages, the highest occupied molecular orbital (HOMO) is spread over the donor ligands and the lowest unoccupied molecular orbital (LUMO) is spread over the acceptor ligands, as shown exemplary for [Pd$_2$**TAA**$_2$**NDI**$_2$]$^{4+}$ (Fig. 24). While conclusions about the donor strength of the excited state cannot be drawn from these ground state calculations, the localization of the HOMO and LUMO show, in accordance with the electrochemical investigation, that the donor ligands possess the largest electron donor strength in the ground state and the acceptor ligands the highest electron affinity in the ground state (Tab. 6). The latter is important regarding the fact that there is another acceptor moiety in the cage: the Pd(II) nodes, as was observed in preceding studies (sections 1.4.4., 3.2.).[1,19] For all cages, the lowest unoccupied molecular orbital with electron density on the Pd(II) nodes lies higher in energy (~ 2.8 eV) than the ones localized on the acceptor ligands (−4.1 to −3.2 eV), meaning that electron transfer to the acceptor ligand is thermodynamically preferred over electron transfer to the Pd(II) node. For all donor moieties, the computed energy levels are smaller than the experimentally obtained ones (entries belonging to the same redox-active moiety are similarly shaded in table 6). The largest divergence is observed for $[\mathrm{Pd}_2\mathbf{PTZ}_2\mathrm{A}_2]^{4+}$ cages ($\Delta E_{\mathrm{HOMO}} \leq 0.43$ eV). While the computed E_{LUMO} values for the $[\mathrm{Pd}_2\mathrm{D}_2\mathbf{FRO}_2]^{4+}$ cages match well, the ones for $[\mathrm{Pd}_2\mathrm{D}_2\mathbf{NDI}_2]^{4+}$ and $[\mathrm{Pd}_2\mathrm{D}_2\mathbf{PMDI}_2]^{4+}$ are underestimated ($\Delta E_{\mathrm{LUMO}} \leq 0.39$ eV). Furthermore, for the $[\mathrm{Pd}_2\mathbf{TAA}_2\mathrm{A}_2]^{4+}$ cages, the difference between the LUMO levels of cages with **NDI** and **PMDI** acceptors are not well captured. The DFT-computations suggest nearly similar LUMO energy levels while electrochemical investigations of ligands, homoleptic cages, and donor-acceptor cages clearly show that the two acceptors differ by around 0.2 eV in their LUMO levels (Tab. 4). Despite these discrepancies, the calculated frontier orbital energy levels are overall for the most part in accordance with the experimentally observed trends in the sense that the ground state donor strength decreases in the order **TAA** > **PTZ** > **CBZ** and the acceptor strength in the order **NDI** > **PMDI** > **FRO**.

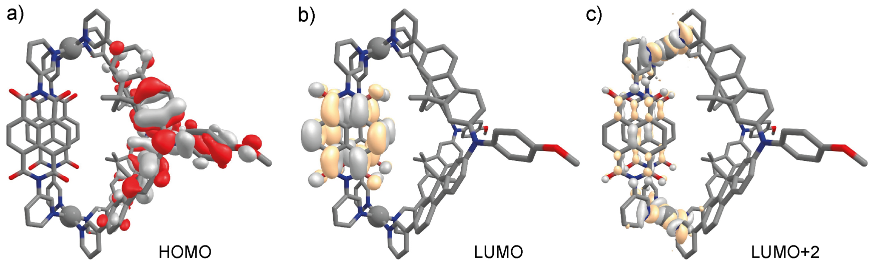

Fig. 24 Visualization of selected molecular orbitals of $[\mathrm{Pd}_2\mathbf{TAA}_2\mathbf{NDI}_2]^{4+}$; a), b) frontier molecular orbitals, c) the lowest unoccupied orbital with electron density on the Pd(II) nodes.

Tab. 6 Overview of experimentally and computationally determined frontier orbital energy levels of the donor-acceptor cages. $^1E_{\mathrm{HOMO/LUMO}} = -E_{1/2} - 4.8$ eV,[28] ^{2} single point energy calculation: B3LYP/Def2-TZVP (with CPCM acetonitrile solvent model, if not stated differently), ^{3}DMSO, ^{4}a reliable value could not be obtained (appendix, section 3.11.6).

	$E_{\mathrm{HOMO,exp}}$ (eV)^1	$E_{\mathrm{LUMO,exp}}$ (eV)^1	$E_{\mathrm{HOMO,DFT}}$ (eV)^2	$E_{\mathrm{LUMO,DFT}}$ (eV)^2	$E_{\mathrm{LUMO(Pd),DFT}}$ (eV)^2
$[\mathrm{Pd}_2\mathbf{CBZ}_2\mathbf{NDI}_2]^{4+}$	-5.66	-^{4}	-5.82	-4.04	-2.86
$[\mathrm{Pd}_2\mathbf{CBZ}_2\mathbf{PMDI}_2]^{4+}$	-5.66	-3.67	-5.80	-3.93	-2.76
$[\mathrm{Pd}_2\mathbf{CBZ}_2\mathbf{FRO}_2]^{4+}$	-5.64	-3.23	-5.81	-3.20	-2.71
$[\mathrm{Pd}_2\mathbf{TAA}_2\mathbf{NDI}_2]^{4+}$	-5.14	-3.89	-5.21	-4.06	-2.76
$[\mathrm{Pd}_2\mathbf{TAA}_2\mathbf{PMDI}_2]^{4+}$	-5.12	-3.68	-5.18	-4.07	-2.79
$[\mathrm{Pd}_2\mathbf{TAA}_2\mathbf{FRO}_2]^{4+}$	-5.14^3	-3.31^3	-5.24	-3.20	-2.72
$[\mathrm{Pd}_2\mathbf{PTZ}_2\mathbf{NDI}_2]^{4+}$	-5.25	-3.89	-5.67	-4.03	-2.89
$[\mathrm{Pd}_2\mathbf{PTZ}_2\mathbf{PMDI}_2]^{4+}$	-5.26	-3.69	-5.58	-3.90	-2.83
$[\mathrm{Pd}_2\mathbf{PTZ}_2\mathbf{FRO}_2]^{4+}$	-5.27	-3.32	-5.66	-3.21	-2.71

Further computations are currently performed by Nicola Bogo (group of Prof. Stein, TU Munich). More precisely, the reorganization energy for charge recombination is calculated using a method introduced by Reimers that is based on curvilinear analysis.[29] For simplification, the free ligands are computed. The reorganization energies and the driving forces will then be compared and their relationship interpreted in the framework of Marcus theory.

3.8. Transient absorption spectroscopy: [Pd$_2$**TAA**$_2$A$_2$]$^{4+}$ and [Pd$_2$**PTZ**$_2$A$_2$]$^{4+}$

Transient absorption spectroscopy on the fs-time scale was applied for obtaining insight into the electron transfer dynamics in the donor-acceptor cages. The six cages [Pd$_2$**TAA**$_2$A$_2$]$^{4+}$ and [Pd$_2$**PTZ**$_2$A$_2$]$^{4+}$ can be excited with the same energy (400 nm, section 3.4.2.), whereby the donor ligand is excited with nearly perfect selectivity, allowing for great comparability of the excited state dynamics across this set of cages. The experiments were carried out in collaboration with Dr. Paul Cesana (group of Prof. Gabriela Schlau-Cohen) at the Massachusetts Institute of Technology during a stay abroad. The data processing and fitting was carried out by Dr. Paul Cesana; the data interpretation was carried out in collaboration.

In general, this technique allows for following the excited state dynamics by using two pulses: a pump pulse which electronically excites the molecules and a time-delayed probe pulse that allows for accessing the absorption spectra of the species that are formed upon photoexcitation. Importantly, an optically gated chopper enables measurement of the absorption with and without the pump pulse. The transient difference spectrum is then obtained by applying $\Delta A = \log(I_{\text{pump off}}/I_{\text{pump on}})$. The 400 nm pump pulse was obtained through second harmonic generation and was operating with an energy of 1 mW (400 nJ/pulse). The probe pulse spanned a range of 450-680 nm. The instrument response function (IRF) was 273 fs as determined via sum frequency generation – frequency resolved optical gating (SFG-FROG). The delay line of the instrument allowed for accessing difference spectra up to a time delay of 800 ps. For more experimental details see appendix, section 3.11.9.

First, the transient difference spectra will be examined in order to assess which processes occurred and which time constants can be extracted. Next, the excited state dynamics of the different cages are compared in a quantitative fashion.

3.8.1. Qualitative analysis of back electron transfer (BET)

The transient difference spectra for the three cages [Pd$_2$**PTZ**$_2$**NDI**$_2$]$^{4+}$, [Pd$_2$**PTZ**$_2$**PMDI**$_2$]$^{4+}$, and [Pd$_2$**PTZ**$_2$**FRO**$_2$]$^{4+}$ at selected time delays are shown in figure 25. For [Pd$_2$**PTZ**$_2$**NDI**$_2$]$^{4+}$, broad absorption between 450-550 nm as well as a band at 600 nm and at 650 nm are observed for the shortest time delay shown (1.5 ps). Comparison of the transient difference spectra with the spectra of the electrochemically oxidized and reduced cage allows for assignment of the bands (Fig. 25d). Within the accessible probe range, the **NDI** radical anion gives rise to the features at 470 and 600 nm in the transient difference spectra while the **PTZ** radical cation absorbs at 520 and > 600 nm. A decrease of ΔA at > 650 nm in the transient difference spectra is unexpected given the absorbance of the **PTZ** radical cation at these wavelengths. Most probably, the decrease is artificial and can be traced back to a lower signal-to-noise ratio at the edge of the probe window. Overall, the transient difference spectra are in accordance with the formation of an LLCS state whose features decrease in intensity at longer time delays owing ground state recovery via charge recombination. However, when comparing the spectrum at 1.5 ps to the ones at longer delay times (e.g. 5 ps, 20 ps), it strikes that the ratios between the absorbances change: the absorbance at 520 nm (**PTZ**$^{\cdot+}$) decreases relative to the one at 470 nm (**NDI**$^{\cdot-}$) and the one at 650 nm (**PTZ**$^{\cdot+}$) decreases relative to the one at 600 nm (**NDI**$^{\cdot-}$). Hence, the features of the donor radical cation decay faster as compared to the features of the acceptor radical anion suggesting the presence of an additional decay pathway for the former. This can be assigned to the decay of the LMCT state. The transient difference spectra of [Pd$_2$**PTZ**$_2$**PMDI**$_2$]$^{4+}$ at early time delays reveal absorption between 450-550 nm with a maximum at 520 nm as well as absorption at > 600 nm. Within the probe range, the **PMDI** radical anion possesses one absorption band at 650 nm. Consequently, the absorption features of **PTZ**$^{\cdot+}$ and **PMDI**$^{\cdot-}$ fully overlap in this wavelength range, complicating a definite conclusion about whether ligand-to-ligand electron transfer occurred. However, the electrochemically generated **PTZ** radical cation possesses weaker absorbance at 650 nm as compared to at 520 nm while in the transient difference spectra, the absorption of the former feature is equal or even larger (depending on the time delay) than the latter. This suggests superposition of the absorption of **PTZ**$^{\cdot+}$ and **PMDI**$^{\cdot-}$ at > 600 nm. Furthermore, the features decay within hundreds of picoseconds, which cannot be explained by the sole formation of the more rapidly decaying LMCT state. For the analogous cage with a **FRO** acceptor, the transient difference spectra at early time delays show three absorption bands at 520 nm, 575 nm, and 650 nm. Again, absorption at 520 nm and > 600 nm can be traced back to the formation of the **PTZ** radical cation. The band at 575 nm can only be explained by parallel formation of the **FRO** radical anion. This species also contributes to the absorbance at around 520 nm. The > 600 nm feature stems from the **PTZ** radical cation only and decays quicker than the features involving the absorption of **FRO**$^{\cdot-}$.

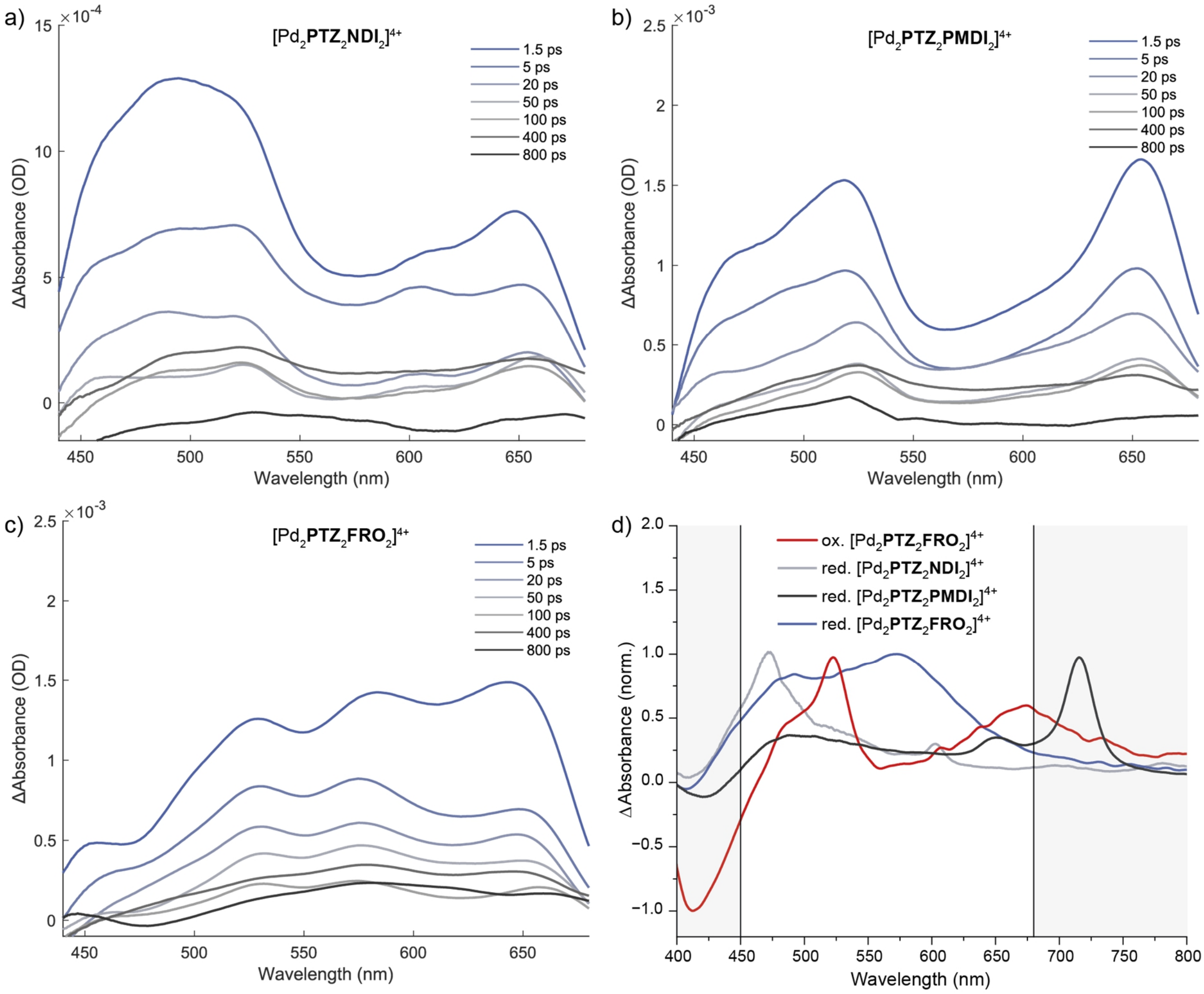

Fig. 25 Transient difference spectra of a) [Pd$_2$**PTZ**$_2$**NDI**$_2$]$^{4+}$; b) [Pd$_2$**PTZ**$_2$**PMDI**$_2$]$^{4+}$; c) [Pd$_2$**PTZ**$_2$**FRO**$_2$]$^{4+}$ at selected time delays; d) Normalized UV-Vis difference spectra of electrochemically generated **PTZ** radical cation and acceptor radical anions in the donor-acceptor cages (solvent for a-d: CH_3CN).

The transient difference spectra of the cages with **TAA** donor will only be discussed briefly since similar processes were observed. For this, the spectra at a time delay of 3 ps are shown in figure 26a. The transient difference spectrum of [Pd$_2$**TAA**$_2$**NDI**$_2$]$^{4+}$ possesses three maxima at 460, 600, and 650 nm. The first one is of highest intensity and can be assigned to an overlap of features of **TAA**$^{\cdot+}$ and **NDI**$^{\cdot-}$. The **NDI** radical anion gives additionally rise to the characteristic feature at 600 nm and the absorbance at > 650 nm can be assigned to the **TAA** radical cation. The spectrum of $[\mathrm{Pd}_2\mathbf{TAA}_2\mathbf{PMDI}_2]^{4+}$ shows two bands at 460 and at 650 nm which can both be assigned to the **TAA** donor radical cation. However, taking a look at the spectrum of the electrochemically generated $\mathbf{TAA}^{\cdot+}$ shows that the oscillator strength at 460 nm is much higher as compared to at 650 nm (only the onset of the low energy feature of $\mathbf{TAA}^{\cdot+}$ is within the probe range). Consequently, the nearly equal intensity of the two features in the TA spectrum hints towards parallel formation of $\mathbf{PMDI}^{\cdot-}$. Finally, the transient difference spectrum of $[\mathrm{Pd}_2\mathbf{TAA}_2\mathbf{FRO}_2]^{4+}$ possesses three bands at 460, 575, and 650 nm. Again, the **TAA** donor radical cation gives rise to the bands at 460 and 650 nm while $\mathbf{FRO}^{\cdot-}$ contributes to the absorbance at 460 nm and gives rise to the feature at 575 nm. Similar to what has been observed for the cages with **PTZ** donor, the features of the **TAA** radical cation decay faster than the features stemming from or involving the respective acceptor radical anion (appendix, section 3.11.9).

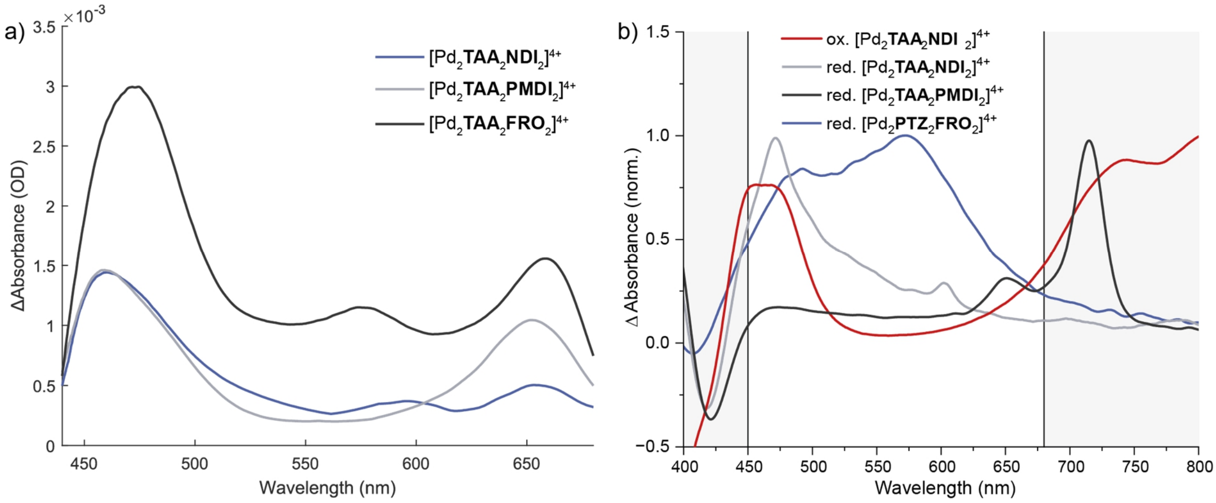

Fig. 26a) Transient difference spectrum of $[\mathrm{Pd}_2\mathbf{TAA}_2\mathbf{NDI}_2]^{4+}$, $[\mathrm{Pd}_2\mathbf{TAA}_2\mathbf{PMDI}_2]^{4+}$, and $[\mathrm{Pd}_2\mathbf{TAA}_2\mathbf{FRO}_2]^{4+}$ at a time delay of 3 ps; b) Normalized UV-Vis difference spectra of electrochemically generated **TAA** radical cation and acceptor radical anions in the donor-acceptor cages (solvent for a,b: CH_3CN).

Overall, the following conclusions can be drawn: 1) from the characteristic features of the radical ions in combination with the long lifetime (hundreds of picoseconds) of the formed species it can be followed that ligand-to-ligand charge separation occurred in all six cages; 2) for all cages, absorption of the singlet excited state of the **PTZ** donor (585 nm) or of the **TAA** donor (550 and 630 nm) is not observed in the accessible time window (see also appendix, section 3.11.9 for shorter time delays); hence, photoinduced electron transfer occurs within the timescale of the IRF; 3) for all combinations, it is observed that the features of the donor radical cation decay faster than the ones of the acceptor radical anion which is assigned to parallelly occurring decay of the LMCT state; 4) the absorbance at the longest time delay is - albeit very noisy - unequal zero. Hence, a small fraction of the charge separated state lives beyond the longest experimentally accessible time delay of 800 ps. Conclusions 2-4) are in accordance with the observations of the group of Prof. Schwarzer on $[\mathrm{Pd}_2\mathbf{PTZ}_2\mathbf{FRO}_2]^{4+}$ and $[\mathrm{Pd}_2\mathbf{TAA}_2\mathbf{FRO}_2]^{4+}$ and hold for all six donor-acceptor cages. This shows that exchanging the acceptor ligand while keeping the overall cage framework unchanged does not significantly alter the excited state processes.

3.8.2. Quantitative analysis of BET

In order to get insight into differences in the electron transfer dynamics between the various cages, the decay traces of the features of the charge separated state were examined. Based on the preceding work on $[\mathrm{Pd}_2\mathbf{PTZ}_2\mathbf{FRO}_2]^{4+}$ and $[\mathrm{Pd}_2\mathbf{TAA}_2\mathbf{FRO}_2]^{4+}$ and on the qualitative analysis, three parallel decay pathways can be assumed: “BET1” corresponds to the decay of the LMCT state and occurs within around 1 ps. “BET2” and “BET3” were assigned to recombination of LLCS state with D and A sitting in *cis*- and *trans*-position and have lifetimes of around 100 ps and > 1 ns, respectively (Fig. 27a). Owing to the accessible time window of up to 800 ps, it is not possible to reliably resolve the slow BET3 dynamics. Therefore, the focus lies first on deciphering relationships between thermodynamics and kinetics for BET2; afterwards, the kinetics for BET1 will be examined.

In the first step, single-wavelength fitting was carried out for multiple decay traces across whole probe range. More precisely, the decay traces were fitted to exponential decay function 4:

$$A = A_0 \cdot e^{-\frac{1}{273\,\mathrm{fs}}} + A_{\mathrm{BET1}} \cdot e^{-\frac{t}{\tau_{\mathrm{BET1}}}} + A_{\mathrm{BET2}} \cdot e^{-\frac{t}{\tau_{\mathrm{BET2}}}} + A_{\mathrm{BET3}} \tag{4}$$

The first component corresponds to the IRF, the second to BET1, the third to BET2 while BET3 is treated as a constant owing to its large lifetime. For confining the analysis to BET1 and BET2, the decay traces were fitted up to a time delay of 400 ps. Inclusion of longer time delays would result in a bias of the lifetime of BET2 to larger values without adding further information. Next, the thus obtained results were used as starting points for global analysis whereby a parallel two component exponential decay model was used. The thereby obtained lifetimes τ_{BET2} range from 51 ps for $[\mathrm{Pd_2}\mathbf{TAA}_2\mathbf{NDI}_2]^{4+}$ (cage with the smallest driving force for BET) to 145 ps for $[\mathrm{Pd_2}\mathbf{TAA}_2\mathbf{FRO}_2]^{4+}$ (cage with the second largest driving force for BET) and are overall in great accordance with the time scales obtained by the group of Prof. Schwarzer. Furthermore, the lifetimes roughly trend in the order $[\mathrm{Pd_2D_2}\mathbf{NDI}_2]^{4+} < [\mathrm{Pd_2D_2}\mathbf{PMDI}_2]^{4+} < [\mathrm{Pd_2D_2}\mathbf{FRO}_2]^{4+}$ for a series of cages with the same donor ligand. Considering the overall driving forces (i.e. cages with **TAA** donor have a smaller driving force for BET than cages with **PTZ** donor), the rough trend that an increase in exergonicity is accompanied by a decrease in the rate constant is obtained, suggesting observation of the Marcus-inverted region effect (Fig. 27b).

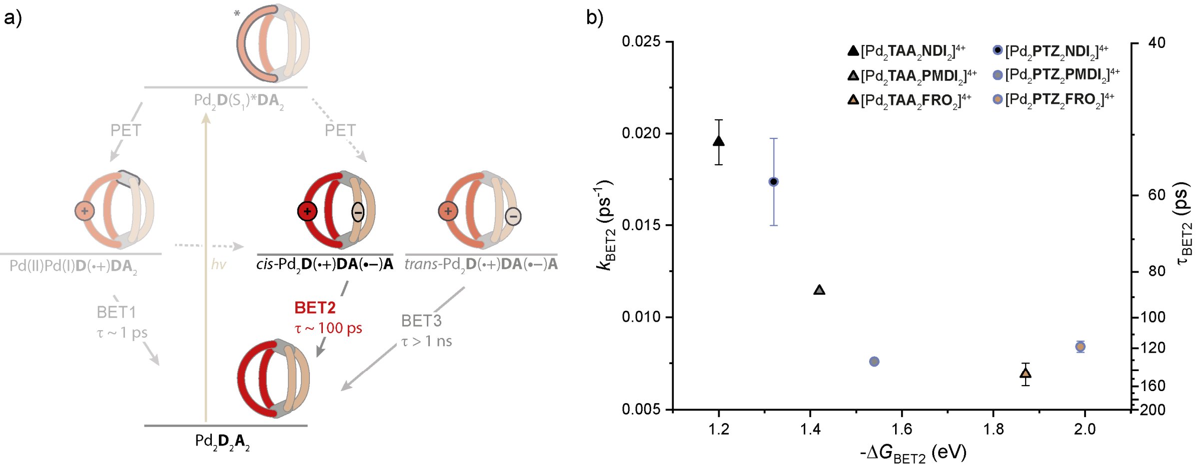

Fig. 27 Kinetics of BET2 (assigned to *cis*-ligand-to-ligand electron transfer): a) schematic overview of the photoinduced processes in *cis*-$\mathrm{Pd_2D_2A_2}$-type cages; b) plot of the rate constant k_{BET2} against the thermodynamic driving force for BET2.

The most significant deviation from this trend is the rate constant for $[\mathrm{Pd_2}\mathbf{PTZ}_2\mathbf{FRO}_2]^{4+}$ which is larger than the one for the corresponding cage with **TAA** donor, while the former cage possesses a larger driving force. For the herein investigated range of driving forces, that is $\Delta G_{\mathrm{BET2}} \leq -1.2$ eV i.e. highly exergonic processes, the inverted region is commonly observed.[25,27,30,31] In the reported systems, the rate constants usually differ by one order of magnitude or more while they are quite similar in the system herein investigated. This makes the overall trend more susceptible for errors in the fitting that can be traced back to mixing-in of the dynamics of the two other BET processes.

This error is not captured in the standard deviation depicted in the graph in figure 27b, which represents the divergence of the values obtained from two separate measurements. Moreover, the electron transfer rate constant can also be affected by the reorganization energy and electronic coupling, which might not be the same for the six cages studied. Therefore, the trend should be viewed with caution.

Single-wavelength fitting followed by global analysis of the decay traces up to 400 ps also provides insight into the dynamics of the decay of the LMCT state (BET1) (Fig. 28a). As it is assumed that the donor ligand but not the acceptor ligand is directly involved in this process, the decay traces of cages carrying the same acceptor but a different donor were compared (Fig. 28c-e). Strikingly, across cages with different acceptor ligands, the dynamics at early time delays are much faster for cages carrying a **TAA** donor as compared to the ones carrying a **PTZ** donor. This is also reflected in the rate constants/lifetimes obtained by global analysis (Fig. 28b): for cages with **TAA** donor, the lifetimes range between 0.4 and 0.6 ps while they range between 1.7 and 2.6 ps for cages with **PTZ** donor. Assuming a charge separated state (PdPd(I)$D^{\cdot+}DA_2$), the driving force for BET1 can be approximated with the halfwave potential of the donors and the computationally obtained orbital energy level of Pd(II) (Tab. 6). This yields $\Delta G_{BET1} = -2.33$ eV for cages with **TAA** donor and $\Delta G_{BET1} = -2.46$ eV for cages with **PTZ** donor. Hence, similar to what has been observed for the thermodynamics-kinetics relationship of BET2, an increase in driving force is accompanied by a deceleration of the electron transfer. In both series [Pd$_2$**PTZ**$_2$A$_2$]$^{4+}$ and [Pd$_2$**TAA**$_2$A$_2$]$^{4+}$ (A = **NDI**, **PMDI**, **FRO**), it is observed that cages with **NDI** acceptor decay faster than cages with **PMDI** acceptor and those faster than the ones with **FRO** acceptor. While an influence of the acceptor ligand on BET1 cannot be excluded (slightly varying conformation and redox potentials) it is probable that the small trend is due to mixing-in of the BET2 dynamics in the obtained rate constant for BET1.

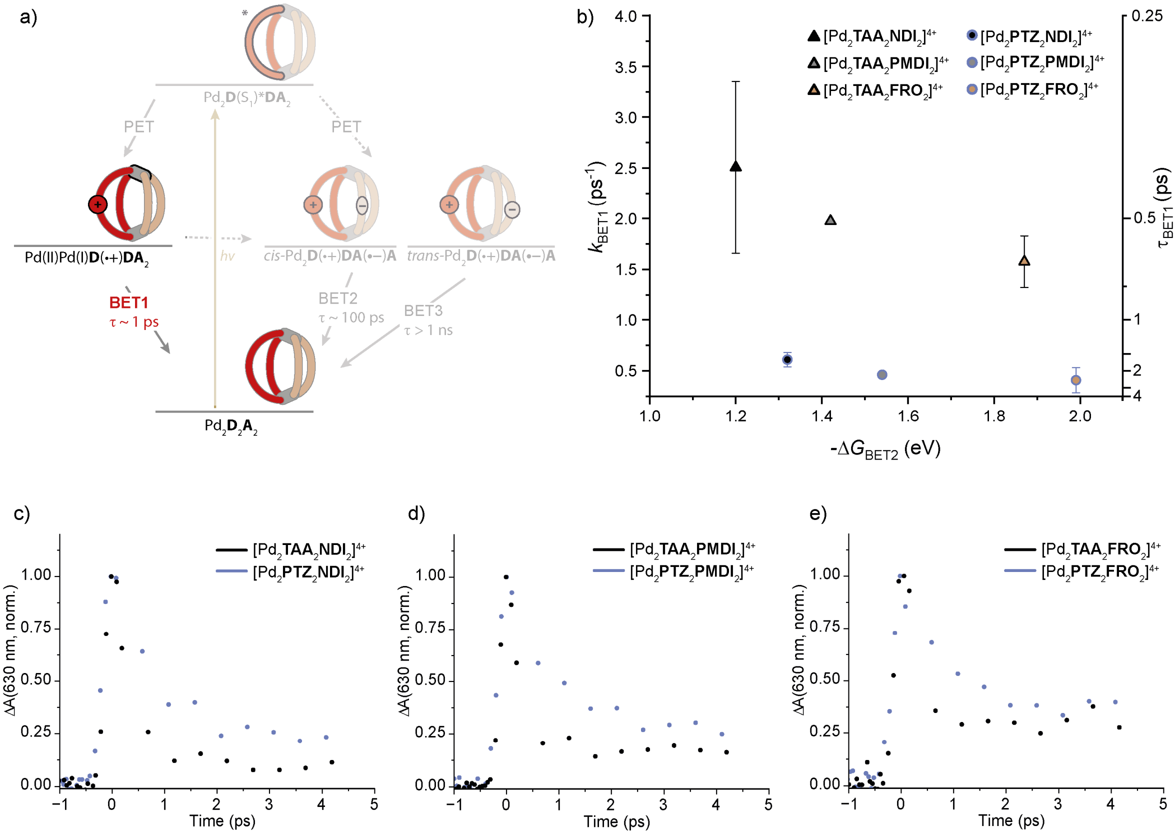

Fig. 28 Kinetics of BET1 (decay of the LMCT state): a) schematic overview of the photoinduced processes in *cis*-$Pd_2D_2A_2$-type cages; b) plot of the rate constant k_{BET1} against the thermodynamic driving force for BET2; c-e) decay traces at 630 nm for c) $[Pd_2D_2$**NDI**$_2]^{4+}$, d) $[Pd_2D_2$**PMDI**$_2]^{4+}$, and e) $[Pd_2D_2$**FRO**$_2]^{4+}$.

3.9. Transient absorption spectroscopy: $[Pd_2$**CBZ**$_2A_2]^{4+}$

Transient absorption spectroscopy on the homoleptic assemblies and donor-acceptor cages $[Pd_2$**CBZ**$_2A_2]^{4+}$ was carried out in collaboration with Dr. Robert Naumann (group of Prof. Katja Heinze, JGU Mainz). Importantly, the used instrument allowed tuning the excitation wavelength ($\lambda \geq 320$ nm), accessing a wide probe window (350-900 nm, 1150-1600 nm), as well as long time delays (fs-ms). Dr. Robert Naumann performed the experiments and processed and fitted the data; the data interpretation was carried out in collaboration.

Pump-pulse excitation of the **NDI** ligand leads to bleaching of the ground state absorption at $\lambda < 400$ nm concomitant with the rise of excited state absorption at 455 and 595 nm (see 150 fs transient, Fig. 29a). This initial spectrum, which can be assigned to the **NDI** singlet excited state,[32] is shorted-lived and transforms into a spectrum with a dominant feature at 470 nm and another feature at 620 nm, resembling the spectrum of the electrochemically generated **NDI** radical anion (Fig. 17). This indicates that a state with charge transfer character is formed. After 100 ps, this state is completely transformed into a triplet state with characteristic features at 454 and 484 nm (Fig. 29a, inset). A similar excited state decay pathway was also observed for a *N*-phenyl,*N*'-alkyl-NDI derivative.[32] For the homoleptic assemblies of **NDI**, photoexcitation is followed by population of the singlet excited state (460, 595 nm), which transforms quickly into a state with peaks at 470 and 605 nm. At long time delays (see transient at 2 ns), solely the features of the **NDI** triplet state remain. While the spectra of ligand and homoleptic assemblies indicate that similar excited states are populated, their dynamics vary. The decay of the absorbance at 595 nm between 1-50 ps is much slower for the free ligand than for the homoleptic assemblies (Fig. 29c). Assuming that this transition majorly corresponds to the transformation of the state with charge transfer character into the triplet state, this observation might be explained by the promotion of ISC through spin-orbit coupling owing to the presence of Pd(II) (heavy atom effect).

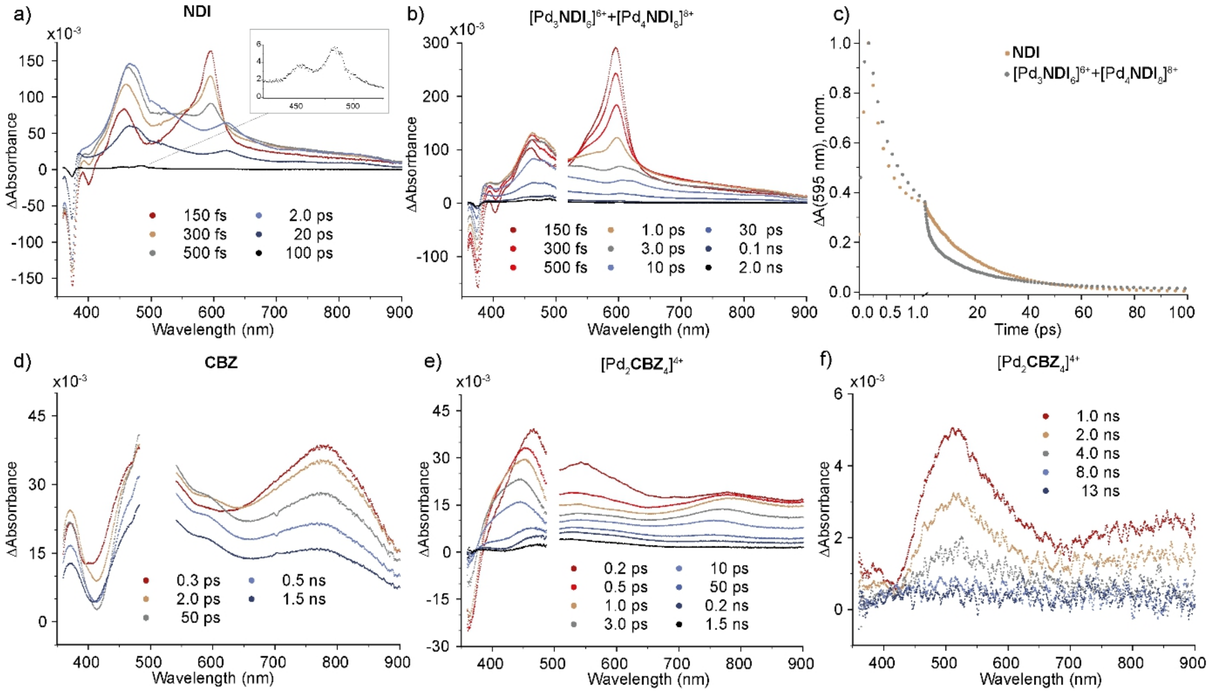

Fig. 29 a) fs-ns Transient difference spectra of ligand **NDI**; b) fs-ns transient difference spectra of $[Pd_3\textbf{NDI}_6]^{6+}$+$[Pd_4\textbf{NDI}_8]^{8+}$; c) decay traces for $\lambda = 595$ nm of **NDI** (beige) and $[Pd_3\textbf{NDI}_6]^{6+}$+$[Pd_4\textbf{NDI}_8]^{8+}$ (gray); d) fs-ns transient difference spectra of ligand **CBZ;** e) fs-ns transient difference spectra of $[Pd_2\textbf{CBZ}_4]^{4+}$; f) sub-ns transient difference spectra of $[Pd_2\textbf{CBZ}_4]^{4+}$; solvent: CH_3CN (a-d), DMSO (e,f), $\lambda_{ex} = 350$ nm.

Photoexcitation of the homoleptic assembly of ligand **PMDI** results in an intense transient absorption feature at 680 nm with a shoulder at 630 nm as well as in a small feature at 420 nm (appendix, section 3.11.9). At a time delay of 2 ns, these absorption features decayed. Presumably, this spectrum can be assigned to the **PMDI** excited singlet state. The free ligand was not investigated owing to its low solubility in acetonitrile. For ligand **FRO**, electronic excitation produces transients with a high intensity feature at 570 nm, shoulders at 460 and 655 nm, and another feature at 360 nm. This spectrum can be assigned to the **FRO** excited singlet state[33] and is in accordance with the investigations of the group of Prof. Schwarzer (section 3.2). In this work here, longer time delays were accessed which showed that the decay of the excited singlet state is over after 50 ns. Furthermore, the homoleptic assemblies of **FRO** were investigated under similar conditions. Up to a time delay of around 15 ns, the transient difference spectra are dominated by the singlet excited state decay, similar to what has been observed for the free ligand. However, after 50 ns, a spectrum with a feature at 490 nm remains. The long lifetime in combination with the fact that it is only observed in the presence of Pd(II) hints towards the formation of a triplet state.

Pump pulse excitation of ligand **CBZ** produces transient difference spectra with peaks at 370 nm, at around 500 nm with a shoulder at 590 nm, as well as at > 700 nm (Fig. 29d). Furthermore, an absorption feature tails into the NIR (appendix, section 3.11.9). This state lives for > 5 ns and can probably be assigned to the excited singlet state of the **CBZ** ligand, in accordance with the observation of steady state fluorescence (section 3.5). At longer time delays (e.g. 15 ns, 1 µs, see appendix, section 3.11.9), broad absorption between 450 nm and 700 nm remains which might be assignable to a triplet state. An overlap of the features of singlet and triplet state of phenyl carbazole has been reported in the literature.[34] Homoleptic cage $[Pd_2\textbf{CBZ}_4]^{4+}$ has been investigated in DMSO owing to its insufficient stability in acetonitrile (appendix, section 3.11.3). Directly after photoexcitation, the Pd(II)-bound **CBZ** shows excited state absorption at 470, 540, and 780 nm (Fig. 29e) as well as in the NIR (appendix, section 3.11.9). The features in the visible region differ from the ones of the free ligand and all features (including the one in the NIR) decay quickly, giving rise to a different spectrum within around 1 ps. More precisely, broad absorption between 400 and 500 nm and another feature at 770 nm are observed. This spectrum is somewhat reminiscent of the spectrum of the **CBZ** radical cation (Fig. 30c,f), indicating that a state with pronounced charge transfer character is populated. At longer time delays (> 0.2 ns, Fig. 29e,f), a feature at 510 nm and a broad feature at > 700 nm is observed that decay within a few ns. Hence, compared to the free ligand the excited state dynamics in the Pd(II) assembly are more complex and the decay is overall quicker, presumably due to the population of state(s) with charge transfer character.

Next, the processes following photoexcitation of the donor-acceptor cages with λ_{ex} = 350nm were investigated. In the case of [Pd$_2$**CBZ**$_2$**NDI**$_2$]$^{4+}$, bleaching of the cage's ground state absorption in the near UV region is observed at early time delays (Fig. 30a). Positive features at 450, 550 (broad), 780 nm arise and can be traced back to the excited state of the Pd(II)-bound **CBZ** ligand. The comparably sharp feature at 595 nm shows that the **NDI** ligand is simultaneously photoexcited. At around 450 nm, the features of both species overlap. Overall, the spectra at early time delays are in great accordance with what has been observed for the corresponding homoleptic assemblies. Within less than a ps, a new spectrum arises which closely resembles the superposition of the spectra of the electrochemically oxidized **CBZ** and reduced **NDI** (Fig. 30c), evidencing that ligand-to-ligand charge separation occurred. More precisely, the 595 nm feature of the **NDI** ligand red shifts to 602 nm and the 780 nm feature of the **CBZ** ligand blue shifts to 725 nm. Moreover, the broad feature of **CBZ**$^{\cdot+}$ at 425 nm and the comparably sharp feature of **NDI**$^{\cdot-}$ at 470 nm overlap between 400 and 500 nm. Additionally, a feature at 840 nm corresponding to **CBZ**$^{\cdot+}$ arises. In the NIR, a band at around 1500 nm is observed (appendix, section 3.11.9). A small portion of the LLCS state lives for > 1 µs (Fig. 30b). Global fitting of the data to a sequential decay model yielded the time constants τ_1 < 100 fs, τ_2 = 780 fs, τ_3 = 15.2 ps, τ_4 = 135 ps, τ_5 = 16.3 ns, τ_6 = 0.4 µs, and τ_7 = 7.3 µs. The evolution associated decay spectra (EADS) of components 3, 4, 5, 6, and 7 closely resemble the features of the LLCS state (appendix, section 3.11.9). Time constants τ_3-τ_7 describe therefore the decay of the LLCS state.

After pump-pulse excitation, the transient difference spectra of [Pd$_2$**CBZ**$_2$**PMDI**$_2$]$^{4+}$ are dominated by the excited state absorption of the Pd(II)-bound **CBZ** ligand at 455, 525, and 780 nm (Fig. 30d, compare to Fig. 29e). Furthermore, the characteristic absorption of the **PMDI** radical anion at 720 nm is visible. The **PMDI** does not absorb at the excitation wavelength suggesting that the **PMDI** radical anion formed through charge transfer from the **CBZ** donor ligand within less than 200 fs. After 0.5 ps, the fraction of cages that underwent LLCS increased, giving rise to absorption between 400 and 500 nm (stemming from both, **CBZ**$^{\cdot+}$ and **PMDI**$^{\cdot-}$), 655 and 720 nm (**PMDI**$^{\cdot-}$), as well as 730 nm (**CBZ**$^{\cdot+}$). Due to the transition of the excited state of the Pd(II)-bound **CBZ** into the **CBZ** radical cation, the 780 nm feature blue shifts within the first ps. After 1 ps, this peak completely overlaps with the feature of **PMDI**$^{\cdot-}$. The spectral features decay on the time constants τ_1 < 100 fs, τ_2 = 500 fs, τ_3 = 2 ps, τ_4 = 150 ps, τ_5 = 1.6 ns, and τ_6 = 1 µs.

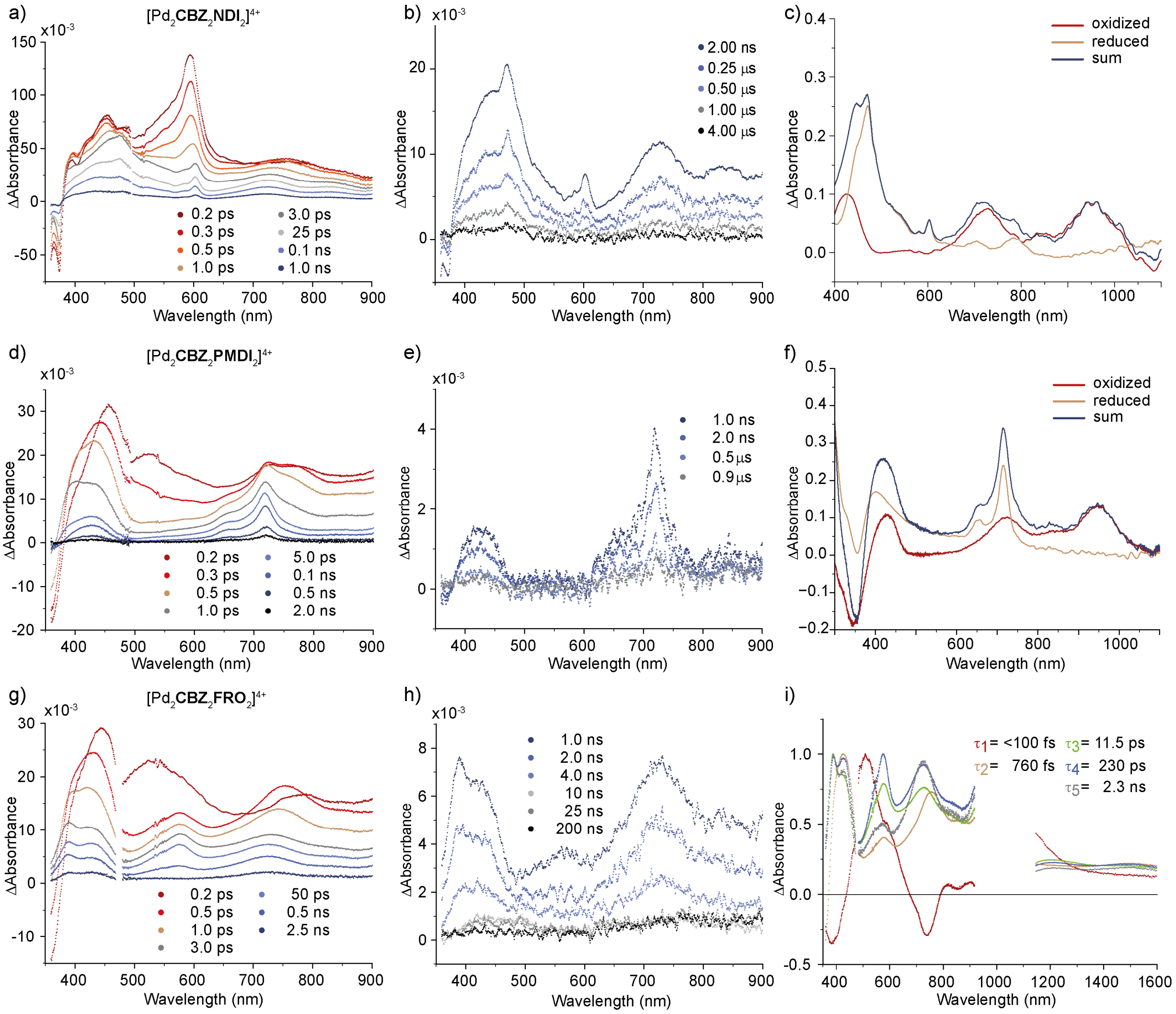

Fig. 30a,b) Selected transient difference spectra of [Pd$_2$**CBZ**$_2$**NDI**$_2$]$^{4+}$(a) fs-ns, b) ns-µs); c) spectra of electrochemically oxidized [Pd$_2$**CBZ**$_2$**NDI**$_2$]$^{4+}$ and reduced ligand **NDI**; d,e) selected transient difference spectra of [Pd$_2$**CBZ**$_2$**PMDI**$_2$]$^{4+}$(d) fs-ns, e) ns-µs); f) spectra of electrochemically oxidized and reduced [Pd$_2$**CBZ**$_2$**PMDI**$_2$]$^{4+}$; g,h) selected transient difference spectra of [Pd$_2$**CBZ**$_2$**FRO**$_2$]$^{4+}$ (g) fs-ns, h) ns-µs); i) fs-ns EADS of [Pd$_2$**CBZ**$_2$**PMDI**$_2$]$^{4+}$ (solvent: CH$_3$CN, λ_{ex} = 350 nm).

The transient of [Pd$_2$**CBZ**$_2$**FRO**$_2$]$^{4+}$ 200 fs after pump-pulse excitation shows the characteristic features of the Pd(II)-bound **CBZ** donor ligand in its excited state (445, 525, 780 nm, Fig. 30g). At a time delay of 500 fs, the LLCS state formed: aside from the characteristic features of **CBZ**$^{\cdot+}$ (425, 730 nm), the feature of the **FRO** radical anion appears at 575 nm. Fitting of the spectral features yielded the time constants $\tau_1 < 100$ fs, $\tau_2 = 760$ fs, $\tau_3 = 11.5$ ps, $\tau_4 = 230$ ps, $\tau_5 = 2.3$ ns, and $\tau_6 = 0.8$ µs and the corresponding EADS for the fs-ns components are shown in figure 30i. Comparison of the spectra of the different components reveals that the intensity of the feature at 575 nm (**FRO**$^{\cdot-}$) decays faster as compared to the feature at 730 nm (**CBZ**$^{\cdot+}$) (compare the EADS of components 3 and 4, where the ratio of the two bands is nearly equal, with components 5). For the µs component, the feature of **FRO**$^{\cdot-}$ is then absent. This cannot be explained by intramolecular charge recombination of the LMCT and the LLCS states only.

Overall, for all three investigated donor-acceptor cages, the population of the electronically excited state is followed by ultrafast electron transfer from the **CBZ** donor to the acceptor ligand. The features of the radical ions decay on various time constants ranging from picoseconds to microseconds. Since the two different intramolecular ligand-to-ligand charge recombination processes (**CBZ**$^{\cdot+}$ and A$^{\cdot-}$ sitting in *cis*- and *trans*-position) as well as possible intermolecular charge recombination between **CBZ**$^{\cdot+}$ and A$^{\cdot-}$ give rise to the same features, the assignment of the rate constants is ambiguous. Intramolecular charge recombination is expected to occur fast and with high efficiency owing to the close proximity of the radical ions. Comparing the intensity of the characteristic acceptor radical anion features in [Pd$_2$**CBZ**$_2$**PMDI**$_2$]$^{4+}$ and [Pd$_2$**CBZ**$_2$**FRO**$_2$]$^{4+}$ reveals that after 0.5 ns, approximately 85% of the LLCS state has already decayed ([Pd$_2$**CBZ**$_2$**PMDI**$_2$]$^{4+}$: ΔA(720 nm, 0.3 ps) = 18.2, ΔA(720 nm, 0.5 ns) = 3.5; ([Pd$_2$**CBZ**$_2$**FRO**$_2$]$^{4+}$: ΔA(575 nm, 0.2 ps) = 20.0, ΔA(575 nm, 0.5 ns) = 3.2; for [Pd$_2$**CBZ**$_2$**NDI**$_2$]$^{4+}$, the features of excited and LLCS state overlap more). Consequently, the picosecond dynamics and possibly also the nanosecond dynamics are highly efficient and presumably stem from intramolecular charge recombination. The lifetime of the dynamic with $\tau \sim 100$ ps (earlier “BET2”, assigned to *cis*-BET) increases in the order τ([Pd$_2$**CBZ**$_2$**NDI**$_2$]$^{4+}$) = 135 ps < τ([Pd$_2$**CBZ**$_2$**PMDI**$_2$]$^{4+}$) = 150 ps < τ([Pd$_2$**CBZ**$_2$**FRO**$_2$]$^{4+}$) = 230 ps in agreement with the increasing driving force. Assuming that the difference in reorganization energy and electronic coupling is small between the cages, this observation supports again that the process lies within the Marcus inverted region. Moreover, these values are in great accordance with the lifetimes of the cages with **TAA** or **PTZ** donor (Fig. 31).

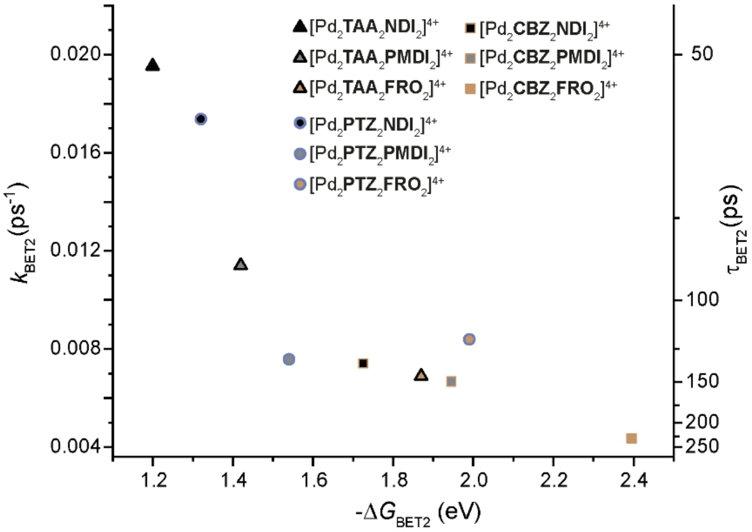

Fig. 31 Plot of the rate constant k_{BET2} and the lifetime τ_{BET2} (reciprocal scale) against the driving force ΔG_{BET2} for *cis*-BET.

In the works on cages with **TAA** and **PTZ** donor ligands, the ~ 1 ns component (“BET3”) was assigned to *trans*-BET. The rate constant was, however, not resolved with certainty owing to the limited time window. Now, having the rate constant k_{BET3} at hand, the damping factor β can be calculated. The damping factor is a measure for the distance-dependence of the electron transfer rate constant. The calculation was carried out with equation 5, assuming that the super exchange mechanism predominates (see below for discussion).[12] The distances d_{cis} and d_{trans} between donor and acceptor were obtained from the DFT models (appendix, section 3.11.8).

$$\frac{k_{\mathrm{BET3}}}{k_{\mathrm{BET2}}} = e^{-\beta(d_{\mathrm{trans}} - d_{\mathrm{cis}})} \tag{5}$$

For cages [Pd$_2$**CBZ**$_2$**PMDI**$_2$]$^{4+}$ and [Pd$_2$**CBZ**$_2$**FRO**$_2$]$^{4+}$, the damping factors 0.76 Å^{-1} and 0.98 Å^{-1} are obtained, respectively. This is a realistic factor considering that Miller and Closs determined a damping factor of 1.01 Å^{-1} for their organic donor-bridge-acceptor system.[35] Hence, the assignment of the dynamic to *trans*-BET is reasonable. The rate constants obtained for the excited state dynamics of cage [Pd$_2$**CBZ**$_2$**NDI**$_2$]$^{4+}$ were not considered here since fitting did not yield a dynamic with a ~ 1 ns lifetime. Owing to concomitant excitation of donor and acceptor in this cage, a larger number of processes occur simultaneously, making the assignment more challenging. The distance-dependence holds also for the forward photoinduced electron transfer; hence, it can be expected that a larger fraction of photoexcited cages undergoes the faster *cis*- as compared to the slower *trans*-PET. The observation that around 85% of the LLCS states have recombined after 0.5 ns therefore further supports that the BET2 dynamic can be assigned to *cis*-BET. The processes with longer lifetimes (~1 µs) are inefficient and might be assignable to bimolecular processes, e.g. the recombination of disproportionated charge separated cages.

Two mechanisms, that represent boundary scenarios, are commonly used for describing electron transfer in donor-bridge-acceptor systems.[36–38] In the incoherent hopping mechanism, the vacant states of the bridge are energetically close to the ones of donor or acceptor and are hence thermally accessible. Therefore, electron transfer occurs stepwise and intermediates carrying an oxidized or reduced bridge moiety (depending on whether the electron transfer is of oxidative or reductive nature) can in principle be observed experimentally. By contrast, the coherent superexchange mechanism predominates when the electronic states of the bridge are energetically separated from the states of the donor and acceptor moieties. The bridge is involved in the electron transfer in the sense that it mediates the coupling between donor and acceptor. For the superexchange mechanism, the electron transfer rate usually decreases exponentially with increasing distance. In contrast, the distance-dependence for electron hopping is typically much weaker. Assignment to one of the two mechanisms can be carried out based on the distance-dependence and/or based on the relative energy levels of the bridge, donor, and acceptor. For the herein described back electron transfer in $[Pd_2D_2A_2]^{4+}$ systems, in which the Pd(II) nodes can be regarded as bridges, only rates for two different distances are available (for intramolecular electron transfer). Resorting to the relative energy levels is therefore advisable. For the hopping mechanism, two electron transfer processes must be thermodynamically feasible: electron transfer from the organic acceptor radical anion to the Pd(II) node ($\mathbf{A}^{\cdot-} \rightarrow$ Pd(II)) as well as from Pd(I) to the donor radical cation (Pd(I) $\rightarrow \mathbf{D}^{\cdot+}$). The second step corresponds to the recombination of the LMCT state and is thermodynamically favored as discussed in section 3.8.2. The first step, however, would be thermodynamically unfavored as the electron affinity of the organic acceptor augments the one of the Pd(II) node ($\Delta(E_{LUMO,Pd(II)} - E_{LUMO,A}) \geq 0.5$ eV, Tab. 6). For the superexchange mechanism, the overall process, i.e. $\mathbf{A}^{\cdot-} \rightarrow \mathbf{D}^{\cdot+}$ must be thermodynamically favored, which is the case (Tab. 5). Based on these considerations, the recombination of the LLCS states is tentatively assigned to the coherent superexchange mechanism which justifies the usage of the exponential distance dependence of the electron transfer rate in equation 5.

3.10. Conclusion and outlook

The SCA strategy was used as a modular approach for accessing a library of nine donor-acceptor cages, possessing the same stoichiometry and stereoconfiguration (*cis*-$Pd_2D_2A_2$) but differing in their (photo)redox active backbones. The structures, ground state photophysical and electrochemical properties were fully characterized. The latter unveiled that the donor and acceptor moieties remain largely independent from each other in the electronic ground state. Furthermore, the thermodynamic driving forces for the forward, photoinduced electron transfer and for the back electron transfer were approximated based on the singlet excited state energies and the half-wave potentials. The processes are exergonic for all cages and differ by up to 1.2 eV – a range in which differences in the electron transfer rate constants can be expected. Insight into the excited state dynamics of the cages was gained by applying pump-probe transient absorption spectroscopy on the femtosecond and nanosecond timescale. Comparison of the transient difference spectra and the spectra of the electrochemically generated cages with oxidized donor or reduced acceptor moieties evidence that ligand-to-ligand electron transfer occurred within all cages. The LLCS state decays on multiple time scales, whereby a time constant of around 100 ps dominates. Excitingly, this dynamic trends with the thermodynamic driving force of the process: the higher the exergonicity, the slower is the charge recombination, indicating that the process falls within the Marcus inverted region. This will enable a more rational design of donor-acceptor cages in the future, for example for applications in photoredox catalysis or for the development of photoactive materials.

For a better understanding of the systems and for promoting their applicability, the following issues could be addressed in the future:

1) Despite the defined structure of the *cis*-$Pd_2D_2A_2$ cages, the different lifetimes of the LLCS state could not be assigned with certainty to a particular process. To gain deeper mechanistical insight, reference cages carrying only one donor and one acceptor sitting either in *cis*- or in *trans*-position could be synthesized by applying strategies for the design of $Pd_2L_2D_1A_1$ cages[13,39] as discussed in section 1.3.3. Importantly, the third ligand L should be innocent in terms of its photophysical and electrochemical properties for preventing interference with the excited state dynamics of the donor-acceptor couple.

2) A major drawback of the systems herein investigated is the formation of an LMCT state that competes with ligand-to-ligand electron transfer, hence reducing the efficiency of the latter. Since the LMCT state decays quickly, it is less attractive for applications. In order to reduce the probability for this process, closed shell metal ions such as Zn(II) could be used as metal nodes. For this, the challenge to develop new strategies and ligand designs for integrative self-sorting in cages bearing other metal centers than the well-studied square-planar Pd(II) must be faced.

3) Moreover, the strategies for the non-statistical self-assembly[13,39] could be used for combining more than two differentiable chromophores that are involved in the cage's excited state pathway. For example, a suitable antenna chromophore could be implemented into a third ligand. Photoexcitation of the latter would be followed by energy transfer to the electron donor, followed by charge separation as described here. This would represent a further step in the direction of the complex photosynthetic system. In order to allow for thorough analysis of the excited state dynamics, chromophores with little overlap of their excited state or radical absorption features should be chosen.

Further photoredox active ligands that could be incorporated in such multichromophore systems are based on BODIPY, diketopyrrolopyrrole, phenoxazine, and PDI, just to name a few. Moreover, it would be interesting to study the potential modulation of the excited state dynamics upon guest binding or changing the solvent.

4) Until now, the donor-acceptor cages have been investigated in solution, meaning that they are randomly oriented with respect to each other. This may be interesting for certain applications such as catalysis. Other applications rely on vectorial electron transfer, as is observed in the photosynthetic system. For achieving this, the donor-acceptor cages must be arranged in an organized fashion, for example through incorporation into vesicular materials (section 4), to ensure productive separation and further transport of the generated charges.[40,41]

3.11. Appendix

3.11.1. General methods

For information about NMR spectroscopic and mass spectrometric experiments see section 2.7. For some compounds, the number of signals in the ^{13}C NMR spectra is smaller than the number of non-equivalent carbon nuclei. This can probably be traced back to signal overlap or low signal intensity.

UV-Vis absorption spectroscopy

UV-Vis spectra were recorded on a DAD HP-8453 UV-Vis spectrometer. The step size was 1 nm. The cuvette pathlength and solvent are indicated below the spectra. The concentration of the compounds was determined by ^{1}H NMR using 1,3,5-trimethoxy benzene as internal standard.

Fluorescence spectroscopy

Fluorescence spectra were recorded on a Jasco FP-8300 fluorimeter. The cuvette pathlength was 4 mm and the step size 0.2 nm.

Cyclic voltammetry

Cyclic voltammograms were recorded using a Metrohm potentiostat PGSTAT101 and the NOVA electrochemistry software (Version 1.9) included in Metrohm Autolab. If not mentioned otherwise, a glassy carbon working electrode and a platinum wire counter electrode were used. The working electrode was polished regularly between the measurements using a polishing powder. As reference electrode Ag/AgNO$_3$ (in acetonitrile or DMSO with 0.1 M TBAPF$_6$) was used. All measurements were performed at room temperature. The samples were degassed via nitrogen purging before scanning at negative potentials. The samples were dissolved in the non-aqueous electrolyte solution (acetonitrile or DMSO with 0.1 M TBAPF$_6$) and filtered prior to the measurement. The concentration of the compounds was determined by ^{1}H NMR using 1,3,5-trimethoxy benzene as internal standard.

Spectroelectrochemistry

For the spectroelectrochemical studies, a thin layer quartz glass spectroelectrochemical cell kit from ALS Japan was used. The optical path length was 0.5 mm if not mentioned otherwise. A gold mesh electrode was used as working electrode. A platinum wire was used as counter electrode and a non-aqueous Ag/AgNO$_3$ (in acetonitrile or DMSO with 0.1 M TBAPF$_6$) as reference electrode. The compounds were oxidized or reduced by bulk electrolysis using the potentiostat PGSTAT101 and the NOVA electrochemistry software (Version 1.9) included in Metrohm Autolab. For the UV-Vis absorption measurements, an AvaLight Deuterium-Halogen light source (200 nm - 1000 nm) was used. For the conduction of the light to the spectroelectrochemical cell and to the DAD AVA-SPEC 2048 spectrometer, an optical fiber with a diameter of 200 µm was used. The data were recorded using AVASOFT 7.5 software. The spectra were smoothed using Origin 2023 software. The sample volume was 300 µL and before the application of negative potentials, the sample was degassed via nitrogen purging. The samples were dissolved in the non-aqueous electrolyte solution (acetonitrile or DMSO with 0.1 M TBAPF$_6$) and filtered prior to the measurement. The concentration of the compounds was determined by ^{1}H NMR using 1,3,5-trimethoxy benzene as internal standard or based on their extinction coefficients.

Transient absorption spectroscopy: $[Pd_2TAA_2A_2]^{4+}$ and $[Pd_2PTZ_2A_2]^{4+}$

The transient absorption spectroscopy setup consists of a regeneratively amplified Ti:Sapphire laser (Libra, Coherent, Santa Clara, CA) producing ~50 fs laser pulses centered around 800 nm at 5 kHz repetition rate. The pump arm consisted of a time-delayed second harmonically generated pulse filtered to 400 +/- 10 nm excitation (Thorlabs FBH400-10) operating at a power of 1 mW (400 nJ/pulse) via focusing the fundamental beam into a BBO crystal. The pump alternated shots at 2.5 kHz using an optically-gated chopper. The probe arm consisted of focusing the fundamental into an Ar-filled tube to generate a white light continuum, which was compressed via prisms and filtered to an effective probe pulse wavelength range of 450-680 nm (Thorlabs FGS600 colored glass filter). The probe arm was detected after non-collinear focusing with a home-built Czerny-Turner spectrograph and was detected with a CCD array (Aviiva EM2, Teledyne e2v) on a shot-to-shot basis. Each two consecutive laser shots were used to calculate the transient absorption spectrum at each time delay using $\Delta A = \log(I_{\text{pump off}}/I_{\text{pump on}})$. For each scan, 2500 transient absorption spectra were collected at each time delay across the transient absorption trace and further traces were repeated and averaged until good signal-to-noise was obtained. The overall instrument time resolution was determined to be 273 fs (cross correlation of 256 fs 400 nm pump and 92 fs white light probe) obtained via SFG-FROG. The measurements were performed with the cages in acetonitrile at OD(400 nm) ≈ 2. Prior to the measurements, the samples were degassed via nitrogen purging.

Transient absorption spectroscopy: $[Pd_2CBZ_2A_2]^{4+}$

fs-Transient absorption experiments were conducted using a Helios pump-probe setup from Ultrafast Systems paired with a regeneratively amplified 1030 nm laser (Pharos, Light Conversion, 1030 nm, < 190 fs, 2 mJ). The effective laser repetition rate of 1 kHz was set via an internal pulse picker. A small portion of the 1030 nm fundamental was directed to the optical delay line and was subsequently used to generate broadband probe light by focusing the beam onto a sapphire for measurements in the Vis/NIR range (450 nm-900 nm). In the UV/Vis spectral range (330 nm-500 nm) the second harmonic was focused onto a second sapphire instead of the fundamental. For measurements in the NIR range (1200-1600 nm), the 1030 nm beam was focused on a YAG crystal. The pump pulse was generated with an optical parametric amplifier (Apollo Y, Ultrafast Systems). ns-Transient absorption spectroscopy experiments were carried out using a modified version of the described fs-transient absorption spectroscopy setup. For this purpose, the Eos add-on has been employed, which uses a photonic crystal fiber-based supercontinuum laser as probe light source. In contrast to the fs measurements, the pump-probe time delay is controlled electronically with a time resolution of < 1 ns. The sample solutions were measured in a 1 mm quartz cuvette. To generate spectra that cover the whole spectral region from 350 nm to 900 nm, the UV/Vis and Vis/NIR part of the transient absorption spectra were recorded separately under identical conditions and were combined using the overlap of both datasets in the visible region (475 nm-525 nm). If not mentioned otherwise, the measurements were performed with the compounds in acetonitrile at OD ≈ 1 at the excitation wavelength. Prior to the measurements, the samples were degassed via argon purging.

3.11.2. Ligand synthesis

Ligands **PTZ**,[16] **PMDI**,[42] and **FRO**[15] were synthesized as reported. Ligands **CBZ** and **NDI**[13] were available in the laboratory.

Ligand **TAA**

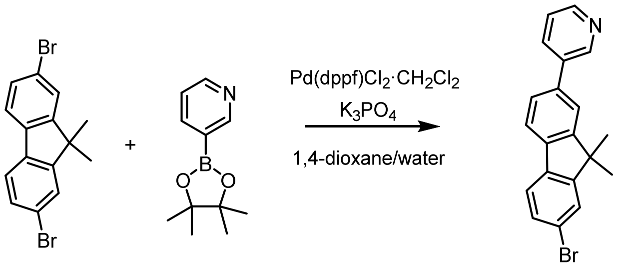

Scheme 1 First step of the synthesis of ligand **TAA**.

Pyridine boronic ester (0.697 g, 3.41 mmol, 1.0 eq.), 2,7-dibromo-9,9-dimethyl-9H-fluorene (3.610 g, 10.26 mmol, 3.0 eq.), and potassium phosphate K_3PO_4 (1.450 g, 6.83 mmol, 2.0 eq.) were combined with a mixture of dioxane and water (50 mL:20 mL) in a Schlenk flask. The solvent was then degassed via argon purging. The catalyst Pd(dppf)Cl_2·CH_2Cl_2 (0.278 g, 0.34 mmol, 0.1 equiv.) was added and after short degassing, the mixture was heated to 90 °C and stirred for 22 h. After cooling to room temperature, DCM was added and the reaction mixture was washed with water and brine. The organic phase was dried with $MgSO_4$, filtered, and concentrated by rotary evaporation. Purification of the crude product was carried out by column chromatography using ethyl acetate as eluent (0.966 g, 2.76 mmol, 81%).

^{1}H NMR (500 MHz, Chloroform-*d*) δ 8.94 (s, 1H), 8.64 (s, 1H), 8.00 (s, 1H), 7.80 (d, *J* = 6.4 Hz, 1H), 7.70 - 7.52 (m, 4H), 7.49 (dd, *J* = 8.0, 1.8 Hz, 1H), 1.54 (s, 6H).

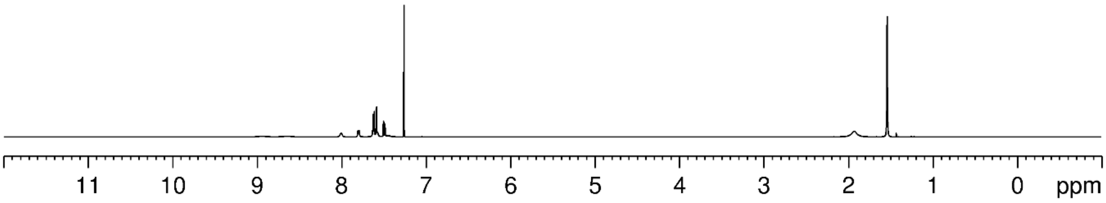

Fig. 32 Full ^{1}H NMR spectrum of the reaction product (500 MHz, 298 K, $CDCl_3$).

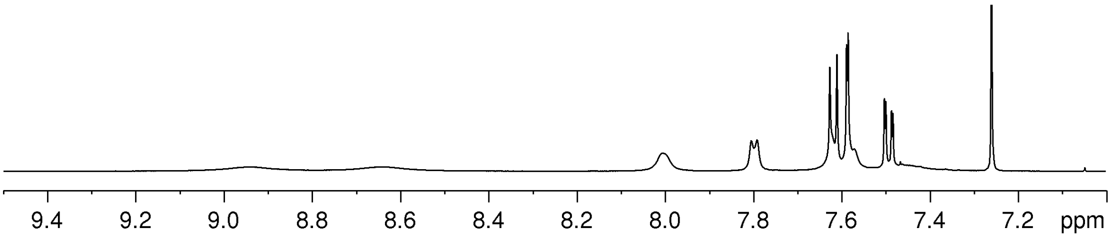

Fig. 33 Partial ^{1}H NMR spectrum of the reaction product (500 MHz, 298 K, $CDCl_3$).

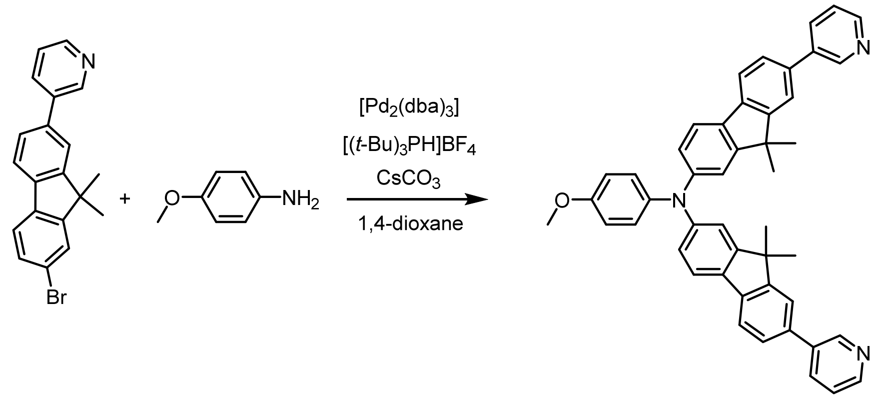

Scheme 2 Synthesis of ligand **TAA**.

p-Anisidine (21.88 mg, 177.66 mmol, 1.0 eq.), 3-(7-bromo-9,9-dimethyl-9H-fluorene-2-yl)pyridine (186.68 mg, 532.99 mmol, 3.0 eq.), caesium carbonate (158.75 mg, 487.23 mmol, 2.7 eq.), and tri-*tert*-butylphosphonium tetrafluoroborate (10.80 mg, 37.31 µmol, 0.2 eq.) were suspended in 1,4-dioxane (15 mL). The reaction mixture was degassed via argon purging. The catalyst tris-(dibenzylidenaceton)-dipalladium(0) (16.88 mg, 18.43 µmol, 0.1 eq.) was added, followed by short degassing. The reaction mixture was then heated to 90 °C and stirred for 16 h. After cooling to room temperature, DCM was added and the reaction mixture was washed with water and brine. The organic phase was dried with $MgSO_4$ and concentrated via rotary evaporation. The crude product was purified by column chromatography with ethyl acetate as eluent, followed by gel permeation chromatography with chloroform as solvent, yielding ligand **TAA** as brown solid (44.12 mg, 0.67 mmol, 38%). Owing to aggregation of the product in chloroform, the NMR spectroscopic characterization was carried out in acetonitrile and DMSO.

^{1}H NMR (500 MHz, DMSO-*d*$_6$) δ 8.98 (dd, *J* = 2.4, 0.9 Hz, 1H), 8.56 (dd, *J* = 4.8, 1.6 Hz, 1H), 8.15 (ddd, *J* = 8.0, 2.4, 1.6 Hz, 1H), 7.91 (d, *J* = 1.8 Hz, 1H), 7.83 (d, *J* = 7.9 Hz, 1H), 7.76 (d, *J* = 8.2 Hz, 1H), 7.70 (dd, *J* = 7.9, 1.7 Hz, 1H), 7.49 (ddd, *J* = 8.4, 4.7, 0.7 Hz,1H), 7.25 (d, *J* = 2.2 Hz, 1H), 7.16 (d, *J* = 8.9 Hz, 1H), 6.99 (d, *J* = 9.0 Hz, 1H), 6.92 (dd, *J* = 8.2, 2.1 Hz, 1H), 3.79 (s, 1H), 1.43 (s, 6H).

^{13}C NMR (176 MHz, CD_3CN) δ 156.49, 155.52, 149.26, 149.14, 148.90, 141.42, 139.99, 137.57, 136.80, 135.05, 133.40, 128.58, 127.16, 124.65, 122.75, 122.39, 122.02, 120.92, 117.99, 115.92, 56.12, 47.81, 27.19.

ESI MS: *m/z* calc. for [**TAA**]$^+$: 661.3088; found: 661.3090

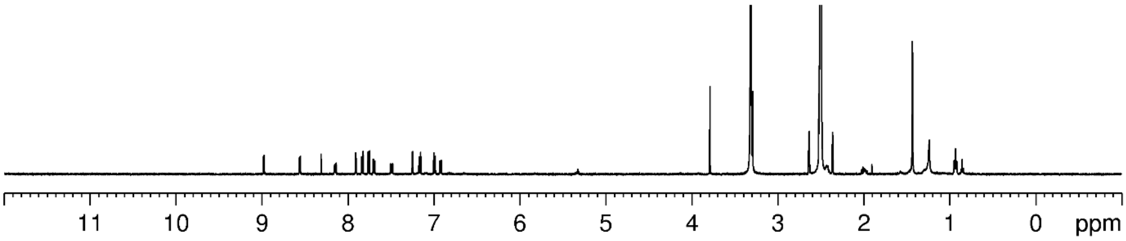

Fig. 34 Full ^{1}H NMR spectrum of ligand **TAA** (500 MHz, 298 K, DMSO-*d*$_6$).

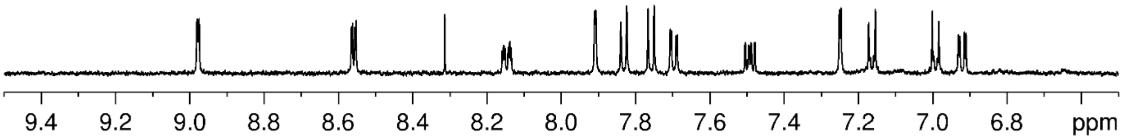

Fig. 35 Partial ^{1}H NMR spectrum of ligand **TAA** (500 MHz, 298 K, DMSO-*d*$_6$).

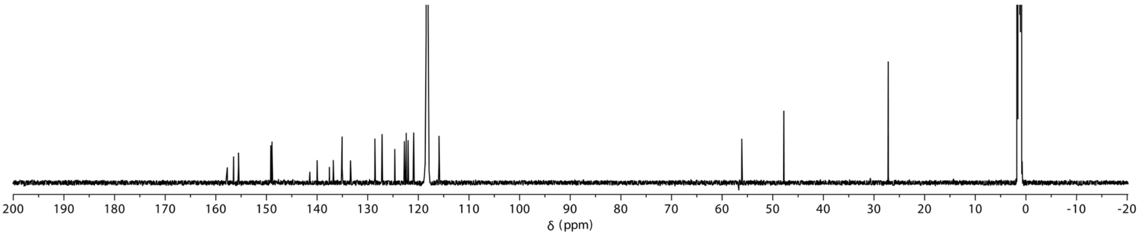

Fig. 36 ^{13}C NMR of ligand **TAA** (176 MHz, 298 K, CD$_3$CN). The data were acquired by Dr. Jacopo Tessarolo.

3.11.3. Self-assembly into cages

The self-assembly of the homoleptic cages [Pd$_2$**CBZ**$_4$]$^{4+}$ and [Pd$_2$**PTZ**$_4$]$^{4+}$ as well as of heteroleptic [Pd$_2$**CBZ**$_2$**NDI**$_2$]$^{4+}$, [Pd$_2$**CBZ**$_2$**PMDI**$_2$]$^{4+}$, [Pd$_2$**CBZ**$_2$**FRO**$_2$]$^{4+}$, [Pd$_2$**TAA**$_2$**NDI**$_2$]$^{4+}$, [Pd$_2$**TAA**$_2$**PMDI**$_2$]$^{4+}$, [Pd$_2$**PTZ**$_2$**NDI**$_2$]$^{4+}$, [Pd$_2$**PTZ**$_2$**PMDI**$_2$]$^{4+}$ is described here. The double cage [Pd$_4$**PTZ**$_8$]$^{8+}$ is published,[16] the heteroleptic cages [Pd$_2$**TAA**$_2$**FRO**$_2$]$^{4+}$ and [Pd$_2$**PTZ**$_2$**FRO**$_2$]$^{4+}$ were synthesized by Dr. Jacopo Tessarolo and Dr. Kai Wu (unpublished).

[Pd$_2$**CBZ**$_4$]$^{4+}$

A solution of ligand **CBZ** (500 µL, 2.8 mM, DMSO-*d*$_6$) was combined with a solution of [Pd(CH$_3$CN)$_4$](BF$_4$)$_2$ (50 µL, 15 mM, DMSO-*d*$_6$). The mixture was heated at 70 °C for one hour. For characterization in acetonitrile, the solvent was removed via lyophilization and the sample suspended in CD$_3$CN via sonication and heating at 70 °C for a short period of time (~ 5 min).

^{1}H NMR (500 MHz, CD$_3$CN) δ 9.32 (s, 1H), 8.76 (d, *J* = 1.7 Hz, 1H), 8.67 (dd, *J* = 5.8, 1.0 Hz, 1H), 8.36 (dt, *J* = 8.2, 2.2, 1.4 Hz, 1H), 8.00 (dd, *J* = 5.5, 2.0 Hz, 2H), 7.91 (dd, *J* = 5.5, 1.9 Hz, 2H), 7.75 (dd, *J* = 8.7, 1.9 Hz, 1H), 7.68 – 7.61 (m, 2H), 7.61 – 7.50 (m, 1.5H), 7.42 (d, *J* = 8.7 Hz, 1H).

^{1}H NMR (700 MHz, DMSO-*d*$_6$) δ 9.52 (s, 1H), 9.13 (d, *J* = 5.8 Hz, 1H), 8.88 (s, 1H), 8.53 (d, *J* = 8.1 Hz, 1H), 8.05 (d, *J* = 8.2 Hz, 2H), 8.00 (d, *J* = 8.1 Hz, 2H), 7.86 (dd, *J* = 8.0, 5.8 Hz, 1H), 7.80 (dd, *J* = 8.6, 1.8 Hz, 1H), 7.70 – 7.64 (m, 1H), 7.60 (d, 1.8 Hz, 1H), 7.57 – 7.52 (m, 0.5H), 7.40 (d, *J* = 8.6 Hz, 1H).

^{13}C NMR (176 MHz, DMSO-*d*$_6$) δ 149.87, 148.73, 141.53, 140.59, 138.77, 138.03, 136.36, 132.42, 130.90, 130.26, 127.47, 127.31, 126.75, 125.86, 124.20, 123.50, 118.42, 118.08, 110.45.

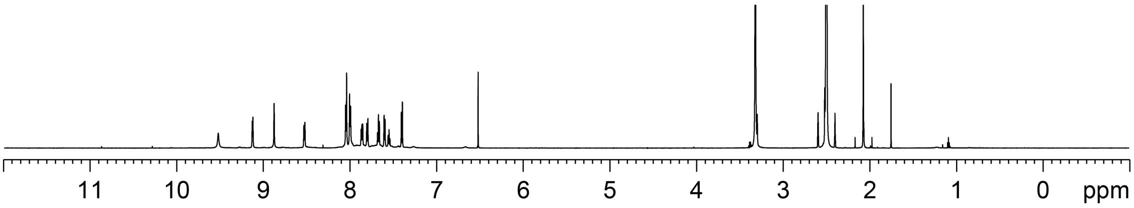

Fig. 37 Full ^{1}H NMR spectrum of [Pd$_2$**CBZ**$_4$]$^{4+}$ (700 MHz, 298 K, DMSO-*d*$_6$).

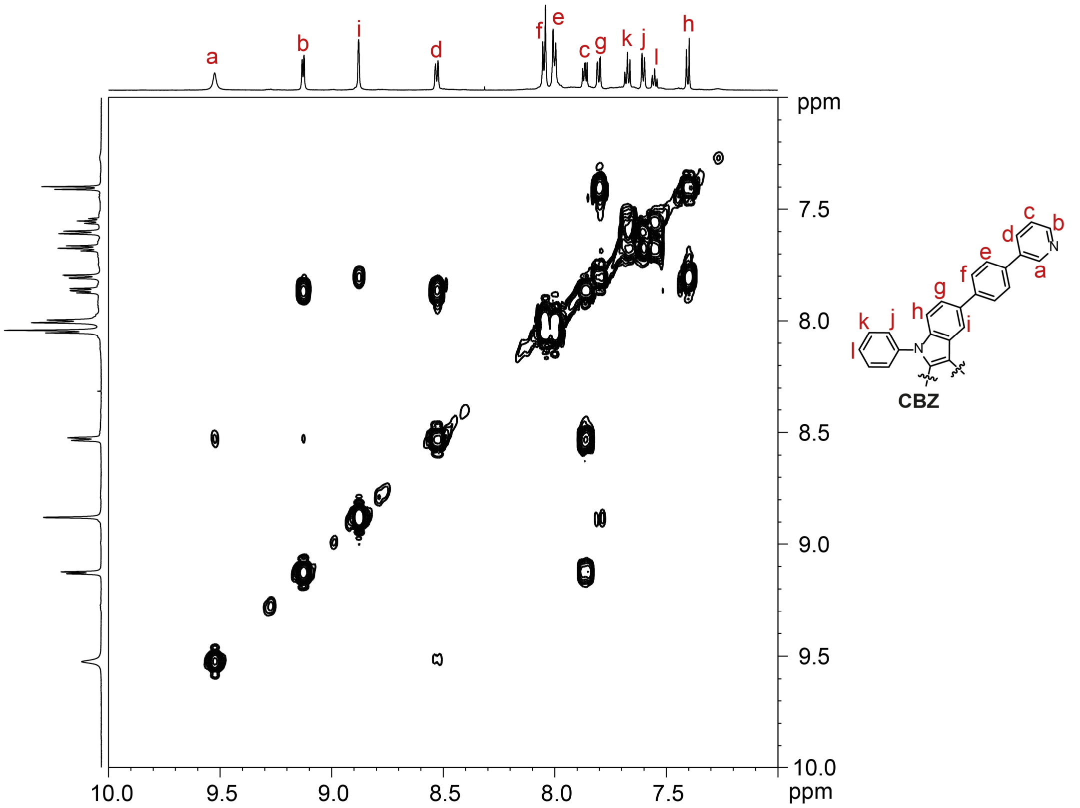

Fig. 38 ^{1}H-^{1}H COSY NMR spectrum of [Pd$_2$**CBZ**$_4$]$^{4+}$ (700 MHz, 298 K, DMSO-d_6).

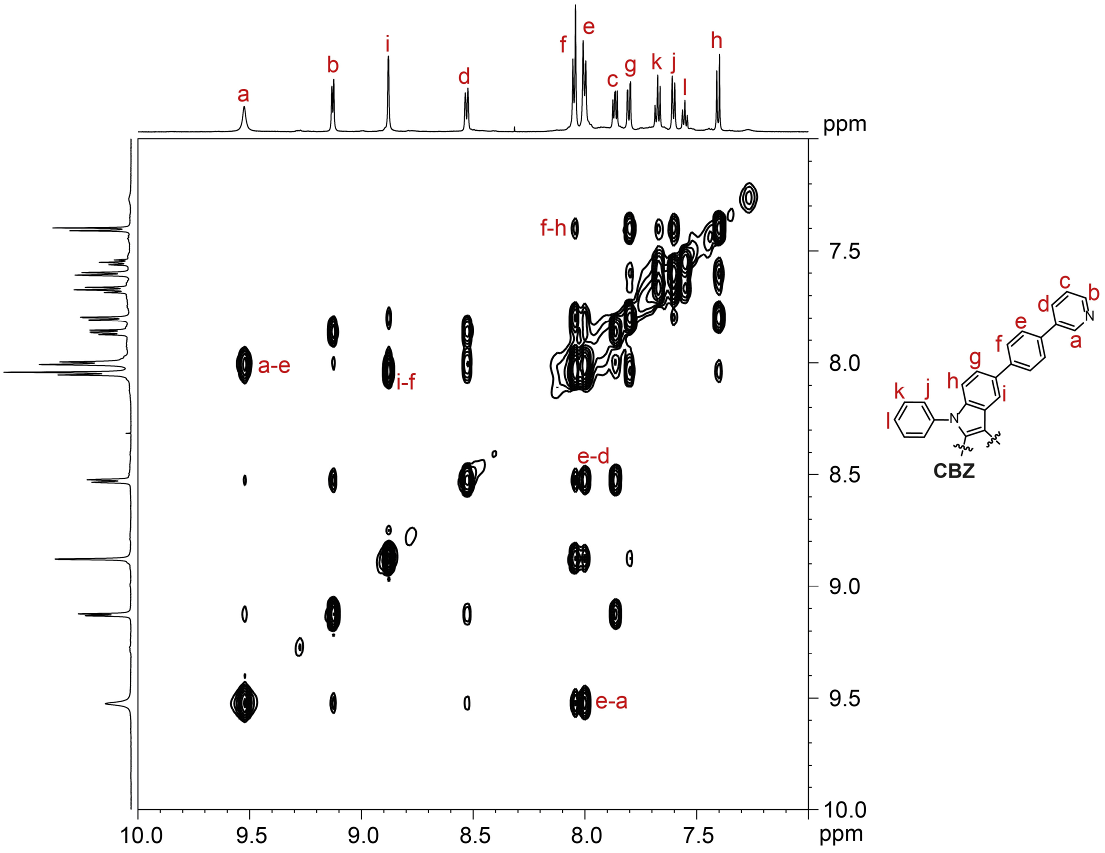

Fig. 39 ^{1}H-^{1}H NOESY NMR spectrum of [Pd$_2$**CBZ**$_4$]$^{4+}$ (700 MHz, 298 K, DMSO-d_6).

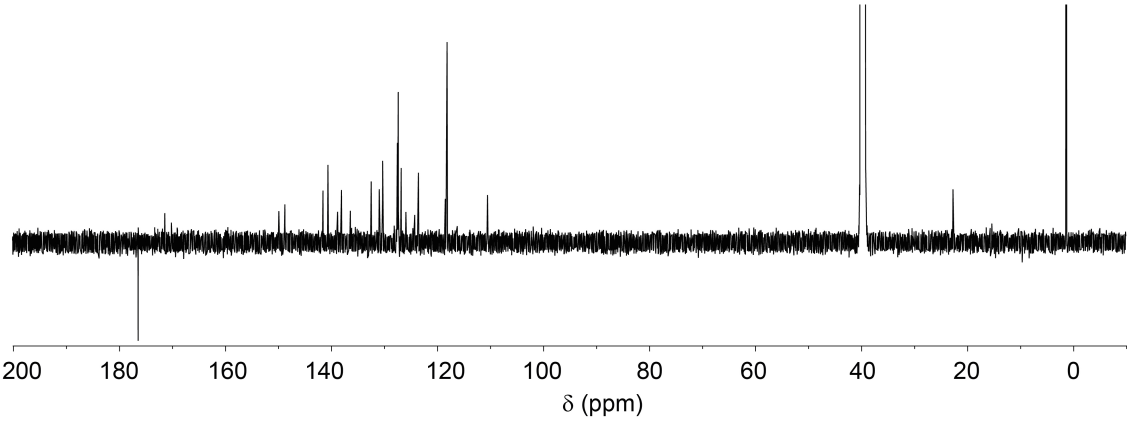

Fig. 40 ^{13}C NMR spectrum of $[Pd_2$**CBZ**$_4]^{4+}$ (176 MHz, 298 K, DMSO-d_6).

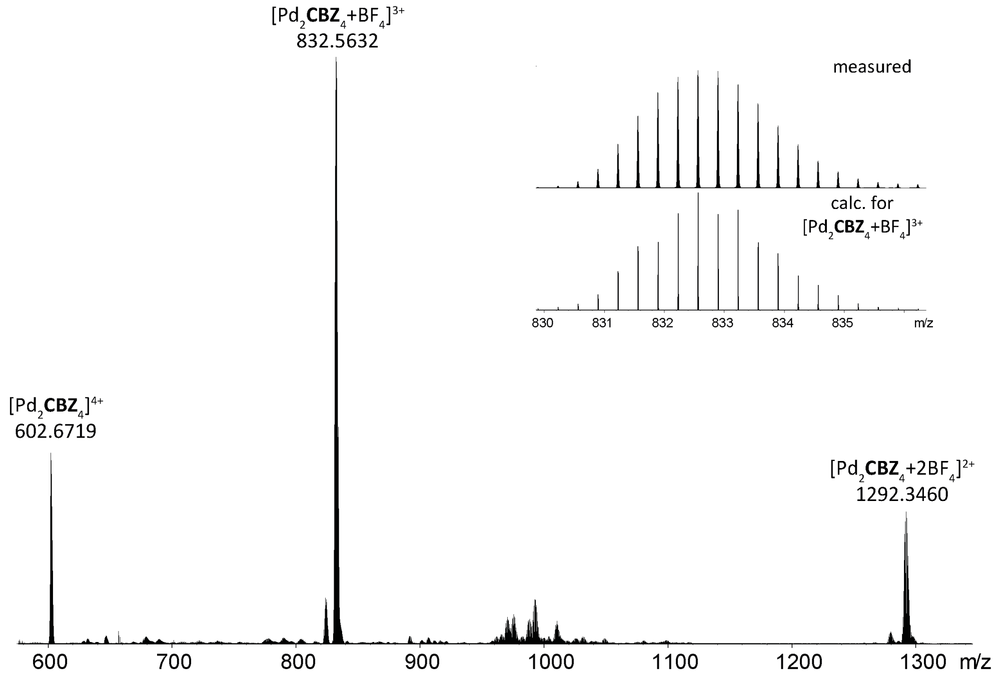

Fig. 41 ESI mass spectrum of $[Pd_2$**CBZ**$_4]^{4+}$, the inset shows the isotopic pattern of $[Pd_2$**CBZ**$_4+BF_4]^{3+}$.

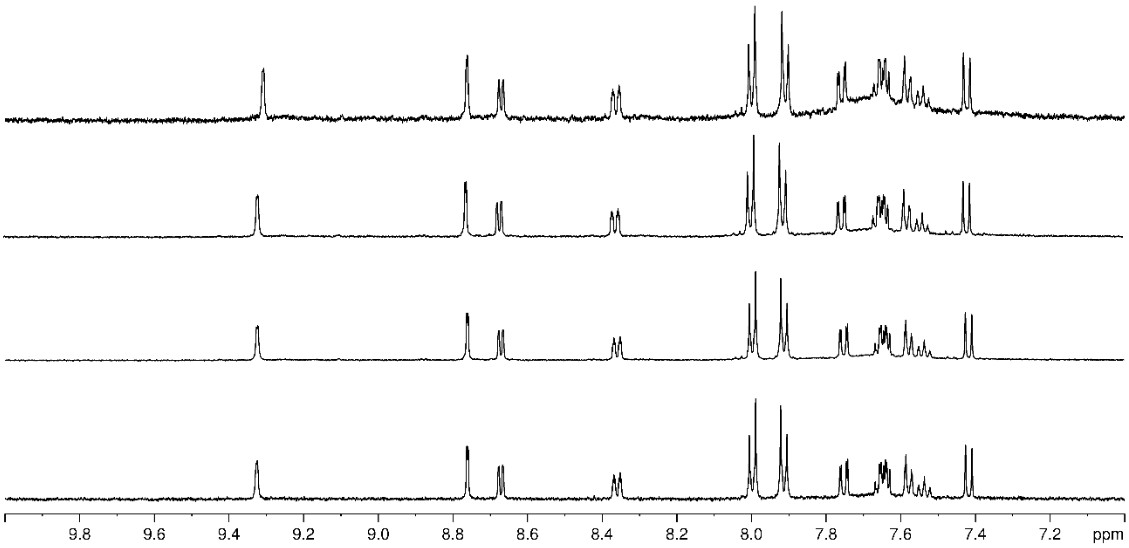

Fig. 42 Stability of [Pd$_2$**CBZ**$_4$]$^{4+}$ in CD$_3$CN; from bottom to top: ^{1}H NMR (500 MHz, 298 K, CD$_3$CN) directly after redissolution in CD$_3$CN, after 12 h, after 36 h, after 4.5 d ("bump" arises between 8 and 7.5 ppm, indicating formation of non-discrete species).

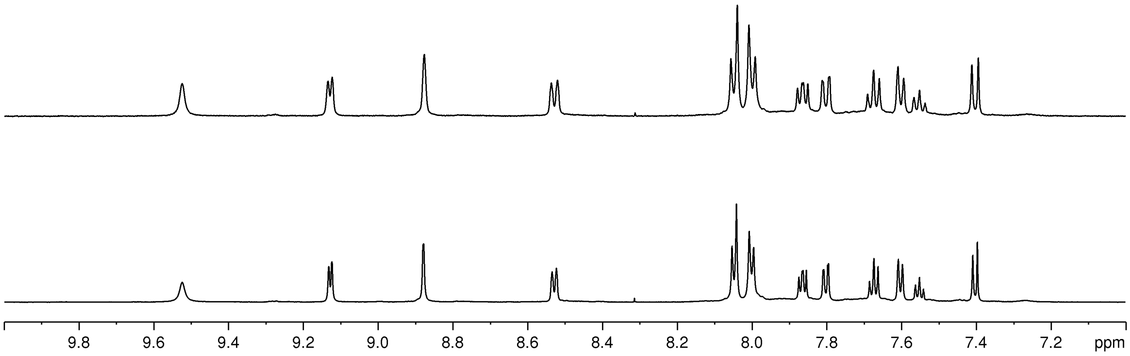

Fig. 43 Stability of [Pd$_2$**CBZ**$_4$]$^{4+}$ in DMSO-*d*$_6$; bottom: ^{1}H NMR (700 MHz, 298 K, DMSO-*d*$_6$) as synthesized, top: ^{1}H NMR (500 MHz, 298 K, DMSO-*d*$_6$) after 19 d.

[Pd$_2$**PTZ**$_4$]$^{4+}$

A solution of **PTZ** (500 µL, 2.8 mM, DMSO-*d*$_6$) was combined with a solution of [Pd(CH$_3$CN)$_4$](BF$_4$)$_2$ (50 µL, 15 mM, DMSO-*d*$_6$). The mixture was heated at 70 °C for one hour. Afterwards, the solvent was removed by lyophilization and the sample dissolved in CD$_3$CN via sonication.

^{1}H NMR (500 MHz, CD$_3$CN) δ 9.19 (d, *J* = 1.8 Hz, 1H), 8.93 (dd, *J* = 6.0, 1.4 Hz, 1H), 8.01 (dt, *J* = 8.0, 1.5 Hz, 1H), 7.57 (dd, *J* = 7.9, 5.9 Hz, 1H), 7.45 – 7.37 (m, 2H), 6.99 (d, *J* = 8.6 Hz, 1H), 3.90 (t, *J* = 7.0 Hz, 1H), 1.76 – 1.69 (m, 1H), 1.42 – 1.38 (m, 1H), 1.29 – 1.23 (m, 2H), 0.82 (t, *J* = 7.0 Hz, 1.5H).

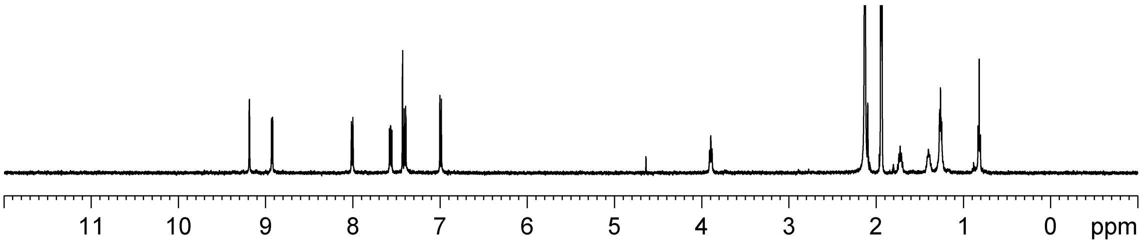

Fig. 44 Full ^{1}H NMR spectrum of [Pd$_2$**PTZ**$_4$]$^{4+}$ (500 MHz, 298 K, CD$_3$CN).

$[Pd_2$**CBZ**$_2$**NDI**$_2]^{4+}$

Solutions of **CBZ** (250 µL, 1.4 mM, CD_3CN), **NDI** (250 µL, 1.4 mM, CD_3CN), and $[Pd(CH_3CN)_4](BF_4)_2$ (30 µL, 15 mM, CD_3CN) were combined. The mixture was heated at 70 °C for 3 days.

^1H NMR (600 MHz, CD_3CN): δ 9.69 (d, *J* = 2.2 Hz, 1H), 9.43 (d, *J* = 2.0 Hz, 1H), 9.22 (d, 1H), 9.18 (s, 1H), 9.07 (d, *J* = 5.9, 1.3 Hz, 1H), 8.90 (s, 1H), 8.74 (s, 1H), 8.33 (dt, *J* = 8.1, 1.7 Hz, 1H), 8.21 (dt, *J* = 8.0, 1.5 Hz, 1H), 8.07 (d, 2H), 7.97 (d, *J* = 8.1 Hz, 2H), 7.87 – 7.78 (m, 4H), 7.71 – 7.66 (m, 0.5H), 7.66 – 7.61 (m, 1H), 7.49 (d, *J* = 8.6 Hz, 1H).

^1H NMR (500 MHz, DMSO-d_6) δ 9.94 (s, 1H), 9.56 (d, *J* = 5.7 Hz, 1H), 9.43 (s, 1H), 9.24 (d, *J* = 5.7 Hz, 1H), 9.20 (s, 1H), 8.92 (s, 1H), 8.53 (d, *J* = 8.2 Hz, 1H), 8.40 (s, 1H), 8.36 (d, *J* = 8.1 Hz, 1H), 8.13 – 7.97 (m, 5H), 7.90 (dd, *J* = 8.6, 1.7 Hz, 1H), 7.73-7.68 (m, 2H), 7.64 (d, *J* = 7.9 Hz, 1H), 7.58 (t, *J* = 7.5 Hz, 0.5H), 7.48 (d, *J* = 8.6 Hz, 1H).

^{13}C NMR (151 MHz, CD_3CN): δ 172.92, 163.87, 163.10, 152.48, 151.47, 149.63, 149.60, 143.33, 142.73, 142.30, 140.31, 139.72, 136.11, 133.58, 133.30, 132.56, 131.90, 131.13, 128.94, 128.79, 128.61, 128.51, 127.94, 127.83, 127.79, 126.80, 125.73, 124.93, 119.95, 111.51.

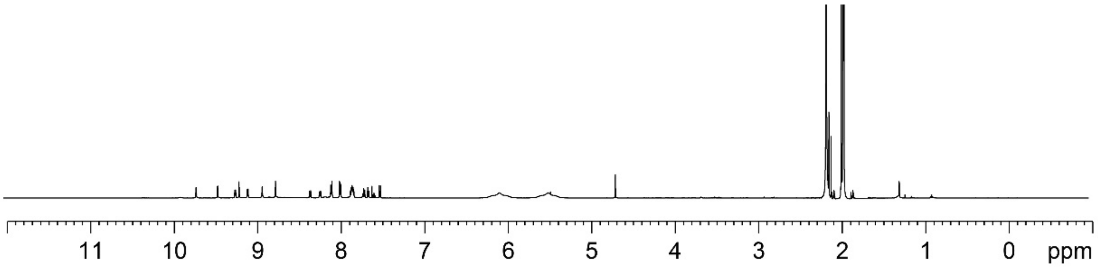

Fig. 45 Full ^1H NMR spectrum of $[Pd_2$**CBZ**$_2$**NDI**$_2]^{4+}$ (600 MHz, 298 K, CD_3CN). The broad signals at δ = 6.07 and 5.48 ppm are due to the heated Pd(II) salt.

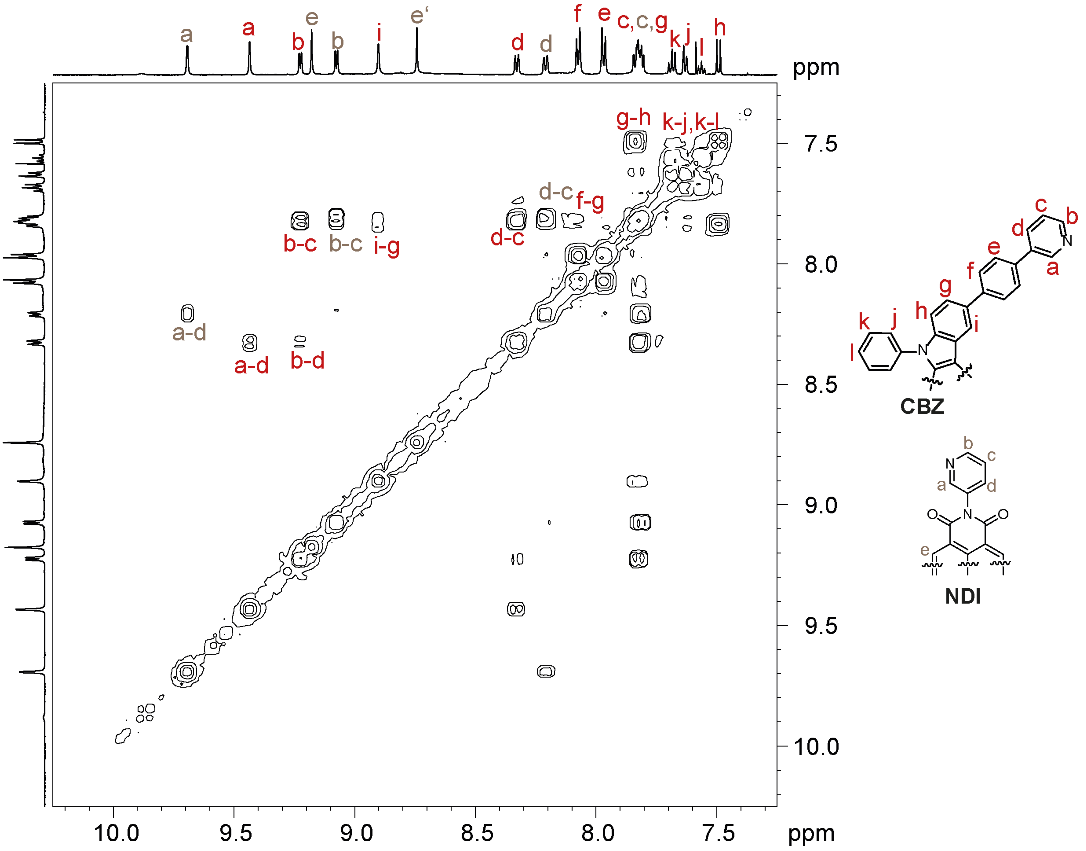

Fig. 46 ^{1}H-^{1}H COSY NMR spectrum of [Pd$_2$**CBZ**$_2$**NDI**$_2$]$^{4+}$ (600 MHz, 298 K, CD$_3$CN).

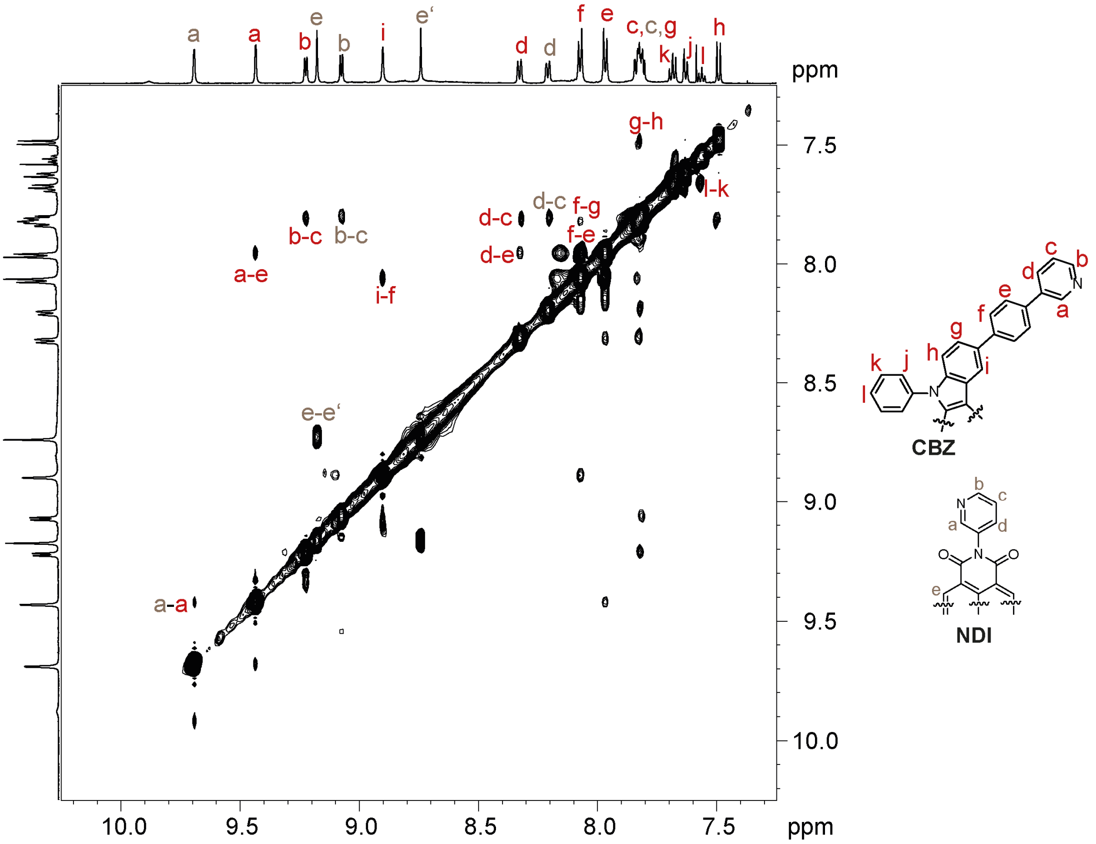

Fig. 47 ^{1}H-^{1}H NOESY NMR spectrum of [Pd$_2$**CBZ**$_2$**NDI**$_2$]$^{4+}$ (600 MHz, 298 K, CD$_3$CN).

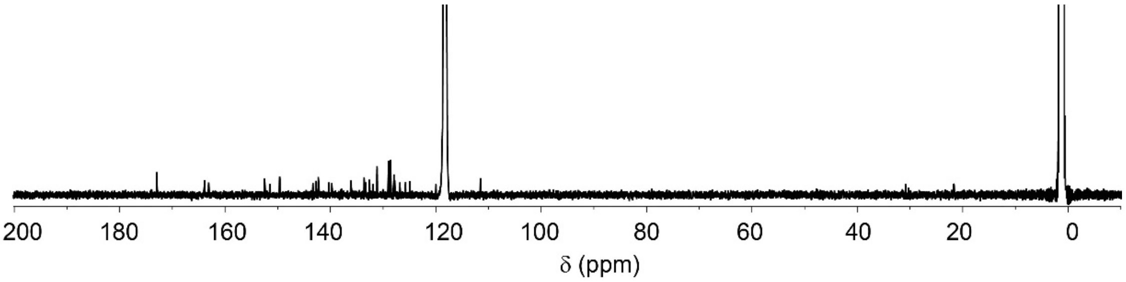

Fig. 48 ^{13}C NMR spectrum of [Pd$_2$**CBZ**$_2$**NDI**$_2$]$^{4+}$ (151 MHz, 298 K, CD$_3$CN).

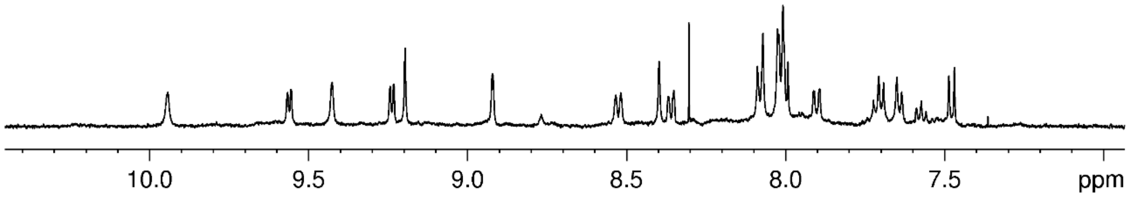

Fig. 49 Partial ^{1}H NMR spectrum of [Pd$_2$**CBZ**$_2$**NDI**$_2$]$^{4+}$ (500 MHz, 298 K, DMSO-d_6).

$[Pd_2\mathbf{CBZ}_2\mathbf{PMDI}_2]^{4+}$

Solutions of **CBZ** (250 µL, 1.4 mM, CD_3CN), **PMDI** (250 µL, 1.4 mM, CD_3CN), and $[Pd(CH_3CN)_4](BF_4)_2$ (30 µL, 15 mM, CD_3CN) were combined. The mixture was heated at 70 °C for 3 days.

^1H NMR (700 MHz, CD_3CN) δ 10.04 (d, *J* = 2.3 Hz, 1H), 9.61 (d, *J* = 2.1 Hz, 1H), 9.21 (d, 1H), 8.97 (d, *J* = 5.8 Hz, 1H), 8.79 (d, *J* = 1.9 Hz, 1H), 8.33 (dt, *J* = 8.1, 1.7 Hz, 1H), 8.22 (dt, *J* = 7.9, 1.6 Hz, 1H), 8.04 (d, *J* = 8.3 Hz, 2H), 7.95 (d, *J* = 8.3 Hz, 2H), 7.84 (dd, *J* = 8.6, 1.9 Hz, 1H), 7.80 (dd, *J* = 8.1, 5.8 Hz, 1H), 7.75 (dd, *J* = 8.0, 5.8 Hz, 1H), 7.68 (t, *J* = 8.0 Hz, 1H), 7.64 – 7.61 (m, 1H), 7.56 (t, *J* = 7.6 Hz, 0.5H), 7.48 (d, *J* = 8.6 Hz, 1H).

^1H NMR (700 MHz, DMSO-d_6) δ 10.25 (s, 1H), 9.84 (s, 1H), 9.55 (d, *J* = 5.9 Hz, 1H), 9.16 (d, *J* = 5.7 Hz, 1H), 8.68 (br, 1H), 8.53 (d, *J* = 8.1 Hz, 1H), 8.28 (d, *J* = 8.0 Hz, 1H), 8.09 – 7.98 (m, 4H), 7.94 (dd, *J* = 8.1, 6.0 Hz, 1H), 7.90 (d, *J* = 8.6 Hz, 2H), 7.71 (t, *J* = 7.9 Hz, 1H), 7.65 (d, *J* = 8.0 Hz, 1H), 7.59 (t, *J* = 7.4 Hz, 0.5H), 7.49 (d, *J* = 8.5 Hz, 1H).

^{13}C NMR (176 MHz, CD_3CN) δ 173.13, 165.43, 151.10, 149.59, 149.08, 143.16, 142.28, 140.18, 139.40, 138.38, 138.24, 137.83, 133.60, 132.41, 132.08, 131.10, 129.03, 128.73, 128.70, 128.55, 128.47, 127.88, 126.66, 124.84, 120.36, 119.54, 111.52.

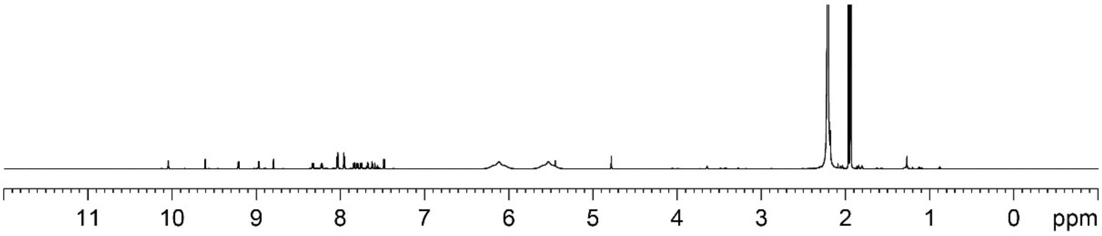

Fig. 50 Full ^1H NMR spectrum of $[Pd_2\mathbf{CBZ}_2\mathbf{PMDI}_2]^{4+}$ (700 MHz, 298 K, CD_3CN). The broad signals at δ = 6.07 and 5.48 ppm are due to the heated Pd(II) salt.

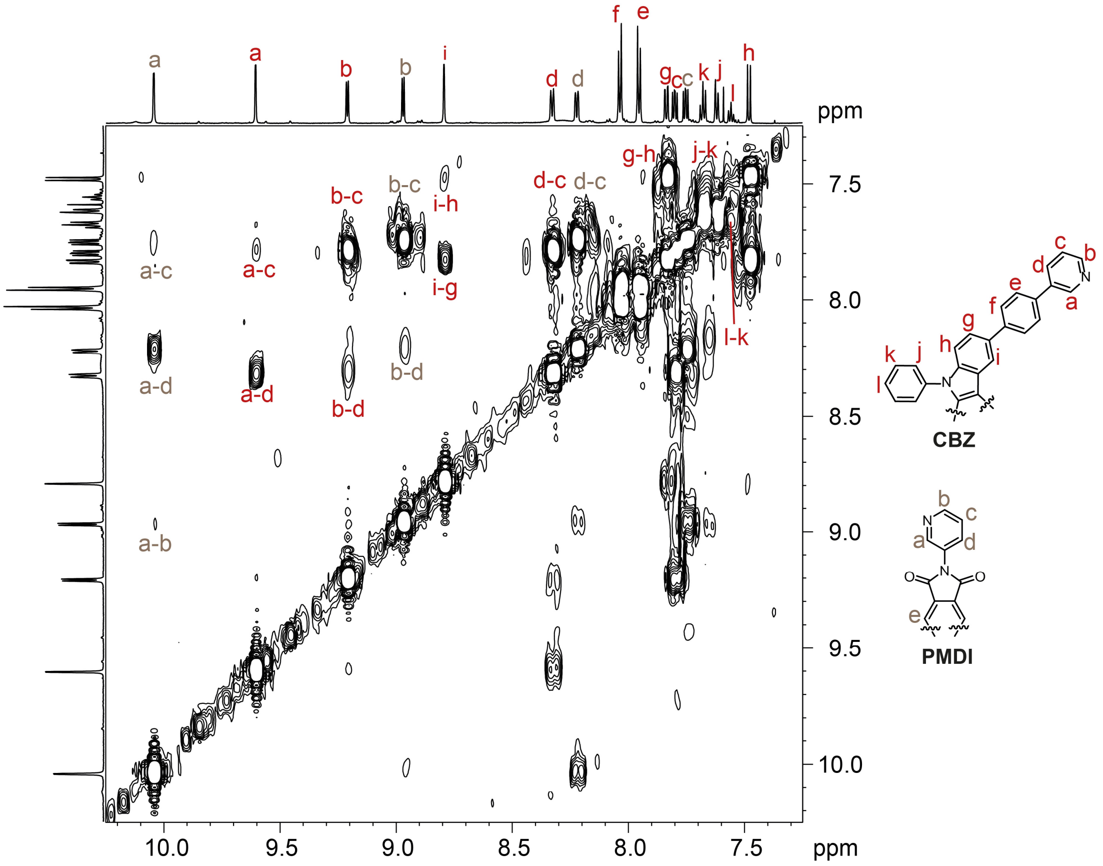

Fig. 51 ^{1}H-^{1}H COSY NMR spectrum of [Pd$_2$**CBZ**$_2$**PMDI**$_2$]$^{4+}$ (700 MHz, 298 K, CD$_3$CN).

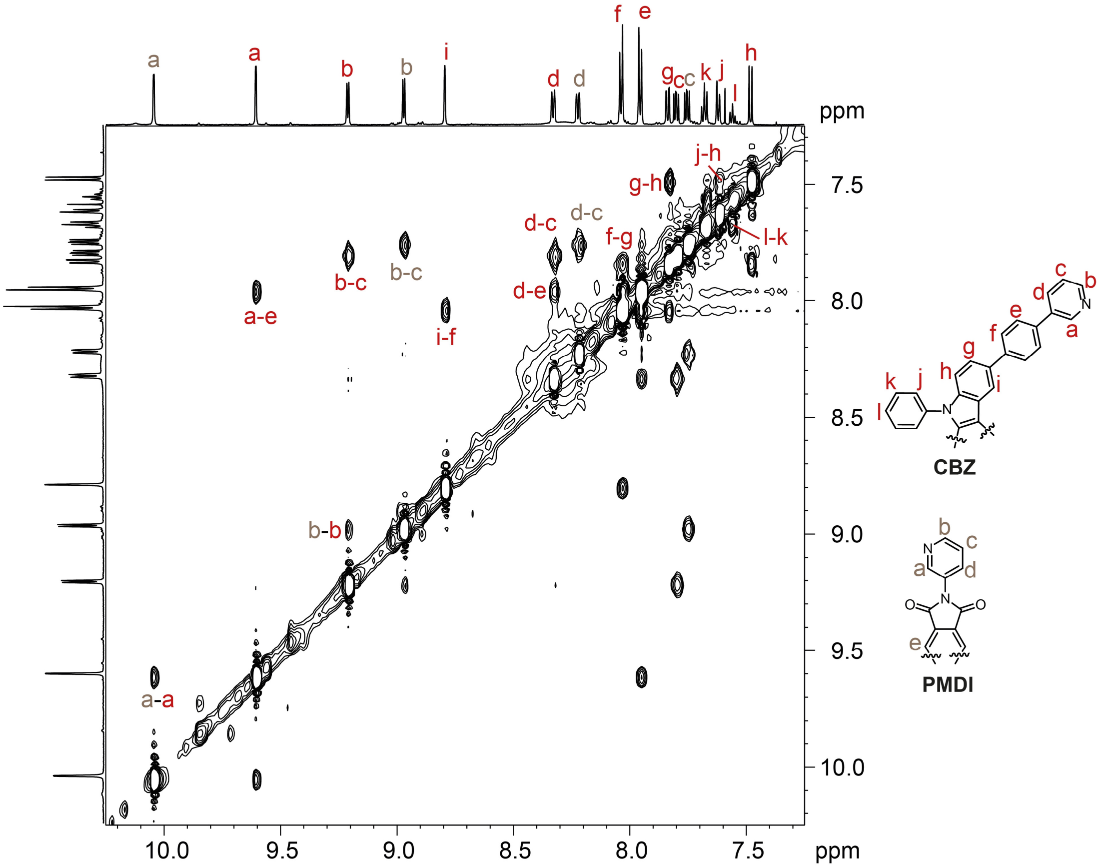

Fig. 52 ^{1}H-^{1}H NOESY NMR spectrum of [Pd$_2$**CBZ**$_2$**PMDI**$_2$]$^{4+}$ (700 MHz, 298 K, CD$_3$CN).

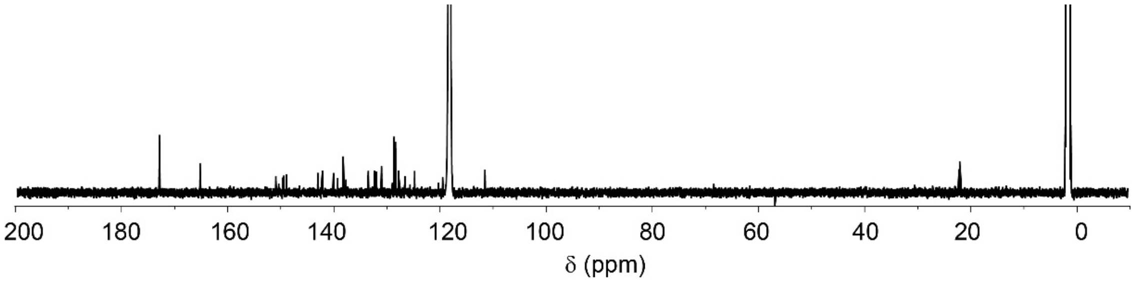

Fig. 53 ^{13}C NMR spectrum of [Pd$_2$**CBZ**$_2$**PMDI**$_2$]$^{4+}$ (176 MHz, 298 K, CD$_3$CN).

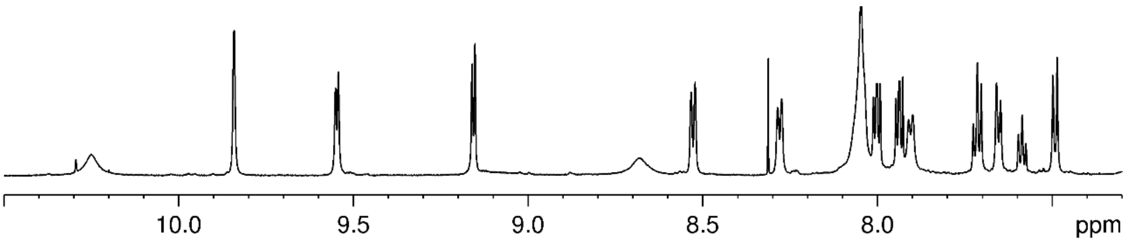

Fig. 54 Full ^{1}H NMR spectrum of [Pd$_2$**CBZ**$_2$**PMDI**$_2$]$^{4+}$ (700 MHz, 298 K, DMSO-d_6).

$[Pd_2\textbf{CBZ}_2\textbf{FRO}_2]^{4+}$

Solutions of **CBZ** (250 µL, 2.8 mM, DMSO-*d*$_6$), **FRO** (250 µL, 2.8 mM, DMSO-*d*$_6$), and $[Pd(CH_3CN)_4](BF_4)_2$ (50 µL, 15 mM, DMSO-*d*$_6$) were combined. The mixture was heated at 70 °C for 1.5 h. Next, the DMSO-*d*$_6$ was removed by lyophilization followed by redissolution of the solid in CD_3CN via sonication and heating at 70 °C.

^1H NMR (700 MHz, CD_3CN) δ 9.86 (s, 1H), 9.64 (s, 1H), 9.30 (dd, *J* = 5.8, 1.3 Hz, 1H), 9.09 (dd, *J* = 5.9, 1.2 Hz, 1H), 8.78 (d, 1.6 Hz, 1H), 8.33 (ddd, *J* = 8.1, 2.1, 1.3 Hz, 1H), 8.24 (d, *J* = 7.9 Hz, 1H), 8.18 (s, 1H), 8.01 (dd, *J* = 5.7, 1.9 Hz, 2H), 7.93 (d, *J* = 7.9 Hz, 2H), 7.85 – 7.77 (m, 4H), 7.70 – 7.63 (m, 2H), 7.62 (dd, *J* = 8.9 Hz, 1.3 Hz, 1H), 7.58 – 7.53 (m, 0.5 H), 7.47 (d, *J* = 8.5, 0.6 Hz, 1H).

^1H NMR (500 MHz, DMSO-*d*$_6$) δ 10.17 (s, 1H), 9.88 (s, 1H), 9.58 (d, *J* = 5.6 Hz, 1H), 9.35 (d, *J* = 5.7 Hz, 1H), 8.89 (s, 1H), 8.53 (d, *J* = 7.9 Hz, 1H), 8.45 (d, *J* = 7.9 Hz, 1H), 8.26 (s, 1H), 8.11 (d, *J* = 8.3 Hz, 2H), 8.06 (d, *J* = 8.2 Hz, 2H), 8.02 – 7.89 (m, 4H), 7.85 (dd, *J* = 7.9, 5.7 Hz, 1H), 7.72 – 7.63 (m, 2H), 7.58-7.54 (m, 0.5H), 7.46 (d, *J* = 8.6 Hz, 1H).

^{13}C NMR (176 MHz, CD_3CN) δ 150.87, 150.13, 149.60, 145.32, 143.44, 142.24, 141.43, 140.39, 140.26, 139.37, 139.27, 137.90, 137.34, 137.06, 135.16, 133.75, 132.74, 131.12, 128.75, 128.66, 128.64, 128.24, 127.87, 127.64, 126.61, 124.93, 123.42, 119.97, 111.48.

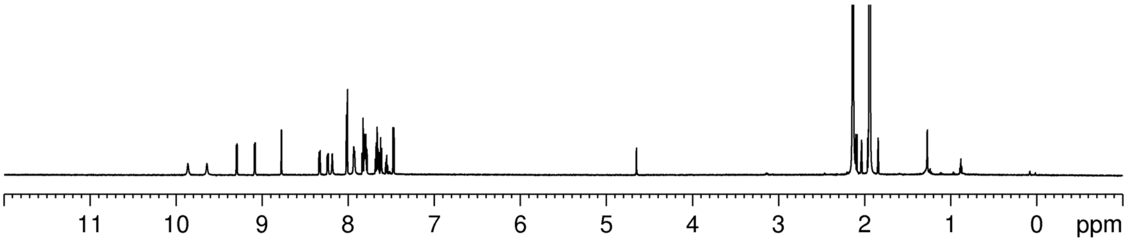

Fig. 55 Full ^1H NMR spectrum of $[Pd_2\textbf{CBZ}_2\textbf{FRO}_2]^{4+}$ (700 MHz, 298 K, CD_3CN).

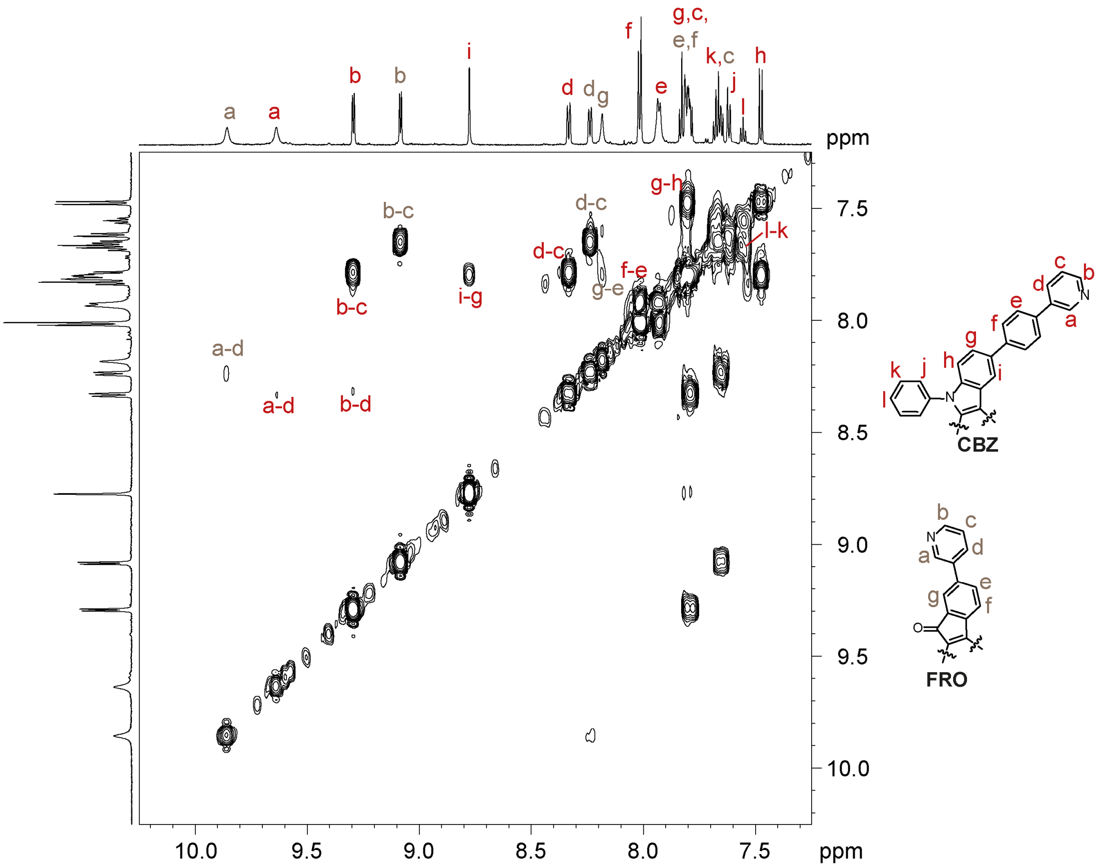

Fig. 56 ^{1}H-^{1}H COSY NMR spectrum of [Pd$_2$**CBZ**$_2$**FRO**$_2$]$^{4+}$ (700 MHz, 298 K, CD$_3$CN).

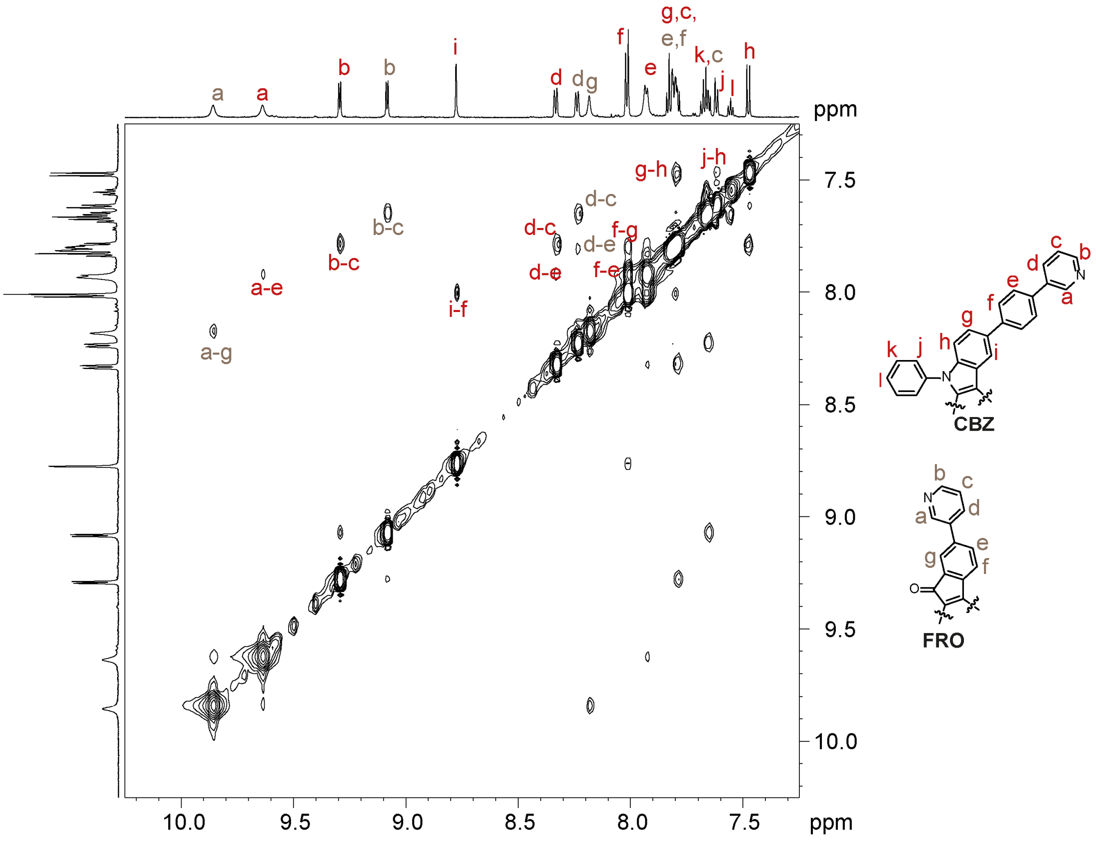

Fig. 57 ^{1}H-^{1}H NOESY NMR spectrum of [Pd$_2$**CBZ**$_2$**FRO**$_2$]$^{4+}$ (700 MHz, 298 K, CD$_3$CN).

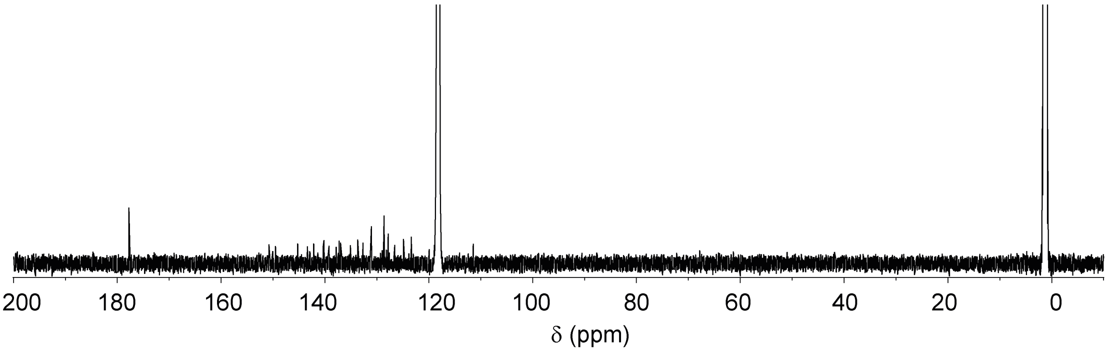

Fig. 58 ^{13}C NMR spectrum of [Pd$_2$**CBZ**$_2$**FRO**$_2$]$^{4+}$ (176 MHz, 298 K, CD$_3$CN). The signal at δ = 177.87 pm stems most probably from an impurity.

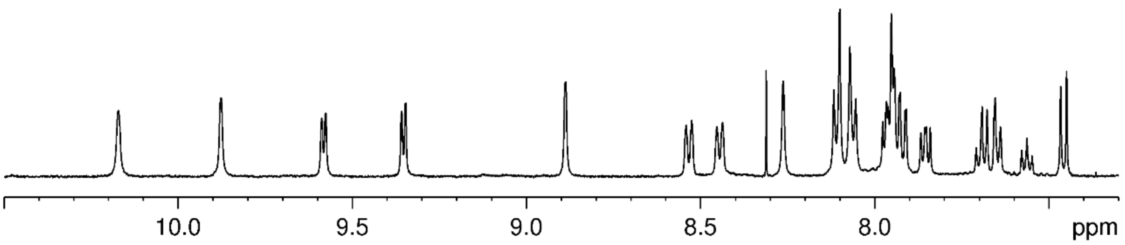

Fig. 59 Partial ^{1}H NMR spectrum of [Pd$_2$**CBZ**$_2$**FRO**$_2$]$^{4+}$ (500 MHz, 298 K, DMSO-*d*$_6$).

$[Pd_2$**TAA**$_2$**NDI**$_2]^{4+}$

Solutions of **TAA** (250 µL, 1.4 mM, CD_3CN), **NDI** (250 µL, 1.4 mM, CD_3CN), and $[Pd(CH_3CN)_4](BF_4)_2$ (30 µL, 15 mM, CD_3CN) were combined. The mixture was heated at 70 °C for 3 days.

^1H NMR (500 MHz, CD_3CN) δ 9.56 (s, 1H), 9.33 (s, 1H), 9.22 (d, *J* = 5.8 Hz, 1H), 9.04 (dd, *J* = 5.9, 1.3 Hz, 1H), 8.74 (s, 1H), 8.64 (s, 1H), 8.28 (d, *J* = 8.0 Hz, 1H), 8.13 (ddd, *J* = 8.1, 2.1, 1.2 Hz, 1H), 7.86 – 7.73 (m, 5H), 7.63 (d, *J* = 8.2 Hz, 1H), 7.54 (d, *J* = 8.0 Hz, 1H), 7.17 (d, *J* = 8.6 Hz, 1H), 7.00 (d, *J* = 8.5 Hz, 1H), 6.70 (d, *J* = 8.1 Hz, 1H), 3.82 (s, 1.5H), 1.71 (s, 3H), 1.57 (s, 3H).

^1H NMR (500 MHz, DMSO-d_6) δ 9.60 – 9.55 (m, 2H), 9.20 (d, *J* = 7.3 Hz, 1H), 9.14 (s, 1H), 8.80 (s, 1H), 8.61 (s, 1H), 8.48 (d, *J* = 8.2 Hz, 1H), 8.30 (d, *J* = 9.1 Hz, 1H), 8.05 – 7.93 (m, 2H), 7.82 (d, *J* = 8.0 Hz, 1H), 7.78 (d, *J* = 2.3 Hz, 1H), 7.76 – 7.66 (m, 2H), 7.63 (d, *J* = 8.0 Hz, 1H), 7.20 (d, *J* = 9.0 Hz, 1H), 7.04 (d, *J* = 9.1 Hz, 1H), 6.61 (dd, *J* = 8.1, 2.1 Hz, 1H), 3.80 (s, 1.5H), 1.67 (s, 3H), 1.52 (s, 3H).

^{13}C NMR (151 MHz, CD_3CN) δ 163.25, 163.08, 158.61, 156.45, 155.83, 152.49, 151.37, 150.11, 149.02, 148.86, 142.72, 141.49, 141.42, 139.73, 136.14, 133.38, 132.23, 131.90, 131.72, 130.27, 128.68, 128.34, 128.03, 127.93, 127.71, 127.58, 122.42, 122.31, 121.88, 121.11, 116.24, 115.90, 56.15, 48.22, 26.94, 26.75.

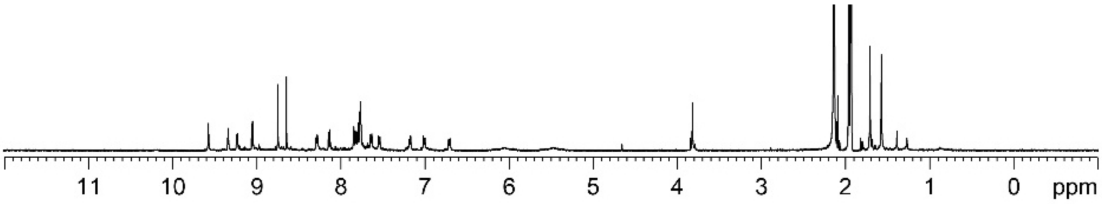

Fig. 60 Full ^1H NMR spectrum of $[Pd_2$**TAA**$_2$**NDI**$_2]^{4+}$ (500 MHz, 298 K, CD_3CN). The broad signals at δ = 6.07 and 5.48 ppm are due to the heated Pd(II) salt.

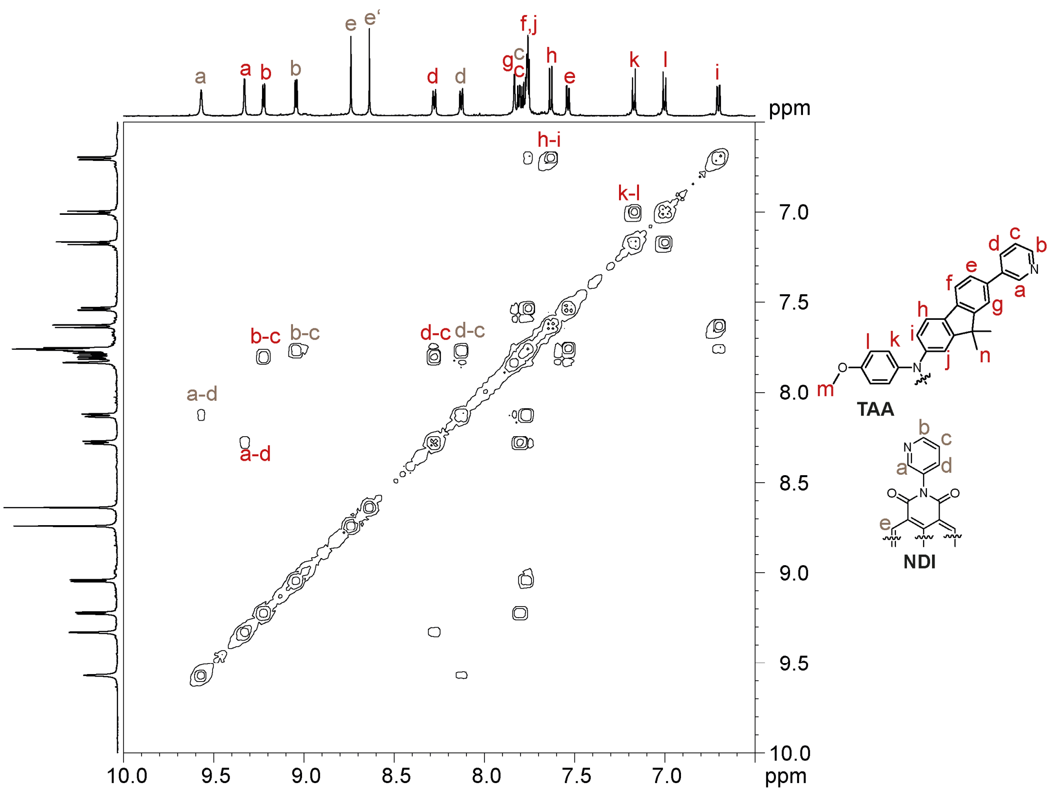

Fig. 61 ^{1}H-^{1}H COSY NMR spectrum of $[Pd_2\mathbf{TAA}_2\mathbf{NDI}_2]^{4+}$ (600 MHz, 298 K, CD_3CN).

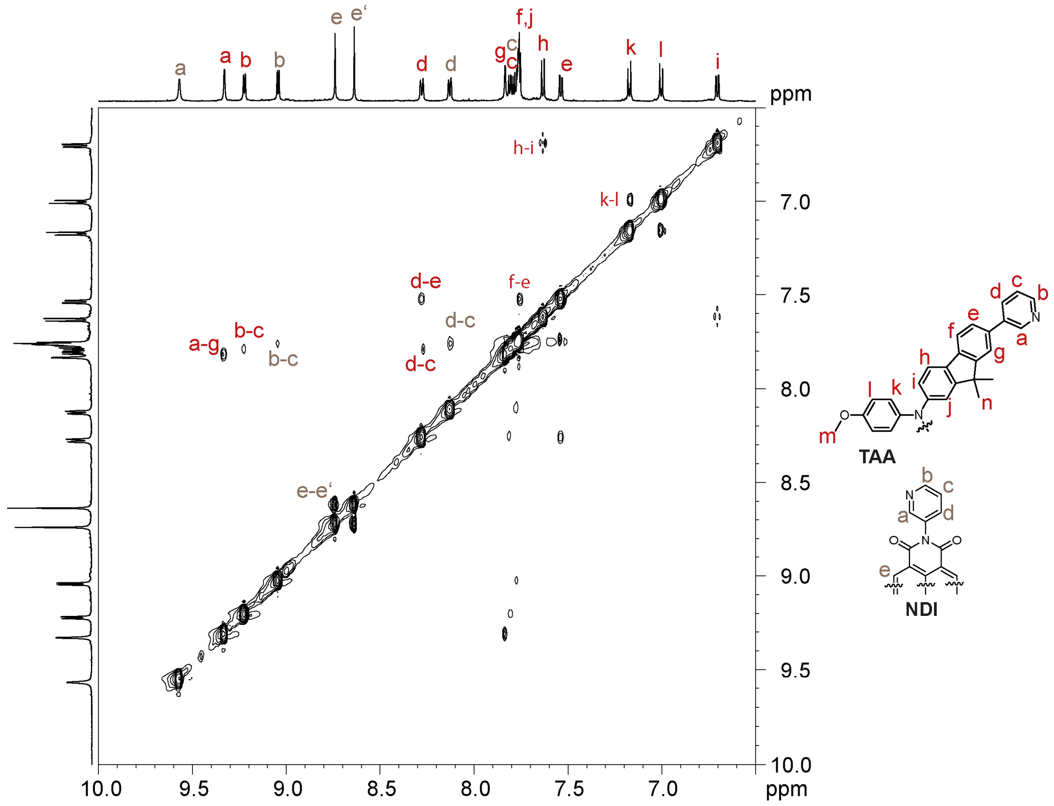

Fig. 62 ^{1}H-^{1}H NOESY NMR spectrum of $[Pd_2\mathbf{TAA}_2\mathbf{NDI}_2]^{4+}$ (600 MHz, 298 K, CD_3CN).

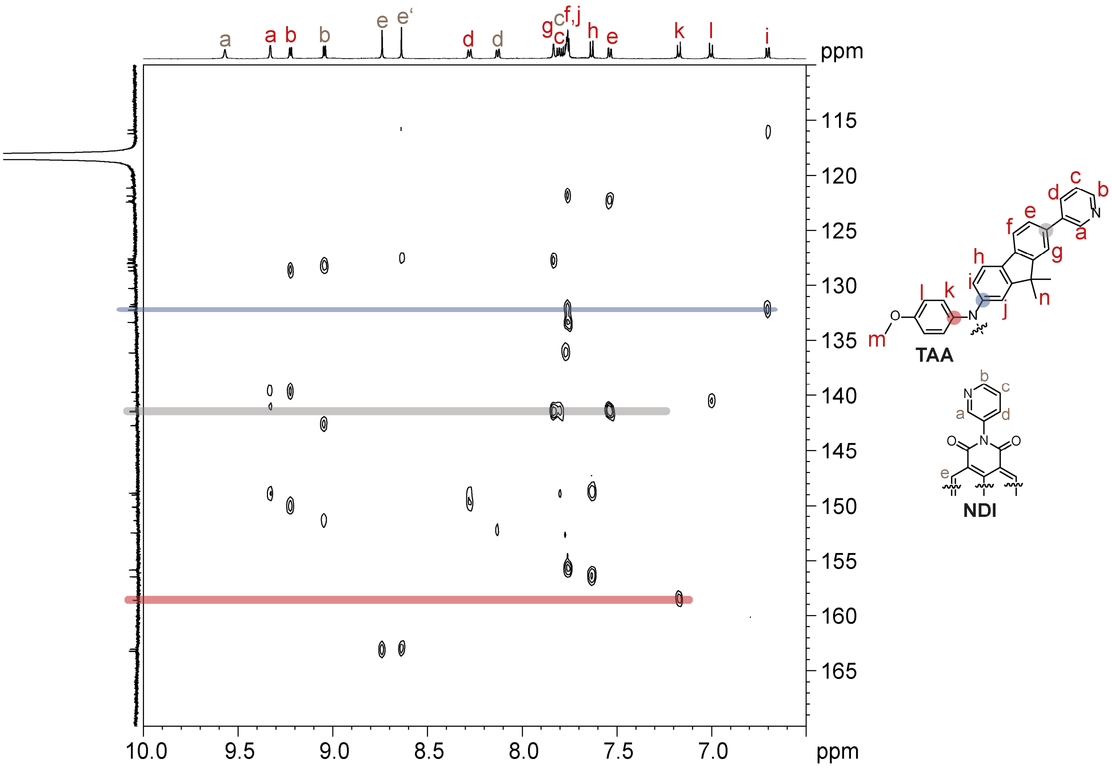

Fig. 63 ^{1}H-^{13}C HMBC NMR spectrum of $[Pd_2$**TAA**$_2$**NDI**$_2]^{4+}$ (600 MHz, 151 MHz, 298 K, CD_3CN).

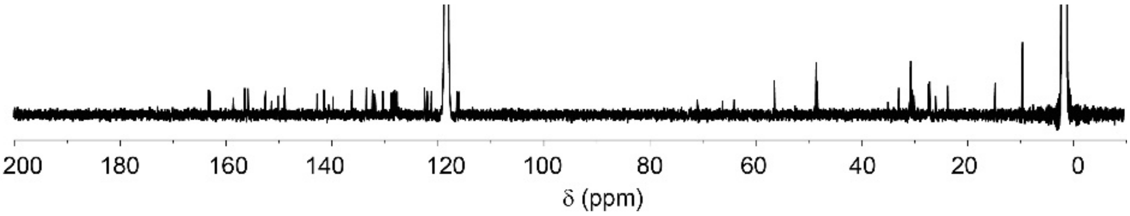

Fig. 64 ^{13}C-NMR spectrum of $[Pd_2$**TAA**$_2$**NDI**$_2]^{4+}$ (151 MHz, 298 K, CD_3CN).

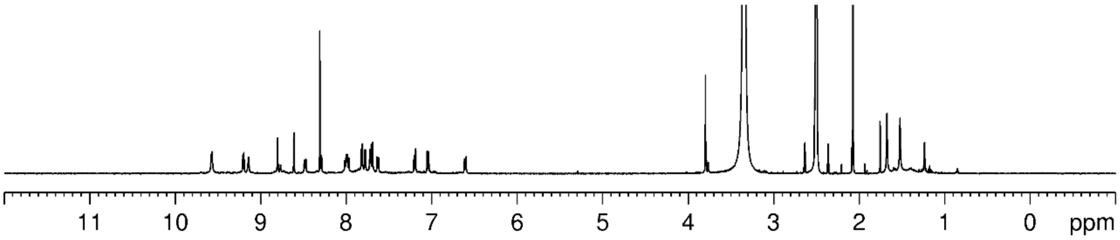

Fig. 65 Full ^{1}H NMR spectrum of $[Pd_2$**TAA**$_2$**NDI**$_2]^{4+}$ (500 MHz, 298 K, DMSO-d_6).

$[Pd_2$**TAA**$_2$**PMDI**$_2]^{4+}$

Solutions of **TAA** (250 µL, 1.4 mM, CD_3CN), **NDI** (250 µL, 1.4 mM, CD_3CN), and $[Pd(CH_3CN)_4](BF_4)_2$ (30 µL, 15 mM, CD_3CN) were combined. The mixture was heated at 70 °C for 3 days.

^{1}H NMR (600 MHz, CD_3CN) δ 9.85 (d, J = 2.3 Hz, 1H), 9.38 (d, J = 2.0 Hz, 1H), 9.21 (dd, J = 5.9, 0.9 Hz, 1H), 9.00 (dd, J = 5.9, 1.2 Hz, 1H), 8.25 (ddd, J = 8.1, 2.0, 1.3 Hz, 1H), 8.21 (ddd, J = 8.2, 2.3, 1.2

Hz, 1H), 7.97 (s, 1H), 7.88 (d, *J* = 1.4 Hz, 1H), 7.82 – 7.70 (m, 3H), 7.64 (d, *J* = 8.1 Hz, 1H), 7.56 (d, *J* = 2.2 Hz, 1H), 7.50 (dd, *J* = 8.0, 1.7 Hz, 1H), 7.16 (dd, *J* = 6.0, 2.3 Hz, 1H), 6.99 (dd, *J* = 6.2, 2.3 Hz, 1H), 6.76 (dd, *J* = 8.1, 2.2 Hz, 1H), 3.81 (s, 1H), 1.62 (s, 3H), 1.55 (s, 3H).

^{1}H NMR (500 MHz, DMSO-d_6) δ 10.15 (s, 1H), 9.59 (d, *J* = 5.7 Hz, 1H), 9.37 (s, 1H), 9.11 (d, *J* = 5.7 Hz, 1H), 8.43 (d, *J* = 8.2 Hz, 1H), 8.21 (d, *J* = 8.5 Hz, 1H), 8.00 (dd, *J* = 8.1, 5.6 Hz, 1H), 7.93 (s, 1H), 7.88 (dd, *J* = 8.2, 5.7 Hz, 1H), 7.84 (d, *J* = 8.0 Hz, 1H), 7.74 (d, *J* = 8.2 Hz, 1H), 7.58 (d, *J* = 8.0 Hz, 1H), 7.36 (s, 1H), 7.16 (d, *J* = 9.0 Hz, 1H), 7.00 (d, *J* = 9.1 Hz, 1H), 6.79 (dd, *J* = 8.1, 2.1 Hz, 1H), 3.78 (s, 1.5H), 1.53 (s, 3H), 1.44 (s, 3H).

^{13}C NMR (151 MHz, CD$_3$CN) δ 165.28, 158.46, 156.11, 155.63, 151.18, 150.29, 149.20, 149.03, 148.29, 141.57, 141.41, 140.50, 139.69, 138.28, 138.02, 133.72, 132.44, 132.06, 129.90, 128.63, 128.46, 128.19, 122.54, 122.26, 122.20, 121.21, 119.86, 116.23, 116.14, 56.12, 47.92, 27.22, 27.06.

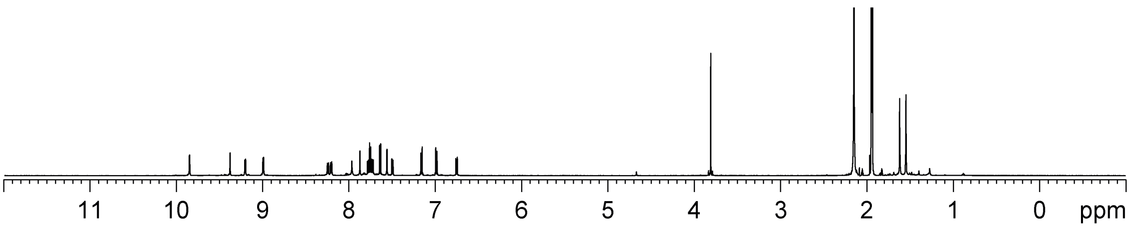

Fig. 66 Full ^{1}H NMR spectrum of [Pd$_2$**TAA**$_2$**PMDI**$_2$]$^{4+}$ (600 MHz, 298 K, CD$_3$CN).

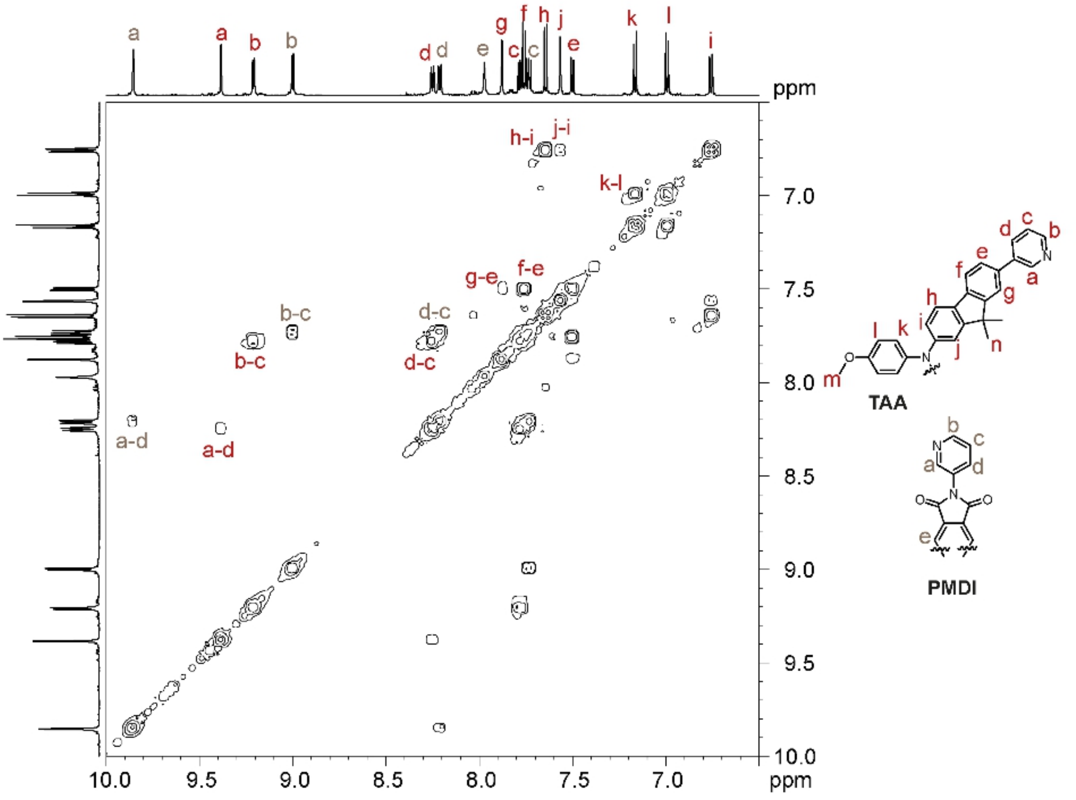

Fig. 67 ^{1}H-^{1}H COSY NMR spectrum of [Pd$_2$**TAA**$_2$**PMDI**$_2$]$^{4+}$ (600 MHz, 298 K, CD$_3$CN).

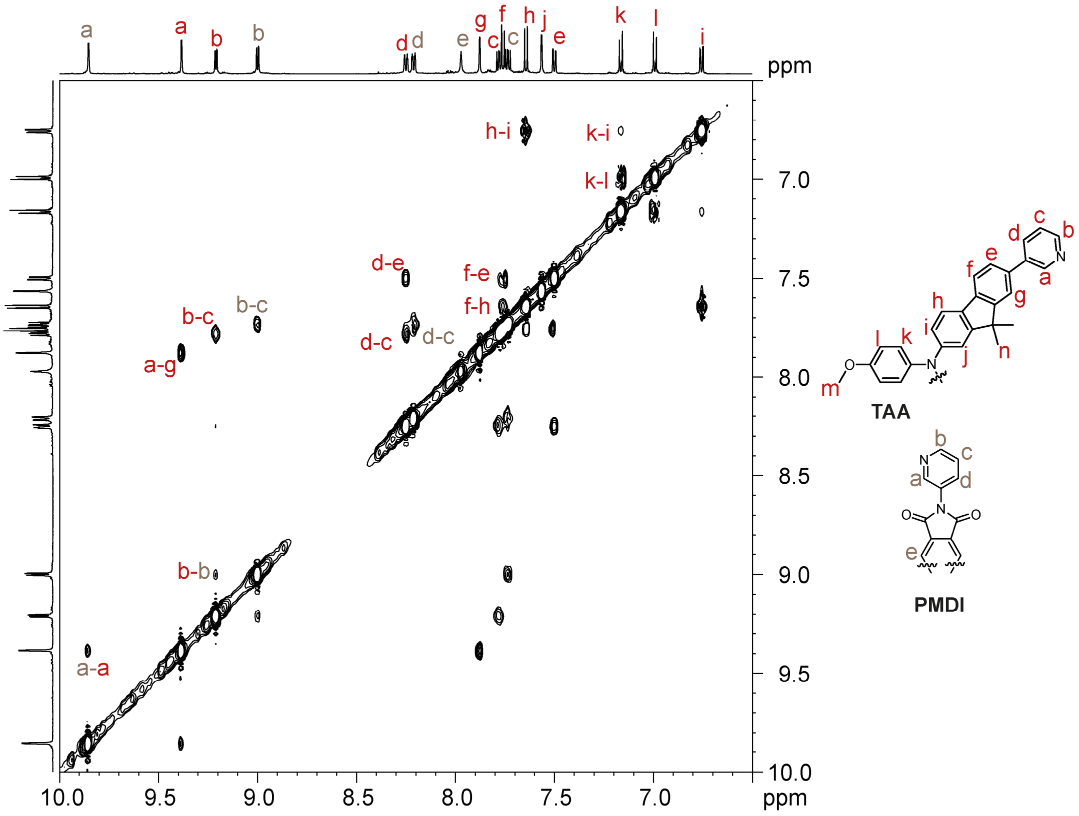

Fig. 68 ^{1}H-^{1}H NOESY NMR spectrum of [Pd$_2$**TAA**$_2$**PMDI**$_2$]$^{4+}$ (600 MHz, 298 K, CD$_3$CN).

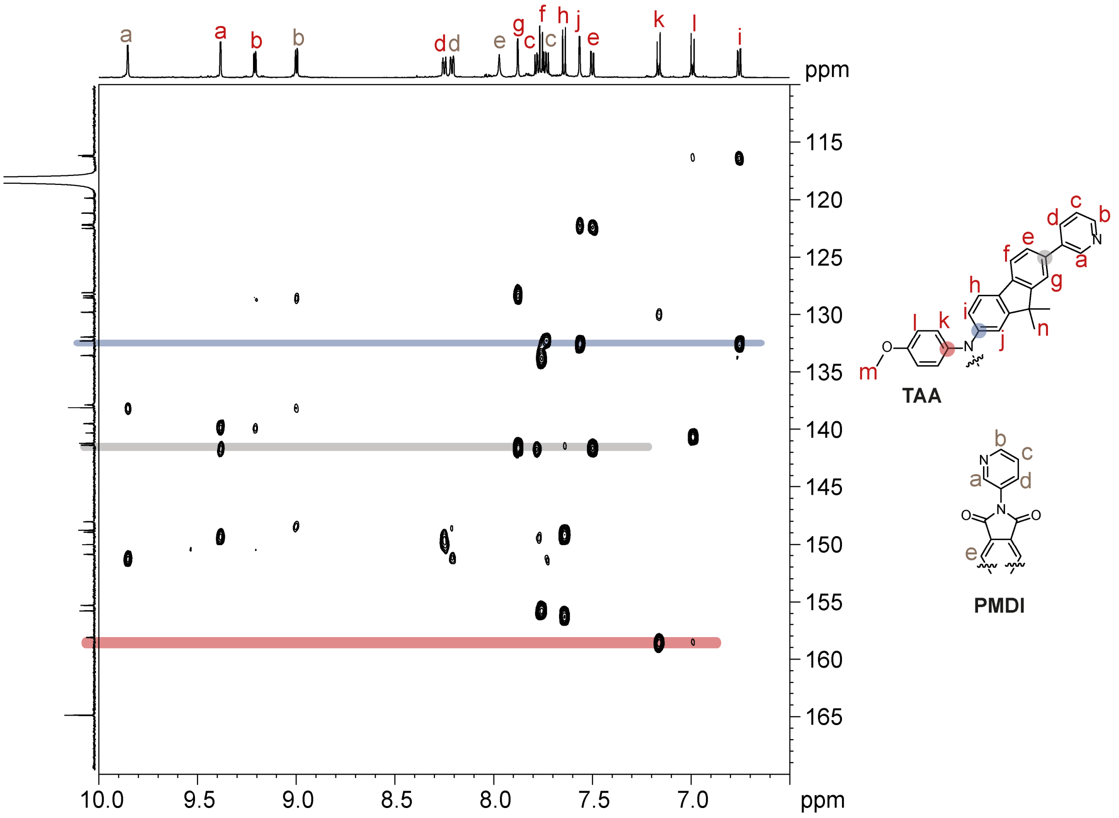

Fig. 69 ^{1}H-^{13}C HMBC NMR spectrum of [Pd$_2$**TAA**$_2$**PMDI**$_2$]$^{4+}$ (600 MHz, 151 MHz, 298 K, CD$_3$CN).

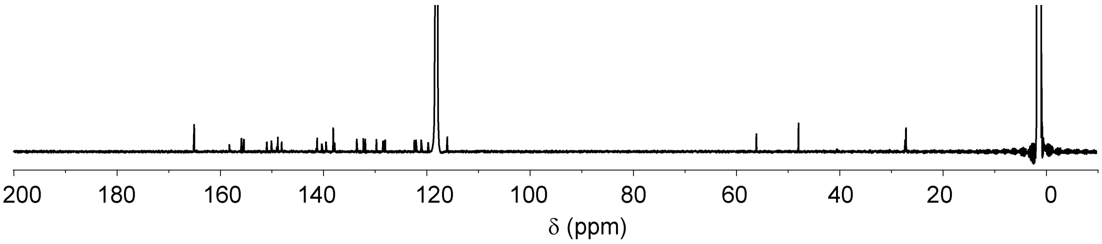

Fig. 70 ^{13}C-NMR spectrum of [Pd$_2$**TAA**$_2$**PMDI**$_2$]$^{4+}$ (151 MHz, 298 K, CD$_3$CN).

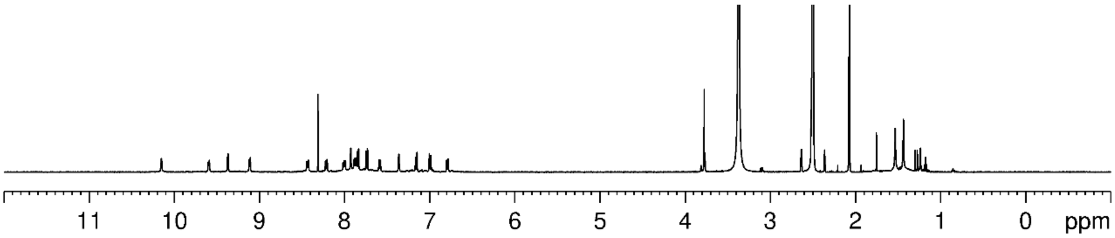

Fig. 71 Full ^{1}H NMR spectrum of [Pd$_2$**TAA**$_2$**PMDI**$_2$]$^{4+}$ (500 MHz, 298 K, DMSO-*d*$_6$).

[Pd$_2$**PTZ**$_2$**NDI**$_2$]$^{4+}$

Solutions of **PTZ** (250 µL, 2.8 mM, DMSO-*d*$_6$), **NDI** (250 µL, 2.8 mM, DMSO-*d*$_6$), and [Pd(CH$_3$CN)$_4$](BF$_4$)$_2$ (50 µL, 15 mM, DMSO-*d*$_6$) were combined. The mixture was heated at 70 °C for 1.5 h. The solvent was then removed by lyophilization and the sample dissolved in CD$_3$CN via sonication.

^{1}H NMR (600 MHz, CD$_3$CN) δ 9.62 (s, 1H), 9.17 (s, 1H), 8.99 – 8.90 (m, 3H), 8.34 (s, 1H), 8.25 (d, *J* = 8.1, 1.8 Hz, 1H), 7.96 (d, *J* = 8.0 Hz, 1H), 7.79 (dd, *J* = 8.1, 5.8 Hz, 1H), 7.64 (dd, *J* = 8.0, 5.9 Hz, 1H), 7.48 (s, 1H), 7.34 (dd, *J* = 8.3, 1.9 Hz, 1H), 6.97 (d, *J* = 8.4 Hz, 1H), 3.87 (t, *J* = 7.1 Hz, 1H), 1.74 – 1.64 (m, 1H), 1.41 – 1.33 (m, 1H), 1.29 – 1.20 (m, 2H), 0.80 (t, *J* = 7.0 Hz, 1.5H).

^{1}H NMR (500 MHz, DMSO-*d*$_6$) δ 9.84 (d, *J* = 2.4 Hz, 1H), 9.25 (s, 2H), 9.09 (d, *J* = 5.8 Hz, 1H), 8.94 (s, 1H), 8.35 (d, *J* = 8.1 Hz, 1H), 8.18 (dt, *J* = 8.0, 1.6 Hz, 1H), 8.13 (s, 1H), 7.92 (dd, *J* = 8.1, 5.8 Hz, 1H), 7.81 (dd, *J* = 8.0, 5.8 Hz, 1H), 7.47 – 7.38 (m, 2H), 7.12 (d, *J* = 8.5 Hz, 1H), 3.89 (t, *J* = 6.8 Hz, 1H), 1.67 – 1.56 (m, 1H), 1.37 – 1.28 (m, 1H), 1.23 – 1.12 (m, 2H), 0.75 (t, 1.5H).

^{13}C NMR (151 MHz, CD$_3$CN) δ 163.74, 163.37, 154.70, 152.15, 152.05, 149.96, 146.62, 142.32, 142.24, 135.61, 133.44, 132.03, 131.86, 131.60, 128.46, 128.44, 127.96, 127.89, 127.81, 124.77, 124.67, 117.14, 116.58, 95.98, 84.78, 48.31, 31.90, 27.03, 26.80, 23.16, 14.13.

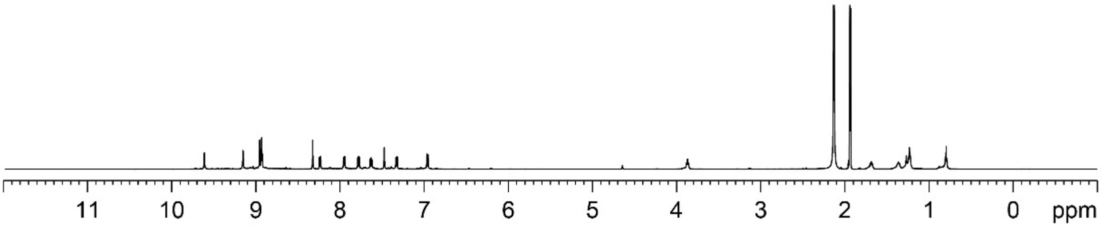

Fig. 72 Full ^{1}H NMR spectrum of [Pd$_2$**PTZ**$_2$**NDI**$_2$]$^{4+}$ (600 MHz, 298 K, CD$_3$CN).

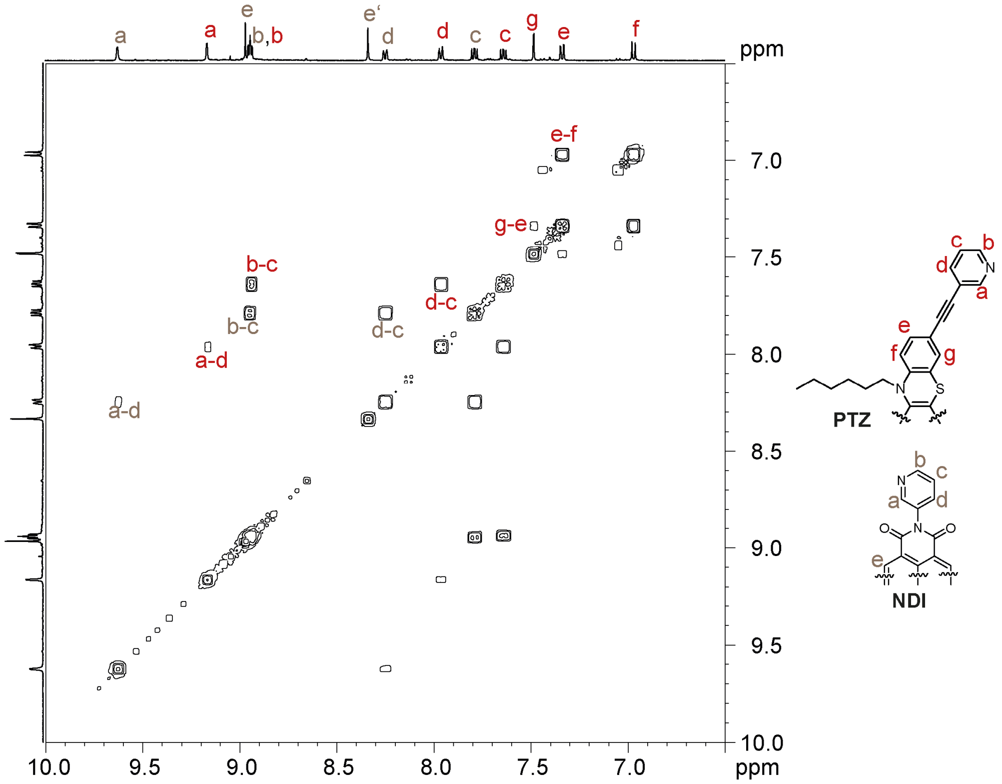

Fig. 73 Partial ^{1}H-^{1}H COSY NMR spectrum of [Pd$_2$**PTZ**$_2$**NDI**$_2$]$^{4+}$ (600 MHz, 298 K, CD$_3$CN).

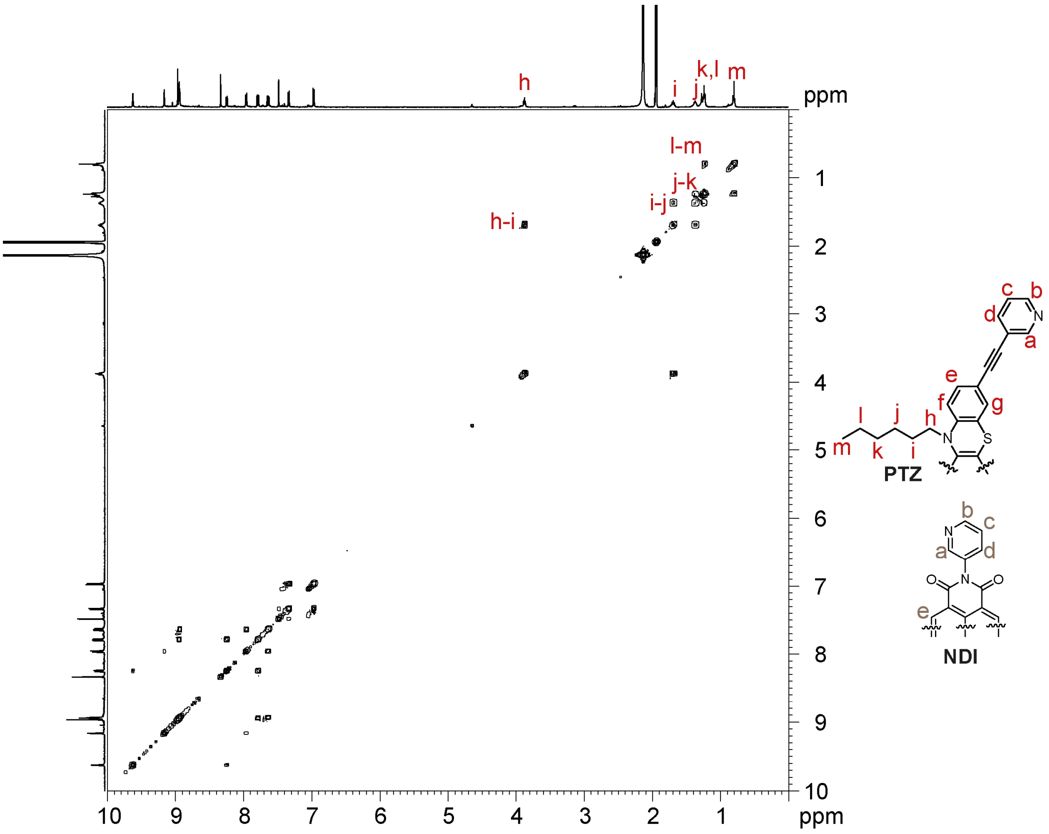

Fig. 74 Full ^{1}H-^{1}H COSY NMR spectrum of [Pd$_2$**PTZ**$_2$**NDI**$_2$]$^{4+}$ (600 MHz, 298 K, CD$_3$CN).

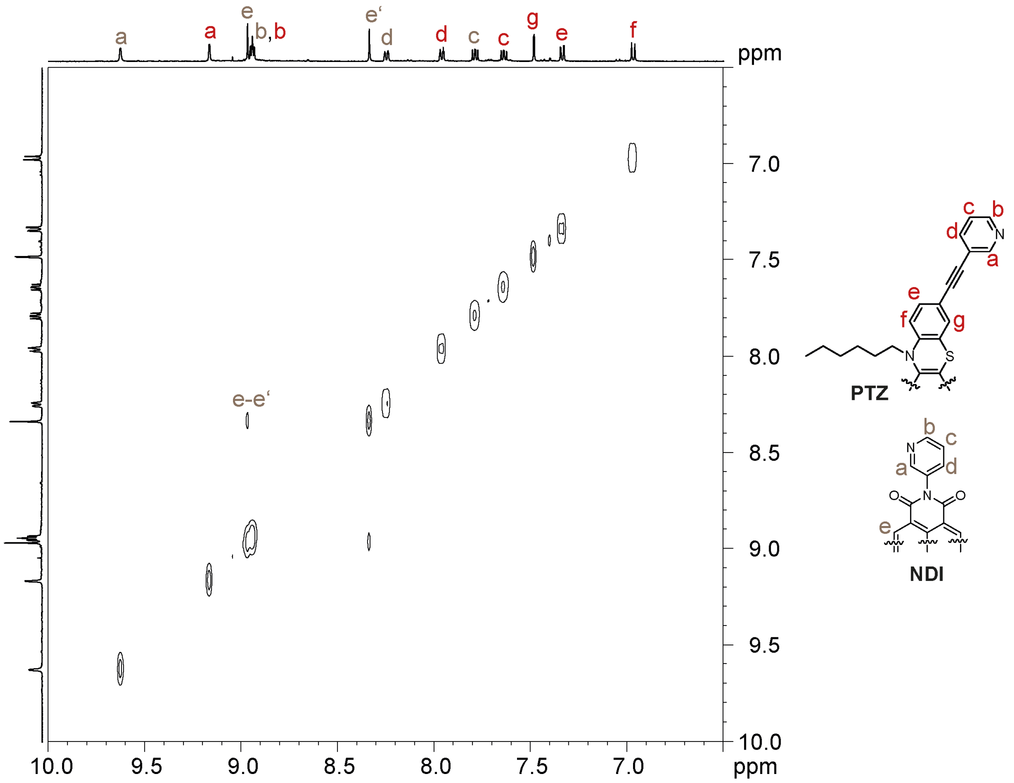

Fig. 75 Partial ^1H-^1H NOESY NMR spectrum of $[Pd_2\mathbf{PTZ}_2\mathbf{NDI}_2]^{4+}$ (600 MHz, 298 K, CD_3CN).

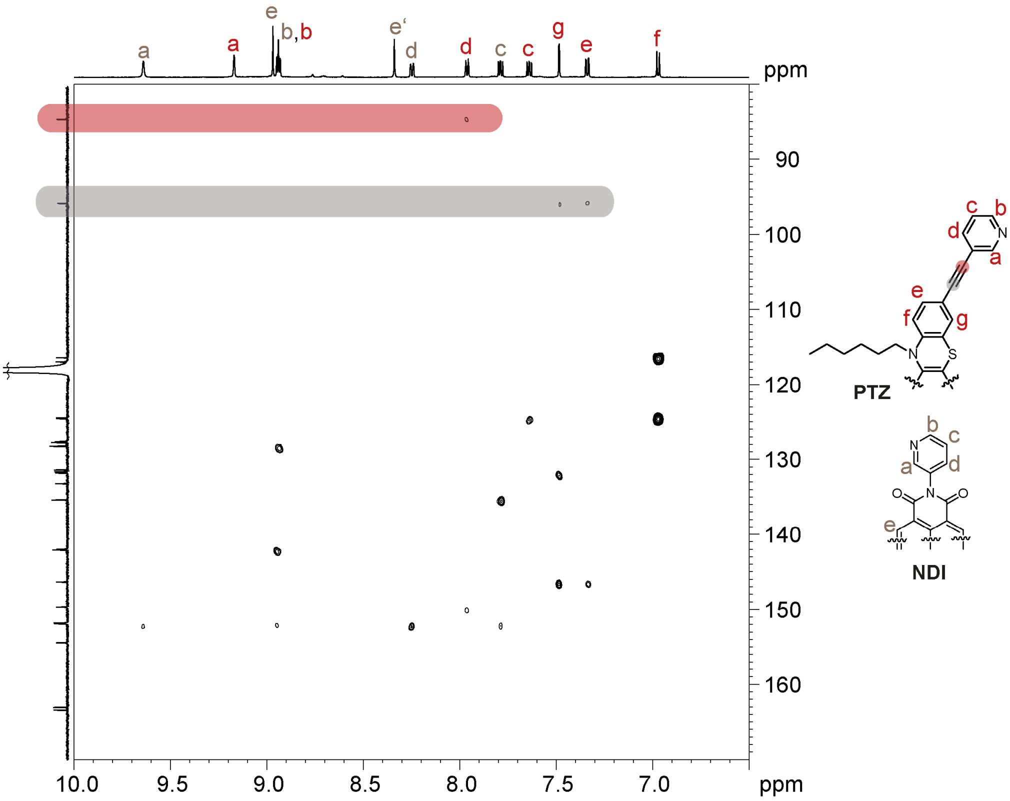

Fig. 76 Partial ^1H-^{13}C HMBC NMR spectrum of $[Pd_2\mathbf{PTZ}_2\mathbf{NDI}_2]^{4+}$ (600 MHz, 151 MHz, 298 K, CD_3CN).

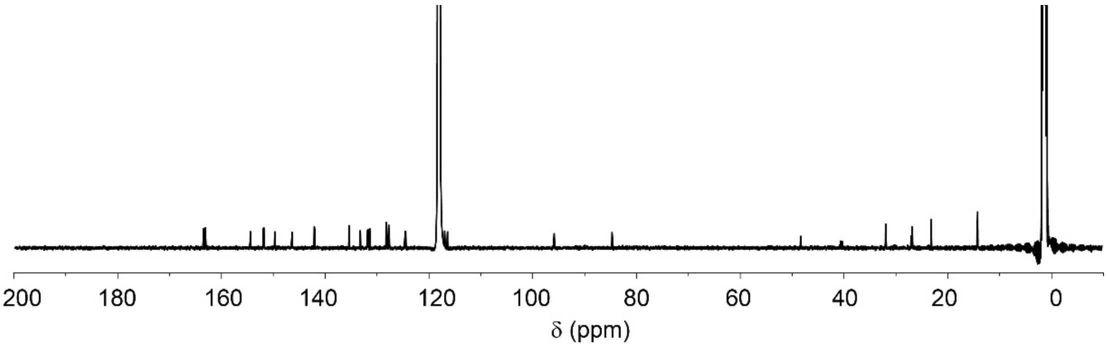

Fig. 77 ^{13}C NMR spectrum of [Pd_2**PTZ**$_2$**NDI**$_2$]$^{4+}$ (151 MHz, 298 K, CD_3CN).

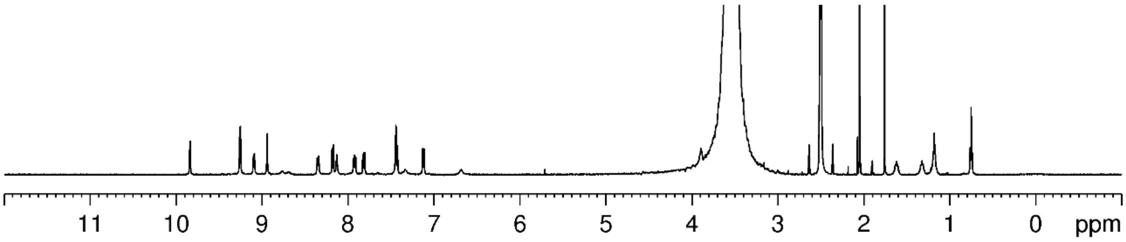

Fig. 78 Full ^{1}H NMR spectrum of [Pd_2**PTZ**$_2$**NDI**$_2$]$^{4+}$ (500 MHz, 298 K, DMSO-*d*$_6$). The broad signals at δ = 7.27 and 6.67 ppm are due to the heated Pd(II) salt.

[Pd_2**PTZ**$_2$**PMDI**$_2$]$^{4+}$

Solutions of **PTZ** (250 µL, 2.8 mM, DMSO-*d*$_6$), **PMDI** (250 µL, 2.8 mM, DMSO-*d*$_6$), and [$Pd(CH_3CN)_4$]$(BF_4)_2$ (50 µL, 15 mM, DMSO-*d*$_6$) were combined. The mixture was heated at 70 °C for 1.5 h. The solvent was then removed by lyophilization and the sample dissolved in CD_3CN via sonication.

^{1}H NMR (600 MHz, CD_3CN) δ 9.94 (s, 1H), 9.32 (s, 1H), 8.94 (dd, *J* = 6.0, 1.3 Hz, 1H), 8.85 (dd, *J* = 5.8, 1.2 Hz, 1H), 8.20 (ddd, *J* = 8.2, 2.2, 1.2 Hz, 1H), 7.95 (dt, *J* = 8.1, 1.6 Hz, 1H), 7.77 – 7.69 (m, 2H), 7.64 (s, 1H), 7.34 (dd, *J* = 8.4, 2.0 Hz, 1H), 6.98 (d, *J* = 8.4 Hz, 1H), 3.89 (t, *J* = 7.1 Hz, 1H), 1.75 – 1.66 (m, 1H), 1.43 – 1.32 (m, 1H), 1.29 – 1.19 (m, 2H), 0.81 (t, *J* = 7.08, 1.5H).

^{1}H NMR (500 MHz, DMSO-*d*$_6$) δ 10.19 (s, 1H), 9.63 (s, 1H), 9.23 (s, 1H), 9.02 (d, *J* = 5.7 Hz, 1H), 8.26 (d, *J* = 8.0 Hz, 1H), 8.19 (dt, *J* = 8.1, 1.5 Hz, 1H), 7.89 (dd, *J* = 8.2, 5.8 Hz, 1H), 7.84 (dd, *J* = 8.0, 5.8 Hz, 1H), 7.63 (s, 1H), 7.42 (d, *J* = 8.2 Hz, 1H), 7.10 (d, *J* = 8.6 Hz, 1H), 3.91 (t, *J* = 6.0 Hz, 1H), 1.70 – 1.58 (m, 1H), 1.40 – 1.31 (m, 1H), 1.29 – 1.10 (m, 2H), 0.78 (t, *J* = 7.0 Hz, 1.5 H).

^{13}C NMR (151 MHz, CD_3CN) δ 165.48, 154.67, 151.39, 149.83, 149.33, 146.58, 141.88, 138.57, 138.36, 132.44, 132.15, 131.83, 128.66, 128.51, 124.79, 124.41, 117.06, 116.44, 96.15, 84.84, 48.30, 31.91, 27.01, 26.81, 23.17, 14.14.

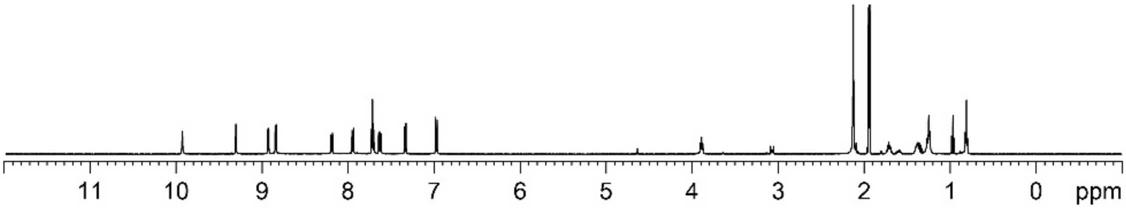

Fig. 79 Full ^{1}H NMR spectrum of [Pd_2**PTZ**$_2$**PMDI**$_2$]$^{4+}$ (600 MHz, 298 K, CD_3CN).

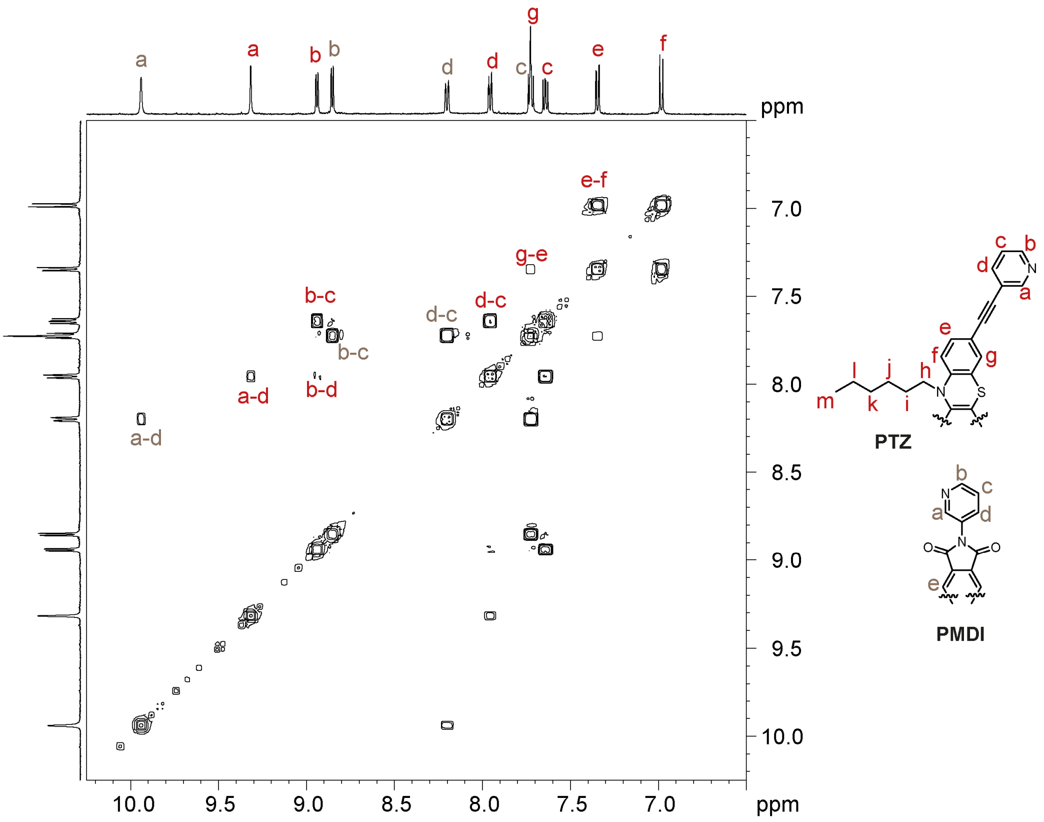

Fig. 80 Partial ^{1}H-^{1}H COSY NMR spectrum of [Pd$_2$**PTZ**$_2$**PMDI**$_2$]$^{4+}$ (600 MHz, 298 K, CD$_3$CN).

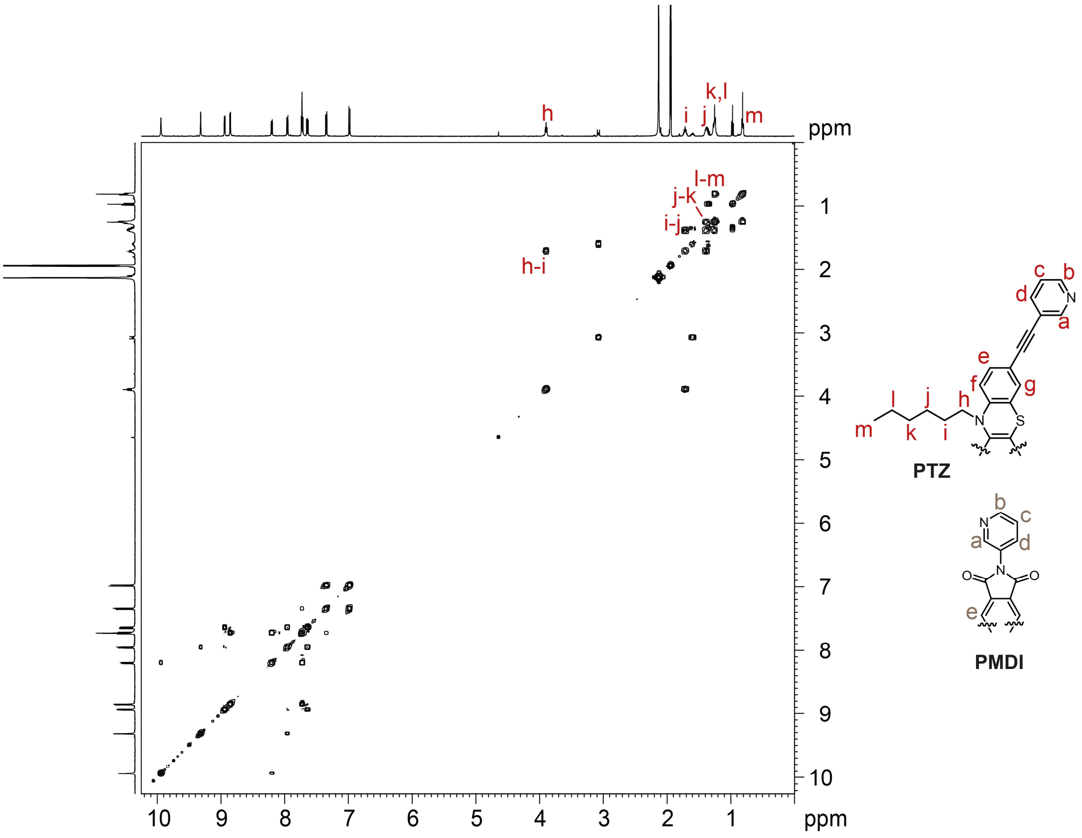

Fig. 81 Full ^{1}H-^{1}H COSY NMR spectrum of [Pd$_2$**PTZ**$_2$**PMDI**$_2$]$^{4+}$ (600 MHz, 298 K, CD$_3$CN).

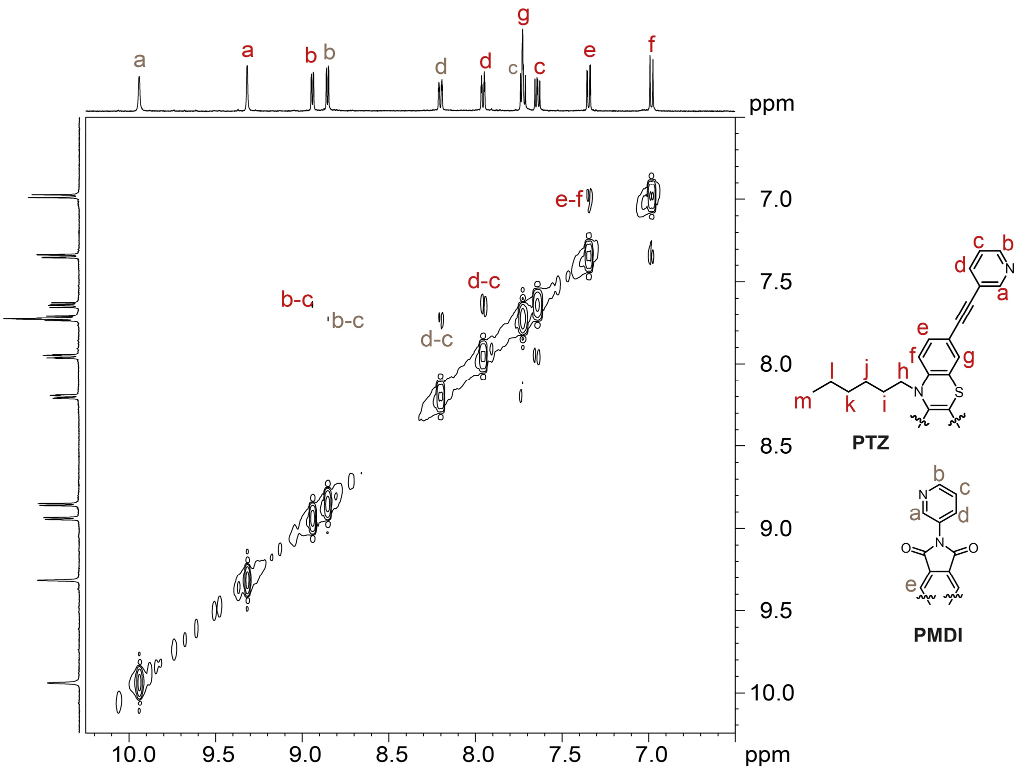

Fig. 82 Partial ^{1}H-^{1}H NOESY NMR spectrum of [Pd$_2$**PTZ**$_2$**PMDI**$_2$]$^{4+}$ (600 MHz, 298 K, CD$_3$CN).

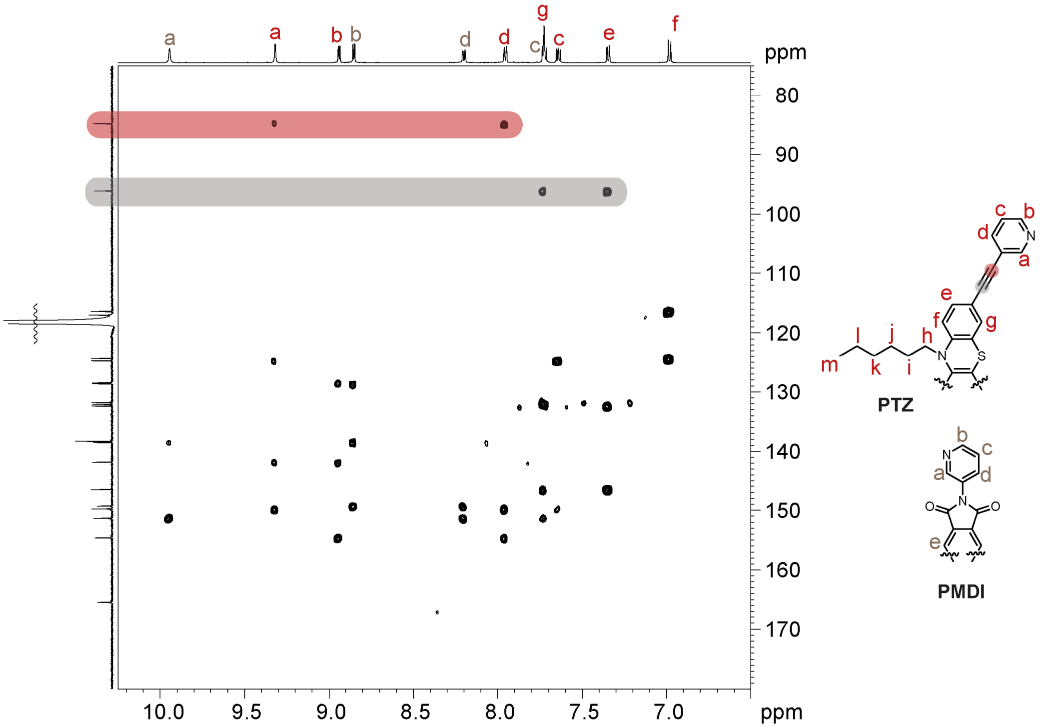

Fig. 83 ^{1}H-^{13}C HMBC NMR spectrum of [Pd$_2$**PTZ**$_2$**PMDI**$_2$]$^{4+}$ (600 MHz, 151 MHz, 298 K, CD$_3$CN).

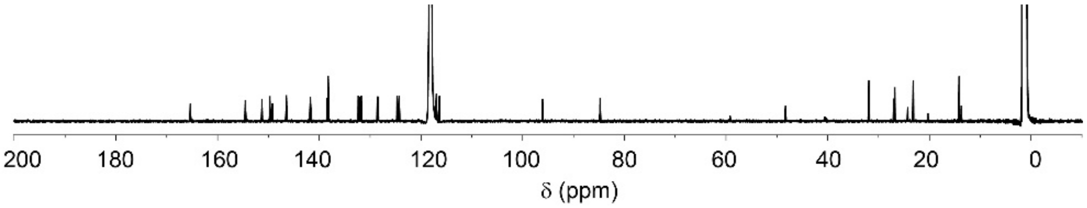

Fig. 84 ^{13}C-NMR spectrum of [Pd$_2$**PTZ**$_2$**PMDI**$_2$]$^{4+}$ (151 MHz, 298 K, CD$_3$CN).

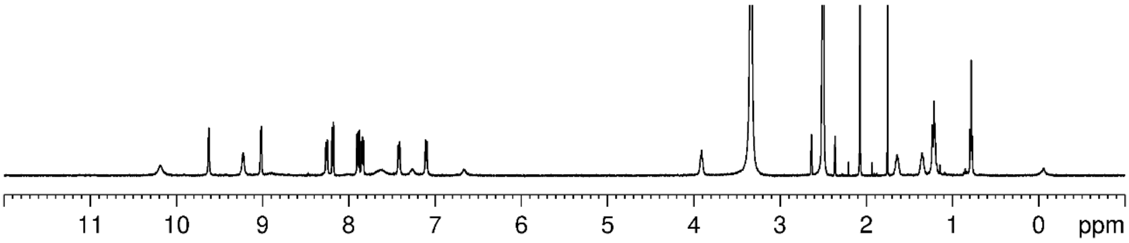

Fig. 85 Full ^{1}H NMR spectrum of [Pd$_2$**PTZ**$_2$**PMDI**$_2$]$^{4+}$ (500 MHz, 298 K, DMSO-d_6). The broad signals at δ = 7.27 and 6.67 ppm are due to the heated Pd(II) salt.

3.11.4. X-ray crystallography

Two of the donor-acceptor cages, $[Pd_2\mathbf{CBZ}_2\mathbf{NDI}_2]^{4+}$ and $[Pd_2\mathbf{TAA}_2\mathbf{NDI}_2]^{4+}$, were investigated with single crystal X-ray crystallography. Noteworthy, crystals of such supramolecular assemblies are highly sensitive towards solvent loss, requiring handling under cryogenic conditions. Due to the small crystal volume, highly brilliant synchrotron radiation was required. The diffraction data were collected during two beamtime shifts at the macromolecular synchrotron beamline P11, PETRA III, at DESY in Hamburg.[43] Macromolecular refinement protocols employing geometrical restraint dictionaries, similarity restraints, and restraints for anisotropic displacement parameters (ADPs) were applied and adapted. Details can be found in the discussions below. The refinement was carried out by Björn Schmidt. He also prepared the texts and tables shown here.

Tab. 7 Crystallographic data of $[Pd_2\mathbf{CBZ}_2\mathbf{NDI}_2]^{4+}$ and $[Pd_2\mathbf{TAA}_2\mathbf{NDI}_2]^{4+}$.

Compound	$[Pd_2\mathbf{CBZ}_2\mathbf{NDI}_2]^{4+}$	$[Pd_2\mathbf{TAA}_2\mathbf{NDI}_2]^{4+}$
Empirical formula	$C_{138}H_{97}B_4F_{16}N_{15}O_{10}Pd_2$	$C_{161}H_{123}B_3F_{12}N_{17}O_{13}Pd_2$
Formula weight	2685.34	2976.99
Temperature [K]	100(2)	100(2)
Crystal system	triclinic	triclinic
Space group (number)	$P\overline{1}$ (2)	$P\overline{1}$ (2)
a [Å]	14.965(3)	17.398(8)
b [Å]	21.519(3)	19.888(8)
c [Å]	22.796(4)	23.964(7)
α [°]	112.928(6)	108.302(4)
β [°]	105.130(14)	104.684(17)
γ [°]	95.821(18)	97.323(12)
Volume [Å^3]	6354.1(18)	7419(5)
Z	2	2
ρ_{calc} [gcm^{-3}]	1.404	1.333
μ [mm^{-1}]	0.461	0.865
F(000)	2732	3054
Crystal size [mm^3]	0.005×0.005×0.060	0.050×0.100×0.300
Crystal color	colorless	yellow
Crystal shape	needle	plate
Radiation	synchrotron (λ = 0.77489 Å)	synchrotron (λ = 1.03321 Å)
2θ range [°]	2.24 to 55.60 (0.83 Å)	2.74 to 50.99 (1.20 Å)
Index ranges	$-17 \leq h \leq 17$ $-24 \leq k \leq 24$ $-26 \leq l \leq 26$	$-14 \leq h \leq 14$ $-16 \leq k \leq 15$ $-18 \leq l \leq 18$
Reflections collected	116680	53488
Independent reflections	18502 R_{int} = 0.1587 R_{sigma} = 0.0731	8059 R_{int} = 0.1478 R_{sigma} = 0.0722
Completeness to θ = 27.706°	80.5%	89.4%
Data / Restraints / Parameters	18502 / 3444 / 1758	8059 / 4058 / 1910
Goodness-of-fit on F^2	1.063	1.204
Final *R* indexes [$I \geq 2\sigma(I)$]	R_1 = 0.0850 wR_2 = 0.2410	R_1 = 0.0945 wR_2 = 0.2729
Final *R* indexes [all data]	R_1 = 0.1106 wR_2 = 0.2650	R_1 = 0.1268 wR_2 = 0.3036
Largest peak/hole [eÅ^{-3}]	1.20/−0.97	0.71/−0.42

Crystal structure of [Pd$_2$TAA$_2$NDI$_2$]$^{4+}$ (LN9m_sq)

Yellow plate-shaped crystals of [Pd$_2$**TAA**$_2$**NDI**$_2$]$^{4+}$ were grown by slow vapor diffusion of methyl *tert*-butyl ether into the solution of [Pd$_2$**TAA**$_2$**NDI**$_2$]$^{4+}$ in acetonitrile at room temperature. Single crystals in mother liquor were pipetted onto a glass slide containing NVH oil. To avoid collapse of the crystal lattice, the crystal was quickly mounted onto a 0.05 mm nylon loop and immediately flash-cooled in liquid nitrogen. Crystals were stored at cryogenic temperature in dry shippers, in which they were safely transported to macromolecular beamline P11 at Petra III, DESY, Hamburg, Germany.[43] A wavelength of λ = 1.03321 Å was chosen using a liquid N$_2$-cooled double-crystal monochromator. Single crystal X-ray diffraction data of several crystals was collected at 100 K on a single-axis goniometer, equipped with an Oxford Cryostream 800 and an Eiger 2x 16M detector. 3600 diffraction images were collected in a 360° ϕ sweep at a detector distance of 154 mm, 0.1° step width and 0.1 seconds exposure time per image. Data integration and reduction were undertaken using XDS.[44] The combined diffraction data of two crystals (x15 & x16) has a completeness of 89.4%. The structure was solved by intrinsic phasing/direct methods using SHELXT[45] and refined with SHELXL[46] using 22 CPU cores for full-matrix least-squares routines on F^2 and ShelXle[47] as a graphical user interface and the DSR program plugin was employed for modeling.[48,49]

Specific refinement details for [Pd$_2$TAA$_2$NDI$_2$]$^{4+}$ (LN9m_sq)

The structure was solved and refined in a triclinic space group $P\bar{1}$ (2) and contains one full coordination cage molecule [Pd$_2$**TAA**$_2$**NDI**$_2$]$^{4+}$ and a half ligand **NDI** in the asymmetric unit. Three tetrafluoroborate counterions were successfully modelled and one of them is outside and two are inside of the cage. One of the inside tetrafluoroborate anions is disordered and both possible positions have an occupancy of around 50%. Furthermore, one methyl *tert*-butyl ether and acetonitrile molecule were modelled outside the coordination cage. Stereochemical restraint dictionaries for the ligands were generated by the GRADE2 program using the GRADE2 Web Server (http://grade2.globalphasing.org) and applied in the refinement. A GRADE2 dictionary for SHELXL contains target values and standard deviations for 1,2-distances (DFIX) and 1,3-distances (DANG), as well as restraints for planar groups (FLAT). All displacements for non-hydrogen atoms were refined anisotropically. The refinement of ADPs for carbon, nitrogen and oxygen atoms was enabled by a combination of similarity restraints (SIMU) and rigid bond restraints (RIGU).[50] The contribution of the electron density from disordered counterions and solvent molecules, which could not be modeled with discrete atomic positions was handled using the SQUEEZE[51] routine in PLATON.[52] The solvent mask file (.fab) computed by PLATON was included in the SHELXL refinement via the ABIN instruction leaving the measured intensities untouched.

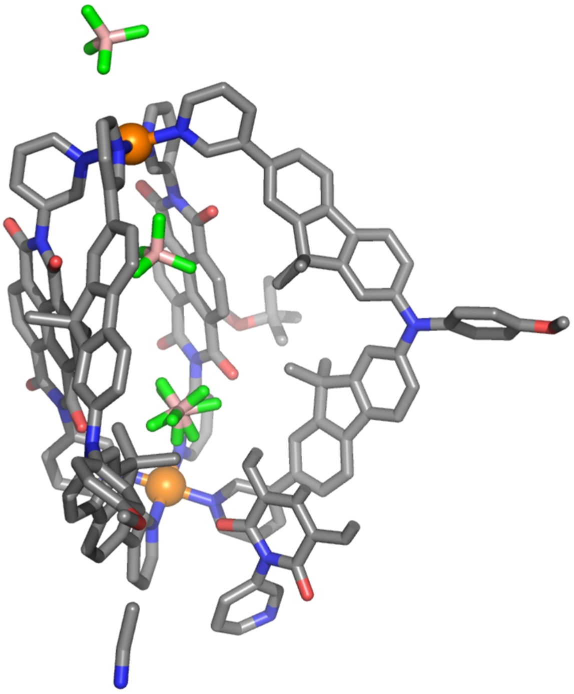

Fig. 86 View of the asymmetric unit of [Pd_2**TAA_2****NDI_2**]$^{4+}$ (LN9m_sq).

Crystal structure of [$Pd_2CBZ_2NDI_2$]$^{4+}$ (LN14u_sq)

Colorless needle-shaped crystals of [Pd_2**CBZ_2****NDI_2**]$^{4+}$ were grown by slow vapor diffusion of tetrahydrofuran into the solution of [Pd_2**CBZ_2****NDI_2**]$^{4+}$ in acetonitrile at room temperature. Single crystals in mother liquor were pipetted onto a glass slide containing NVH oil. To avoid collapse of the crystal lattice, the crystal was quickly mounted onto a 0.05 mm nylon loop and immediately flash-cooled in liquid nitrogen. Crystals were stored at cryogenic temperature in dry shippers, in which they were safely transported to macromolecular beamline P11 at Petra III, DESY, Hamburg, Germany.[43] A wavelength of λ = 0.77489 Å was chosen using a liquid N2-cooled double-crystal monochromator. Single crystal X-ray diffraction data of several crystals was collected at 100 K on a single-axis goniometer, equipped with an Oxford Cryostream 800 and an Eiger 2x 16M detector. 3600 diffraction images were collected in a 360° ϕ sweep at a detector distance of 154 mm, 0.1° step width and 0.1 seconds exposure time per image. Data integration and reduction were undertaken using XDS.[44] The combined diffraction data of two crystals (x14 & x15) has a completeness of 79.8%. The structure was solved by intrinsic phasing/direct methods using SHELXT[45] and refined with SHELXL[46] using 22 CPU cores for full-matrix least-squares routines on F^2 and ShelXle[47] as a graphical user interface and the DSR program plugin was employed for modeling.[48,49]

Specific refinement details for [$Pd_2CBZ_2NDI_2$]$^{4+}$ (LN14u_sq)

The structure was solved and refined in a triclinic space group $P\bar{1}$ (2) and therefore contains one full coordination cage molecule [Pd_2**CBZ_2****NDI_2**]$^{4+}$ in the asymmetric unit. Four tetrafluoroborate counterions were successfully modelled and two of them are outside and two are inside of the cage. The two outside tetrafluoroborate anions are disordered and free variables were used for refinement of occupancy factors. Furthermore, two tetrahydrofuran molecules outside of the cage and one acetonitrile molecule in the cavity were modelled. Stereochemical restraint dictionaries for the ligands were generated by the GRADE2 program using the GRADE2 Web Server (http://grade2.globalphasing.org) and applied in the refinement. A GRADE2 dictionary for SHELXL contains target values and standard deviations for 1,2-distances (DFIX) and 1,3-distances

(DANG), as well as restraints for planar groups (FLAT). All displacements for non-hydrogen atoms were refined anisotropically. The refinement of ADPs for carbon, nitrogen and oxygen atoms was enabled by a combination of similarity restraints (SIMU) and rigid bond restraints (RIGU).[50] The contribution of the electron density from disordered counterions and solvent molecules, which could not be modeled with discrete atomic positions was handled using the SQUEEZE[51] routine in PLATON.[52] The solvent mask file (.fab) computed by PLATON was included in the SHELXL refinement via the ABIN instruction leaving the measured intensities untouched.

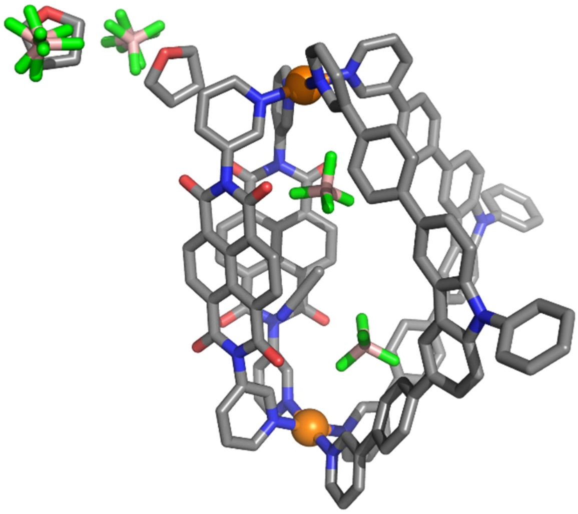

Fig. 87 View of the asymmetric unit of [Pd$_2$**CBZ**$_2$**NDI**$_2$]$^{4+}$ (LN14u_sq).

3.11.5. UV-Vis absorption spectroscopy

The UV-Vis absorption spectra of ligands **CBZ**, **NDI**, and **PMDI**, of the homoleptic assemblies [Pd$_2$**CBZ**$_4$]$^{4+}$, [Pd$_2$**PTZ**$_4$]$^{4+}$, [Pd$_3$**NDI**$_6$]$^{6+}$ + [Pd$_4$**NDI**$_8$]$^{8+}$, [Pd$_3$**PMDI**$_6$]$^{6+}$, and [Pd$_3$**FRO**$_6$]$^{6+}$ as well as of all nine heteroleptic cages are described here. The spectra of ligand **PTZ** and double cage [Pd$_4$**PTZ**$_8$]$^{8+}$[16] as well as of ligand **FRO** are published.[15] Ligand **TAA** and its homoleptic cage were investigated by Dr. Jacopo Tessarolo (unpublished).

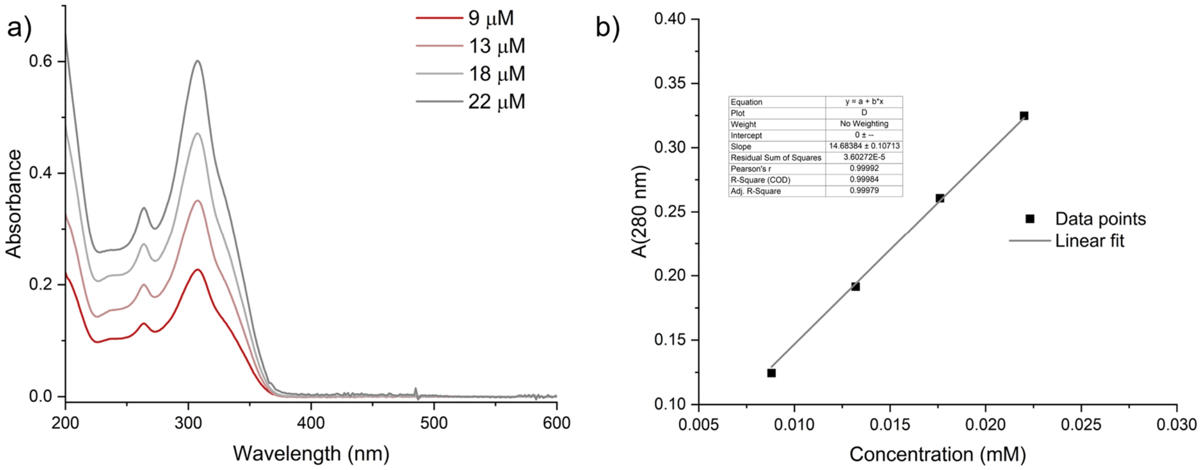

Equation	y = a + b*x
Plot	D
Weight	No Weighting
Intercept	0 ± --
Slope	14.68384 ± 0.10713
Residual Sum of Squares	3.60272E-5
Pearson's r	0.99992
R-Square (COD)	0.99984
Adj. R-Square	0.99979

Fig. 88a) UV-Vis absorption spectra of ligand **CBZ** at different concentrations (CH_3CN, 4 mm cuvette pathlength; b) linear fit of the absorbance at 280 nm against the ligand concentration for the determination of the extinction coefficient (ε(280 nm) = 3.67 mM^{-1}·mm^{-1}).

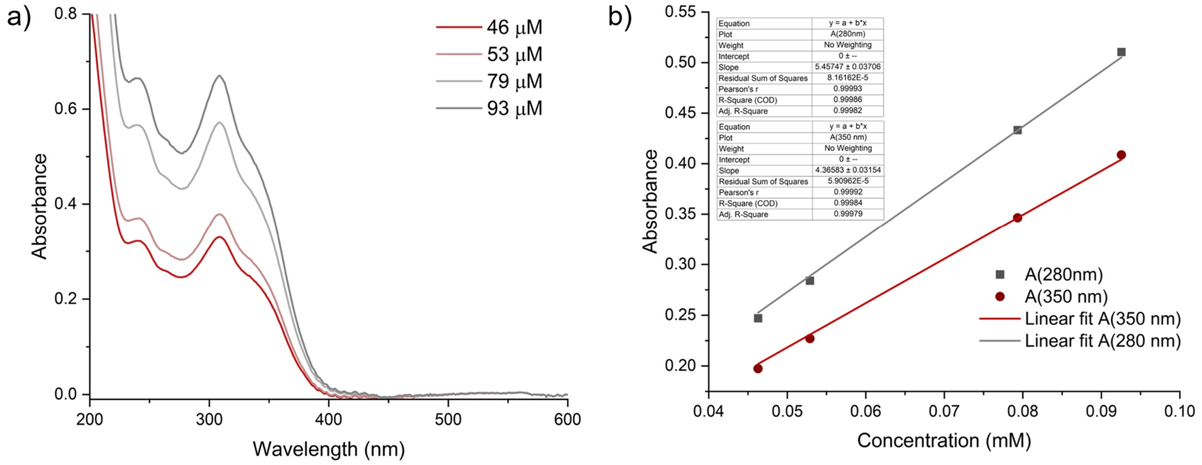

Equation	y = a + b*x
Plot	A(280nm)
Weight	No Weighting
Intercept	0 ± --
Slope	5.45747 ± 0.03706
Residual Sum of Squares	8.16162E-5
Pearson's r	0.99993
R-Square (COD)	0.99986
Adj. R-Square	0.99982

Equation	y = a + b*x
Plot	A(350 nm)
Weight	No Weighting
Intercept	0 ± --
Slope	4.36583 ± 0.03154
Residual Sum of Squares	5.90962E-5
Pearson's r	0.99992
R-Square (COD)	0.99984
Adj. R-Square	0.99979

Fig. 89a) UV-Vis absorption spectra of [Pd$_2$**CBZ**$_4$]$^{4+}$ at different ligand concentrations (CH_3CN, 1 mm cuvette pathlength; b) linear fit of the absorbance at 280 nm and at 350 nm against the ligand concentration for the determination of the extinction coefficient (ε(280 nm) = 5.46 mM^{-1}·mm^{-1}, ε(350 nm) = 4.37 mM^{-1}·mm^{-1}).

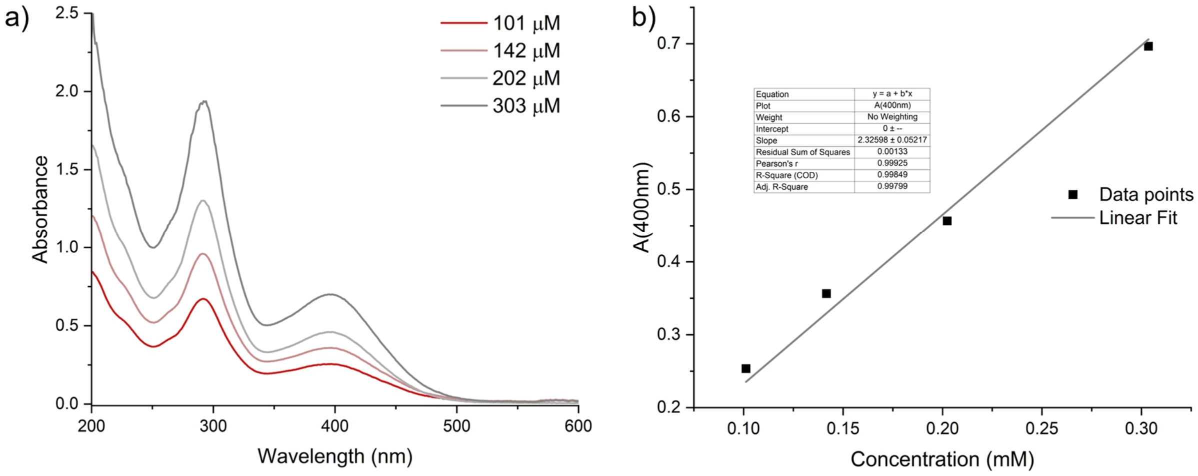

Equation	y = a + b*x
Plot	A(400nm)
Weight	No Weighting
Intercept	0 ± --
Slope	2.32598 ± 0.05217
Residual Sum of Squares	0.00133
Pearson's r	0.99925
R-Square (COD)	0.99849
Adj. R-Square	0.99799

Fig. 90a) UV-Vis absorption spectra of $[Pd_2\mathbf{PTZ}_4]^{4+}$ at different ligand concentrations (CH_3CN, 1 mm cuvette pathlength); b) linear fit of the absorbance at 400 nm against the ligand concentration for the determination of the extinction coefficient (ε(400 nm) = 2.33 $mM^{-1}\cdot mm^{-1}$).

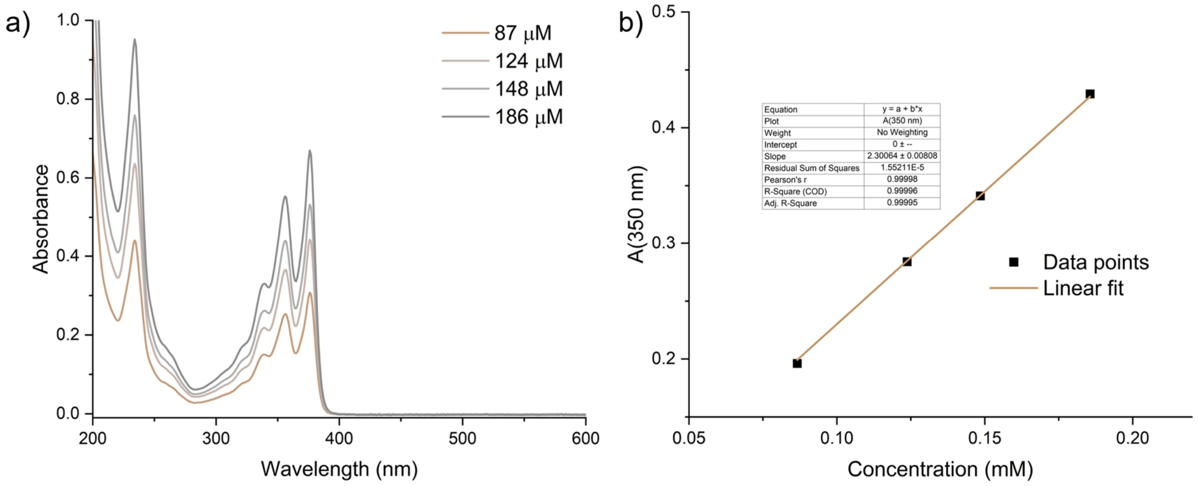

Equation	y = a + b*x
Plot	A(350 nm)
Weight	No Weighting
Intercept	0 ± --
Slope	2.30064 ± 0.00808
Residual Sum of Squares	1.55211E-5
Pearson's r	0.99998
R-Square (COD)	0.99996
Adj. R-Square	0.99995

Fig. 91a) UV-Vis absorption spectra of **NDI** at different concentrations (CH_3CN, 1 mm cuvette pathlength); b) linear fit of the absorbance at 350 nm against the ligand concentration for the determination of the extinction coefficient (ε(350 nm) = 2.30 $mM^{-1}\cdot mm^{-1}$).

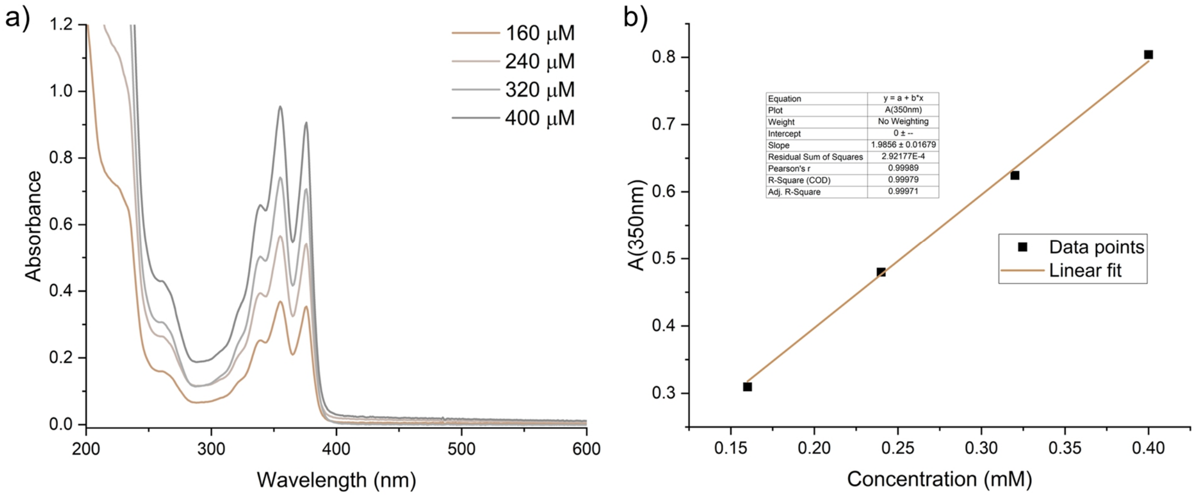

Equation	y = a + b*x
Plot	A(350nm)
Weight	No Weighting
Intercept	0 ± --
Slope	1.9856 ± 0.01679
Residual Sum of Squares	2.92177E-4
Pearson's r	0.99989
R-Square (COD)	0.99979
Adj. R-Square	0.99971

Fig. 92a) UV-Vis absorption spectra of $[Pd_3\mathbf{NDI}_6]^{6+}$+$[Pd_4\mathbf{NDI}_8]^{8+}$at different ligand concentrations (CH_3CN, 1 mm cuvette pathlength); b) linear fit of the absorbance at 350 nm against the ligand concentration for the determination of the extinction coefficient (ε(350 nm) = 1.99 $mM^{-1}\cdot mm^{-1}$).

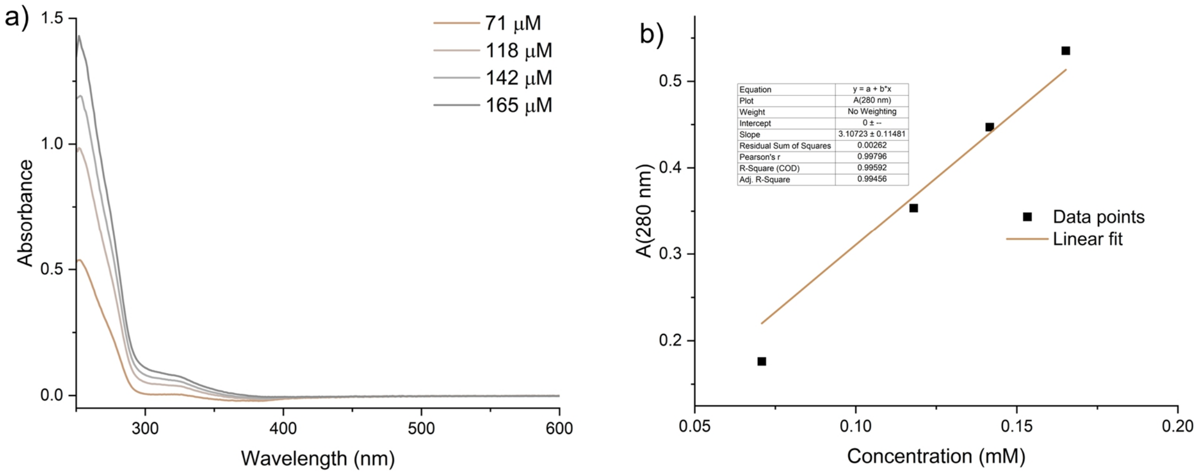

Equation	y = a + b*x
Plot	A(280 nm)
Weight	No Weighting
Intercept	0 ± --
Slope	3.10723 ± 0.11481
Residual Sum of Squares	0.00262
Pearson's r	0.99796
R-Square (COD)	0.99592
Adj. R-Square	0.99456

Fig. 93a) UV-Vis absorption spectra of **PMDI** at different concentrations (DMSO, 1 mm cuvette pathlength); b) linear fit of the absorbance at 280 nm against the ligand concentration for the determination of the extinction coefficient (ε(280 nm) = 3.11 $mM^{-1} \cdot mm^{-1}$).

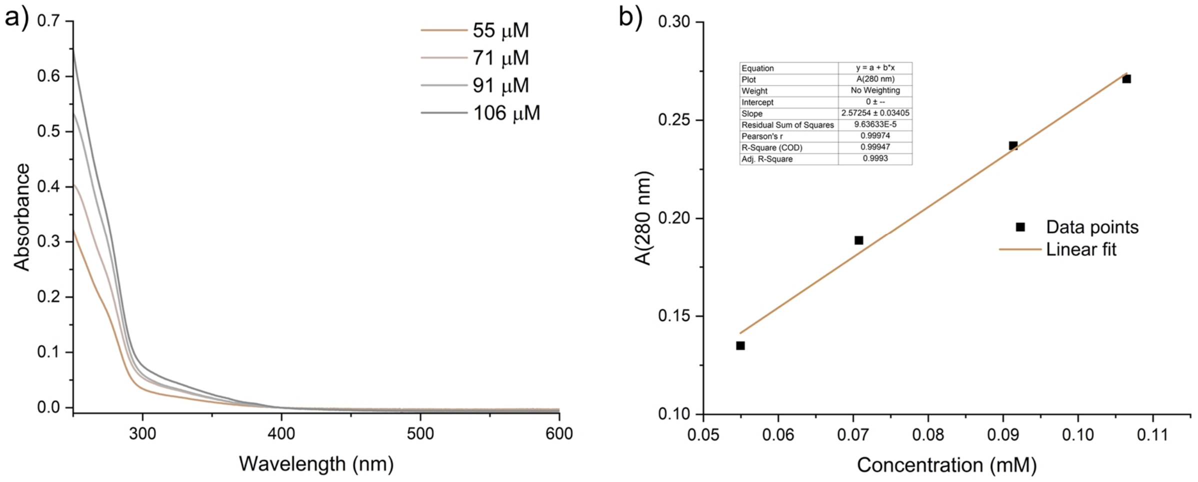

Equation	y = a + b*x
Plot	A(280 nm)
Weight	No Weighting
Intercept	0 ± --
Slope	2.57254 ± 0.03405
Residual Sum of Squares	9.63633E-5
Pearson's r	0.99974
R-Square (COD)	0.99947
Adj. R-Square	0.9993

Fig. 94a) UV-Vis absorption spectra of $[Pd_3$**PMDI**$_6]^{6+}$ at different ligand concentrations (DMSO, 1 mm cuvette pathlength); b) linear fit of the absorbance at 280 nm against the ligand concentration for the determination of the extinction coefficient (ε(280 nm) = 2.57 $mM^{-1} \cdot mm^{-1}$).

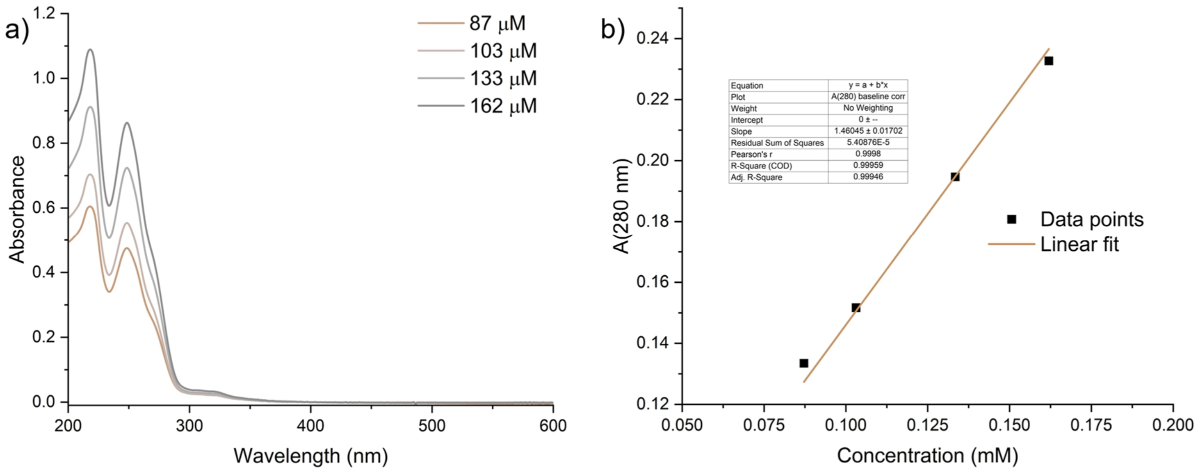

Equation	y = a + b*x
Plot	A(280) baseline corr
Weight	No Weighting
Intercept	0 ± --
Slope	1.46045 ± 0.01702
Residual Sum of Squares	5.40876E-5
Pearson's r	0.9998
R-Square (COD)	0.99959
Adj. R-Square	0.99946

Fig. 95a) UV-Vis absorption spectra of $[Pd_3$**PMDI**$_6]^{6+}$ at different ligand concentrations (CH_3CN, 1 mm cuvette pathlength); b) linear fit of the absorbance at 280 nm against the ligand concentration for determination of the extinction coefficient (ε(280 nm) = 1.46 $mM^{-1} \cdot mm^{-1}$).

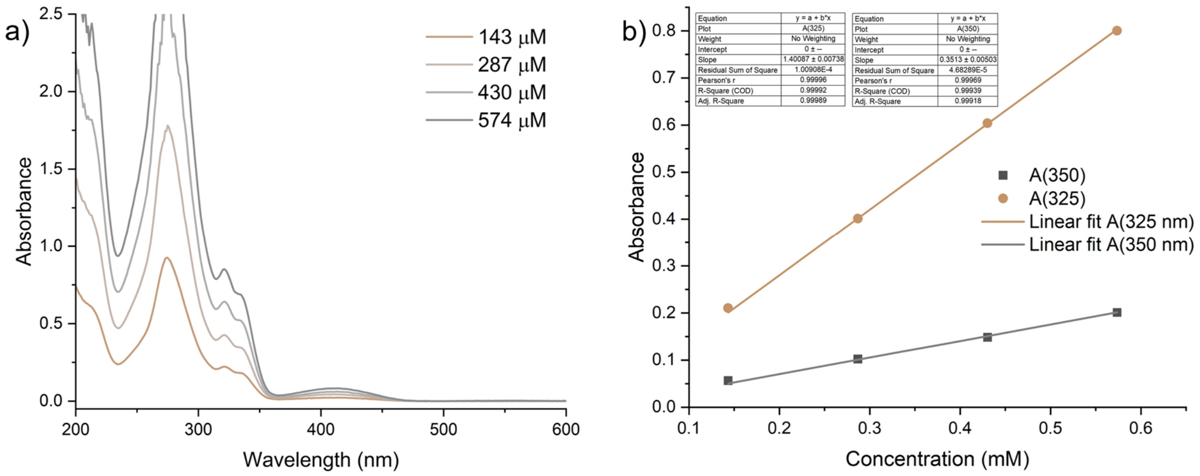

Equation	y = a + b*x
Plot	A(325)
Weight	No Weighting
Intercept	0 ± --
Slope	1.40087 ± 0.00738
Residual Sum of Square	1.00908E-4
Pearson's r	0.99996
R-Square (COD)	0.99992
Adj. R-Square	0.99989

Equation	y = a + b*x
Plot	A(350)
Weight	No Weighting
Intercept	0 ± --
Slope	0.3513 ± 0.00503
Residual Sum of Square	4.68289E-5
Pearson's r	0.99969
R-Square (COD)	0.99939
Adj. R-Square	0.99918

Fig. 96a) UV-Vis absorption spectra of $[Pd_3\mathbf{FRO}_6]^{6+}$ (with trace amounts of $[Pd_4\mathbf{FRO}_8]^{8+}$) at different ligand concentrations (CH_3CN, 1 mm cuvette pathlength); b) linear fit of the absorbance at 325 nm and at 350 nm against the ligand concentration for determination of the extinction coefficient (ε(325 nm) = 1.40 $mM^{-1}\cdot mm^{-1}$, ε(350 nm) = 0.35 $mM^{-1}\cdot mm^{-1}$).

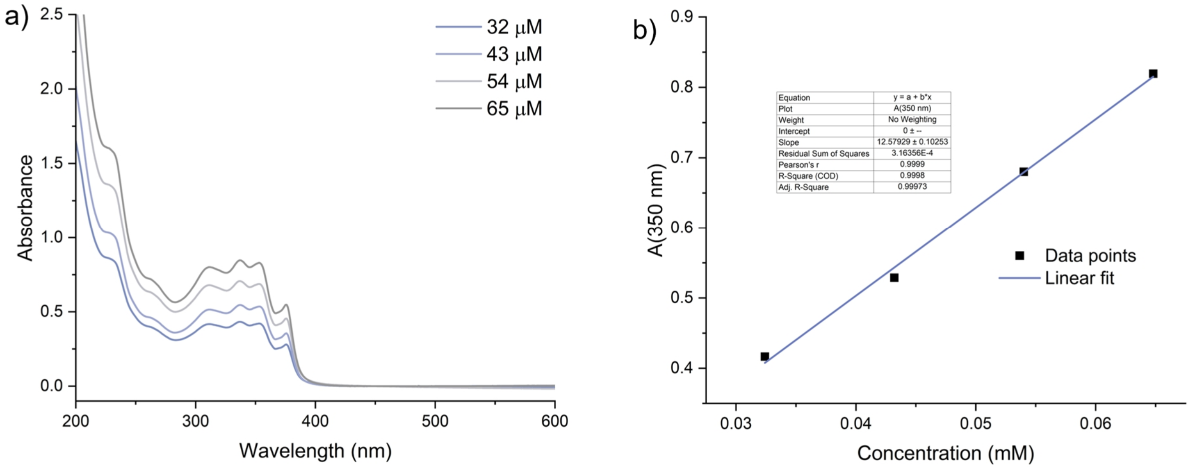

Equation	y = a + b*x
Plot	A(350 nm)
Weight	No Weighting
Intercept	0 ± --
Slope	12.57929 ± 0.10253
Residual Sum of Squares	3.16356E-4
Pearson's r	0.9999
R-Square (COD)	0.9998
Adj. R-Square	0.99973

Fig. 97a) UV-Vis absorption spectra of $[Pd_2\mathbf{CBZ}_2\mathbf{NDI}_2]^{4+}$ at different cage concentrations (CH_3CN, 1 mm cuvette pathlength; b) linear fit of the absorbance at 350 nm against the cage concentration for determination of the extinction coefficient (ε(350 nm) = 12.58 $mM^{-1}\cdot mm^{-1}$).

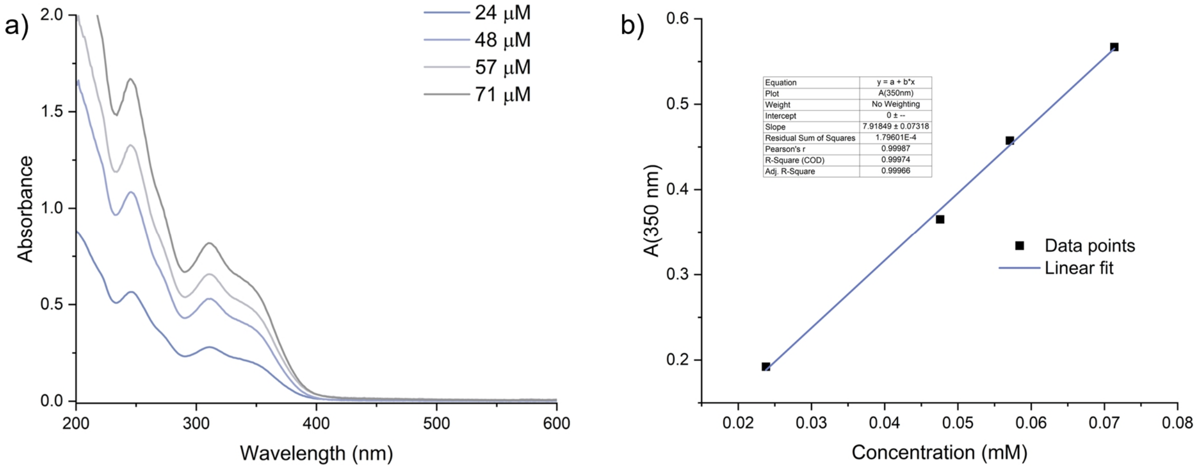

Equation	y = a + b*x
Plot	A(350nm)
Weight	No Weighting
Intercept	0 ± --
Slope	7.91849 ± 0.07318
Residual Sum of Squares	1.79601E-4
Pearson's r	0.99987
R-Square (COD)	0.99974
Adj. R-Square	0.99966

Fig. 98a) UV-Vis absorption spectra of $[Pd_2\mathbf{CBZ}_2\mathbf{PMDI}_2]^{4+}$ at different cage concentrations (CH_3CN, 1 mm cuvette pathlength; b) linear fit of the absorbance at 350 nm against the cage concentration for determination of the extinction coefficient (ε(350 nm) = 7.92 $mM^{-1}\cdot mm^{-1}$).

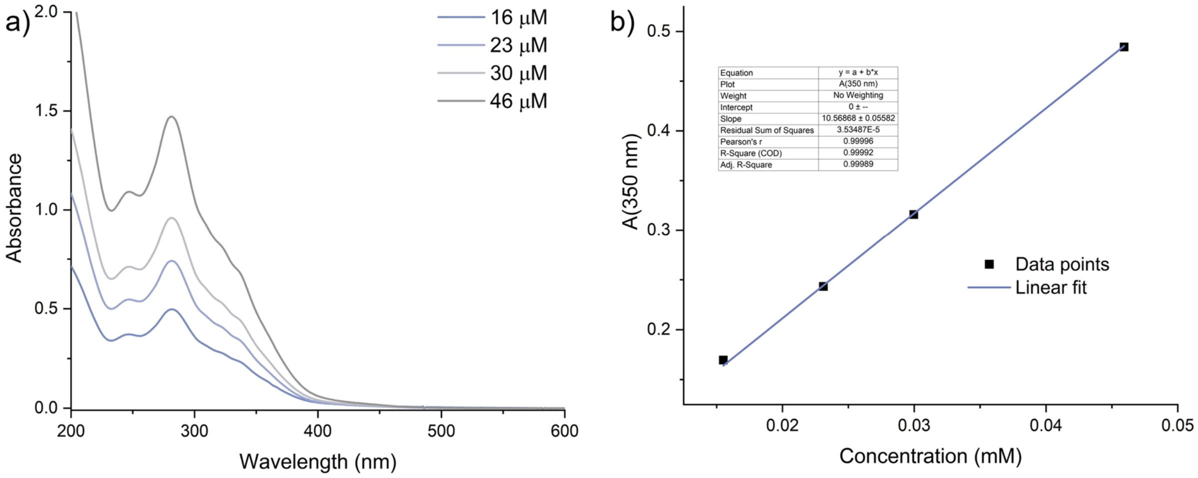

Equation	y = a + b*x
Plot	A(350 nm)
Weight	No Weighting
Intercept	0 ± --
Slope	10.56868 ± 0.05582
Residual Sum of Squares	3.53487E-5
Pearson's r	0.99996
R-Square (COD)	0.99992
Adj. R-Square	0.99989

Fig. 99a) UV-Vis absorption spectra of $[\mathrm{Pd_2}\mathbf{CBZ}_2\mathbf{FRO}_2]^{4+}$ at different cage concentrations (CH_3CN, 1 mm cuvette pathlength; b) linear fit of the absorbance at 350 nm against the cage concentration for determination of the extinction coefficient (ε(350 nm) = 10.57 $mM^{-1}\cdot mm^{-1}$).

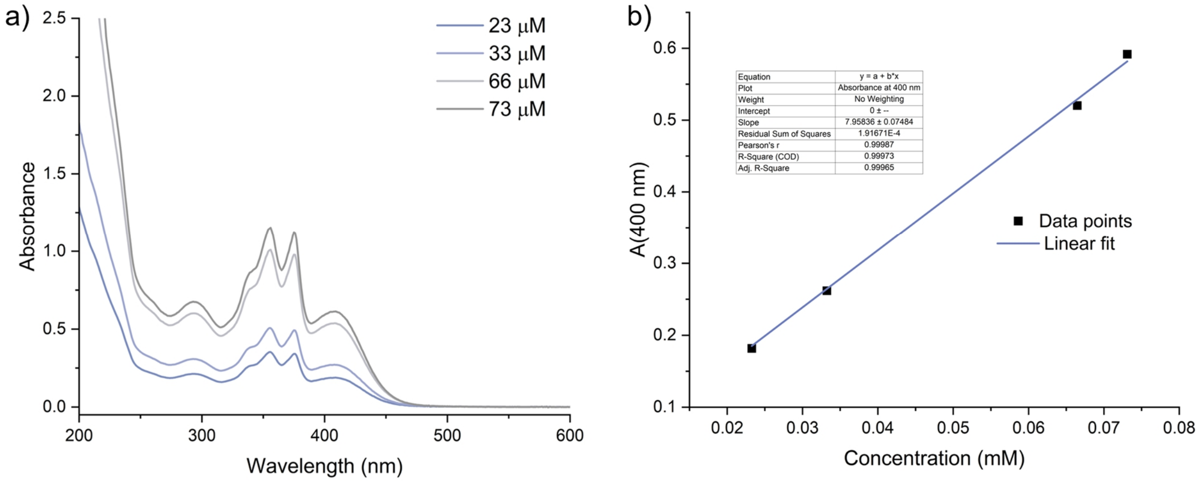

Equation	y = a + b*x
Plot	Absorbance at 400 nm
Weight	No Weighting
Intercept	0 ± --
Slope	7.95836 ± 0.07484
Residual Sum of Squares	1.91671E-4
Pearson's r	0.99987
R-Square (COD)	0.99973
Adj. R-Square	0.99965

Fig. 100a) UV-Vis absorption spectra of $[\mathrm{Pd_2}\mathbf{TAA}_2\mathbf{NDI}_2]^{4+}$ at different cage concentrations (CH_3CN, 1 mm cuvette pathlength; b) linear fit of the absorbance at 400 nm against the cage concentration for determination of the extinction coefficient (ε(400 nm) = 7.96 $mM^{-1}\cdot mm^{-1}$).

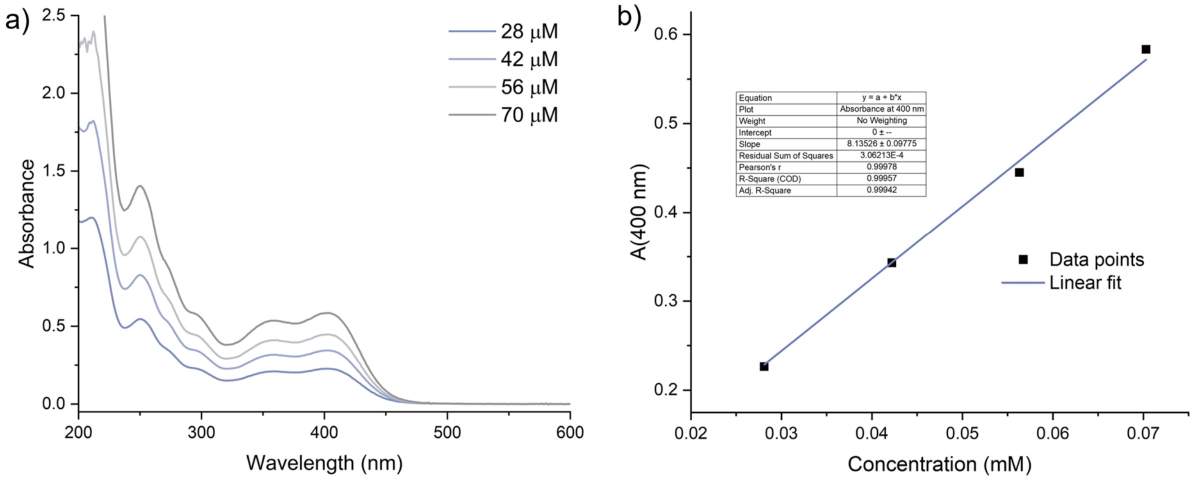

Equation	y = a + b*x
Plot	Absorbance at 400 nm
Weight	No Weighting
Intercept	0 ± --
Slope	8.13526 ± 0.09775
Residual Sum of Squares	3.06213E-4
Pearson's r	0.99978
R-Square (COD)	0.99957
Adj. R-Square	0.99942

Fig. 101a) UV-Vis absorption spectra of $[\mathrm{Pd_2}\mathbf{TAA}_2\mathbf{PMDI}_2]^{4+}$ at different cage concentrations (CH_3CN, 1 mm cuvette pathlength; b) linear fit of the absorbance at 400 nm against the cage concentration for determination of the extinction coefficient (ε(400 nm) = 8.14 $mM^{-1}\cdot mm^{-1}$).

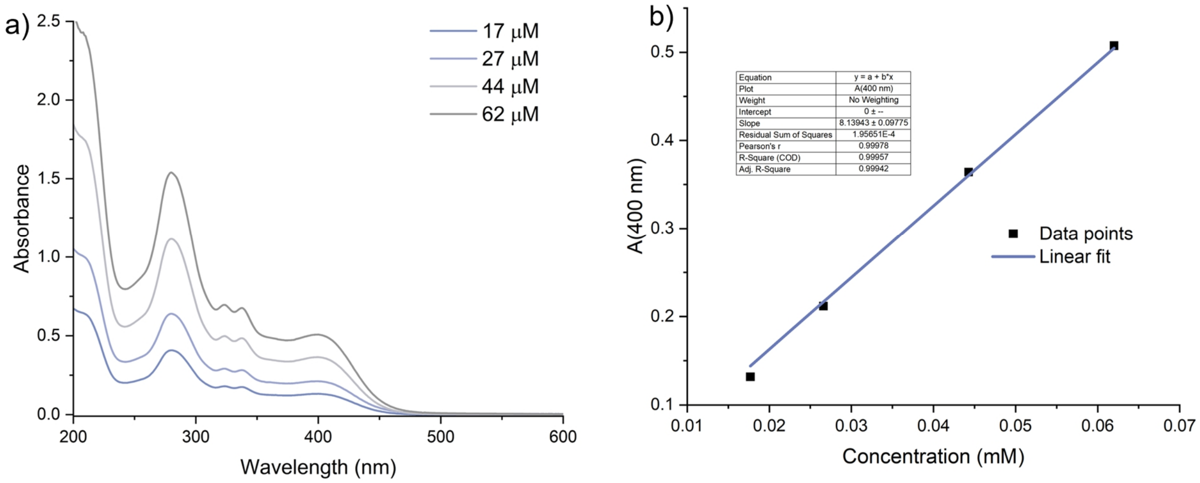

Fig. 102a) UV-Vis absorption spectra of $[\mathrm{Pd}_2\mathbf{TAA_2FRO_2}]^{4+}$ at different cage concentrations (CH_3CN, 1 mm cuvette pathlength; b) linear fit of the absorbance at 400 nm against the cage concentration for determination of the extinction coefficient ($\varepsilon(400\ \mathrm{nm}) = 8.14\ \mathrm{mM^{-1}\cdot mm^{-1}}$).

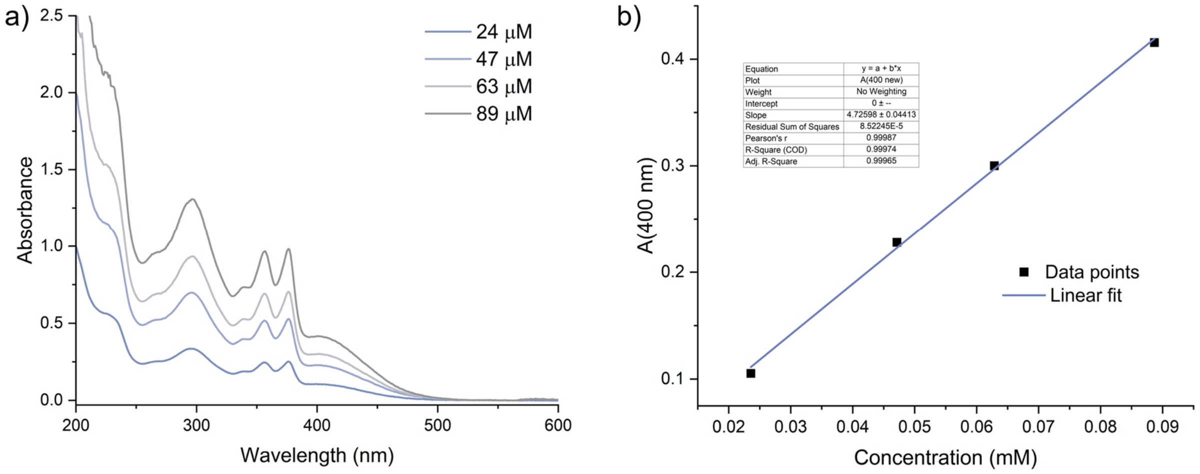

Fig. 103a) UV-Vis absorption spectra of $[\mathrm{Pd}_2\mathbf{PTZ_2NDI_2}]^{4+}$ at different cage concentrations (CH_3CN, 1 mm cuvette pathlength; b) linear fit of the absorbance at 400 nm against the cage concentration for determination of the extinction coefficient ($\varepsilon(400\ \mathrm{nm}) = 4.73\ \mathrm{mM^{-1}\cdot mm^{-1}}$).

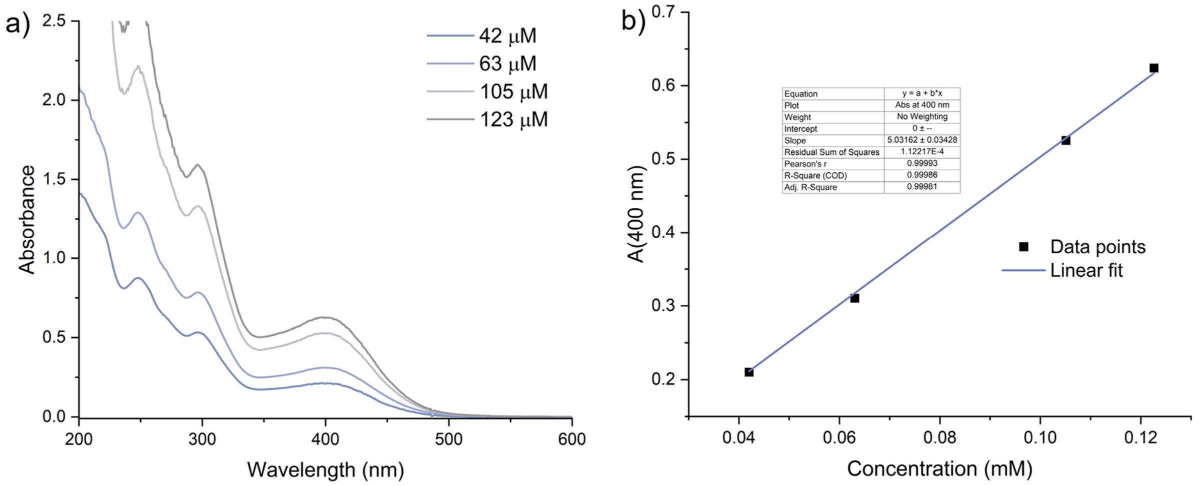

Fig. 104a) UV-Vis absorption spectra of $[\mathrm{Pd}_2\mathbf{PTZ_2PMDI_2}]^{4+}$ at different cage concentrations (CH_3CN, 1 mm cuvette pathlength; b) linear fit of the absorbance at 400 nm against the cage concentration for determination of the extinction coefficient ($\varepsilon(400\ \mathrm{nm}) = 5.03\ \mathrm{mM^{-1}\cdot mm^{-1}}$).

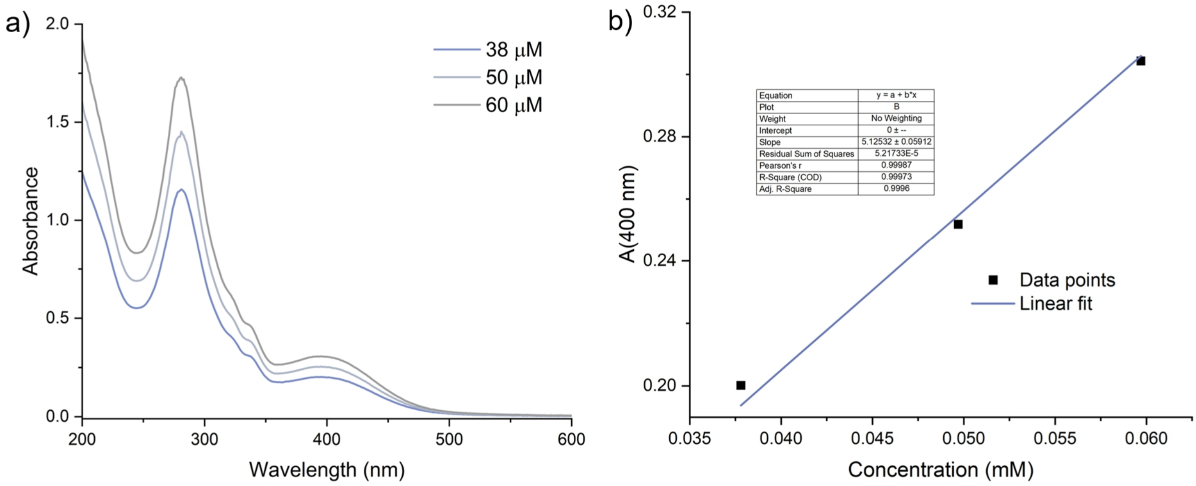

Equation	y = a + b*x
Plot	B
Weight	No Weighting
Intercept	0 ± --
Slope	5.12532 ± 0.05912
Residual Sum of Squares	5.21733E-5
Pearson's r	0.99987
R-Square (COD)	0.99973
Adj. R-Square	0.9996

Fig. 105a) UV-Vis absorption spectra of $[Pd_2\textbf{PTZ}_2\textbf{FRO}_2]^{4+}$ at different cage concentrations (CH_3CN, 1 mm cuvette pathlength; b) linear fit of the absorbance at 400 nm against the cage concentration for determination of the extinction coefficient (ε(400 nm) = 5.13 $mM^{-1} \cdot mm^{-1}$).

3.11.6. Electrochemistry

The cyclic voltammograms of the ligands **CBZ**, **TAA**, **NDI**, **PMDI**, **FRO** and of the homoleptic assemblies $[Pd_3\textbf{NDI}_6]^{6+}$ + $[Pd_4\textbf{NDI}_8]^{8+}$ and $[Pd_3\textbf{PMDI}_6]^{6+}$ are shown here (the electrochemical characterization of $[Pd_2\textbf{CBZ}_4]^{4+}$ was hampered by its poor solubility in the electrolyte solution). The cyclic voltammograms and the spectroelectrochemical characterization of the heteroleptic cages $[Pd_2\textbf{CBZ}_2\textbf{NDI}_2]^{4+}$, $[Pd_2\textbf{CBZ}_2\textbf{FRO}_2]^{4+}$, $[Pd_2\textbf{TAA}_2\textbf{PMDI}_2]^{4+}$, $[Pd_2\textbf{PTZ}_2\textbf{NDI}_2]^{4+}$, $[Pd_2\textbf{PTZ}_2\textbf{PMDI}_2]^{4+}$ is shown here (for $[Pd_2\textbf{CBZ}_2\textbf{PMDI}_2]^{4+}$, $[Pd_2\textbf{TAA}_2\textbf{NDI}_2]^{4+}$ and $[Pd_2\textbf{PTZ}_2\textbf{FRO}_2]^{4+}$ see main text). Ligand **PTZ** and homoleptic $[Pd_4\textbf{PTZ}_8]^{8+}$ are published. [1] Cage $[Pd_2\textbf{TAA}_2\textbf{FRO}_2]^{4+}$ and homoleptic $[Pd_3\textbf{FRO}_6]^{6+}$ was investigated by Dr. Jacopo Tessarolo (unpublished).

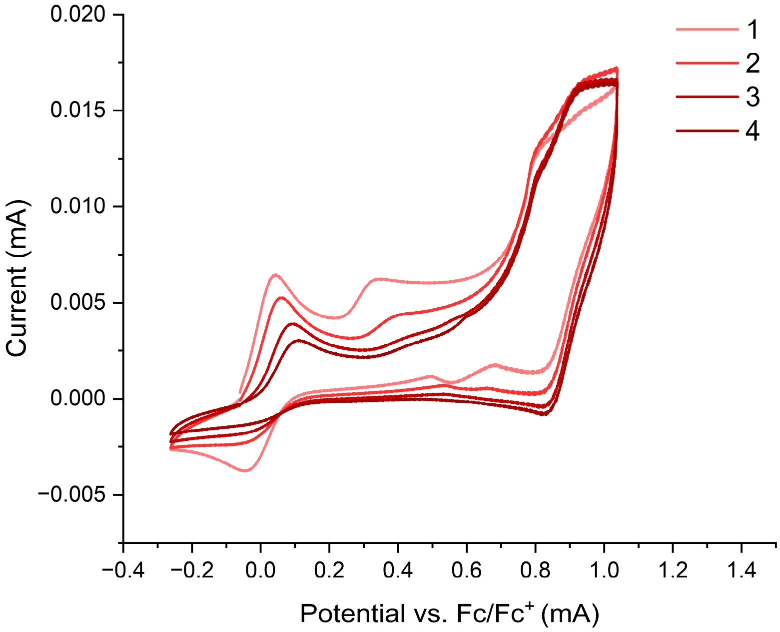

Fig. 106 CV of ligand **CBZ** over four cycles, see color code for cycle number (c = 480 µM, CH_3CN, 0.1 M $TBAPF_6$, WE: glassy carbon, CE: platinum wire, RE: $Ag/AgNO_3$, scan rate: 0.1 $V \cdot s^{-1}$). The CVs suggest that the oxidation product with $E_{p/2}$ ~ 0.8 V is transformed into a species with $E_{p/2}$ ~ 0.88 V. This behavior was not observed in the cage and therefore not investigated further.

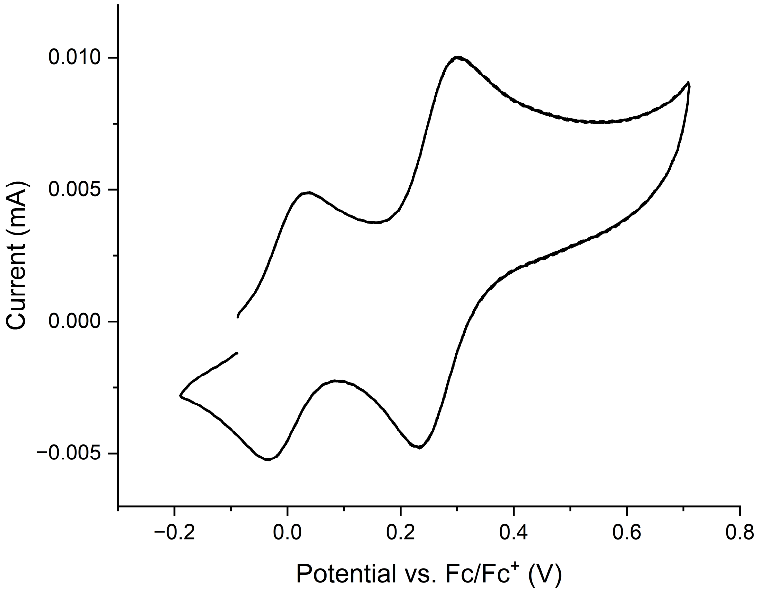

Fig. 107 CV of ligand **TAA** (c = 310 µM, CH_3CN, 0.1 M $TBAPF_6$, WE: glassy carbon, CE: platinum wire, RE: Ag/$AgNO_3$, scan rate: 0.1 V·s^{-1}).

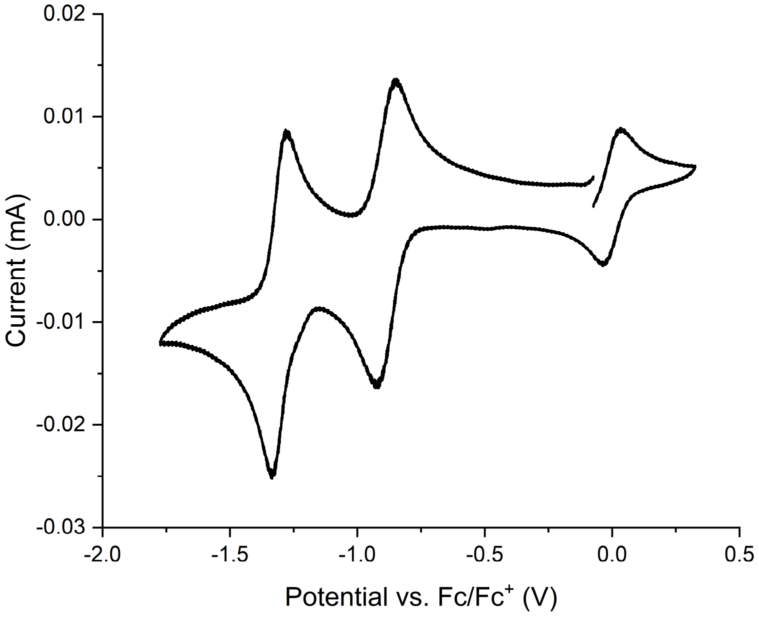

Fig. 108 CV of ligand **NDI** (c=540 µM, CH_3CN, 0.1 M $TBAPF_6$, WE: glassy carbon, CE: platinum wire, RE: Ag/$AgNO_3$, scan rate: 0.1 V·s^{-1}).

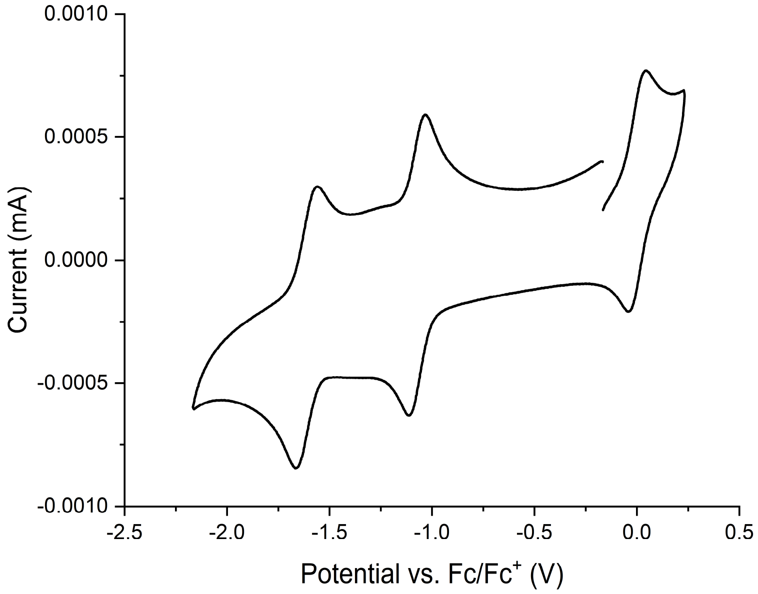

Fig. 109 CV of ligand **PMDI** (c = 50 µM, DMSO, 0.1 M $TBAPF_6$, WE: platinum disc, CE: platinum wire, RE: $Ag/AgNO_3$, scan rate: 0.1 $V·s^{-1}$).

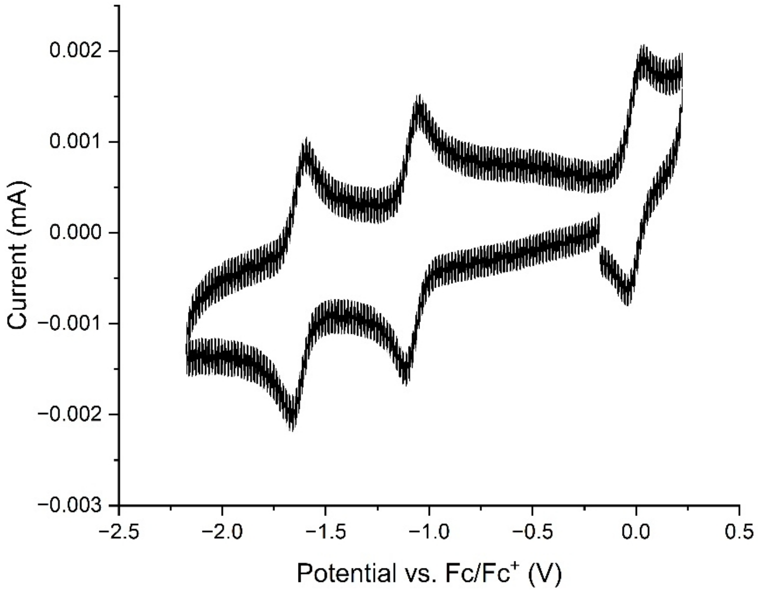

Fig. 110 CV of ligand **PMDI** (c = 50 µM, DMSO, 0.1 M $TBAPF_6$, WE: glassy carbon, CE: platinum wire, RE: $Ag/AgNO_3$, scan rate: 0.1 $V·s^{-1}$).

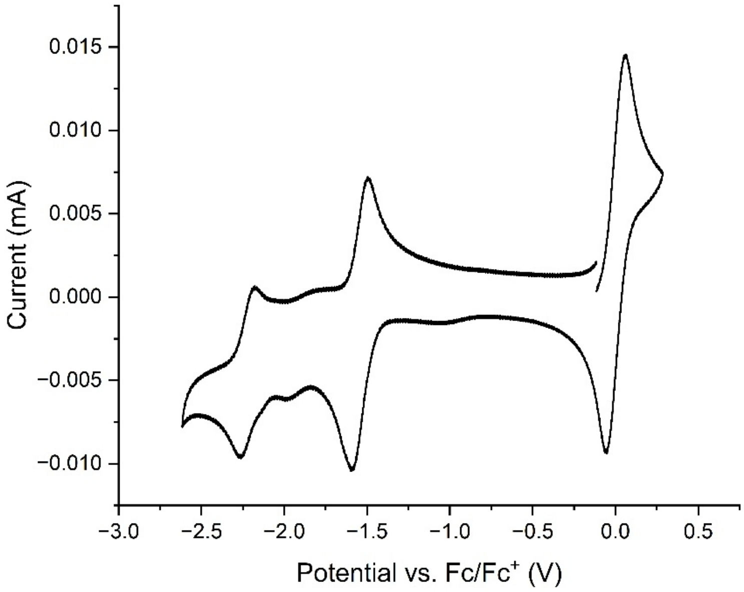

Fig. 111 CV of ligand **FRO** (*c* = 1.4 mM, DMSO, 0.1 M TBAPF$_6$, WE: glassy carbon, CE: platinum wire, RE: Ag/AgNO$_3$, scan rate: 0.1 V·s^{-1}).

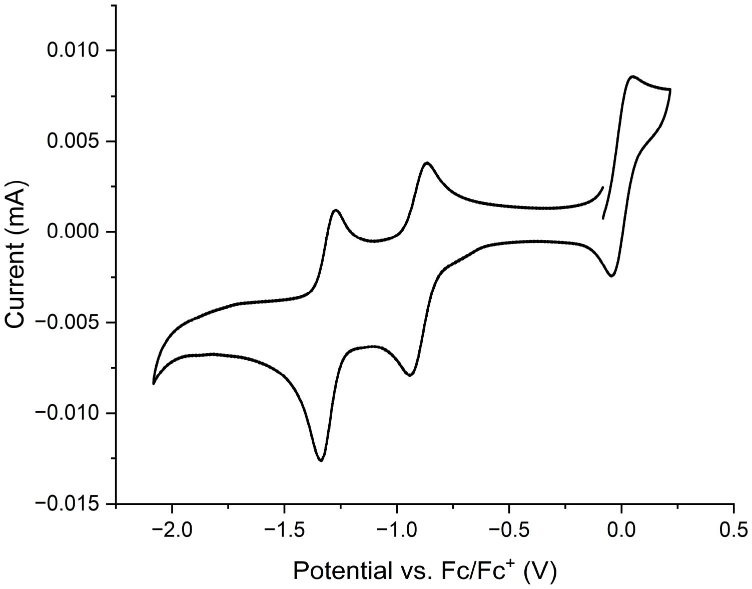

Fig. 112 CV of [Pd$_3$**NDI**$_6$]$^{6+}$ + [Pd$_4$**NDI**$_8$]$^{8+}$ ((c(ligand) = 400 µM, CH$_3$CN, 0.1 M TBAPF$_6$, WE: glassy carbon, CE: platinum wire, RE: Ag/AgNO$_3$, scan rate: 0.1 V·s^{-1}).

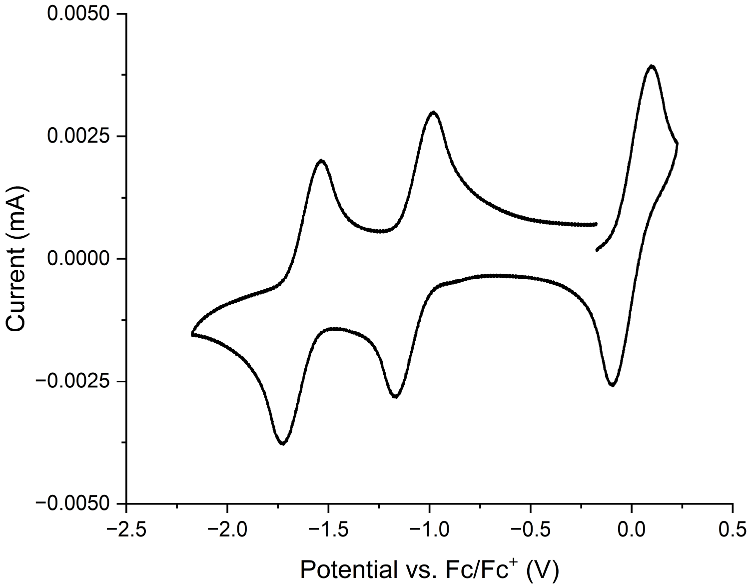

Fig. 113 CV of $[Pd_3\textbf{PMDI}_6]^{6+}$ (c(ligand) = 400 µM, DMSO, 0.1 M $TBAPF_6$, WE: platinum, CE: platinum wire, RE: $Ag/AgNO_3$, scan rate: 0.1 $V{\cdot}s^{-1}$).

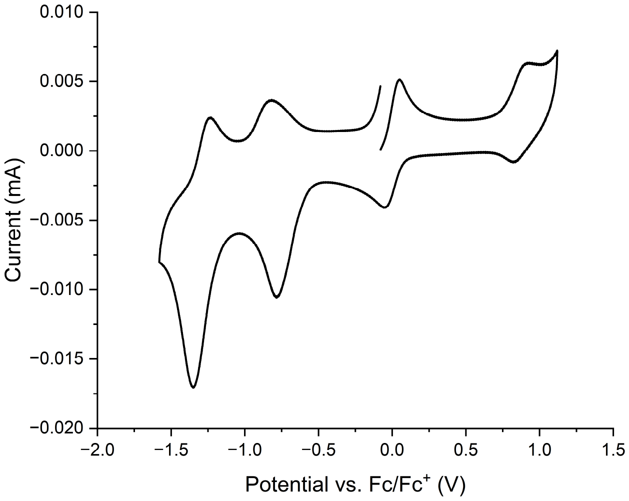

Fig. 114 CV of $[Pd_2\textbf{CBZ}_2\textbf{NDI}_2]^{4+}$ (c(cage) = 110 µM, CH_3CN, 0.1 M $TBAPF_6$, WE: glassy carbon, CE: platinum wire, RE: $Ag/AgNO_3$, scan rate: 0.1 $V{\cdot}s^{-1}$). The first reduction event occurs at less negative potentials (−0.78 V) than the corresponding oxidation event (−0.83 V), suggesting that the two events do not stem from the same compound. Therefore, a reliable half-wave potential for the first reduction event of the **NDI** ligand could not be obtained for this cage.

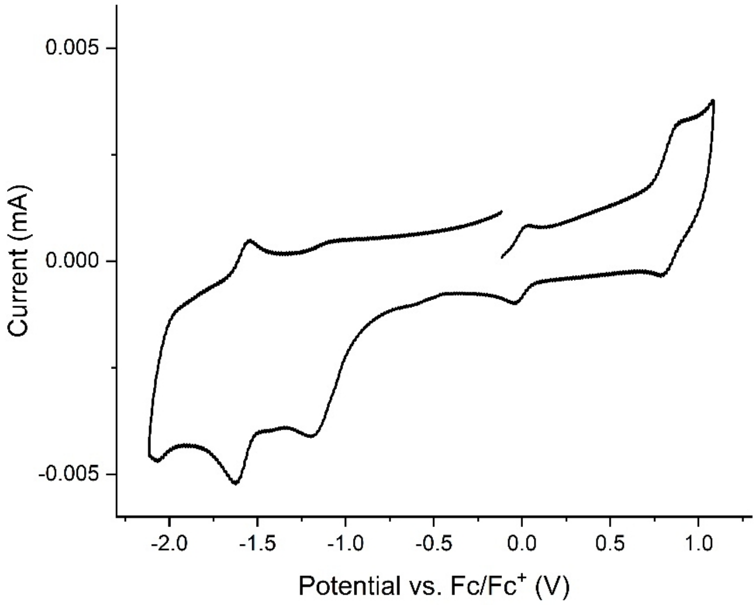

Fig. 115 CV of $[Pd_2$**CBZ**$_2$**FRO**$_2]^{4+}$ (CH_3CN, 0.1 M $TBAPF_6$, WE: glassy carbon, CE: platinum wire, RE: $Ag/AgNO_3$, scan rate: 0.05 V·s^{-1}). The concentration was not determined. The reduction event at ~−1.2 V stems probably from residual oxygen.

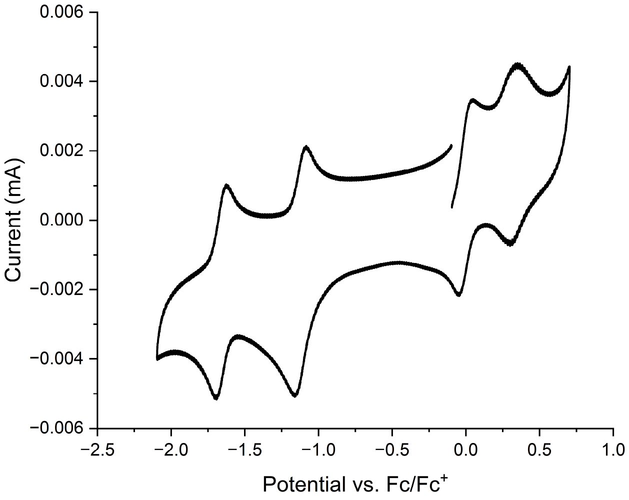

Fig. 116 CV of $[Pd_2$**TAA**$_2$**PMDI**$_2]^{4+}$ (c(cage) = 20 µM, CH_3CN, 0.1 M $TBAPF_6$, WE: glassy carbon, CE: platinum wire, RE: $Ag/AgNO_3$, scan rate: 0.1 V·s^{-1}).

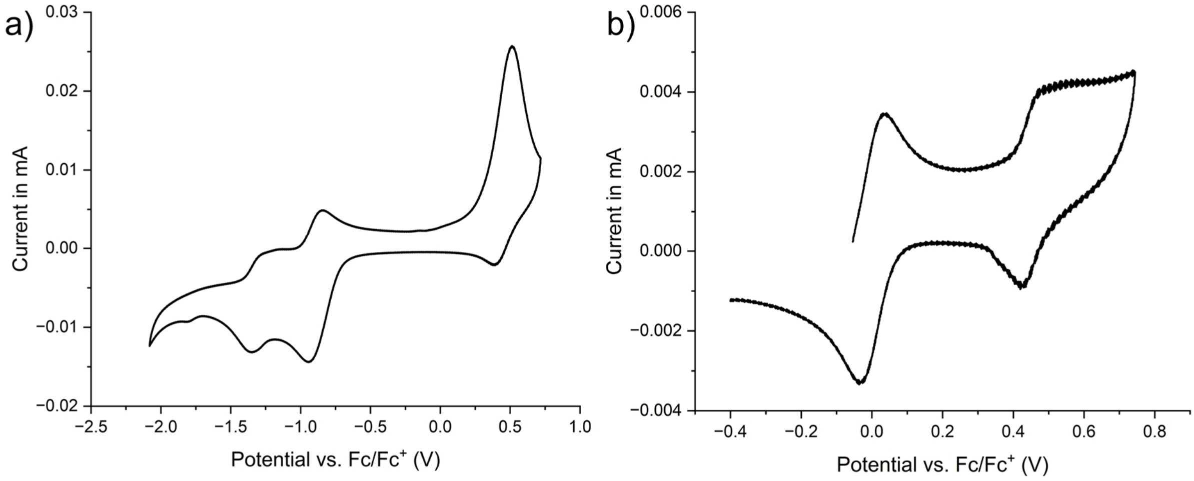

Fig. 117 CV of [Pd$_2$**PTZ**$_2$**NDI**$_2$]$^{4+}$ a) Full CV, b) partial CV with ferrocene (*c*(cage) = 80 µM, CH_3CN, 0.1 M $TBAPF_6$, WE: glassy carbon, CE: platinum wire, RE: Ag/$AgNO_3$, scan rate: 0.1 V·s^{-1}).

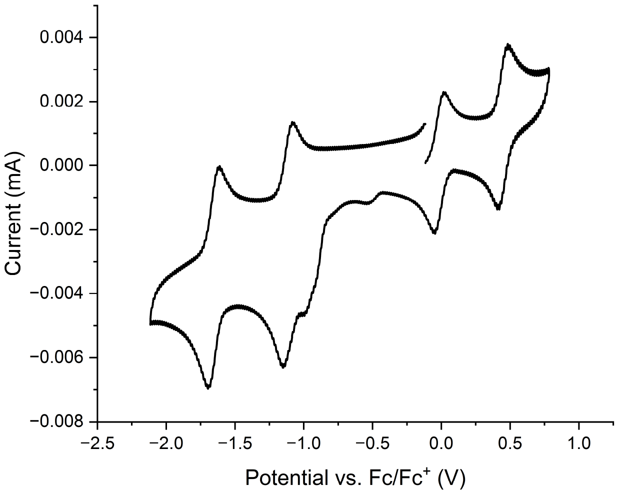

Fig. 118 CV of [Pd$_2$**PTZ**$_2$**PMDI**$_2$]$^{4+}$ (*c*(cage) = 160 µM, CH_3CN, 0.1 M $TBAPF_6$, WE: glassy carbon, CE: platinum wire, RE: Ag/$AgNO_3$, scan rate: 0.05 V·s^{-1}).

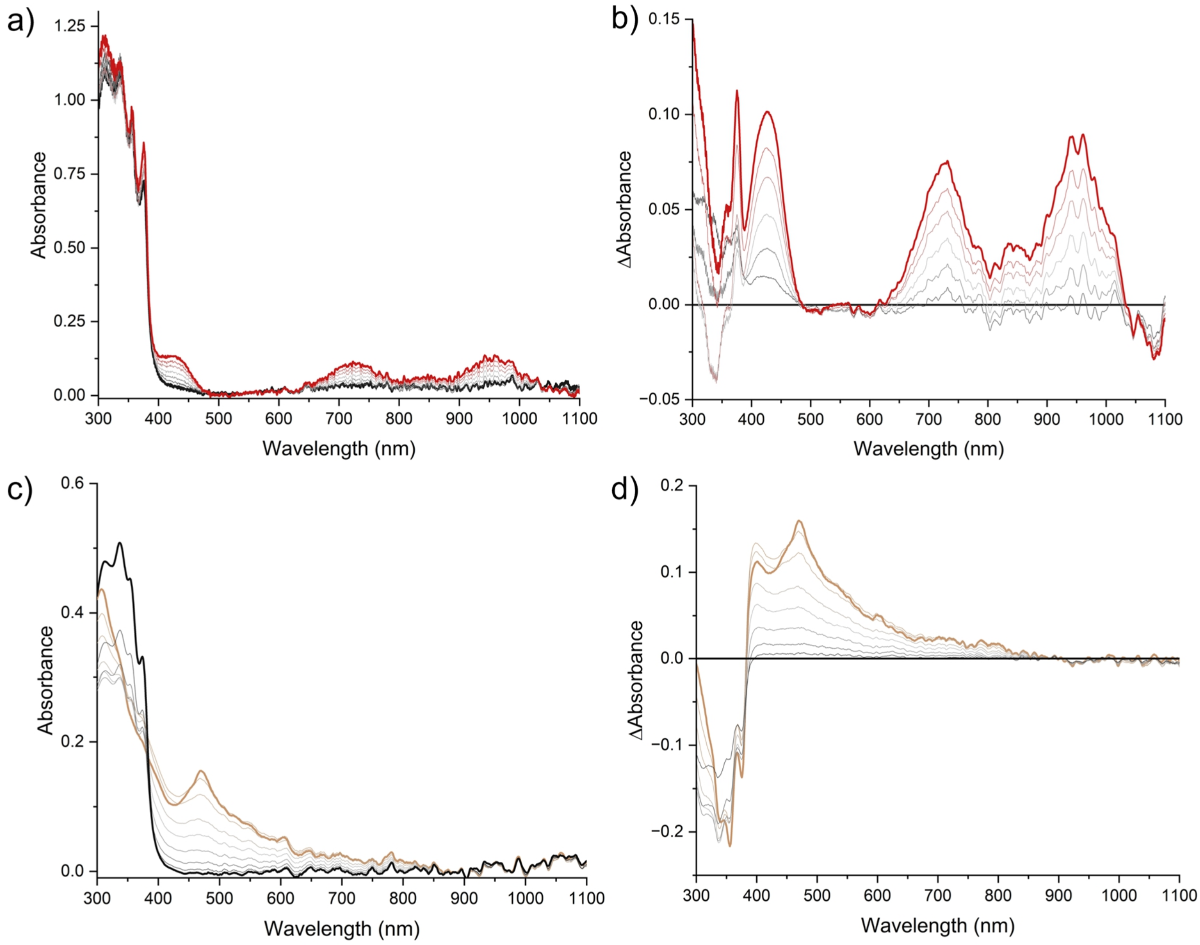

Fig. 119 Spectroelectrochemical characterization of $[Pd_2\textbf{CBZ}_2\textbf{NDI}_2]^{4+}$ a) UV-Vis spectra upon oxidation (+1.2 V), b) difference spectra upon oxidation (+1.2 V), c) UV-Vis absorption spectra upon reduction (−1.2 V), d) difference spectra upon reduction (−1.2 V) (*c*(cage) = 90 µM (a,b), 45 µM (c,d), CH_3CN, 0.1 M $TBAPF_6$, WE: gold gauze, CE: platinum wire, RE: $Ag/AgNO_3$, cuvette pathlength: 0.5 mm).

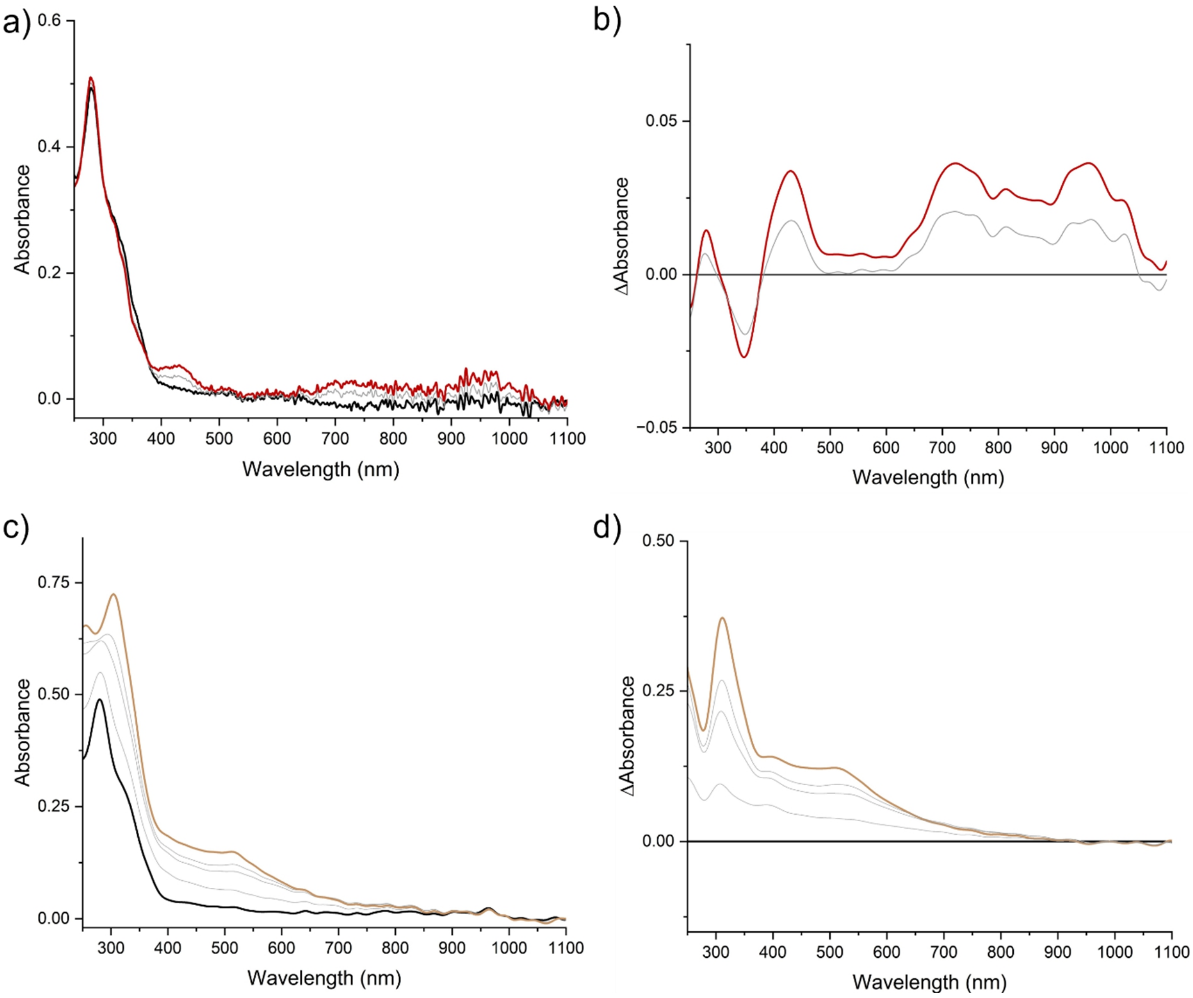

Fig. 120 Spectroelectrochemical characterization of $[Pd_2\mathbf{CBZ}_2\mathbf{FRO}_2]^{4+}$ a) UV-Vis spectra upon oxidation (+1.0 V), b) difference spectra upon oxidation (+1.0 V), c) UV-Vis absorption spectra upon reduction (−1.7 V), d) difference spectra upon reduction (−1.7 V) (*c*(cage) = 35 μM, CH_3CN, 0.1 M $TBAPF_6$, WE: gold gauze, CE: platinum wire, RE: $Ag/AgNO_3$, cuvette pathlength: 0.5 mm).

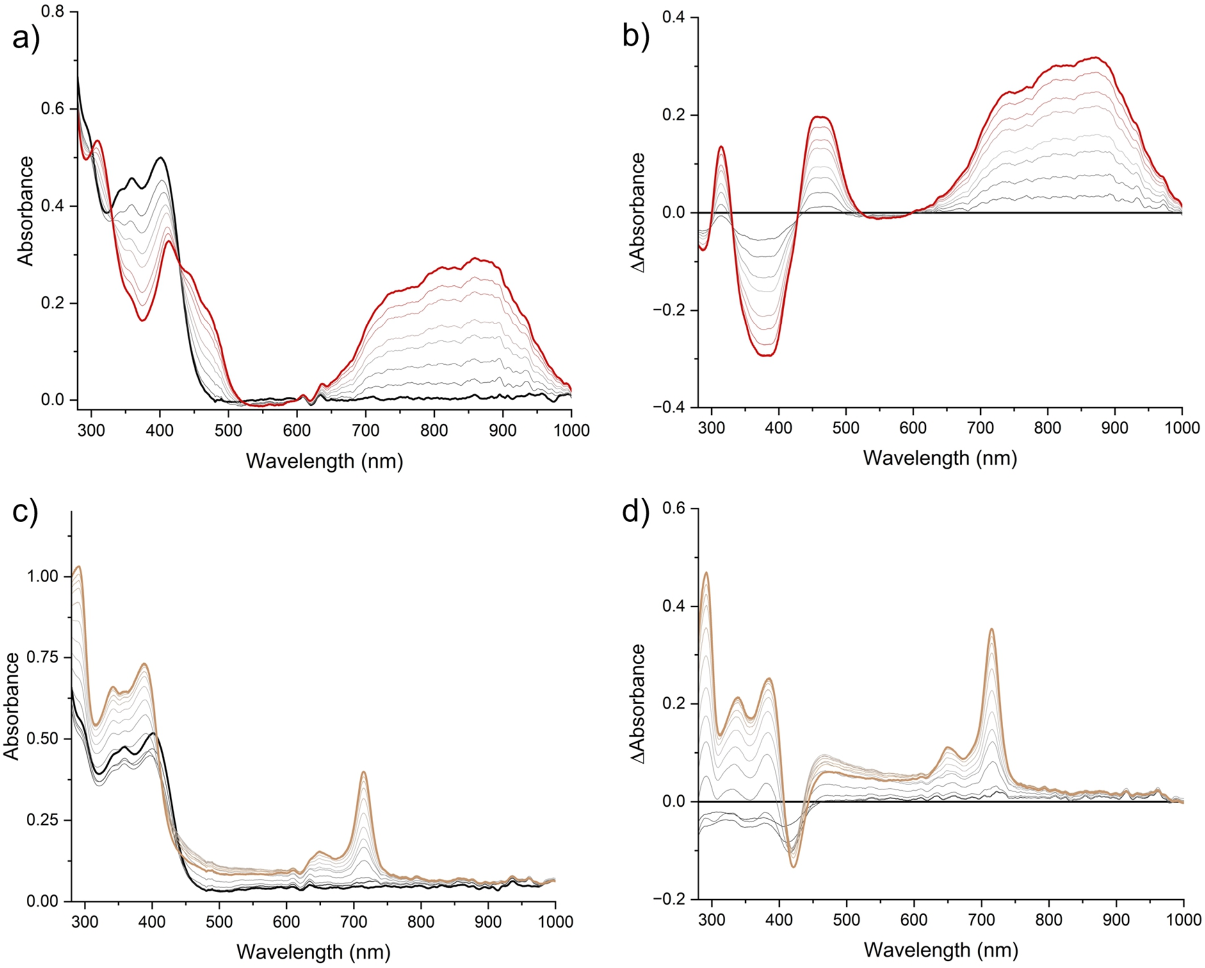

Fig. 121 Spectroelectrochemical characterization of [Pd_2**TAA**$_2$**PMDI**$_2$]$^{4+}$ a) UV-Vis spectra upon oxidation (+0.5 V), b) difference spectra upon oxidation (+0.5 V), c) UV-Vis absorption spectra upon reduction (−1.3 V), d) difference spectra upon reduction (−1.3 V) (*c*(cage) = 120 µM, CH_3CN, 0.1 M $TBAPF_6$, WE: gold gauze, CE: platinum wire, RE: $Ag/AgNO_3$, cuvette pathlength: 0.5 mm).

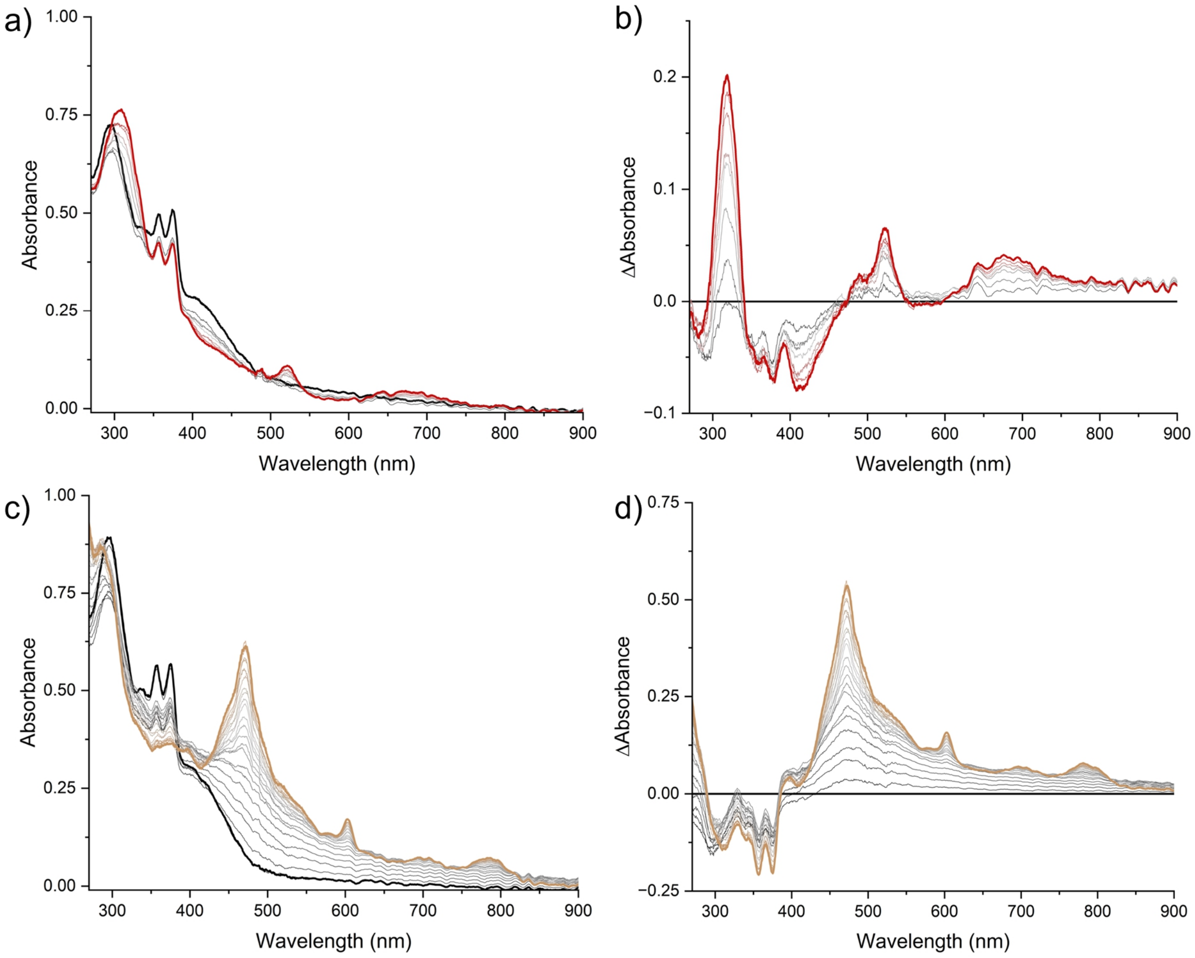

Fig. 122 Spectroelectrochemical characterization of $[Pd_2\mathbf{PTZ}_2\mathbf{NDI}_2]^{4+}$ a) UV-Vis spectra upon oxidation (+0.6 V), b) difference spectra upon oxidation (+0.6 V), c) UV-Vis absorption spectra upon reduction (−1.1 V), d) difference spectra upon reduction (−1.1 V) (*c*(cage) = 100 μM, CH_3CN, 0.1 M $TBAPF_6$, WE: gold gauze, CE: platinum wire, RE: $Ag/AgNO_3$, cuvette pathlength: 0.5 mm).

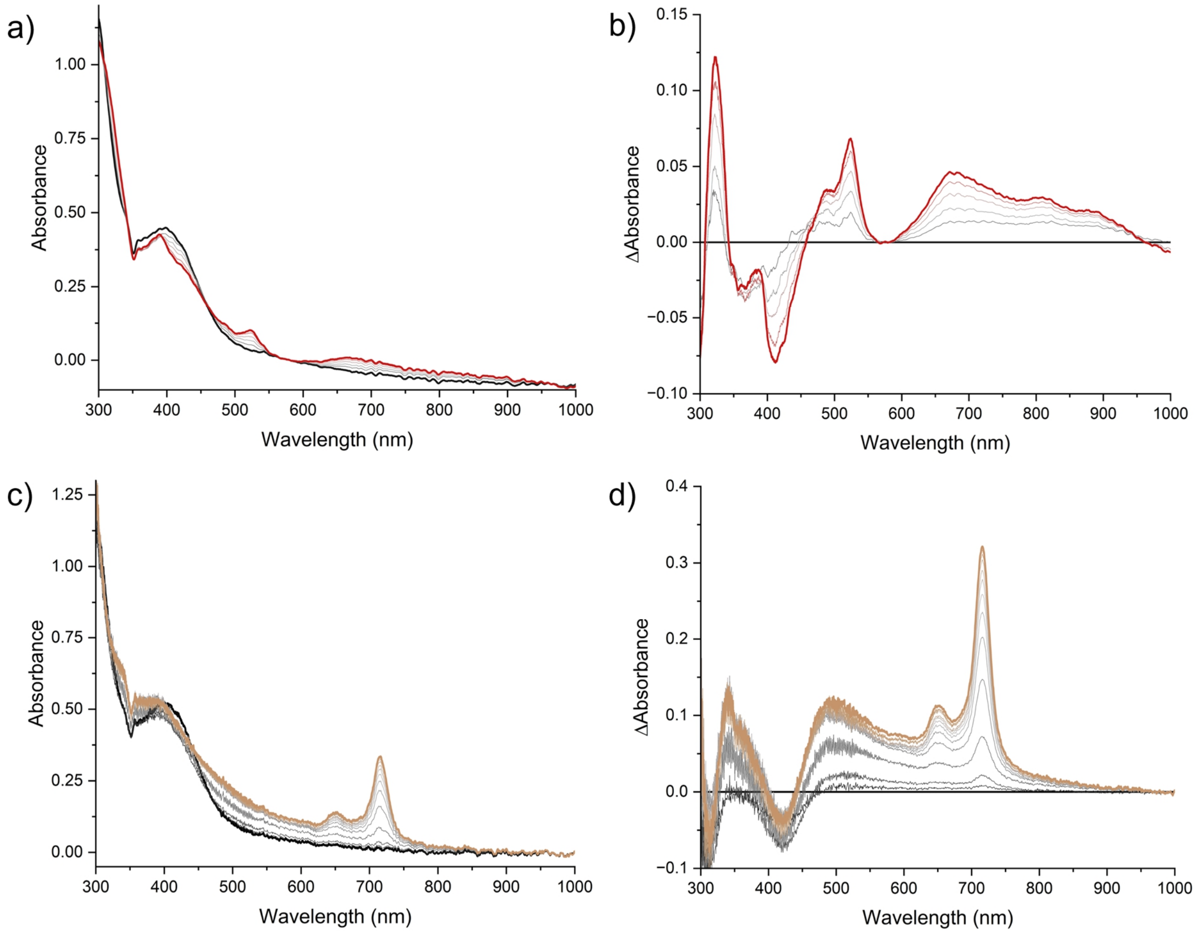

Fig. 123 Spectroelectrochemical characterization of $[Pd_2\mathbf{PTZ_2PMDI_2}]^{4+}$ a) UV-Vis spectra upon oxidation (+0.7 V), b) difference spectra upon oxidation (+0.7 V), c) UV-Vis absorption spectra upon reduction (−1.3 V), d) difference spectra upon reduction (−1.3 V) (*c*(cage) = 160 µM, CH_3CN, 0.1 M $TBAPF_6$, WE: gold gauze, CE: platinum wire, RE: $Ag/AgNO_3$, cuvette pathlength: 0.5 mm).

3.11.7. Computational studies

Models of the cages [Pd$_2$**CBZ**$_2$**PMDI**$_2$]$^{4+}$, [Pd$_2$**CBZ**$_2$**FRO**$_2$]$^{4+}$, [Pd$_2$**TAA**$_2$**PMDI**$_2$]$^{4+}$, [Pd$_2$**TAA**$_2$**FRO**$_2$]$^{4+}$, [Pd$_2$**PTZ**$_2$**NDI**$_2$]$^{4+}$, [Pd$_2$**PTZ**$_2$**PMDI**$_2$]$^{4+}$, and [Pd$_2$**PTZ**$_2$**FRO**$_2$]$^{4+}$ were built with the software Spartan;[53] for [Pd$_2$**CBZ**$_2$**NDI**$_2$]$^{4+}$ and [Pd$_2$**TAA**$_2$**NDI**$_2$]$^{4+}$, the X-ray crystal structures were used. First, a geometry optimization on the PM6 level was carried out using Spartan or Gaussian 16.[54] Next, a DFT geometry optimization was carried out (B3LYP/Def2-SVP) using either Gaussian 16 or ORCA 5.0.2 software.[55] The DFT-optimized structures were then subjected to a single point energy calculation (B3LYP/Def2-TZVP). For orbital visualization, ChemCraft 1.8 was used.[56] Selected orbital energy levels are listed in table 8 and the corresponding orbital lobes are visualized in figures 124-132.

Tab. 8 Orbital energy levels for ligand and donor acceptor cages in eV.

Compound	HOMO-1	HOMO	LUMO	LUMO+1	LUMO+2	LUMO+3	LUMO+4	LUMO+5
[Pd$_2$**CBZ**$_2$**NDI**$_2$]$^{4+}$	-5.83	-5.82	-4.04	-3.97	-2.92	-2.90	-2.72	-2.70
[Pd$_2$**CBZ**$_2$**PMDI**$_2$]$^{4+}$	-5.83	-5.80	-3.93	-3.84	-2.96	-2.91	-2.76	-2.76
[Pd$_2$**CBZ**$_2$**FRO**$_2$]$^{4+}$	-5.82	-5.81	-3.20	-3.11	-2.71	-2.69	-2.47	-2.45
[Pd$_2$**TAA**$_2$**NDI**$_2$]$^{4+}$	-5.22	-5.21	-4.06	-4.05	-2.76	-2.73	-2.71	-2.63
[Pd$_2$**TAA**$_2$**PMDI**$_2$]$^{4+}$	-5.21	-5.18	-4.07	-3.86	-3.01	-2.93	-2.79	-2.76
[Pd$_2$**TAA**$_2$**FRO**$_2$]$^{4+}$	-5.25	-5.24	-3.20	-3.10	-2.72	-2.68	-2.46	-2.44
[Pd$_2$**PTZ**$_2$**NDI**$_2$]$^{4+}$	-5.68	-5.67	-4.03	-4.02	-2.89	-2.87	-2.71	-2.70
[Pd$_2$**PTZ**$_2$**PMDI**$_2$]$^{4+}$	-5.66	-5.58	-3.90	-3.84	-2.96	-2.92	-2.83	-2.82
[Pd$_2$**PTZ**$_2$**FRO**$_2$]$^{4+}$	-5.67	-5.66	-3.21	-3.11	-2.79	-2.78	-2.71	-2.59
NDI			-3.66					
PMDI			-3.50					
FRO			-2.86					
CBZ		-5.61						
TAA		-5.05						
PTZ		-5.43						

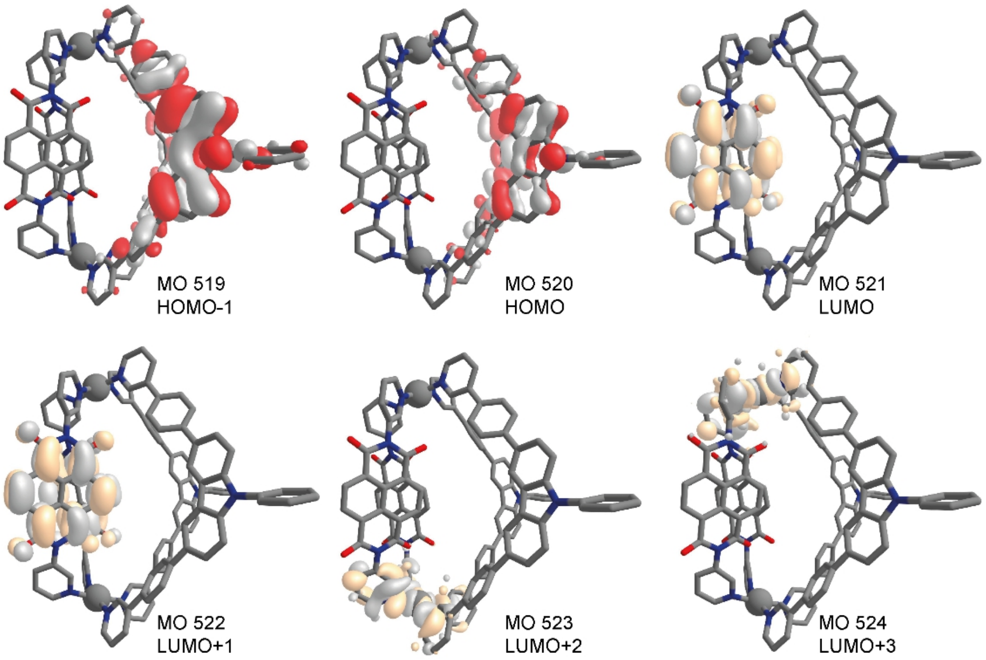

Fig. 124 Selected molecular orbitals of [Pd$_2$**CBZ**$_2$**NDI**$_2$]$^{4+}$. The calculated structure should be regarded with caution owing to the twisting of the **NDI** ligand.

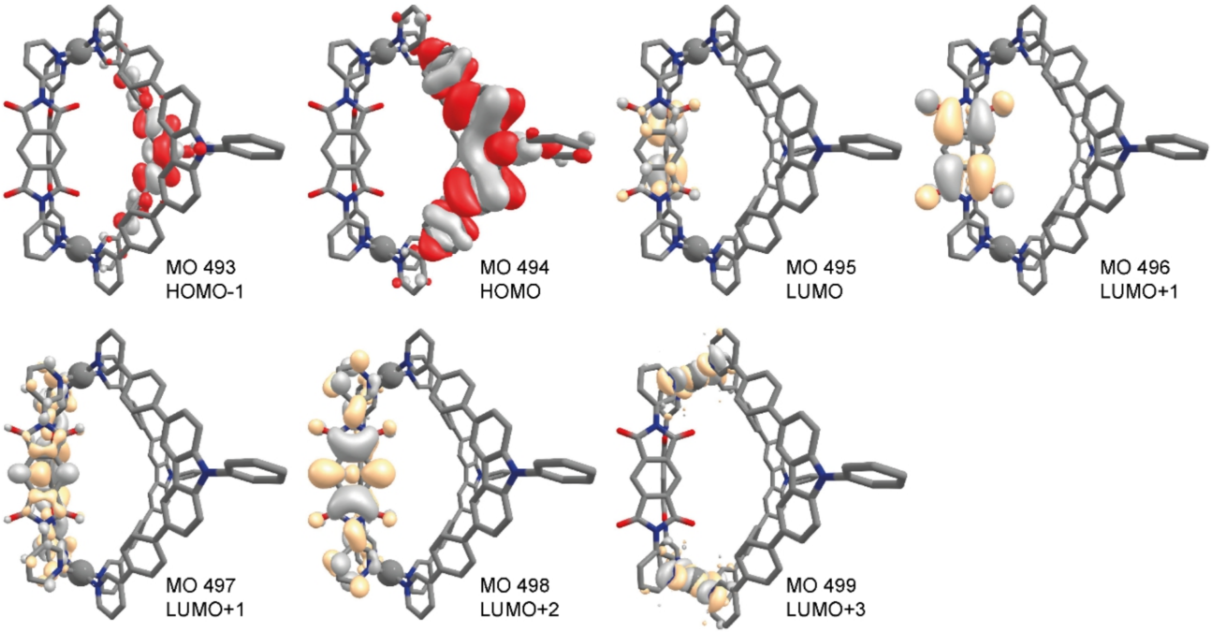

Fig. 125 Selected molecular orbitals of [Pd$_2$**CBZ**$_2$**PMDI**$_2$]$^{4+}$.

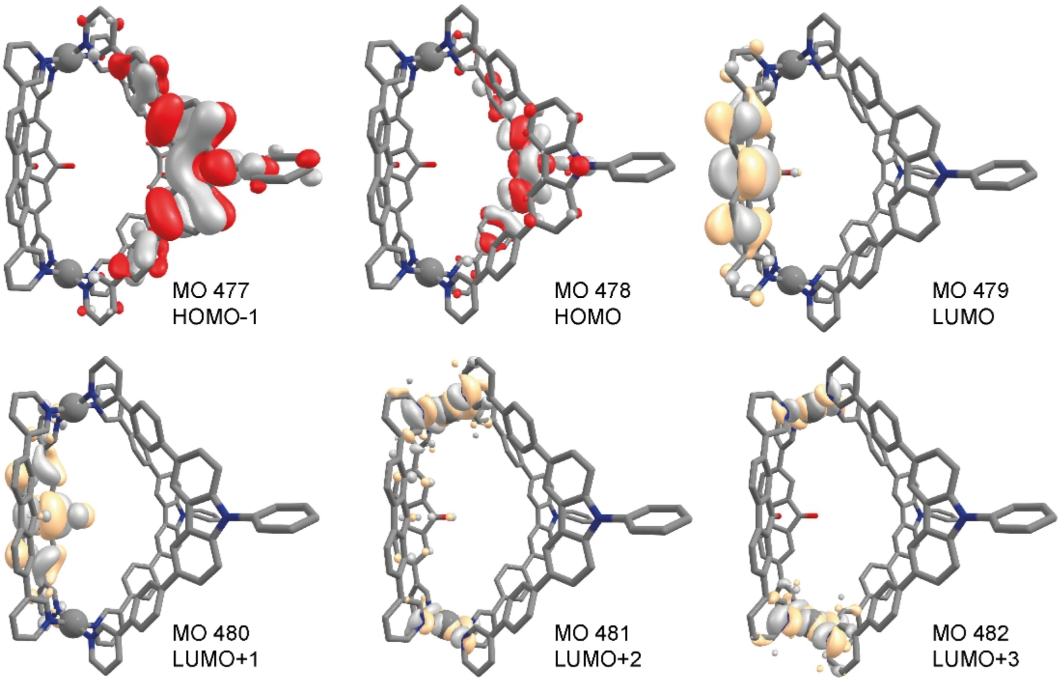

Fig. 126 Selected molecular orbitals of [Pd$_2$**CBZ**$_2$**FRO**$_2$]$^{4+}$.

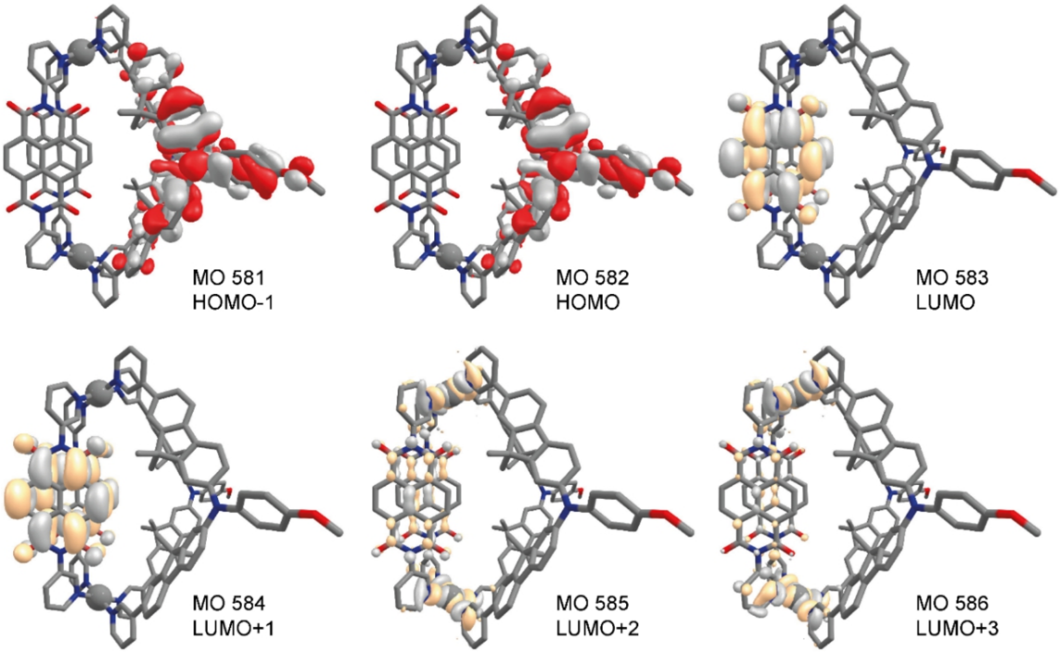

Fig. 127 Selected molecular orbitals of [Pd$_2$**TAA$_2$NDI$_2$**]$^{4+}$.

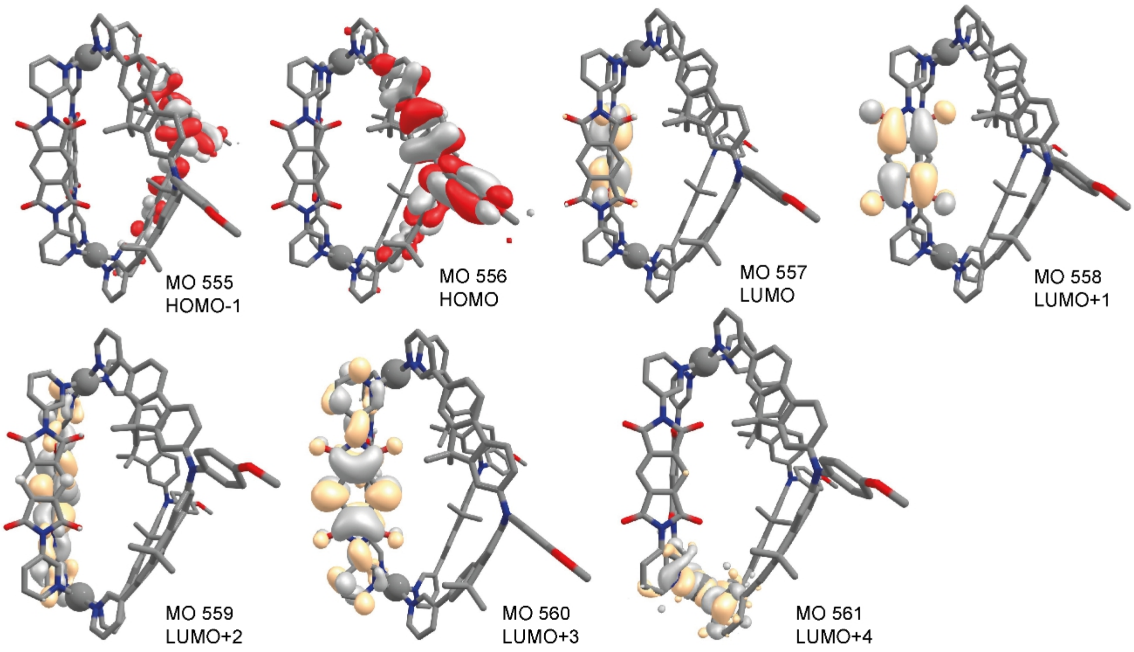

Fig. 128 Selected molecular orbitals of [Pd$_2$**TAA$_2$PMDI$_2$**]$^{4+}$.

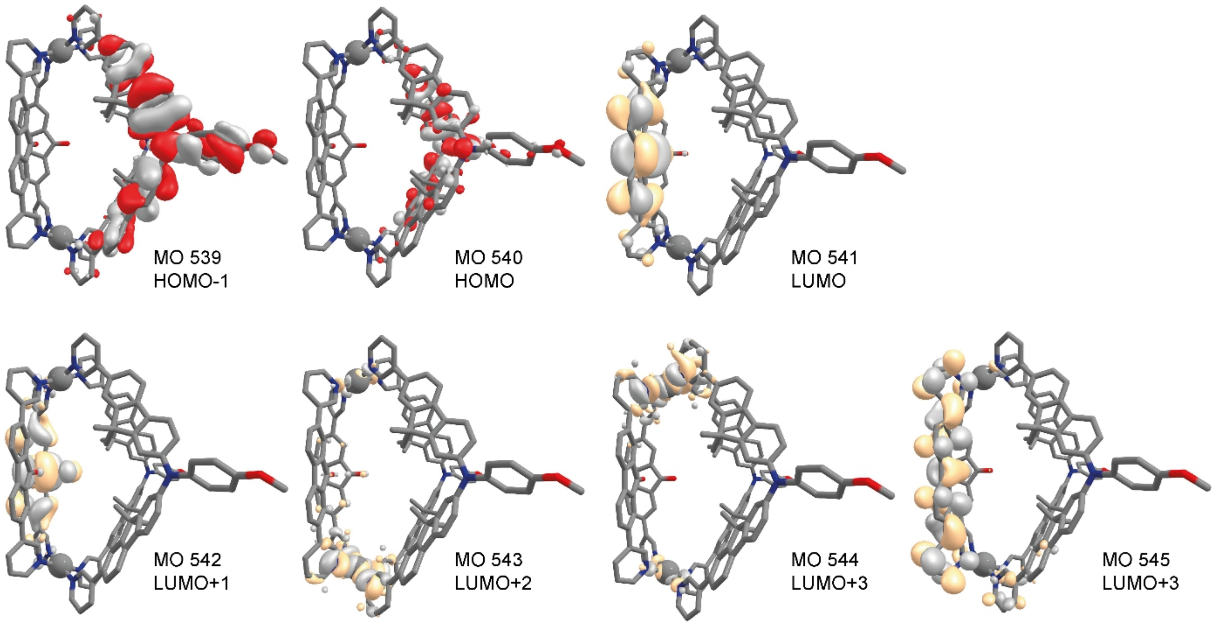

Fig. 129 Selected molecular orbitals of [Pd$_2$**TAA**$_2$**FRO**$_2$]$^{4+}$.

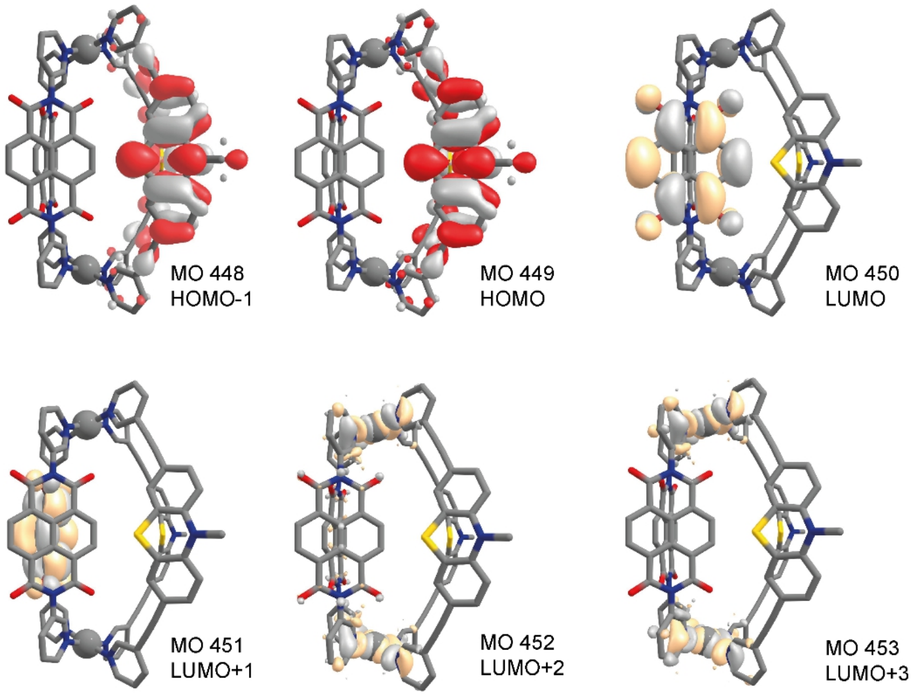

Fig. 130 Selected molecular orbitals of [Pd$_2$**PTZ**$_2$**NDI**$_2$]$^{4+}$.

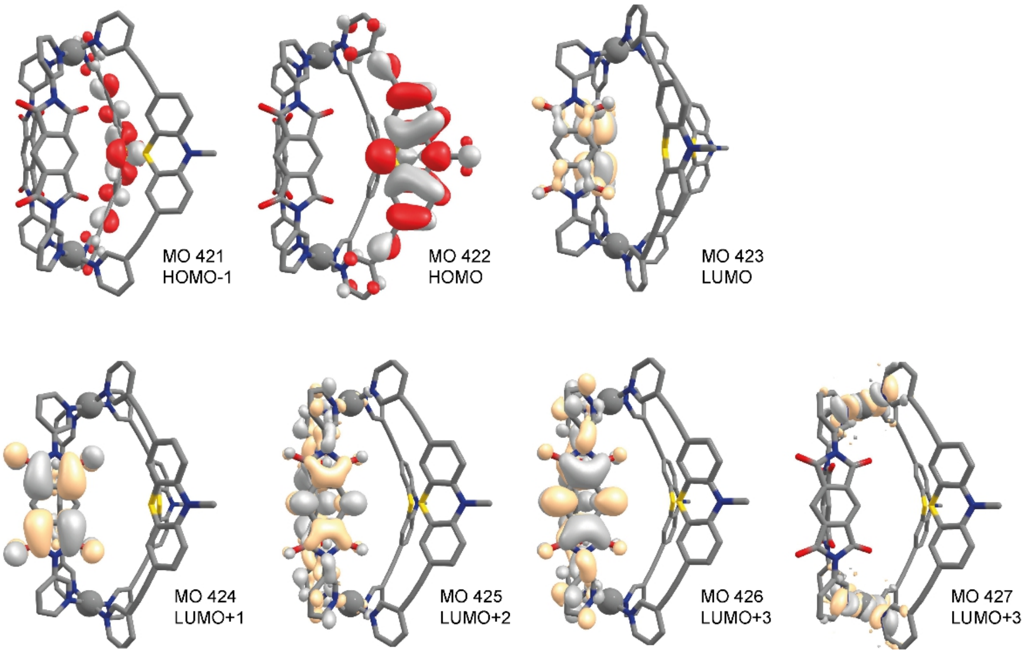

Fig. 131 Selected molecular orbitals of $[\mathrm{Pd}_2\mathbf{PTZ}_2\mathbf{PMDI}_2]^{4+}$.

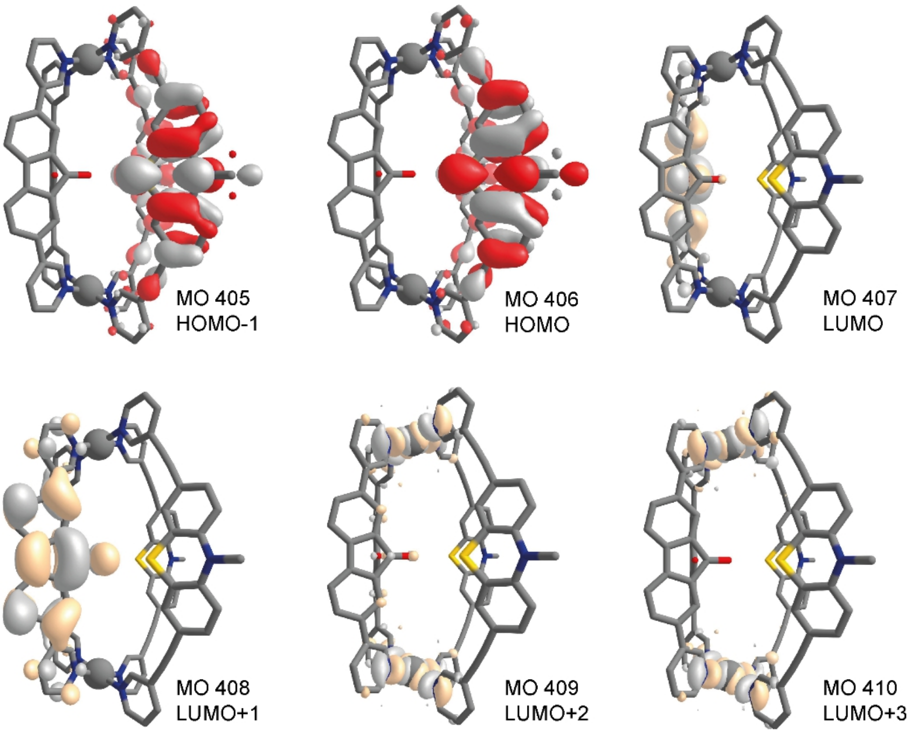

Fig. 132 Selected molecular orbitals of $[\mathrm{Pd}_2\mathbf{PTZ}_2\mathbf{FRO}_2]^{4+}$.

3.11.8. Calculation of the Coulomb term and ligand-to-ligand distances

The Coulomb term was calculated with equation 6 with $e = -1.602 \cdot 10^{-19}$ C, $\varepsilon_0 = 8.854187 \frac{\mathrm{C}^2 \cdot \mathrm{s}^2}{\mathrm{kg} \cdot \mathrm{m}^3}$, $\varepsilon_\mathrm{r} = 37.5$ (for acetonitrile). For the ligand-to-ligand distance d_DA, an average distance $d_\mathrm{cis,av}$ was used for all three cages carrying the same donor ligand (Tab. 9).

$$\frac{e^2}{4\pi\varepsilon_0\varepsilon_\mathrm{r} d_\mathrm{DA}} \tag{6}$$

The distances between donor and acceptor ligands were measured based on the DFT-optimized structures (3.11.7) between the atoms of the ligand backbones (Fig. 133). Table 9 lists the averages d_cis of the measured distances, e.g. for the *cis*-electron transfer in $[\mathrm{Pd_2}\mathbf{CBZ}_2\mathbf{NDI}_2]^{4+}$ the average over the distance between the two ligand pairs, was considered. For $[\mathrm{Pd_2}\mathbf{CBZ}_2\mathbf{PMDI}_2]^{4+}$, the average over four distances was measured and for $[\mathrm{Pd_2}\mathbf{PTZ}_2\mathbf{PMDI}_2]^{4+}$ the average over eight distances.

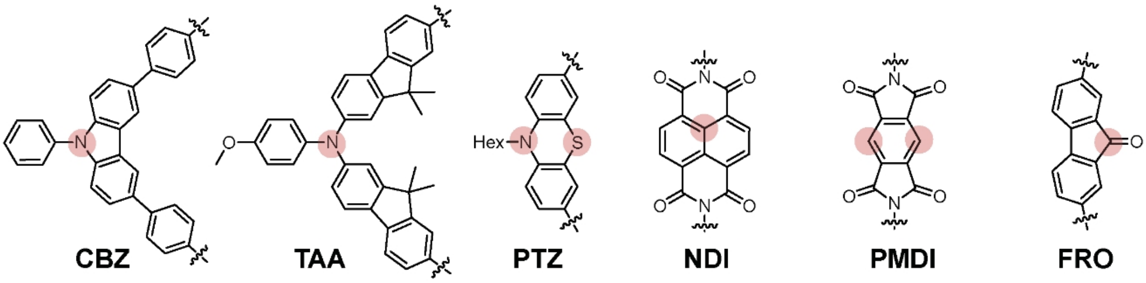

Fig. 133 Atoms of the central backbones of the ligands used for measuring the ligand-to-ligand distances.

Tab. 9 Ligand-to-ligand distances measured based on the DFT-optimized cage structures.

	d_cis/ Å	$d_\mathrm{cis,av}$/ Å	d_trans/ Å
$[\mathrm{Pd_2}\mathbf{CBZ}_2\mathbf{NDI}_2]^{4+}$	10.99	11.32	14.49
$[\mathrm{Pd_2}\mathbf{CBZ}_2\mathbf{PMDI}_2]^{4+}$	11.45		14.85
$[\mathrm{Pd_2}\mathbf{CBZ}_2\mathbf{FRO}_2]^{4+}$	11.52		13.87
$[\mathrm{Pd_2}\mathbf{TAA}_2\mathbf{NDI}_2]^{4+}$	10.55	10.43	14.06
$[\mathrm{Pd_2}\mathbf{TAA}_2\mathbf{PMDI}_2]^{4+}$	10.30		13.88
$[\mathrm{Pd_2}\mathbf{TAA}_2\mathbf{FRO}_2]^{4+}$	10.45		12.85
$[\mathrm{Pd_2}\mathbf{PTZ}_2\mathbf{NDI}_2]^{4+}$	8.08	7.85	11.10
$[\mathrm{Pd_2}\mathbf{PTZ}_2\mathbf{PMDI}_2]^{4+}$	8.31		10.65
$[\mathrm{Pd_2}\mathbf{PTZ}_2\mathbf{FRO}_2]^{4+}$	7.15		10.13

3.11.9. Transient absorption spectroscopy

Transient absorption spectroscopy: $[Pd_2TAA_2A_2]^{4+}$ and $[Pd_2PTZ_2A_2]^{4+}$

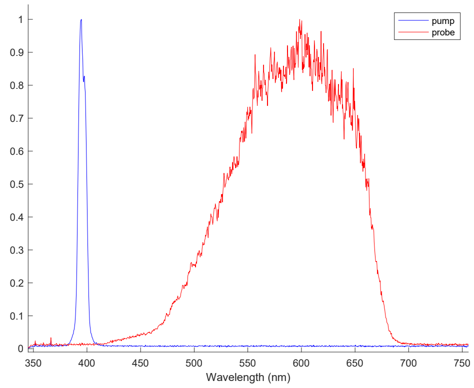

Fig. 134 Pump and probe spectra.

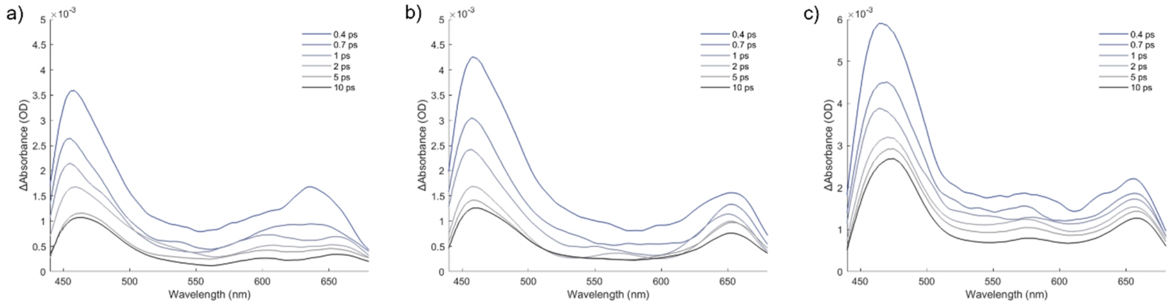

Fig. 135 Transient difference spectra at early time delays a) $[Pd_2\mathbf{TAA}_2\mathbf{NDI}_2]^{4+}$, b) $[Pd_2\mathbf{TAA}_2\mathbf{PMDI}_2]^{4+}$, and c) $[Pd_2\mathbf{TAA}_2\mathbf{FRO}_2]^{4+}$.

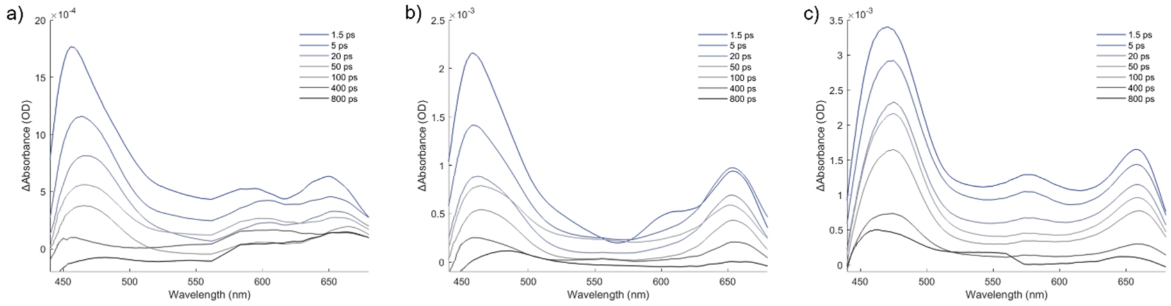

Fig. 136 Transient difference spectra at various time delays a) $[Pd_2\mathbf{TAA}_2\mathbf{NDI}_2]^{4+}$, b) $[Pd_2\mathbf{TAA}_2\mathbf{PMDI}_2]^{4+}$, and c) $[Pd_2\mathbf{TAA}_2\mathbf{FRO}_2]^{4+}$.

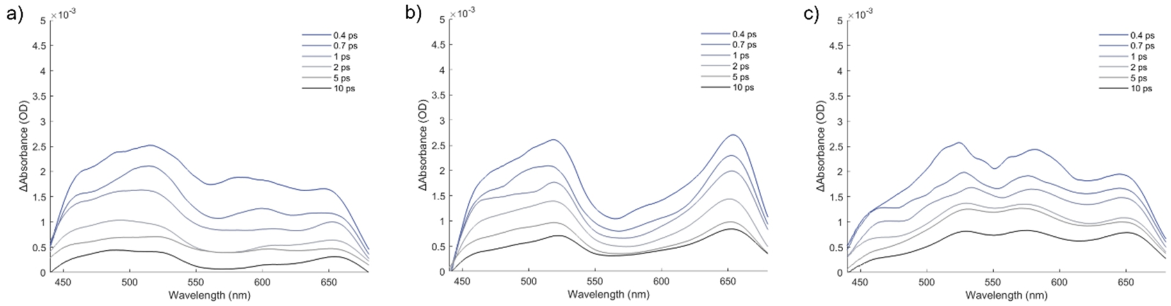

Fig. 137 Transient difference spectra at early time delays a) $[Pd_2\textbf{PTZ}_2\textbf{NDI}_2]^{4+}$, b) $[Pd_2\textbf{PTZ}_2\textbf{PMDI}_2]^{4+}$, and c) $[Pd_2\textbf{PTZ}_2\textbf{FRO}_2]^{4+}$.

Global analysis for the transient absorption data was performed using the Glotaran software[57] after single wavelength kinetic fitting was performed using Matlab. Based on the results of the preceding work (section 3.2.), charge separation from the donor species (**PTZ** or **TAA**) to the acceptor species (**PMDI**, **NDI**, or **FRO**) is assumed to have occurred within the instrument response time. Therefore, relaxation is the only process left to occur, and all samples were fit to a parallel two component exponential decay model. The results of this model for each sample are summarized in table 10, and the resultant species associated spectra (SAS) for each sample are shown in figure 138.

Tab. 10 Rate constants k_{BET1}, k_{BET2} and lifetimes τ_{BET1}, τ_{BET2} obtained from global analysis.

	k_{BET1} (ps^{-1})	τ_{BET1} (ps)	k_{BET2} (ps^{-1})	τ_{BET2} (ps)
$[Pd_2\textbf{TAA}_2\textbf{NDI}_2]^{4+}$	3.10	0.322	2.04×10^{-2}	49.04
	1.91	0.524	1.87×10^{-2}	53.55
Average	2.50	0.423	1.96×10^{-2}	51.30
Standard Deviation	0.841	0.143	1.20×10^{-3}	3.19
$[Pd_2\textbf{TAA}_2\textbf{PMDI}_2]^{4+}$	1.97	0.507	1.14×10^{-2}	87.65
$[Pd_2\textbf{TAA}_2\textbf{FRO}_2]^{4+}$	1.75	0.570	7.33×10^{-3}	136.38
	1.40	0.716	6.47×10^{-3}	154.53
Average	1.58	0.643	6.90×10^{-3}	145.46
Standard Deviation	0.247	0.103	6.08×10^{-4}	12.84
$[Pd_2\textbf{PTZ}_2\textbf{NDI}_2]^{4+}$	0.658	1.52	1.90×10^{-2}	52.50
	0.559	1.79	1.57×10^{-2}	63.77
Average	0.608	1.65	1.74×10^{-2}	58.14
Standard Deviation	7.00×10^{-2}	0.19	2.33×10^{-3}	7.97
$[Pd_2\textbf{PTZ}_2\textbf{PMDI}_2]^{4+}$	0.463	2.16	7.58×10^{-3}	131.76
$[Pd_2\textbf{PTZ}_2\textbf{FRO}_2]^{4+}$	0.322	3.11	8.18×10^{-3}	122.19
	0.495	2.02	8.61×10^{-3}	116.18
Average	0.408	2.56	8.40×10^{-3}	119.18
Standard Deviation	0.122	0.77	3.04×10^{-4}	4.25

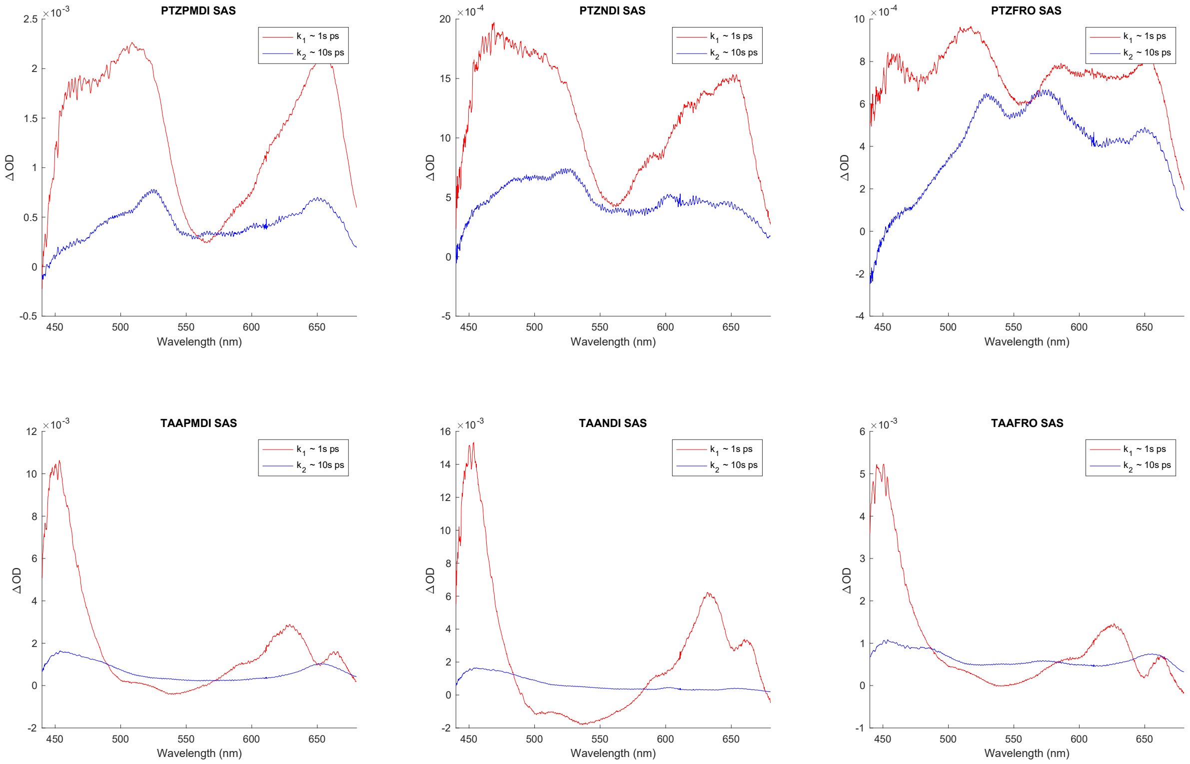

Fig. 138 Species associated decay spectra (SAS) for [Pd$_2$**PTZ**$_2$**PMDI**$_2$]$^{4+}$ (top left), [Pd$_2$**PTZ**$_2$**NDI**$_2$]$^{4+}$ (top, middle), [Pd$_2$**PTZ**$_2$**FRO**$_2$]$^{4+}$ (top, right), Pd$_2$**TAA**$_2$**PMDI**$_2$]$^{4+}$ (top left), [Pd$_2$**TAA**$_2$**NDI**$_2$]$^{4+}$ (top, middle), [Pd$_2$**TAA**$_2$**FRO**$_2$]$^{4+}$ (top, right).

Transient absorption spectroscopy: $[\mathrm{Pd_2}\mathbf{CBZ}_2\mathrm{A_2}]^{4+}$

All assemblies except for $[\mathrm{Pd_2}\mathbf{CBZ}_4]^{4+}$ can be synthesized in acetonitrile, i.e. they are the thermodynamic product in this solvent. Aiming at investigating all assemblies in the same solvent, cage $[\mathrm{Pd_2}\mathbf{CBZ}_4]^{4+}$ was synthesized in DMSO and redissolved in acetonitrile after removal of the DMSO via lyophilization. However, the cage does not possess sufficient stability in acetonitrile (appendix, section 3.11.3; for shipping of the solution, the sample should be stable for > 1 week). By contrast, the cage was shown to be stable in DMSO for > 2 weeks (appendix, section 3.11.3) and was therefore investigated in this solvent.

Preprocessing of the data, including chirp and baseline correction, were performed using the Surface Xplorer 4.3.0 software from Ultrafast Systems. The open source Python based data analysis tool KiMoPack 7.4.9 was employed for global analysis of the TA data. The data were fitted to a sequential decay model.

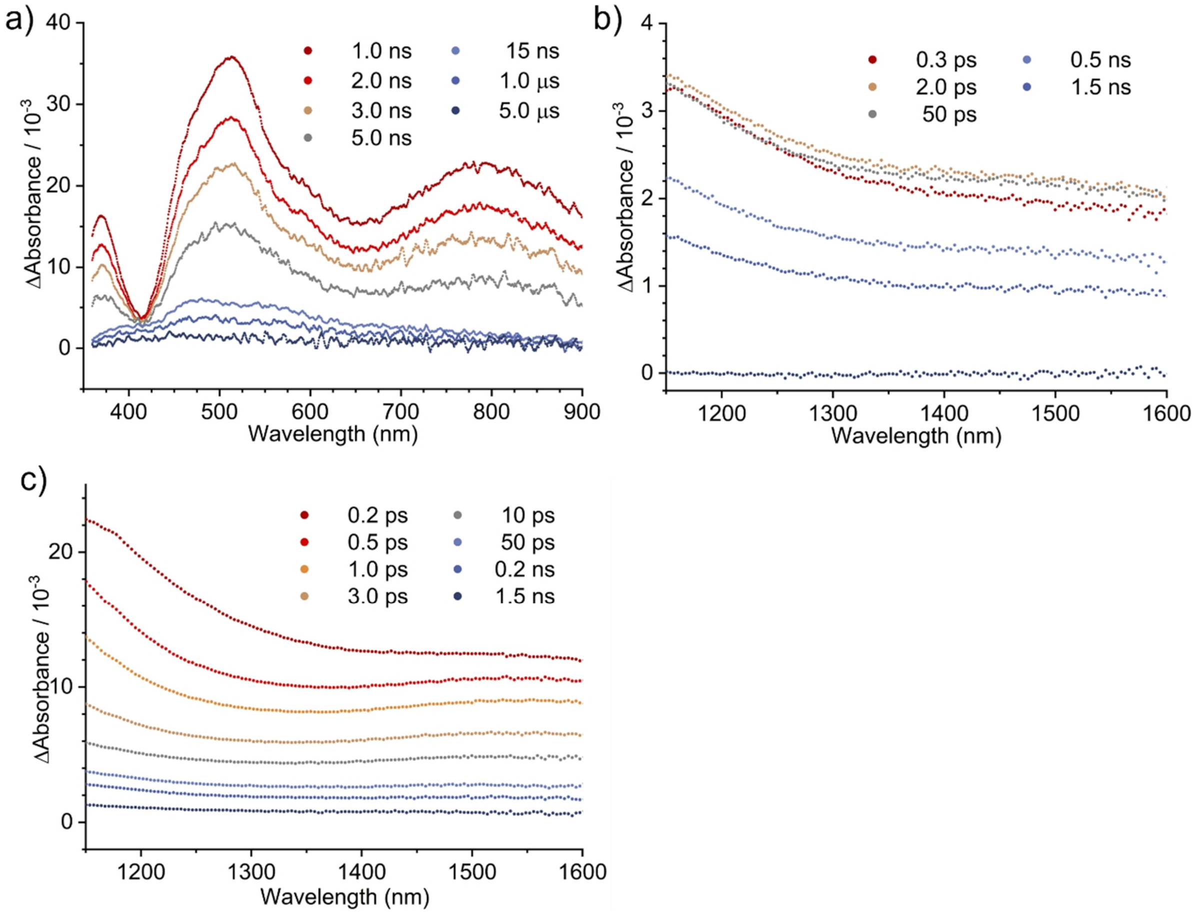

Fig. 139 Selected ns-transient difference spectra of ligand **CBZ** in the UV-Vis (a) and NIR region(b) (solvent: CH_3CN, λ_{ex} = 350 nm); selected ns-transient difference spectra of $[\mathrm{Pd_2}\mathbf{CBZ}_4]^{4+}$ in the NIR region (solvent: DMSO, λ_{ex} = 350 nm).

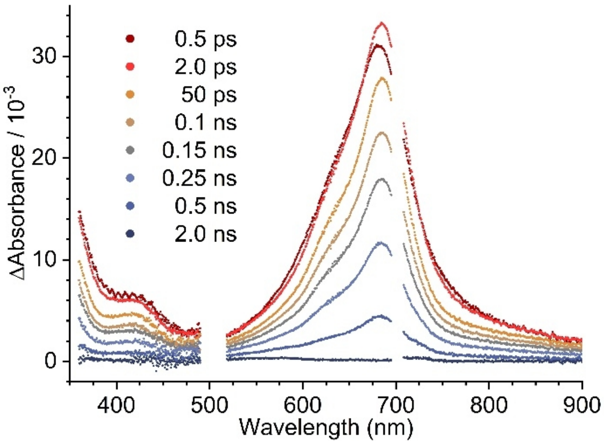

Fig. 140 Selected fs-transient difference spectra of ligand **PMDI** in the UV-Vis region (solvent: CH_3CN, λ_{ex} = 350 nm).

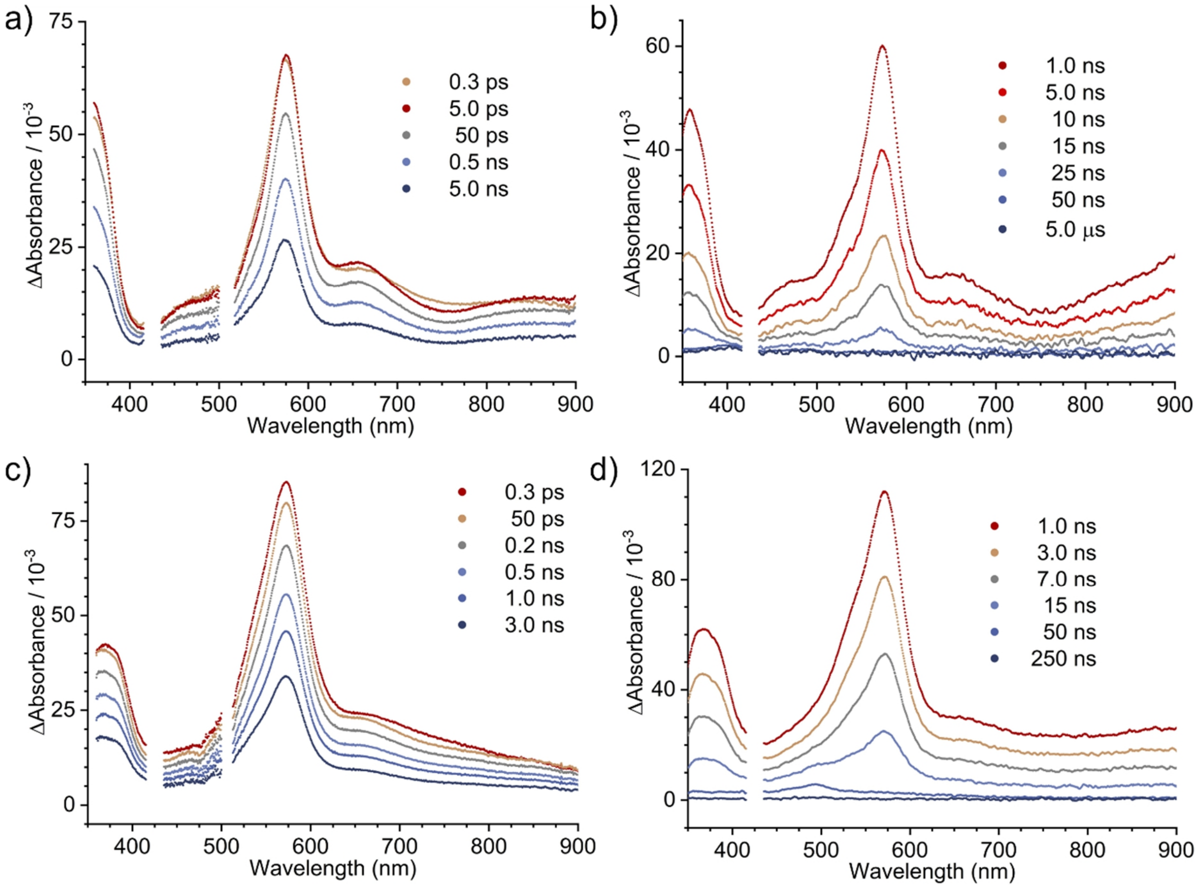

Fig. 141 Selected transient difference spectra of ligand **FRO** (a) fs-ns, b) ns-µs) and of the homoleptic assemblies of **FRO** (c) fs-ns, d) ns-µs) (solvent: CH_3CN, λ_{ex} = 425 nm).

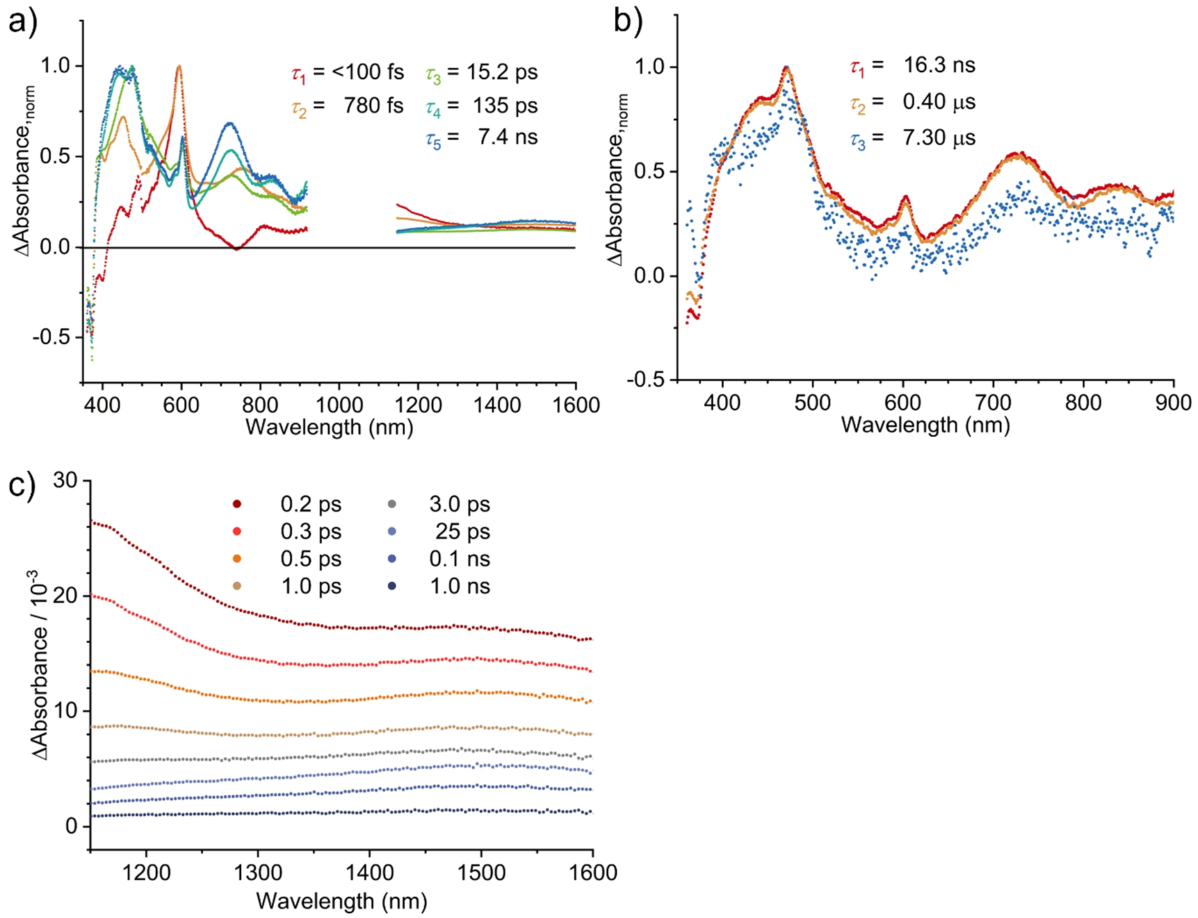

Fig. 142 EADS of [Pd$_2$**CBZ**$_2$**NDI**$_2$]$^{4+}$ (a) fs-ns, b) ns-µs); c) selected transient difference spectra of [Pd$_2$**CBZ**$_2$**NDI**$_2$]$^{4+}$ in the NIR region (solvent: CH$_3$CN, λ_{ex} = 350 nm).

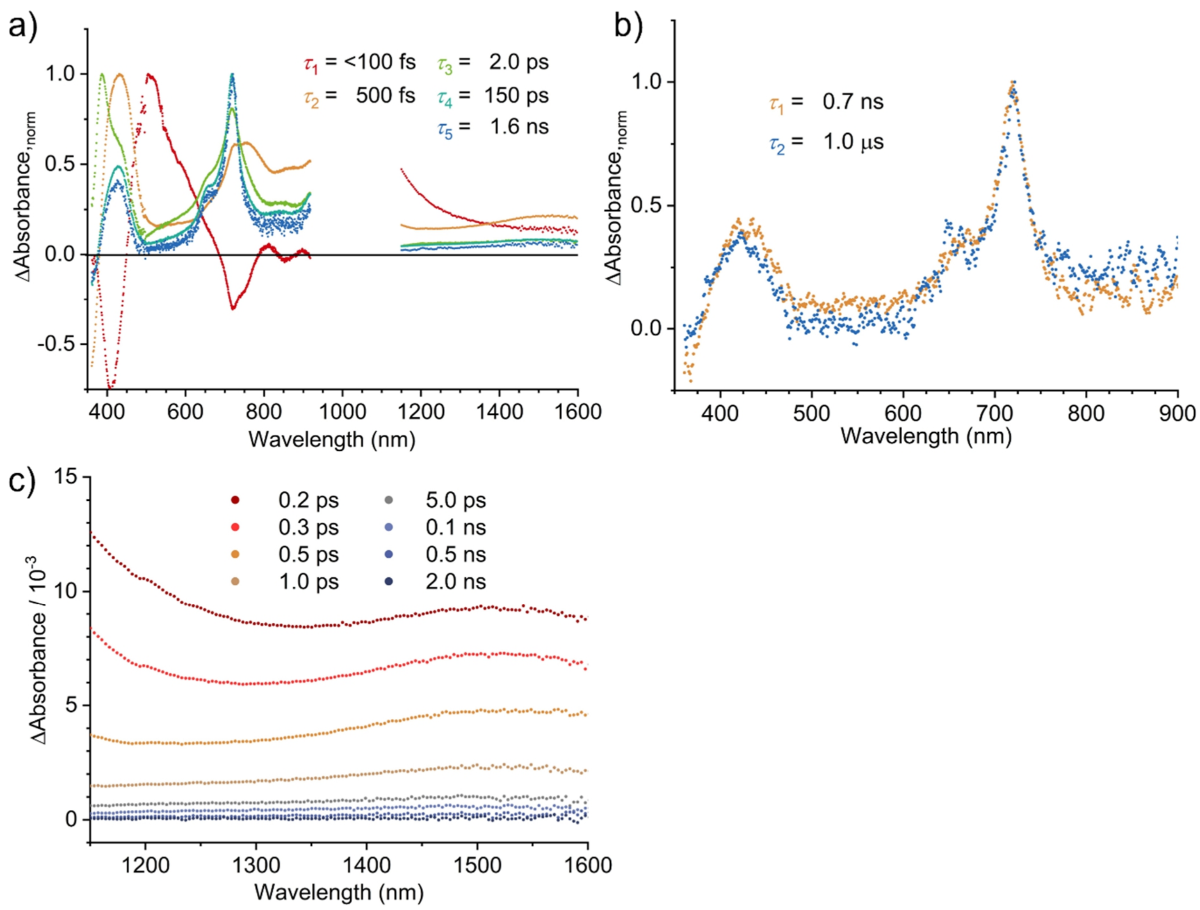

Fig. 143 EADS of [Pd$_2$**CBZ**$_2$**PMDI**$_2$]$^{4+}$ (a) fs-ns, b) ns-µs); c) selected transient difference spectra of [Pd$_2$**CBZ**$_2$**PMDI**$_2$]$^{4+}$ in the NIR region (solvent: CH$_3$CN, λ_{ex} = 350 nm).

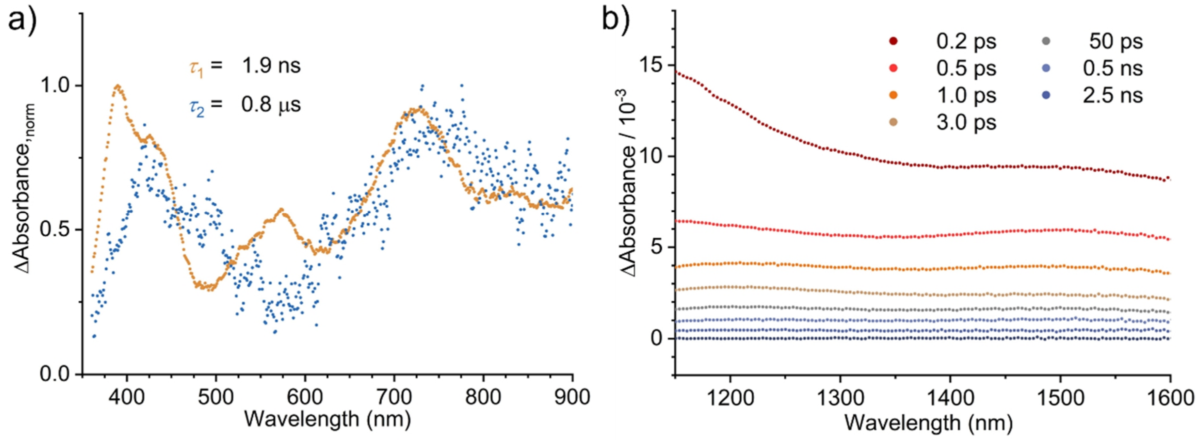

Fig. 144a) ns-µs EADS of [Pd$_2$**CBZ**$_2$**FRO**$_2$]$^{4+}$; b) selected transient difference spectra of [Pd$_2$**CBZ**$_2$**FRO**$_2$]$^{4+}$ in the NIR region (solvent: CH$_3$CN, λ_{ex} = 350 nm).

3.12. References

[1] M. Frank, J. Ahrens, I. Bejenke, M. Krick, D. Schwarzer, G. H. Clever, *J. Am. Chem. Soc.* **2016**, *138*, 8279.

[2] R. Ham, C. J. Nielsen, S. Pullen, J. N. H. Reek, *Chem. Rev.* **2023**, *123*, 5225.

[3] Y. Xue, X. Hang, J. Ding, B. Li, R. Zhu, H. Pang, Q. Xu, *Coord. Chem. Rev.* **2021**, *430*, 213656.

[4] S. Fukuzumi, K. Ohkubo, T. Suenobu, *Acc. Chem. Res.* **2014**, *47*, 1455.

[5] Y. Hou, X. Zhang, K. Chen, D. Liu, Z. Wang, Q. Liu, J. Zhao, A. Barbon, *J. Mater. Chem. C* **2019**, *7*, 12048.

[6] A. Leo, F. Ambrosio, A. Landi, A. Peluso, *Chemistry* **2023**, *5*, 97.

[7] D. Rehm, A. Weller, *Isr. J. Chem.* **1970**, *8*, 259.

[8] J. Ahrens, M. Frank, G. H. Clever, D. Schwarzer, *Phys. Chem. Chem. Phys.* **2017**, *19*, 13596.

[9] R. Sugimura, S. Suzuki, M. Kozaki, K. Keyaki, K. Nozaki, H. Matsushita, N. Ikeda, K. Okada, *Res. Chem. Intermed.* **2013**, *39*, 185.

[10] K. Kimoto, T. Satoh, M. Iwamura, K. Nozaki, T. Horikoshi, S. Suzuki, M. Kozaki, K. Okada, *J. Phys. Chem. A* **2016**, *120*, 8093.

[11] F. Zieschang, M. H. Schreck, A. Schmiedel, M. Holzapfel, J. H. Klein, C. Walter, B. Engels, C. Lambert, *J. Phys. Chem. C* **2014**, *118*, 27698.

[12] G. L. Closs, J. R. Miller, *Science* **1988**, *240*, 440.

[13] K. Wu, E. Benchimol, A. Baksi, G. H. Clever, *Nat. Chem.* **2024**, *16*, 584.

[14] W. M. Bloch, Y. Abe, J. J. Holstein, C. M. Wandtke, B. Dittrich, G. H. Clever, *J. Am. Chem. Soc.* **2016**, *138*, 13750.

[15] J. Tessarolo, H. Lee, E. Sakuda, K. Umakoshi, G. H. Clever, *J. Am. Chem. Soc.* **2021**, *143*, 6339.

[16] M. Frank, J. Hey, I. Balcioglu, Y. Chen, D. Stalke, T. Suenobu, S. Fukuzumi, H. Frauendorf, G. H. Clever, *Angew. Chem. Int. Ed.* **2013**, *52*, 10102.

[17] N. J. Hestand, F. C. Spano, *Chem. Rev.* **2018**, *118*, 7069.

[18] F. D. Lewis, R. L. Letsinger, M. R. Wasielewski, *Acc. Chem. Res.* **2001**, *34*, 159.

[19] S. Ganta, J.-H. Borter, C. Drechsler, J. J. Holstein, D. Schwarzer, G. H. Clever, *Org. Chem. Front.* **2022**, *9*, 5485.

[20] N. Elgrishi, K. J. Rountree, B. D. McCarthy, E. S. Rountree, T. T. Eisenhart, J. L. Dempsey, *J. Chem. Educ.* **2018***, 95,* 197.

[21] S. Guha, F. S. Goodson, R. J. Clark, S. Saha, *CrystEngComm* **2011**, *14*, 1213.

[22] S. Guha, F. S. Goodson, L. J. Corson, S. Saha, *J. Am. Chem. Soc.* **2012**, *134*, 13679.

[23] A. Viehbeck, M. J. Goldberg, C. A. Kovac, *J. Electrochem. Soc.* **1990**, *137*, 1460.

[24] A. Avestro, D. M. Gardner, N. A. Vermeulen, E. A. Wilson, S. T. Schneebeli, A. C. Whalley, M. E. Belowich, R. Carmieli, M. R. Wasielewski, J. F. Stoddart, *Angew. Chem. Int. Ed.* **2014**, *53*, 4442.

[25] T. Honda, T. Nakanishi, K. Ohkubo, T. Kojima, S. Fukuzumi, *J. Am. Chem. Soc.* **2010**, *132*, 10155.

[26] S. S. Jayanthi, P. Ramamurthy, *J. Phys. Chem. A* **1997**, *101*, 2016.

[27] E. Prasad, K. R. Gopidas, *J. Am. Chem. Soc.* **2000**, *122*, 3191.

[28] J. Pommerehne, H. Vestweber, W. Guss, R. F. Mahrt, H. Bässler, M. Porsch, J. Daub, *Adv. Mater.* **1995**, *7*, 551.

[29] J. R. Reimers, *J. Chem. Phys.* **2001**, *115*, 9103.

[30] A. L. Jones, K. S. Schanze, *J. Phys. Chem. A* **2020**, *124*, 21.

[31] B. Balan, K. R. Gopidas, *Chem. Eur. J.* **2006**, *12*, 6701.

[32] P. Ganesan, J. Baggerman, H. Zhang, E. J. R. Sudhölter, H. Zuilhof, *J. Phys. Chem. A* **2007**, *111*, 6151.

[33] L. A. Estrada, J. E. Yarnell, D. C. Neckers, *J. Phys. Chem.* **2011**, *115*, 6366.

[34] G. L. Thornton, R. Phelps, A. J. Orr-Ewing, *Phys. Chem. Chem. Phys.* **2021**, *23*, 18378.

[35] G. L. Closs, L. T. Calcaterra, N. J. Green, K. W. Penfield, J. R. Miller, *J. Phys. Chem.* **1986**, *90*, 3673.

[36] M. Gilbert, B. Albinsson, *Chem. Soc. Rev.* **2014**, *44*, 845.

[37] M. Natali, S. Campagna, F. Scandola, *Chem. Soc. Rev.* **2014**, *43*, 4005.

[38] W. B. Davis, W. A. Svec, M. A. Ratner, M. R. Wasielewski, *Nature* **1998**, *396*, 60.

[39] E. Benchimol, I. Regeni, B. Zhang, M. Kabiri, J. J. Holstein, G. H. Clever, *J. Am. Chem. Soc.* **2024**, *146*, 6905.

[40] J. N. Robinson, D. J. Cole-Hamilton, *Chem. Soc. Rev.* **1991**, *20*, 49.

[41] N. Sinambela, J. Bösking, A. Abbas, A. Pannwitz, *ChemBioChem* **2021**, *22*, 3140.

[42] E. Benchimol, A. Rivoli, M. Kabiri, B. Zhang, J. J. Holstein, P. Ballester, G. H. Clever, *J. Am. Chem. Soc.* **2025**, *147*, 3823.

[43] A. Burkhardt, T. Pakendorf, B. Reime, J. Meyer, P. Fischer, N. Stübe, S. Panneerselvam, O. Lorbeer, K. Stachnik, M. Warmer, P. Rödig, D. Göries, A. Meents, *Europ. Phys. J. Plus* **2016**, *131*, 56.

[44] W. Kabsch, *Acta Crystallogr. Sect. D* **2010**, 66, 125.

[45] G. M. Sheldrick, *Acta Crystallogr. Sect. A* **2015**, *71*, 3.

[46] G. M. Sheldrick, *Acta Crystallogr. Sect. C* **2015**, *71*, 3.

[47] C. B. Hübschle, G. M. Sheldrick, B. Dittrich, *J. Appl. Crystallogr.* **2011**, *44*, 1281.

[48] D. Kratzert, J. J. Holstein, I. Krossing, *J. Appl. Crystallogr.* **2015**, *48*, 933.

[49] D. Kratzert, I. Krossing, *J. Appl. Crystallogr.* **2018**, *51*, 928.

[50] A. Thorn, B. Dittrich, G. M. Sheldrick, *Acta Crystallogr. Sect. A* **2012**, *68*, 448.

[51] A. L. Spek, *Acta Crystallogr. Sect. C* **2015**, *71*, 9.

[52] A. L. Spek, *Acta Crystallogr. Sect. D* **2009**, *65*, 148.

[53] Wavefunc on, Inc., Spartan`18 Parallel Suite, Irvine (USA), **2018**.

[54] M. J. Frisch, G. W. Trucks, H. B. Schlegel et al., Gaussian, Inc., Gaussian 16, Revision C.01, Wallingford CT (USA), **2016**.

[55] F. Neese, *Wiley Interdiscip. Rev.: Comput. Mol. Sci.* **2022**, *12*, e1606.

[56] Zhurko, G. and Zhurko, D. Chemcraft Graphical Program for Visualization of Computed Results. http://www.chemcraftprog.com/, **2015**.

[57] J. J. Snellenburg, S. P. Laptenok, R. Seger, K. M. Mullen, I. H. M. van Stokkum, *J. Stat. Softw.* **2012**, *49*, 1.

4. Amphiphilic donor-acceptor cages

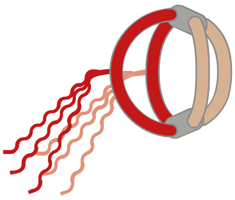

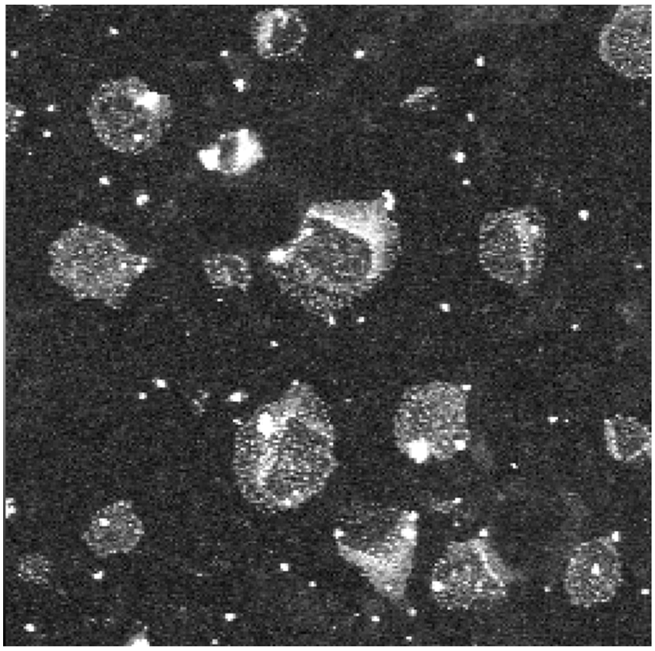

4.1. Motivation

Having established *cis*-[$Pd_2D_2A_2$]$^{4+}$ cages as a reliable platform for the formation of light-induced charge separated states, their incorporation into vesicular materials is envisioned. In section 3, the donor-acceptor cages were studied in solution, meaning that they are randomly oriented relative to each other. For certain applications, for example for the generation of an electrochemical gradient, vectorial electron transfer (i.e. electron transfer in one direction) is desirable. For achieving this, donor-acceptor systems can be incorporated into higher order materials such as vesicles.[1,2] Enriching the different solvent environments in the compartmentalized media with suitable redox active compounds can then allow for multiple consecutive electron transfer steps. Aside from the just mentioned directionality, this bears the advantage of an increased distance between electron and hole. In analogy to the stepwise electron transfer in the photosynthetic reaction center (section 1.2.), this would prolong the lifetime of the charge separated state and make it available for conversion into other usable forms of energy.

Bhosale and coworkers reported on photoinduced electron transfer across a lipid bilayer which resulted in the build-up of a pH gradient.[3] For achieving this, a donor-spacer-acceptor system, modified with multiple octyl chains, was embedded into the lipid membrane of liposomes (Fig. 1). The donor-spacer-acceptor system consisted of a zinc porphyrin donor, bridged via thiophenes to an NDI acceptor. The inner compartment of the liposomes was loaded with sulfonato naphthoquinone (Q) as electron acceptor and EDTA was used as a sacrificial electron donor residing in the bulk phase. 8-hydroxypyrene-1,3,6-trisulfonate (HPTS) served as a pH indicator. Photoinduced charge separation within the donor-spacer-acceptor dyad leads to transmembrane electron transfer: the oxidized zinc porphyrin is reduced by EDTA and the NDI acceptor shuttles the electron to a quinone. The reduced quinone catches protons from its environment, thus increasing the basicity of the inner compartment, resulting in a detectable change in the fluorescence of the indicator HPTS.

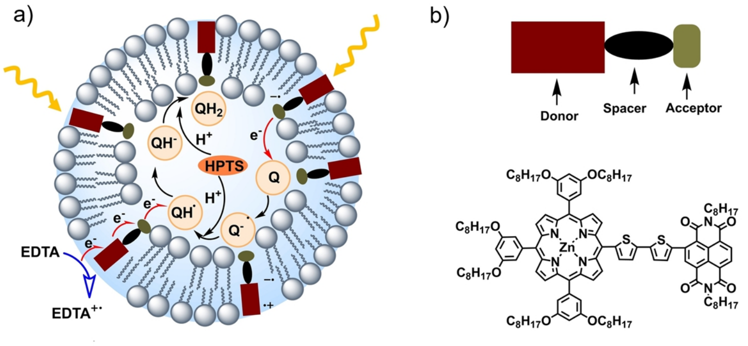

Fig. 1 Transmembrane photoinduced electron transfer leads to the generation of a pH gradient; a) overview of photoinduced processes; b) structure of donor-spacer-acceptor dyad embedded in the lipide bilayer. Reprinted from ref.[1] (*open access*).

In preceding works of Clever and coworkers, amphiphilic Pd(II) based cages were accessed by anisotropic decoration of the cage with solubility-controlling groups, using the SCA approach.[4] For this, the well-known set of geometrically complementary ligands based on acridone and phenanthrene was employed (Fig. 2). The former ligand was equipped with dodecyl chains and the latter carries methoxy substituents. In combination with the charged metal centers, the design of cage **CGA-1** therefore gives rise to a gemini-type amphiphile. In suitable polar organic solvents, such as acetonitrile, higher order self-assembly into vesicular structures with diameters larger than 100 nm was observed. Moreover, **CGA-1** was shown to stabilize oil-in-oil emulsions for up to 24 h (Fig. 2 bottom).

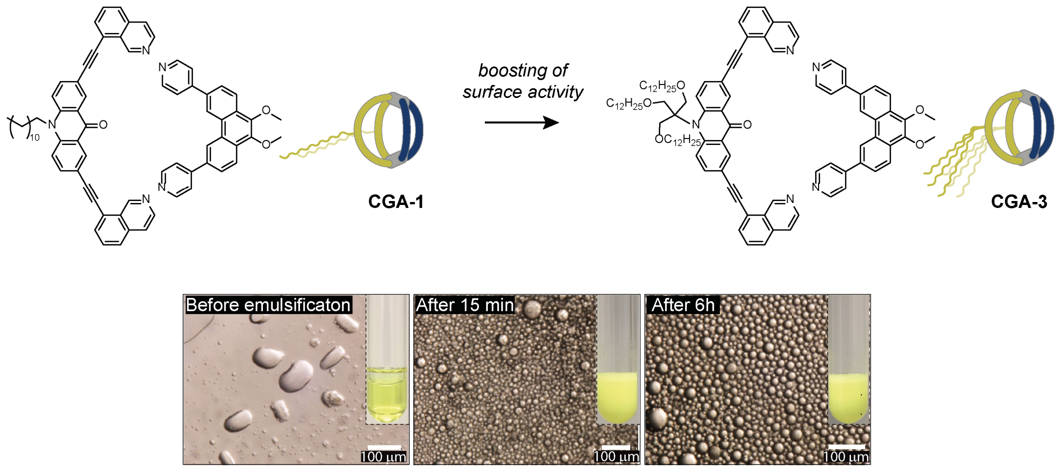

Fig. 2 Top: evolution of cage-based amphiphiles **CGA-1** and **CGA-3**; bottom: stabilization of a 4:1 acetonitrile:hexadecane emulsion by **CGA-1** (left: solvent mixture (phases are separated), middle and right: stable emulsion after homogenization in the presence of **CGA-1**). Reprinted from ref[4] (*open access*).

In a later work, cage **CGA-1** was appended with three nonpolar chains at the acridone ligand, giving rise to cage **CGA-3** (Fig. 2, top).[5] This structural modification translated into improved surface activity; the same oil-in-oil emulsion was stabilized for a longer period of time by **CGA-3** as compared to **CGA-1**. In addition, **CGA-3** but not **CGA-1** was able to form a foam when air was passed through the sample. The oil-in-oil emulsions stabilized by **CGA-3** were utilized as a template for the synthesis of different metal-oxides capsules. In another fashion, the same group reported on a homoleptic amphiphilic cage Pd_2L_4 with L having cholesterol appendices.[6] The latter are oriented in a common direction which gives, in combination with the Pd(II) metal centers, rise to an anisotropic polarity profile. Oil-in-oil emulsions stabilized by this cage were used as medium for organic polycondensation reactions.

In order to achieve photoredox active soft materials, the approaches for the synthesis of cage-based amphiphiles and for the design of donor-acceptor cages are combined in this work. Cage $[Pd_2\mathbf{CBZ}_2\mathbf{FRO}_2]^{4+}$, thoroughly studied in section 3, is structurally modified for changing its polarity profile. For this, ligand $^{\mathbf{Do}}\mathbf{CBZ}$, a derivative of ligand **CBZ** equipped with three dodecyloxy chains, is synthesized as the nonpolar part of the amphiphile (Fig. 3). The analogous ligand with methoxy substituents ($^{\mathbf{Me}}\mathbf{CBZ}$) should display the same electronic properties as $^{\mathbf{Do}}\mathbf{CBZ}$ while resembling commonly investigated dinuclear cages with regards to its solubility properties. Therefore, $^{\mathbf{Me}}\mathbf{CBZ}$ is synthesized as a reference compound. Self-assembly into $[Pd_2{}^{\mathbf{Me}}\mathbf{CBZ}/{}^{\mathbf{Do}}\mathbf{CBZ}_2\mathbf{FRO}_2]^{4+}$ is studied as well as the potential formation of higher order assemblies in polar solvents. Moreover, the incorporation of the cages into aqueous micellar solutions is targeted. In comparison to assemblies solely based on the amphiphilic cage, such materials feature an aqueous (bulk) and nonpolar environment (micellar core) which might allow for easy partitioning of redox compounds based on their solubility properties.

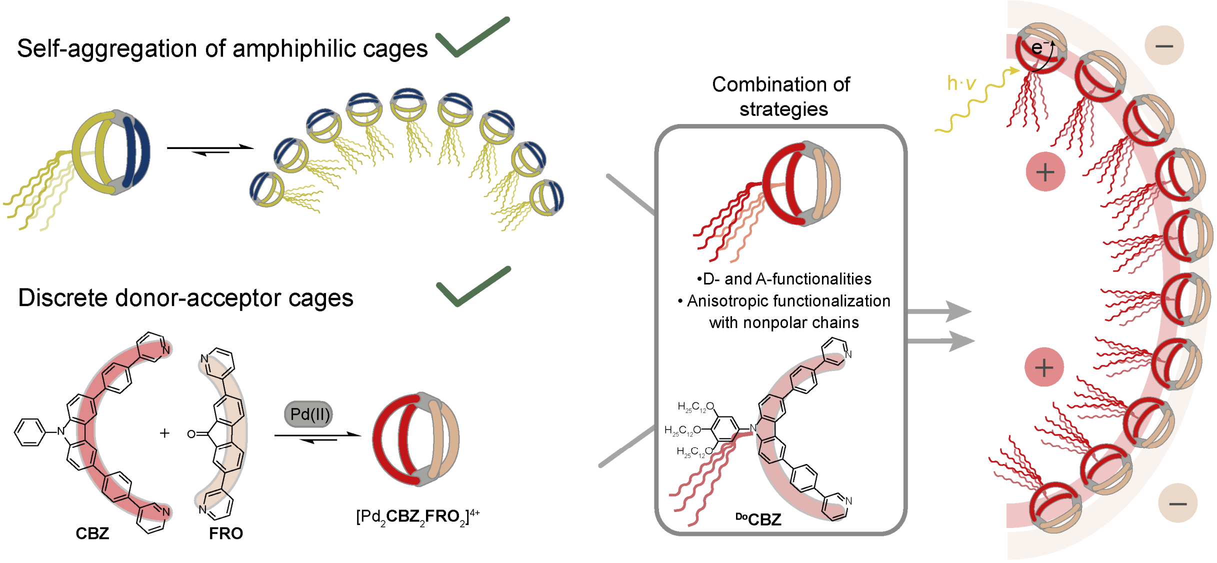

Fig. 3 Strategy for achieving higher order self-assembly of amphiphilic donor-acceptor cages through the design of shape complementary ligands with photoredox properties and suitable solubility properties. On the right side, a possible arrangement of the amphiphilic cages is shown in a schematic fashion.

4.2. Ligand synthesis and self-assembly into cages

The hydrophobic donor ligand **^{Do}CBZ** and the reference ligand **^{Me}CBZ** were synthesized in two steps. First, commercially available 3,6-dibromo-9*H*-carbazole was reacted with a phenyl pyridine boronic ester in a Suzuki cross coupling to yield an unsubstituted carbazole-based ligand **^{NH}CBZ**. Next, **^{NH}CBZ** was reacted with either 5-bromo-1,2,3-tri(dodecyloxy)benzene or 5-bromo-1,2,3-tri(methoxy)benzene in a Buchwald-Hartwig amination to yield ligands **^{Do}CBZ** and **^{Me}CBZ**, respectively. The synthetic details can be found in the appendix, section 4.6.2.

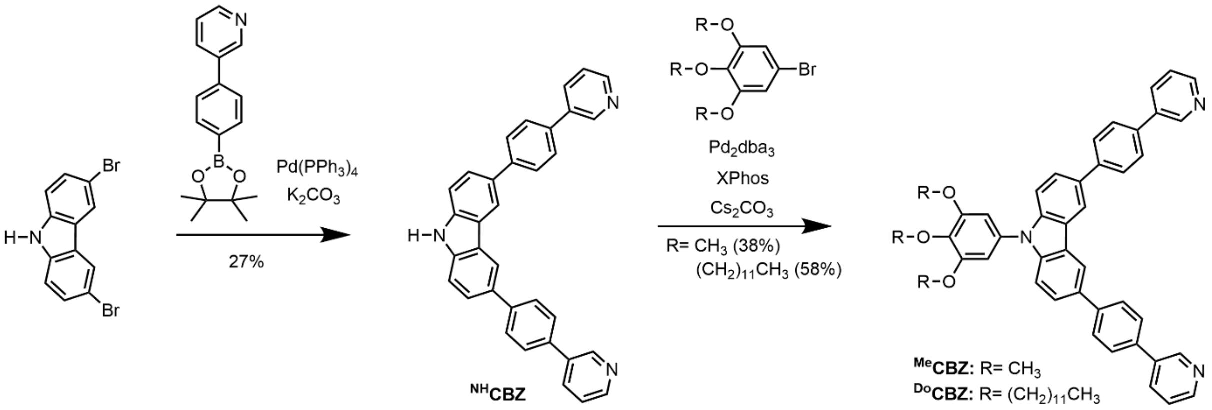

Scheme 1 Synthesis of ligands **^{Me}CBZ** and **^{Do}CBZ** via Suzuki cross-coupling (1st step) and Buchwald-Hartwig amination (2nd step).

For the self-assembly into heteroleptic [Pd$_2$**^{Me}CBZ/^{Do}CBZ$_2$FRO$_2$**]$^{4+}$, the two ligands and [Pd(CH$_3$CN)$_4$](BF$_4$)$_2$ were combined in DMSO-*d*$_6$ and the mixture was heated at 70 °C for 1.5 h. While **^{Me}CBZ** possesses great solubility in DMSO, it was not possible to dissolve or suspend **^{Do}CBZ** in this solvent. Therefore, solutions of **^{Do}CBZ** and **FRO** in CDCl$_3$ were combined and their ratio was adjusted to 1:1 by ^{1}H NMR. Afterwards, the solvent was removed, DMSO-*d*$_6$ as well as [Pd(CH$_3$CN)$_4$](BF$_4$)$_2$ were added, and the reaction was performed as stated above. For characterizations in acetonitrile, the DMSO-*d*$_6$ was removed via lyophilization, followed by suspension of the cage in acetonitrile.

The characterization of the reference cage [Pd$_2$**^{Me}CBZ$_2$FRO$_2$**]$^{4+}$ and the amphiphilic cage [Pd$_2$**^{Do}CBZ$_2$FRO$_2$**]$^{4+}$ and is shown in figure 4. The ^{1}H NMR spectra of the heteroleptic cages are stacked with the ^{1}H NMR spectra of the corresponding homoleptic cages and ligands. The acceptor ligand **FRO** assembles in DMSO-*d*$_6$ into a three-membered ring [Pd$_3$**FRO$_6$**]$^{6+}$ (II, Fig. 4).[7] The self-assembly of ligand **^{Me}CBZ** with Pd(II) leads to a downfield shift of the signals of the pyridine protons in the ^{1}H NMR spectrum (III,IV). A single set of signals is observed in the ^{1}H NMR spectrum which can probably be assigned to a lantern-shaped cage [Pd$_2$**^{Me}CBZ$_4$**]$^{4+}$, similar to the analogous ligand without methoxy substituents (section 3.11.3.). The ^{1}H NMR spectrum of the heteroleptic assembly of **^{Me}CBZ** and **FRO** features one set of signals (V). Furthermore, the ESI mass spectrum unequivocally confirms that the assembly has the sum formula [Pd$_2$**^{Me}CBZ$_2$FRO$_2$**]$^{4+}$. In agreement with this, a hydrodynamic radius of 12.1 Å is obtained by DOSY NMR. Coordination of dodecyloxy-chain decorated ligand **^{Do}CBZ** to Pd(II) leads to a severely broadened ^{1}H NMR spectrum (VII). This contrasts previous works, in which defined signals for Pd$_2$L$_4$-type cages were obtained for ligands based on dodecyl- or octadecyl-acridone[4] and cholesteryl carbazole.[6] The ^{1}H NMR spectrum for a homoleptic assembly of a tris-dodecyloxy-functionalized acridone based ligand was not reported.[5] As compared to a ligand with only one alkyl chain, the assembly of ligand **^{Do}CBZ** stands out with increased amphiphilicity owing to the three dodecyloxy chains per ligand, probably inducing aggregation and hence broadening of the spectrum. On the contrary, the ^{1}H NMR spectrum of the heteroleptic assembly of $^{\mathrm{Do}}$**CBZ** and **FRO** shows one set of well-separated signals, similar to reference cage [Pd$_2$$^{\mathrm{Me}}$**CBZ**$_2$**FRO**$_2$]$^{4+}$ (VIII). The ESI mass spectrum shows prominent peaks for [Pd$_2$$^{\mathrm{Do}}$**CBZ**$_2$**FRO**$_2$]$^{4+}$ and [Pd$_2$$^{\mathrm{Do}}$**CBZ**$_2$**FRO**$_2$+BF$_4$]$^{3+}$. Furthermore, a hydrodynamic radius of 13.3 Å was obtained by ^{1}H DOSY NMR. The slightly larger value as compared to the reference cage (ΔR_H = 1.2 Å) can be traced back to the long alkyl chains of ligand $^{\mathrm{Do}}$**CBZ**. Hence, the NMR spectroscopic characterization of the amphiphilic assembly in DMSO does not give any indications for the presence of higher order assemblies. However, amphiphilic cage **CGA-1** also showed defined signals in the ^{1}H NMR spectrum in DMSO while formation of vesicles in this solvent was visualized by liquid-cell transmission electron microscopy (LC-TEM).[4]

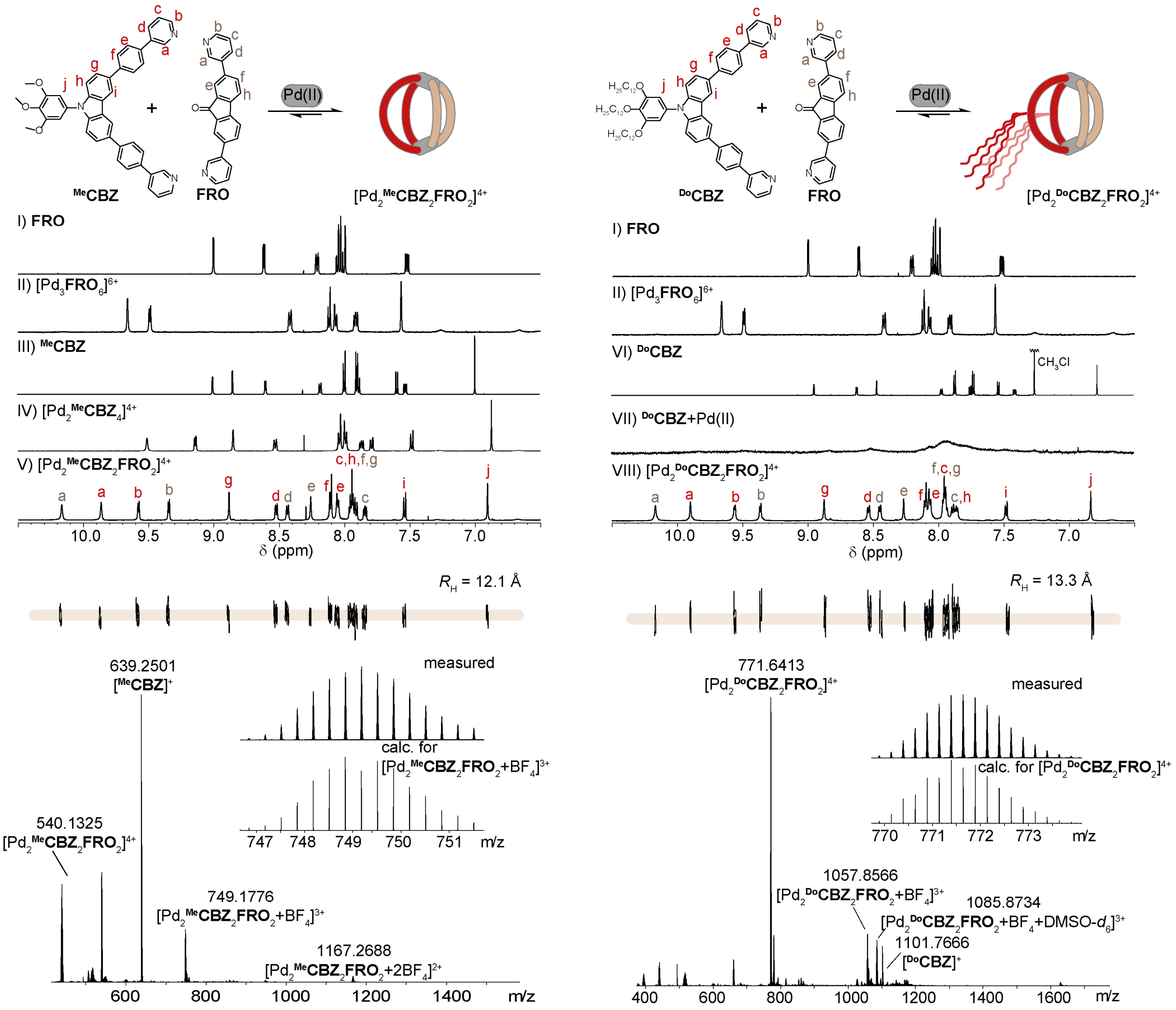

Fig. 4 Self-assembly scheme and structural characterization of [Pd$_2$$^{\mathrm{Me}}$**CBZ**$_2$**FRO**$_2$]$^{4+}$ (left) and [Pd$_2$$^{\mathrm{Do}}$**CBZ**$_2$**FRO**$_2$]$^{4+}$ (right); top: self-assembly scheme, middle: stack of partial ^{1}H NMR spectra of the ligands (I),III): 500,600 MHz, 298 K, DMSO-*d*$_6$, VI) 700 MHz, 298 K, CDCl$_3$), the homoleptic assemblies (II),IV),VII) 500 MHz, 298 K, DMSO-*d*$_6$), and the heteroleptic cages (V),VIII): 600 MHz, 298 K, DMSO-*d*$_6$), ^{1}H DOSY NMR of the heteroleptic cages (500 MHz, 298 K, DMSO-*d*$_6$); bottom: ESI mass spectrum of the heteroleptic cages.

In order to obtain first insights into the photophysical properties of the cages, solutions of [Pd$_2$$^{\mathrm{Me}}$**CBZ**$_2$**FRO**$_2$]$^{4+}$ and [Pd$_2$$^{\mathrm{Do}}$**CBZ**$_2$**FRO**$_2$]$^{4+}$ were investigated with UV-Vis absorption spectroscopy (appendix, section 4.6.5). Both cages show strong absorption in the UV region with an absorption maximum at around 280 nm. The similar absorption patterns and extinction coefficients of

$[Pd_2{}^{Me}\mathbf{CBZ_2FRO_2}]^{4+}$ and $[Pd_2{}^{Do}\mathbf{CBZ_2FRO_2}]^{4+}$ support that the electronic structures of the chromophoric moieties of amphiphilic and reference cage are analogous, as anticipated.

4.3. Characterization of higher-order assemblies

For getting an idea about the size of possible higher order assemblies, the systems were investigated with dynamic light scattering (DLS). The intensity-weighted distribution of hydrodynamic diameters of $[Pd_2{}^{Me}\mathbf{CBZ_2FRO_2}]^{4+}$ and $[Pd_2{}^{Do}\mathbf{CBZ_2FRO_2}]^{4+}$ in DMSO and of $[Pd_2{}^{Do}\mathbf{CBZ_2FRO_2}]^{4+}$ in acetonitrile are shown in Fig. 5a-c. In each case, the DLS data between 1 and 1000 nm show a monomodal size distribution, i.e. a distribution with one maximum. For one of the measurements with $[Pd_2{}^{Do}\mathbf{CBZ_2FRO_2}]^{4+}$ in DMSO or acetonitrile, respectively, a shoulder at smaller diameters was observed. The Z-average (mean size) and peak maxima will not be compared since they differed for the same cage when the experiment was repeated (appendix, section 4.6.4). However, all measurements yielded a distribution of diameters that lies within 20 and 800 nm, Z-averages of 90 to 180 nm, and polydispersity indices (PDI) between 0.15 and 0.41. The latter attests a moderate heterogeneity of the hydrodynamic diameters. Overall, the size of the higher order assemblies is of the same order of magnitude as compared to **CGA-3** (d = 200-500 nm).[5] The reference cage in $[Pd_2{}^{Me}\mathbf{CBZ_2FRO_2}]^{4+}$ in acetonitrile did not yield reliable results. The reasons for this might be a low concentration of larger assemblies, resulting in a small signal intensity, or a high polydispersity.

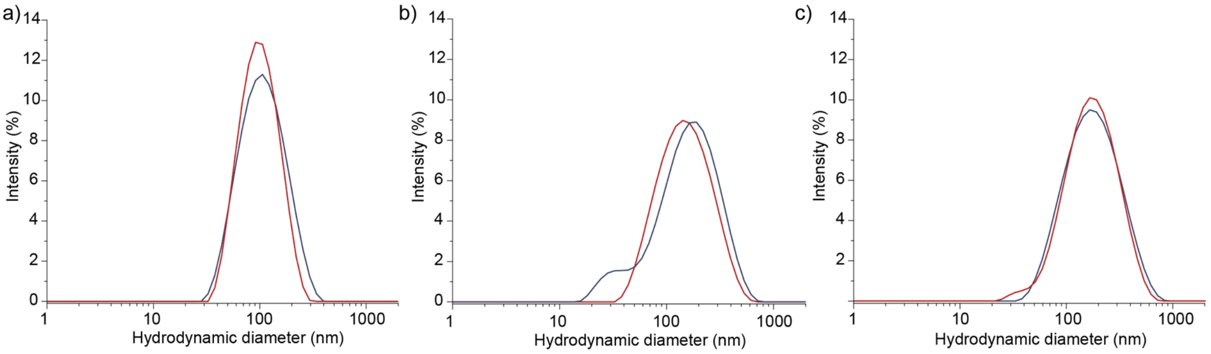

Fig. 5 DLS data of a) $[Pd_2{}^{Me}\mathbf{CBZ_2FRO_2}]^{4+}$ in DMSO, b) $[Pd_2{}^{Do}\mathbf{CBZ_2FRO_2}]^{4+}$ in DMSO, c) $[Pd_2{}^{Do}\mathbf{CBZ_2FRO_2}]^{4+}$ in acetonitrile. Two consecutive measurements were performed with each sample.

The DLS measurements provide information about the hydrodynamic radius of a sphere with a similar diffusion coefficient as compared to the investigated species.[8] In order to get insight into the shape of the higher order assemblies, cage $[Pd_2{}^{Do}\mathbf{CBZ_2FRO_2}]^{4+}$ was investigated with scanning transition electron microscopy (STEM). The sample was dried on the specimen before investigation; therefore, acetonitrile was used as volatile solvent. The STEM images show agglomerates with diameters of 50-100 nm (Fig. 6). Bright boundaries or lines on the agglomerates suggest that they burst upon drying, resulting in boundaries of higher density of the material. Furthermore, the agglomerates show bright dot-like spots, suggesting the accumulation of heavy elements. Usage of energy-dispersive X-ray spectroscopy (EDS) allowed for elemental mapping. This showed that the bright spots stem from accumulation of Pd (Fig. 6d). This might be attributable to the access of Pd(II) salt added for ascertaining the integrity of the cage at low concentrations. The larger agglomerates show an increased abundance of nitrogen, oxygen, and fluorine, i.e. elements of the organic ligand and the counter anions, suggesting that they consist of the cages. However, no increased abundance of Pd was found in these larger assemblies (appendix, section 4.6.4). The STEM measurement of cage $[Pd_2{}^{Do}\mathbf{CBZ_2FRO_2}]^{4+}$ was repeated with a smaller excess of the Pd(II) salt but no agglomerates were observed. By contrast, the experiment with a modified version of the cage ($[Pd_2{}^{Do}\mathbf{CBZ_2}{}^{Me}\mathbf{FRO_2}]^{4+}$), more precisely with a **FRO** acceptor ligand equipped with methoxy groups at the pyridines, showed approximately spherical aggregates with diameters of around 50 nm and no bright spots that would stem from Pd accumulation (appendix, section 4.6.4). Again, the agglomerates did not show an increased abundance of Pd, leaving their composition ambiguous.

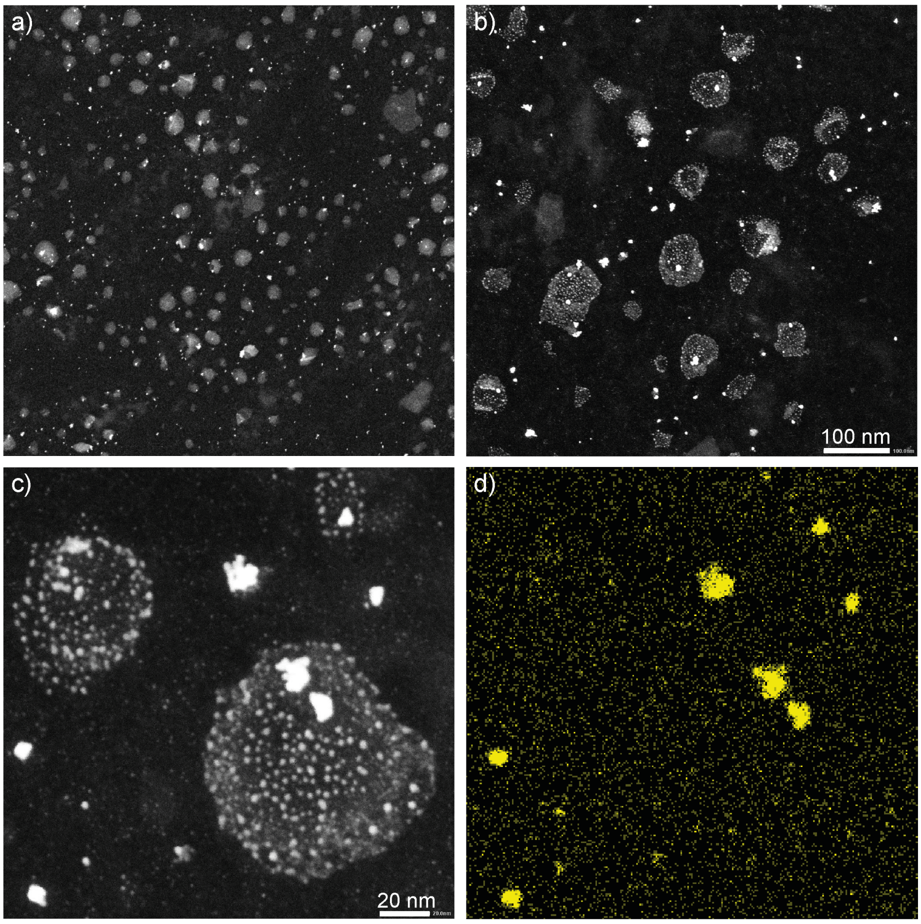

Fig. 6a-c) STEM images of a dried solution of $[\mathrm{Pd}_2{}^{\mathrm{Do}}\mathbf{CBZ}_2\mathbf{FRO}_2]^{4+}$ in acetonitrile, d) EDS map of an STEM image showing the distribution of Pd.

4.4. Incorporation of amphiphilic cages into polymeric micelles

The amphiphilic nature of $[\mathrm{Pd}_2{}^{\mathrm{Do}}\mathbf{CBZ}_2\mathbf{FRO}_2]^{4+}$ holds promise for its incorporation into micelles. Amphiphilic block copolymers were envisioned for this purpose owing to their reliable micelle formation and their readily adjustable polarity profile.[9] The polymer used herein consists of a polar part based on *N,N*-dimethylacrylamide and a nonpolar part based on dodecylacrylate (Scheme 2). In water, the polymer forms micelles with a hydrodynamic diameter of 50 nm, as obtained through DLS measurements (appendix, section 4.6.6). The polymer synthesis and the characterization of the micelles was carried out by Janick Wesselmann (group of Prof. Weberskirch, TU Dortmund).

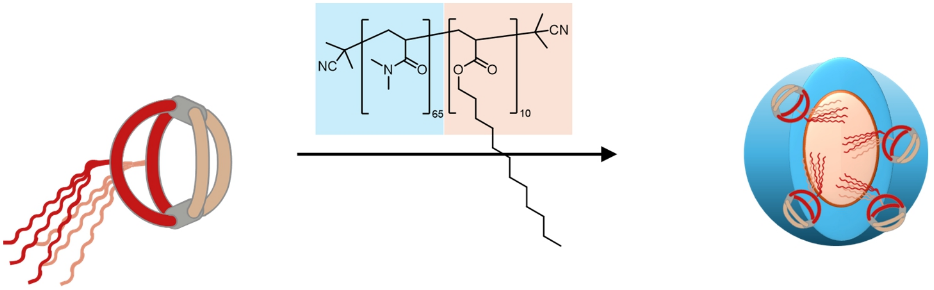

Scheme 2 Incorporation of $[\mathrm{Pd}_2{}^{\mathrm{Do}}\mathbf{CBZ}_2\mathbf{FRO}_2]^{4+}$ into polymeric micelles consisting of amphiphilic block copolymers (blue: polar part, beige: nonpolar part).

In the first approach, a micellar solution in water was prepared and added to a dried sample of the cage $[\mathrm{Pd}_2{}^{\mathrm{Do}}\mathbf{CBZ}_2\mathbf{FRO}_2]^{4+}$. As a control experiment, pure water was added to the cage. In order to trigger integration of the cage into the micelles or possible solubilization in water, respectively, the samples were treated with ultrasound and heated (appendix, section 4.6.6). The samples were then filtered and measured by UV-Vis absorption spectroscopy. The cage in acetonitrile possesses an absorption maximum at 280 nm and smaller features between 300 and 400 nm (appendix, section 4.6.5) while the solution of the polymers only shows a tail in the UV region (Fig. 7a, (II)). Hence, any absorption peaks in the UV region would indicate solubilization of the cage in the aqueous medium. The sample that contained only the cage does not show absorption in the UV-Vis region which can be traced back to the insolubility of the cage in water (I). The absorption pattern of the sample which contained both, the cage and the polymer, is similar to the spectrum of the polymer alone, suggesting that incorporation of the cage was not successful (III).

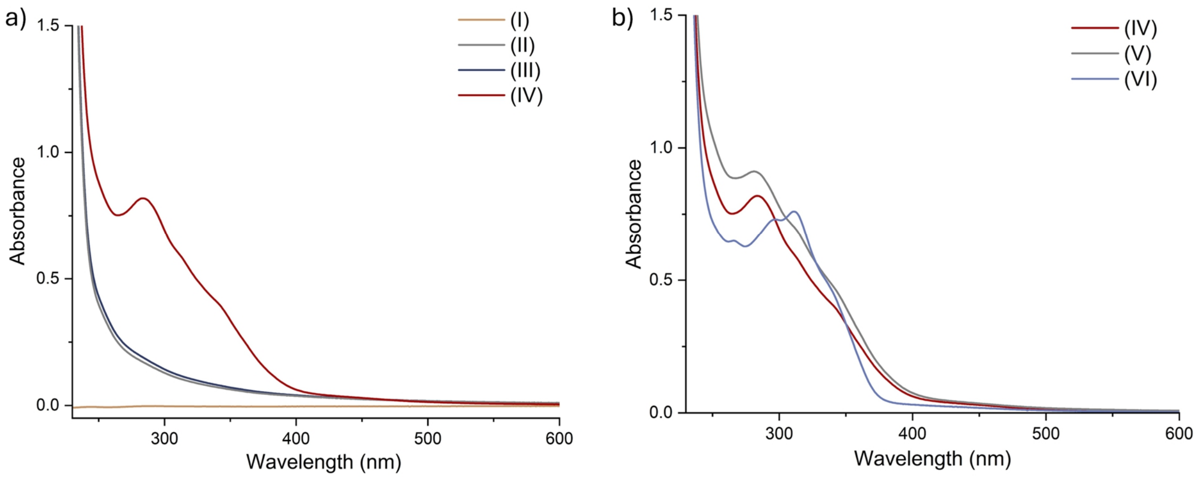

Fig. 7 UV-Vis absorption spectra of (I) $[\mathrm{Pd}_2{}^{\mathrm{Do}}\mathbf{CBZ}_2\mathbf{FRO}_2]^{4+}$, (II) the polymer, (III) $[\mathrm{Pd}_2{}^{\mathrm{Do}}\mathbf{CBZ}_2\mathbf{FRO}_2]^{4+}$ + polymer, combined in water, (IV) $[\mathrm{Pd}_2{}^{\mathrm{Do}}\mathbf{CBZ}_2\mathbf{FRO}_2]^{4+}$ + polymer, combined in DMSO, (V) $[\mathrm{Pd}_2{}^{\mathrm{Me}}\mathbf{CBZ}_2\mathbf{FRO}_2]^{4+}$ + polymer, combined in DMSO, (VI) ${}^{\mathrm{Do}}\mathbf{CBZ}$ + **FRO** + polymer, combined in DMSO (solvent: water, cuvette pathlength: 1mm).

In the second approach a solution of the polymer in DMSO was combined with a solution of the cage $[\mathrm{Pd}_2{}^{\mathrm{Do}}\mathbf{CBZ}_2\mathbf{FRO}_2]^{4+}$ in DMSO. The mixture was sonicated and heated, followed by removal of the solvent via lyophilization. Next, water was added and the sample was again sonicated, heated, and filtered. Investigation by UV-Vis absorption spectroscopy showed a peak at around 300 nm with two shoulders at lower energies along with the characteristic tail stemming from the absorption of the polymer (IV). This indicates that the cage or its components were incorporated into the micelles.

In order to test whether the amphiphilic nature of the cage is a prerequisite for their integration into the micelles, the same experiment was repeated with reference cage $[\mathrm{Pd}_2{}^{\mathrm{Me}}\mathbf{CBZ}_2\mathbf{FRO}_2]^{4+}$. The UV-Vis absorption spectrum of this sample closely resembles the spectrum obtained with

$[\mathrm{Pd}_2{}^{\mathrm{Do}}\mathbf{CBZ}_2\mathbf{FRO}_2]^{4+}$ (V). The difference in the absorption intensity can possibly be traced back to an error in the concentration of the sample of the cage in DMSO used for the incorporation experiment. Overall, this result suggests that the amphiphilicity is not needed for incorporation of the cage into the micelles or that the reference cage exhibits sufficient amphiphilicity even without the dodecyl chains. Lastly, the role of cage integrity was tested by repeating the experiment with the ligands only (**FRO** and $^{\mathrm{Me}}$**CBZ** owing to the poor solubility of $^{\mathrm{Do}}$**CBZ** in DMSO). Again, an absorption maximum at around 300 nm was observed, pointing towards incorporation of the ligands into the micelles (VI). The absorption pattern differs from the ones obtained with the cages. More precisely, the feature at 280 nm is less broad and the overall spectrum is blue shifted. This supports that the cage did not disassemble upon integration into the micelles in the experiments described beforehand. That the ligands are incorporated into the micelles is not surprising since the micellar core is nonpolar and provides therefore a suitable environment for organic compounds. This is well-known and commonly exploited in micellar catalysis[10] and for drug delivery.[11] Overall, the experiments show that by premixing the polymer and the cage or ligands in DMSO, a solvent which dissolves all of the mentioned components, solubilization of the cages or ligands in the aqueous micellar solution is observed while the compounds are water insoluble. However, conclusions about the arrangement of the compounds in the micelles, e.g. incorporation into the micellar core or into the corona, cannot be drawn. This might have an important effect on whether the cages can promote transmembrane electron transfer.

4.5. Conclusion and outlook

In conclusion, an amphiphilic donor-acceptor cage $[\mathrm{Pd_2}{}^{\mathrm{Do}}\mathbf{CBZ_2FRO_2}]^{4+}$ based on a carbazole donor ligand $^{\mathrm{Do}}$**CBZ** modified with three dodecyloxy chains, as well as a reference cage $[\mathrm{Pd_2}{}^{\mathrm{Me}}\mathbf{BZ_2FRO_2}]^{4+}$ whose donor ligand $^{\mathrm{Me}}$**CBZ** lacks the nonpolar chains, were synthesized successfully. While ligand $^{\mathrm{Do}}$**CBZ** and its homoleptic assembly have different solubility properties as compared to ligand $^{\mathrm{Me}}$**CBZ** and its homoleptic assembly, the two heteroleptic cages cleanly assembled and solubilized in DMSO. DLS measurements of DMSO solutions of the cages $[\mathrm{Pd_2}{}^{\mathrm{Me}}\mathbf{CBZ_2FRO_2}]^{4+}$ and $[\mathrm{Pd_2}{}^{\mathrm{Do}}\mathbf{CBZ_2FRO_2}]^{4+}$ suggest that higher order assemblies with diameters of 100 to 200 nm are formed. A clear difference between the higher order assembly of the amphiphilic and the reference cage could not be identified. Analysis of the amphiphilic cage with TEM supported the formation of roughly spherical agglomerates in acetonitrile. However, a higher abundance of Pd as compared to the background could not be observed. The composition of the agglomerates remains therefore ambiguous. Lastly, the incorporation of cage $[\mathrm{Pd_2}{}^{\mathrm{Do}}\mathbf{CBZ_2FRO_2}]^{4+}$ into polymeric micelles was studied with the overall aim to trigger transmembrane photoinduced charge separation. Investigation with UV-Vis absorption spectroscopy revealed that the cage can be solubilized in the aqueous micellar medium when polymer and cage are mixed in advance in DMSO, a solvent which dissolves both compounds. The reference cage and the free ligands were incorporated into the micelles via the same procedure.

For unravelling potential differences in the higher order self-assembly of the amphiphilic cage and the reference cage, the DLS measurements could be repeated with both cages at various concentrations. Moreover, it would be interesting to investigate whether the higher order self-assembly affects the excited state dynamics; for this, transient absorption spectroscopy should be applied. Aiming at achieving transmembrane electron transfer, the aqueous micellar solutions with incorporated cages $[\mathrm{Pd_2}{}^{\mathrm{Do}}\mathbf{CBZ_2FRO_2}]^{4+}$ can be enriched with suitable second electron donors and acceptors. For example, tetrathiafulvalene (TTF) can be used as second donor and dimethyl viologen ($\mathrm{DMV^{2+}}$) as second acceptor and as redox indicator (Fig. 8). TTF can readily be functionalized with alkyl chains which should increase its affinity for the nonpolar micellar core. $\mathrm{DMV^{2+}}$, on the other hand, is water soluble and should therefore reside in the bulk phase. While electron transfer between TTF and $\mathrm{DMV^{2+}}$ would be energetically uphill in their electronic ground states, electron transfer from TTF to the cage in its charge separated state as well as from the charge separated state of the cage to $\mathrm{DMV^{2+}}$ is thermodynamically feasible. The latter process would result in the formation of a DMV radical cation with an intense blue color.[12] TTF would then act as sacrificial electron donor for regenerating the neutral **CBZ** in the cage.

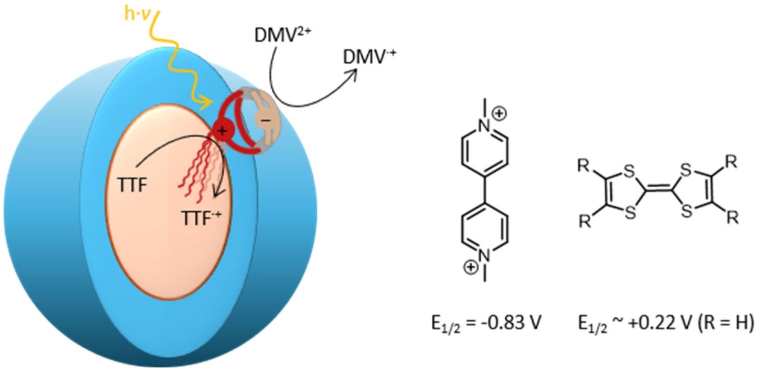

Fig. 8 Schematic illustration of transmembrane electron transfer with donor-acceptor cages incorporated into the micellar interface and TTF as second donor as well as $\mathrm{DMV^{2+}}$ as second acceptor and redox indicator. For achieving localization of the TTF in the micellar core, a nonpolar derivative (e.g. R = dodecyl) should be employed. Half-wave potentials against $\mathrm{Fc/Fc^{+}}$ in acetonitrile are taken from refs[13,14].

4.6. Appendix

4.6.1. General methods

For chemicals, NMR spectroscopy, mass spectrometry, and UV-Vis absorption spectroscopy, see chapters 2.7.1 and 3.11.1. For some compounds, the number of signals in the ^{13}C NMR spectra is smaller than the number of non-equivalent carbon nuclei. This can probably be traced back to signal overlap or low signal intensity.

Dynamic light scattering (DLS)

The measurements were performed on a Zetasizer nano-ZS (Malvern Instruments, Malvern, UK) using a 10x10 mm quartz glass cuvette. All measurements were performed at 298 K. The intensity-weighted diameters are given. For each sample, two consecutive measurements were performed.

Scanning transmission electron microscopy (STEM)

All measurements were carried out by or with Dr. Yen-Ting Chen at ZEMOS, Ruhr-University Bochum. A JEOL JEM-2800 with Schottky field emission cathode, operating at 200 kV, was used. For the STEM images, HAADF, BF, SEM detectors were equipped. For BF and HAADF, the collection angles were 28 mrad and 34-157 mrad, respectively. Dual SDD X-ray detectors were used for the EDS mapping. The EDS signal was detected with a solid angle of 0.95 srad and with a spectral resolution of 133 eV. The STEM resolution was 0.19 nm. The spherical aberration was 0.7 mm and the chromatic aberration was 1.3 mm.

4.6.2. Ligand synthesis

Ligand $^{\mathbf{NH}}$**CBZ**

3,6-dibromo-9*H*-carbazole (1.210 g, 3.72 mmol, 1.0 eq.) was combined with 4-(4-pyridyl)-phenylboronic acid pinacol ester (3.140 g, 11.17 mmol, 3.0 eq.), and potassium carbonate (1.540 g, 11.17 mmol, 3.0 eq.) and suspended in a mixture of dioxane and water (4:1). The reaction mixture was thoroughly degassed and tetrakis(triphenylphosphine)-palladium (0.215 g, 0.19 mmol, 0.05 eq.) was added. After further degassing, the reaction mixture was heated to 90° C and stirred overnight. After cooling to room temperature, the reaction mixture was extracted with DCM and washed with brine. The combined organic phases were then dried with $MgSO_4$ and the solvent was evaporated *in vacuo*. After washing with cold diethyl ether and acetonitrile, the product was obtained as a white powder (0.475 g, 1.00 mmol, 27%).

^{1}H NMR (500 MHz, DMSO-d_6) δ 11.46 (s, 1H), 8.99 (d, *J* = 2.4 Hz, 1H), 8.70 (s, 1H), 8.59 (dd, *J* = 4.7, 1.6 Hz, 1H), 8.20 – 8.14 (m, 1H), 7.96 (d, *J* = 8.4 Hz, 2H), 7.88 (d, *J* = 8.4 Hz, 2H), 7.83 (dd, *J* = 8.5, 1.8 Hz, 1H), 7.61 (d, *J* = 8.4 Hz, 1H), 7.52 (dd, *J* = 7.9, 4.7 Hz, 1H).

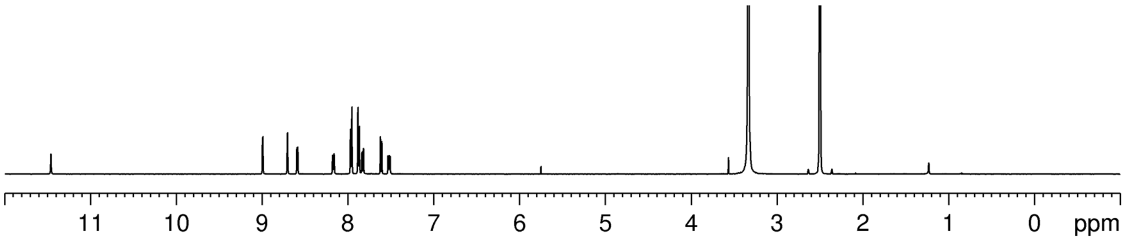

Fig. 9 Full ^{1}H NMR spectrum of ligand $^{\mathbf{NH}}$**CBZ** (500 MHz, 298 K, DMSO-d_6).

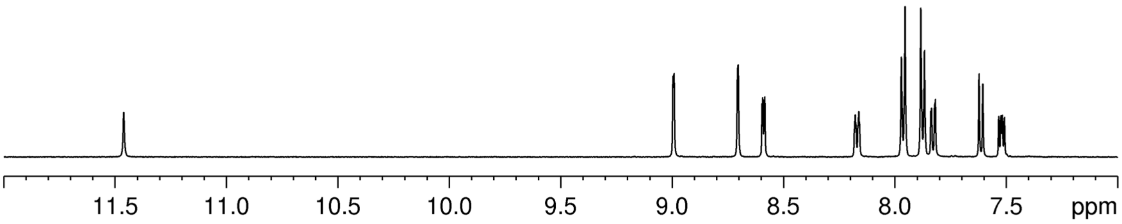

Fig. 10 Partial ^{1}H NMR spectrum of ligand ^{NH}**CBZ** (500 MHz, 298 K, DMSO-d_6).

Ligand ^{Do}**CBZ**

Compound ^{NH}**CBZ** (0.480 g, 1.01 mmol, 1.0 eq.) was combined with 5-bromo-1,2,3-tris(dodecyloxy)-benzene (0.720 g, 1.01 mmol, 1.0 eq.), XPhos (0.145 g, 0.30 mmol, 0.3 eq.), and cesium carbonate (0.925 g, 2.84 mmol, 2.8 eq.) were suspended in dioxane. The reaction mixture was thoroughly degassed and tris(dibenzylidenaceton)-dipalladium(0) (0.093 g, 0.10 mmol, 0.1 eq.) was added. After further degassing, the reaction mixture was heated to 100 °C and stirred overnight. After evaporation of the solvent, the crude product was purified by column chromatography using ethyl acetate as eluent. The product was then concentrated and addition of cold ethyl acetate led to precipitation (0.646 g, 0.59 mmol, 58%).

^{1}H NMR (700 MHz, Chloroform-*d*) δ 8.95 (d, *J* = 2.4, 0.9 Hz, 1H, a), 8.62 (dd, *J* = 4.8, 1.6 Hz, 1H, b), 8.47 (d, *J* = 1.7 Hz, 1H, g), 7.99 – 7.95 (m, 1H, d), 7.89 – 7.85 (m, 2H, e), 7.75 (dd, *J* = 8.5, 1.8 Hz, 1H, h), 7.74 – 7.71 (m, 2H, f), 7.53 (d, 1H, i), 7.41 (dd, *J* = 8.4, 4.8, 1H, c), 6.78 (s, 1H, j), 4.10 (t, *J* = 6.6 Hz, 1H, p), 4.00 (t, *J* = 6.5 Hz, 1.5H, k), 1.88 – 1.79 (m, 3H, l, q), 1.60 – 1.52 (m, 1H, r), 1.52 – 1.45 (m, 2H, m), 1.44 – 1.19 (m, 21H, n, s), 0.93 – 0.82 (m, 4.5H, o, t).

^{13}C NMR (176 MHz, Chloroform-*d*) δ 154.08, 148.42, 148.22, 141.79, 137.74, 141.30, 136.39, 136.04, 134.32, 132.66, 132.42, 123.9, 127.97, 127.62, 125.68, 123.69, 118.88, 110.61, 105.67, 73.71, 69.41, 32.01, 31.98, 30.49, 29.86, 29.85, 29.83, 29.78, 29.76, 29.72, 29.70, 29.49, 29.47, 29.42, 29.40, 26.24, 26.15, 22.77, 22.74, 14.18, 14.17.

ESI MS: *m/z* calc. for [^{Do}**CBZ**]$^+$: 1101.7681; found: 1101.7666

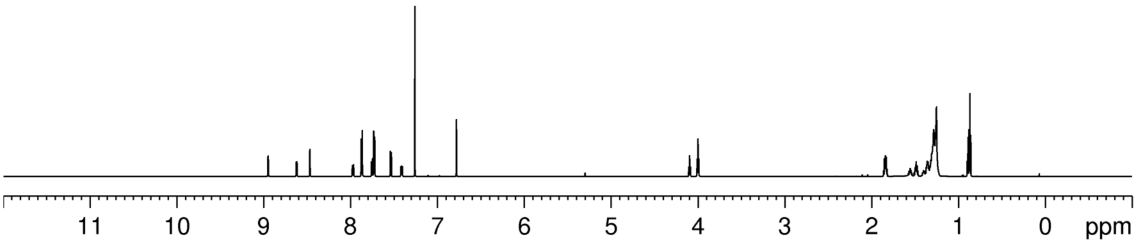

Fig. 11 Full ^{1}H NMR spectrum of ligand ^{Do}**CBZ** (700 MHz, 298 K, CDCl$_3$).

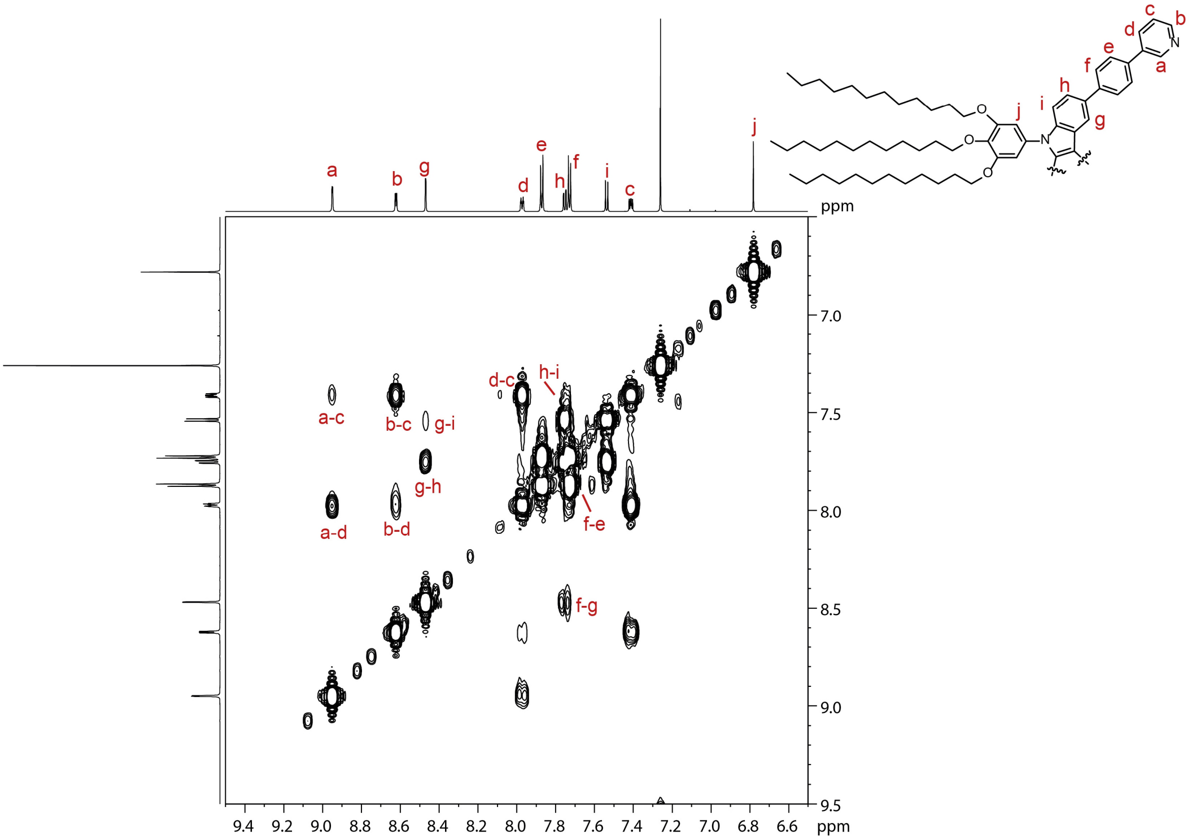

Fig. 12 Partial ^{1}H,^{1}H COSY NMR of ligand **^{Do}CBZ** (700 MHz, 298 K, CDCl$_3$).

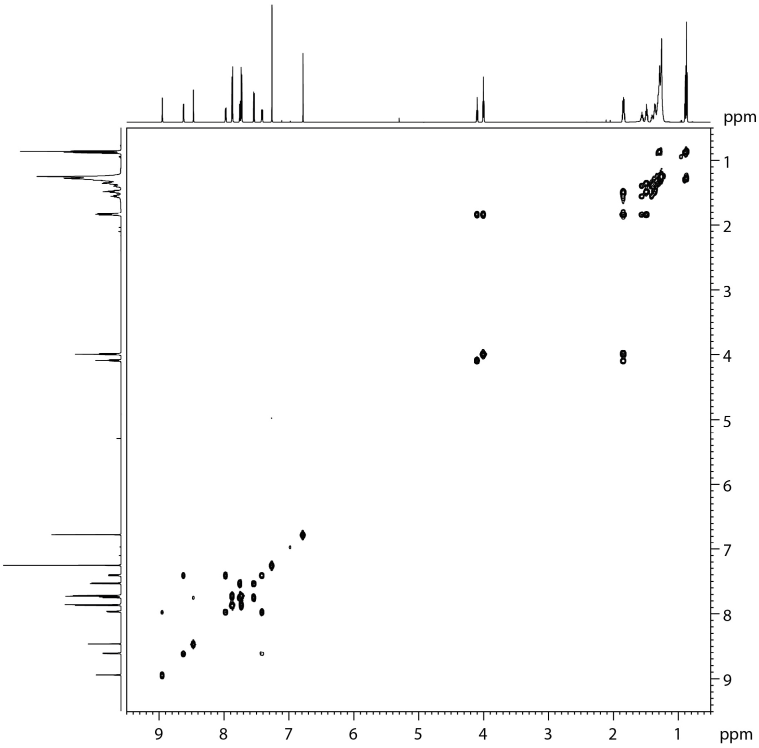

Fig. 13 Full ^{1}H,^{1}H COSY NMR of ligand **^{Do}CBZ** (700 MHz, 298 K, CDCl$_3$).

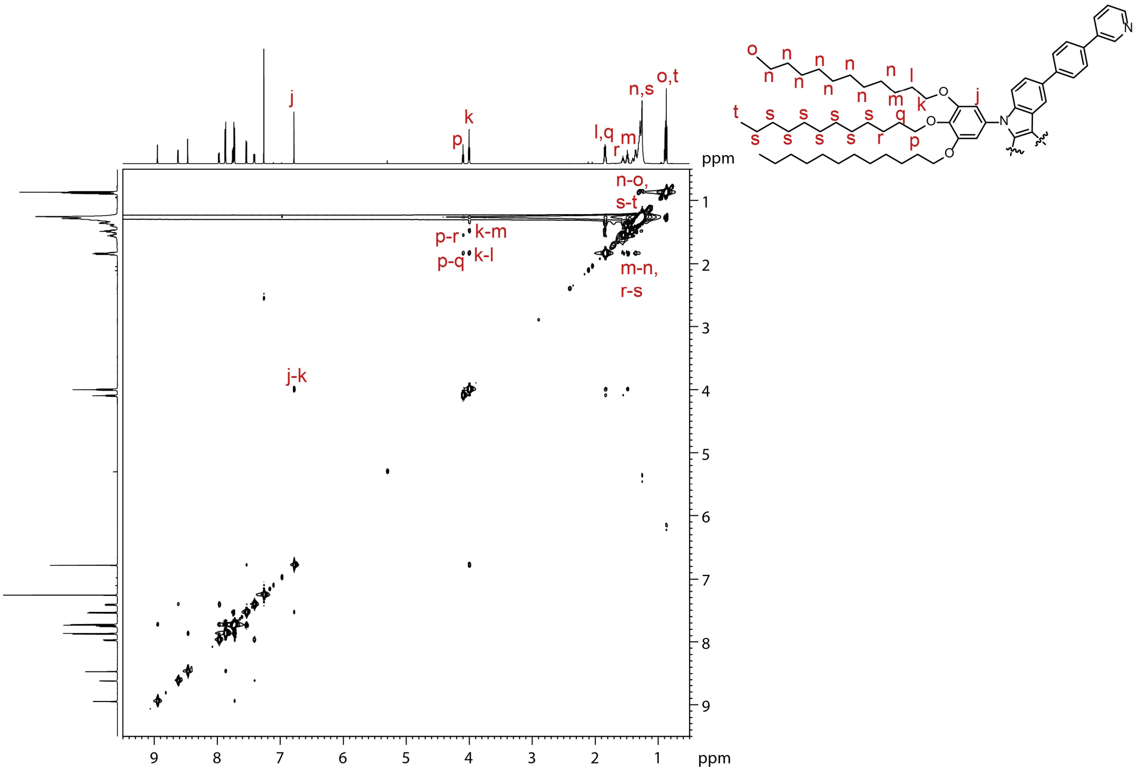

Fig. 14 Full ^{1}H,^{1}H NOESY NMR of ligand $^{\text{Do}}$**CBZ** (700 MHz, 298 K, CDCl$_3$).

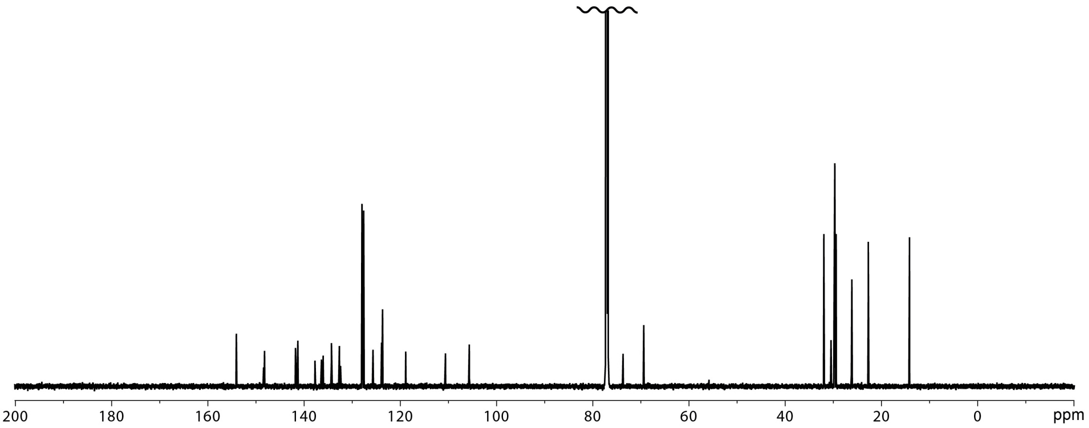

Fig. 15 ^{13}C NMR of ligand $^{\text{Do}}$**CBZ** (176 MHz, 298 K, CDCl$_3$).

Ligand $^{\text{Me}}$**CBZ**

Compound $^{\text{NH}}$**CBZ** (0.600 g, 1.27 mmol, 1.0 eq.) was combined with 5-bromo-1,2,3-trimethoxybenzene (0.313 g, 1.27 mmol, 1.0 eq.), XPhos (0.181 g, 0.38 mmol, 0.3 eq.), and cesium carbonate (1.160 g, 3.55 mmol, 2.8 eq.) were suspended in dioxane. The reaction mixture was thoroughly degassed and tris(dibenzylidenaceton)-dipalladium(0) (0.116 g, 127 µmol, 0.1 eq.) was added. After further degassing, the reaction mixture was heated to 100 °C and stirred overnight. After evaporation of the solvent, the crude product was purified by column chromatography using ethyl acetate as eluent. Further purification was carried out by gel permeation chromatography (GPC) using chloroform as eluent (0.311 g, 0.49 mmol, 38%).

^{1}H NMR (600 MHz, DMSO-d_6) δ 9.00 (d, J = 2.4, 1H, a), 8.85 (d, J = 1.9, 1H, g), 8.60 (dd, J = 4.7, 1.6 Hz, 1H, b), 8.18 (ddd, J = 8.0, 2.5, 1.6 Hz, 1H, d), 8.02 – 7.96 (m, 2H, e), 7.92 – 7.85 (m, 3H, f, h), 7.59 (d, *J* = 8.5, 1H, i), 7.53 (ddd, *J* = 7.9, 4.7, 0.8 Hz, 1H, c), 7.00 (s, 1H, j), 3.87 (s, 4H, k), 3.81 (s, 2H, l).

^{13}C NMR (151 MHz, DMSO-d_6) δ 153.87, 148.44, 147.55, 140.55, 140.45, 136.87, 135.27, 135.14, 133.92, 132.34, 131.57, 127.39, 127.26, 125.31, 123.92, 123.58, 118.92, 110.71, 104.37, 60.21, 56.24.

ESI MS: *m/z* calc. for [$^{\text{Me}}$**CBZ**]$^+$: 639.2516; found: 639.2501

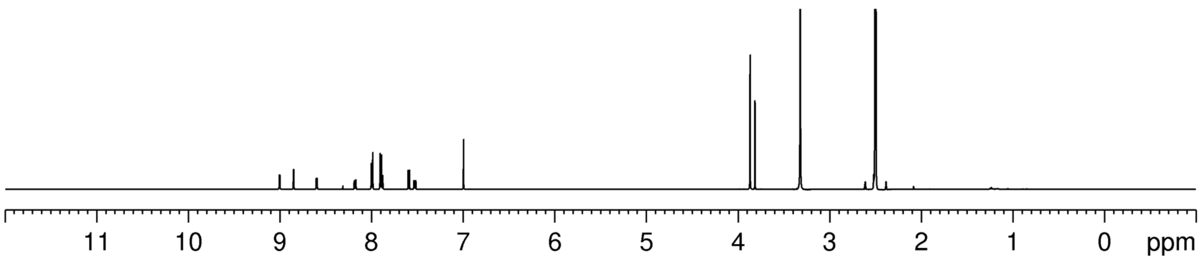

Fig. 16 Full ^{1}H NMR spectrum of ligand $^{\text{Me}}$**CBZ** (600 MHz, 298 K, DMSO-d_6).

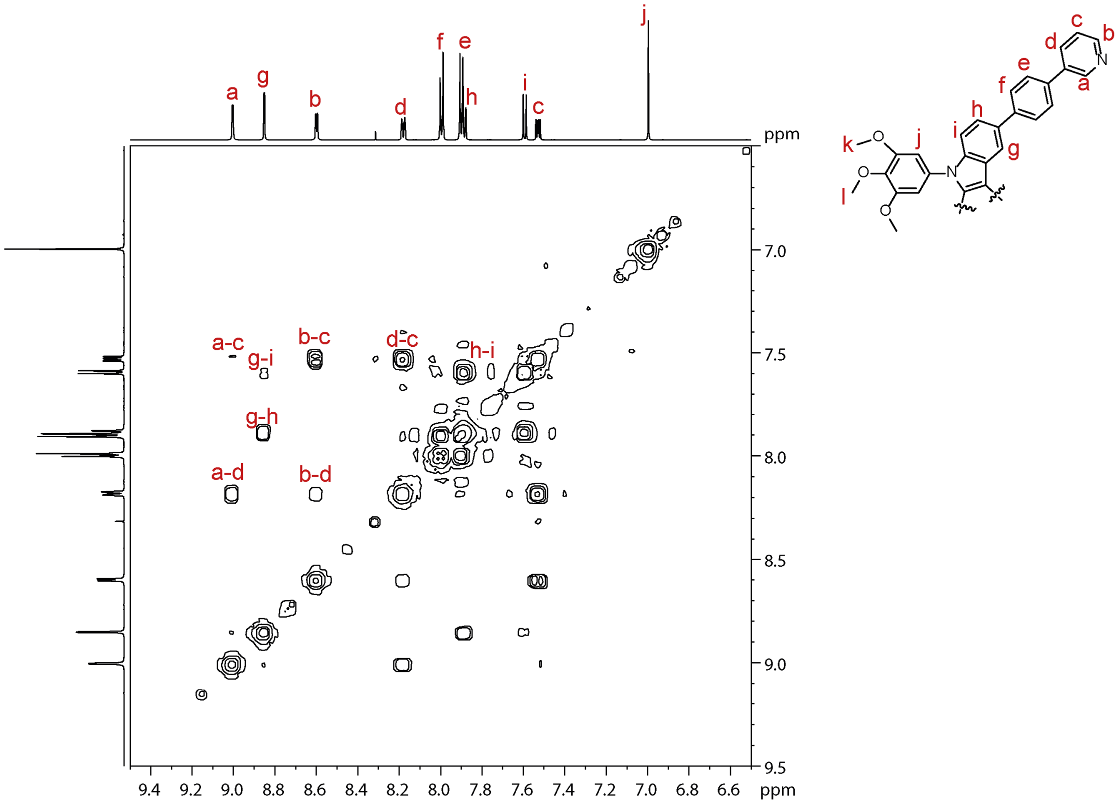

Fig. 17 Partial ^{1}H,^{1}H COSY NMR of ligand $^{\text{Me}}$**CBZ** (600 MHz, 298 K, DMSO-d_6).

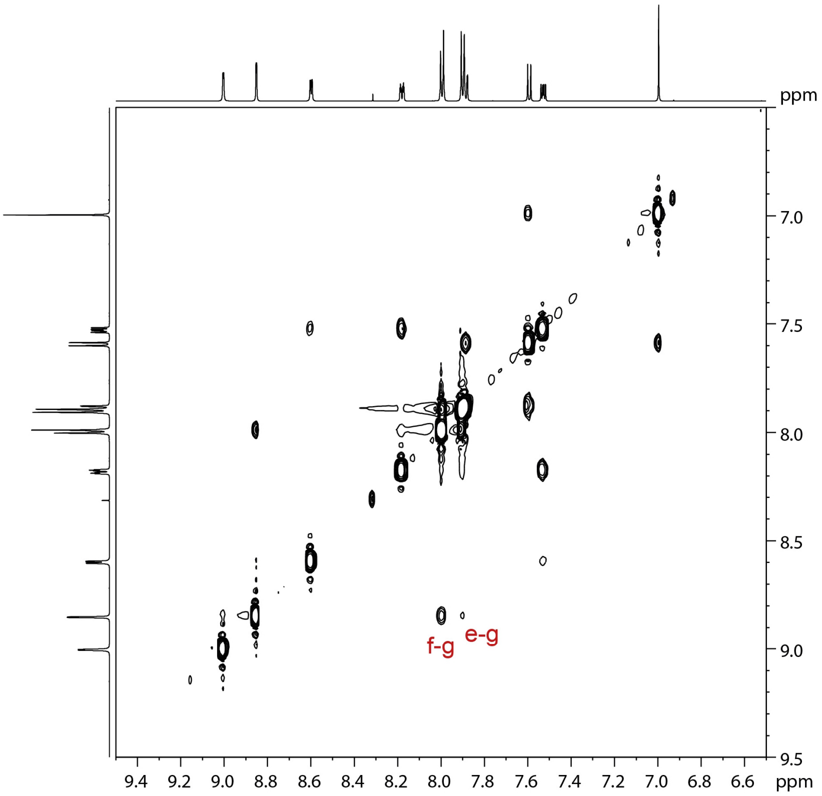

Fig. 18 Partial ^{1}H,^{1}H NOESY NMR of ligand $^{\mathrm{Me}}$**CBZ** (600 MHz, 298 K, DMSO-d_6).

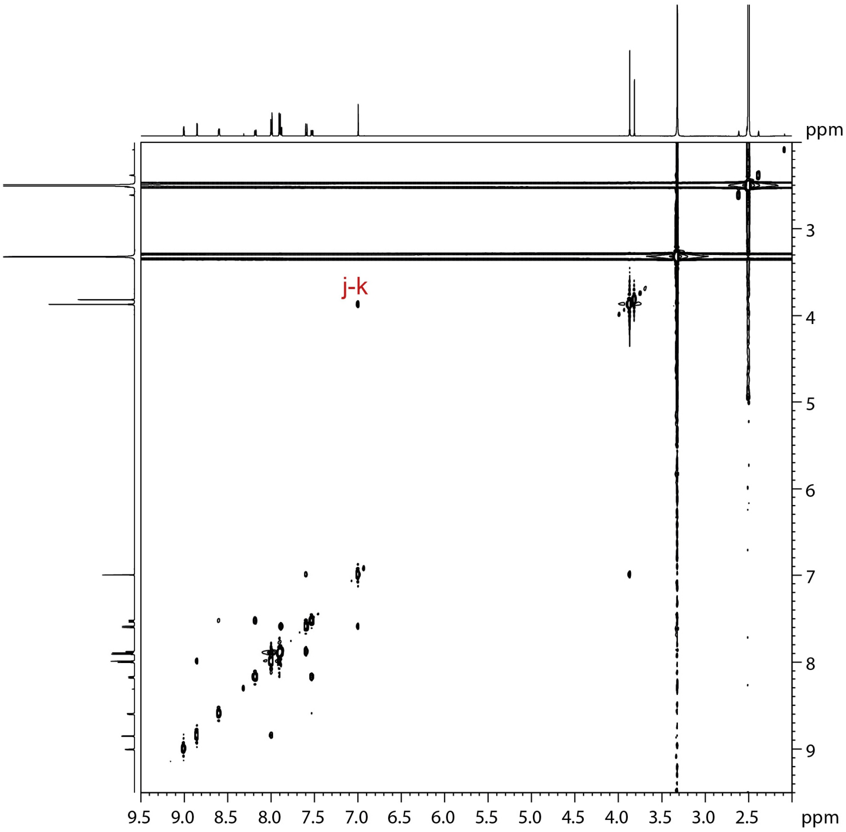

Fig. 19 Full ^{1}H,^{1}H NOESY NMR of ligand $^{\mathrm{Me}}$**CBZ** (600 MHz, 298 K, DMSO-d_6).

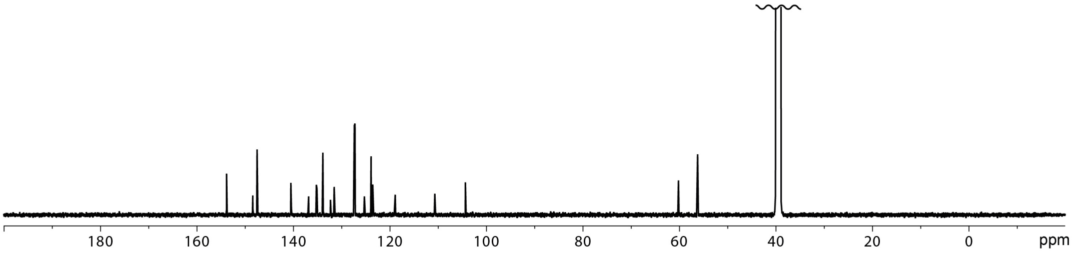

Fig. 20 ^{13}C NMR of ligand $^{\mathrm{Me}}$**CBZ** (151 MHz, 298 K, DMSO-d_6).

4.6.3. Self-assembly into cages

$[\mathrm{Pd}_2{}^{\mathrm{Me}}\mathbf{CBZ}_4]^{4+}$

A solution of $^{\mathrm{Me}}$**CBZ** (500 µL, 1.4 mM, DMSO-d_6) was combined with a solution of $[\mathrm{Pd(CH_3CN)_4}](\mathrm{BF_4})_2$ (30 µL, 15 mM, DMSO-d_6). The mixture was heated at 70 °C for 1.5 h.

^{1}H NMR (600 MHz, DMSO-d_6) δ 9.50 (s, 1H, a), 9.14 (d, *J* = 5.7, 1H, b), 8.85 (s, 1H, g), 8.53 (d, *J* = 8.2, 1H, d), 8.04 (d, *J* = 8.2 Hz, 2H, f), 7.99 (d, *J* = 8.3 Hz, 2H, e), 7.87 (dd, *J* = 8.0, 5.8 Hz, 1H, c), 7.79 (dd, *J* = 8.6, 1.7 Hz, 1H, h), 7.49 (d, *J* = 8.6 Hz, 1H, i), 6.88 (s, 1H, j), 3.80 – 3.74 (m, 1.5H, k, l).

^{13}C NMR (151 MHz, DMSO-d_6) δ 171.41, 153.81, 149.87, 148.62, 141.63, 140.80, 138.80, 138.04, 132.39, 131.92, 130.76, 127.46, 127.30, 125.87, 123.27, 118.24, 118.07, 110.90, 104.52, 60.18, 56.14.

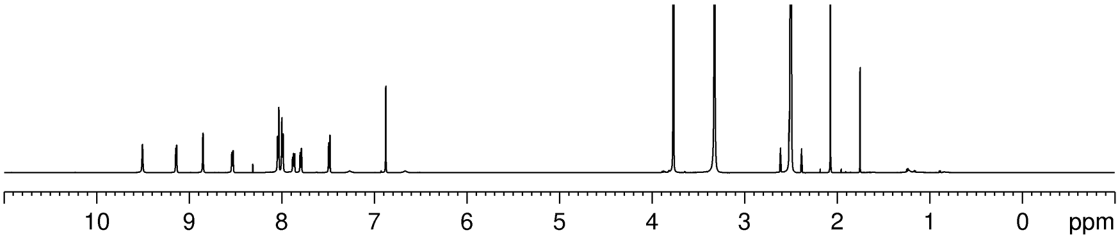

Fig. 21 Full ^{1}H NMR spectrum of $[\mathrm{Pd}_2{}^{\mathrm{Me}}\mathbf{CBZ}_4]^{4+}$ (600 MHz, 298 K, DMSO-d_6).

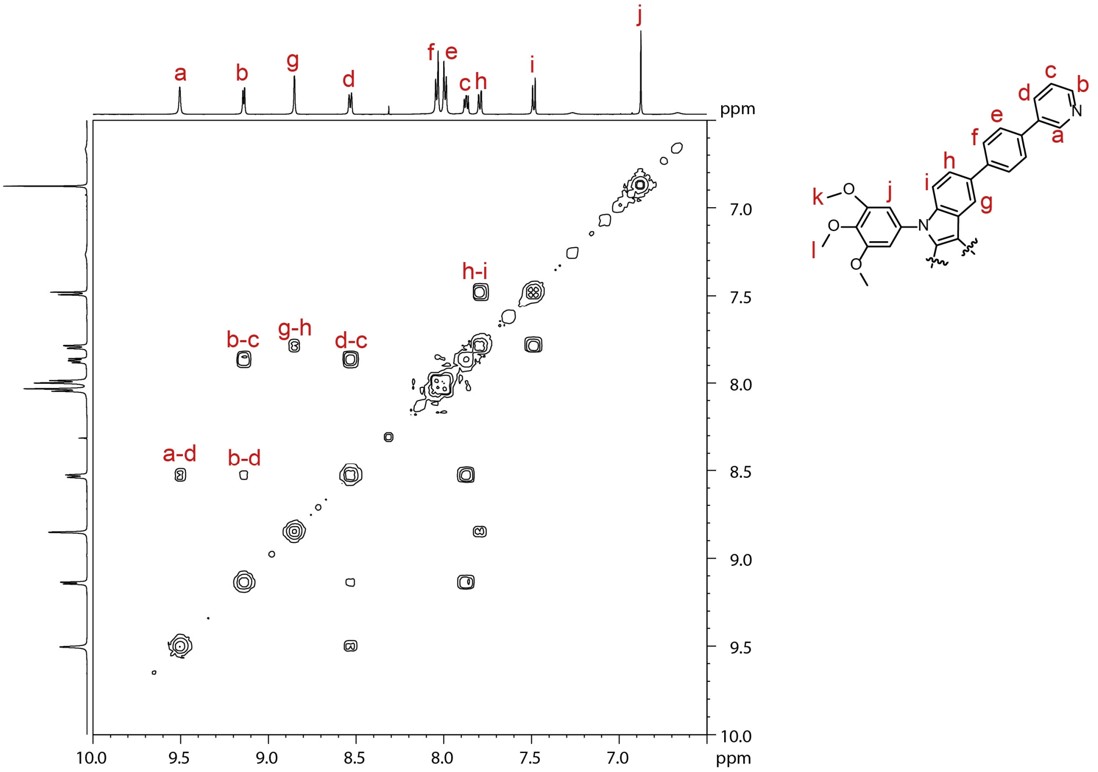

Fig. 22 Partial ^{1}H,^{1}H COSY NMR spectrum of $[\mathrm{Pd_2}^{\mathrm{Me}}\mathbf{CBZ}_4]^{4+}$ (600 MHz, 298 K, DMSO-d_6).

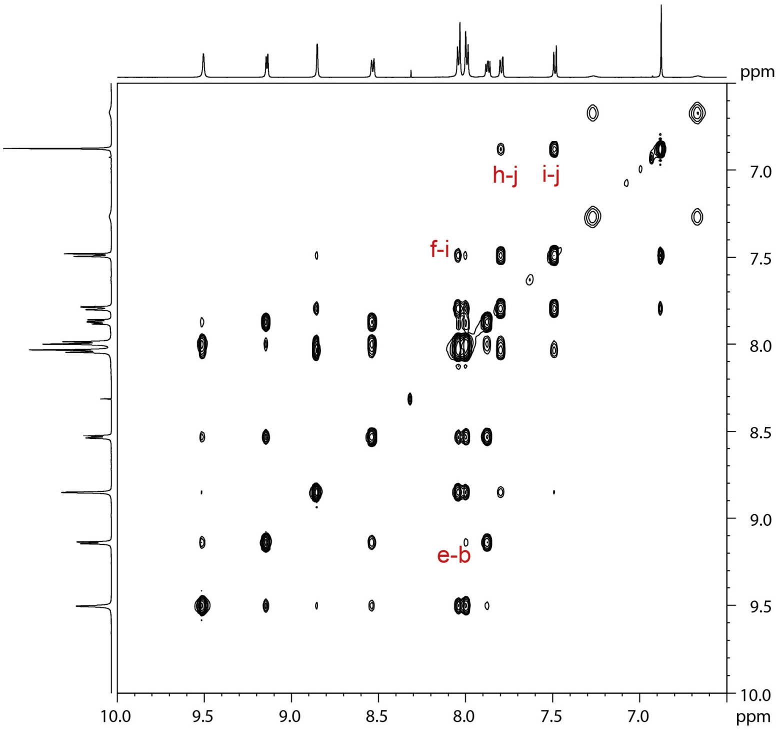

Fig. 23 Partial ^{1}H,^{1}H NOESY NMR spectrum of $[\mathrm{Pd_2}^{\mathrm{Me}}\mathbf{CBZ}_4]^{4+}$ (600 MHz, 298 K, DMSO-d_6).

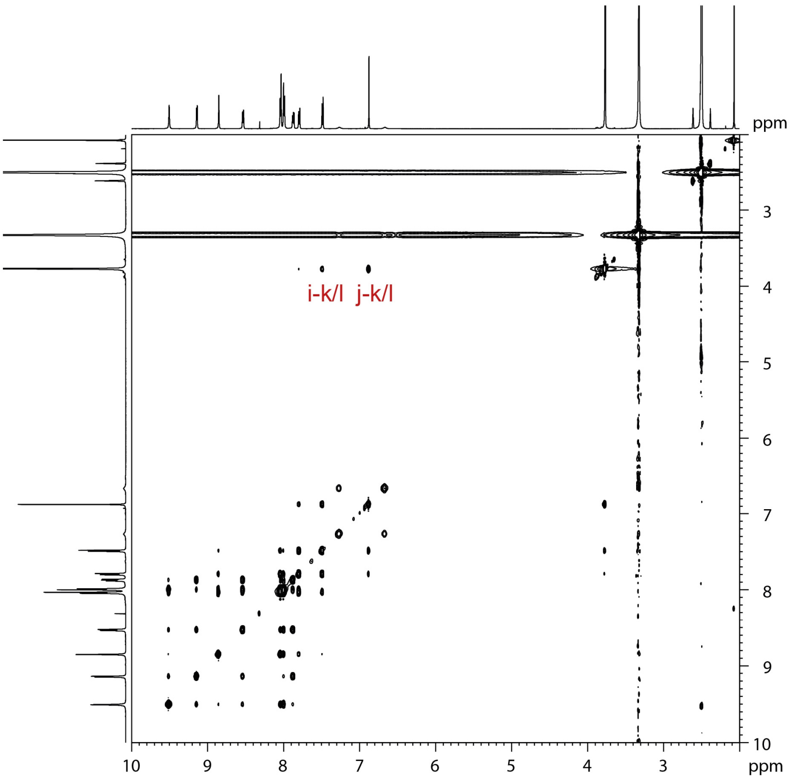

Fig. 24 Full ^{1}H,^{1}H NOESY NMR spectrum of $[Pd_2$^{Me}**CBZ**$_4]^{4+}$ (600 MHz, 298 K, DMSO-d_6).

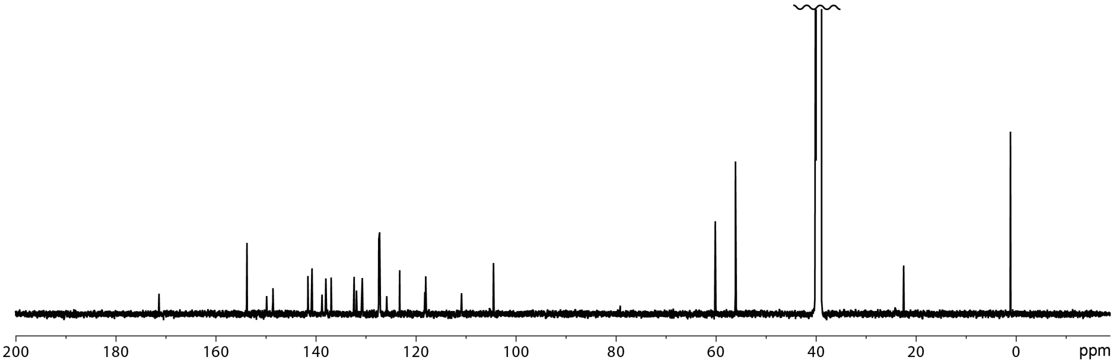

Fig. 25 ^{13}C NMR of $[Pd_2$^{Me}**CBZ**$_4]^{4+}$ (151 MHz, 298 K, DMSO-d_6).

$[Pd_2$^{Me}**CBZ**$_2$**FRO**$_2]^{4+}$

A solution of ^{Me}**CBZ** (250 µL, 1.4 mM, DMSO-d_6) and **FRO** (250 µL, 1.4 mM, DMSO-d_6) were combined with a solution of $[Pd(CH_3CN)_4](BF_4)_2$ (40 µL, 15 mM, DMSO-d_6). The mixture was heated at 70 °C for 1.5 h. For characterizations in acetonitrile, the DMSO-d_6 was removed by lyophilization and the sample suspended in acetonitrile via sonication and heating at 70 °C.

^{1}H NMR (600 MHz, DMSO-d_6) δ 10.17 (s, 1H, a), 9.87 (s, 1H, a), 9.58 (d, *J* = 5.5 Hz, 1H, b), 9.35 (d, *J* = 5.7, Hz, 1H, b), 8.89 (s, 1H, g), 8.52 (d, *J* = 8.1 Hz, 1H, d), 8.44 (d, *J* = 7.5 Hz, 1H, d), 8.26 (s, 1H, e), 8.11 (d, *J* = 8.2 Hz, 2H, f), 8.05 (d, *J* = 8.1 Hz, 2H, e), 7.98 – 7.88 (m, 4H, f, d, c, h), 7.85 (dd, *J* = 7.8, 5.7 Hz, 1H, c), 7.54 (d, *J* = 8.6 Hz, 1H, i), 6.91 (s, 1H, j), 3.79 (s, 2H, k), 3.77 (s, 1H, l).

^{13}C NMR (151 MHz, DMSO-d_6) δ 192.22, 171.65, 153.92, 150.17, 149.37, 148.87, 143.90, 141.42, 140.88, 138.28, 138.15, 137.87, 137.77, 137.02, 136.13, 135.09, 134.80, 132.36, 130.59, 127.77, 127.18, 126.98, 125.41, 123.37, 122.92, 121.89, 118.45, 118.16, 111.05, 104.41, 60.26, 56.26.

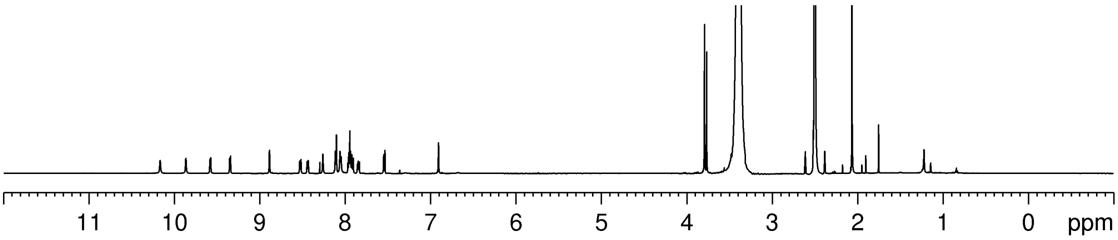

Fig. 26 Full ^{1}H NMR spectrum of $[\mathrm{Pd}_2{}^{\mathrm{Me}}\mathbf{CBZ}_2\mathbf{FRO}_2]^{4+}$ (600 MHz, 298 K, DMSO-d_6).

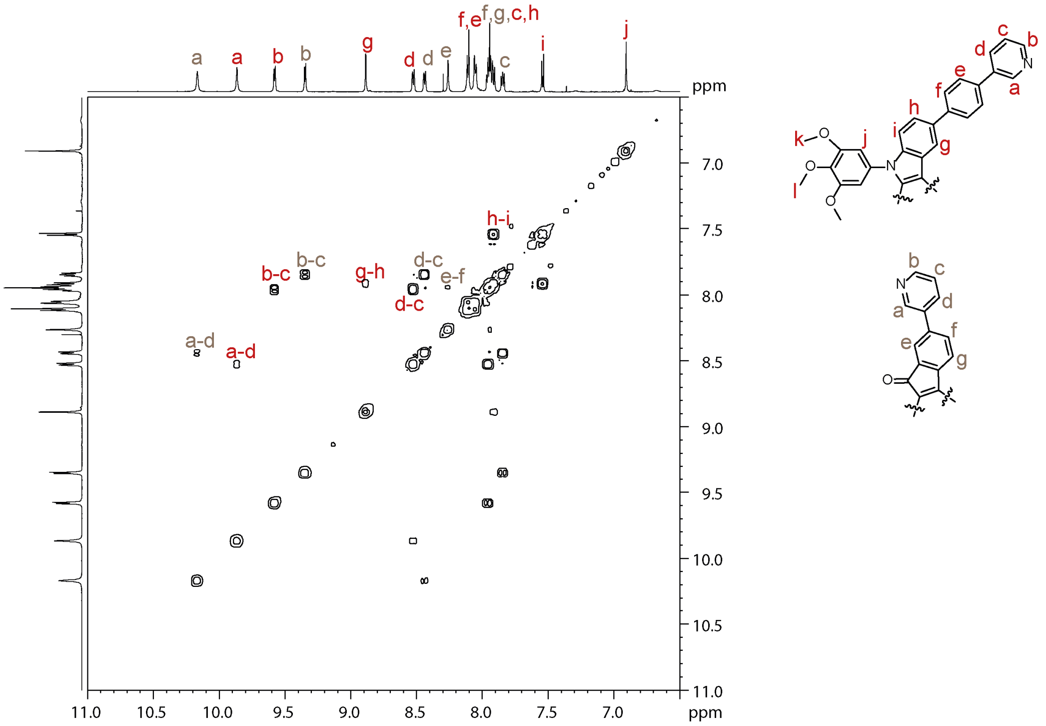

Fig. 27 Partial ^{1}H,^{1}H COSY NMR spectrum of $[\mathrm{Pd}_2{}^{\mathrm{Me}}\mathbf{CBZ}_2\mathbf{FRO}_2]^{4+}$ (600 MHz, 298 K, DMSO-d_6).

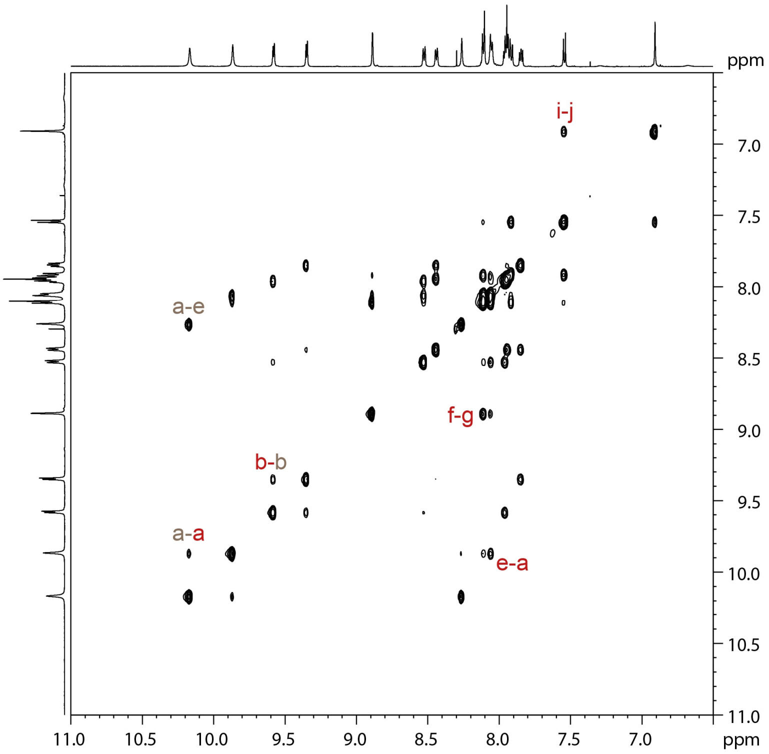

Fig. 28 Partial ^{1}H,^{1}H NOESY NMR spectrum of [Pd$_2$$^{\mathrm{Me}}$**CBZ**$_2$**FRO**$_2$]$^{4+}$ (600 MHz, 298 K, DMSO-*d*$_6$).

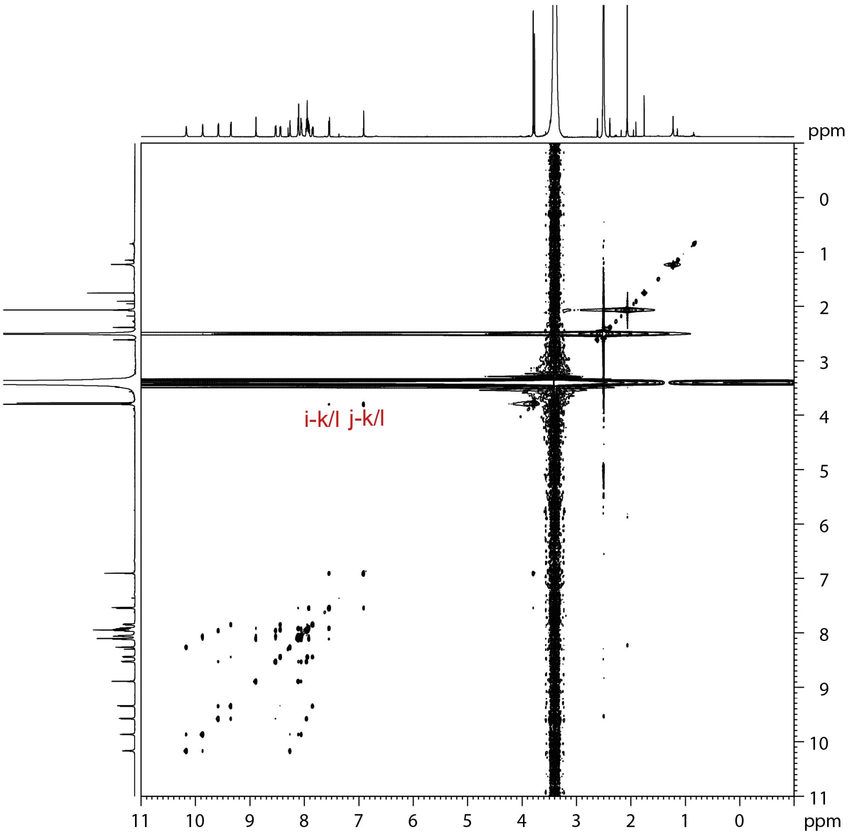

Fig. 29 Full ^{1}H,^{1}H NOESY NMR spectrum of [Pd$_2$$^{\mathrm{Me}}$**CBZ**$_2$**FRO**$_2$]$^{4+}$ (600 MHz, 298 K, DMSO-d_6).

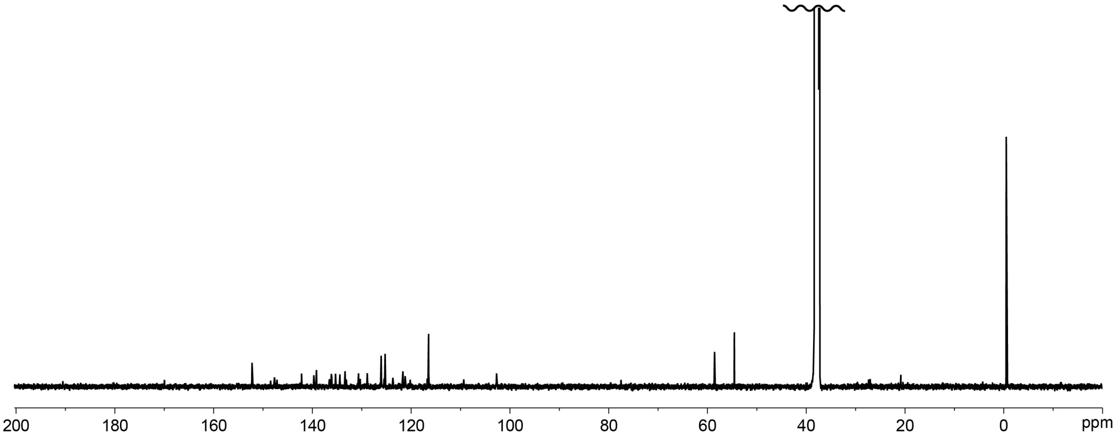

Fig. 30 ^{13}C NMR spectrum of [Pd$_2$$^{\mathrm{Me}}$**CBZ**$_2$**FRO**$_2$]$^{4+}$ (151 MHz, 298 K, DMSO-d_6).

[Pd$_2$$^{\mathrm{Do}}$**CBZ**$_2$**FRO**$_2$]$^{4+}$

A solution of $^{\mathrm{Do}}$**CBZ** (250 µL, 1.4 mM, CDCl$_3$) was combined with a solution of **FRO** (250 µL, 1.4 mM, CDCl$_3$). A ligand-to-ligand ratio of 1:1 was ensured by ^{1}H NMR spectroscopy. Afterwards, the solvent was evaporated. Next, 500 µL DMSO-d_6 and a solution of [Pd(CH$_3$CN)$_4$](BF$_4$)$_2$ (30 µL, 15 mM, DMSO-d_6) were added. The mixture was heated at 70 °C for 1.5 h. For characterizations in acetonitrile, the DMSO-d_6 was removed by lyophilization and the sample suspended in acetonitrile via sonication and heating at 70 °C.

^{1}H NMR (600 MHz, DMSO-d_6) δ 10.17 (s, 1H, a), 9.90 (s, 1H, a), 9.56 (d, J = 5.7 Hz, 1H, b), 9.36 (d, J = 5.8 Hz, 1H, b), 8.87 (s, 1H, g), 8.53 (d, J = 8.1 Hz, 1H, d), 8.45 (d, J = 7.9 Hz, 1H, d), 8.27 (s, 1H, e), 8.16 – 8.00 (m, 4H, f, e), 8.00 – 7.91 (m, 3H, f, g, c), 7.91 – 7.81 (m, 2H, c, h), 7.48 (d, J = 8.5 Hz, 1H, i), 6.83 (s, 1H, j), 3.98 – 3.91 (m, 3H, k, p), 1.72 – 1.63 (m, 3H, l, q), 1.52 – 1.43 (m, 1H, r), 1.43 – 1.35 (m, 2H, m), 1.34 – 1.12 (m, 24H, n, s), 0.88 – 0.80 (m, 3H, o, t).

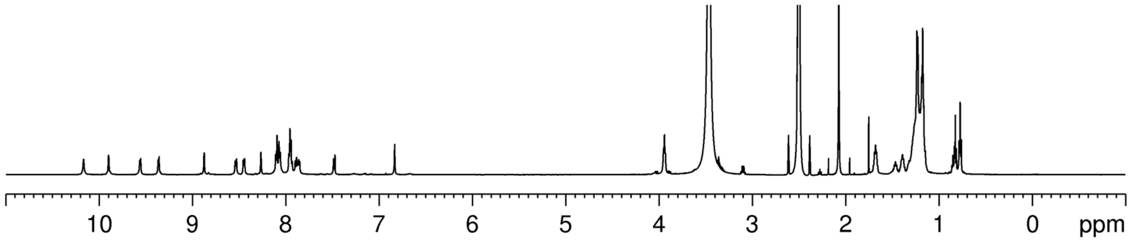

Fig. 31 Full ^{1}H NMR spectrum of [Pd$_2$$^{\mathrm{Do}}$**CBZ**$_2$**FRO**$_2$]$^{4+}$ (600 MHz, 298 K, DMSO-*d*$_6$).

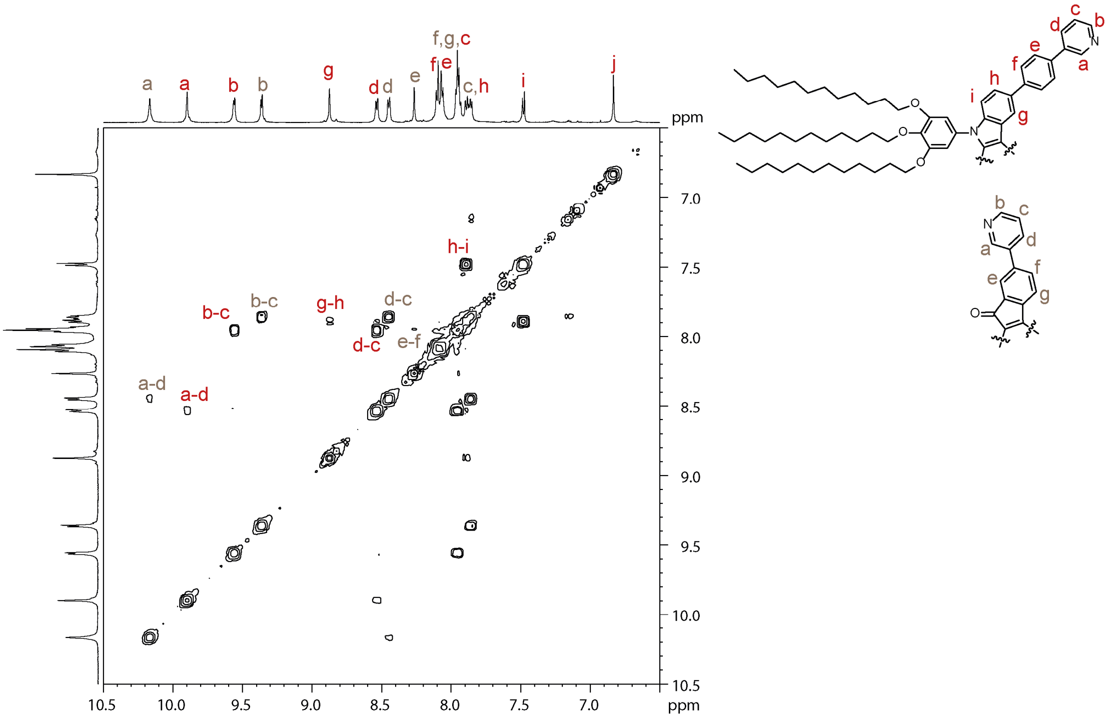

Fig. 32 Partial ^{1}H,^{1}H COSY NMR spectrum of [Pd$_2$$^{\mathrm{Do}}$**CBZ**$_2$**FRO**$_2$]$^{4+}$ (600 MHz, 298 K, DMSO-*d*$_6$).

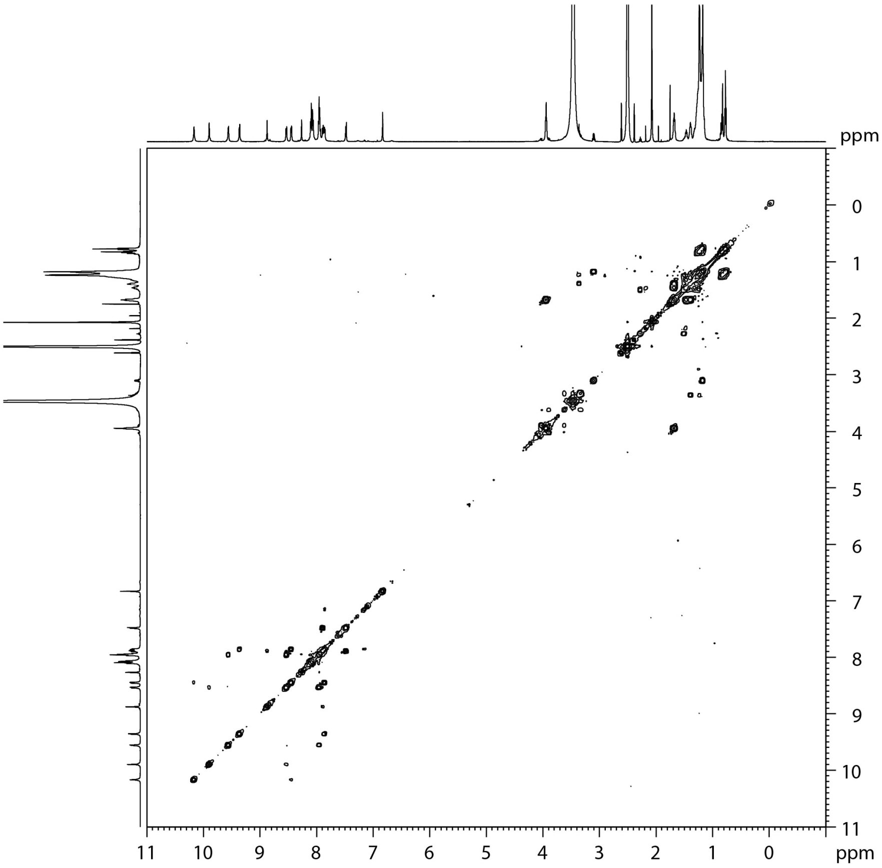

Fig. 33 Full ^{1}H,^{1}H COSY NMR spectrum of $[\mathrm{Pd}_2{}^{\mathbf{Do}}\mathbf{CBZ}_2\mathbf{FRO}_2]^{4+}$ (600 MHz, 298 K, DMSO-d_6).

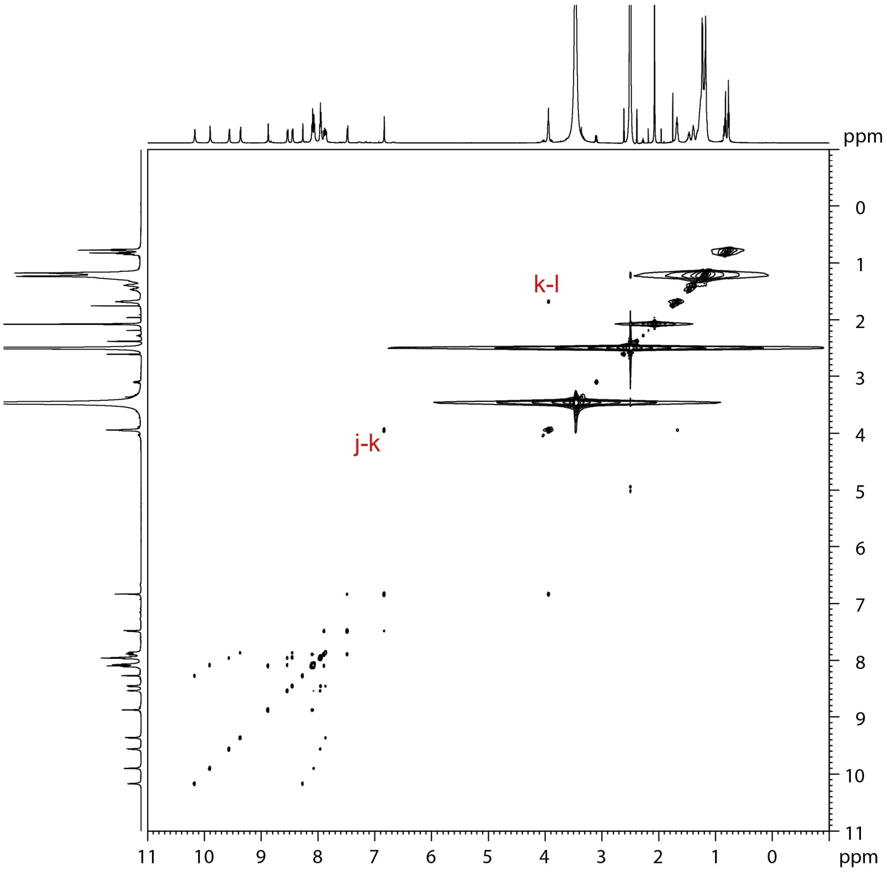

Fig. 34 Full ^{1}H,^{1}H COSY NMR spectrum of $[Pd_2{}^{Do}\mathbf{CBZ}_2\mathbf{FRO}_2]^{4+}$ (600 MHz, 298 K, DMSO-d_6).

4.6.4. Characterization of higher-order assemblies

DLS measurements

A solution of the cages ($[Pd_2{}^{Me}\mathbf{CBZ}_2\mathbf{FRO}_2]^{4+}$ in DMSO: c(cage) = 63 µM, $[Pd_2{}^{Do}\mathbf{CBZ}_2\mathbf{FRO}_2]^{4+}$ in DMSO: c(cage) = 35 µM, $[Pd_2{}^{Do}\mathbf{CBZ}_2\mathbf{FRO}_2]^{4+}$ in acetonitrile: c(cage) = 14 µM, $[Pd_2{}^{Do}\mathbf{CBZ}_2{}^{Me}\mathbf{FRO}_2]^{4+}$ in acetonitrile: c(cage) = 10 µM) was filtered through a 0.2 µm syringe filter and vortexed.

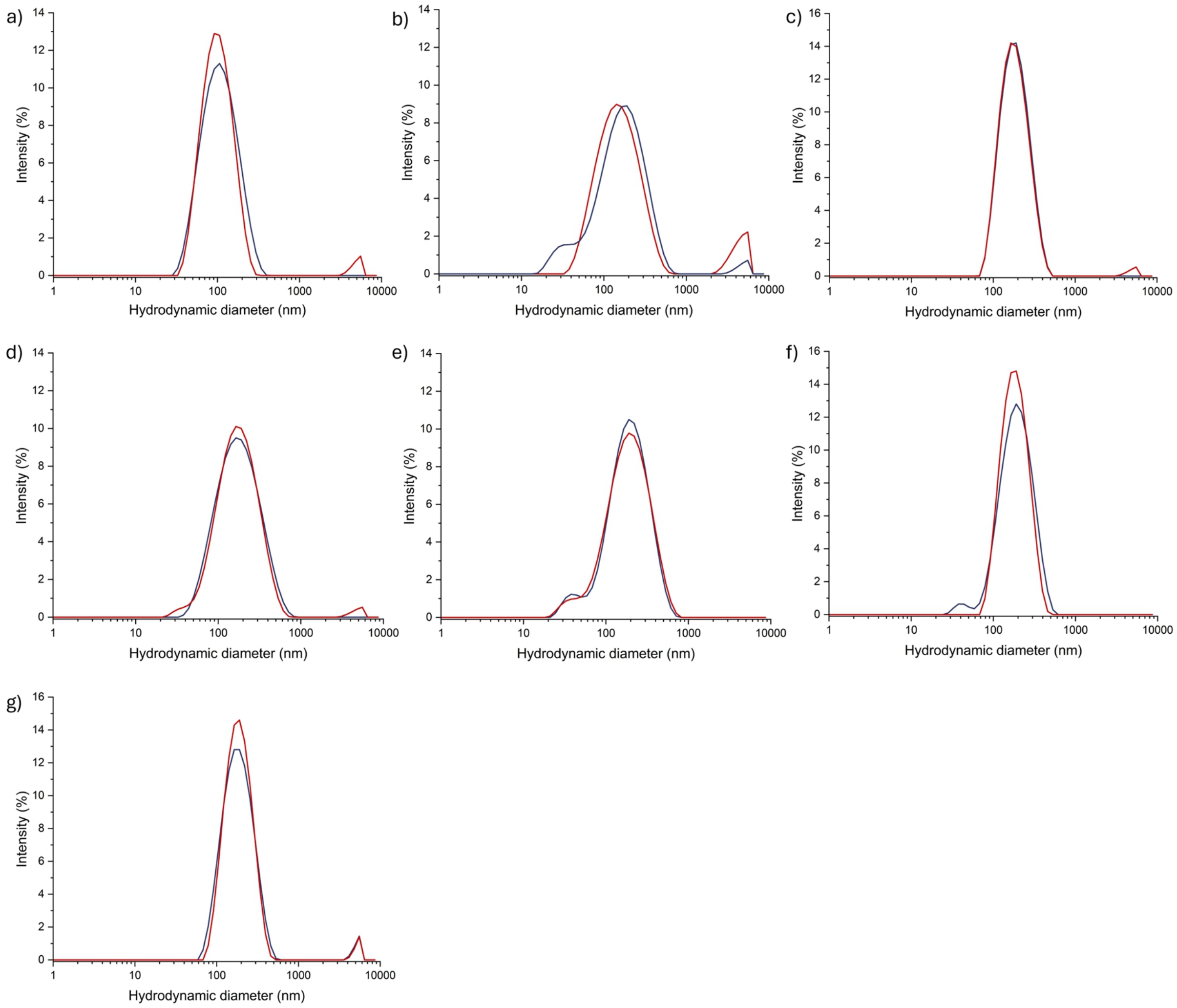

Fig. 35 DLS data for a) $[\mathrm{Pd}_2{}^{\mathrm{Me}}\mathbf{CBZ}_2\mathbf{FRO}_2]^{4+}$ (DMSO, LN522), b) $[\mathrm{Pd}_2{}^{\mathrm{Do}}\mathbf{CBZ}_2\mathbf{FRO}_2]^{4+}$ (DMSO, LN541), c) $[\mathrm{Pd}_2{}^{\mathrm{Do}}\mathbf{CBZ}_2\mathbf{FRO}_2]^{4+}$ (DMSO, LN529), d) $[\mathrm{Pd}_2{}^{\mathrm{Do}}\mathbf{CBZ}_2\mathbf{FRO}_2]^{4+}$ (acetonitrile, LN567), e) $[\mathrm{Pd}_2{}^{\mathrm{Do}}\mathbf{CBZ}_2\mathbf{FRO}_2]^{4+}$ (acetonitrile, LN541), f) $[\mathrm{Pd}_2{}^{\mathrm{Do}}\mathbf{CBZ}_2{}^{\mathrm{Me}}\mathbf{FRO}_2]^{4+}$ (acetonitrile, LN649), g) $[\mathrm{Pd}_2{}^{\mathrm{Do}}\mathbf{CBZ}_2{}^{\mathrm{Me}}\mathbf{FRO}_2]^{4+}$ (acetonitrile, LN649-3).

Tab. 1 DLS data for amphiphilic and reference cages in DMSO and acetonitrile. The approximate peak width refers to the peak < 1000 nm.

Cage	Peak maximum	Z-Average	Approx. peak width	PDI
$[\mathrm{Pd}_2{}^{\mathrm{Me}}\mathbf{CBZ}_2\mathbf{FRO}_2]^{4+}$ (DMSO, LN522)	106, 91	86, 89	30-400, 30-300	0.28, 0,26
$[\mathrm{Pd}_2{}^{\mathrm{Do}}\mathbf{CBZ}_2\mathbf{FRO}_2]^{4+}$ (DMSO, LN541)	190, 142	131, 120	20-700, 30-600	0.39, 0.41
$[\mathrm{Pd}_2{}^{\mathrm{Do}}\mathbf{CBZ}_2\mathbf{FRO}_2]^{4+}$ (DMSO, LN529)	164, 190	164, 164	70-550, 70-550	0.22, 0.20
$[\mathrm{Pd}_2{}^{\mathrm{Do}}\mathbf{CBZ}_2\mathbf{FRO}_2]^{4+}$ (acetonitrile, LN567)	164, 164	148, 150	30-800, 30-700	0.25, 0.25
$[\mathrm{Pd}_2{}^{\mathrm{Do}}\mathbf{CBZ}_2\mathbf{FRO}_2]^{4+}$ (acetonitrile, LN541)	190, 190	155, 151	20-800, 20-700	0.26, 0.27
$[\mathrm{Pd}_2{}^{\mathrm{Do}}\mathbf{CBZ}_2{}^{\mathrm{Me}}\mathbf{FRO}_2]^{4+}$ (acetonitrile, LN649)	190, 190	166, 161	30-600, 70-450	0.18, 0.15
$[\mathrm{Pd}_2{}^{\mathrm{Do}}\mathbf{CBZ}_2{}^{\mathrm{Me}}\mathbf{FRO}_2]^{4+}$ (acetonitrile, LN649-3)	164, 190	175, 180	60-550, 70-450	0.26, 0.26

TEM measurements

Solutions of the cages $[\mathrm{Pd}_2{}^{\mathrm{Do}}\mathbf{CBZ}_2\mathbf{FRO}_2]^{4+}$ and $[\mathrm{Pd}_2{}^{\mathrm{Do}}\mathbf{CBZ}_2{}^{\mathrm{Me}}\mathbf{FRO}_2]^{4+}$ in acetonitrile were filtered through a 0.2 µm syringe filter to reach cage concentrations of 14 µM and 10 µM, respectively. Afterwards, the samples were vortexed.

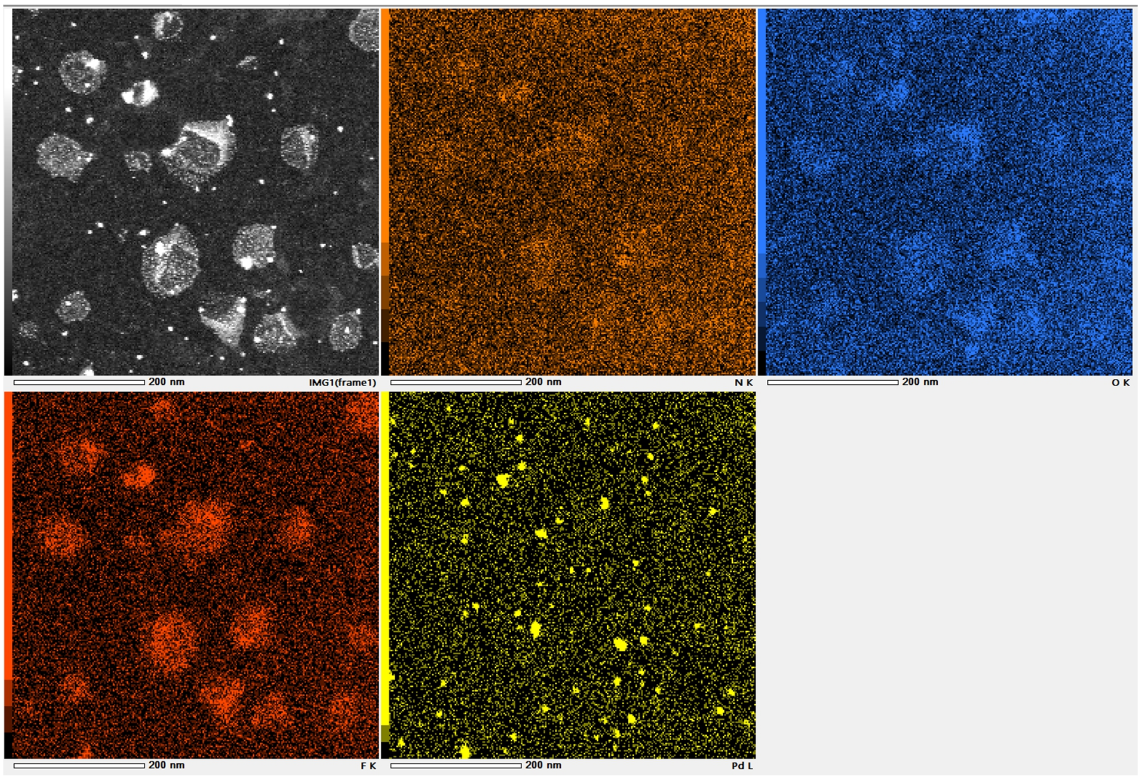

Fig. 36 STEM-EDS analysis of $[\mathrm{Pd}_2{}^{\mathrm{Do}}\mathbf{CBZ}_2\mathbf{FRO}_2]^{4+}$, a) STEM image, b-e) EDS analysis (b) nitrogen, c) oxygen, d) fluorine, e) palladium).

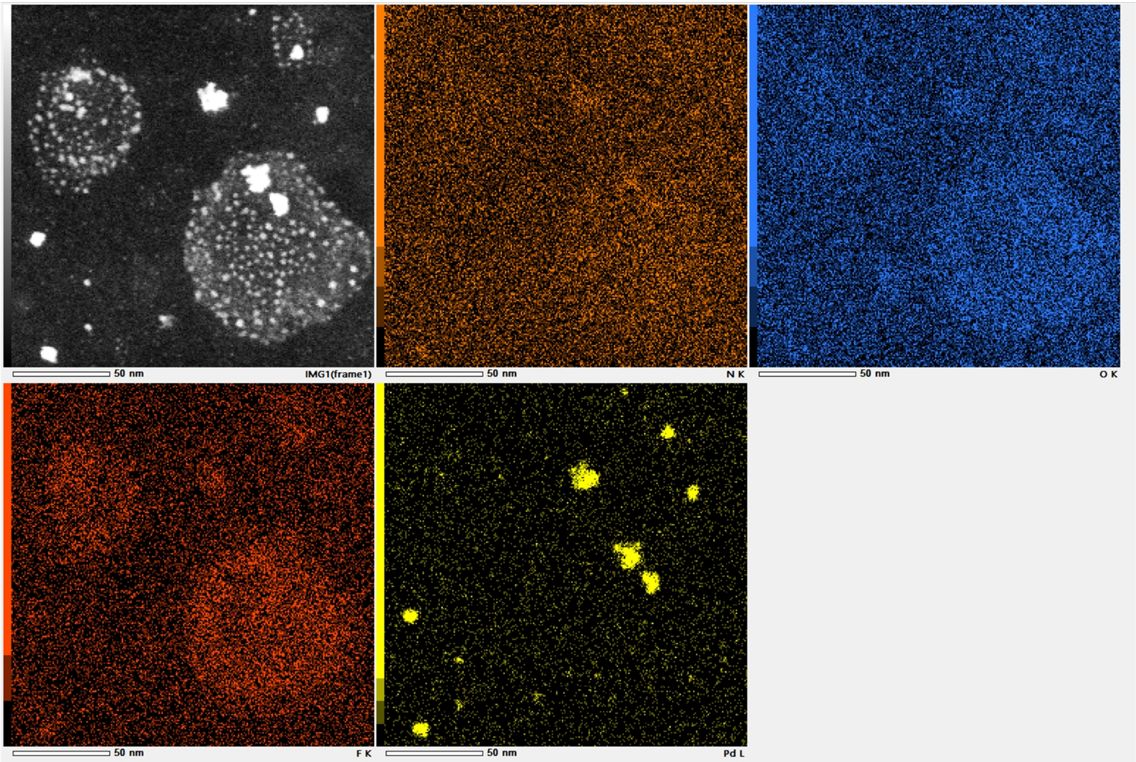

Fig. 37 STEM-EDS analysis of $[\mathrm{Pd}_2{}^{\mathrm{Do}}\mathbf{CBZ}_2\mathbf{FRO}_2]^{4+}$, a) STEM image, b-e) EDS analysis (b) nitrogen, c) oxygen, d) fluorine, e) palladium).

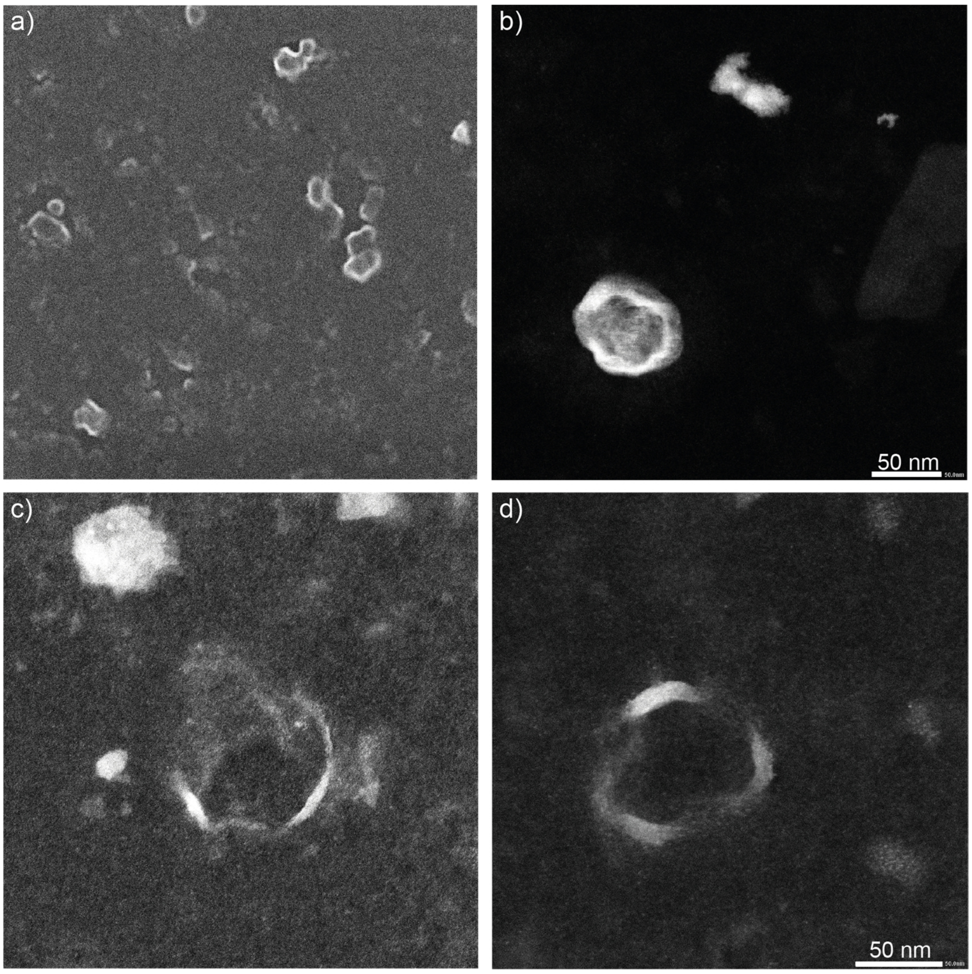

Fig. 38 STEM images of $[\mathrm{Pd}_2{}^{\mathrm{Do}}\mathbf{CBZ}_2{}^{\mathrm{Me}}\mathbf{FRO}_2]^{4+}$, a) secondary electron image (SEI), b-d) side stream dark field (SDF) images.

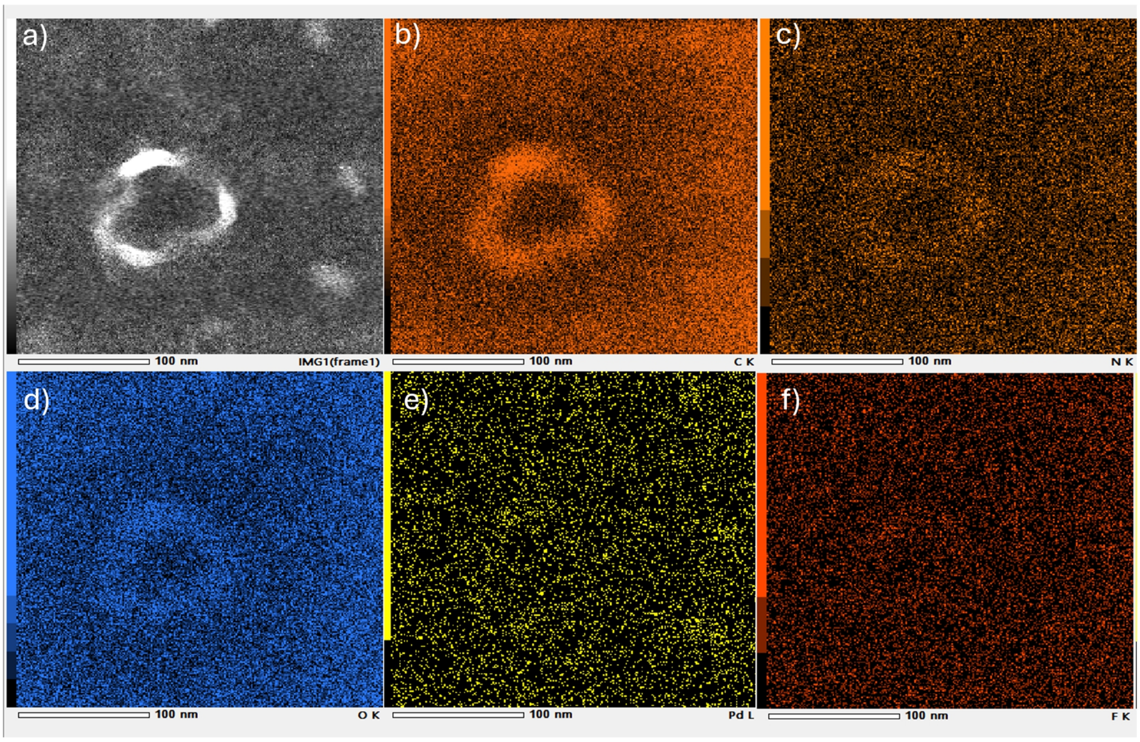

Fig. 39 STEM-EDS analysis of $[\mathrm{Pd}_2{}^{\mathrm{Do}}\mathbf{CBZ}_2{}^{\mathrm{Me}}\mathbf{FRO}_2]^{4+}$, a) STEM image, b-e) EDS analysis (b) carbon, c) nitrogen, d) oxygen, e) palladium, f) fluorine).

4.6.5. Photophysical characterization

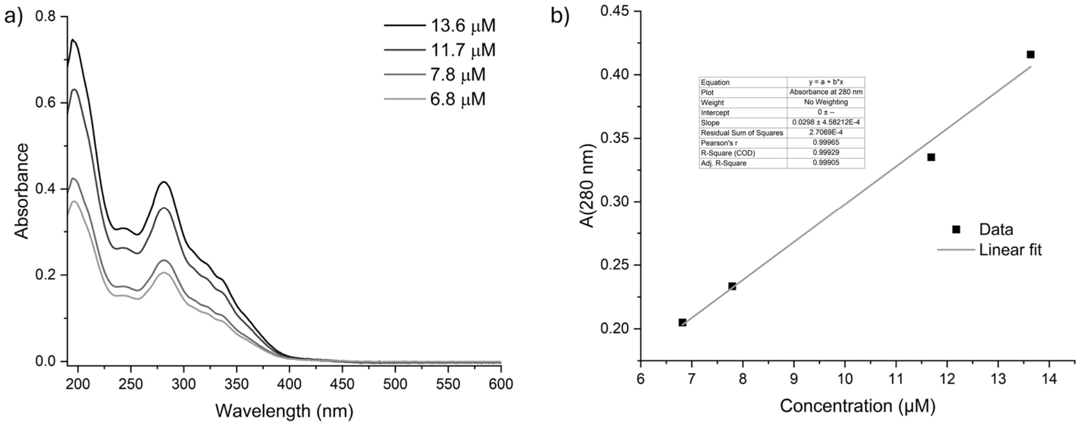

Fig. 40a) UV-Vis absorption spectra of [Pd$_2$$^{\mathrm{Do}}$**CBZ**$_2$**FRO** $_2$]$^{4+}$ at different concentrations (CH_3CN, 1 mm cuvette pathlength); b) linear fit of the absorbance at 280 nm against the cage concentration for determination of the extinction coefficient (ε(280 nm) = 29.8 mM^{-1} mm^{-1}.

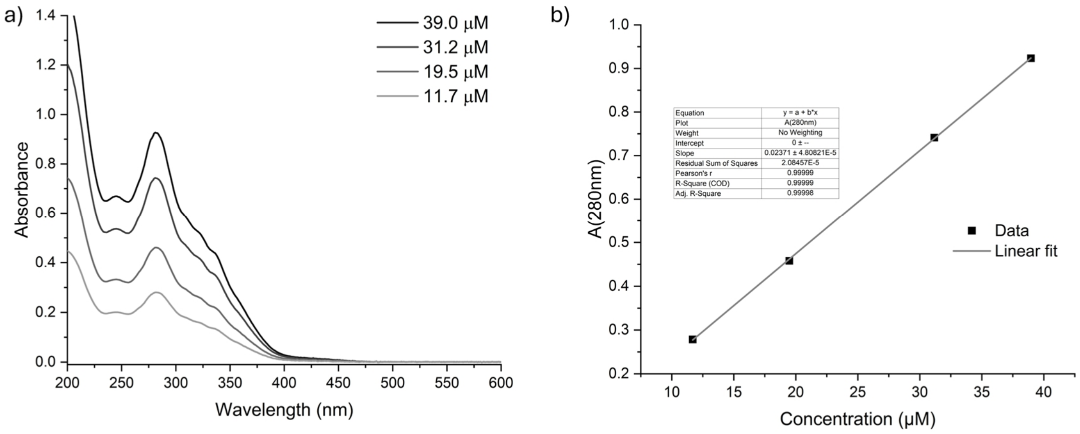

Fig. 41a) UV-Vis absorption spectra of [Pd$_2$$^{\mathrm{Me}}$**CBZ**$_2$**FRO** $_2$]$^{4+}$ at different concentrations (CH_3CN, 1 mm cuvette pathlength); b) linear fit of the absorbance at 280 nm against the cage concentration for determination of the extinction coefficient (ε(280 nm) = 23.7 mM^{-1} mm^{-1}.

4.6.6. Incorporation of amphiphilic cages into polymeric micelles

The synthesis of the amphiphilic block copolymer "WJ-270R" as well as its characterization (shown below) was carried out by Janick Wesselmann, group of Prof. Weberskirch.

Tab. 2 Characterization of the amphiphilic block copolymer ("WJ-270R") and its micellar solution. [a]degree of polymerization determined by ^{1}H-NMR end group analysis (rounded to the penultimate digit), x = n,n-dimethylacrylamide, y = n-dodecyl acrylate; [b] determined by SEC (3 g/L in DMF + 5 g/L LiBr, rounded to the penultimate digit); [c] mean hydrodynamic diameter and polydispersity over five single measurements, determined by DLS (1 g/L in H_2O, treated with ultrasound for 10 min, filtrated trough 220 nm syringe filter and conditioned for 24 h at 25 °C prior to measurement).

Entry	P_x [a]	P_y [a]	$M_{n,NMR.}$ [a] (g·mol^{-1})	$M_{n,SEC}$ [b] (g·mol^{-1})	Đ [b]	$d_{h,}$ [c] [nm]	PDI [c]
WJ-270R	65	10	8983	8280	1.25	96.41 ± 0.69	0.234 ± 0.009

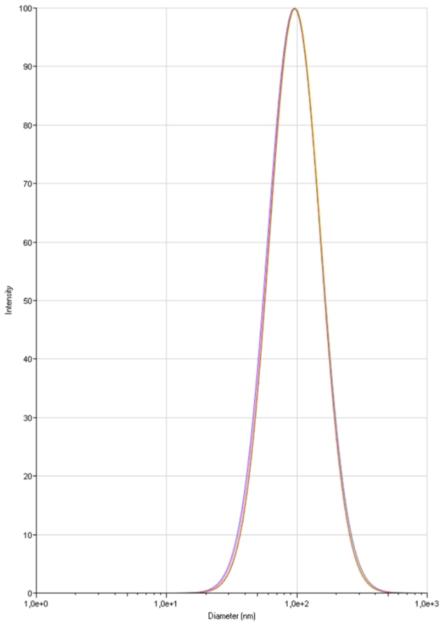

Fig. 42 DLS data of a micellar solution of the amphiphilic block copolymer WJ-270R (1 g/L in water).

Sample I

A solution of cage $[\mathrm{Pd}_2{}^{\mathrm{Do}}\mathbf{CBZ}_2\mathbf{FRO}_2]^{4+}$ (125 µL, 0.33 mM, DMSO-d_6) was dried via lyophilization. Then, water (825 µL, miliQ grade) was added. This was followed by sonication for 10 min and heating at 70 °C for 10 min. Afterwards, the sample was filtered through an Eppendorf filter (0.45 µm pore size).

Sample II

A 1.00 mM solution of the polymer in water (miliQ grade) was prepared. The sample was sonicated for 10 min. Afterwards, the sample was filtered through a syringe filter (0.2 µm pore size).

Sample III

A solution of cage $[\mathrm{Pd}_2{}^{\mathrm{Do}}\mathbf{CBZ}_2\mathbf{FRO}_2]^{4+}$ (125 µL, 0.33 mM, DMSO-d_6) was dried via lyophilization. Then, a solution of the polymer (825 µL, 1.00 mM, miliQ grade water) was added. This was followed by sonication for 10 min and heating at 70 °C for 10 min. Afterwards, the sample was filtered through a syringe filter (0.2 µm pore size).

Samples IV

A solution of cage $[\mathrm{Pd}_2{}^{\mathrm{Do}}\mathbf{CBZ}_2\mathbf{FRO}_2]^{4+}$ (125 µL, 0.33 mM, DMSO-d_6) was combined with a solution of the polymer (825 µL, 1.00 mM, DMSO-d_6). The mixture was sonicated for 10 min and then heated at 70 °C for 10 min. Next, the DMSO-d_6 was removed via lyophilization. Then, water (825 µL, miliQ grade) was added. This was followed by sonication for 10 min and heating at 70 °C for 10 min. Afterwards, the sample was filtered through a syringe filter (0.2 µm pore size).

Samples V

A solution of cage $[\mathrm{Pd}_2{}^{\mathrm{Me}}\mathbf{CBZ}_2\mathbf{FRO}_2]^{4+}$ (125 µL, 0.33 mM, DMSO-d_6) was combined with a solution of the polymer (825 µL, 1 mM, DMSO-d_6). The mixture was sonicated for 10 min and then heated at 70 °C for 10 min. Next, the DMSO-d_6 was removed via lyophilization. Then, water (825 µL, miliQ grade) was added. This was followed by sonication for 10 min and heating at 70 °C for 10 min. Afterwards, the sample was filtered through a syringe filter (0.2 µm pore size).

Sample VI

A mixture of ligands ^{Me}**CBZ** and **FRO** (60 µL of each ligand, 1.40 mM, DMSO-d_6) was combined with a solution of the polymer (825 µL, 1.00 mM, DMSO-d_6). The mixture was sonicated for 10 min and then heated at 70 °C for 10 min. Next, the DMSO was removed via lyophilization. Then, water (825 µL, miliQ grade) was added. This was followed by sonication for 10 min and heating at 70 °C for 10 min. Afterwards, the sample was filtered through a syringe filter (0.2 µm pore size).

4.7. References

[1] N. Sinambela, J. Bösking, A. Abbas, A. Pannwitz, *ChemBioChem* **2021**, *22*, 3140.

[2] M. Grätzel in *Supramolecular Photochemistry* (Ed.: V. Balzani) Reidel, Dodrecht, **1987**, p. 435-454.

[3] M. M. A. Kelson, R. S. Bhosale, K. Ohkubo, L. A. Jones, S. V. Bhosale, A. Gupta, S. Fukuzumi, S. V. Bhosale, *Dye. Pigment.* **2015**, *120*, 340.

[4] S. Saha, B. Holzapfel, Y.-T. Chen, K. Terlinden, P. Lill, C. Gatsogiannis, H. Rehage, G. H. Clever, *J. Am. Chem. Soc.* **2018**, *140*, 17384.

[5] S. Saha, Y. Chen, S. Ganta, M. Gilles, B. Holzapfel, P. Lill, H. Rehage, C. Gatsogiannis, G. H. Clever, *Chem. Eur. J.* **2022**, *28*, e202103406.

[6] S. Ganta, C. Drechsler, Y. Chen, G. H. Clever, *Chem. Eur. J.* **2022**, *28*, e202104228.

[7] J. Tessarolo, H. Lee, E. Sakuda, K. Umakoshi, G. H. Clever, *J. Am. Chem. Soc.* **2021**, *143*, 6339.

[8] J. Stetefeld, S. A. McKenna, T. R. Patel, *Biophys. Rev.* **2016**, *8*, 409.

[9] M. K. Škopić, C. Gramse, R. Oliva, S. Pospich, L. Neukirch, M. Manisegaran, S. Raunser, R. Winter, R. Weberskirch, A. Brunschweiger, *Chem. Eur. J.* **2021**, *27*, 10048.

[10] T. Dwars, E. Paetzold, G. Oehme, *Angew. Chem. Int. Ed.* **2005**, *44*, 7174.

[11] Z. Ahmad, A. Shah, M. Siddiq, H.-B. Kraatz, *RSC Adv.* **2014**, *4*, 17028.

[12] M. Kathiresan, B. Ambrose, N. Angulakshmi, D. E. Mathew, D. Sujatha, A. M. Stephan, *J. Mater. Chem. A* **2021**, *9*, 27215.

[13] D. Canevet, M. Sallé, G. Zhang, D. Zhang, D. Zhu, *Chem. Commun.* **2009**, 2245

[14] T. P. Vaid, M. S. Sanford, *Chem. Commun.* **2019**, *55*, 11037.

Abbreviations

A	Acceptor
ABI	Adjacent backbone interaction
ATP	Adenosine triphosphate
BChl *a*	Bacteriochlorophyll *a*
BET	Back electron transfer
BPhe	Bacteriopheophytin
BODIPY	Boron dipyrromethene
CD	Circular dichroism
CPL	Circularly polarized luminescence
CSE	Coordination sphere engineering
CV	Cyclic voltammetry
D	Donor
DCM	dichloromethane
DFT	Density functional theory
DMSO	Dimethyl sulfoxide
DMV	Dimethyl viologen
DOSY	Diffusion-ordered spectroscopy
DPP	Diketopyrrolopyrrole
EADS	Evolution associated decay spectra
en	Ethylenediamine
ESI	Electrospray ionization
Fig.	Figure
FRET	Förster resonance energy transfer
HGCS	Host-to-guest charge separated state
HOMO	Highest occupied molecular orbital
IC	Intersystem crossing
IR	Infrared
ISC	Intersystem crossing
LLCS	Ligand-to-ligand charge separated state
LMCT	Ligand-to-metal charge transfer
LUMO	Lowest unoccupied molecular orbital
MLCT	Metal-to-ligand charge transfer
MOF	Metal-organic framework

NMR	Nuclear magnetic resonance
OTf	Triflate
PAH	Polyaromatic hydrocarbons
PET	Photoinduced electron transfer
QY	Quantum yield
RC	Reaction center
RhB	Rhodamine B
SCA	Shape complementary assembly
Tab.	Table
TPE	Tetraphenylethylene
TTF	Tetrathiafulvalene
UV	ultraviolet

Other scientific contributions

I have structured and written a review article on coordination assemblies with bis-pyridyl ligands and Pd(II). Various homoleptic topologies ranging from di- to octanuclear assemblies are discussed along with the factors governing their formation. Additionally, the literature on integrative self-sorting into heteroleptic cages, orientational self-sorting of asymmetric ligands, and chiral self-sorting was reviewed.

In collaboration with my former colleagues Dr. Elie Benchimol and Dr. Alexandre Walther, we compiled a review article covering works on chromophore-based coordination cages. Here, I wrote the chapters on photoinduced energy transfer and photoinduced electron transfer.

In collaboration with Dr. Jennifer Bouzeid, group of Prof. Goeb and Prof. Sallé (University of Angers) and Dr. Elie Benchimol, we investigated redox-active heteroleptic coordination cages. I assembled a series of tetranuclear cages with tetrathiafulvalene-based ligands and different bis-pyridyl counter ligands.

For a collaborative project with the group of Prof. Kast (TU Dortmund), I investigated the solvent-dependent equilibrium between homo- and heteroleptic assemblies and helped writing the manuscript (*Angew. Chem.* **2024**, e202416076).

For a systematic study on photoinduced energy transfer in coordination cages, a project led by Dr. Elie Benchimol, I investigated the electrochemical properties of the corresponding cages.

I translated various papers of the group which were published in the journal Angewandte Chemie (*Angew. Chem. Int. Ed.* **2024**, *63*, e202404682, *Angew. Chem. Int. Ed.* **2022**, *61*, e202209305, *Angew. Chem. Int. Ed.* **2023**, 202308288, *Angew. Chem. Int. Ed.* **2022**, *61*, e202205725). Additionally, I wrote short articles about selected research topics of the Clever lab for the faculty website (e.g. “Mehrkomponenten Assemblierungen mit chiroptischen Eigenschaften”, „Photoschaltbare Koordinationskäfige”) and for the RESOLV blog (“Towards light harvesting in coordination cages”).

Acknowledgements

First, I'd like to thank my supervisor, Prof. Guido Clever, for giving me the opportunity to pursue the PhD in his group. Starting off with the PhD after being half-way through the masters was not only a great acknowledgement for my work but also one of the most exciting (and challenging!) steps in my life. Thank you for all the scientific ideas that greatly shaped the projects as well as for the responsibilities I was allowed to take over within the group. Thank you for the freedom I had regarding the projects - whether it was working in the lab or writing reviews, I was free to choose. Also, thank you for the trust you've placed in me by letting me handle multiple collaborations on my own. All of this allowed me to grow in a way that would not have been possible otherwise.

I also would like to thank Prof. Andreas Steffen for taking over the role as second examiner and for fruitful discussions on electron transfer.

To my students: Mert, Shaian, Lukas, Thokozire, DongHee, Daniel - thank you for the hard work in the lab. A special thanks goes to Mert and Shaian who worked for a longer period of time with me. My projects wouldn't be as they are now without your work, thank you for the efforts you've put into the ligand synthesis and crystal set ups!

I also would like to thank my collaborators, Paul (Schlau-Cohen group), Robert (Heinze group), Adrian and Fabio (Havenith group), Yen-Ting (ZEMOS), Janick (Weberskirch group). I learned a lot by working with you and through all of the discussions.

Elie, thank you so much for all the support in the last years and for sincerely caring! Thank you for always being up to scientific discussions, no matter the time or day in the week. I am so grateful that you were part of my PhD journey.

Paul, thank you for all the time we've spent together in the laser lab, for introducing me into the method, for all the time and energy you've put into the project, and for all the scientific discussions.

For proof-reading, I would like to thank Alexandre, Elie, Paul, Armin, Björn, Robert, and Erti! Your input helped me improve this dissertation. I'd like to thank the whole Clever lab for the continuous support and friendship, thank you Alex (thank you for reminding me to take holidays!), Aleks, Armin, David (thanks for lifting my mood so many times!), Lars, Björn (thank you for all the NMR samples you've measured, for handling my crystals, and for much more help in the lab!), Malavika, Jenny, Kathrin, Joseph, Aiswarya, Christoph (thanks for helping me solving multiple problems with computing my cages!) and all! A big thank you goes also to former group members who supported me in the beginning of my PhD: thank you Kristina, thank you Irene! Maike, thank you for shipping multiple samples to different collaborators and dealing with me under time pressure. Laura, Franzi, thank you for introducing me into mass spectrometry and for all your help. Thank you Gabi, Christina, Birgit, and Astrid for help with contracts, holidays, and much more.

I also would like to thank RESOLV - Cluster of Excellence for funding my PhD, for giving me the opportunity to conduct research abroad, and for the network I was able to build within the graduate school. Sedakat, thank you for all the organizational effort and for being available for administrative matter.

Ibrahim, Maria, thank you for cheering me up during tough times and for making life away from the desk and the lab so enjoyable.

Lastly, I would like to thank my parents. Thank you for supporting me in every single step of my life and for always making me a priority. You encouraged me in my academic journey even though it came with less time to spend as a family. I can always count on your support and advice, and I am so so thankful for that.